CYCLIC PERFORMANCE OF ELLIPTICAL HOLLOW SECTIONS – A FINITE ELEMENT STUDY

A thesis submitted for the degree of

Doctor of Philosophy

by

V R Narēndra Bābu Perumāḷḷa

DEPARTMENT OF CIVIL ENGINEERING

INDIAN INSTITUTE OF TECHNOLOGY GUWAHATI

ASSAM, INDIA

Dedicated

To

My Parents and Well Wishers

CERTIFICATE

This is to certify that the work embodied in this thesis entitled *"**Cyclic Performance of Elliptical Hollow Sections – A Finite Element Study**"* is being submitted by Mr **V R Narēndra Bābu Perumāḷḷa**, to the Indian Institute of Technology Guwahati, India for the award of the degree of **Doctor of Philosophy** in Civil Engineering and this is a record of authentic research work carried out by the candidate as a research scholar under my supervision and guidance.

The thesis work, in my opinion, is worthy of considering for the award of the degree of **Doctor of Philosophy** as per the regulations of the Institute.

Date: 15th March 2021

Place: IIT Guwahati

Dr Konjengbam Darunkumar Singh
Professor
Structural Engineering Division
Department of Civil Engineering
Indian Institute of Technology Guwahati

DECLARATION

I hereby declare that the work embodied in this thesis entitled "***Cyclic Performance of Elliptical Hollow Sections – A Finite Element Study***" represents a record of research work carried out and submitted by me to the Indian Institute of Technology Guwahati, India is a partial fulfilment as per the regulations of the Institute for the award of the degree of **Doctor of Philosophy** in Civil Engineering, under the supervision of **Dr Konjengbam Darunkumar Singh**, Professor at Department of Civil Engineering, Indian Institute of Technology Guwahati, India.

I certify that the research work contained in this thesis is authentic, except where due acknowledgement is made, and that it has not been previously included in a thesis, dissertation or report submitted to this Institute *or* any other institution *or* university for a degree, diploma *or* other qualifications.

Date: 15th March 2021

Place: IIT Guwahati

Mr V R Narēndra Bābu Perumāḷḷa
Research Scholar (Roll No. 126104009)
Structural Engineering Division
Department of Civil Engineering
Indian Institute of Technology Guwahati

ACKNOWLEDGEMENT

The work presented in this thesis would not have been possible without my close association with many people who were always there when I needed them the most. The following acknowledgements are an account of the gratitude and indebtedness I feel towards them for giving me the guidance, inspiration, moral and financial supports, which have helped me make this thesis a possibility.

I express my deep sense of obligation and sincere thanks to my supervisor **Prof. Konjengbam Darunkumar Singh** from the Department of Civil Engineering, Indian Institute of Technology Guwahati (IITG) for his invaluable guidance, expertise, patience, moral and financial supports and constant encouragements throughout my doctoral period. It's his vigour and hunger to thrive in adverse situations, which have inspired me to thrive for excellence and nothing less. From day one, he had instilled the desire for learning in me. His attitude of living every moment as it comes, making serendipitous observation and transforming them to novel possibilities, correlating ideas and interpreting the obvious has helped me come a long way and will always guide me hereafter. He made me realize what I will always remember, "*Never stop learning; for when we stop learning, we stop growing*" and "*When the going gets tough, the tough get going*". I would never know where and when to stop thanking him for what he has been to me. Without his arduous dedication, the completion of this work would be impossible.

I am thankful to Prof. Sudip Talukdar, Prof. Arbind Kr. Singh and Dr Hrishikesh Sharma, my Doctoral Committee (DC) members from the Department of Civil Engineering at IITG, who have contributed their valuable suggestions and expert opinions throughout this work.

I offer my heartfelt thanks to the Heads of the Department of Civil Engineering, IITG during this research work for providing me with all the support and facilities. This gratitude is also extended to the people from the Department of Civil Engineering, IITG for providing me with an ideal environment for carrying out this research work.

Particular thanks are owed to my senior colleagues at IITG, Dr Longshithung Patton, Dr Khwairakpam Sachidananda and Dr Sonu J K for their guidance during my first incursions in the Finite Element Modelling. For making this research work easier, I am also thankful to my colleagues at IITG, Dr Tekcham Gishan Singh, Dr Ricky Lalthazuala, Dr Sanasam Vipej Devi, Dr Ningthoukhongjam Sukumar Singh, Dr G R Patil, Mr Suman Kr. Mushahary, Mr Prasanta

Kar, Dr Jyotirmoy Haloi, Dr Smriti Jain, Dr Vijayan Chelliah, Dr Anupoju Rājeev, Dr N Venkata Satish Laveti, Dr Maharshi Kintāda, and Dr Subrat Kr. Mallick.

My sincere thanks to the anonymous reviewers of the journal articles and conference papers published in-accordance-with the research work of this thesis for their many insightful comments and critical suggestions.

I also thankfully acknowledge the support from Dr Kartik Prasad, Scientist, Mechanical Behaviour Group, Defence Metallurgical Research Laboratory (DMRL), Defence Research Development Organisation (DRDO), Hyderabad, India for providing the data of the axially loaded strain-controlled Low-Cycle-Fatigue (LCF) laboratory experiments on IS 2062:E250A (Fe410W-A) mild steel specimens, which is used in understanding the calibration procedure for estimating the Non-Linear Combined (isotopic/kinematic) Hardening Material (NLCHM) model of the metallic materials.

I gratefully thank my friend, Dr Madhup Pandey from the Hong Kong Polytechnic University (HKPU *or* PolyU) for rendering some literature support to the research work in this thesis by mailing the requested articles.

I have spent memorable time at IITG with many friends and groups that became a part of my life. I would like to acknowledge such close friends for their moral support and motivation, which drives me to give my best. Thanks to Neeraj Mishra, Rahul Vinod Upputuri, Santhosh Chandra Budde, Jeevan Rāthod Dese, Harish Krishna Nanduri, Sathish Baagadi, Shravan Kr. Burra, Mahesh Nāga, Subba Rao Pichuka, Dinesh Kr. Vallipshetty, Pranit Khelurkar, Amit Desai…..*the list is endless*…

My special gratitude to Sujith Kr. Pesala, Pradeep Reddy Nāga, Mohammed Farook, Tharun Kariveda, Om Prakāsh Reddy Thaduru, Jeevan Rāthod, Laxmi Sai Krishna Bonda, Bharadwāja Komanduru, Shravan Kr. Pārthasārathy, Devabrat Borgohain, Mohit Mishra, Swapnika Bhrugumalla and Bindu Sri Vishnumolakala for being with me in thick and thins of my life during this work, I find myself lucky to have friends like them in my life.

Apart from my doctoral study supervisor, Prof. Konjengbam Darunkumar Singh, I also convey special thanks to my other guardians at IITG, Prof. Mallikarjuna Chunchu, Prof. Mohammad Qureshi and Prof. Poulose Poulose for the care and support they have provided.

A special word of thanks goes to Dr G Gerald Moses and Dr G RāmaKrishna, Professors at the Department of Civil Engineering, Pondicherry Engineering College (PEC), India for motivating me to pursue higher studies after my B.Tech study.

Also, a very big thanks to those who brought harder and tougher times in my personal and research life during my doctoral period, due to which I have drawn additional commitment and focus towards a substantial bettering of the work in this thesis.

As it would be impossible to thank everyone individually, this acknowledgement as an expression of my deep gratitude is to all those others who helped me in any way in the successful completion of this thesis.

Words are insufficient to express gratitude to the doctors and other medical staff of Palnadu COVID-19 care centre at Piduguralla (Andhra Pradesh, India) for their care and dedication shown towards me when I was admitted there with severe COVID in October 2020 and then suffered with long COVID until December 2020.

Last but not least, I record my utmost gratitude to the people who mean the world to me, my parents (Laxmi Kumāri and Venkata Sivannārāyana), sister (Renuka), brother (Nikhil Bābu) and uncles (Maddu Rāmānjineyulu and Bhishma Gajavelli) for their selfless support and encouragement during the entire period of the research work in this thesis.

V R Narēndra Bābu Perumāḷḷa

Guwahati, 15th March 2021

This page is intentionally left blank

ABSTRACT

At the beginning of the 21st century, especially in Canada, Hong-Kong, Western Europe and western half of Southern Europe, Elliptical-Hollow-Section (EHS) became increasingly preferable over conventional Circular and Rectangular-Hollow-Sections (CHSs and RHSs) owing to its aesthetic and structural advantages. Numerous practical applications of EHS in various structural configurations are catalogued in this thesis. The majority of the research on EHSs in the literature focused mainly on their behaviour under axial compression, bending and combined axial compression and bending loading conditions and development of design rules for their cross-section classification. However, those design guidelines are eventually proven to be detrimental in terms of optimised structural performance. Further, very few studies were carried out to assess the performance of EHS members under the influence of cyclic loading. Thus, in light of the increasing implementation of Hollow-Structural-Sections (HSSs) into the earthquake-resistant structural configurations, the main objective of the research in this thesis encompasses the behaviour of EHS members under cyclic loading.

In the current study, the feasibility of the existing cross-section classification criteria specified in the design codes for CHSs and the equivalent CHS diameter expressions for EHS suggested in the previous studies for the loading cases of axial compression and bending are assessed based on the experimental and numerical findings detailed in the literature. Then, expressions for cross-section capacity prediction curves for local buckling and material strain hardening effects are formulated based on the Direct-Strength-Method (DSM) approach through a lower bound fit for an exhaustive data of structural carbon steel CHSs found in the literature. Also, a unified set of cross-section slenderness limits for CHS members is proposed. Later, to promote applicability of the proposed CHS cross-section classification criteria also to the EHSs, improved empirical expressions for the equivalent CHS diameter of EHS according to the Equivalent-Resistance-Capacity-Method (ERCM) are derived by using the available data of EHSs from the literature alongside the proposed CHS cross-sectional capacity curves. Further, the plastic interaction response analyses and the expressions for the equivalent CHS diameter for compact and plastic EHSs under combinations of axial-compression, uni-axial bending and bi-axial bending loads are also presented.

The structural performance of EHS members under the Extremely-Low-Cycle-Fatigue (ELCF) load is examined in this study through numerical investigations by employing a Non-Linear

Combined (isotropic/kinematic) Hardening Material (NLCHM) model in the general Finite-Element (FE) package, Abaqus.

The response of FE modelled EHS steel braces with constant cross-sectional steel area and wall thickness under cyclic axial displacement loading history is analysed at various displacement ductility levels. It is observed that *a*/*b* ratio has less significance on normalized cyclic compressive resistance and energy dissipation values at cyclic displacements of higher displacement ductility levels for EHS braces with non-dimensional global slenderness ratio greater than ~0.8. A set of equations for cyclic post-buckling compressive resistance, mid-length lateral deflection, and energy dissipation curves of EHS braces at various displacement ductility levels are also proposed.

Analysis of the data from the non-linear FE simulations carried out on EHS steel cantilever member models with equal length and cross-sectional area under ELCF uni-directional flexural load along major and minor axes separately is also presented herein. The *a/b* ratio and shell thickness values of EHS cantilever models are varied between 1–2.33 and 4–6 mm respectively. A set of predictive equations for cyclic rotation capacity and flexural over-strength with-respect-to the cross-section slenderness are derived based on the FE analyses data. It is observed that the cyclic rotation capacity and flexural over-strength are not significantly affected by *a*/*b* ratio.

Lastly, the structural behaviour analysis of EHS steel cantilever columns under the combined action of constant axial compressive load and ELCF uni-directional flexural load along the major or minor axis is presented herein by performing a series of non-linear FE simulations. Under various axial load levels, the interaction between axial compressive load and the cyclic moment is interpreted. Further, the developed expressions for estimating the hysteretic properties like cyclic ductility and energy dissipation capacities with-respect-to the non-dimensional global slenderness of the column and the applied axial compressive load level are also proposed.

This page is intentionally left blank

This page is intentionally left blank

CONTENTS

This page is intentionally left blank

LIST OF TABLES

LIST OF FIGURES

ABBREVIATIONS

AESS	Architecturally-Exposed-Structural-Steel
AIJ	Architectural Institute of Japan
AISC	American Institute of Steel Construction
AISI	American Iron and Steel Institute
ANSI	American National Standards Institute
AS	Australian Standard
ASCE	American Society of Civil Engineers
ASME	American Society of Mechanical Engineers
ASTM	American Society for Testing and Materials
ATC	Applied Technology Council
BS	British Standard
CBF	Concentrically Braced Frame
CF	Cold-Formed
CFEHS	Concrete-Filled-EHS
CFST	Concrete-Filled Steel Tube
CHS	Circular-Hollow-Section
COV	Coefficient of Variation
CS	Carbon-Steel
CSA	Canadian Standards Association
CSS	Cyclic-Stress-Strain
CUFSM	Constrained and Unconstrained Finite Strip Method
CUREE	Consortium of Universities for Research in Earthquake Engineering
DL	Dead Load
DSM	Direct-Strength-Method
EC3	Eurocode3

ECCS	European Convention for Constructional Steelwork
EHS	Elliptical-Hollow-Section
ELCF	Extremely-Low-Cycle-Fatigue
EN	European Norm
ENA	Elastic-Neutral-Axis
ERCM	Equivalent-Resistance-Capacity-Method
EWM	Effective-Width-Method
EXP	Experiment
FE	Finite-Element
FEA	Finite-Element Analysis
FEM	Finite Element Method
FEMA	Federal Emergency Management Agency
GMINA	Geometrically and Materially Non-linear Analysis with Imperfections
HCF	High-Cycle-Fatigue
HF	Hot-Finished
HSS	Hollow-Structural-Section
IS	Indian Standard
LCF	Low-Cycle-Fatigue
LL	Live Load
LRFD	Load and Resistance Factor Design
NASA	National Aeronautics and Space Administration
NLCHM	Non-Linear Combined (isotropic/kinematic) Hardening Material
NLGEOM	Non-Linear Geometry
NZS	New-Zealand Standard
OHS	Oval-Hollow-Section
PNA	Plastic-Neutral-Axis
RHS	Rectangular-Hollow-Section

RRD	Reference-Resistance-Design
SAC	Joint venture of SEA, ATC and CUREE
SAE	Society of Automotive Engineers
SEA	Structural Engineers Association
SHS	Hollow-Structural-Section
SS	Stainless Steel

This page is intentionally left blank

NOTATION

Latin Lower-Case Letters

a	Larger outer radius of EHS
a_m	Larger radius of EHS cross-section mean-profile
b	Smaller outer radius of EHS
b_{iso}	Isotropic hardening exponent of the material
b_m	Smaller radius of EHS cross-section mean-profile
c_{PNA}	Distance from the extreme compressive fibre to PNA in EHS cross-section under N_h in Figure 5.1
d_{PNA}	Distance from the extreme compressive fibre to PNA in EHS cross-section under N_n in Figure 5.2
f_{cr}	Critical elastic local buckling stress of CHS
f_t	Coefficient dependant on the thickness and larger outer diameter of EHS
$f_{y.mea}$	Monotonic tensile yield stress of steel
h	PNA shift from minor axis in EHS cross-section due to N_h in Figure 5.1
h_m	Coefficient dependant on the geometry of the mean profile of the EHS cross-section
h_{mn}	PNA shift from major axis in EHS cross-section due to N_n in Figure 5.2
k	Radial distance of EHS cross-sectional mean-profile element with Ω in Figure 2.2
k_1	Corresponding radial distance of θ_1 in Figure 5.4
k_2	Corresponding radial distance of θ_2 in Figure 5.4
k_h	Radial distance of EHS cross-sectional mean-profile element with Ω_h in Figure 5.1

k_n	Radial distance of EHS cross-sectional mean-profile element with Ω_n in Figure 5.2
k_r	Corresponding radial distance of θ_r in Figure 5.4
m_{ry}	Interaction exponent of normalised M_{lpy} dependent on r
m_{rz}	Interaction exponent of normalised M_{lpz} dependent on r
n	Axial compressive load level ratio
n_h	Normalised N_h factor
n_n	Normalised N_n factor
n_{ry}	Interaction exponent of normalised N_h dependent on r
n_{rz}	Interaction exponent of normalised N_n dependent on r
r	Cross-sectional aspect ratio of EHS
$r_{g.y}$	Radius of gyration about axis *y*-*y*
$r_{g.z}$	Radius of gyration about axis *z*-*z*
r_{gy}	Radius of gyration
r_{mid}	Mean *or* mid-profile radius of the CHS cross-section
r_{st}	Strain hardening ratio of steel
$s_{cy.}$	Cyclic flexural-overstrength of a beam
t	Uniform cross-sectional thickness of HSS *or* EHS
w	PNA shift from EHS cross-section centre due to N_c in Figure 5.4
x_{ip}	Coefficient dependent on δ_{ei} and α_I in imperfection sensitivity study
z_r	Interaction exponent of normalised $M_{lpz.r}$ dependent on r

Latin Upper-Case Letters

A	Cross-sectional area of EHS
$A_{cmp.h}$	Area of EHS cross-section effective under N_h
$A_{cmp.n}$	Area of EHS cross-section effective under N_n
A_v	Area of the cross-section under V_p
B	Smaller outer diameter of EHS
B_{RHS}	Width of the equivalent RHS cross-section of EHS
C_{kin}	Kinematic hardening constant of the material
C_φ	Calibration coefficient as per AISI S100-16 (2016)
D	Outer diameter of CHS
D_{bi}	Depth of the cross-section under tension *or* compression for EHS under bi-axial bending
D_{eq}	Equivalent CHS diameter of EHS
$\bar{E}_{cy.mjr}$	Cyclic energy dissipation capacity of the column under axial compression and major axis cyclic bending
$\bar{E}_{cy.mnr}$	Cyclic energy dissipation capacity of the column under axial compression and minor axis cyclic bending
E	Modulus of elasticity
$E_{e.cy}$	Product of M_{er} and θ_y
$E_{tot.cy}$	Cumulative cyclic energy dissipation of the column up to the displacement load cycle with θ equal to $\theta_{0.85u}$
F_c	Post local buckling cyclic compressive resistance of the brace exhibited after $F_{cr.\max}$
$F_{cr.LnS}$	Predictive CHS *or* EHS cross-sectional axial-compressive-resistance-capacity for local buckling and strain hardening

$F_{cr.max}$	Peak cyclic compressive resistance of the brace
$F_{cr.max.}$	Maximum axial compressive strength of EHS
$F_{cr.Pl}$	Predictive CHS cross-sectional axial-compressive-resistance-capacity by Plantema (1946)
F_m	Mean value of fabrication factor as per AISI S100-16 (2016)
H	Larger outer diameter of EHS
H_c	Lateral cyclic displacement load at tip of the cantilever column
H_{RHS}	Depth of the equivalent RHS cross-section of EHS
H_{y0}	Lateral resistance of the member corresponding to δ_{yo}
I	Area moment of inertia of HSS cross-section
I_y	Second moment of inertia about axis *y-y*
I_z	Second moment of inertia about axis *z-z*
K_{eff}	Effective length factor based on boundary conditions
L	Length of a cantilever HSS member
L_{br}	Length of HSS brace member
L_{eff}	Effective length of the member
L_{ub}	Length of uniform bending moment region in CHS
M	Bending moment acting on HSS cross-section
$M_{AISC360}$	Maximum cross-sectional moment resistance of CHS member as per AISC 360-16 (2016)
M_{AS4100}	Maximum cross-sectional moment resistance of CHS member as per AS 4100:1998 (2016)
M_{ay}	Resulting bending moment component reduced normally about the EHS cross-sectional minor axis
M_{ay}	Bending moment resistance component about axis *y-y* of EHS cross-section due to the applied loads

M_{az}	Resulting bending moment component reduced normally about the EHS cross-sectional major axis
M_{az}	Bending moment resistance component about axis *z-z* of EHS cross-section due to the applied loads
M_{Cy}	Cyclic moment
M_{dy}	Major axis bending moment for the design under the presence of N_h
$M_{dy.r}$	Design major axis bending moment for EHS under bi-axial bending
M_{dz}	Minor axis bending moment for the design under the presence of N_n
$M_{dz.r}$	Design minor axis bending moment for EHS under bi-axial bending
M_e	Elastic section bending moment of HSS
M_{EC3}	Maximum cross-sectional moment resistance of CHS member as per EC3: EN 1993-1-1 (2005) and EN 1993-1-6 (2007)
M_{er}	Reduced yield section moment capacity of the member due to N_a
M_{ey}	Elastic section bending moment of EHS cross-section about axis *y-y*
M_{ez}	Elastic section bending moment of EHS cross-section about axis *z-z*
M_{lpy}	Plastic state limiting moment acting about the minor axis in the presence of N_h
$M_{lpy.c}$	Plastic state limiting moment component acting about EHS cross-sectional minor axis under bi-axial bending and N_c
$M_{lpy.r}$	Plastic state limiting moment component acting about the minor axis under bi-axial bending of EHS in Figure 5.3
M_{lpz}	Plastic state limiting moment acting about the major axis in the presence of N_n
$M_{lpz.c}$	Plastic state limiting moment component acting about EHS cross-sectional major axis under bi-axial bending and N_c

$M_{lpz.r}$	Plastic state limiting moment component acting about the major axis under bi-axial bending of EHS in Figure 5.3
M_m	Mean value of material factor as per AISI S100-16 (2016)
M_p	Plastic section bending moment of HSS
M_{pr}	Reduced plastic section moment capacity of the member due to N_a
M_{py}	Plastic section bending moment of EHS cross-section about axis *y-y*
M_{pz}	Plastic section bending moment of EHS cross-section about axis *z-z*
M_u	Maximum cross-sectional moment resistance of CHS member
$M_{u.pr}$	Predictive max. cross-sectional moment resistance of CHS member
M_{uCy}	Maximum cyclic moment
N_a	Resulting axial compressive component on EHS
N_c	Axial compressive force on EHS subjected to bi-axial bending
N_{cr}	Elastic critical buckling load of the member
N_h	Axial compressive force on EHS subjected to major axis bending
N_n	Axial compressive force on EHS subjected to minor axis bending
N_y	Compression yield capacity of EHS
P_M	Mean perimeter of EHS cross-section
P_m	Mean of the normalised resistance dataset
Q_∞	Isotropic hardening constant of the material
$R_{cy.}$	Rotation capacity of a beam
T	Time duration of ELCF load
V_F	COV of fabrication factor as per AISI S100-16 (2016)
V_M	COV of material factor as per AISI S100-16 (2016)
V_P	COV of the normalised resistance dataset

V_p	Plastic section shear force developed due to cyclic bending
V_Q	COV of load effect as per AISI S100-16 (2016)
V_u	Maximum value of V_p
W_{el}	Elastic section modulus of HSS cross-section
W_{ey}	Elastic section modulus of EHS cross-section about axis *y-y*
W_{ez}	Elastic section modulus of EHS cross-section about axis *z-z*
W_{pl}	Plastic section modulus of HSS cross-section
W_{py}	Plastic section modulus of EHS cross-section about axis *y-y*
W_{pz}	Plastic section modulus of EHS cross-section about axis *z-z*
$W_{\mu\delta.4}$	Energy dissipation of the brace during first loading cycle at μ_δ of 4
$W_{\mu\delta.4cum}$	Cumulative energy dissipation of the brace after the first loading cycle at μ_δ of 4

Greek Lower-Case Letters

α	Coefficient dependent on r_{st} and $\bar{\lambda}$
α_e	Elastic reduction factor as per RRD
α_G	Geometric nonlinearity factor as per RRD
α_g	Global imperfection factor
α_I	Imperfection sensitivity factor as per RRD
α_{mj}	Proportion of the EHS cross-sectional depth in compression under N_h
α_{mn}	Proportion of the EHS cross-sectional depth in compression under N_n
β	First-order reliability index calculated as per AISI S100-16 (2016)

β_b	Coefficient dependent on μ_δ, α and $\overline{\lambda}$
β_l	Local imperfection factor
β_o	Target reliability index
β_p	Plastic range factor of CHS bending capacity curve as per RRD
γ	PNA inclination angle measured with-respect-to the major axis *z*–*z* under bi-axial bending of EHS in Figure 5.3
γ_c	PNA inclination angle measured with-respect-to EHS cross-sectional major axis *z*–*z* in Figure 5.4
γ_{kin}	Kinematic hardening rate of the material
γ_{M0}	Partial factor as per EC3: EN 1993-1-1 (2005)
δ	Displacement load applied on the member
δ_u	Displacement load corresponding to $\theta_{0.85u}$
δ_{uCy}	Displacement load corresponding to θ_u
δ_y	Applied displacement on the member at the yield level
δ_{yo}	δ_y in the absence of N_a
ε	Steel strength normalisation factor in Eurocodes
$\varepsilon_{y.mea}$	Monotonic yield strain of steel
η_{in}	Plastic severity factor *or* elastic-plastic interaction exponent of CHS bending capacity curve as per RRD
θ	Drift angle of the member made at the end *or* joint
$\theta_{0.85u}$	Column rotation corresponding to 0.85 times M_{uCy} in the post-peak zone of M_{Cy}-θ envelope
θ_1	Inclination angle of the PNA intersection point-1 on mid-profile of EHS cross-section measured with-respect-to EHS cross-sectional major axis *z*–*z* in Figure 5.4

θ_2	Inclination angle of the PNA intersection point-2 on mid-profile of EHS cross-section measured with-respect-to EHS cross-sectional major axis *z*–*z* in Figure 5.4
θ_b	Intersection angle of D_{bi} and $\overline{T_1T_2}$ for the EHS under bi-axial bending
θ_p	Elastic component of member rotation upon reaching the resistance level of M_p
θ_r	Inclination angle of $\overline{R_1R_2}$ measured with-respect-to the major axis *z*–*z* for the EHS in Figure 5.4
θ_t	Chord $\overline{T_1T_2}$ inclination angle measured with-respect-to the major axis *z*–*z* under bi-axial bending of EHS in Figure 5.3
θ_u	Limiting member rotation at which the moment resistance falls back below M_p
θ_w	Intersection angle of normal to the PNA from the centre of EHS cross-section and $\overline{R_1R_2}$ in Figure 5.4
θ_y	Column rotation corresponding to M_{er} prior to the peak zone of M_{Cy}-θ envelope
θ_{y0}	θ corresponding to δ_{yo}
$\kappa_{lpy.r}$	Bending curvature due to $M_{lpy.r}$
$\kappa_{lpz.r}$	Bending curvature due to $M_{lpz.r}$
$\overline{\lambda}$	Non-dimensional global slenderness of the member
$\overline{\lambda}_{RHSc}$	Equiv. RHS cross-section slenderness of EHS under axial compression
$\overline{\lambda}_{cs}$	CHS *or* EHS cross-section slenderness of as per AISC 360-16 (2016) and CSA S16-14 (2014)
$\overline{\lambda}_{cs.E}$	CHS *or* EHS cross-section slenderness of as per EC3: EN 1993-1-1 (2005)

$\overline{\lambda}_{cs.IA}$	CHS *or* EHS cross-section slenderness of as per AS 4100:1998 (2016) and IS 800 (2007)
$\overline{\lambda}_{l.b}$	Critical elastic local buckling slenderness of CHS *or* EHS cross-section
$\overline{\lambda}_{osb}$	Plastic *or* squash limit relative slenderness of CHS as per RRD
$\overline{\lambda}_{psb}$	Elastic limit relative slenderness of CHS as per RRD
$\overline{\lambda}_{sb}$	CHS *or* EHS cross-section relative slenderness as per RRD
σ	Material stress
$\sigma\|_0$	Initial yield stress of the material with zero equivalent plastic strain
υ	Poisson's ratio
φ	Resistance factor as per AISI S100-16 (2016)
ψ	Parametric form of Ω
ψ_{bi}	Parametric form of γ
ψ_h	ψ in case of combined axial compressive and major axis bending loads on EHS
ψ_n	ψ in case of combined axial compressive and minor axis bending loads on EHS
ω_{g0}	Global imperfection amplitude
ω_{l0}	Local imperfection amplitude
ω_{lcs}	Dimensionless length parameter-2 in geometric nonlinearity and imperfection sensitivity analyses of thin CHS under as per RRD

Greek Upper-Case Letters

Δ_{mid}	Lateral deflection at mid-length of the HSS brace

Ω	Polar central angle for each element measured counter-clockwise with-respect-to the major axis of the EHS cross-section
Ω_h	Ω in case of combined axial compressive and major axis bending loads on EHS
Ω_{lcs}	Dimensionless length parameter-1 in geometric nonlinearity and imperfection sensitivity analyses of thin CHS as per RRD
Ω_n	Ω in case of combined axial compressive and minor axis bending loads on EHS

This page is intentionally left blank

CHAPTER 1

INTRODUCTION

In this chapter, a comprehensive description of the structural background on Elliptical-Hollow-Sections (EHSs) and the practicality of existing cross-sectional slenderness equations are introduced. Subsequently, the research problem highlighting the significance of devising the improved cross-section slenderness parameters and analysing the cyclic performance of EHSs is expressed. Further details like the general aim, scope, and limitations of this research work and the specific objectives which are intended to be accomplished through this research along with the methodology adopted are also presented. Lastly, an overview of the dissertation is specified.

1.1 BACKGROUND

The first and foremost experiment on Elliptical-Hollow-Section (EHS) was conducted by Robert Stephenson on August 6th, 1845 and it is a transverse bending test on a malleable iron specimen (Fairbairn 1849, Clark and Stephenson 1850). But, it was Isambard Kingdom Brunel who first used elliptical tubular sections as the arch-ribs in the superstructure of the Royal Albert Bridge (see Figure 2.1) around 1858 over the River Tamar at Saltash, UK (Brunel 1870, Whitbread 1969). Almost three-quarters of a century later, Lundquist and Burke (1935) performed tests on thin-walled duralumin EHSs as part of the strength assessment project on aircraft structural components. Later, Kempner (1962), Kempner and Chen (1966, 1967, 1969), Hutchinson (1968), Tennyson and Muggeridge (1969), Feinstein et al. (1971), Chen and Kempner (1976) and Tvergaard (1976) conducted the investigations on thin-walled EHSs to address the buckling and post-buckling behaviour of tubular thin-walled Circular Hollow Sections (CHSs) which had turned out as non-circular *or* slightly elliptical (*or* oval) after their improper fabrication. At the beginning of the 21st century, the resurgent EHSs have gained prominence as Architecturally-Exposed-Structural-Steel (AESS) members in places like Canada, Hong-Kong, Western Europe and western half of Southern Europe (Packer 2008, Boake 2015) owing to their distinct superior structural and aesthetical advantages over Circular--Hollow-Section (CHS), Square--Hollow-Section (SHS) and Rectangular-Hollow-Sections (RHSs) (Chan 2007, Chan and Gardner 2008a, Packer et al. 2009, Zhao and Packer 2009).

1.1.1 Merits of EHS

Unlike rectangular, square and other polygonal Hollow-Structural-Sections (HSSs) with sharp corners and flat faces; **circular**, **flat-oval, tunnel** and **elliptical** (see Figure 2.1) HSSs with curved faces are known to exhibit relatively higher impact load endurance due to their streamlined surface finishing with a lesser degree of local-imperfections (Packer and Henderson 1992, Wardenier et al. 2010). EHS members under torsion and compression loads are structurally more efficient because of their larger ratio of the radius of gyration to the cross-sectional steel area (Wardenier et al. 2010, AISI S100-16C 2016). EHS can deliver higher flexural rigidity than a CHS of equal wall-thickness and cross-sectional steel area due to the disposition of weaker and stronger principal axis directions while preserving a smooth curved

shape (Packer 2008, Boake 2015). Consequently, for a structural member, EHS could be a more productive alternative for RHS and CHSs with more methodical usage of the material in a variety of major structural configurations (Chan and Gardner 2009).

1.1.2 Practical Applications of EHS

Notable implementations of EHSs comprise arch-ribs, beams, vertical and inclined columns, braces, struts, *etc*. The extensive range of these practices (see Figure 2.1) in various structures like office, residential, recreational, educational, hospital and airport terminal buildings; railway bridges; pedestrian footbridges; railway, market and bus-stop platforms due to the contemporary architectural design demands showcases the vibrancy of EHSs.

1.2 MOTIVATION AND OBJECTIVES

1.2.1 Motivation

Since the resurgence of EHS in the construction steel market in 1994 (Packer 2008), the performance of EHS members in a variety of structural configurations (*e.g.*, skeleton, wall-bearing, and long-span steel framings) under various loading patterns is examined in terms of various aspects like local and global slenderness parameters, ductility and design strength curves through numerous experimental and Finite-Element-Analysis (FEA) programs.

Performance of EHS involving in various structural connections was examined by Bortolotti et al. (2003), Pietrapertosa and Jaspart (2003), Choo et al. (2003), Willibald et al. (2006a, 2006b) and Haque and Packer (2012). The development of slenderness parameters and design rules for cross-sectional and member capacities of EHS structural members under axial compression was carried out by Chan and Gardner (2008b); Ruiz-Terán and Gardner (2008), Theofanous et al. (2009a), Silvestere and Gardner (2011), Haque et al. (2012), Abela and Gardner (2012), McCann et al. (2016), Lan et al. (2018) and Chen and Young (2018). On the other hand, the research comprising design aspects such as cross-section and member classification criteria, local and global stability and strengths for EHS members under bending load has been pursued by Chan and Gardner (2008a), Chan and Gardner (2009), Theofanous et al. (2009b), Law and Gardner (2012), Haque et al. (2012), Xu et al. (2017), McCann et al.

(2018), Lan et al. (2019) and Chen and Young (2019). While investigations on the structural performance of EHSs under combined axial compression and bending loading through experimental testing and numerical modelling were conducted by Nowzartash and Mohareb (2009), Gardner et al. (2011), Law and Gardner (2013a, 2013b).

Apart from the aforementioned studies on EHSs, investigations carried out by Yang et al. (2008), Zhao and Packer (2009), Dai and Lam (2010), Lam et al. (2010), Lam and Testo (2011), Sheehan et al. (2012), Jamaluddin et al. (2013), Uenaka (2014), Chan et al. (2015), Liu et al. (2017), Yang et al. (2017), Mahgub et al. (2017), Ding et al. (2017), Qiu (2017), Cai et al. (2018), Hassanein et al. (2018), *etc.*, focussed on the behaviour of Concrete-Filled-EHSs (CFEHSs) under various loading conditions. The performance of CFEHSs under elevated temperature conditions is also examined by Espinós et al. (2011, 2014, 2015).

All most all the up-to-date research on EHSs focused on their performance under combinations of constant and monotonically applied loads, only Fang et al. (2018) carried out investigations on EHSs to assess their performance under the influence of Extremely-Low-Cycle-Fatigue (ELCF) loading. Therefore, in the light of the increasing implementation of HSSs into the earthquake-resistant and light-weight structural configurations and the expectations of the engineers and architects on EHS to make a crafty impression in the dominion of AESS, the lack of sufficient reliable research on the cyclic behaviour of EHSs is the main motive behind framing the objectives (see Section 1.2.2) catalogued herein.

1.2.2 Objectives

For any HSS member, the determination of cross-section slenderness parameter which characterises the cross-sectional stability is a basic requirement of the designer (Gardner and Nethercot 2011). Chan (2007), Chan and Gardner (2008a, 2008b) and Gardner et al. (2011) proposed an equivalent CHS diameter methodology for EHSs under combinations of axial compression and bending loads with an intent to make the CHS cross-section classification criteria specified in various design standards also applicable for EHSs. However, these guidelines are eventually found to be detrimental in terms of optimised structural performance (*discussed later in* Chapter 2). Despite the surging interest in the usage of EHSs and the availability of significant research related to the development of the design approaches, there is no design standard available to date with the provisions of cross-section classification

information and design strength curves for EHSs as per the authors' knowledge. Also, with time, significant inconsistencies (*discussed later in* Chapter 2) among the cross-sectional slenderness limits for CHSs specified in various international design standards (BS 5950:Part-1 1990, EN 1993-1-1 2005, IS 800 2007, CSA S16-14 2014, AISC 360-16 2016, AS 4100:1998 2016) are reported in the literature (Elchalakani et al. 2002a, 2002c, Rondal et al. 2003, Rotter and Sadowski 2014). Thus, within this context, the following are the auxiliary objectives of the research presented in this thesis.

1. To establish a unified set of cross-sectional resistance capacity curves and slenderness limits for CHSs under axial compression and bending loads that can be used uniformly across various global design standards, by using a comprehensive data of CHS results from the literature.
2. To develop improved expressions of equivalent CHS diameter of EHS for axial compression and bending loading cases using the data of EHS analysis results from the literature, while maintaining consistency with the proposed CHS cross-section strength curves and classification criteria.
3. To analyse the plastic-interaction response and formulate expressions for the equivalent CHS diameter of compact and plastic EHSs under combinations of axial-compression, uni-axial bending and bi-axial bending loads based on the fundamentals of Cartesian and Polar co-ordinate geometries and the approach described in Gardner et al. (2011).

While the primary objective of the research in this thesis is to examine the behaviour of EHS members under ELCF loading through FEAs and thus provide reliable design guidance for their practical implementation into the earthquake-resistant structures. Firstly, it is resolved to investigate the effect of cross-sectional aspect ratio and non-dimensional brace slenderness on cyclic post-buckling compressive resistance, mid-length lateral deflection, and energy dissipation at various displacement ductility levels by analyzing the hysteresis response of EHS steel braces under cyclic axial displacement loading history.

Later, it is opted to carry out non-linear Finite-Element (FE) simulations on EHS steel cantilever member models under ELCF uni-directional flexural load along major and minor axes separately. Based on the FEAs data, the evaluation of cyclic rotation capacity and flexural over-strength of EHS cantilever sections with-respect-to the cross-section slenderness is to be conducted.

Lastly, it is aimed herein to carry out the structural behaviour assessment of EHS steel cantilever columns under the combined action of constant axial compressive load and ELCF uni-directional bending load along the major *or* minor axis through a series of non-linear FE simulations. Under various axial load levels, the interaction between axial compressive load and the cyclic moment is to be interpreted. Further, the effects of non-dimensional global slenderness and compressive axial load level on cyclic ductility and cyclic energy dissipation capacity of the columns are also to be examined.

1.3 SCOPE AND LIMITATIONS

The chief interest of the research in this thesis is to develop reliable design guidance for the practical implementation of EHSs into the structures that are susceptible to ELCF type loadings. Due to the financial and logistical constraints for conducting experiments, parametric studies are reported herein by using the data from previous studies and the data obtained by performing FEAs using the general FE software package, Abaqus (2009). No experimental work is carried out as a part of the research in this thesis.

Consequently, before the execution of parametric study on EHS members under ELCF loading by FEAs, the FE modelling approaches adopted are substantiated by accurately replicating the hysteretic behaviour of HSS members subjected to cyclic axial *or* bending loads in the independent experimental programs conducted by others (*e.g.*, Nip, 2009; Fadden, 2013). Also, the FE modelling patterns adopted herein are inspired by those described in Nip (2009) and Chan (2007) and Fadden (2013). While the Non-Linear Combined (isotropic/kinematic) Hardening Material (NLCHM) model parameters for the FE models of the EHS members analysed under cyclic displacement loading are adopted from the works of Nip (2009).

According to EN 1993-1-1 (2005), the performance of Cold-Formed (CF) and Hot-Finished (HF) HSSs do not differ with-regard-to the tension and bending resistances. But the scenario is different in case of the compression resistance. Due to the presence of higher residual stress in CF HSSs, separate compression buckling curves are recommended for CF and HF HSSs in Eurocode 3 (EC3): EN 1993-1-1 (2005) (Puthli and Packer 2013, Androić et al. 2014). Unlike the effect of cross-sectional profile on the cyclic performance of EHS members, the effect of residual stresses is not within the scope of the research presented in this thesis. Therefore, the

EHS braces are modelled as HF members while the EHS cantilevers are modelled as CF members so that the modelling of residual stresses is ignored.

Initial geometric imperfections are incorporated into the FE models using appropriate deformed shapes corresponding to the lowest buckling modes of the elastic eigenvalue buckling analyses carried out using Abaqus (2009). While, the imperfection amplitudes used in the FEAs are derived based on the EC3 guidelines (EN 1993-1-1 2005, EN 1993-1-6 2007) and the recommendations from Nip (2009), Ashraf et al. (2006), Gardner (2002) and Schafer and Peköz (1998a). Any in-depth parametric studies related to geometric imperfection amplitudes are not performed as a part of the research presented in this thesis.

Further, this thesis is structured as a monograph. Apart from the literature review presented in **Chapter 2**, efforts are made to make it more intelligible to the reader by incorporating all the other relevant literature in the subsequent chapters wherever found to be necessary for its completeness.

1.4 ORGANIZATION OF THE THESIS

The framework of the thesis is described as follows:

In **Chapter 2**, a review of the literature that is relevant to the research in this thesis is chronicled. An overview of the important topics, as well as the available design guidance followed by the identification of shortcomings and possible gap areas from a critical survey of the extensive literature are detailed.

Chapters 3, **4** and **5** make up the preliminary and fundamental part of the research in this thesis focusing on the cross-sectional slenderness parameters and classification criteria for EHSs. The outcomings from these chapters are derived by carrying out a systematic analytics of the literature data covering the existing design theories and models based on theoretical, numerical and experimental investigations. In **Chapter 3**, improved expression of the equivalent CHS diameter for the EHSs under axial compression considering the local buckling and material strain-hardening effects is formulated. Similarly, in **Chapter 4**, improved expressions of the equivalent CHS diameter for the EHSs under bending are formulated. In **Chapter 5,** modified equivalent CHS diameter equations for the compact EHSs under the interaction of axial

compression and bending loads are devised by using the expressions formulated in **Chapters 3** and **4** and based on the shift and orientations of the cross-sectional Plastic-Neutral-Axis (PNA).

Chapters 6, **7** and **8** comprise detailing of the tasks performed to accomplish the main objectives and the respective findings of the research in this thesis based on the FEAs carried out using Abaqus (2009). In **Chapter 6,** the performance analysis of EHS brace members under axial cyclic displacement loading is reported. Similarly, in **Chapter 7**, the behaviour of EHS cantilever members under cyclic uni-axial (major *or* minor axial) bending load is explained. In **Chapter 8**, the assessment details of the response of compact EHS cantilever column members under the interaction of the combined cyclic uni-axial (major *or* minor axial) bending and axial compressive loads are presented.

In **Chapter 9**, the important findings from the research in this thesis and possible research areas that could be explored in the future as an extension to the research in this thesis are summarised, thereby concluding the thesis.

Figure 1.1 *The Royal Albert Bridge, London, UK*

[This image file is licensed under the Creative Commons Attribution 2.0 Generic license, **Source:** Oxyman (2011)]

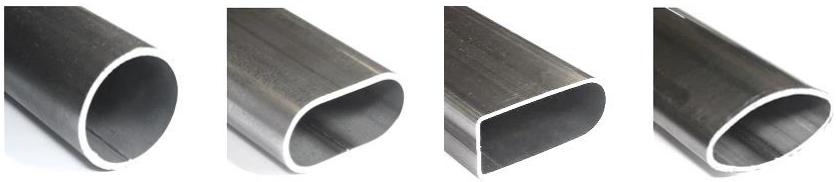

a) Circular **b)** Flat-Oval **c)** Tunnel **d)** Elliptical

Figure 1.2 *Closed thin-walled HSSs with curved surfaces*

[**Source:** Steel Tube Direct, STD (2014)]

Figure 1.3 *Some structural implementations of EHS*

a) Highland Society Bridge, Braemar, UK [**Source:** Chan et al. (2010b)]

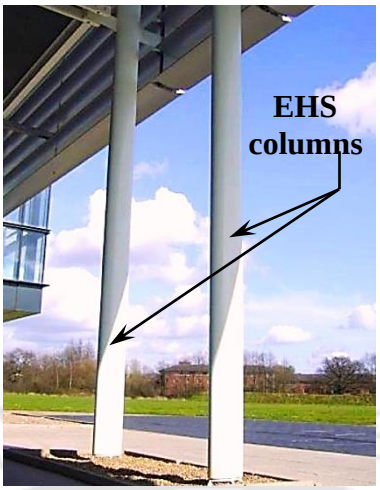

d) Zeeman Building, University of Warwick, UK [**Source:** Chan et al. (2010b)]

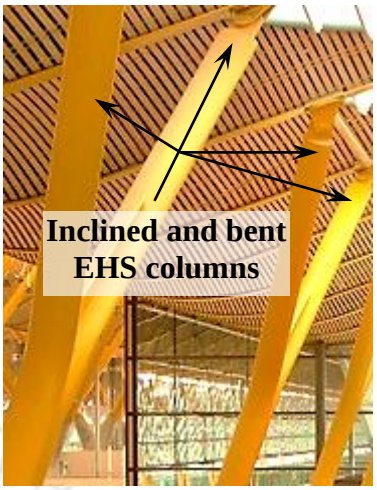

g) Terminal 4, Barajas Airport, Madrid, Spain [**Source:** Pezoa (2014)]

b) DLR Station, Stratford, London, UK [**Source:** Boyle (2014)]

e) Dugald Stewart Building, University of Edinburgh, UK [**Source:** LEAPS (2015)]

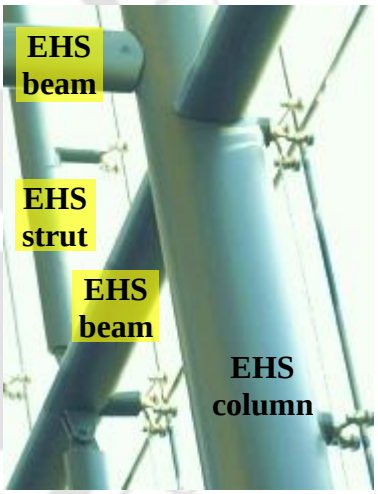

h) Odeon Cinemas, Paradise St., Liverpool, UK [**Source:** TSE (2018)]

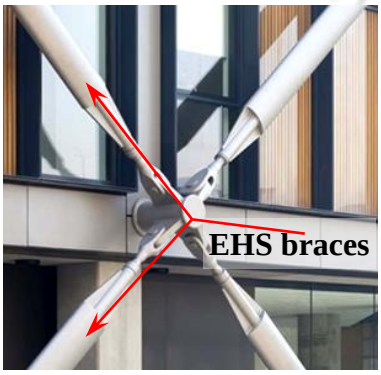

c) NEO Bankside Edifice, London, UK [**Source:** RSHP (2017)]

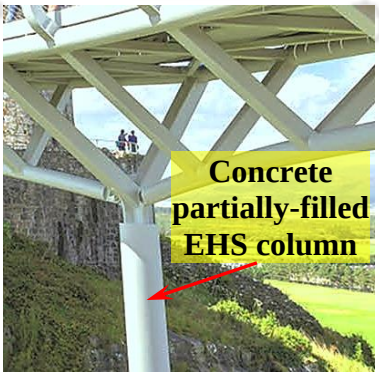

f) Harlech Castle Footbridge, Wales, UK [**Source:** BCSA (2016)]

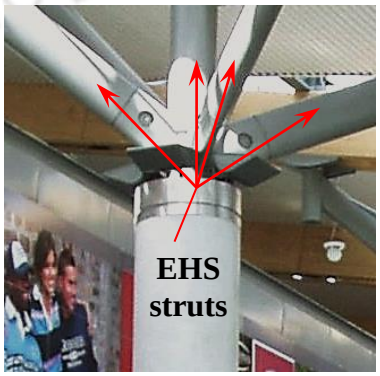

i) Cork Airport, Cork, Ireland, UK [**Source:** WRM (2016)]

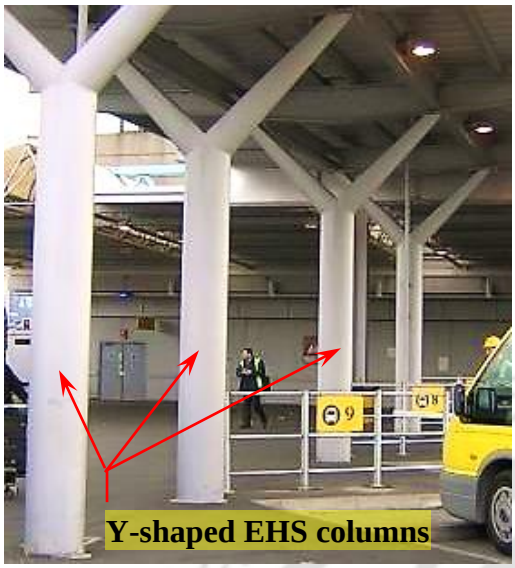

j) Terminal 3 Coach Station, Heathrow Airport, UK [**Source:** SDB (2015)]

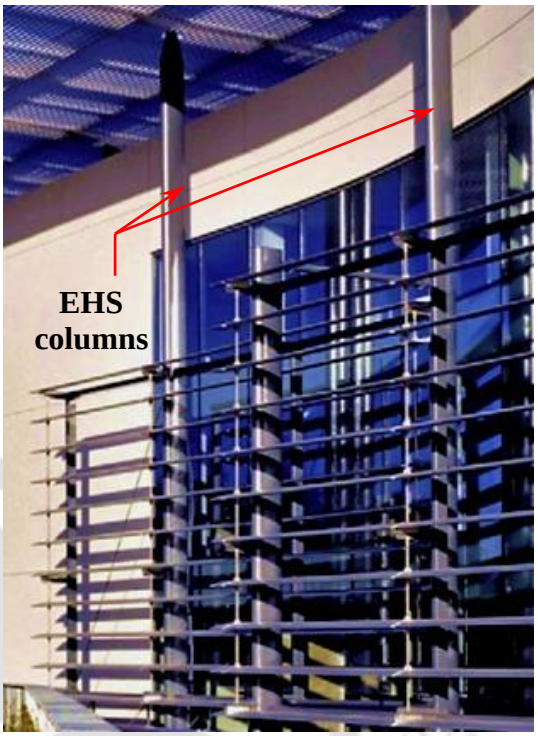

m) Airside Business Park, Dublin Airport, Swords, UK [**Source:** Corus (2008)]

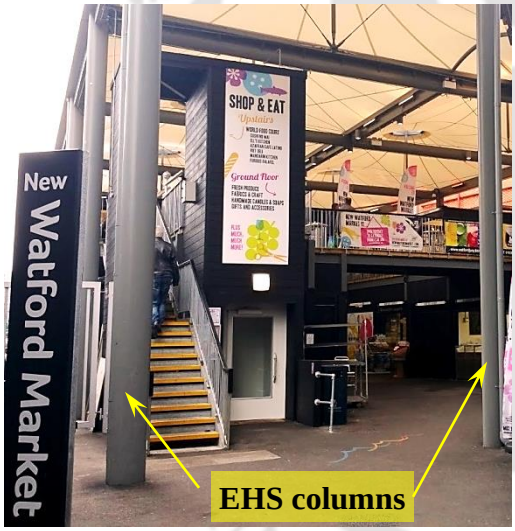

k) New Watford Market, Watford, UK [**Source:** Ogle (2015)]

l) Heathrow Airport, London, UK [**Source:** Boake (2015)]

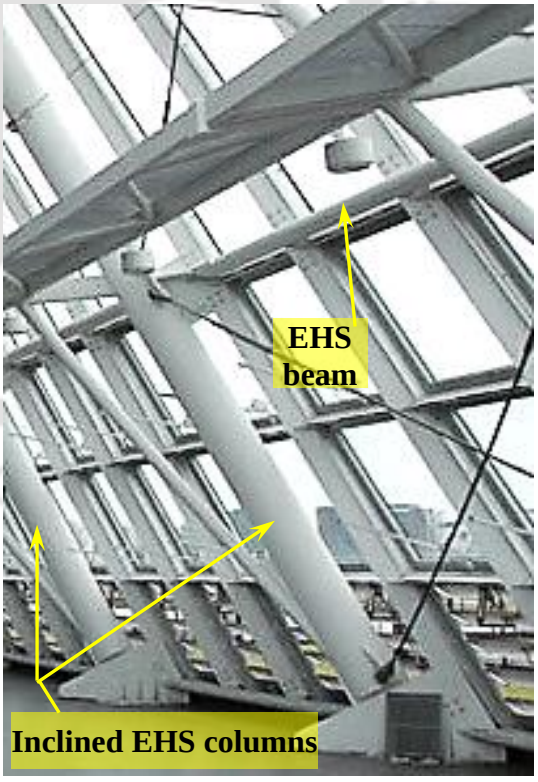

n) Angel's Hospital, Mestre, Venice, Italy [**Source:** Engel and Badia (2013)]

o) New Science Wing, Kimbolton School, Huntingdon, UK [**Source:** RHP (2015)]

p) Shane Homes YMCA, Calgary, Canada [**Source:** Livesey (2018)]

q) Oculus Teaching Building, University of Warwick, UK [**Source:** Short (2018)]

r) IFC mall near the MTR HK Station, Hong Kong [**Source:** Klook (2016)]

s) Delpark Homes Centre Oshawa, Canada [**Source:** Szekely (2013)]

CHAPTER 2

LITERATURE REVIEW

In this chapter, a systematic review identifying, analysing and assessing the available research work covering a broad range of subject areas which are pertinent to the topic of this dissertation and state-of-the-art specifications on the relevant research agendas specified in the previous chapter are presented. The concise review focussing on discussing existing theories, innovative methodological approaches, and exploring necessary modifications to the existing design guidance based on the strengths and weaknesses observed from the critical re-evaluation of the available research data is detailed. Subsequently, the research gap and priorities are highlighted.

2.1 OUTLINE OF LITERATURE REVIEW

The chapter begins with the introduction of the cross-sectional geometric profile and mechanical characteristics of a structural steel EHS. Later, the current state of the research in the field of cross-sectional stability of EHS members in terms of slenderness parameters and classification criteria under various loading conditions is reviewed before discussing the significance of assessing the cyclic performance of structural members and the different cyclic loading patterns those are being used for their testing and design purposes. Further, some relevant FE modelling terminology like the material model, mesh elements and Eigen-buckling analysis are discussed. Lastly, the deductions made from the information discussed in this chapter highlighting the necessity and possible ways to address the research objectives specified in the previous chapter (Chapter 1) are summarised.

2.2 CROSS-SECTIONAL PROPERTIES

2.2.1 General

The basic cross-sectional properties of structural steel EHSs are discussed in this section. Between the 4th and 2nd centuries BC, ancient Greek mathematicians like Menaechmus, Archimedes and Apollonius, *etc.*, had pioneered the philosophical works on geometry of ellipse from the theory of conic sections (Hayman 1628, Toomer 1990, Rashed 2015). EHSs possess a cross-sectional profile of an ellipse with wall-thickness, *t*, one smaller outer diameter $\left(B=2b\right)$ and one larger outer diameter $\left(H=2a\right)$ along minor and major axes of symmetry, respectively as shown in Figure 2.1. The cross-sectional aspect ratio, *r* (= a/b) is defined as the ratio of major (*or* semi-major) axis diameter to minor (*or* semi-minor) axis diameter.

Based on EN 10210-2 (2006) recommendations, the approximate formulae for the properties like the radius of gyration, r_{gy}, cross-sectional area, *A*, area moment of inertia, *I*, elastic section modulus, W_{el} and plastic section modulus, W_{pl} of EHS under bending moment, *M* about either principal axis are presented in Table 2.1. While, the mean perimeter, P_M value of EHSs can be determined using the following Equation 2.1, which is pioneered by Ramanujan (Almkvist and Berndt 2016).

$$P_M = \pi\left(a_m + b_m\right)\left(1 + \frac{3h_m}{10 + \sqrt{4 - 3h_m}}\right) \tag{2.1}$$

where $a_m = \left(2a - t\right)/2$, $b_m = \left(2b - t\right)/2$, $h_m = \left(a_m - b_m\right)^2 / \left(a_m + b_m\right)$ and Ω is the Polar central angle for each element measured counter-clockwise with-respect-to the *z*-*z* axis (*i.e.*, the major axis) as shown in Figure 2.1.

The mid-surface of EHS cross-section has a major axis diameter $2a_m$ and minor axis diameter $2b_m$ as shown in Figure 2.2. ψ is the respective parametric angle of Ω. Ω is positive (*+ve*) when measured in the counter-clockwise direction with-respect-to the major axis diameter as indicated in Figure 2.2 Any point with Cartesian coordinates (*z*, *y*) shown in Figure 2.2 can be represented as (k, Ω) in the Polar co-ordinate form, where k is the respective radial distance expressed in Equation 2.2. Also, the relation between Ω and ψ is expressed in Equation 2.3.

$$k = \sqrt{a_m^2 \cos^2\psi + b_m^2 \sin^2\psi} = \frac{a_m b_m}{\sqrt{a_m^2 \sin^2\Omega + b_m^2 \cos^2\Omega}} \tag{2.2}$$

$$\Omega = \sin^{-1}\left(\frac{b_m \cdot \sin\psi}{k}\right) = \sin^{-1}\left(\frac{b_m \cdot \sin\psi}{\sqrt{a_m^2 \cos^2\psi + b_m^2 \sin^2\psi}}\right) \tag{2.3}$$

In the Cartesian plane, the standard form for the mid-surface (*or* median) profile of an EHS shown in Figure 2.2 can be described as follows:

$$\left(\frac{z}{a_m}\right)^2 + \left(\frac{y}{b_m}\right)^2 = 1 \tag{2.4}$$

For the range of thickness, t value of EHSs available in the market (EN 10210-2 2006) and with an aspect ratio (r) range of 1 – 4, the approximate relation between a_m and b_m can be expressed as follows:

$$\frac{b_m^2}{a_m^2} = \frac{0.0399 + 0.2454r - 0.024r^2}{1 - 2.0152r + 1.2772r^2} \tag{2.5}$$

By integrating along the circumference of the elliptic median profile, the equations for mean perimeter, P_M; area of cross-section, A and respective second moments of the area about minor and major axes, I_y and I_z are as follows:

$$P_M = 4a_m \int_0^{\frac{\pi}{2}} \sqrt{\sin^2\psi + \frac{b_m^2}{a_m^2}\cos^2\psi} \cdot d\psi \tag{2.6}$$

$$A = P_M \times t = 4a_m t \int_0^{\frac{\pi}{2}} \sqrt{\sin^2\psi + \frac{b_m^2}{a_m^2}\cos^2\psi} \cdot d\psi \tag{2.7}$$

$$I_y = 4a_m^3 t \int_0^{\frac{\pi}{2}} \cos^2\psi \sqrt{\sin^2\psi + \frac{b_m^2}{a_m^2}\cos^2\psi} \cdot d\psi \tag{2.8}$$

$$I_z = 4a_m b_m^2 t \int_0^{\frac{\pi}{2}} \sin^2\psi \sqrt{\sin^2\psi + \frac{b_m^2}{a_m^2}\cos^2\psi} \cdot d\psi \tag{2.9}$$

By integrating along the circumference of the elliptic median profile, the respective expressions for the elastic section moduli of EHS under major and minor axes bending, W_{ey} and W_{ez} are as follows (Chan 2007, Chan and Gardner 2008a):

$$W_{ey} = \frac{I_y}{a} = \frac{4a_m^3 t}{a} \int_0^{\frac{\pi}{2}} \cos^2\psi \sqrt{\sin^2\psi + \frac{b_m^2}{a_m^2}\cos^2\psi} \cdot d\psi \tag{2.10}$$

$$W_{ez} = \frac{I_z}{b} = \frac{4a_m b_m^2 t}{b} \int_0^{\frac{\pi}{2}} \sin^2\psi \sqrt{\sin^2\psi + \frac{b_m^2}{a_m^2}\cos^2\psi} \cdot d\psi \tag{2.11}$$

Similarly, the respective expressions for the plastic section moduli of EHS under major and minor axes bending, W_{py} and W_{pz} are as follows:

$$W_{py} = 4a_m^2 t \int_0^{\frac{\pi}{2}} \cos\psi \sqrt{\sin^2\psi + \frac{b_m^2}{a_m^2}\cos^2\psi} \cdot d\psi \tag{2.12}$$

$$W_{pz} = 4a_m b_m t \int_0^{\frac{\pi}{2}} \sin\psi \sqrt{\sin^2\psi + \frac{b_m^2}{a_m^2}\cos^2\psi} \cdot d\psi \tag{2.13}$$

The yield and plastic section moment resistances for the case of major axis bending can be evaluated by using Equations 2.14 and 2.15, respectively where the measured monotonic tensile yield strength of steel is represented by $f_{y.mea}$.

$$M_e = M_{ey} = W_{ey} \times f_{y.mea} = \frac{4a_m^3 t f_{y.mea}}{a} \int_0^{\frac{\pi}{2}} \cos^2\psi \sqrt{\sin^2\psi + \frac{b_m^2}{a_m^2}\cos^2\psi} \cdot d\psi \tag{2.14}$$

$$M_p = M_{py} = W_{py} \times f_{y.mea} = 4a_m^2 t f_{y.mea} \int_0^{\frac{\pi}{2}} \cos\psi \sqrt{\sin^2\psi + \frac{b_m^2}{a_m^2}\cos^2\psi} \cdot d\psi \tag{2.15}$$

Similarly, the yield and plastic section moment resistances for the case of minor axis bending can be evaluated by using Equations 2.16 and 2.17, respectively.

$$M_e = M_{ez} = W_{ez} \times f_{y.mea} = \frac{4a_m b_m^2 t f_{y.mea}}{b} \int_0^{\frac{\pi}{2}} \sin^2\psi \sqrt{\sin^2\psi + \frac{b_m^2}{a_m^2}\cos^2\psi} \cdot d\psi \tag{2.16}$$

$$M_p = M_{pz} = W_{pz} \times f_{y.mea} = 4a_m b_m t f_{y.mea} \int_0^{\frac{\pi}{2}} \sin\psi \sqrt{\sin^2\psi + \frac{b_m^2}{a_m^2}\cos^2\psi} \cdot d\psi \tag{2.17}$$

Cross-sectional squash load *or* axial compressive yield capacity N_y can be computed by using any one of the Equations 2.18 and 2.19.

$$N_y = P_M \times t \times f_{y.mea} = 4a_m t f_{y.mea} \int_0^{\frac{\pi}{2}} \sqrt{\sin^2\psi + \frac{b_m^2}{a_m^2}\cos^2\psi} \cdot d\psi \tag{2.18}$$

$$N_y = P_M \times t \times f_{y.mea} = \pi t f_{y.mea}\left(a_m + b_m\right)\left(1 + \frac{3h_m}{10 + \sqrt{4 - 3h_m}}\right) \tag{2.19}$$

Chan (2007) estimated that the maximum deviation of the perimeter of an ellipse value calibrated using Equation 2.1 compared to the exact value calibrated using Equation 2.6 is only -0.04%. Thus, the alternate expressions presented in Table 2.1 are used during the research work of this dissertation for calibrating the cross-sectional properties of EHSs to avoid the complexities in using Equations 2.6–2.13. M_{ay} and M_{az} in Table 2.1 are the resultant components of the applied moment, M along the respective principal axes.

2.2.2 Equivalent CHS Geometry

The cross-sectional profile of a typical CHS with wall-thickness, t and outer diameter, D is shown in Figure 2.3. CHS is a special case of an EHS with unity as the cross-sectional aspect ratio, r (= a/b) such that $D = 2a = 2b$. The concept of the equivalent CHS diameter, D_{eq} of an EHS stems from extensive analytical work of Kempner (1962) and Kempner and Chen (1974) based on a conservatively approximate estimation of local buckling stress for Oval–Hollow–Sections (OHSs) and EHSs with moderate eccentricities by substituting their radius of curvature at the point of initiation of local buckling into the classical critical buckling stress equation (Lorenz 1908, 1911, Timoshenko 1910, Southwell 1914, Timoshenko and Gere 1961) of a CHS (Nowzartash and Mohareb 2009, Gardner et al. 2011).

EHSs being sensitive to imperfections (Kempner and Chen 1974), practically their actual buckling load is reasonably much lower than the buckling load predicted by the classical critical buckling theory (von Kármán and Tsien 1941, Hutchinson 1968). So, it is understood that the

approach adopted by Kempner (1962) and Kempner and Chen (1974) is not assessed for the extent of conservatism in estimating the actual maximum stress.

Yet, Gardner and colleagues (Gardner and Ministro 2004, Gardner 2005, Gardner and Chan 2007, Chan and Gardner 2008a, 2008b, Gardner et al. 2011) have suggested the expressions for the equivalent CHS diameter of an EHS with equal wall thickness based on the radius of curvature at the point of initiation of local buckling, with an intent to make the existing CHS cross-section classification criteria applicable for the EHSs also.

According to the concept put forward by Kempner (1962) and Kempner and Chen (1974), Gardner and Chan (2007) and Chan and Gardner (2008b) suggested the following Equation 2.20 for the equivalent CHS diameter of the EHS under pure axial compression.

$$D_{eq} = D_{eq.c1} = 2\frac{a^2}{b} = 2ra \tag{2.20}$$

Further research by Ruiz-Terán and Gardner (2008) on the elastic buckling of elliptical tubes revealed conservatism in Kempner's (Kempner 1962, Kempner and Chen 1969, 1974, Feinstein et al. 1971) predictive formula (Equation 2.20) for EHSs with higher aspect ratios and tube thicknesses.

Following analytical and numerical studies, an improved expression for the elastic buckling stress of a uniformly compressed EHS was derived and hence a revised expression (Equations 2.21a and 2.21b) for the equivalent CHS diameter was proposed.

$$D_{eq} = D_{eq.c2} = 2a\left[1 + f_t\left(\frac{a}{b} - 1\right)\right] \tag{2.21a}$$

$$f_t = 1 - 2.3\left(\frac{t}{2a}\right)^{0.6} \tag{2.21b}$$

Also, Gardner and Chan (2007) and Chan and Gardner (2008a) proposed the following expressions (Equations 2.22 and 2.23) of the equivalent CHS diameter.

For EHS under major axis bending:

$$D_{eq} = D_{CGb.mj} = \begin{cases} 0.8\dfrac{a^2}{b} = 0.4ra & if \quad r > 1.357 \\ 2\dfrac{b^2}{a} = 2\dfrac{a}{r^2} & if \quad r \le 1.357 \end{cases} \tag{2.22}$$

For EHS under minor axis bending:

$$D_{eq} = D_{CGb.mn} = 2\frac{a^2}{b} = 2ar \tag{2.23}$$

It was understood that for EHS under minor axis bending, similar to EHS under axial compression, local buckling initiates at the point of maximum radius of curvature of the cross-sectional profile, which coincides with the most heavily compressed part of the cross-section. But for EHS under major axis bending, local buckling initiates neither at the point of maximum radius of curvature of the cross-sectional profile *nor* at the extreme compressive fibre of the cross-section (*i.e.*, at the point minimum radius of curvature).

Following experimental and analytical works, Gardner et al. (2011) formulated the equivalent CHS diameter equations for EHSs under combined axial compression and uniaxial bending based on the location of plastic *or* elastic neutral-axis at the cross-sectional level and Equations 2.20–2.23. Also, the experimental and numerical data were used to develop and recommend the plastic and elastic interaction formulae for the design of EHSs under combined loading.

However, Packer and colleagues (Zhao and Packer 2009, Haque et al. 2012) reported some conservatism involved in using those expressions (Equations 2.20-2.23). Fang et al. (2018) observed that the EHSs which are classified as Class 4 (Slender sections) based on the Equation 2.20, exhibited significant cyclic energy dissipation capacities under combined axial compression and cyclic bending loads. Previous studies (Chan and Gardner 2008a, 2008b, McCann et al. 2016) also indicated different strength curves with-respect-to the cross-sectional aspect ratio of the EHS based on those equivalent CHS diameter formulae (Equations 2.20-2.23) and thus implying different slenderness limits for different aspect ratios alongside the conservatism expressed by Packer and associates (Zhao and Packer 2009, Haque et al. 2012).

2.2.3 Equivalent RHS Geometry

While Chan and Gardner (2008a, 2008b), Ruiz-Terán and Gardner (2008) and Gardner et al. (2011) focussed on establishing equivalency between EHS and CHS cross-sections, so that the CHS slenderness limits can be used for EHSs too, Zhao and Packer (2009) and Haque et al. (2012) suggested that determining an equivalent RHS profile for EHS would be more worthwhile so that the RHS cross-section slenderness limits can be used for EHSs too. Zhao and Packer (2009) and Haque et al. (2012) proposed the equivalent RHS concept such that both the EHS and the respective equivalent RHS have the same cross-sectional area. Equations for determining the cross-sectional dimensions of the equivalent RHS profile for EHSs proposed by Haque et al. (2012) are as follows:

$$B_{RHS} = \frac{A - 4at + 4t^2}{2t} \quad \text{for EHSs under axial compression } \textit{or} \text{ major axis bending;}$$
$$= \frac{A - 4bt + 4t^2}{2t} \quad \text{for EHSs under minor axis bending} \tag{2.24}$$

$$H_{RHS} = 2a \quad \text{for EHSs under axial compression } \textit{or} \text{ major axis bending;}$$
$$= 2b \quad \text{for EHSs under minor axis bending} \tag{2.25}$$

where B_{RHS} and H_{RHS} are the width and depth of the equivalent RHS cross-section, respectively.

The equivalent RHS cross-sectional profile is shown schematically in Figure 2.4. Zhao and Packer (2009) and Haque et al. (2012) observed that the local buckling failure mode of EHS stub columns in axial compression exhibits a pattern similar to that of plate buckling (*or* the buckling mode of a RHS) rather than the circumferential shell buckling mode of a CHS.

2.2.4 Local Slenderness

As with any new cross-sectional shape, the demand for carrying out investigations on various aspects like cross-sectional slenderness parameters, classification criteria and design strength

curves for EHSs is growing since 2003, to accredit the inclusion of its design guidelines in various codal specifications. Before assessing the design strength of a structural member, it is essential to classify the cross-section based on the cross-sectional slenderness ratio to assess the cross-sectional performance (Ziemian 2010, Gardner and Nethercot 2011, Bernuzzi and Cordova 2016).

For classifying cross-sections under axial compression, stub-column tests are necessitated. A stub-column is a member sufficiently short to prevent global member buckling when compressed, but adequately long enough to contain the same initial residual stress pattern as a much longer member cut from the same stock so that it shall not experience flexural or torsional buckling in the elastic or plastic range (Yu and Tall 1971, Ziemian 2010, Bernuzzi and Cordova 2016). Therefore, almost all the axial compressive resistance of the stub-column is driven by local buckling only. The stub-column test procedure and fabrication of stub-column specimens depending on whether unconnected or welded endplates are used shall meet requirements as per the specifications of EC3: EN 1993-1-3 (2006), AISI S902-13 (2013) and stub-column test memorandum from Ziemian (2010). The stub-column test provides not only the local buckling resistance of the member for a particular cross-section but also the mechanical properties of the material averaging out the structural imperfections of the cross-section profile fabricated especially by cold-forming process due, for instance, to the presence of residual stresses *or* different local failure strengths in various parts of the profile (flat portion, corners, web, flanges, *etc.*) (Yu and Tall 1971, Ziemian 2010, Bernuzzi and Cordova 2016).

For classifying cross-sections under bending, tests shall be performed by applying a bending moment without the simultaneous presence of axial, shear, *or* torsional forces. Pure bending occurs only when the member is under a constant bending moment *or* couple as the shear force is equal to zero. In reality, a state of pure bending does not practically exist, because such a state needs a weightless member. The state of pure bending is an approximation made to derive the related formulae. In case of a point load *or* a uniformly distributed load applied on cantilever sections (*i.e.*, ordinary *or* simple bending), shear stresses are also induced in addition to the normal bending stresses but the effect of the shear stresses can be made negligible if a larger length-to-depth ratio of the member is maintained (Roylance 2000).

The cross-section classification specified in various design specifications, *viz.*, Australian Standards (AS/NZS 4600:2005 2010, AS 4100:1998 2016), EC3 Part 1-1 (EN 1993-1-1 2005), American Specifications (AISC 360-16 2016), Indian Standard (IS 800 2007), *etc.*, is based on

a cross-sectional non-dimensional slenderness parameter which is generally designated as the fundamental attribute of the effective section that is susceptible to local buckling under external loading. Local buckling has the effect of reducing the load-resistance capacity of the cross-section due to the reduction in stiffness and strength of the locally buckled portions. Therefore, it is desirable to avoid local buckling before yielding of the member. However, it should be remembered that local buckling does not always spell disaster.

When local buckling occurs, structural members do not fail but can continue to resist additional loading beyond their initial bucking range. It is quite common that loads at failure may be considerably higher than those at which local buckling occurs. This is due to the redistribution of the longitudinal stresses within the member from the flexible parts to stiffer parts of the component portions, *i.e.*, a uniformly distributed stress (less than the critical stress) in the pre-buckling stage would be redistributed into non-uniform stress (exceeding the critical stress) in the post-buckling stage of the component portion where local buckling is likely to occur (Bambach and Rasmussen 2004, Bambach 2006). The term 'effective width' was coined by von Kármán (1932, 1941) to resolve the stress redistribution problem and later on, this concept became the instrumental notion behind the development of the **Effective-Width-Method (EWM)** by Winter(1947) (Hancock 2003, Bambach 2006). von Kármán (1932, 1941) termed the dimension of the stiffer region the ''effective width'' of the plate element of the cross-section under compressive stress (Bambach 2006). Each plate *or* portion in a cross-section is reduced to its effective width, and this reduction from the gross cross-section to the effective cross-section again is the fundamental notion behind the evolution of the EWM (Schafer 2008). The effective cross-section provides a clear model for the locations in the cross-section where the material is ineffective in resisting the load, *i.e.*, the most unfavourable (the slenderest) portions of the cross-section (Schafer 2008, Bock and Real 2015).

From the 1990s to the first two decades of the 21st century, most of the customary classical design approaches for structural steel members specified in various design specifications, *viz.*, Australian Standards (AS/NZS 4600:2005 2010, AS 4100:1998 2016), EC3 Part 1-1 (EN 1993-1-1 2005), American Specifications (AISC 360-16 2016), Indian Standard (IS 800 2007), *etc.*, adopt the modified *or* unified version of EWM for estimating the cross-sectional design strength and deformation capacities (Schafer and Peköz 1998a). The modified *or* unified version of EWM accounts for the stress gradient in both stiffened and unstiffened portions of the cross-section (DeWolf et al. 1973, Kalyanaraman 1976, Kalyanaraman and Peköz 1978,

Desmond et al. 1981a, 1981b, Bock and Real 2015); residual stress and geometric imperfections (Liew et al. 1989); and perforations (Yu and Davis 1973, Miller and Peköz 1994).

In the EWM, the cross-section classification is performed based on the cross-sectional non-dimensional slenderness parameter. The cross-sectional non-dimensional slenderness parameter is obtained by normalizing the effective width with-respect-to the wall thickness. For CHSs, most of the dimensions like effective-width and the perimeter can be expressed as factorized terms of the cross-sectional outer diameter *D*. For classifying the cross-section of a CHS member, the cross-section slenderness parameter is specified as $\frac{D}{t\varepsilon^2}$ by reducing $\frac{D}{t}$ ratio with the factor ε^2 ($=235/f_{y.mea}$) in EC3 Part 1-1 (EN 1993-1-1 2005). The reduction factor ε^2 is used to attain normalisation among the CHSs made of various $f_{y.mea}$ values. The EWM offers an obvious means to incorporate local-global buckling interaction where reduced cross-section properties influence global buckling (although specifications often simplify this interaction somewhat). However, the commonly assumed two-dimensional non-linear stress distribution to explain the effective width of a plate is itself an approximation, representing the average of the longitudinal membrane stress and ignoring variation in stress through the thickness as well as variation in stress along the length of the plate. Thus, the true "effective width" is far more complicated than the typically assumed values for it (Schafer 2008). While the existing effective width equations only correlate to the average membrane stress conditions in a plate.

The EWM leads to the notion of neutral axis shift in the cross-section due to local-buckling because once the respective effective width of each element *or* portion of the cross-section is estimated, the gross neutral axis is unlikely to be at the same location as the effective neutral axis (Schafer 2008, Ziemian 2010). However, there are shortcomings for the EWM because of the consideration of this neutral axis shift. The EWM ignores inter-element (*i.e.*, between the flange and the web) equilibrium and compatibility in determining the elastic buckling behaviour with the evolution of complex cross-sectional shapes. While practising the EWM, incorporation of the competing buckling modes, such as distortional buckling can be awkward (Schafer 2008). By the 1990s, practising the EWM seemed to be a cumbersome task due to the complications involved in determining the governing non-dimensional slenderness parameter and the resulting effective properties of the members with

a) globally stepped, tapered, curved, perforated, spiralled, and twisted profiles; a variety of hybrid cross-sections (*e.g.*, multiple-skinned, dumbbell-shaped, *etc.*,) involving the interaction among various elements (*i.e.*, web, flange, weld) of the cross-section (Han et al. 2014);

b) edge and/or intermediate stiffeners; and

c) material based hybrid sections or elements (*i.e.*, web, flange, stiffener and weld elements with two *or* more material properties).

To overcome these difficulties, the **Direct-Strength-Method (DSM)** approach which involves the utilization of numerical elastic buckling solutions for the entire member or cross-section was put forward by Schafer and Peköz (1998a, 1998b). If the effective width (*or* effective section) is the fundamental notion behind the EWM, then the elastic stability of the whole cross-section (*or* whole member) is the basic idea behind the DSM. Further, the DSM assumes that local buckling behaviour can also be predicted by utilizing the elastic critical local buckling stress of the whole section with an appropriate capacity design curve for local instability of the sections (Hancock et al. 2001).

The DSM is driven by the idea that if a designer determines all of the elastic instabilities for the gross section, *i.e.*, local, distortional, and global buckling, and also determines the moment (*or* load) that causes the section to yield, then the cross-sectional (*or* member) strength can be directly determined (Bock and Real 2015). The DSM relies on the estimation of elastic local, global and distorsional buckling stresses using numerical software based on the Constrained and Unconstrained Finite Strip Method (CUFSM) (Schafer and Ádány 2006) *or* the Finite Element Method (FEM). The DSM has its genesis in the design technique for the distortional buckling of thin-walled sections developed by Hancock et al. (1994). The method is essentially evolved from the procedure of establishing the column curves for global buckling, but with application to local and distortional buckling instabilities and appropriate consideration of post-buckling reserve and interaction in these modes (Schafer 2008).

Local buckling curves for estimating section capacity according to DSM are specified in AISI S100-16 (2016) and AS/NZS 4600:2005 (2010), except for the closed cylindrical tubular sections. Albeit, the DSM is proposed to assess the capacity of a section due to its local buckling behaviour, it is found that the capacity of a non-slender cross-section is not only due to local buckling but also due to the material strain hardening effect (Kato 1990, Gardner 2008,

Buchanan et al. 2016, Gardner et al. 2017, Zhao et al. 2017, Lan et al. 2018, Zhao and Gardner 2018). So, the DSM design predictions show a degree of conservativeness for the cross-sections (*or* members) with lower slenderness values. It is assessed that for cross-sections with the section slenderness less than the elastic-slenderness limit, the effect of local buckling decreases, while the effect of material strain hardening increases over the section capacity with a decrease in cross-section slenderness (Kato 1990, Gardner 2008, Buchanan et al. 2016, Gardner et al. 2017, Zhao et al. 2017, Lan et al. 2018, Zhao and Gardner 2018).

The non-dimensional slenderness measure of the entire CHS cross-section shown in Figure 2.3 based on the critical elastic local buckling approach can be expressed as follows (Ma et al. 2018):

$$\bar{\lambda}_{l.b} = \frac{\sqrt{f_{y.mea}}}{\sqrt{f_{cr}}} = \frac{\sqrt{f_{y.mea}}}{\sqrt{\frac{E}{\sqrt{3\left(1-\nu^2\right)}} \times \frac{2t}{D}}} \tag{2.26}$$

where f_{cr} is the critical elastic local buckling stress (Timoshenko and Gere 1961). E is the initial elastic modulus of the material and υ is the Poisson's ratio within the elastic range of the material.

The normalised cross-section slenderness parameter for a CHS according to various design standards can be represented by the following expressions.

$$\bar{\lambda}_{cs} = \left(\frac{D}{t}\right)\left(\frac{f_{y.mea}}{E}\right) \quad \text{as per AISC 360-16 (2016) and CSA S16-14 (2014)} \tag{2.27}$$

$$\bar{\lambda}_{cs.E} = \left(\frac{D}{t}\right)\left(\frac{f_{y.mea}}{235}\right) \quad \text{as per EC3: EN 1993-1-1 (2005)} \tag{2.28}$$

$$\bar{\lambda}_{cs.IA} = \left(\frac{D}{t}\right)\left(\frac{f_{y.mea}}{250}\right) \quad \text{as per AS 4100:1998 (2016) and IS 800 (2007)} \tag{2.29}$$

For CHSs, dimensions like the effective-width and the perimeter can be expressed as factorized terms of *D*. The following Equation 2.30 is deduced from Equations 2.26–2.29.

$$\bar{\lambda}_{cs.E} = \frac{250}{235}\bar{\lambda}_{cs.IA} = \frac{E}{235}\bar{\lambda}_{cs} = \frac{1.1547E}{235\sqrt{1-\nu^2}}\bar{\lambda}_{l.b}^2 \tag{2.30}$$

Further, from Equation 2.30, the following expression in Equation 2.31 is obtained by assuming 210000 MPa and 0.3 as approximate values of E and υ for steel, respectively.

$$\bar{\lambda}_{cs.E} \approx 1.064\bar{\lambda}_{cs.IA} \approx 893.62\bar{\lambda}_{cs} \approx 1081.683\bar{\lambda}_{l.b}^2 \tag{2.31}$$

In Table 2.2, cross-section classification slenderness limits for CHSs under axial compression and bending loading cases specified in various international design standards are shown. In the case of axial compression, the cross-sections are classified as yielding and non-yielding sections with-respect-to the yield limit (see Table 2.2). The cross-sections capable of exhibiting a compressive resistance more than *or* equal to the respective yield resistance are known as yielding sections else known as non-yielding *or* slender sections. In the case of bending, cross-sections are classified depending on their moment-rotation characteristics (see Figure 2.5) and the ultimate state material response during exhibiting their moment resistance, M (see Figure 2.6). The moment-rotation characteristics of general CHS cross-sections are illustrated in Figure 2.5. It is assumed that the cross-sections are subjected to an increasing bending moment, and variation of stress in the cross-sections is presented in Figure 2.6. The codes also specify the limiting slenderness values (see Table 2.2), which enables the classification to be made as follows:

- ***Slender cross-sections***: These are the cross-sections with a sufficiently larger slenderness ratio in which yield in the extreme fibres cannot be attained because of premature local buckling in the elastic range. These sections are generally classified as Class 4.

- ***Elasto-plastic or semi-compact cross-sections***: These are the cross-sections in which only some of the outermost fibres are capable of reaching a stress level σ equal to $f_{y.mea}$ because local buckling would prevent the development of the full-plastic moment resistance M_p While the remaining fibres of the cross-section are only capable of exhibiting a σ value lesser than $f_{y.mea}$. Such sections can develop only yield moment resistance M_e *or* a moment resistance with a magnitude between M_e and M_p (*i.e.*, $M_e \leq M < M_p$). These sections are generally classified as Class 3. Apart from the local buckling, material in-elastic squashing can also be observed in these cross-sections.

- ***Compact cross-sections***: These are the cross-sections in which all the fibres are capable of reaching a stress level σ equal to *or* greater than $f_{y.mea}$ by developing a moment of resistance with a magnitude greater than *or* equal to M_p (*i.e.*, $M \geq M_p$). After attaining the state of the full-plastic moment M_p these cross-sections require an infinite strain at the neutral axis which is practically impossible to achieve and thus any attempt at increasing the bending load at this point simply results in more rotation, once the cross-section has sufficient ductility. These sections are generally classified as Class 1 *or* Class 2. Class 2 cross-sections are those in which all the fibres are capable of reaching a stress level σ equal to $f_{y.mea}$, but have inadequate plastic hinge rotation capacity for formation of plastic mechanism due to local buckling. But the cross-sections which could attain their full-plastic moment M_p and allow sufficient higher rotation at *or* above this moment so that redistribution of bending moments can take place in the structure until complete plastic hinge failure mechanism is formed fall under Class 1 category. However, there are two types of Class 1 cross-sections. Cross-sections in which all the fibres are capable of reaching a stress level σ only equal to $f_{y.mea}$, and the cross-sections in which some of the outermost fibres are capable of reaching a stress level σ beyond $f_{y.mea}$ because of material strain-hardening. Due to strain hardening of the material, the cross-sections can sustain a small amount of extra moment.

Strain hardening (also called cold working) is an important metallic material strengthening process that involves plastically deforming the material during manufacturing (involves forming processes such as rolling, forging, and extrusion) *or* loading (involves externally applied mechanical loads) to greatly increase the number of dislocations. Dislocations form at the grain boundaries, free surfaces, and at the interfaces between the lattice matrix and second phase particles. A large number of dislocations can also be formed by homogenous nucleation via a mechanism called the Frank–Read source. The formation of these dislocations occurs when a stress level σ greater than the yield strength $f_{y.mea}$ is reached in the fibres of the cross-section. However, creating many dislocations is not sufficient by itself to greatly increase the strength. Strain hardening requires the dislocations to interact and impede each other's movement. The strain field surrounding a dislocation repulses further cumulative dislocations, and these forces impede the movement of dislocations when in close contact. As the dislocation motion becomes more restricted the applied stress level σ required to deform the material must be increased beyond the yield strength $f_{y.mea}$ and higher, thus translating into higher strength. Further, when two dislocation lines cross, they become entangled, thus impeding their movement and thereby increasing the strength. As the resistance to dislocation motion rises

with their density, the strength of the material and thus the cross-section improves (Mouritz 2012). It can be seen in Table 2.2 that the Slender (Class 4) and Elasto-plastic (Class 3) sections are separated by the Yield limit while the Elasto-plastic (Class 3) and Compact (Class 2 and Class 1) sections are separated by the Compact limit. Although EC3 Part 1-1 (EN 1993-1-1 2005) specifies guidelines for the design of elastic CHSs under bending, it is to be noted that the design cross-sectional moment resistance of elastic CHSs is regulated by EC3 Part 1-6 (EN 1993-1-6 2007).

Some codal specifications like EC3: EN 1993-1-1 (2005) and AS 4100:1998 (2016) also recommend slenderness limits separating Class 1 and Class 2 sections with different rotation-capacity criteria. However, the significance of those slenderness limits with-respect-to the objectives of the research in this thesis is negligible as it is essential only to find out if the cross-section of a CHS *or* an EHS member to be used for resisting cyclic (ELCF) loads belong to Compact section category *or* not but not required to check whether the cross-sections belong to Class 1 *or* Class 2 category.

Conveniently, CHS can be assumed as a special case of EHSs with a cross-sectional aspect ratio of unity (*i.e.*, $r = a/b = 1$). Therefore, Equations 2.26–2.31 and the CHS cross-section classification criteria will be used for the cross-section classification of EHS members in the further chapters based on the concept of the equivalent CHS diameter. And, Equations 2.26–2.29 are expressed in terms of D_{eq} for both CHS and EHSs in the following equations.

$$\bar{\lambda}_{l.b} = \frac{\sqrt{f_{y.mea}}}{\sqrt{f_{cr}}} = \frac{\sqrt{f_{y.mea}}}{\sqrt{\frac{E}{\sqrt{3\left(1-\nu^2\right)}} \times \frac{2t}{D_{eq}}}} \tag{2.32}$$

$$\bar{\lambda}_{cs} = \left(\frac{D_{eq}}{t}\right)\left(\frac{f_{y.mea}}{E}\right) \quad \text{as per AISC 360-16 (2016) and CSA S16-14 (2014)} \tag{2.33}$$

$$\bar{\lambda}_{cs.E} = \left(\frac{D_{eq}}{t}\right)\left(\frac{f_{y.mea}}{235}\right) \quad \text{as per EC3: EN 1993-1-1 (2005)} \tag{2.34}$$

$$\bar{\lambda}_{cs.IA} = \left(\frac{D_{eq}}{t}\right)\left(\frac{f_{y.mea}}{250}\right) \quad \text{as per AS 4100:1998 (2016) and IS 800 (2007)} \tag{2.35}$$

2.3 EXTREMELY–LOW–CYCLE–FATIGUE (ELCF) LOAD

2.3.1 General

With progressive cyclic loading, even at a stress amplitude much below a given material's yield limit (*i.e.*, at stress amplitudes considerably smaller than the 'safe' stress levels estimated based on static fracture analyses) (Suresh, 1998), the resulting localized permanent microscopic damage at the crystalline grain interface level in association with nucleation, dislocation restructuring (hardening/softening) and re-crystallization may accumulate further and develop into cracks *or* other macroscopic damage, eventually leading to failure of the component (Lee et al. 2005, Dowling 2012). This process of progressive damage initiating at the material level of the component due to cyclic loading is being referred to as 'fatigue'. When such damage results due to the application of external stresses or strains, it is called 'mechanical fatigue'. The early work on fatigue in the 1830s and subsequent efforts up to the 1960s are reviewed by Mann (2013).

Cyclic tests resulting mechanical fatigue is customarily being classified as 'High-Cycle-Fatigue (HCF)' *or* 'Low-Cycle-Fatigue (LCF)' tests based on the number of cycles to failure and the extent of plastic straining at the physically damaged location (*i.e.*, the most stressed location of the specimen *or* the mechanical component), which in turn depends on the properties of the metallic material and the magnitude of the applied nominal cyclic stress *or* strain. The arbitrary, but commonly accepted, the splitting line between HCF and LCF failures is considered to be about 5×10^4 to 5×10^5 fatigue-life cycles. However, there is not a fixed rule to separate the LCF from the HCF fields (Davoli 1999). As a rule of thumb, cyclic loadings in which test regimes are usually stress-controlled and typically involve a very high number of cycles, typically 5×10^6 cycles *or* greater to cause failure are conventionally being referred to as 'HCF' and generally in such tests the elastic strain amplitude is higher than the plastic strain amplitude, where the material deforms primarily elastically and the number of cycles for failure is characterized in terms of the stress amplitude (Grover 1966, Davoli 1999, Nicholas 2006). Conversely, the term LCF (*or* Oligo-Cyclic-Fatigue) refers to cyclic load where plastic strain dominates and the number of cycles to failure generally ranges from 10^2 to 5×10^4 (Coffin 1959, Sorenson and Clemett 1962, ASME-LCF 1963, Grover 1966, Davoli 1999) and the term '**Extremely-Low-Cycle-Fatigue (ELCF)**' is characterized by large inelastic strain amplitudes (several times of the yield strain) and extremely fewer cycles to fracture, typically less than 100 cycles (Shimada et al. 1987, Kuroda 2002).

Often ignored in the primitive fatigue design concept and frequently appearing in the later phases of product development, LCF was identified as the basis for explaining a compressor-rotor failure that occurred during the development of a turbojet engine (Sorenson and Clemett 1962). Gradually, the developments of the aeronautical industry followed by nuclear programs were powerful stimulants, then, in boosting enhancements in the field of 'fatigue research'. Instead of focussing on stress-based approaches alone in the 1960s, Coffin (1959, 1962) at 'General Electric' and Manson (1962, 1964, 1966) at NASA proposed a strain-based fatigue model by establishing the strain-life (ε-N) curve for a metallic material based on the applied strain amplitude levels for LCF and ELCF loading conditions (Van 1999). This new way of studying fatigue found a great number of spectators from then onwards. The strain-controlled LCF and ELCF testing became a necessity for metallic components from a variety of industries like aeronautical, civil and mechanical and nuclear engineering, *etc.*, that require integrity assessment under small to a very small number of severe strain loading cycles (approximately ranging from 50 to 5×10^4 cycles) (Grover 1966, Polák 1991, Van 1999, Nip et al. 2010b, Nussbaumer et al. 2011).

Notable applications of LCF and ELCF failure assessment are Zircaloy components like fuel cladding, pressure and calandria tubes, *etc.*, in nuclear reactor plants (O'Donnell and Langer 1964, Northwood 1985); compressor-rotor of turbojet engine (Sorenson and Clemett 1962, Pakhomenkov et al. 2017); fuel tank membrane of pressure vessels such as liquid-propellant and solid-propellant tanks of rocket motor systems in missiles (Bagby 1960, Grover 1966, Skvortsov et al. 2017); ship hull structures like brackets, stiffeners, shells, *etc.* (Gross 1963, Rolfe and Munse 1963, Masubuchi 1980, Aung 2007); attachment surfaces between the blade and the turbine disk connected by the dovetail or the fir tree in the power generation *or* propulsion sectors (Tepper 1976, DeLuca 2001); aircraft landing gear components like swinging levers, wheel flanges, *etc.* (Franco et al. 2006, Bagnoli and Bernabei 2008, Bagnoli et al. 2008, Divakaran et al. 2015); and various components of earthquake resistant civil engineering structures like braces, beams, columns, *etc* (Han et al. 2003, Nip et al. 2010b, Haddad 2015, Liao et al. 2016). The corresponding ELCF and LCF strengths are relevant in the case of loadings such as those occurring during earthquakes, where usually key components of the structures experience only small numbers of stress cycles of high magnitude and significant inelastic deformations (Nip et al. 2010a, Nussbaumer et al. 2011).

2.3.2 Cyclic Loading Histories

All structural elements can be estimated to have limited strength and deformation capacities, and collapse safety, as well as damage control, depending on our ability to assess these cyclic capacities (involves cyclic- ductility, over-strength, rotation capacity, energy dissipation index, *etc.*,) with some confidence. Unfortunately, the cyclic- strength and deformation capacities of an old structural component depend (sometimes weakly and sometimes strongly) on its cumulative damage, which implies that every such component has a permanent memory of past damaging events and at any instance, in time the damage propagation in the component starts with effectuating the already accumulated deterioration in its state of health from the past excursions (*or* cycles) (FEMA P695 2009, Krawinkler 2009). Thus, the performance of an old structural component depends on the history of previously applied damaging cycles, and to the best of the authors' knowledge, the only reasonable way to assess the consequences of history (short of developing complex analytical models that can be used for damage state predictions) is to replicate the load and deformation histories that component had undergone in an earthquake (*or* several earthquakes if this is appropriate). It is essential to testing (in addition to analytical modelling) to evaluate the performance of many conventional old structural components for their retrofitting *or* replacement, and also particularly of new and innovative components (*or* systems) that show much promise for the enhanced cyclic performance.

With the advancements in the seismic performance enhancement systems during the last decade of the 20th century, the need for representative cyclic loading histories became prevalent as the performance-based seismic design involving estimation of the cumulative damage in terms of cyclic capacities and failure modes was considered as a more widely accepted alternative to routine code design (FEMA P695 2009, Krawinkler 2009). In the development of a cyclic loading protocol, the number and amplitudes of cycles of the loading history to be applied to the specimen can be derived from analytical studies in which models of representative structural systems are subjected to representative earthquake ground motions and the response is statistically evaluated (FEMA P695 2009, Krawinkler 2009). However, any loading protocol will always be a compromise that will provide deformation histories whose authenticity will depend on many parameters. There are many decisions and judgmental steps to be taken to develop a compromise loading history that is conservative but statistically representative of the full range of ground motions and structural configurations. Such decisions and steps involved in the derivation of loading protocols for cyclic testing are too elaborate to enumerate herein. Therefore, the reader is referred to the following relevant guideline

documents for such detailed information: ECCS (1986), ATC-24 (1992), Krawinkler (1996), Krawinkler et al. (2000), FEMA 461 (2007), AISC-341 (2016) and Tsitos and Elghazouli (2017), *etc*.

Following is a detailed description regarding some of the strain-controlled quasi-static cyclic loading protocols for testing the steel structures which are currently being utilised widely.

- ***ATC-24 Protocol*** (ATC-24 1992): This protocol is specifically developed for components of steel structures, which is one of the first formal protocols developed in the U.S. for seismic performance evaluation of components using a cyclic loading history (see Figure 2.7a). It uses the yield deformation of the structural component, δ_y, as the reference for increasing the amplitude of cycles. The loading history contains at least 6 elastic cycles (*i.e.*, amplitude < δ_y), followed by nine cycles with three cycles of amplitude δ_y, three cycles of amplitude $2\delta_y$, and three more cycles of amplitude $3\delta_y$, and further followed by pairs of cycles whose amplitude increases in increments of δ_y until severe cyclic deterioration occurs. This protocol was employed in Phase I of the SAC (a joint venture of Structural Engineers Association (SEA) of California, Applied Technology Council (ATC) and Consortium of Universities for Research in Earthquake Engineering (CUREE)) steel program. In the SAC Phase I experiments, it was found that inconsistent measures of "yield deformation" were employed by different investigators (for test control, δ_y had to be predicted before the test), which led to results that were difficult to compare with each other. Thus, the choice of a "yield deformation" as the test control parameter appears to be a little ambiguous. This discovery came too late to prevent the adoption of this protocol in the 1997 AISC Seismic Provisions for qualification testing of steel components.

- ***SAC Protocol*** (ANSI/AISC 341-16 2016): The SAC loading protocol shown in Figure 2.7b is specifically developed for steel moment frames, which uses story drift rather than yield deformation as the amplitude control parameter because of the δ_y ambiguity. The story yield drift of steel frame structures is confined to a rather narrow range around 0.01 radians, which permits an approximate correlation between the ATC-24 and SAC protocols. The SAC protocol contains a greater number of small (elastic) cycles (which were added because of the observed Northridge weld fractures that occurred before yielding took place), two cycles of an intermediate amplitude of 0.015 radians, but slightly fewer cycles of larger amplitude. In general, the two protocols are very similar in cumulative damage potential, but because of the commitment to story drift as the control parameter, the SAC

protocol should not be applied to configurations other than steel beam-to-column assemblies that are representative of typical stories. The November 2000 Supplement #2 of the 1997 AISC Seismic Provisions has replaced the ATC-24 (1992) protocol with the SAC protocol.

• ***FEMA 461 Protocol*** (FEMA 461 2007): This protocol was developed originally for testing of drift sensitive non-structural components but is applicable in general also to drift sensitive structural components. Structural components that may be tested as per this protocol include shear walls, beam-column assemblies, and frame assemblies (see Figure 2.7c). It uses a targeted maximum deformation amplitude, δ_m, and a targeted smallest deformation amplitude, δ_0, as reference values, and a predetermined number of increments, n, to determine the loading history (a value of $n \geq 10$ is recommended). The amplitude a_i of the step-wise increasing deformation cycles is given by the equation $a_{i+1}/a_n = 1.4(a_i/a_n)$, where a_1 is equal to δ_0 (or a value close to it) and a_n is equal to δ_m (or a value close to it). Two cycles are to be executed for each amplitude. If the last damage state has not yet occurred at the target value δ_m, the loading history shall be continued by using further increments of the amplitude of $0.3\delta_m$.

• ***ECCS Protocol*** (ECCS 1986): This protocol also uses the yield deformation of the structural component, δ_y, as the reference for increasing the amplitude of cycles. The applied axial displacement (δ) history contains one cycle at each level of 0.25, 0.5, 0.75 and $1.0\delta_y$, followed by three cycles at each level of 2, 4, 6, $8\delta_y$, *etc.*, as shown in Figure 2.7d. The axial yield displacement δ_y of each specimen was taken as the product of the length of the member and the measured weighted yield strain of the cross-section. The axial displacement δ shall be applied at a strain rate which is within the recommended range for quasi-static testing (BS 7270 2006). This protocol is very good to interpret the member behaviour during laboratory tests and to make their results comparable at an international level, but it is very far from the real behaviour when the structure is subjected to an actual earthquake (Gioncu and Mazzolani 2013).

2.4 CYCLIC HARDENING MATERIAL MODEL

Given the same geometry, material, and support conditions, the difference between the performances of a steel structural component under externally applied cyclic (axial *or* flexural) and monotonic (*or* constant) loads is essentially due to the difference in the material characteristics under these loads. Mostly, the LCF and ELCF tests are to be carried out in a strain-controlled environment. When a specimen *or* component of a metallic material is subjected to cycles of constant- *or* varying-strain amplitude, large changes normally occur in its flow stress; depending on the material chemical composition and its processing history, hardening *or* softening may occur (Laird 1977, Basan et al. 2010). It often happens that a metallic material subjected to cyclic strains will harden rapidly in the first few applications of loading, but the hardening rate decreases with accumulating strains and eventually reaches zero, at the point where the material response is described as being "stabilized" *or* "saturated" (Laird 1977). If the material behaviour before reaching the stabilized state at any strain amplitude is required, such as when specifying the material model in a numerical simulation, a constitutive model of cyclic plasticity is needed. The characteristics of non-linear stress-strain response of physically deformed solids under cyclic loading are mathematically described using the theory of cyclic plasticity. The significant facets of cyclic plasticity include Cyclic-Stress-Strain (CSS) curve, strain-life curve, fracture energy-life curve, and constitutive material modelling. The CSS curve characterizes the stabilized hysteretic response only, although it gives an overview of material response under ELCF conditions at various strain amplitude levels. But, an appropriate constitutive material model that can predict the accurate material response before reaching the stabilized sate under cyclic loading is needed for specifying material model parameters in a numerical simulation study (Novak 2016). As the CSS curve, strain-life curve and fracture energy-life curve do not fall within the scope of the research objectives in this thesis, the detailing of these facets is not presented herein. Therefore, the reader is referred to the following for such detailed information on the CSS curve, strain-life curve and fracture energy-life curve: SAE J1099 (1997), Suresh (1998), Hales et al. (2002), Lee et al. (2005), Nip et al. (2010a), Bruneau et al. (2011), Dowling (2012), ASTM E606/E606M (2012), *etc*.

To date, a vast amount of literature (Armstrong and Frederick 1966, Chaboche 1986, White 1988, Lemaitre and Chaboche 1994, Portella and Rie 1998, Dunne and Petrinic 2005, Ottosen and Ristinmaa 2005, Chen and Han 2007, Chaboche 2008, Halama et al. 2012a, Ziegler 2012,

Xu et al. 2016) is existing on the evolution of constitutive elastoplastic material model relations. For metallic materials, how the plastic strains reform the yield function is defined by '*hardening rules*'. Cyclic hardening in structural steels can be classified into isotropic and kinematic components.

The isotropic hardening rule assumes that the yield surface expands uniformly in all directions with increasing stress beyond the elastic domain of the material. This implies that, if the yield strength in tension and compression are initially equal (yield surface is symmetric about the stress axes), they increase accordingly and remain equal as the yield surface increases with plastic strain. Essentially, isotropic hardening just means if the material is loaded up to a certain yield point which is beyond its elastic domain in tension, then it will not yield during the subsequent compression loading (*i.e.*, after unloading from the yield point in the tension) until it reaches the same magnitude of the yield point which was reached during the tension loading previously. Isotropic hardening rule is not applicable to model the components which are subjected to cyclic loading as it predicts that after a few cycles, the material just hardens until it responds elastically. Under cyclic loading, the hardening of a material in tension will lead to softening in the subsequent compression and this effect is called the Bauschinger (1886a, 1886b) effect. In inelastic deformation processes involving recurrent reversal of stress (such as metalworking, high-intensity seismic loading, *etc.*,), the Bauschinger (1886a) effect is very significant and cannot be ignored (Bower 2009). To model the Bauschinger effect, the kinematic hardening rule needs to be used. In this case, the yield surface remains in the same shape and size but merely translates in stress space with a shift of the centre. The kinematic hardening rule assumes that the material can soften in subsequent compression loading.

Cyclic plasticity characteristics of materials are defined by a constitutive model which is based on the rational combination of non-linear isotropic and kinematic hardening components. At the end of the 20th century, Chaboche et al. (1979) and Lemaitre and Chaboche (1994) developed a constitutive Non-Linear Combined (isotropic-kinematic) Hardening Material (NLCHM) model which takes care of the metallic material behaviour under ELCF load before reaching the stabilized state as well (Marquis 2001). The NLCHM model assumes uniform expansion and translation of the yield surface in the stress space, simultaneously (Lemaitre and Chaboche 1994, Marquis 2001, Dunne and Petrinic 2005, Silvestre et al. 2015). The evolution of material yield surface domain in the stress space is the basis of the methodology involved in developing the NLCHM model. The evolutions of this domain are driven by the plastic flow.

The domain size of the yield surface is governed by a so-called 'nonlinear isotropic hardening component'. While the position of the yield surface is controlled by a so-called 'nonlinear kinematic hardening component'. The non-linear isotropic hardening component was derived using isotropic work-hardening rule by Hodge et al. (1956) and Hill (1966), considering Voce's flow rule (Voce 1948) based on the yield criterion by von Mises (1913, 1928). While the procedure for the estimation of non-linear kinematic hardening component was developed by Chaboche (1974, 1986, 2008) using the material yield surface transition mechanism addressed by Armstrong and Frederick (1966) which takes the Bauschinger (1886a, 1886b) effect of metallic materials into account (Marquis 2001).

Since the 1990s, engineers involved in the ELCF design and assessment activities are increasingly tending to use the constitutive NLCHM model in some of the commercially available finite element software packages like Abaqus, Ansys, *etc* (Doghri 1993, Payne 2000). The NLCHM model parameters are successfully being used to simulate and predict the ELCF behaviour of a component *or* structure before the initiation of the fatigue crack propagation. Also, the design of steel structural components which are susceptible to ELCF conditions, based on iterative tests on full-scale models is still a difficult, time-consuming and expensive task to perform. After the Northridge Earthquake in 1994 and the Kobe Earthquake in 1995, the increased emphasis on specifying design standards for steel structural components under ELCF conditions using FE simulation techniques had triggered an urge in the estimation of constitutive NLCHM model parameters of the 'constructional steels'. In this regard, the reader is referred to the following examples of such works: Tremblay et al. (1995), Usami (1996), Ballio et al. (1997), Bernuzzi et al. (2000), Astaneh-Asl (2003), Nastar et al. (2013), *etc*. One of the most important design considerations which must be made during simulations and virtual testing of product *or* component models is the proper choice of material model (Anderson et al. 2015).

The commonly adopted calibration procedure for computing the constitutive NLCHM model parameters is comprehensively chronicled in Chaboche (1986), Marquis (2001), Imaoka (2008), Nip et al. (2010a), Abaqus 6.9-EF (2009), Halama et al. (2012a) and Novak (2016). Due to the upsurge in the evolution of precise and enhanced fatigue measurement tools of the process automation and instrumentation market during the first two decades of the 21st century, conducting studies to estimate the NLCHM model parameters of the metallic materials picked the pace significantly (see Table 2.3). Eventually, the construction of the CSS curve of a

metallic material has become just as a by-product of such cyclic endurance tests (Hales et al. 2002). The NLCHM model parameters and Poisson's ratio, υ values of various engineering metallic materials at ambient temperature conditions, covering a wide range of $f_{y.mea}$, obtained from various sources are catalogued in Table 2.3. In Table 2.3, $\sigma\big|_0$ is the initial yield stress with zero equivalent plastic strain, Q_∞ is the isotropic hardening constant representing the maximum change in the size of the yield surface, and b_{iso} is the isotropic hardening exponent representing the rate at which the size of the yield surface changes as plastic strain increases. Q_∞ can be either positive *or* negative, indicating cyclic hardening *or* softening, respectively. While C_{kin} and γ_{kin} are the kinematic hardening constant and the rate of kinematic hardening, respectively and can be calibrated using the stabilized hysteretic responses from the strain-controlled cyclic tests. The shift in the center of the yield surface in the stress space under the applied cyclic load is termed as backstress. The ratio $\frac{C_{kin}}{\gamma_{kin}}$ is the maximum change in backstress and γ_{kin} determines the rate at which the backstress varies as the plastic strain increases.

Due to the financial and logistical constraints for conducting experiments, parametric studies are reported herein (in Chapters **6**, **7** and **8**) by performing the FE simulations using the general FE software package, Abaqus (2009). The NLCHM model parameters for performing these FE simulations are chosen from Table 2.3. During the first two decades of the 21st century, Nip et al. (2010b), Salawdeh and Goggins (2013), Haddad et al. (2011a), Fadden and McCormick (2014), Haddad (2015), Zhou et al. (2018), and Fang et al. (2018) are among those who had successfully employed the NLCHM model parameters in FE studies to accurately simulate the experimental cyclic behaviour steel HSS members.

2.5 HSSs UNDER CYCLIC LOADING

2.5.1 Significance of ELCF in Structural Design

Structures subjected to repeated cyclic loadings, such as large variations in temperature, seismic loads, traffic loads, and high-pressure cycles from water waves can undergo progressive, localized and permanent structural change due to the action of fluctuating strains at nominal stresses that have maximum values less than (and often much less than) the tensile

strength of the material. This phenomenon is mechanical fatigue and is represented by a loss of resistance in the structures with time. This fatigue may even culminate into cracks and cause fractures after a sufficient number of fluctuations by yielding of the net section *or* by brittle fracture. A typical failure of structural elements under the ELCF regime is an earthquake-induced fracture (Shimada et al. 1987, Kuroda 2002). The behaviour and economical design of the structural members under this form of loading are certainly expected to be controlled by their geometry, local detailing, workmanship and by the hysteretic properties of their constituent material (*e.g.,* carbon steel and stainless steel, high-strength and very high-strength steels, *etc*.,), which can be assessed through fatigue testing at high strain amplitudes (Nip 2009, Nip et al. 2010a, 2010b, Roberti et al. 2011, Gioncu and Mazzolani 2013).

More importantly, ELCF fracture is often considered as the governing limit state in steel structures subjected to severe earthquakes and therefore, strain-controlled ELCF testing at high strain amplitudes is considered as a valuable method for testing energy-dissipating components (Ballio and Castiglioni 1995, Uriz 2005, Fell et al. 2006, Fell 2008). Maintaining overall structural integrity without collapse is one of the primary objectives of the seismic-resistant structural design. The behaviour of steel structural members under repeated cyclic loads is highly influential in the context of earthquake-resistant design, because the true characteristic behaviour of these members may differ from the ideal reference of the perfect elastic-plastic behaviour (ECCS 1986).

Structural damage and failure under ELCF loading are analogous to the plastic and/or unstable behaviour of structural members like beams, columns and braces (Elchalakani et al. 2003, Choi and Park 2010, Nip et al. 2010b). HSS beam and columns in seismic low and mid-rise frames provide large beneficial assistance in terms of reduced seismic weight, lesser surface area per length of the member, decreased lateral bracing, applications in modular construction and unique retrofit techniques (Nishikawa et al. 1998, Fadden and McCormick 2014). Also, thin-walled steel HSSs are being preferred over their reinforced concrete counterparts because of their higher stiffness to cross-sectional area ratio. Severe earthquakes like 1985 Mexico City and 1995 Hyogo-ken-Nanbu (Kobe) earthquakes have shown that these HSS components are pregnable to local buckling under cyclic lateral loading (Bruneau et al. 1996, Bruneau 1998).

After the 1994 Northridge and the 1995 Hyōgo-ken Nanbu (Kobe) earthquakes, the seismic design codes were revised to account for larger deformation ductility demands to structures (FEMA 350 2000, Midorikawa et al. 2003). Ductility and energy-absorption capacity are

important elements of seismic resistant steel member design. Nowadays, for economic reasons, the concept of ductility-based design has become cardinal during the design of structural resistance to severe earthquakes, which is a shift away from the strength-based design. Ductility is the parameter that personifies the maximum deformability of a structure or structural member under various loading conditions without collapsing or failure. The ductility-based design draws attention to both strength and ductility. The design strength of a section can be substantially reduced if it can provide a good deformation capacity beyond the elastic limit.

Today, fatigue design rules are present in many different Eurocode parts: EN 1993-1-9 (2005), EN 1993-1-11 (2006), EN 1993-2 (2006), *etc*. General design rules for earthquake resistant structures, including a section for steel structures, are specified in EN 1998-1 (2004) and AISC 341-16 (2016). All these standards are based on the recommendations of the European Convention for Constructional Steelwork (ECCS/CECM/EKS) for steel (ECCS 1986).

2.5.2 HSS Members under Cyclic Axial Load

In the early days, models were proposed to predict the area under the hysteresis loops, which represents the amount of energy dissipation of structural members under cyclic loading. It was understood that the non-dimensional global slenderness ratio $\bar{\lambda}$ was the most important parameter influencing the energy dissipation and fracture life-based on the hysteretic behaviour of braces (Popov et al. 1979, Jain et al. 1980, Popov and Black 1981). Codes typically impose an upper limit on $\bar{\lambda}$ of bracing members in Concentrically Braced Frames (CBFs), which is specified as 2.0 in EC8 (EN 1998-1 2004). $\bar{\lambda}$ can be expressed as follows:

$$\bar{\lambda} = \sqrt{\frac{N_y}{N_{cr}}} = \sqrt{\frac{A \times f_{y.mea}}{N_{cr}}} = \sqrt{\frac{P_M \times t \times f_{y.mea}}{N_{cr}}} \tag{2.36}$$

where, $f_{y.mea}$ is the measured material tensile yield stress and A is the cross-sectional area. While N_{cr} is the elastic critical buckling load of the member (Yoo and Lee 2011).

Various experimental programs (summarised in Table 2.4) conducted on SHS, RHS and CHS bracing members under cyclic loading revealed that their geometric and material properties affect the corresponding hysteresis behaviour and fracture life of the brace. These studies also revealed that the drop in compressive resistance was more rapid in slender members than stocky

members, resulting in a few cycles of inelastic response and a smaller amount of energy dissipation. However, braces with higher $\bar{\lambda}$ values exhibited a delayed local buckling, resulting in less deterioration in the buckling strength at the mid-length plastic hinge and thus longer fracture life. Results of all the experimental tests summarised in Table 2.4 indicated a decrease in the maximum compressive load capacity with an increasing number of cycles, with the largest reduction occurring after the first buckling cycle. These studies also unveiled that all the specimens exhibited residual elongation with most of the tensile elongation and inelastic strains within the mid-length plastic hinge zone (Tremblay 2002).

Besides gauging the post-buckling compressive resistance, lateral deflection at plastic hinge near mid-length, and cyclic energy dissipation at various displacement ductility levels, Lee and Goel (1987), Tang and Goel (1989), Archambault et al. (1995), Shaback and Brown (2003), Goggins et al. (2005, 2006), Nip et al. (2010b), Haddad et al. (2011b) and Xu et al. (2020), *etc.*, have also evaluated the fracture life of hollow steel braces. However, gradually, the attention later altered towards the fracture ductility from the failure features and fracture life. Shaback and Brown (2003) and Huang (2009) observed that the bracing members with a smaller local slenderness ratio fractured later than those with a larger local slenderness ratio. Goggins et al. (2006) and Haddad et al. (2011b) independently focussed on the estimation of the cyclic energy life of the specimens by conducting the experiments on SHS and RHS bracing members. Apart from experimenting on carbon steel HSS braces, Nip et al. (2010b) conducted experimental investigations on stainless steel HSS bracing members and found that the stainless steel members exhibited higher energy dissipation at higher ductility levels.

2.5.3 HSS Members under Cyclic Bending Load

Unlike the number of testing programs conducted for studying the cyclic axial performance of HSSs, the number of testing programs conducted for studying their cyclic bending performance is limited. Apart from the cyclic hardening properties of the steel, the cross-sectional slenderness parameters such as width-to-thickness and depth-to-thickness ratios play a crucial role in the cyclic bending performance of the HSSs (Elchalakani et al. 2004, Guerrero et al. 2007, Fadden and McCormick 2014). It is understood that steel beams need to undergo a ductile flexural pattern with a high cyclic rotation capacity essential to ensure that a determined portion of the input seismic energy is dissipated by inelastic cyclic behaviour. Rotation capacity

represents the ability of a flexural member to fulfil the rotational prerequisite in terms of rotation ductility. Elchalakani et al. (2004) conducted cyclic bending tests on cold-formed carbon-steel (CF-CS) CHSs and determined fully ductile section slenderness limits for the respective target structure ductility index values suitable for the seismic-resistant design specified in the New Zealand (NZS 1170.5 2004) and European (EN 1998-1 2004) codes.

Lee et al. (2001) and Chang and Pan (2009) conducted cyclic bending experiments on stainless steel CHSs and examined the effect of ovalisation (Change in diameter of the section in the plane of bending). Lee et al. (2001) also observed that the magnitude of the maximum ovalisation reached was higher in sections with higher cross-section slenderness than those with lower cross-section slenderness. Brescia (2008) conducted cyclic bending tests on RHS moment-restraint connections and observed that the plastic hinge typically forms at a distance of 1.2 times the flange width from the base of the connection. An extensive experimental study by D'Aniello et al. (2012) on CS RHS cantilever beams revealed that cyclic rotation capacity is much lower than monotonic rotation capacity. D'Aniello et al. (2012) interpreted that cyclic rotation capacity (*or* cyclic ductility) is influenced by cross-section slenderness. While cyclic flexural over-strength is influenced by the post-yield cyclic hardening properties of steel. Further, D'Aniello et al. (2012) proposed empirical formulations for cyclic rotation capacity and cyclic flexural over-strength of RHSs. Shariati et al. (2014) experimentally analysed the effect of the cut-out on cyclic flexural bending moment and energy dissipation of stainless steel (SS) CHS cantilever members.

After a comprehensive FE study on cold-formed carbon steel (CF-CS) RHSs under cyclic bending load, Fadden and McCormick (2014) proposed 12.1 and 28.4 as limiting width-to-thickness and depth-to-thickness ratios, respectively for the sections to have 80% of the overall maximum moment at a cyclic rotation level of 0.04 rad. As per FEMA-350 (2000) and the AISC seismic design provisions (AISC 360-16 2016, ANSI/AISC 341-16 2016, ANSI/AISC 358-16 and ANSI/AISC 358-18s 2018) for special moment resisting frames, a fully restrained connection in a steel moment-resisting frame must be able to possess 80% of its maximum overall moment at an interstory drift of 0.04 rad and can completely fail to exhibit almost zero resistance beyond an interstory drift of 0.06 rad.

2.5.4 HSS Members under Combined Cyclic Bending and Axial Loads

An understanding of the cyclic bending behaviour of HSSs is essential for moment frame systems to ensure strong-column weak-beam design requirements (Brescia 2008, Wang et al. 2008). The collapse mechanism of medium-to-low rise steel frames is designed to ensure the formation of plastic hinges at both the beam ends and at the column bases (Akiyama 1985, AIJ 1990, Mazzolani and Piluso 1997, Gioncu and Mazzolani 2013). Compared with the beam hinges, the column bases are more critical and their behaviour is more complex due to the presence of varying axial loads (Wang et al. 2008).

To date, a very limited number of quasi-static cyclic load testing programs (Hashimoto et al. 1996, Nishikawa et al. 1996, 1998, Mamaghani et al. 1997, Nakamura et al. 1997, Usami and Ge 1998, Kurata et al. 2005, Nakashima and Liu 2005, Mamaghani 2008, Fang et al. 2018) on steel HSS columns were carried out to examine their cyclic plastic deformation behaviour under the presence of axial compressive load. Usually, these tests were continued until the specimens completely lost their axial load capacities. Strength deterioration induced by local buckling and collapse limit of the test specimens were quantified in terms of the local slenderness and axial load ratios. Except for Nakashima and Liu (2005), Kurata et al. (2005), and Fang et al. (2018) others performed studies on CHS and RHS bridge pier specimens. While Nakashima and Liu (2005) and Kurata et al. (2005) performed tests on SHS moment frame column specimens. To date, only Fang et al. (2018) analysed the cyclic behaviour of EHS columns. Besides reiterating the importance of global and local section slenderness limits, these studies have also focussed on other important facets like ductility and energy dissipation capacities and the interaction between axial load and moment due to lateral cyclic bending.

2.6 SUMMARY

An overview of the subject areas which are focussed within the research of this thesis, in particular, the cross-section classification of EHS members and the material model to be employed during the FE study are presented. It is learnt that the equivalent CHS diameter formulae (Equations 2.20–2.23) intended to be used for classifying the cross-section of EHS members are inconsistent and highly conservative. To date, no internationally recognised design standard provides guidelines for classifying the EHS cross-sections and the design of EHS members.

From the 1980s to the 2010s, different testing protocols are developed and employed to determine the cyclic performance to prove the adequacy of structural detail to fulfil the demands of local ductility as specified by seismic design recommendations in a conservative, yet not too conservative manner. Nonetheless, there can be no unique and "the best" cyclic loading history because no two seismic actions are alike. The cyclic loading histories of these four protocols (see Figure 2.7) presented herein are rather similar and are expected to produce similar performance assessments (Krawinkler 2009). But, the SAC (2016) and FEMA 461 (2007) protocols shall be used to test beam-column assemblies, and frame assemblies only. While the ECCS (1986) and ATC-24 (1992) protocols are preferable for testing the steel components (bracing elements) which are likely to be subjected to cyclic axial displacement loadings.

Post the 1994 Northridge and the 1995 Hyōgo-ken Nanbu Kobe earthquakes, capacity design provisions are included in most modern seismic design specifications to ensure reasonable ductility and energy dissipation capacities in seismic resisting systems. The performance of HSSs under cyclic loading is being estimated in terms of vital facets like the cyclic resistance, displacement/rotation ductility, and energy dissipation capacities; and the interaction among various externally applied loads based on the extent of cyclic plastification of the material at the local buckling zone. Thus, the cross-sectional slenderness of the structural members plays an important role under cyclic loading. During the first two decades of the 21st century, due to the time-saving and financial reasons, there is an increasing trend in conducting FE studies to analyse the cyclic behaviour of HSS members by employing the NLCHM model parameters.

To date, only Fang et al. (2018) carried out cyclic tests on EHS members. In light of the increasing implementation of EHSs into the light-weight structural configurations, there is a lack of sufficient reliable research and design guidelines for their cross-section classification and cyclic performance. So, the improvement of the equivalent CHS diameter formulae for various loading conditions and the understanding of the cyclic behaviour of EHS members are essential to promote their consistent application.

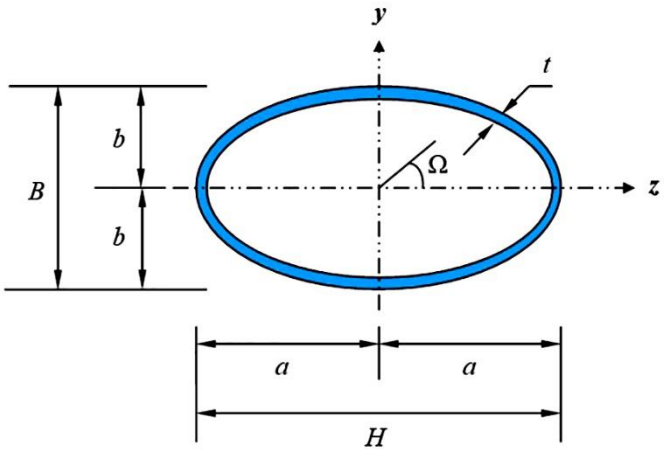

Figure 2.1 *Basic cross-sectional profile of an EHS*

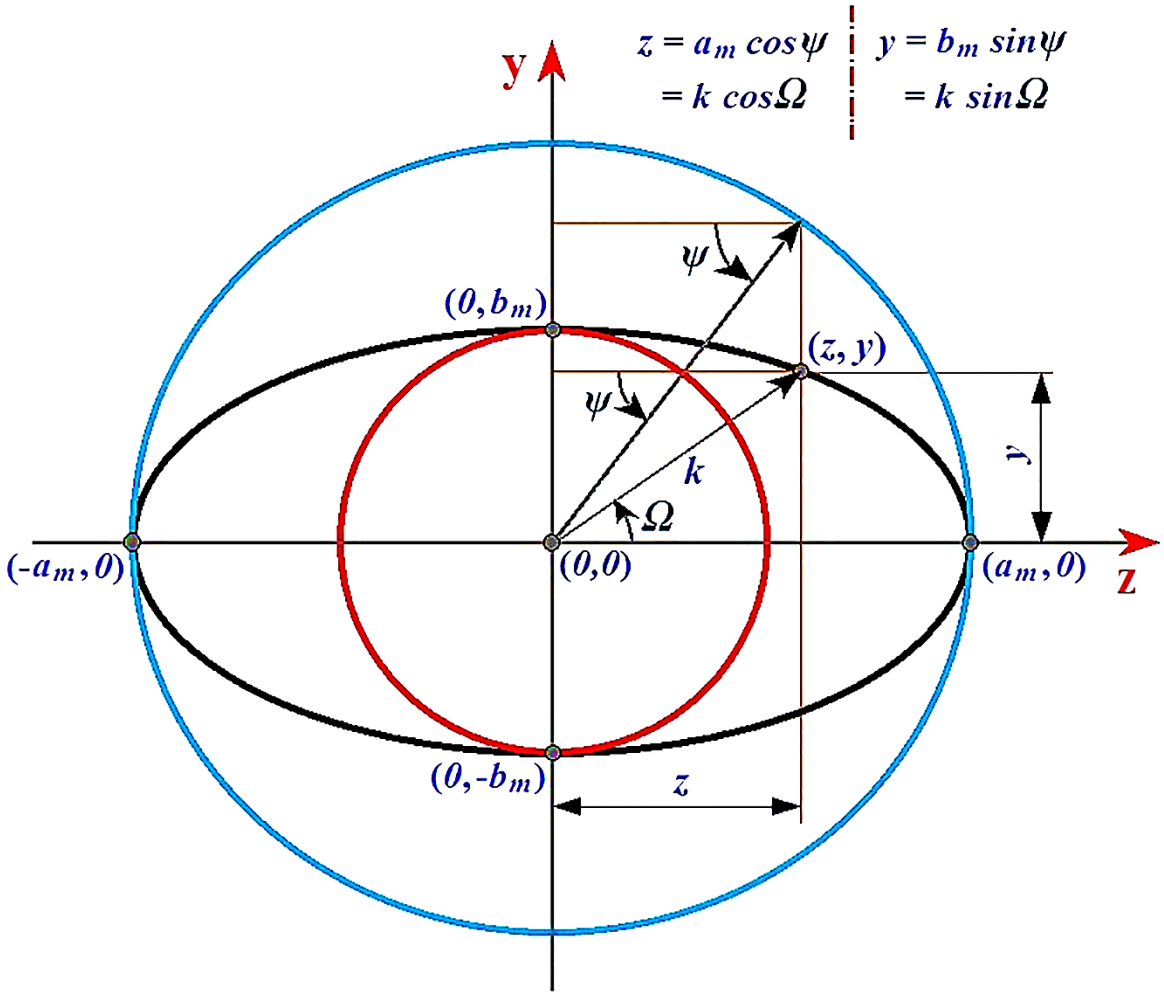

Figure 2.2 *Mid-surface (or median) profile of an EHS cross-section*

.

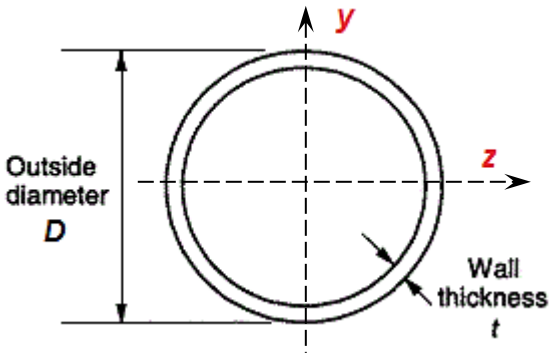

Figure 2.3 *Basic cross-sectional profile of a CHS*

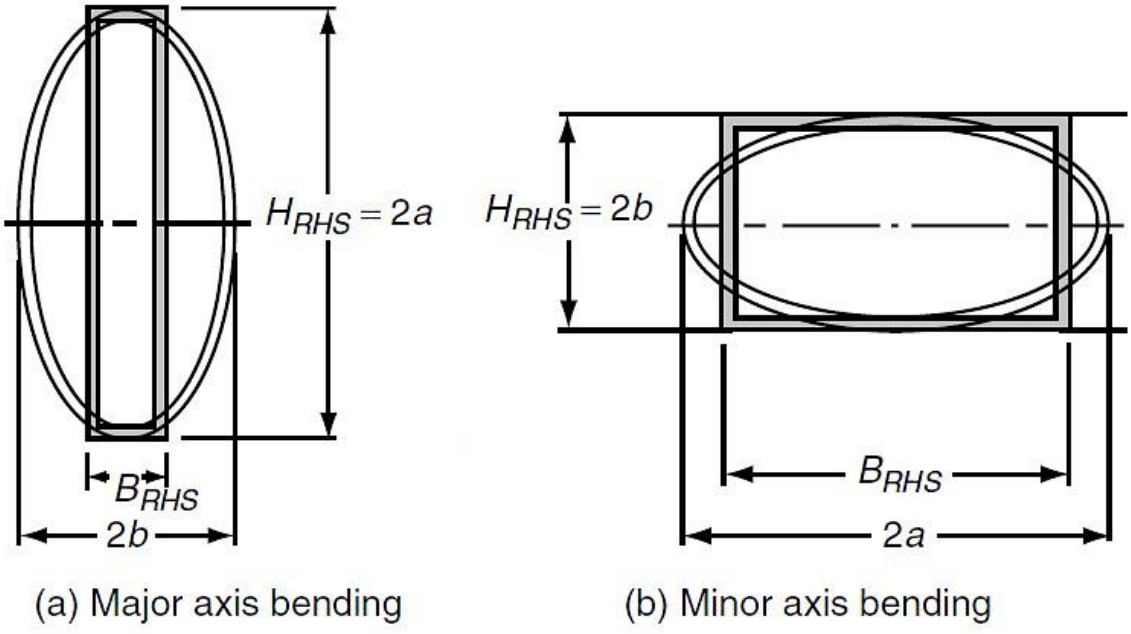

Figure 2.4 *Graphical interpretation of typical cross-sectional profiles of EHS and the respective equivalent RHS without corner radii*

[**Source:** Haque et al. (2012)]

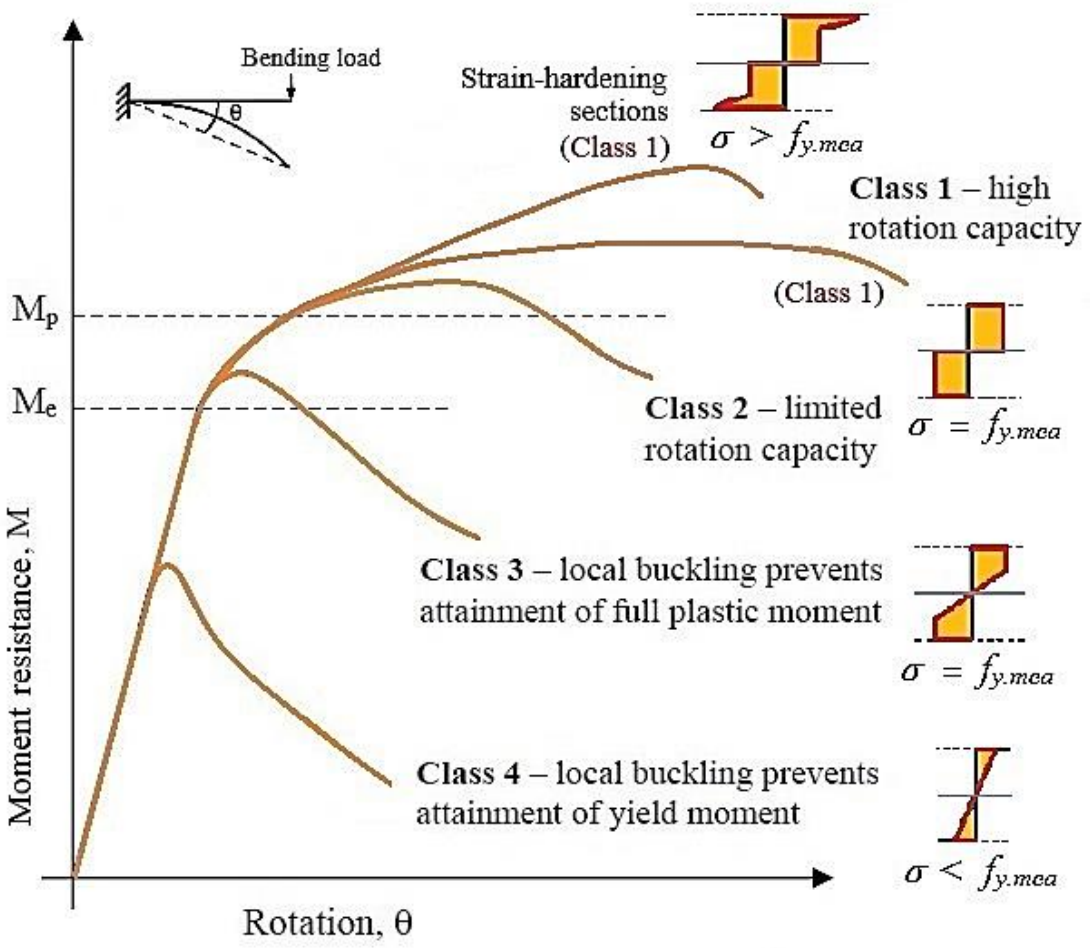

Figure 2.5 *Typical moment-rotation response of CHSs under bending*

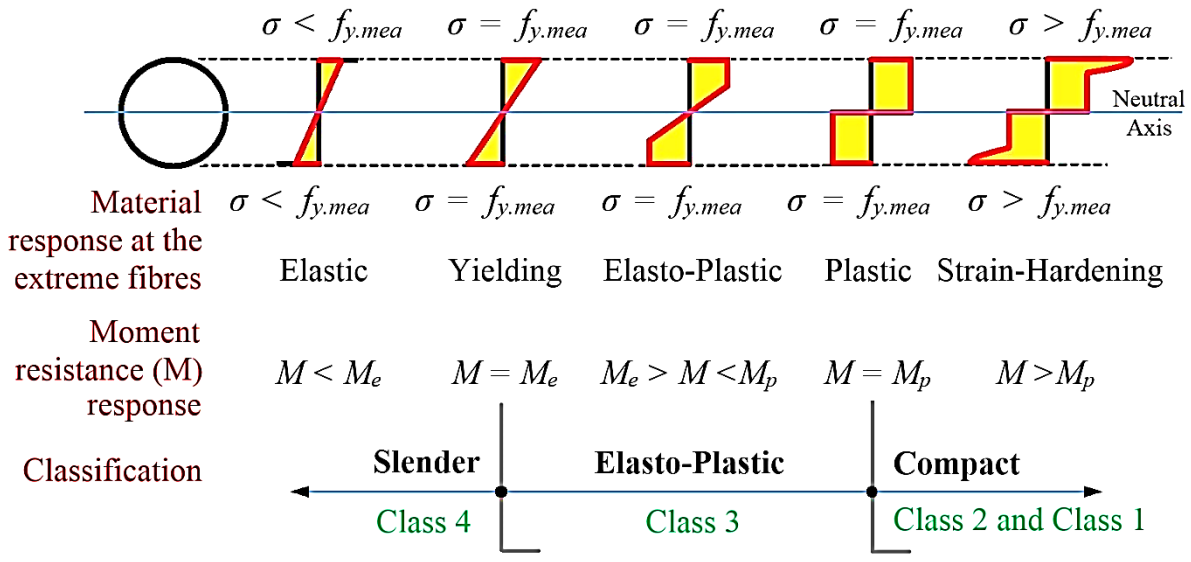

Figure 2.6 *Typical ultimate state stress blocks of CHSs under bending*

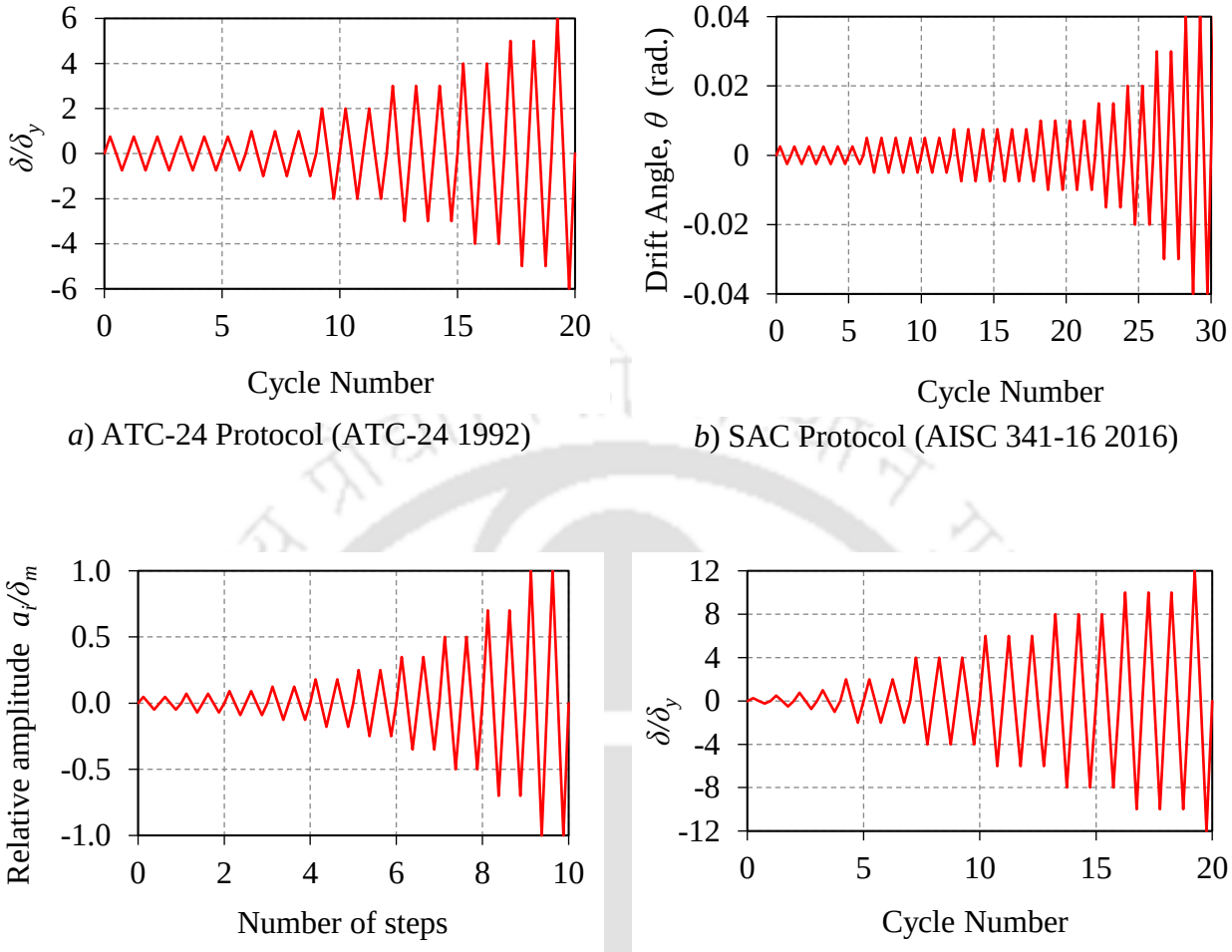

a) ATC-24 Protocol (ATC-24 1992)

b) SAC Protocol (AISC 341-16 2016)

c) FEMA 461 Protocol (FEMA 2007)

d) ECCS Protocol (ECCS 1986)

Figure 2.7 *Strain-controlled quasi-static cyclic loading histories for steel components*

Table 2.1 *Approximate formulae for determining the cross-sectional properties of EHSs*

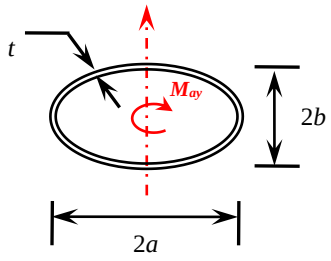	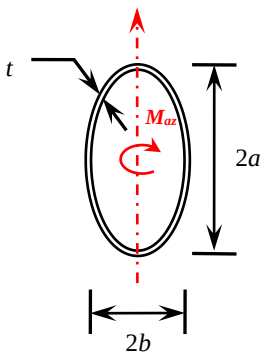
Major axis bending (*or*) Bending moment about the minor axis	Minor axis bending (*or*) Bending moment about the major axis
$r_{g.y}=\frac{1}{2}\times\sqrt{\frac{a^3b-(a-t)^3(b-t)}{ab-(a-t)(b-t)}}$	$r_{g.z}=\frac{1}{2}\times\sqrt{\frac{ab^3-(a-t)(b-t)^3}{ab-(a-t)(b-t)}}$
$A=P_M\times t$	$A=P_M\times t$
$I_y=\frac{A}{4}\times\left[\frac{a^3b-(a-t)^3(b-t)}{ab-(a-t)(b-t)}\right]$	$I_z=\frac{A}{4}\times\left[\frac{ab^3-(a-t)(b-t)^3}{ab-(a-t)(b-t)}\right]$
$W_{ey}=\frac{A}{4a}\times\left[\frac{a^3b-(a-t)^3(b-t)}{ab-(a-t)(b-t)}\right]$	$W_{ez}=\frac{A}{4b}\times\left[\frac{ab^3-(a-t)(b-t)^3}{ab-(a-t)(b-t)}\right]$
$W_{py}=\frac{4A}{3\pi}\times\left[\frac{a^2b-(a-t)^2(b-t)}{ab-(a-t)(b-t)}\right]$	$W_{pz}=\frac{4A}{3\pi}\times\left[\frac{ab^2-(a-t)(b-t)^2}{ab-(a-t)(b-t)}\right]$

Table 2.2 *Cross-section classification slenderness limits for CHSs under axial compression and bending loading cases specified in various international design standards*

Design Standard	Slenderness parameter	Axial-compression	Bending	
		Yield limit	Compact limit	Yield limit
AS 4100:1998 (2016)	$\bar{\lambda}_{cs.IA}$	82	50	120
IS 800 (2007)	$\bar{\lambda}_{cs.IA}$	88	52	146
EN 1993-1-1 (2005)	$\bar{\lambda}_{cs.E}$	90	70	90
AISC 360-16 (2016)	$\bar{\lambda}_{cs}$	0.11	0.07	0.31
CSA S16-14 (2014)	$\bar{\lambda}_{cs}$	0.11	0.0857	0.3143

Table 2.3 *NLCHM model parameters and other mechanical properties of various metallic materials*

Metallic material	Source	E (**GPa**)	υ	$f_{y.mea}$ (**MPa**)	No. of backstresses	$\sigma\|_0$ (**MPa**)	C_{kin} (**MPa**)	γ_{kin}	Q_∞ (**MPa**)	b_{iso}
1200 Gr. UHS	Javidan et al. (2017)	209	0.30	1247	1	1110	140200	239.45	296.6	16.55
HSA/HSB800	Javidan et al. (2017)	205	0.30	772	1	740	30990	141.15	196.5	14.55
EH47	Jiang et al. (2017)	190	0.30	534	1	500	296717	4815	132	122
API X65	Li et al. (2017) and Pereira et al. (2016)	207	0.30	595	3	468	75000 6000 50	900 35 2	55.63	3.53
R7T	Halama et al. (2012a)	175	0.30	515	2	500	264156 20973	873 1	-320	30
TRIP 700	Broggiato et al. (2008)	195	0.30	513	1	483	16100	129.8	51.4	24.8
20MnMoNi55	Pirondi et al. (2006)	200	0.29	495	1	429	11431	128.9	-41.5	0.1141
G40.21-350WT	Tremblay et al. (2006)	206	0.30	367	1	352	8000	75	110	4
ASTM A500 Gr.B	Fell (2008)	201	0.30	462	1	462	2220	25	81	5.7
ASTM A53 Gr.B	Fell (2008)	201	0.30	359	1	345	3372	26	90	7
BCR295	Suzuki (2018)	198	0.30	420	1	430	1236	14	0	0
DP 600	Broggiato et al. (2008)	182	0.29	415	1	349.4	17400	125.9	50.1	27.5
ASTM A992	Fell (2008)	201	0.30	399	1	345	3448	38	118	5
ASTM A572 Gr.50 / HSLA50-HDG	Taherizadeh et al. (2009)	204	0.29	412	1	394.5	5000	140	180	7
ASTM A572Gr.50	Wen (2012)	205	0.30	380	2	362	3625 711	39.46 3.39	417	4.53
CSA 300W (44W)	Wen (2012)	207	0.30	336	2	332	3965 583	29.30 2.37	448	3.03
S355J2H	Nip et al. (2010a)	215	0.30	385	1	461	23554	139	55	2.38
S235JRH	Nip et al. (2010a)	205	0.30	410	1	282	122400	430	35	1.12
S355	Krolo et al. (2016)	185	0.30	390	3	386	5327 1725 1120	75 16 10	20.8	3.2
S275/ ASTM 529 Gr.42	Krolo et al. (2016)	207	0.30	333	3	285	13921 4240 1573	765 52 14	25.6	4.4
Q345B	Shi et al. (2013)	205	0.30	383	4	363.3	7993 6773 2854 1450	175 116 34 29	21	1.2
Q460C	Shi et al. (2013)	208	0.30	489	4	444	4924 3101 2730 1450	154 120 31 26	25	1.2
ASTM A992	Elkady and Lignos (2015)	205	0.30	383	1	369	6895	25	172	2
ASTM A653 Gr.50 / ZAR-345	Padilla-Llano et al. (2015)	203.4	0.30	369	1	416.6	114.7	3.012	295.9	3.468
ASTM A106B	Zakavi et al. (2017)	209	0.30	328	1	257.4	2763.69	17.66	135.9	4.76
ASTM A36	Payne (2000)	190	0.28	285	1	351.6	3447	50	137.89	10

Table 2.3 (**Cont'd.**)

Metallic material	Source	E (**GPa**)	υ	$f_{y.mea}$ (**MPa**)	No. of backstresses	$\sigma\|_0$ (**MPa**)	C_{kin} (**MPa**)	γ_{kin}	Q_∞ (**MPa**)	b_{iso}
JIS SS400	Jin et al. (2016)	200	0.26	265	2	256	1617.2 54	10.7 0	320	20
BS-4360-43A	Zakavi et al. (2010)	209	0.30	305	1	261	2473.36	24.62	82.16	3.74
AISI/SAE 1010 cold-rolled	Doghri (1993)	210	0.30	305	1	200	25500	81	2000	0.26
LYP SLY100 /Q100 / LY100	Wang et al. (2016)	193	0.30	88	4	48	32123 630 128 482	850 89 20 0.5	198	5
AKDQ-HDG	Taherizadeh et al. (2009)	207	0.31	189	1	158.5	2500	50	210	8
AISI 325/A 276 /UNS S32550 /EN 1.4507/F255	Broggiato et al. (2008)	190	0.29	585	1	371.8	18300	39.5	61.3	33.6
EN 1.4301/1.4307	Nip et al. (2010a)	195	0.29	510	1	237	105800	224	478	1.49
S220503/ S31803/ EN 1.4462	Chang et al. (2019)	226	0.29	532	4	299	65020 41222 31286 23210	662 417 319 249	62	6.6
SS 316	Dutta et al. (2010)	193	0.28	267	1	225	42096	594.45	60	9.71
SS 316L	Halama et al. (2012b)	193	0.28	258	5	130	456250 70520 17380 7670 5860	21538 3373 1451 771 459	225	12
SS 304	Badnava et al. (2012)	193	0.31	288	3	225	63000 41000 1650	8950 500 6	215	15
SS316 L (N)	Roy et al. (2012)	200	0.29	275	1	211	57805	619.04	42.3	21.6
S31608/ AISI 316 /EN 1.4401	Wang et al. (2014)	208	0.30	338	1	234	56760	420	77	10.5
SS 304L	Zehsaz et al. (2016)	198	0.31	288	1	236.7	4402.7	11.04	109.6	17.8
SA 333 Gr.6 C-Mn	Bhowmick and Shit (2016)	200	0.30	304	1	275	32000	214	18.5	2.5
SPRC	Zhao and Lee (2000)	155	0.30	256	1	240	14600	125	12.3	26.6
SPCEN	Zhao and Lee (2000)	153	0.30	137	1	108	23700	416	35.7	67.8
XN40F	Leen et al. (2010)	162	0.28	172	1	125	82000	656	50	35
CuAg0.10 EN H040 R220 alloy	Novak et al. (2015)	117	0.34	130	1	74	46250	617.2	-72.3	2.352
Al 7075-T6 alloy	Agius et al. (2017)	69	0.33	495	3	465	41 71 2100	35.304 242 0	15	6.8
7A04 Al alloy	Wang and Wang (2016)	72	0.32	545	3	521.11	83.92 33.33 12.74	0.78 0.80 0.88	60.2	26.63
AA6022-T43	Taherizadeh et al. (2009)	69	0.33	159	1	136	1400	20	110	7.5
EN AW-5754-O Al alloy	Chaparro et al. (2008)	68	0.33	106	1	73.2	60.5	117.5	146.8	9.6

Table 2.4 *Summary of experimental investigations on HSS tubes under cyclic axial loading*

Reference	Cross-section	Brace Material
Popov et. al. (1979)	CHS	carbon steel
Black et al. (1980)	SHS and CHS	carbon steel
Jain et al. (1980)	SHS and RHS	carbon steel
Popov and Black (1981)	SHS and CHS	carbon steel
Gugerli (1982)	RHS	carbon steel
Lee and Goel (1987)	SHS	carbon steel
Archambault et al. (1995)	SHS and RHS	carbon steel
Walpole (1996)	RHS	carbon steel
Elchalakani et al. (2003)	CHS	carbon steel
Shaback and Brown (2003)	SHS	carbon steel
Yang and Mahin (2005)	SHS	carbon steel
Goggins et al. (2006)	SHS and RHS	carbon steel
Fell et al. (2006)	SHS and CHS	carbon steel
Han et al. (2007)	SHS	carbon steel
Tremblay et al. (2008)	RHS and CHS	carbon steel
Nip et al. (2010b)	SHS and RHS	carbon and stainless steels
Huang (2009)	SHS	carbon steel
Haddad et al. (2011b)	SHS	carbon steel
Takeuchi and Matsui (2011)	CHS	carbon steel
Gabor et al. (2012)	CHS	carbon steel
Sheehan and Chan (2014)	CHS	carbon steel

CHAPTER 3

ELLIPTICAL-HOLLOW-SECTIONS UNDER AXIAL COMPRESSION

In this chapter, the suitability of the equivalent Circular-Hollow-Section (CHS) diameter expressions for the Elliptical-Hollow-Sections (EHSs) under pure axial compression proposed in earlier studies is assessed with-respect-to the EC3: EN 1993-1-1 (2005) CHS cross-section design criteria. Later, to promote consistent application of the cross-section slenderness parameter limits and design strength curves specified for CHSs, also to the EHSs, an improved empirical expression for the equivalent CHS diameter is derived using the data of EHS stub column analyses from the literature, based on a novel Equivalent-Resistance-Capacity-Method (ERCM). Additionally, a unified empirical expression based on the Direct-Strength-Method (DSM) approach for predicting the axial compressive capacity is also determined by using an exhaustive data of EHS and CHS stub-column analyses from the literature.

3.1 EQUIVALENT CHS DIAMETER

Ever since Gardner and Chan (2007), Chan and Gardner (2008b) and Ruiz-Terán and Gardner (2008) proposed expressions (Equations 2.20 and 2.21) for the equivalent CHS diameter of EHS, many additional independent experimental and FE programs (Zhao and Packer 2009, Gardner et al. 2011, Lam and Testo 2011, Haque and Packer 2012, Jamaluddin et al. 2013, Chan et al. 2015, McCann et al. 2016, Liu et al. 2017, Cai et al. 2018, Chen and Young 2018) were carried out on EHS stub-columns. But, Ruiz-Terán and Gardner (2008) proposed Equations 2.21a and 2.21b as an improvement. Yet, Zhao and Packer (2009) reported significant conservatism involved in using those Equations 2.21a and 2.21b for predicting the maximum cross-sectional axial compressive strength, $F_{cr.max}$. Therefore, firstly, the efficiency of the Equations 2.21a and 2.21b is assessed by utilizing all the available data from the EHS stub column studies (see Tables 3.1 and 3.2) carried out till date while verifying consistency with the CHS cross-section classification criteria specified in EC3: EN 1993-1-1 (2005). The data including geometrical, material and other cross-sectional strength properties of the tested EHS stub-columns and EHS stub-column FE models from the literature are calibrated and catalogued in this chapter using the formulae provided in Section 2.2.1.

The plot in Figure 3.1 contains the data of the respective ratio of maximum axial compressive strength, $F_{cr.max.}$ to the axial yield capacity, N_y $\left(= A \cdot f_{y.mea}\right)$ against the equivalent CHS slenderness, $\frac{D_{eq.c2}}{t\varepsilon^2}$ (also catalogued in Table 3.1) using Equations 2.21a and 2.21b. Vertical reference line indicates the slenderness limit $\left(=90\right)$, while the horizontal reference line indicates the theoretical limit $\left(=1.0\right)$ of $\frac{F_{cr.\max.}}{A.f_{y.mea}}$ ratio between yielding and non-yielding (Slender) CHSs under axial compression according to EC3: EN 1993-1-1 (2005).

Further, $\frac{F_{cr.\max.}}{A.f_{y.mea}}$ ratio values of EHS stub-column FE models of Chen and Young (2018) and EHS stub-column FE models with Class-A imperfections of McCann et al. (2016) listed in Table 3.2 are plotted against their respective equivalent CHS slenderness, $\frac{D_{eq.c2}}{t\varepsilon^2}$ (Tabulated in Table 3.2) using Equations 2.21a and 2.21b in Figures 3.2a and 3.2b, respectively. It is

understood that McCann et al. (2016) performed FE study on slender (Class 4) EHSs under axial compression by considering perfectly elastic-plastic material model and then proposed different cross-sectional strength curves with-respect-to the cross-sectional aspect ratio of EHSs after using Equation. 2.20 for obtaining the cross-section slenderness values.

The dotted bordered box and the triangle in Figures 3.1 and 3.2a respectively, both starting from the slenderness limit of 90 (*i.e.*, at $\frac{D_{eq.c2}}{t\varepsilon^2} = 90$) suggests significant conservatism in using Equations 2.21a and 2.21b. Also, Chen and Young (2018) found that the influence of residual stress on the structural response of cold-formed steel EHS stub-columns is negligible. Although Equations 2.21a and 2.21b are proposed by Ruiz-Terán and Gardner (2008) in an attempt to align the $\frac{F_{cr.\max.}}{A.f_{y.mea}}$ data of EHSs consistently towards the CHS classification criteria (*i.e.*, EHS columns with $\frac{a}{b} = 1$), a scatter of data with-respect-to $\frac{a}{b}$ is significantly observed in Figure 3.2b.

3.1.1 Equivalent-Resistance-Capacity-Method (ERCM)

The equivalent CHS diameter of an EHS can be obtained for distinct variables like cross-sectional area; the radius of curvature at the point of initiation of local buckling, *e.g.*, Chan and Gardner (2008a, 2008b), Gardner and Chan (2007); normalized cross-sectional resistance capacity; *etc*. Also, the cross-section classification criteria are governed by the limiting state resistance capacity of the effective portion due to local buckling and material-strain-hardening effects, *e.g.*, Mazzolani et al. (1999), Gardner and Nethercot (2011). Thus, the expression in Equation 3.1 for D_{eq} of an EHS under axial compression is derived based on the Equivalent-Resistance-Capacity-Method (ERCM) to bring into the use of CHS slenderness classification limits to EHSs too.

$$D_{eq} = D_{eq.c3} = 2a\left[0.1011\frac{a^2}{b^2} - 0.0774\frac{a}{b} + 0.9763\right]\left(\frac{t}{P_M}\right)^{118.35-\sqrt{118.38^2-\left(\frac{a}{b}-3.64\right)^2}} \quad (3.1)$$

According to ERCM, both the EHS and the respective equivalent CHS with outer diameter $D_{eq.c3}$ based on Equation 3.1 shall exhibit the same value of $\frac{F_{cr.\max.}}{A.f_{y.mea}}$, provided both the EHS and CHS have the same $f_{y.mea}$ and t values. Equation 3.1 is obtained empirically based on ERCM by using t, P_M, a, $\frac{a}{b}$, $\frac{F_{cr.\max.}}{A.f_{y.mea}}$ values of EHS stub-columns from Tables 3.1 and 3.2 and slenderness limit (*i.e.*, $\frac{D_{eq.c3}}{t\varepsilon^2}=90$ for $\frac{F_{cr.\max.}}{A.f_{y.mea}}=1$) between EC3: EN 1993-1-1 (2005) Class 3 and Class 4 CHS cross-sections. Similar to Equations 2.21a and 2.21b, $D_{eq.c3}$ in Equation 3.1 is also dependent on relative thickness, $\frac{t}{P_M}$ and cross-section aspect ratio, $\frac{a}{b}(=r)$ of EHS.

$\frac{F_{cr.\max.}}{A.f_{y.mea}}$ values of EHS stub-column models of Chen and Young (2018) and EHS stub-column models with Class A imperfections of McCann et al. (2016) listed in Table 3.2 are plotted against their respective newly proposed equivalent CHS slenderness $\left(\frac{D_{eq.c3}}{t\varepsilon^2}\right)$ using Equation 3.1 in Figures 3.3a and 3.3b, respectively. Also, the $\frac{F_{cr.\max.}}{A.f_{y.mea}}$ ratio values of EHS stub-columns tested in various experimental programs listed in Table 3.1 are plotted against their $\frac{D_{eq.c3}}{t\varepsilon^2}$ values in Figure 3.4. The conservatism observed in Figures 3.1 and 3.2a because of using Equations 2.21a and 2.21b is significantly reduced in Figures 3.3a and 3.4 by using Equation 3.1. Also, the scatter observed in Figure 3.2b is significantly reduced in Figure 3.3b. Further, it is to be noted that Equation 3.1 is best applicable for EHSs with $\frac{a}{b}(=r)$ values ranging between 1.0 and 3.5.

Zhao and Packer (2009) adopted the equivalent RHS approach by assuming the major axis diameter, *2a* of EHS as the depth, H_{RHS} (larger dimension between cross-sectional depth and width) of the equivalent RHS to assess the slenderness of the EHS section under pure axial compression (see Equation 2.25). Zhao and Packer (2009) and Haque et al. (2012) concluded that adopting the equivalent RHS approach in determining the cross-section slenderness for

EHSs with $\frac{a}{b}(=r)$ of 2.0 showed good compatibility towards the EC3: EN 1993-1-1 (2005) RHS classification criteria under pure compression. The RHS cross-section slenderness, $\bar{\lambda}_{RHSc}$ under axial compression is calibrated as per the following expression.

$$\bar{\lambda}_{RHSc} = \frac{H_{RHS} - 3t}{t\varepsilon} = \frac{2a - 3t}{t\varepsilon} \tag{3.2}$$

In Figure 3.5, $\frac{F_{cr.\max.}}{A.f_{y.mea}}$ ratio values of EHS stub-columns tested in various experimental programs listed in Table 3.1 are plotted against their respective $\bar{\lambda}_{RHSc}$ values (calibrated in Table 3.1). Comparing Figure 3.4 with Figure 3.5, quite similar cross-sectional classification of EHSs is observable based on the proposed equivalent CHS slenderness using Equation 3.1 and the equivalent RHS slenderness using Equation 3.2 proposed by Zhao and Packer (2009). Therefore, it is recommended that Equation 3.1 can be preferably used to classify the EHS cross-sections under axial compression.

3.2 AXIAL COMPRESSIVE CAPACITY

3.2.1 Capacity Prediction Curves

In addition to the data of EHS stub-column members in Tables 3.1 and 3.2, test data of CHS stub column sections obtained from the literature (see Tables 3.3 and 3.4) are also used to derive a unified expression to predict the cross-sectional axial-compressive-resistance-capacity for local buckling and strain hardening, $F_{cr.LnS}$ of EHS and CHS members based on the DSM approach.

In addition to the machined hot-rolled seamless steel tube stub-column specimen data from Wilson and Newmark (1933), AISI S100-16C (2016) also consider manually fabricated hot-rolled steel specimen data from Wilson and Newmark (1933) and Wilson (1937). But the manual fabrication of a hollow cylindrical specimen from a very thin hot-rolled steel sheet using a weld can induce a large number of additional local imperfections which ultimately results in a significant reduction of cross-sectional strength. It is also understood that all the hollow cylindrical shell specimens of Wilson (1937) are longer than the maximum stub-column

length limit specified in EN 1993-1-3 (2006), AISI S902-13 (2013) and stub-column test memorandum from Ziemian (2010). Hence, only machined hot-rolled seamless steel tube specimens of Wilson and Newmark (1933) are considered in this study.

The cross-sectional non-dimensional slenderness parameters $\bar{\lambda}_{l.b}$, $\bar{\lambda}_{cs}$, $\bar{\lambda}_{cs.E}$ and $\bar{\lambda}_{cs.IA}$ for EHS (*or* CHS) members under axial compression with an equivalent diameter $D_{eq.c3}$ and wall thickness t are obtained in Tables 3.1–3.4 by substituting the respective $D_{eq}\left(=D_{eq.c3}\right)$ value from Equation 3.1 in Equations 2.32–2.35, respectively. $\frac{F_{cr.\max.}}{A.f_{y.mea}}$ values of EHS stub-columns listed in Tables 3.1 and 3.2 and CHS stub-columns listed in Tables 3.3 and 3.4 are plotted against their respective $\bar{\lambda}_{l.b}$ value in Figure 3.6 and against their respective $\frac{1}{\bar{\lambda}_{cs}}$ value in Figure 3.7. Using the data plotted in Figures 3.6 and 3.7, the proposed expressions for predicting $F_{cr.LnS}$ of EHS and CHS members based on DSM approach indicating a lower bound curve (also shown in Figures 3.6 and 3.7) for the $\frac{F_{cr.\max.}}{A.f_{y.mea}}$ values, barring few inconsistent data are calibrated and expressed in the following Equations 3.3–3.6.

$$\frac{F_{cr.LnS}}{A.f_{y.mea}}=\begin{cases}\dfrac{0.0413}{\bar{\lambda}_{l.b}}+\left(\dfrac{0.0985}{\bar{\lambda}_{l.b}}\right)^2-\left(\dfrac{0.0781}{\bar{\lambda}_{l.b}}\right)^3+0.7446 & if \quad 0.125\le\bar{\lambda}_{l.b}<0.5963\\ \dfrac{1.789-1.0069\bar{\lambda}_{l.b}+0.3527\bar{\lambda}_{l.b}^2}{1-0.2266\bar{\lambda}_{l.b}+1.9733\bar{\lambda}_{l.b}^2} & if \quad 0.5963\le\bar{\lambda}_{l.b}\le 2.4\end{cases} \tag{3.3}$$

$$\frac{F_{cr.LnS}}{A.f_{y.mea}}=\begin{cases}\left(\dfrac{1}{484.341\bar{\lambda}_{cs}}\right)^{0.5}+\dfrac{1}{85.149\bar{\lambda}_{cs}}-\left(\dfrac{1}{135.441\bar{\lambda}_{cs}}\right)^{1.5}+0.7446 & if \quad 0.02\le\bar{\lambda}_{cs}<0.4303\\ \dfrac{1.789-0.9152\bar{\lambda}_{cs}^{0.5}+0.2914\bar{\lambda}_{cs}}{1-0.206\bar{\lambda}_{cs}^{0.5}+1.6302\bar{\lambda}_{cs}} & if \quad 0.4303\le\bar{\lambda}_{cs}\le 6\end{cases} \tag{3.4}$$

$$\frac{F_{cr.LnS}}{A.f_{y.mea}} = \begin{cases} \left(\frac{1.845}{\bar{\lambda}_{cs.E}}\right)^{0.5} + \frac{10.4948}{\bar{\lambda}_{cs.E}} - \left(\frac{6.5979}{\bar{\lambda}_{cs.E}}\right)^{1.5} + 0.7446 & if \quad 16.9 \le \bar{\lambda}_{cs.E} < 384.554 \\ \frac{1598.686 - 27.3585\bar{\lambda}_{cs.E}^{-0.5} + 0.2914\bar{\lambda}_{cs.E}}{893.62 - 6.1581\bar{\lambda}_{cs.E}^{-0.5} + 1.6302\bar{\lambda}_{cs.E}} & if \quad 384.554 \le \bar{\lambda}_{cs.E} \le 5400 \end{cases} \tag{3.5}$$

$$\frac{F_{cr.LnS}}{A.f_{y.mea}} = \begin{cases} \left(\frac{1.7343}{\bar{\lambda}_{cs.IA}}\right)^{0.5} + \frac{9.8651}{\bar{\lambda}_{cs.IA}} - \left(\frac{6.202}{\bar{\lambda}_{cs.IA}}\right)^{1.5} + 0.7446 & if \quad 15.89 \le \bar{\lambda}_{cs.IA} < 361.48 \\ \frac{1502.76 - 26.525\bar{\lambda}_{cs.IA}^{-0.5} + 0.2914\bar{\lambda}_{cs.IA}}{840 - 5.9704\bar{\lambda}_{cs.IA}^{-0.5} + 1.6302\bar{\lambda}_{cs.IA}} & if \quad 361.48 \le \bar{\lambda}_{cs.IA} \le 5040 \end{cases} \tag{3.6}$$

Respective Plantema's (Plantema 1946) cross-sectional capacity, $F_{cr.Pl}$ values of EHS and CHSs are also calibrated and tabulated in Tables 3.1–3.4 according to Equation 3.7. Plantema's (Plantema 1946) prediction curve is also plotted in Figures 3.6 and 3.7 using Equations 3.7 and 3.8 for comparison purpose.

$$\frac{F_{cr.Pl}}{A.f_{y.mea}} = \begin{cases} 1 & if \quad \bar{\lambda}_{l.b} < 0.304 \\ \left(\frac{1}{5.72\bar{\lambda}_{l.b}}\right)^2 + 0.667 & if \quad 0.304 \le \bar{\lambda}_{l.b} < 0.604 \\ \left(\frac{1}{1.921\bar{\lambda}_{l.b}}\right)^2 & if \quad 0.604 \le \bar{\lambda}_{l.b} \end{cases} \tag{3.7}$$

$$\frac{F_{cr.Pl}}{A.f_{y.mea}} = \begin{cases} 1 & if \quad \bar{\lambda}_{cs} < 0.112 \\ \frac{0.037}{\bar{\lambda}_{cs}} + 0.667 & if \quad 0.112 \le \bar{\lambda}_{cs} < 0.441 \\ \frac{0.328}{\bar{\lambda}_{cs}} & if \quad 0.441 \le \bar{\lambda}_{cs} \end{cases} \tag{3.8}$$

3.2.2 Yield and Elastic Slenderness Limits

From Figure 3.6, the abscissa value of 0.2751 $\left(=\bar{\lambda}_{l.b}\right)$ at which the ordinate becomes unity for the proposed design curve that represents Equation 3.3 is chosen as the yield limit. The point of convergence of the two components of the cross-sectional axial-compressive-resistance-capacity curve defined by Equations 3.3–3.6 beneath the yield limit (see Figures 3.6 and 3.7) is assumed as the elastic limit. From Figure 3.6, the elastic limit is obtained as $\bar{\lambda}_{l.b}=0.5963$. The sections with the elastic limit as cross-section slenderness exhibit a cross-section capacity equal to 0.839 times of axial yield capacity, N_y $\left(=A\cdot f_{y.mea}\right)$.

Table 3.5 shows a slight contrast between the existing and the proposed cross-section classification slenderness limits for CHSs under axial compression according to various international design standards (BS 5950:Part-1 1990, EN 1993-1-1 2005, IS 800 2007, CSA S16-14 2014, AISC 360-16 2016, AS 4100:1998 2016) and Equations 3.4–3.6. However, it should be noted that the new slenderness limits put forward in Table 3.5 shall have the same value when normalized with-respect-to any of the slenderness parameters specified in Equations 2.33–2.35. Therefore, the proposed Equation 3.1 for the equivalent CHS diameter for EHSs under pure axial compression also justifies the cross-section classification as per various international design standards (BS 5950:Part-1 1990, EN 1993-1-1 2005, IS 800 2007, CSA S16-14 2014, AISC 360-16 2016, AS 4100:1998 2016).

Further, using any of the Equations 2.20 and 2.21 to calibrate the equivalent CHS diameter for EHS under axial compression will enforce the designer to propose *or* use a higher yield limit than the existing yield limit for CHS as Equations 2.20 and 2.21 are already proved to be conservative. Lan et al. (2018) suggested yield limit for $\bar{\lambda}_{l.b}$ of CHS and EHSs as 0.35 by using Equation 2.20, while Fang et al. (2018) observed significant cyclic energy dissipation capacities by the EHSs which are classified as Class 4 sections (*i.e.*, elastic sections) based on the Equations 2.20 and 2.21.

From Figure 3.7, for yielding *or* fully-effective cross-sections with $\bar{\lambda}_{cs.E}\le 81.88$ (*i.e.*, $\bar{\lambda}_{cs}\le 0.0916$), it can be estimated that the $F_{cr.\max.}$ of the EHSs (*or* CHSs) is only due to the material plastification and/or strain hardening effects. From the interpretation of the yield and

elastic limits, it is assessed that the $F_{cr.\max.}$ of the EHSs (*or* CHSs) with $0.0916 < \bar{\lambda}_{cs} < 0.4303$ (*i.e.,* for the elastic-plastic buckling sections) is due to the elastic buckling and mild inelastic squashing effects, with the increasing local buckling and decreasing inelastic squashing effects with-respect-to the increment in the cross-section slenderness. Also, it can be seen that the $F_{cr.\max.}$ of the EHSs (*or* CHSs) with $\bar{\lambda}_{cs} \geq 0.4303$ (*i.e.,* for elastic buckling sections) is exclusively due to elastic buckling.

3.3 RELIABILITY ANALYSIS

The reliability of the proposed design curves expressed in the form of Equations 3.3–3.6 for EHS and CHSs is evaluated using reliability analysis to bestow their practice. Reliability analysis for the design of steel structural members is detailed in Ellingwood et al. (1980), Victorsson (2011) and North American specifications (AISI S100-16 2016). A target reliability index, β_o of 2.5 is specified as a lower limit for structural members relative to the load combination $1.2DL+1.6LL$ (1.2×Dead Load + 1.6×Live Load) and a fixed dead-to-live load ratio of 0.2 is to be utilised according to the LRFD (Load and Resistance Factor Design) of North American specifications (AISI S100-16 2016). The equation for calibrating the first-order reliability index, β according to North American specifications (AISI S100-16 2016) is as follows:

$$\beta = \frac{\ln\left(\frac{C_\varphi}{\varphi}.M_m.F_m.P_m\right)}{\sqrt{V_M^2 + V_F^2 + V_P^2 + V_Q^2}} \tag{3.9}$$

The statistical parameters M_m and F_m are the mean values of material and fabrication factors, respectively. V_M, V_F, and V_Q are the respective coefficients of variation of material factor, fabrication factor and load effect. C_φ is the calibration coefficient. These values are specified in North American specifications (AISI S100-16 2016), where $M_m = 1.10$, $F_m = 1.00$, $V_M = 0.10$, $V_F = 0.05$, $V_Q = 0.21$ and $C_\varphi = 1.521$. Resistance factor, φ for steel structural members under axial compression is taken as 0.85 for LRFD method as per North American specifications (AISI S100-16 2016). The statistical parameters P_m and V_P are the mean value and coefficient of variation (COV) of all the ratios of test-result (*or* FE analysis result) to proposed-predicted-

value for axial-compressive-capacity of EHS (*or* CHS) stub column member obtained from any of the Equations 3.3–3.6 (*i.e.*, $\frac{F_{cr.\max.}}{F_{cr.LnS}}$ ratios). Respective $F_{cr.LnS}$ and $\frac{F_{cr.\max.}}{F_{cr.LnS}}$ ratio of all the EHS and CHS members considered in this study are calibrated and tabulated in Tables 3.1–3.4 using Equations 3.3–3.6. From Tables 3.1–3.4, 1.127 and 0.182 are the respective values of P_m and V_P of all the $\frac{F_{cr.\max.}}{F_{cr.LnS}}$ ratios. Based on Equation 3.9, β of the proposed Equations 3.3–3.6 is found to be 2.66. The P_m and V_P of all the $\frac{F_{cr.\max.}}{F_{cr.Pl}}$ ratios in Tables 3.1–3.4 are 1.334 and 0.404, respectively. Based on Equation 3.9, β of Plantema's (Plantema 1946) Equations 3.7 and 3.8 is found to be 2.06.

Hence, the proposed design curve representing Equations 3.3-3.6 has β value greater than the target value of 2.5. And, Plantema's (Plantema 1946) curve representing Equations 3.7 and 3.8 has β value lesser than the target value of 2.5 and this could be largely due to non-consideration of the material strain hardening effect in the yielding sections.

3.4 SUMMARY

Based on an exhaustive data from the literature on carbon steel EHSs under axial compression and the existing classification criteria for CHSs, this chapter addresses the discrepancies and inconsistencies associated with the usage of the expressions proposed for the equivalent CHS diameter of EHS in the earlier studies. Hence, new expressions are developed for the same according to a novel Equivalent-Resistance-Capacity-Method (ERCM) approach. The key findings obtained using the ERCM for CHS and EHSs under pure axial compression are listed below.

- A new empirical expression for the equivalent CHS diameter of EHS, D_{eq} is derived by using the experimental and FE analyses results from the literature on EHS stub-columns, to make the existing CHS cross-section classification criteria in various design standards (BS 5950:Part-1 1990, EN 1993-1-1 2005, IS 800 2007, CSA S16-14 2014, AISC 360-16 2016, AS 4100:1998 2016) applicable to EHSs also.

- The expressions for predicting the cross-sectional resistance capacity of EHS and CHS members with-respect-to their cross-section slenderness calibrated using $D_{eq.c3}$ are also proposed.

The cross-sectional yield and elastic slenderness limits for assessing the EHS (*or* CHS) members under pure axial compression are also established.

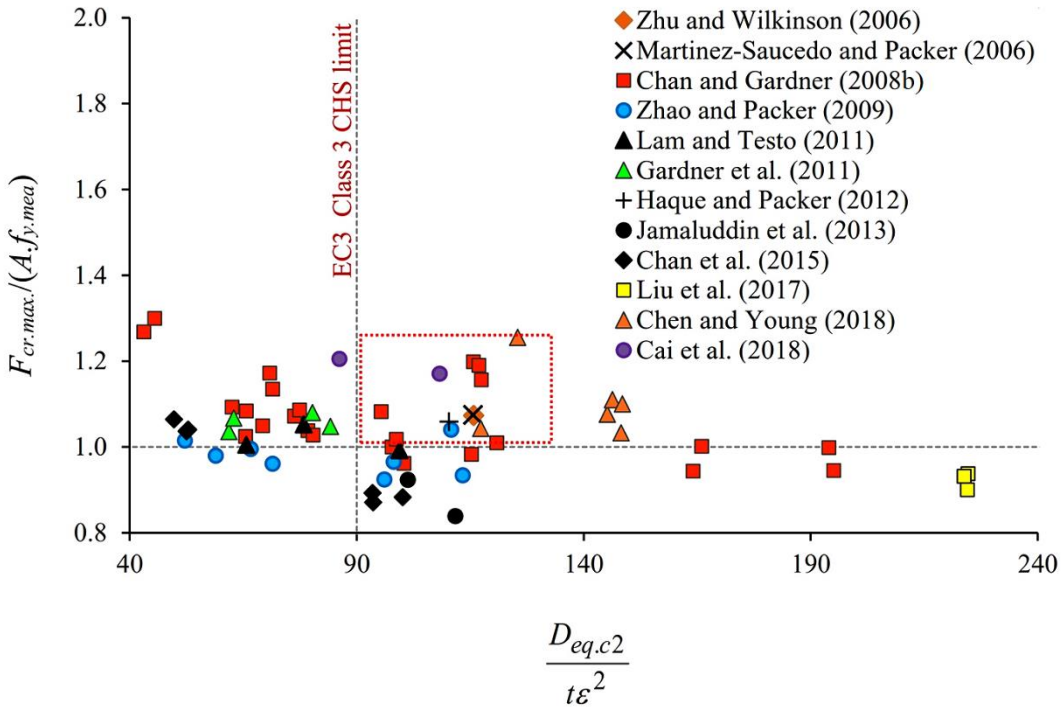

Figure 3.1 *Normalized axial compressive capacity Versus equiv. CHS slenderness by Ruiz-Terán and Gardner (2008) for EHS stub columns of experimental programs*

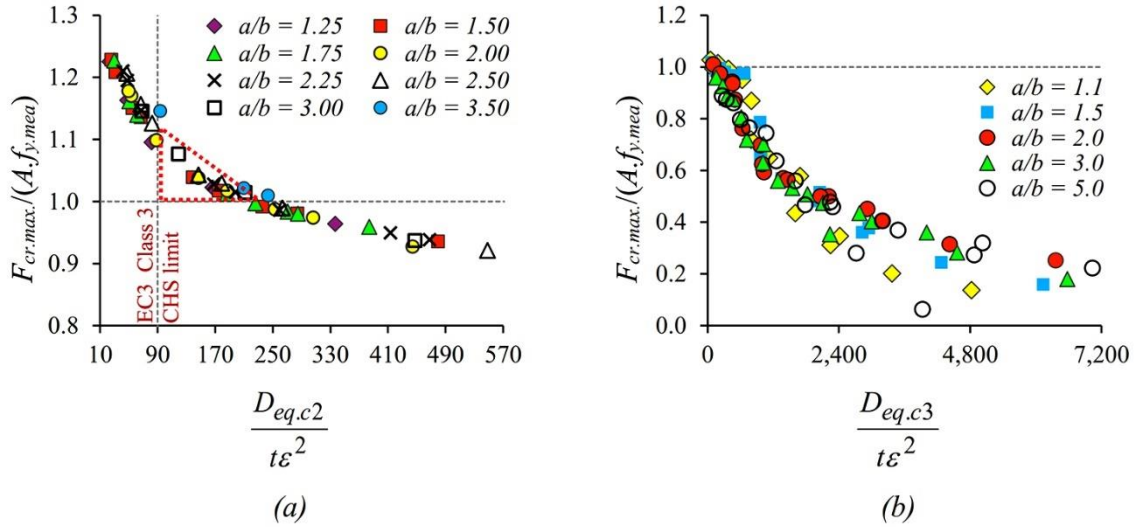

Figure 3.2 *Normalized axial compressive capacity Versus equiv. CHS slenderness by Ruiz-Terán and Gardner (2008) for EHS stub-columns, (a) FE models of Chen and Young (2018); (b) FE models of McCann et al. (2016)*

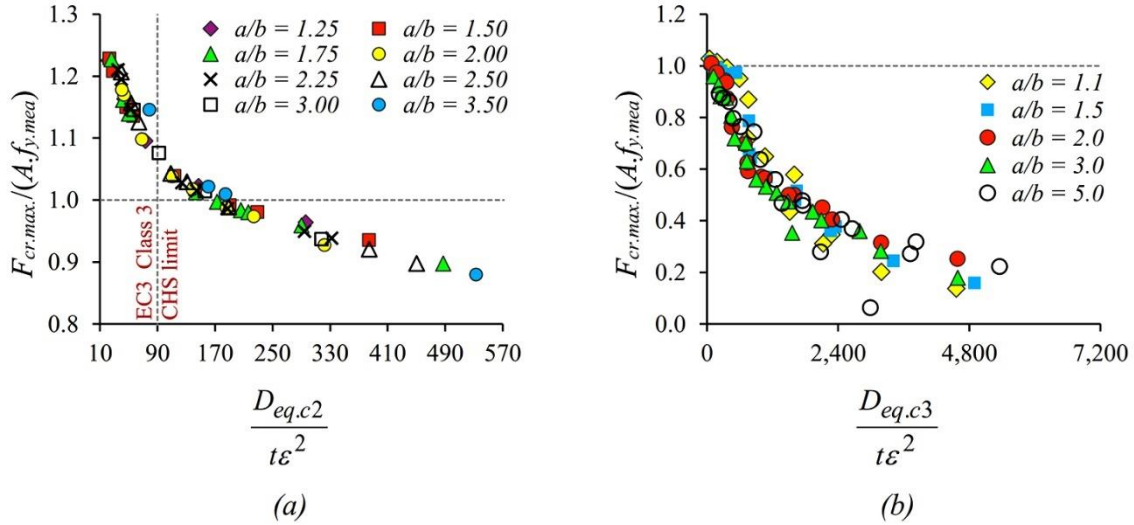

Figure 3.3 *Normalized axial compressive capacity Versus proposed equiv. CHS slenderness for EHS stub-columns, (a) FE models of Chen and Young (2018); (b) FE models of McCann et al. (2016)*

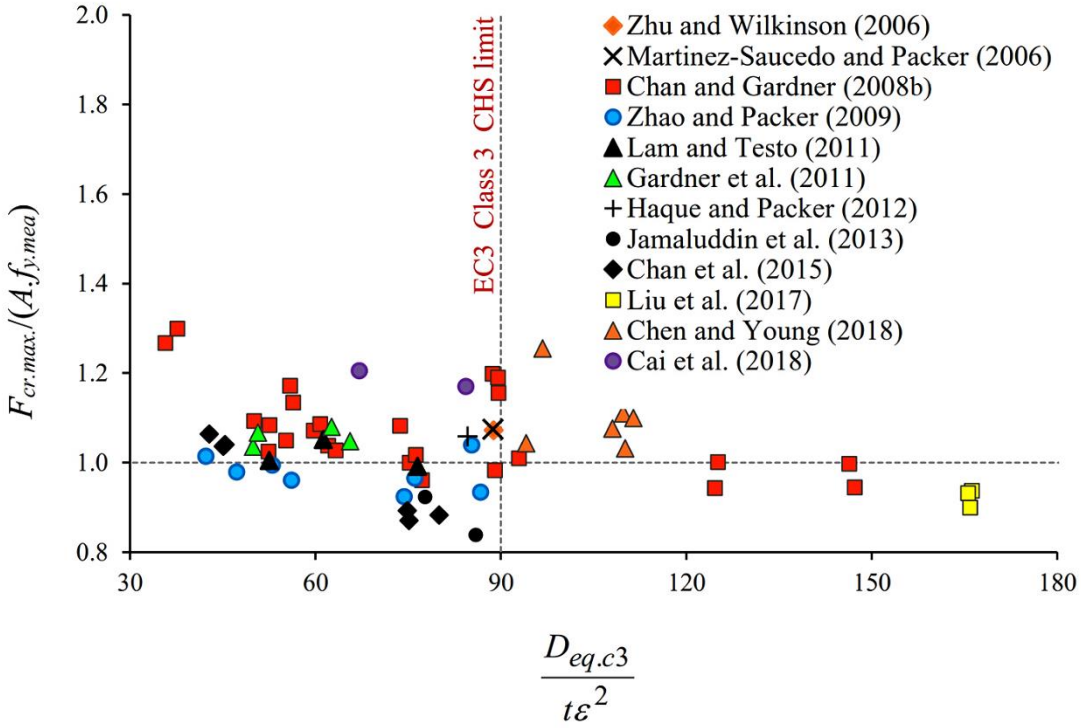

Figure 3.4 *Normalized axial compressive capacity Versus proposed equiv. CHS slenderness for EHS stub-columns of experimental programs*

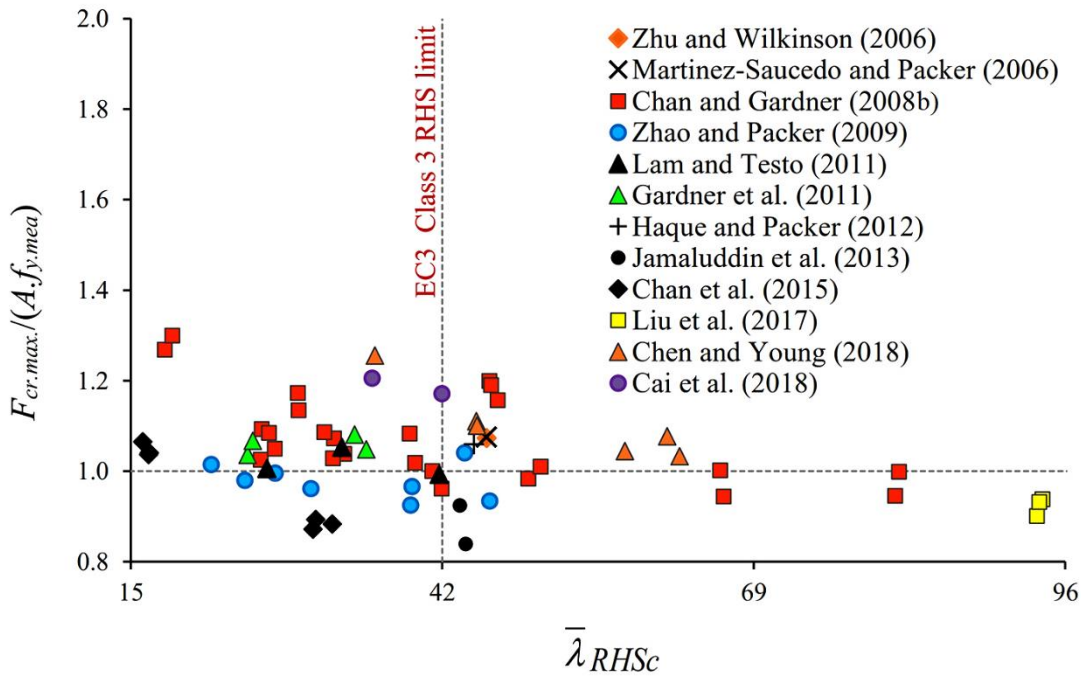

Figure 3.5 *Normalized axial compressive capacity Versus equiv. RHS slenderness by Zhao and Packer (2009) for EHS stub-columns of experimental programs*

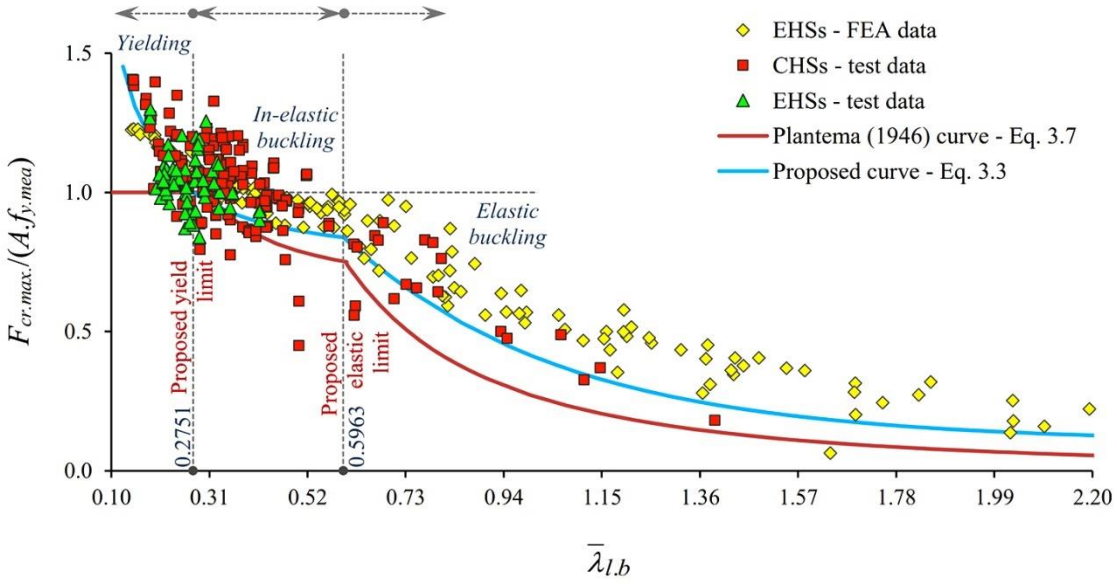

Figure 3.6 *Normalized axial compressive capacity Versus cross-sectional local buckling slenderness of CHS and EHSs of various experimental and FE programs*

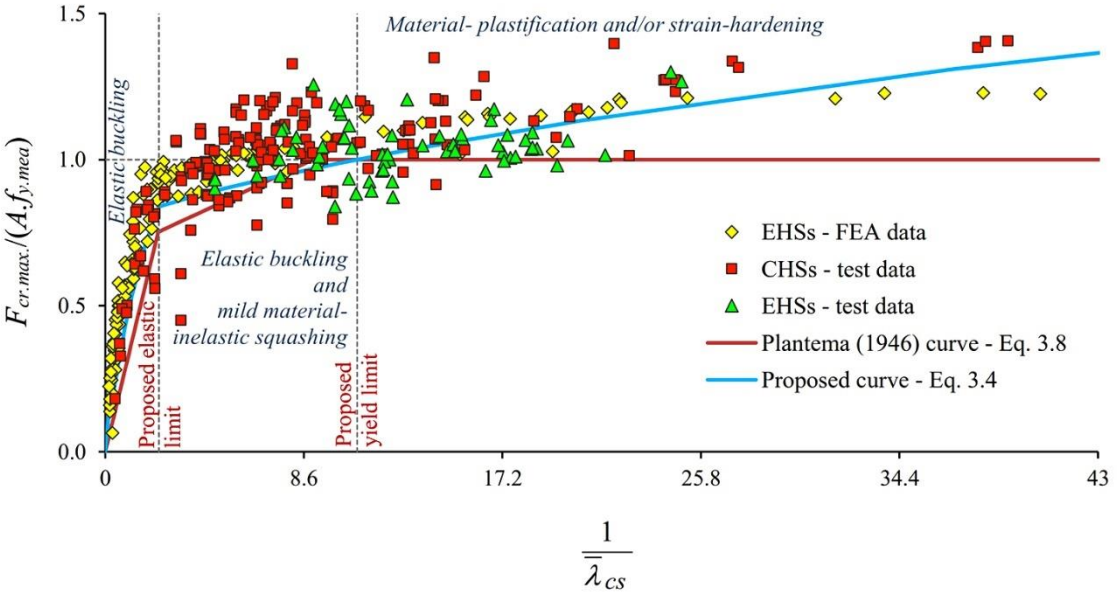

Figure 3.7 *Normalized axial compressive capacity Versus inversed-AISC cross-section slenderness (AISC 360-16, 2016) of CHS and EHSs of various experimental and FE programs*

Table 3.1 *Properties of EHS stub-columns in various experimental investigations*

Reference	$2a$ (mm)	$2b$ (mm)	t (mm)	P_M (mm)	E (GPa)	$f_{y.mea}$ (MPa)	$F_{cr.max.}$ (kN)	$\frac{F_{cr.\max.}}{A.f_{y.mea}}$	$\bar{\lambda}_{RHSc}$	$\frac{D_{eq.c2}}{t\varepsilon^2}$	$D_{eq.c3}$ (mm)	$\frac{D_{eq.c3}}{t\varepsilon^2}$	$\bar{\lambda}_{cs}$	$\bar{\lambda}_{l.b}$	$F_{cr.Pl}$ (kN)	$\frac{F_{cr.\max.}}{F_{cr.Pl}}$	$F_{cr.LnS}$ (kN)	$\frac{F_{cr.\max.}}{F_{cr.LnS}}$
Zhu and Wilkinson (2006)	221.2	110.9	5.9	518.2	215	421.4	1392	1.073	45.9	115.8	314.0	94.8	0.097	0.283	1297	1.073	1285	1.083
Martinez-Saucedo and Packer (2006)	221.2	110.9	5.9	518.2	216	421	1393	1.075	45.8	115.7	314.0	94.7	0.097	0.282	1296	1.075	1285	1.084
Chan and Gardner (2008b)	150.4	75.6	4.2	352.3	217.4	380	538	0.962	42.0	100.4	213.3	82.5	0.083	0.263	560	0.962	569	0.946
	150.5	75.4	4.2	351.9	217.7	373	554	1.000	41.1	97.8	213.7	80.4	0.081	0.259	554	1.000	566	0.979
	150.2	75.8	5.1	349.3	216.9	374	689	1.038	33.5	79.3	212.4	66.5	0.067	0.236	664	1.038	702	0.981
	150.2	75.7	5.1	349.0	217.2	364	700	1.072	32.6	76.3	212.6	64.1	0.065	0.231	653	1.072	696	1.005
	148.7	76	6.3	343.2	217.7	381	896	1.093	26.4	62.6	208.7	54.0	0.054	0.211	820	1.093	907	0.988
	148.8	76	6.3	343.3	215.2	400	935	1.084	27.0	65.7	209.0	56.6	0.057	0.218	862	1.084	942	0.992
	149.8	74.9	6.5	343.1	212.1	406	931	1.025	26.3	65.5	213.1	56.5	0.058	0.219	908	1.025	990	0.940
	150.2	75.2	6.3	344.8	221.1	415	952	1.050	27.5	69.3	213.6	59.5	0.059	0.220	907	1.049	987	0.965
	150.1	75.1	8.7	337.4	209.5	369	1367	1.268	18.0	43.1	213.4	38.7	0.040	0.182	1078	1.268	1278	1.069
	149.2	75.1	8.5	336.1	216.7	386	1435	1.300	18.6	45.5	211.3	40.8	0.041	0.184	1104	1.300	1303	1.101
	299.7	150	8.0	702.1	217.7	415	2777	1.199	46.1	115.7	425.9	94.6	0.096	0.281	2316	1.199	2300	1.208
	300.0	149.8	8.0	702.4	209.6	419	2792	1.190	46.3	116.9	427.1	95.5	0.100	0.288	2346	1.190	2311	1.208
	301.6	148.9	7.8	704.7	215.1	405	2574	1.156	46.8	117.5	432.2	95.5	0.098	0.284	2226	1.156	2202	1.169
	395.7	207.4	7.6	947.6	222.0	434	2961	0.944	66.4	164.1	547.4	132.5	0.132	0.330	2973	0.996	2967	0.998
	399.4	202.7	7.7	948.2	221.2	424	3081	1.002	66.1	166.0	563.0	132.8	0.133	0.331	2908	1.060	2905	1.061
	394.6	209.5	9.6	942.2	191.8	396	3521	0.983	49.5	115.3	541.6	95.1	0.109	0.300	3582	0.983	3482	1.011
	396.2	207.2	9.6	942.3	202.4	406	3693	1.010	50.5	120.9	548.8	99.2	0.108	0.299	3657	1.010	3562	1.037
	402.2	200.4	12.0	937.1	215.2	388	4727	1.083	39.2	95.4	573.1	78.8	0.080	0.258	4367	1.083	4467	1.058
	402.3	199.5	12.1	935.9	215.0	402	4623	1.018	39.7	98.7	575.0	81.5	0.083	0.262	4541	1.018	4617	1.001
	400.5	199.5	14.4	925.5	220.1	387	5610	1.086	31.8	77.4	570.9	65.2	0.065	0.231	5165	1.086	5504	1.019
	399.6	201.9	14.4	926.9	220.1	408	5610	1.028	32.5	80.4	564.7	67.9	0.068	0.236	5457	1.028	5769	0.972
	403.5	201.2	15.4	930.1	221.2	377	6310	1.172	29.5	70.8	574.6	60.1	0.059	0.221	5383	1.172	5840	1.080
	403.4	200.6	15.4	929.3	221.3	380	6159	1.135	29.6	71.5	575.5	60.6	0.060	0.222	5428	1.135	5880	1.048
	492.4	261.2	7.6	1188.9	219.9	409	3684	0.998	81.6	194.0	676.2	155.1	0.156	0.359	3335	1.105	3411	1.080
	488.4	259.1	7.6	1179.1	227.7	417	3546	0.945	81.3	195.1	670.9	156.0	0.152	0.354	3416	1.038	3480	1.019
Lam and Testo (2011)	150.4	75.6	4.2	352.2	217.5	376.5	550	0.992	41.8	99.4	213.2	81.7	0.083	0.261	554	0.992	564	0.975
	150.2	75.7	5.1	349.3	217.1	369	689	1.052	33.3	78.3	212.6	65.7	0.066	0.234	655	1.052	695	0.992
	148.8	75.5	6.3	342.6	216.5	400.5	872	1.005	26.8	65.6	209.8	56.6	0.057	0.217	867	1.005	949	0.919
Gardner et al. (2011)	150.3	75.8	4.9	350.1	211.8	377	671	1.048	35.4	84.2	198.3	65.6	0.073	0.245	640	1.048	667	1.006
	150.1	76.0	4.9	349.9	213.0	365	676	1.080	34.4	80.2	197.5	62.6	0.069	0.239	626	1.080	659	1.026
	148.2	76.1	6.7	341.0	216.3	410	973	1.036	25.2	61.8	192.2	49.9	0.054	0.212	939	1.036	1039	0.936
	148.9	76.1	6.6	342.5	216.6	408	990	1.067	25.6	62.9	193.7	50.7	0.055	0.213	928	1.067	1023	0.968

Table 3.1 (*Cont'd.****)***

Reference	$2a$ (mm)	$2b$ (mm)	t (mm)	P_M (mm)	E (GPa)	$f_{y.mea}$ (MPa)	$F_{cr.max.}$ (kN)	$\frac{F_{cr.\max.}}{A.f_{y.mea}}$	$\bar{\lambda}_{RHSc}$	$\frac{D_{eq.c2}}{t\varepsilon^2}$	$D_{eq.c3}$ (mm)	$\frac{D_{eq.c3}}{t\varepsilon^2}$	$\bar{\lambda}_{cs}$	$\bar{\lambda}_{l.b}$	$F_{cr.Pl}$ (kN)	$\frac{F_{cr.\max.}}{F_{cr.Pl}}$	$F_{cr.LnS}$ (kN)	$\frac{F_{cr.\max.}}{F_{cr.LnS}}$
Zhao and Packer (2009)	150.2	75.2	4.5	350.3	217.3	395	577	0.925	39.3	96.1	199.5	74.3	0.080	0.258	624	0.925	638	0.904
	150.5	75.3	5.4	348.2	217.3	358	648	0.961	30.6	71.5	199.4	56.1	0.061	0.224	674	0.961	728	0.890
	150.1	75.4	6.6	344.1	217.3	369	816	0.980	24.9	59.0	197.4	47.2	0.051	0.205	833	0.980	933	0.874
	200.2	100.1	5.2	469.3	215.1	397	905	0.934	46.1	113.3	266.9	86.7	0.095	0.280	969	0.934	963	0.939
	200.0	100.4	6.1	466.5	215.1	411	1129	0.965	39.4	98.2	265.2	76.0	0.083	0.262	1169	0.965	1189	0.949
	200.6	100.0	8.2	460.8	215.1	383	1435	0.995	27.5	66.7	265.6	53.0	0.058	0.219	1442	0.995	1573	0.912
	200.2	100.4	9.7	455.8	215.1	367	1650	1.015	22.0	52.2	263.1	42.3	0.046	0.195	1626	1.015	1864	0.885
	220.7	110.7	6.2	516.4	214.1	421	1393	1.040	43.9	110.8	293.2	85.3	0.094	0.278	1339	1.040	1334	1.044
Haque and Packer (2012)	221.2	110.9	5.9	518.2	210.1	401.5	1309	1.059	44.8	110.3	294.2	84.6	0.095	0.280	1236	1.059	1229	1.065
Jamaluddin et al. (2013)	150.3	75.2	4.2	351.4	201.0	424	525	0.839	44.0	111.7	200.0	85.9	0.100	0.288	626	0.839	616	0.852
	197.8	100.1	5.2	464.9	209.0	363	811	0.924	43.5	101.2	261.6	77.7	0.087	0.269	878	0.924	885	0.916
Chan et al. (2015)	120.4	60.0	5.4	275.0	219.9	599	775	0.871	30.8	93.6	159.2	75.1	0.080	0.258	890	0.871	910	0.851
	120.2	59.5	5.2	274.7	204.1	612	772	0.883	32.5	100.2	159.7	80.0	0.092	0.276	874	0.883	873	0.884
	120.1	59.7	5.3	274.4	202.9	586	761	0.893	31.0	93.5	159.1	74.8	0.087	0.268	852	0.893	860	0.884
	120.2	58.1	9.0	261.4	201.6	565	1415	1.064	16.1	49.8	160.3	42.8	0.050	0.203	1329	1.064	1497	0.945
	120.3	57.5	8.9	261.2	198.1	583	1405	1.037	16.6	52.5	161.7	45.1	0.053	0.210	1355	1.037	1504	0.934
	120.3	57.5	8.9	261.2	197.4	587	1420	1.041	16.6	52.9	161.7	45.4	0.054	0.211	1365	1.041	1511	0.940
Liu et al. (2017)	200.0	100.5	2.6	477.3	185.0	376.4	421	0.900	93.6	224.5	269.3	165.9	0.211	0.417	394	1.069	417	1.009
	201.0	101.5	2.6	480.4	185.0	376.4	441	0.938	94.0	224.7	269.8	166.2	0.211	0.418	396	1.114	420	1.051
	201.2	101.7	2.6	480.9	185.0	376.4	440	0.932	93.8	223.8	269.9	165.6	0.210	0.417	398	1.106	422	1.044
Chen and Young (2018)	141.2	87.2	2.9	354.8	208.0	388	423	1.044	57.9	117.3	167.5	94.1	0.106	0.296	405	1.044	395	1.069
	150.4	51.1	5.0	321.7	205.0	410	820	1.256	36.2	125.5	274.5	96.8	0.111	0.303	653	1.256	633	1.295
	148.7	71.6	2.8	348.5	210.0	341	352	1.076	61.5	145.2	204.7	108.0	0.121	0.316	318	1.106	313	1.124
	148.4	71.2	2.7	347.6	210.0	341	331	1.033	62.6	148.3	204.9	110.1	0.123	0.319	310	1.068	306	1.082
	176.6	65.7	4.8	386.7	200.0	418	863	1.110	45.0	146.4	296.9	109.8	0.129	0.326	742	1.164	737	1.171
	176.8	64.8	4.8	386.1	200.0	418	854	1.100	45.0	148.5	301.4	111.5	0.131	0.329	737	1.159	735	1.162
Cai et al. (2018)	204.9	105.9	6.2	481.8	201.1	462.3	1622	1.171	42.0	108.3	266.7	84.3	0.099	0.285	1386	1.171	1369	1.185
	204.3	102.9	6.6	476.0	206.3	383.2	1442	1.205	35.9	86.2	270.0	67.1	0.076	0.251	1196	1.205	1235	1.167

Table 3.2 *Properties of EHS stub-columns in various FE studies*

Reference	$2a$ (mm)	$2b$ (mm)	t (mm)	P_M (mm)	E (GPa)	$f_{y.mea}$ (MPa)	$F_{cr.max.}$ (kN)	$\frac{F_{cr.\max.}}{A.f_{y.mea}}$	$\frac{D_{eq.c2}}{t\varepsilon^2}$	$D_{eq.c3}$ (mm)	$\frac{D_{eq.c3}}{t\varepsilon^2}$	$\bar{\lambda}_{cs}$	$\bar{\lambda}_{l.b}$	$F_{cr.Pl}$ (kN)	$\frac{F_{cr.\max.}}{F_{cr.Pl}}$	$F_{cr.LnS}$ (kN)	$\frac{F_{cr.\max.}}{F_{cr.LnS}}$
McCann et al. (2016)	242.0	220.0	8.7	699.1	216.0	390.6	2441	1.027	49.4	248.2	47.4	0.052	0.206	2376	1.027	2656	0.919
	242.0	220.0	4.2	713.2	216.0	390.6	1162	0.993	103.4	248.7	98.4	0.107	0.297	1170	0.993	1141	1.019
	242.0	220.0	2.1	719.8	216.0	390.6	578	0.978	208.1	249.2	197.3	0.215	0.421	496	1.165	526	1.098
	242.0	220.0	1.5	721.7	216.0	390.6	411	0.972	292.1	249.5	276.4	0.301	0.498	334	1.231	365	1.127
	242.0	220.0	1.0	723.3	216.0	390.6	270	0.957	439.0	249.7	415.1	0.452	0.611	205	1.318	231	1.171
	242.0	220.0	0.7	724.2	216.0	390.6	188	0.950	628.1	250.0	593.6	0.646	0.730	101	1.871	130	1.444
	242.0	220.0	8.7	699.1	216.0	1500	9262	1.015	189.8	248.2	182.1	0.198	0.405	15102	0.613	8199	1.130
	242.0	220.0	4.2	713.2	216.0	1500	4377	0.974	397.1	248.7	378.0	0.411	0.583	3583	1.221	3782	1.157
	242.0	220.0	2.1	719.8	216.0	1500	1972	0.870	799.3	249.2	757.5	0.824	0.825	902	2.185	1260	1.565
	242.0	220.0	1.5	721.7	216.0	1500	1053	0.648	1121.5	249.5	1061.5	1.155	0.977	461	2.283	697	1.511
	242.0	220.0	1.0	723.3	216.0	1500	627	0.578	1686.0	249.7	1594.1	1.734	1.197	205	3.057	332	1.888
	242.0	220.0	0.7	724.2	216.0	1500	263	0.346	2412.1	250.0	2279.5	2.480	1.431	101	2.615	172	1.525
	242.0	220.0	8.7	699.1	216.0	3000	18116	0.993	379.5	248.2	364.3	0.396	0.572	15102	1.200	15397	1.177
	242.0	220.0	4.2	713.2	216.0	3000	6461	0.719	794.3	248.7	756.1	0.823	0.824	3583	1.803	5000	1.292
	242.0	220.0	2.1	719.8	216.0	3000	1973	0.435	1598.6	249.2	1515.1	1.648	1.167	902	2.187	1450	1.361
	242.0	220.0	1.5	721.7	216.0	3000	1010	0.311	2243.1	249.5	2123.1	2.310	1.381	461	2.190	781	1.293
	242.0	220.0	1.0	723.3	216.0	3000	437	0.201	3371.9	249.7	3188.2	3.469	1.693	205	2.129	379	1.153
	242.0	220.0	0.7	724.2	216.0	3000	209	0.137	4824.3	250.0	4559.0	4.960	2.024	101	2.079	211	0.992
	274.8	183.2	8.7	699.9	216.0	390.6	2421	1.018	71.1	313.2	59.8	0.065	0.232	2378	1.018	2533	0.956
	274.8	183.2	4.2	713.9	216.0	390.6	1155	0.986	152.9	315.7	124.9	0.136	0.335	1100	1.050	1103	1.047
	274.8	183.2	2.1	720.4	216.0	390.6	580	0.981	312.8	318.1	251.8	0.274	0.476	474	1.223	514	1.128
	274.8	183.2	1.5	722.3	216.0	390.6	401	0.949	441.4	319.2	353.7	0.385	0.564	323	1.243	358	1.122
	274.8	183.2	1.0	723.8	216.0	390.6	275	0.974	667.1	320.6	532.9	0.580	0.692	160	1.722	199	1.381
	274.8	183.2	0.7	724.8	216.0	390.6	156	0.787	957.9	321.8	764.2	0.831	0.829	78	1.996	109	1.426
	274.8	183.2	8.7	699.9	216.0	1200	7272	0.995	218.6	313.2	183.8	0.200	0.406	6225	1.168	6560	1.108
	274.8	183.2	4.2	713.9	216.0	1200	3480	0.967	469.9	315.7	383.8	0.418	0.587	2719	1.280	3025	1.150
	274.8	183.2	2.1	720.4	216.0	1200	1194	0.658	961.0	318.1	773.4	0.841	0.834	708	1.687	994	1.201
	274.8	183.2	1.5	722.3	216.0	1200	740	0.569	1356.0	319.2	1086.7	1.182	0.988	361	2.052	547	1.352
	274.8	183.2	1.0	723.8	216.0	1200	448	0.516	2049.3	320.6	1637.2	1.781	1.213	160	2.804	260	1.724
	274.8	183.2	0.7	724.8	216.0	1200	230	0.377	2942.9	321.8	2347.8	2.554	1.453	78	2.937	135	1.703
	274.8	183.2	8.7	699.9	216.0	2500	14429	0.948	455.4	313.2	383.0	0.417	0.587	11505	1.254	12799	1.127
	274.8	183.2	4.2	713.9	216.0	2500	4828	0.644	978.9	315.7	799.7	0.870	0.848	2826	1.709	4003	1.206
	274.8	183.2	2.1	720.4	216.0	2500	1826	0.483	2002.2	318.1	1611.3	1.753	1.203	708	2.580	1148	1.591
	274.8	183.2	1.5	722.3	216.0	2500	978	0.361	2825.1	319.2	2264.0	2.463	1.427	361	2.713	618	1.583
	274.8	183.2	1.0	723.8	216.0	2500	443	0.245	4269.4	320.6	3410.8	3.711	1.751	160	2.770	301	1.471
	274.8	183.2	0.7	724.8	216.0	2500	202	0.159	6131.0	321.8	4891.2	5.321	2.097	78	2.584	169	1.193
	300.0	150.0	8.7	700.4	216.0	390.6	2404	1.010	98.9	399.1	76.3	0.083	0.262	2380	1.010	2421	0.993
	300.0	150.0	4.2	714.1	216.0	390.6	1128	0.963	216.4	404.7	160.2	0.174	0.379	1030	1.095	1069	1.056

Table 3.2 (**Cont'd.**)

Reference	$2a$ (mm)	$2b$ (mm)	t (mm)	P_M (mm)	E (GPa)	$f_{y.mea}$ (MPa)	$F_{cr.max.}$ (kN)	$\frac{F_{cr.\max.}}{A.f_{y.mea}}$	$\frac{D_{eq.c2}}{t\varepsilon^2}$	$D_{eq.c3}$ (mm)	$\frac{D_{eq.c3}}{t\varepsilon^2}$	$\bar{\lambda}_{cs}$	$\bar{\lambda}_{l.b}$	$F_{cr.Pl}$ (kN)	$\frac{F_{cr.\max.}}{F_{cr.Pl}}$	$F_{cr.LnS}$ (kN)	$\frac{F_{cr.\max.}}{F_{cr.LnS}}$
McCann et al. (2016)	300.0	150.0	2.1	720.5	216.0	390.6	557	0.943	447.1	410.0	324.5	0.353	0.540	456	1.222	503	1.108
	300.0	150.0	1.5	722.3	216.0	390.6	323	0.763	633.0	412.6	457.2	0.497	0.641	279	1.157	327	0.987
	300.0	150.0	1.0	723.9	216.0	390.6	197	0.697	959.8	415.8	691.1	0.752	0.788	123	1.597	168	1.174
	300.0	150.0	0.7	724.8	216.0	390.6	113	0.570	1381.5	418.6	993.9	1.081	0.945	60	1.880	90	1.261
	300.0	150.0	8.7	700.4	216.0	900	5341	0.974	227.8	399.1	175.7	0.191	0.397	4719	1.132	4949	1.079
	300.0	150.0	4.2	714.1	216.0	900	2360	0.874	498.5	404.7	369.0	0.402	0.576	2049	1.152	2276	1.037
	300.0	150.0	2.1	720.5	216.0	900	807	0.593	1030.1	410.0	747.8	0.814	0.820	549	1.470	764	1.057
	300.0	150.0	1.5	722.3	216.0	900	551	0.565	1458.6	412.6	1053.6	1.146	0.973	279	1.973	421	1.308
	300.0	150.0	1.0	723.9	216.0	900	325	0.499	2211.6	415.8	1592.4	1.732	1.196	123	2.637	200	1.629
	300.0	150.0	0.7	724.8	216.0	900	185	0.405	3183.2	418.6	2290.1	2.492	1.435	60	3.079	103	1.794
	300.0	150.0	8.7	700.4	216.0	1800	10272	0.936	455.6	399.1	351.4	0.382	0.562	8377	1.226	9280	1.107
	300.0	150.0	4.2	714.1	216.0	1800	3373	0.625	997.1	404.7	738.1	0.803	0.814	2205	1.530	3057	1.104
	300.0	150.0	2.1	720.5	216.0	1800	1362	0.500	2060.2	410.0	1495.6	1.627	1.159	549	2.481	880	1.547
	300.0	150.0	1.5	722.3	216.0	1800	881	0.451	2917.2	412.6	2107.1	2.292	1.376	279	3.156	472	1.865
	300.0	150.0	1.0	723.9	216.0	1800	410	0.315	4423.2	415.8	3184.8	3.465	1.692	123	3.326	228	1.801
	300.0	150.0	0.7	724.8	216.0	1800	230	0.252	6366.4	418.6	4580.2	4.983	2.029	60	3.833	126	1.824
	326.0	108.7	8.7	701.0	216.0	390.6	2285	0.959	154.3	610.4	116.6	0.127	0.324	2284	1.001	2265	1.009
	326.0	108.7	4.2	714.1	216.0	390.6	1033	0.882	343.4	623.5	246.7	0.268	0.471	943	1.096	1021	1.012
	326.0	108.7	2.1	720.3	216.0	390.6	425	0.719	716.6	636.0	503.4	0.548	0.673	354	1.201	432	0.984
	326.0	108.7	1.5	722.0	216.0	390.6	297	0.702	1017.9	642.1	711.5	0.774	0.800	179	1.657	246	1.208
	326.0	108.7	1.0	723.5	216.0	390.6	150	0.532	1548.2	649.5	1079.6	1.175	0.985	79	1.905	120	1.257
	326.0	108.7	0.7	724.4	216.0	390.6	70	0.354	2233.0	656.1	1557.9	1.695	1.183	38	1.827	62	1.132
	326.0	108.7	8.7	701.0	216.0	700	3950	0.925	276.5	610.4	209.0	0.227	0.433	3542	1.115	3781	1.045
	326.0	108.7	4.2	714.1	216.0	700	1693	0.806	615.5	623.5	442.2	0.481	0.630	1432	1.182	1656	1.022
	326.0	108.7	2.1	720.3	216.0	700	593	0.560	1284.2	636.0	902.1	0.981	0.900	354	1.675	516	1.148
	326.0	108.7	1.5	722.0	216.0	700	385	0.508	1824.2	642.1	1275.0	1.387	1.071	179	2.147	280	1.374
	326.0	108.7	1.0	723.5	216.0	700	220	0.435	2774.5	649.5	1934.7	2.105	1.319	79	2.791	132	1.673
	326.0	108.7	0.7	724.4	216.0	700	128	0.360	4001.7	656.1	2792.0	3.038	1.584	38	3.335	68	1.866
	326.0	108.7	8.7	701.0	216.0	1150	6148	0.877	454.2	610.4	343.4	0.374	0.556	5373	1.144	5945	1.034
	326.0	108.7	4.2	714.1	216.0	1150	2173	0.630	1011.2	623.5	726.4	0.790	0.808	1432	1.518	1975	1.100
	326.0	108.7	2.1	720.3	216.0	1150	826	0.475	2109.7	636.0	1482.0	1.612	1.154	354	2.334	567	1.457
	326.0	108.7	1.5	722.0	216.0	1150	501	0.402	2996.9	642.1	2094.7	2.279	1.372	179	2.795	303	1.653
	326.0	108.7	1.0	723.5	216.0	1150	235	0.283	4558.1	649.5	3178.5	3.458	1.690	79	2.981	146	1.616
	326.0	108.7	0.7	724.4	216.0	1150	105	0.179	6574.3	656.1	4586.9	4.990	2.030	38	2.728	81	1.298
	346.0	69.2	8.7	703.4	216.0	390.6	2126	0.889	263.8	1188.8	227.1	0.247	0.452	1952	1.089	2100	1.012
	346.0	69.2	4.2	715.7	216.0	390.6	935	0.796	595.4	1208.6	478.3	0.520	0.656	740	1.263	884	1.057
	346.0	69.2	2.1	721.5	216.0	390.6	377	0.637	1251.5	1227.6	971.6	1.057	0.935	184	2.053	272	1.384
	346.0	69.2	1.5	723.1	216.0	390.6	198	0.468	1782.2	1236.8	1370.5	1.491	1.110	93	2.126	147	1.345
	346.0	69.2	1.0	724.5	216.0	390.6	79	0.280	2717.0	1248.1	2074.5	2.257	1.365	41	1.925	69	1.141

Table 3.2 (**Cont'd.**)

Reference	$2a$ (mm)	$2b$ (mm)	t (mm)	P_M (mm)	E (GPa)	$f_{y.mea}$ (MPa)	$F_{cr.max.}$ (kN)	$\frac{F_{cr.\max.}}{A.f_{y.mea}}$	$\frac{D_{eq.c2}}{t\varepsilon^2}$	$D_{eq.c3}$ (mm)	$\frac{D_{eq.c3}}{t\varepsilon^2}$	$\bar{\lambda}_{cs}$	$\bar{\lambda}_{l.b}$	$F_{cr.Pl}$ (kN)	$\frac{F_{cr.\max.}}{F_{cr.Pl}}$	$F_{cr.LnS}$ (kN)	$\frac{F_{cr.\max.}}{F_{cr.LnS}}$
McCann et al. (2016)	346.0	69.2	0.7	725.3	216.0	390.6	13	0.064	3925.0	1258.0	2987.1	3.250	1.639	20	0.630	36	0.347
	346.0	69.2	8.7	703.4	216.0	500	2676	0.875	337.7	1188.8	290.7	0.316	0.511	2399	1.116	2628	1.018
	346.0	69.2	4.2	715.7	216.0	500	1150	0.765	762.1	1208.6	612.3	0.666	0.742	740	1.553	969	1.187
	346.0	69.2	2.1	721.5	216.0	500	424	0.560	1602.0	1227.6	1243.8	1.353	1.057	184	2.311	286	1.485
	346.0	69.2	1.5	723.1	216.0	500	249	0.459	2281.4	1236.8	1754.4	1.909	1.256	93	2.672	153	1.626
	346.0	69.2	1.0	724.5	216.0	500	134	0.369	3477.9	1248.1	2655.5	2.889	1.545	41	3.248	73	1.838
	346.0	69.2	0.7	725.3	216.0	500	81	0.319	5024.3	1258.0	3823.8	4.160	1.854	20	4.046	39	2.070
	346.0	69.2	8.7	703.4	216.0	700	3689	0.861	472.7	1188.8	407.0	0.443	0.605	3173	1.162	3538	1.042
	346.0	69.2	4.2	715.7	216.0	700	1566	0.744	1066.9	1208.6	857.2	0.933	0.878	740	2.117	1067	1.468
	346.0	69.2	2.1	721.5	216.0	700	507	0.478	2242.8	1227.6	1741.3	1.894	1.251	184	2.760	301	1.682
	346.0	69.2	1.5	723.1	216.0	700	308	0.405	3193.9	1236.8	2456.2	2.672	1.486	93	3.303	162	1.899
	346.0	69.2	1.0	724.5	216.0	700	138	0.273	4869.1	1248.1	3717.7	4.045	1.828	41	3.364	80	1.738
	346.0	69.2	0.7	725.3	216.0	700	79	0.223	7034.1	1258.0	5353.3	5.824	2.194	20	3.957	45	1.744
Chen and Young (2018)	500.0	250.0	25.0	1135.4	208.0	388	12887	1.170	53.5	658.1	43.5	0.049	0.201	11013	1.170	12450	1.035
	250.0	200.0	20.0	646.7	208.0	388	6148	1.225	23.2	264.7	21.9	0.025	0.143	5018	1.225	6754	0.910
	150.0	100.0	12.0	359.5	208.0	388	2056	1.228	25.7	169.2	23.3	0.026	0.147	1674	1.228	2214	0.929
	210.0	120.0	16.0	479.0	208.0	388	3650	1.227	29.9	254.2	26.2	0.030	0.156	2974	1.227	3808	0.958
	300.0	200.0	20.0	731.4	208.0	388	6858	1.208	31.5	339.1	28.0	0.032	0.162	5676	1.208	7144	0.960
	180.0	80.0	12.0	387.7	208.0	388	2185	1.210	41.7	255.2	35.1	0.040	0.181	1805	1.210	2145	1.018
	250.0	100.0	16.0	527.9	208.0	388	3954	1.207	47.4	385.3	39.8	0.045	0.193	3277	1.207	3781	1.046
	270.0	120.0	16.0	587.5	208.0	388	4359	1.195	48.0	383.8	39.6	0.045	0.192	3647	1.195	4212	1.035
	150.0	75.0	8.0	339.1	208.0	388	1240	1.178	49.6	197.2	40.7	0.046	0.195	1053	1.178	1208	1.026
	150.0	50.0	8.0	310.9	208.0	388	1105	1.145	68.3	275.1	56.8	0.064	0.230	965	1.145	1031	1.072
	210.0	120.0	10.0	497.5	208.0	388	2242	1.162	51.1	256.1	42.3	0.048	0.199	1930	1.162	2196	1.021
	250.0	100.0	12.0	539.8	208.0	388	2906	1.156	66.8	388.3	53.4	0.060	0.223	2513	1.156	2718	1.069
	180.0	80.0	8.0	399.7	208.0	388	1423	1.147	67.1	257.6	53.2	0.060	0.223	1241	1.147	1343	1.059
	350.0	100.0	16.0	717.0	208.0	388	5101	1.146	93.8	762.3	78.7	0.089	0.271	4451	1.146	4475	1.140
	250.0	200.0	10.0	678.0	208.0	388	3060	1.163	48.2	265.9	43.9	0.050	0.202	2631	1.163	2967	1.031
	150.0	100.0	6.0	378.1	208.0	388	1013	1.150	55.0	170.5	46.9	0.053	0.209	880	1.150	978	1.035
	350.0	200.0	14.0	837.3	208.0	388	5184	1.140	61.9	428.0	50.5	0.057	0.217	4548	1.140	4977	1.042
	500.0	200.0	20.0	1091.4	208.0	388	9536	1.126	82.5	780.2	64.4	0.073	0.245	8470	1.126	8826	1.080
	300.0	200.0	10.0	762.5	208.0	388	3360	1.136	66.9	341.7	56.4	0.064	0.229	2958	1.136	3164	1.062
	150.0	50.0	5.0	319.6	208.0	388	667	1.076	119.0	279.0	92.1	0.104	0.293	620	1.076	607	1.099
	500.0	250.0	16.0	1162.8	208.0	388	7929	1.098	88.1	663.9	68.5	0.077	0.253	7218	1.098	7436	1.066
	250.0	200.0	6.0	690.5	208.0	388	1761	1.096	81.8	266.7	73.4	0.083	0.262	1608	1.096	1636	1.077
	500.0	200.0	12.0	1115.3	208.0	388	5416	1.043	146.7	790.4	108.8	0.123	0.319	5027	1.077	4959	1.092
	350.0	100.0	8.0	739.9	208.0	388	2347	1.022	209.8	779.0	160.8	0.182	0.387	2000	1.174	2084	1.126
	150.0	75.0	3.0	354.3	208.0	388	428	1.038	146.9	201.0	110.6	0.125	0.321	397	1.078	393	1.090

Table 3.2 (**Cont'd.**)

Reference	$2a$ (mm)	$2b$ (mm)	t (mm)	P_M (mm)	E (GPa)	$f_{y.mea}$ (MPa)	$F_{cr.max.}$ (kN)	$\frac{F_{cr.\max.}}{A_c f_{y.mea}}$	$\frac{D_{eq.c2}}{t\varepsilon^2}$	$D_{eq.c3}$ (mm)	$\frac{D_{eq.c3}}{t\varepsilon^2}$	$\bar{\lambda}_{cs}$	$\bar{\lambda}_{l.b}$	$F_{cr.Pl}$ (kN)	$\frac{F_{cr.\max.}}{F_{cr.Pl}}$	$F_{cr.LnS}$ (kN)	$\frac{F_{cr.\max.}}{F_{cr.LnS}}$
Chen and Young (2018)	250.0	100.0	5.0	560.6	208.0	388	1120	1.029	179.1	397.0	131.1	0.148	0.350	997	1.123	1012	1.106
	180.0	80.0	3.5	413.3	208.0	388	577	1.028	168.1	262.5	123.8	0.140	0.340	523	1.104	526	1.096
	150.0	50.0	3.0	325.5	208.0	388	384	1.014	211.3	283.2	155.9	0.176	0.381	332	1.157	345	1.114
	350.0	100.0	7.0	742.7	208.0	388	2037	1.010	243.5	782.2	184.5	0.208	0.415	1704	1.195	1803	1.130
	150.0	100.0	2.5	389.0	208.0	388	392	1.039	138.8	172.2	113.7	0.128	0.326	360	1.088	358	1.095
	270.0	120.0	4.5	622.1	208.0	388	1102	1.015	198.5	395.1	145.0	0.164	0.368	970	1.136	998	1.104
	500.0	250.0	8.0	1187.1	208.0	388	3748	1.017	186.5	672.8	138.9	0.157	0.360	3327	1.127	3405	1.101
	350.0	200.0	5.0	865.0	208.0	388	1700	1.013	186.7	434.8	143.6	0.162	0.366	1502	1.131	1544	1.101
	300.0	200.0	4.0	781.1	208.0	388	1234	1.018	175.1	345.2	142.5	0.161	0.365	1087	1.135	1117	1.105
	500.0	200.0	7.0	1130.2	208.0	388	3037	0.989	263.4	801.2	189.0	0.214	0.420	2579	1.177	2737	1.110
	250.0	100.0	3.5	565.1	208.0	388	759	0.989	263.4	400.6	189.0	0.214	0.420	645	1.177	684	1.110
	270.0	120.0	3.5	625.2	208.0	388	837	0.986	259.6	397.3	187.4	0.212	0.418	715	1.171	758	1.105
	250.0	200.0	3.0	699.9	208.0	388	833	1.023	166.4	267.8	147.4	0.167	0.371	724	1.150	747	1.115
	210.0	120.0	2.5	520.6	208.0	388	503	0.997	225.9	261.6	172.8	0.195	0.402	432	1.164	455	1.107
	500.0	250.0	6.0	1193.2	208.0	388	2743	0.987	252.9	676.5	186.2	0.210	0.417	2341	1.171	2480	1.106
	150.0	100.0	1.5	392.1	208.0	388	226	0.992	235.7	173.1	190.6	0.215	0.422	191	1.183	203	1.114
	350.0	200.0	3.5	869.6	208.0	388	1162	0.984	271.0	437.2	206.2	0.233	0.439	975	1.191	1043	1.113
	150.0	75.0	1.5	358.9	208.0	388	203	0.974	306.3	203.7	224.2	0.253	0.457	170	1.198	183	1.111
	210.0	120.0	2.0	522.1	208.0	388	397	0.980	285.1	262.5	216.7	0.245	0.450	331	1.198	356	1.115
	150.0	50.0	1.5	329.9	208.0	388	180	0.937	447.4	289.0	318.1	0.359	0.545	148	1.217	163	1.102
	300.0	200.0	2.5	785.8	208.0	388	748	0.981	284.3	346.9	229.1	0.259	0.462	617	1.211	667	1.121
	180.0	80.0	1.5	419.3	208.0	388	232	0.949	413.6	267.5	294.4	0.333	0.524	190	1.220	209	1.110
	270.0	120.0	2.0	629.7	208.0	388	459	0.939	467.7	402.3	332.1	0.375	0.557	374	1.226	414	1.108
	210.0	120.0	1.5	523.6	208.0	388	292	0.959	384.0	263.6	290.2	0.328	0.520	238	1.230	261	1.120
	500.0	250.0	3.5	1200.9	208.0	388	1512	0.927	444.1	683.4	322.4	0.364	0.549	1253	1.206	1385	1.092
	500.0	200.0	3.5	1140.6	208.0	388	1427	0.921	548.2	815.1	384.5	0.434	0.599	1165	1.224	1293	1.103
	350.0	100.0	2.5	755.6	208.0	388	645	0.880	740.5	807.1	533.0	0.602	0.705	399	1.616	505	1.278
	250.0	200.0	1.5	704.6	208.0	388	395	0.964	336.6	268.9	296.0	0.334	0.526	402	0.983	351	1.127
	250.0	100.0	1.5	571.1	208.0	388	298	0.898	643.9	409.1	450.3	0.509	0.648	214	1.393	254	1.176
	300.0	200.0	1.5	788.9	208.0	388	430	0.935	479.5	348.8	384.0	0.434	0.599	347	1.237	384	1.120
	350.0	200.0	1.5	875.8	208.0	388	458	0.898	649.0	442.8	487.4	0.551	0.674	304	1.507	371	1.233

Table 3.3 *Properties of CHS stub-columns in various experimental investigations*

Reference	D (mm)	t (mm)	P_M (mm)	E (GPa)	$f_{y.mea}$ (MPa)	$F_{cr.max.}$ (kN)	$\frac{F_{cr.\max.}}{Af_{y.mea}}$	$\frac{D_{eq.c3}}{t\varepsilon^2}$	$\bar{\lambda}_{cs}$	$\bar{\lambda}_{l.b}$	$F_{cr.Pl}$ (kN)	$\frac{F_{cr.\max.}}{F_{cr.Pl}}$	$F_{cr.LnS}$ (kN)	$\frac{F_{cr.\max.}}{F_{cr.LnS}}$
Ostapenko and Gunzelman (1978)	1787	7.2	5593	203.4	377.2	12313	0.814	401.5	0.464	0.619	10693	1.152	12177	1.011
	1533	7.3	4794	203.4	372.1	11511	0.889	335.4	0.388	0.566	9873	1.166	10945	1.052
	1203	7.3	3757	203.4	372.1	9549	0.941	263.2	0.304	0.501	8004	1.193	8746	1.092
Grimm (1979)	772	9.9	2396	203.4	239.1	6007	1.056	79.4	0.092	0.275	5688	1.056	5687	1.056
	770	6.7	2398	203.4	203.8	3302	1.004	99.5	0.115	0.308	3252	1.015	3172	1.041
	1021	6.7	3189	203.3	203.8	4369	0.999	132.1	0.153	0.355	3977	1.099	4055	1.077
	1532	6.7	4792	203.6	203.8	5784	0.880	198.1	0.229	0.435	5448	1.062	5818	0.994
	585	9.7	1807	203.5	337.5	6344	1.069	86.6	0.100	0.287	5934	1.069	5849	1.085
	601	2.0	1881	203.9	366.3	1180	0.844	462.9	0.533	0.664	860	1.373	1038	1.137
	1531	6.6	4792	203.1	622.8	16207	0.829	621.9	0.720	0.771	8910	1.819	11956	1.355
O'Shea and Bridge (1997)	165	2.8	509.7	200.6	363.3	523	1.001	90.7	0.106	0.296	522	1.001	510	1.025
	190	1.9	591	204.7	256.4	284	0.967	107.2	0.123	0.319	284	1.000	281	1.013
	190	1.5	592.4	207.4	306.1	239	0.868	163.4	0.185	0.391	239	1.001	250	0.958
	190	1.1	593.6	178.4	185.7	109	0.876	133.3	0.176	0.381	109	0.998	114	0.961
	190	1.1	593.7	188.3	206.7	117	0.862	151.1	0.189	0.395	118	0.998	123	0.954
	190	1.1	593.7	188.3	206.7	116	0.855	151.1	0.189	0.395	118	0.990	123	0.946
	190	0.9	594.4	177.0	210.7	93	0.862	198.8	0.264	0.467	87	1.069	94	0.988
Fujimoto et al. (1997)	149	3.0	459	206.0	283	462	1.202	60.8	0.069	0.239	384	1.202	404	1.142
	239	4.7	736.3	206.0	284	1328	1.348	61.5	0.070	0.241	985	1.348	1034	1.285
	301	3.0	936.7	206.0	283	785	1.000	122.9	0.140	0.340	731	1.074	736	1.067
	450	3.0	1405	206.0	283	1131	0.961	183.7	0.210	0.416	993	1.139	1051	1.076
	122	4.5	369.2	206.0	579	1068	1.101	66.4	0.076	0.250	970	1.101	1004	1.064
	239	9.0	722.9	206.0	482	3825	1.220	54.6	0.062	0.227	3136	1.220	3369	1.135
	238	4.5	733.7	206.0	579	1776	0.921	129.5	0.148	0.349	1769	1.004	1796	0.989
	237	4.5	730.7	206.0	504	1863	1.119	112.8	0.129	0.326	1589	1.172	1579	1.180
	360	4.5	1117	206.0	579	2790	0.950	196.0	0.224	0.430	2445	1.141	2605	1.071
	108	6.5	319.1	206.0	835	1949	1.131	59.4	0.068	0.237	1724	1.131	1821	1.070
	160	9.1	474.2	206.0	820	3793	1.070	61.4	0.070	0.240	3546	1.070	3723	1.019
	222	6.5	677.4	206.0	835	3844	1.050	122.2	0.139	0.339	3412	1.127	3434	1.119
	160	4.8	487.9	206.0	772	1900	1.060	110.7	0.126	0.323	1721	1.104	1706	1.114
	336	6.5	1036	206.0	835	5763	1.030	185.0	0.211	0.418	4713	1.223	4994	1.154
Johansson and Gylltoft (2002)	159	4.8	484.6	206.0	433	920	0.913	61.2	0.070	0.240	1007	0.913	1058	0.870
Zhao et al. (2002)	48.4	2.8	143.3	200.0	425	228	1.337	31.3	0.037	0.174	171	1.337	206	1.104
	101.8	3.1	310.2	200.0	410	414	1.050	57.4	0.067	0.236	394	1.050	417	0.993
Zhao (2000)	32	1.5	95.8	200.1	1372	236	1.166	121.7	0.143	0.344	187	1.259	189	1.247
	32	1.5	95.8	203.7	1369	239	1.183	121.4	0.140	0.340	188	1.271	189	1.262
	32.1	1.7	95.4	207.0	1349	267	1.193	106.1	0.120	0.315	218	1.225	214	1.245
	32.1	1.8	95.4	201.7	1351	263	1.167	105.7	0.123	0.319	218	1.206	215	1.222
	32	2.0	94.3	200.4	1350	301	1.194	93.0	0.109	0.300	252	1.194	245	1.228
	32	2.0	94.3	197.7	1348	305	1.230	94.2	0.112	0.304	247	1.233	240	1.271
	38.3	1.6	115.3	203.8	1405	291	1.151	146.9	0.169	0.374	224	1.301	231	1.258
	38.2	1.5	115.3	205.9	1366	290	1.203	145.6	0.166	0.370	214	1.352	221	1.311
	38.3	1.8	114.9	197.8	1350	328	1.201	125.4	0.149	0.351	250	1.313	254	1.292
	38.4	1.8	114.9	197.0	1341	320	1.154	121.9	0.145	0.347	256	1.252	259	1.237
	38.3	2.0	114.2	195.0	1349	366	1.212	112.5	0.136	0.335	284	1.289	285	1.286
	38.3	2.0	114.3	193.8	1366	368	1.197	113.4	0.137	0.337	288	1.278	289	1.273
Giakoumelis and Lam (2004)	114	3.9	346.1	207.0	343	539	1.173	43.1	0.049	0.201	459	1.173	520	1.037
	115	5.0	345.8	207.0	365	806	1.272	35.7	0.041	0.183	634	1.272	749	1.076
Teng and Hu (2007)	162	4.2	495.9	201.0	333.6	718	1.033	54.9	0.064	0.230	695	1.033	742	0.967
Martinez-Saucedo and Packer (2006)	168.5	4.9	514.2	196.0	498	1213	0.969	73.2	0.088	0.269	1252	0.969	1261	0.962

Table 3.3 (*Cont'd.****)***

Reference	D (mm)	t (mm)	P_M (mm)	E (GPa)	$f_{y.mea}$ (MPa)	$F_{cr.max.}$ (kN)	$\frac{F_{cr.max.}}{Af_{y.mea}}$	$\frac{D_{eq.c3}}{t\varepsilon^2}$	$\bar{\lambda}_{cs}$	$\bar{\lambda}_{l.b}$	$F_{cr.Pl}$ (kN)	$\frac{F_{cr.max.}}{F_{cr.Pl}}$	$F_{cr.LnS}$ (kN)	$\frac{F_{cr.max.}}{F_{cr.LnS}}$
Elchalakani et al. (2002b)	114.4	5.9	341	200	454	927	1.013	37.5	0.044	0.191	915	1.013	1061	0.874
	114.4	4.7	344.9	200	416	719	1.075	43.6	0.051	0.206	669	1.075	749	0.960
	114.4	3.5	348.7	200	453	560	1.022	63.7	0.075	0.249	548	1.022	568	0.986
	114.4	3.0	350.3	200	430	454	1.018	70.9	0.083	0.262	446	1.018	453	1.002
	139.7	3.4	428.2	200	379	584	1.052	66.0	0.078	0.253	555	1.052	572	1.022
	139.7	2.9	429.7	200	357	457	1.013	72.4	0.085	0.265	451	1.013	457	1.000
	165.2	3.4	508.3	200	433	674	0.890	88.7	0.104	0.293	757	0.890	741	0.909
	165.2	2.9	510	200	395	553	0.947	96.0	0.113	0.305	581	0.951	565	0.979
Jiao and Zhao (2003)	75.4	1.6	232	198.7	1377	547	1.064	275.2	0.326	0.519	402	1.363	441	1.241
	75.5	1.6	232.2	198.7	1377	549	1.060	273.9	0.324	0.517	405	1.357	444	1.236
	75.3	1.6	231.6	198.7	1377	547	1.065	274.9	0.325	0.518	401	1.364	440	1.243
	57.4	1.6	175.3	197.6	1360	425	1.087	203.2	0.242	0.447	321	1.325	344	1.235
	57.5	1.6	175.5	198.2	1360	430	1.105	204.6	0.243	0.448	319	1.349	342	1.256
	57.4	1.6	175.3	197.7	1360	423	1.088	204.4	0.243	0.448	318	1.328	342	1.237
	38.2	1.6	115.1	192	1398	298	1.172	144.2	0.176	0.382	223	1.337	232	1.287
	38.2	1.6	115	192	1398	295	1.161	144.1	0.176	0.382	223	1.324	231	1.275
Sakino et al. (2004)	149.0	3.0	459	209	283	462	1.201	60.8	0.068	0.238	384	1.201	406	1.139
	301.0	3.0	936.7	209	283	787	1.004	122.9	0.138	0.338	734	1.073	737	1.068
	450.0	3.0	1405	209	283	1135	0.965	183.7	0.207	0.413	996	1.140	1053	1.078
	122.0	4.5	369.2	203	579	1066	1.098	66.4	0.077	0.252	970	1.098	1001	1.065
	238.0	4.5	733.7	203	579	1769	0.917	129.5	0.150	0.352	1762	1.004	1792	0.987
	360.0	4.5	1117	203	579	2779	0.946	196.0	0.227	0.433	2438	1.140	2602	1.068
	108.0	6.5	319.1	197	835	1941	1.126	59.4	0.071	0.242	1724	1.126	1805	1.075
	222.0	6.5	677.4	197	835	3835	1.048	122.2	0.146	0.347	3369	1.138	3413	1.123
	336.0	6.5	1036	197	835	5783	1.034	185.0	0.221	0.427	4670	1.238	4971	1.163
Baig et al. (2006)	160.0	2.5	495	203	245	290	0.957	66.9	0.078	0.253	303	0.957	312	0.929
	111.3	2.5	341.8	203	245	237	1.132	46.5	0.054	0.211	209	1.132	232	1.022
Guo et al. (2016)	150.0	2.0	465.1	188	190	186	1.052	60.8	0.076	0.251	177	1.052	183	1.018
	150.0	2.0	465.1	188	190	195	1.100	60.8	0.076	0.251	177	1.100	183	1.065
	150.0	2.0	465.1	188	190	197	1.115	60.8	0.076	0.251	177	1.115	183	1.078
	200.0	2.0	622.3	188	190	188	0.795	81.1	0.101	0.289	236	0.795	233	0.808
	200.0	2.0	622.3	188	190	211	0.892	81.1	0.101	0.289	236	0.892	233	0.907
	200.0	2.0	622.3	188	190	210	0.886	81.1	0.101	0.289	236	0.886	233	0.901
	250.0	2.0	779.4	188	190	252	0.851	101.4	0.127	0.324	284	0.887	282	0.895
	250.0	2.0	779.4	188	190	272	0.917	101.4	0.127	0.324	284	0.956	282	0.964
	250.0	2.0	779.4	188	190	272	0.918	101.4	0.127	0.324	284	0.958	282	0.966
	300.0	2.0	936.6	188	190	276	0.776	121.7	0.152	0.355	324	0.852	330	0.836
	300.0	2.0	936.6	188	190	348	0.978	121.7	0.152	0.355	324	1.074	330	1.054
	300.0	2.0	936.6	188	190	321	0.902	121.7	0.152	0.355	324	0.991	330	0.972
	400.0	2.0	1251	188	190	400	0.842	162.3	0.203	0.409	404	0.991	426	0.939
	400.0	2.0	1251	188	190	410	0.863	162.3	0.203	0.409	404	1.016	426	0.962
	600.0	2.0	1879	188	190	435	0.609	243.5	0.304	0.501	563	0.772	615	0.707
	600.0	2.0	1879	188	190	321	0.449	243.5	0.304	0.501	563	0.570	615	0.522
Ma et al. (2016)	89.0	3.0	270.4	209	1054	886	1.050	135.2	0.152	0.354	768	1.154	783	1.132
	89.0	2.9	270.5	209	1054	898	1.071	136.1	0.153	0.356	762	1.179	777	1.156
	89.0	3.9	267.5	210	1053	1171	1.069	102.8	0.115	0.308	1083	1.081	1057	1.108
	89.0	3.9	267.4	205	1180	1375	1.114	114.6	0.131	0.329	1171	1.175	1167	1.178
	89.1	3.9	267.7	205	1180	1365	1.102	114.4	0.131	0.329	1175	1.161	1172	1.165
	108.2	3.9	327.8	215	1180	1671	1.108	139.7	0.153	0.355	1372	1.218	1399	1.195
	133.4	3.9	407.0	204	1159	2018	1.094	168.7	0.194	0.401	1581	1.276	1661	1.215
	133.7	3.9	407.8	204	1159	1985	1.069	168.2	0.194	0.400	1594	1.245	1674	1.186
	139.5	5.9	419.8	194	1014	3344	1.327	101.9	0.123	0.319	2436	1.373	2405	1.390
Ahn et al. (2016)	48.6	1.8	147.1	205	276	96	1.315	31.8	0.036	0.174	73	1.315	89	1.084
	60.5	1.8	184.5	205	276	128	1.397	39.6	0.045	0.194	92	1.397	106	1.213
	77.3	2.1	236.3	205	276	157	1.147	43.4	0.050	0.203	137	1.147	154	1.017

Table 3.3 (*Cont'd.****)***

Reference	D (mm)	t (mm)	P_M (mm)	E (GPa)	$f_{y.mea}$ (MPa)	$F_{cr.max.}$ (kN)	$\frac{F_{cr.\max.}}{Af_{y.mea}}$	$\frac{D_{eq.c3}}{t\varepsilon^2}$	$\bar{\lambda}_{cs}$	$\bar{\lambda}_{l.b}$	$F_{cr.Pl}$ (kN)	$\frac{F_{cr.\max.}}{F_{cr.Pl}}$	$F_{cr.LnS}$ (kN)	$\frac{F_{cr.\max.}}{F_{cr.LnS}}$
Chan et al. (2015)	95.5	5.3	283.5	209.8	480	917	1.272	36.9	0.041	0.185	721	1.272	849	1.080
	95.5	5.3	283.5	207.0	472	903	1.273	36.3	0.041	0.184	709	1.273	835	1.081
	95.5	5.4	283.2	208.4	476	897	1.232	35.9	0.040	0.183	728	1.232	861	1.042
	95.6	7.5	276.9	205.3	411	1200	1.406	22.3	0.026	0.145	854	1.406	1138	1.055
	95.6	7.4	277.2	207.5	424	1203	1.383	23.4	0.026	0.148	870	1.383	1148	1.047
	95.6	7.4	277.2	206.4	418	1204	1.404	23.0	0.026	0.147	857	1.404	1135	1.061
Wang et al. (2017)	139.9	6.0	421.0	196.1	740	2194	1.184	74.2	0.089	0.271	1854	1.184	1863	1.178
	138.5	6.0	416.5	196.1	740	2149	1.168	73.2	0.088	0.269	1840	1.168	1854	1.159
	140.4	5.9	422.7	196.1	740	2204	1.200	75.5	0.090	0.273	1836	1.200	1840	1.198
	180.6	5.9	548.9	196.1	740	2728	1.134	96.3	0.115	0.309	2375	1.149	2318	1.177
	180.6	5.9	549.0	196.1	740	2759	1.151	96.6	0.116	0.309	2365	1.167	2309	1.195
	181.2	5.9	551.0	196.1	740	2724	1.127	96.5	0.116	0.309	2386	1.141	2330	1.169
	209.1	5.9	638.7	196.1	740	3074	1.106	112.3	0.135	0.333	2618	1.174	2620	1.173
	210.2	5.9	641.9	196.1	740	3109	1.106	112.1	0.134	0.333	2650	1.173	2652	1.172
	210.0	5.9	641.5	196.1	740	3073	1.099	112.6	0.135	0.334	2632	1.168	2635	1.166
	242.1	6.0	741.9	196.1	740	3497	1.065	127.8	0.153	0.356	2983	1.172	3043	1.149
	240.6	6.0	737.3	196.1	740	3467	1.066	127.4	0.153	0.355	2957	1.173	3015	1.150
	240.4	6.0	736.7	196.1	740	3447	1.050	126.1	0.151	0.353	2993	1.152	3047	1.131
	270.9	5.9	832.8	196.1	740	3897	1.068	144.5	0.173	0.378	3213	1.213	3330	1.170
	269.6	5.8	829.1	196.1	740	3822	1.078	147.3	0.176	0.382	3109	1.229	3230	1.183
	270.0	5.9	830.0	196.1	740	3843	1.057	144.0	0.173	0.378	3205	1.199	3320	1.157
	360.5	5.8	1114.7	196.1	740	4716	0.981	195.3	0.234	0.440	3968	1.189	4247	1.110
	360.6	5.8	1115.0	196.1	740	4734	0.982	195.0	0.234	0.439	3977	1.190	4256	1.112
	359.0	5.9	1109.8	196.1	740	4785	0.993	193.1	0.231	0.437	3986	1.200	4262	1.123
	389.9	5.9	1206.9	196.1	740	5143	0.979	209.4	0.251	0.455	4277	1.203	4606	1.117
	390.2	5.9	1207.6	196.1	740	5185	0.980	208.1	0.249	0.454	4313	1.202	4643	1.117
	391.5	5.8	1212.1	196.1	740	5176	0.990	212.1	0.254	0.458	4249	1.218	4581	1.130
	420.5	5.8	1303.1	196.1	740	5484	0.974	227.4	0.273	0.474	4521	1.213	4901	1.119
	421.4	5.8	1306.2	196.1	740	5455	0.968	228.3	0.274	0.475	4521	1.207	4902	1.113
	421.2	5.9	1305.4	196.1	740	5499	0.971	227.0	0.272	0.474	4545	1.210	4927	1.116
Ross (1978)	380	7.9	1169.4	212	308	3444	1.207	63.1	0.070	0.240	2853	1.207	2996	1.150
	380	7.9	1169.4	214	271	3222	1.284	55.5	0.061	0.224	2510	1.284	2709	1.189
	560	8.0	1734.9	212	308	4459	1.043	92.0	0.102	0.290	4275	1.043	4200	1.062
Wilson and Newmark (1933)	364.9	0.36	1145.6	200	296	40	0.327	1273.8	1.497	1.112	27	1.490	43	0.942
	389.2	0.84	1220.7	200	296	200	0.657	584.5	0.687	0.753	145	1.376	192	1.041
	373.2	0.53	1171.1	200	296	91	0.500	898.0	1.055	0.934	57	1.610	84	1.086
	366.7	0.40	1151.3	200	296	66	0.489	1163.2	1.367	1.063	33	2.036	51	1.306
	358.0	0.23	1124.4	200	296	14	0.181	1995.2	2.344	1.392	11	1.294	18	0.762
	363.7	0.34	1142.1	200	296	42	0.370	1354.1	1.591	1.147	24	1.793	38	1.122
	372.4	0.51	1168.7	200	296	84	0.475	923.6	1.085	0.947	53	1.572	80	1.054
	383.9	0.74	1204.3	200	296	169	0.642	658.2	0.773	0.799	112	1.514	153	1.104

Table 3.4 *Properties of CHS stub-columns in various experimental investigations reported in AISI S100-16C* (2016)

Reference	$\frac{F_{cr.\max.}}{A.f_{y.mea}}$	$\frac{D_{eq.c3}}{t\varepsilon^2}$	$\bar{\lambda}_{cs}$	$\bar{\lambda}_{l.b}$	$\frac{F_{cr.\max.}}{F_{cr.Pl}}$	$\frac{F_{cr.\max.}}{F_{cr.LnS}}$
University of Alberta	0.762	703.1	0.787	0.806	1.827	1.326
	0.670	578.5	0.647	0.731	1.322	1.019
	0.618	538.3	0.602	0.705	1.134	0.897
	0.592	418.5	0.468	0.622	0.845	0.739
	0.559	415.7	0.465	0.620	0.792	0.695
Lehigh University	0.820	672.6	0.753	0.789	1.881	1.382
	0.828	487.6	0.546	0.671	1.378	1.131
	0.804	424.2	0.475	0.626	1.163	1.011
	0.879	346.1	0.387	0.566	1.152	1.040
	0.928	270.6	0.303	0.500	1.176	1.076
	0.951	234.8	0.263	0.466	1.177	1.089
	0.988	202.6	0.227	0.433	1.190	1.116
	0.874	201.3	0.225	0.431	1.052	0.986
	0.970	198.7	0.222	0.429	1.163	1.092
	0.988	138.7	0.155	0.358	1.092	1.068
	0.998	134.2	0.150	0.352	1.093	1.075
	0.994	120.2	0.134	0.333	1.055	1.054
	1.011	102.2	0.114	0.307	1.021	1.048
	1.072	88.6	0.099	0.286	1.072	1.086
	1.059	80.9	0.090	0.273	1.059	1.057
University of Tokyo	0.890	503.4	0.563	0.682	1.529	1.240
	0.758	241.2	0.270	0.472	0.942	0.870
	0.964	172.2	0.193	0.399	1.122	1.069
	1.029	157.8	0.177	0.382	1.174	1.130
	1.075	142.2	0.159	0.363	1.195	1.165
	1.024	131.9	0.148	0.349	1.116	1.100
	1.000	126.3	0.141	0.342	1.076	1.067
	1.059	125.3	0.140	0.340	1.138	1.129
	1.032	122.8	0.137	0.337	1.102	1.097
	1.020	105.5	0.118	0.312	1.040	1.062
	1.117	104.6	0.117	0.311	1.136	1.161
	1.043	101.0	0.113	0.306	1.049	1.079
	1.023	99.4	0.111	0.303	1.023	1.055

Table 3.5 *Existing and proposed cross-section classification slenderness limits for CHSs under axial compression*

Design Standard	Slenderness parameter	Yield limit		Elastic limit	
		Existing	Proposed	Existing	Proposed
AS 4100:1998 (2016)	$\bar{\lambda}_{cs.IA}$	82	76.97	—	361.48
IS 800 (2007)	$\bar{\lambda}_{cs.IA}$	88	76.97	—	361.48
BS 5950: Part-1 (1990)	$\bar{\lambda}_{cs.E}$	93.6	81.88	—	384.62
EN 1993-1-1 (2005)	$\bar{\lambda}_{cs.E}$	90	81.88	—	384.62
AISC 360-16 (2016)	$\bar{\lambda}_{cs}$	0.11	0.092	—	0.4303
CSA S16-14 (2014)	$\bar{\lambda}_{cs}$	0.11	0.092	—	0.4303

This page is intentionally left blank

CHAPTER 4

ELLIPTICAL-HOLLOW-SECTIONS UNDER BENDING

In this chapter, an expression for the cross-sectional bending capacity curve is proposed based on the Direct-Strength-Method (DSM) approach using comprehensive data from the literature on structural carbon steel Circular-Hollow-Sections (CHSs). Also, a unified set of elastic, yield and compact cross-sectional slenderness limits for assessing the CHS and EHS members under bending is proposed. Later, according to the Equivalent-Resistance-Capacity-Method (ERCM), improved empirical expressions for the equivalent CHS diameter of Elliptical-Hollow-Section (EHS) are derived using the proposed CHS bending capacity prediction curve and the data of EHSs from the literature. Finally, the proposed expression for the bending resistance curve based on the DSM is also transformed into the generalized form of the traditional cylindrical shell buckling capacity curve as a practical solution, in harmony with the newly introduced Reference-Resistance-Design (RRD) guidelines (Rotter 2013, 2016a, 2016b, EN 1993-1-6: A1 2017).

4.1 BENDING CAPACITY

Of late, significant inconsistencies (*discussed further in* Section 4.1.2) among the cross-sectional compact and yield section slenderness limits for CHSs under bending specified in various international design standards (BS 5950:Part-1 1990, EN 1993-1-1 2005, IS 800 2007, CSA S16-14 2014, AISC 360-16 2016, AS 4100:1998 2016) are reported in the literature (Elchalakani et al. 2002a, 2002c, Rondal et al. 2003, Rotter and Sadowski 2014). Hence, in the interest of promoting the reliable application of the CHS cross-section classification criteria also to the EHSs, firstly, it is aimed to establish the moment resistance capacity prediction curve and the cross-section slenderness limits for CHSs which can be used uniformly across those design standards, by using a comprehensive data of results from the literature on CHS bending experimental programs (Donnell 1934, Coutie and Maunder 1963, Khaliq and Schilling 1964, Jirsa et al. 1972, Sherman 1976, 1979, 1984, 1985, Korol 1978, Stephens et al. 1982, Sedlacek et al. 1998, Al-Shawi 2001, Elchalakani et al. 2002a, 2002c, Jiao and Zhao 2004, Poonaya et al. 2009, Haedir et al. 2009, Guo et al. 2013, Nghiem et al. 2018).

4.1.1 Capacity Prediction Curves

In Tables 4.1 and 4.2, experimental data consisting of the ultimate cross-sectional moment of resistance, M_u exhibited by hot-finished (HF) and cold-formed (CF) CHSs under bending load in various independently conducted programs are tabulated. Also, the respective cross-sectional geometry; material yield strength; and cross-sectional strength properties calibrated by using the formulae provided in Section 2.2.1 with an assumption of $D = 2a = 2b$ for CHSs are compiled. The cross-sectional non-dimensional slenderness parameters $\bar{\lambda}_{l.b}$, $\bar{\lambda}_{cs}$, $\bar{\lambda}_{cs.E}$, and $\bar{\lambda}_{cs.IA}$ for CHS members with an outer diameter D and wall thickness t are obtained from Equations 2.26–2.29, respectively.

$\frac{M_u}{M_e}$ ratio of the test specimens in Table 4.1, is plotted against their respective $\bar{\lambda}_{l.b}$ value in Figure 4.1 and against their respective $\frac{1}{\bar{\lambda}_{cs}}$ value in Figure 4.2. According to the data plotted in Figures 4.1 and 4.2, the proposed expressions for estimating $M_{u.pr}$ based on the DSM

approach indicating a lower bound curve fit, barring few inconsistent data are calibrated and expressed in the Equations 4.1–4.4 in terms of $\bar{\lambda}_{l.b}$, $\bar{\lambda}_{cs}$, $\bar{\lambda}_{cs.E}$, and $\bar{\lambda}_{cs.IA}$, respectively. Where $M_{u.pr}$ is the predictive ultimate cross-sectional moment resistance-capacity according to Equations 4.1–4.4.

$$\frac{M_{u.pr}}{M_e} = \begin{cases} \dfrac{0.5948}{\bar{\lambda}_{l.b}} - \left(\dfrac{0.3605}{\bar{\lambda}_{l.b}}\right)^2 + \left(\dfrac{0.2693}{\bar{\lambda}_{l.b}}\right)^3 \\ \qquad\qquad\qquad\qquad\qquad\qquad if \quad 0.1 \le \bar{\lambda}_{l.b} < 0.621 \\ -\left(\dfrac{0.1996}{\bar{\lambda}_{l.b}}\right)^4 + \left(\dfrac{0.1393}{\bar{\lambda}_{l.b}}\right)^5 \end{cases} \tag{4.1}$$

$$\begin{cases} -\dfrac{0.0826}{\bar{\lambda}_{l.b}} + \left(\dfrac{0.5013}{\bar{\lambda}_{l.b}}\right)^2 + \left(\dfrac{0.6722}{\bar{\lambda}_{l.b}}\right)^3 \\ \qquad\qquad\qquad\qquad\qquad\qquad if \quad 0.621 \le \bar{\lambda}_{l.b} \le 2.1 \\ -\left(\dfrac{0.7113}{\bar{\lambda}_{l.b}}\right)^4 + \left(\dfrac{0.5669}{\bar{\lambda}_{l.b}}\right)^5 \end{cases}$$

$$\frac{M_{u.pr}}{M_e} = \begin{cases} \dfrac{0.6544}{\bar{\lambda}_{cs}^{0.5}} - \left(\dfrac{0.3966}{\bar{\lambda}_{cs}^{0.5}}\right)^2 + \left(\dfrac{0.2963}{\bar{\lambda}_{cs}^{0.5}}\right)^3 \\ \qquad\qquad\qquad\qquad\qquad\qquad if \quad 0.0121 \le \bar{\lambda}_{cs} < 0.4668 \\ -\left(\dfrac{0.2196}{\bar{\lambda}_{cs}^{0.5}}\right)^4 + \left(\dfrac{0.1533}{\bar{\lambda}_{cs}^{0.5}}\right)^5 \end{cases} \tag{4.2}$$

$$\begin{cases} -\dfrac{0.0908}{\bar{\lambda}_{cs}^{0.5}} + \left(\dfrac{0.5515}{\bar{\lambda}_{cs}^{0.5}}\right)^2 + \left(\dfrac{0.7396}{\bar{\lambda}_{cs}^{0.5}}\right)^3 \\ \qquad\qquad\qquad\qquad\qquad\qquad if \quad 0.4668 \le \bar{\lambda}_{cs} \le 5.338 \\ -\left(\dfrac{0.7826}{\bar{\lambda}_{cs}^{0.5}}\right)^4 + \left(\dfrac{0.6237}{\bar{\lambda}_{cs}^{0.5}}\right)^5 \end{cases}$$

$$\frac{M_{u.pr}}{M_e} = \begin{cases} \dfrac{19.5623}{\bar{\lambda}_{cs.E}^{0.5}} - \left(\dfrac{11.8558}{\bar{\lambda}_{cs.E}^{0.5}}\right)^2 + \left(\dfrac{8.8574}{\bar{\lambda}_{cs.E}^{0.5}}\right)^3 \\ \qquad\qquad\qquad\qquad\qquad\qquad if \quad 10.81 \le \bar{\lambda}_{cs.E} < 417.14 \\ -\left(\dfrac{6.5646}{\bar{\lambda}_{cs.E}^{0.5}}\right)^4 + \left(\dfrac{4.5827}{\bar{\lambda}_{cs.E}^{0.5}}\right)^5 \end{cases} \tag{4.3}$$

$$\begin{cases} -\dfrac{2.7143}{\bar{\lambda}_{cs.E}^{0.5}} + \left(\dfrac{16.4863}{\bar{\lambda}_{cs.E}^{0.5}}\right)^2 + \left(\dfrac{22.1092}{\bar{\lambda}_{cs.E}^{0.5}}\right)^3 \\ \qquad\qquad\qquad\qquad\qquad\qquad if \quad 417.14 \le \bar{\lambda}_{cs.E} \le 4770.14 \\ -\left(\dfrac{23.3946}{\bar{\lambda}_{cs.E}^{0.5}}\right)^4 + \left(\dfrac{18.6446}{\bar{\lambda}_{cs.E}^{0.5}}\right)^5 \end{cases}$$

$$\frac{M_{u.pr}}{M_e} = \begin{cases} \dfrac{18.9648}{\bar{\lambda}_{cs.IA}^{0.5}} - \left(\dfrac{11.4937}{\bar{\lambda}_{cs.IA}^{0.5}}\right)^2 + \left(\dfrac{8.5869}{\bar{\lambda}_{cs.IA}^{0.5}}\right)^3 \\ \qquad\qquad\qquad\qquad\qquad\qquad if \quad 10.164 \le \bar{\lambda}_{cs.IA} < 392.11 \\ -\left(\dfrac{6.3641}{\bar{\lambda}_{cs.IA}^{0.5}}\right)^4 + \left(\dfrac{4.4427}{\bar{\lambda}_{cs.IA}^{0.5}}\right)^5 \end{cases} \tag{4.4}$$

$$\begin{cases} -\dfrac{2.6314}{\bar{\lambda}_{cs.IA}^{0.5}} + \left(\dfrac{15.9827}{\bar{\lambda}_{cs.IA}^{0.5}}\right)^2 + \left(\dfrac{21.434}{\bar{\lambda}_{cs.IA}^{0.5}}\right)^3 \\ \qquad\qquad\qquad\qquad\qquad\qquad if \quad 392.11 \le \bar{\lambda}_{cs.IA} \le 4483.92 \\ -\left(\dfrac{22.6801}{\bar{\lambda}_{cs.IA}^{0.5}}\right)^4 + \left(\dfrac{18.0751}{\bar{\lambda}_{cs.IA}^{0.5}}\right)^5 \end{cases}$$

Along with the proposed curve representing Equation 4.1 in Figure 4.1, the CHS cross-sectional bending capacity prediction curves specified in various international design standards are also plotted.

The expression for the normalized cross-sectional moment resistance prediction curve for CHSs as per AS 4100:1998 (2016) is as follows:

$$\frac{M_{AS4100}}{M_e} = \begin{cases} 1.2732 & if \quad 0 \le \bar{\lambda}_{lb} \le 0.2218 \\ -2.2431\bar{\lambda}_{lb} + 1.7707 & if \quad 0.2218 < \bar{\lambda}_{lb} \le 0.3436 \\ 3.9369\bar{\lambda}_{lb}^2 - 5.3245\bar{\lambda}_{lb} + 2.3602 & if \quad 0.3436 < \bar{\lambda}_{lb} \le 0.5743 \\ \dfrac{18084.0374 - 9520.6426\bar{\lambda}_{lb} + 1179.1142\bar{\lambda}_{lb}^2}{1 - 124140.275\bar{\lambda}_{lb} + 282876.012\bar{\lambda}_{lb}^2} & if \quad 0.5743 < \bar{\lambda}_{lb} \le 2.1 \end{cases} \tag{4.5}$$

The expression for the normalized cross-sectional moment resistance prediction curve for CHSs as per EC3: EN 1993-1-1 (2005) is as follows:

$$\frac{M_{EC3}}{M_e} = \begin{cases} 1.2732 & if \quad 0 \le \bar{\lambda}_{lb} \le 0.2548 \\ 1 & if \quad 0.2548 < \bar{\lambda}_{lb} \le 0.293 \\ -\dfrac{0.026}{\bar{\lambda}_{lb}} + \dfrac{0.1817}{\bar{\lambda}_{lb}^2} - \dfrac{0.0258}{\bar{\lambda}_{lb}^3} & if \quad 0.293 < \bar{\lambda}_{lb} \le 2.1 \end{cases} \tag{4.6}$$

Although, EC3: EN 1993-1-1 (2005) specifies guidelines for the design of elastic CHSs under bending, it is to be noted that the design cross-sectional moment resistance of elastic CHSs is regulated by EC3: EN 1993-1-6 (2007).

The expression for the normalized cross-sectional moment resistance prediction curve for CHSs as per AISC 360-16 (2016) is as follows:

$$\frac{M_{AISC360}}{M_e} = \begin{cases} 1.2732 & if \quad 0 \le \bar{\lambda}_{lb} \le 0.2405 \\ 1 - \dfrac{0.0086}{\bar{\lambda}_{lb}} + \dfrac{0.0179}{\bar{\lambda}_{lb}^2} & if \quad 0.2405 < \bar{\lambda}_{lb} \le 0.5061 \\ -\dfrac{0.0421}{\bar{\lambda}_{lb}} + \dfrac{0.2967}{\bar{\lambda}_{lb}^2} & if \quad 0.5061 < \bar{\lambda}_{lb} \le 2.1 \end{cases} \tag{4.7}$$

However, it should be noted that the curves represented by Equations 4.5–4.7 in Figure 4.1 are extrapolated beyond their specified maximum slenderness values to match the slenderness range of the proposed curve represented by Equation 4.1. Similar extrapolation is carried out by Elchalakani (2014). Also, Donnell (1934) conducted bending tests on CHSs with $\bar{\lambda}_{l.b}$ values as high as ~ 2.1 and McCann et al. (2018) carried out FE study on bending of EHSs with $\bar{\lambda}_{l.b}$ values as high as ~ 1.65. Further, the $\frac{M_u}{M_p}$ ratio of the tested specimens which is mentioned in Table 4.1 is plotted against their respective $\bar{\lambda}_{l.b}$ value in Figure 4.3. Maintaining consistency with the $M_{u.pr}$ values based on Equations 4.1–4.4, Equations 4.8–4.11 are obtained. A plot of the lower bound fit curve representing Equation 4.8 is also shown in Figure 4.3.

$$\frac{M_{u.pr}}{M_p} = \begin{cases} \dfrac{0.4557}{\bar{\lambda}_{l.b}} - \left(\dfrac{0.298}{\bar{\lambda}_{l.b}}\right)^2 + \left(\dfrac{0.2172}{\bar{\lambda}_{l.b}}\right)^3 & if \quad 0.1 \le \bar{\lambda}_{l.b} < 0.621 \\ -\left(\dfrac{0.1566}{\bar{\lambda}_{l.b}}\right)^4 + \left(\dfrac{0.1085}{\bar{\lambda}_{l.b}}\right)^5 & \end{cases} \tag{4.8}$$

$$\begin{cases} \dfrac{0.0488}{\bar{\lambda}_{l.b}} - \left(\dfrac{0.7192}{\bar{\lambda}_{l.b}}\right)^2 + \left(\dfrac{1.1643}{\bar{\lambda}_{l.b}}\right)^3 & if \quad 0.621 \le \bar{\lambda}_{l.b} \le 2.1 \\ -\left(\dfrac{1.0343}{\bar{\lambda}_{l.b}}\right)^4 + \left(\dfrac{0.7686}{\bar{\lambda}_{l.b}}\right)^5 & \end{cases}$$

$$\frac{M_{u.pr}}{M_p} = \begin{cases} \dfrac{0.5014}{\bar{\lambda}_{cs}^{0.5}} - \left(\dfrac{0.3279}{\bar{\lambda}_{cs}^{0.5}}\right)^2 + \left(\dfrac{0.239}{\bar{\lambda}_{cs}^{0.5}}\right)^3 & \\ & if \quad 0.0121 \le \bar{\lambda}_{cs} < 0.4668 \\ -\left(\dfrac{0.1723}{\bar{\lambda}_{cs}^{0.5}}\right)^4 + \left(\dfrac{0.1194}{\bar{\lambda}_{cs}^{0.5}}\right)^5 & \end{cases}$$

$$\begin{cases} \dfrac{0.0537}{\bar{\lambda}_{cs}^{0.5}} - \left(\dfrac{0.7913}{\bar{\lambda}_{cs}^{0.5}}\right)^2 + \left(\dfrac{1.281}{\bar{\lambda}_{cs}^{0.5}}\right)^3 & \\ & if \quad 0.4668 \le \bar{\lambda}_{cs} \le 5.338 \\ -\left(\dfrac{1.1379}{\bar{\lambda}_{cs}^{0.5}}\right)^4 + \left(\dfrac{0.8456}{\bar{\lambda}_{cs}^{0.5}}\right)^5 & \end{cases}$$

(4.9)

$$\frac{M_{u.pr}}{M_p} = \begin{cases} \dfrac{14.9875}{\bar{\lambda}_{cs.E}^{0.5}} - \left(\dfrac{9.8009}{\bar{\lambda}_{cs.E}^{0.5}}\right)^2 + \left(\dfrac{7.1435}{\bar{\lambda}_{cs.E}^{0.5}}\right)^3 & \\ & if \quad 10.81 \le \bar{\lambda}_{cs.E} < 417.14 \\ -\left(\dfrac{5.1504}{\bar{\lambda}_{cs.E}^{0.5}}\right)^4 + \left(\dfrac{3.5685}{\bar{\lambda}_{cs.E}^{0.5}}\right)^5 & \end{cases}$$

$$\begin{cases} \dfrac{1.605}{\bar{\lambda}_{cs.E}^{0.5}} - \left(\dfrac{23.6538}{\bar{\lambda}_{cs.E}^{0.5}}\right)^2 + \left(\dfrac{38.2927}{\bar{\lambda}_{cs.E}^{0.5}}\right)^3 & \\ & if \quad 417.14 \le \bar{\lambda}_{cs.E} \le 4770.14 \\ -\left(\dfrac{34.0171}{\bar{\lambda}_{cs.E}^{0.5}}\right)^4 + \left(\dfrac{25.2785}{\bar{\lambda}_{cs.E}^{0.5}}\right)^5 & \end{cases}$$

(4.10)

$$\frac{M_{u.pr}}{M_p} = \begin{cases} \dfrac{14.5298}{\bar{\lambda}_{cs.IA}^{0.5}} - \left(\dfrac{9.5016}{\bar{\lambda}_{cs.IA}^{0.5}}\right)^2 + \left(\dfrac{6.9253}{\bar{\lambda}_{cs.IA}^{0.5}}\right)^3 \\ \qquad\qquad if \quad 10.164 \le \bar{\lambda}_{cs.IA} < 392.11 \\ -\left(\dfrac{4.9931}{\bar{\lambda}_{cs.IA}^{0.5}}\right)^4 + \left(\dfrac{3.4595}{\bar{\lambda}_{cs.IA}^{0.5}}\right)^5 \end{cases} \tag{4.11}$$

$$\begin{cases} \dfrac{1.556}{\bar{\lambda}_{cs.IA}^{0.5}} - \left(\dfrac{22.9314}{\bar{\lambda}_{cs.IA}^{0.5}}\right)^2 + \left(\dfrac{37.1232}{\bar{\lambda}_{cs.IA}^{0.5}}\right)^3 \\ \qquad\qquad if \quad 392.11 \le \bar{\lambda}_{cs.IA} \le 4483.92 \\ -\left(\dfrac{32.9782}{\bar{\lambda}_{cs.IA}^{0.5}}\right)^4 + \left(\dfrac{24.5064}{\bar{\lambda}_{cs.IA}^{0.5}}\right)^5 \end{cases}$$

Elchalakani et al. (2002c, 2002a) and Elchalakani (2014) observed that there is a reduction in the ultimate moment resistance capacity, M_u of CHSs under bending due to ovalisation instability. CHS buckling under bending is a complex phenomenon due to the interaction of two different modes of instability, namely, ovalisation and bifurcation. Apart from the bifurcation mode which is similar to the classical local buckling of cylinders in axial compression, ovalisation is another form of theoretical local instability associated with the bending of CHSs (Sherman 1992). The phenomenon and effects of ovalisation instability of cylindrical tubular metal sections under bending are well documented in the literature (Brazier 1927, Karamanos 2002, Houliara and Karamanos 2011, Xu et al. 2017, Wang et al. 2018a). In the past, evidence of both ovalisation and wave buckles are observed from bending tests of CHS members with a long unstiffened region of constant bending along the length (Sherman 1992, Wang et al. 2018a).

In Table 4.2, the data of CHSs under bending with ovalisation restraint from the literature (Sherman 1976, 1979, 1985) reported in Sherman (1992) is presented. It is observable from Figure 4.4 that the proposed design curve represented by Equation 4.1 conservatively predicts the moment resistance capacity of the CHSs under bending (see Table 4.2) with ovalisation restraint. A better interpretation of such conservatism during the design due to the ovalisation effect on M_u of CHSs based on a non-dimensional length parameter involving the length of

the uniform bending moment region, L_{ub} and cross-sectional geometric details alongside $\bar{\lambda}_{cs.E}$ can also be seen in a 3-D plot by Wang et al. (2018a). However, Wang et al. (2018a) observed that the ovalisation restrained CHS members with $\bar{\lambda}_{cs.E} \sim 100$ exhibited an increase in M_u only around 5% when compared with those without ovalisation restraints. While Rotter and Sadowski (2017) found that a significant decrease in M_u due to ovalisation instability occurs only in CHS members with $\bar{\lambda}_{cs.E} > 140$, *i.e.*, the yield *or* the slender cross-sectional limit suggested by Rotter and Sadowski (2017). As mentioned earlier, L_{ub} plays a significant role in inducing the ovalisation instability to the bending performance of CHS members. Even for very long CHS members with $\bar{\lambda}_{cs.E} > 140$, ovalisation instability can be constrained to the fullest with the usage of stiffening rings at regular intervals along the length.

Unlike the design procedures in AS 4100:1998 (2016), EC3: EN 1993-1-1 (2005) and AISC 360-16 (2016) where the cross-sectional bending resistance is estimated largely based on empirical relationships involving limited parameters like the cross-sectional geometry and material properties *E* and υ, EN 1993-1-6 (2007) of EC3 offers provisions for the same with the inclusion of additional parameters relating to the mechanical phenomena like strain hardening, geometric non-linearity, material non-linearity, and imperfection sensitivity by considering the CHSs as thin tubular cylindrical shells. Also, the EC3: EN 1993-1-1 (2005) design curve (Equation 4.6) possesses a strangely large step change in predictive resistance between the specified compact and yielding sections, which leads to a dramatic drop in assessed bending resistance at the specified yield slenderness limit (Rotter and Sadowski 2017). According to EC3: EN 1993-1-6 (2007), the CHSs with $r_{mid} \geq 25t$ are considered as thin tubular cylindrical shells. r_{mid} is the mid-profile radius of the CHS cross-section expressed in the following Equation 4.12.

$$r_{mid} = 0.5(D - t) \tag{4.12}$$

The EC3: EN 1993-1-6 (2007) shell buckling capacity design provisions are developed by Rotter (1999, 2002). The strain hardening phenomenon was ignored in the initial proposals and was later included with modifications (Rotter 2005, 2006) to the guidelines thereby eliminating

the plastic plateau in the traditional shell buckling capacity curve for stress design (Rotter 2011). Further developments in this regard involve devising a hand calculation method, termed Reference-Resistance-Design (RRD) by Rotter (2013, 2016a, 2016b, 2017) for estimating the parameters attributing various mechanical phenomena which define the profile of the traditional shell buckling capacity curve based on extensive GMINA (Geometrically and Materially Non-linear Analysis with Imperfections included) calculations. RRD is included in EC3: EN 1993-1-6 (2007) through an amendment (EN 1993-1-6:A1 2017) which additionally created a new normative Annex E. However, it is understood that practical appropriateness of these developments of shell buckling RRD procedures is still uptaking. Therefore, an attempt is made herein to bring the proposed bending resistance curve for CHSs represented by Equations 4.1–4.4 and 4.8–4.11 to the form of RRD based traditional shell buckling capacity curve.

The essential feature of the traditional shell buckling capacity curve is that the cross-section is categorized among one of the three domains which are clearly defined based on two limiting conditions: one based on the pure material failure and the other based on the elastic stability failure (Rotter 2005, Doerich and Rotter 2011). The interposing relation between the two is defined using the ‘‘relative slenderness’’ of the cross-section as the measure between them. The relative slenderness, $\bar{\lambda}_{sb}$ is defined in dimensionless terms as follows:

$$\bar{\lambda}_{sb} = \sqrt{\left(M_p / M_{cr}\right)} \tag{4.13}$$

M_p and M_{cr} are the full plastic and linear elastic critical cross-sectional moment resistances, respectively. Ignoring length effects, M_p and M_{cr} for steel thin cylindrical CHSs can be expressed from small displacement theory as follows (Chen et al. 2008, Rotter and Sadowski 2014, Wang et al. 2020):

$$M_p \approx 4 t r_{mid}^2 f_{y.mea} \tag{4.14}$$

$$M_{cr} = \frac{\pi}{\sqrt{3\left(1-\upsilon^2\right)}} E t^2 r_{mid} \approx 1.9007 E t^2 r_{mid} \tag{4.15}$$

It is understood that apart from Equations 2.15 and 2.17 and the expressions in Table 2.1 with an assumption of $D = 2a = 2b$ for CHSs, Equation 4.14 can also be used for obtaining M_p of thin cylindrical CHSs with $r_{mid} \geq 15t$. After substituting Equations 4.14 and 4.15 in Equation 4.13, the following Equation 4.16 is obtained.

$$\bar{\lambda}_{sb} = 1.4507\sqrt{\left(\frac{r_{mid}}{t}\right)\left(\frac{f_{y.mea}}{E}\right)} \tag{4.16}$$

Rotter and Sadowski (2014) related $\bar{\lambda}_{sb}$ to $\bar{\lambda}_{cs.E}$ using the following assumption for thin cylindrical CHS shells.

$$\sqrt{r_{mid}} \approx \sqrt{0.5D} \tag{4.17}$$

By substituting Equation 4.17 in Equation 4.16 and by using Equation 2.27, the following Equation 4.18 is obtained.

$$\bar{\lambda}_{sb} \approx 1.0258\sqrt{\left(\frac{D}{t}\right)\left(\frac{f_{y.mea}}{E}\right)} \approx 1.0258\bar{\lambda}_{cs}^{0.5} \tag{4.18}$$

Later, from Equations 2.31 and 4.18 and with an assumption that $E \approx 210000$ MPa, the following Equation 4.19 is obtained (Rotter and Sadowski 2014).

$$\bar{\lambda}_{cs.E} \approx \frac{4.044E\bar{\lambda}_{sb}^2}{1000} \approx 849.24\bar{\lambda}_{sb}^2 \tag{4.19}$$

By substituting Equation 4.19 in Equation 4.10, the CHS cross-sectional capacity prediction curve equation under bending in terms of EC3: EN 1993-1-6 (2007) relative slenderness, $\bar{\lambda}_{sb}$ is as follows:

$$\frac{M_{u.pr}}{M_p} = \begin{cases} \dfrac{0.5143}{\bar{\lambda}_{sb}} - \left(\dfrac{0.3363}{\bar{\lambda}_{sb}}\right)^2 + \left(\dfrac{0.2451}{\bar{\lambda}_{sb}}\right)^3 \\ -\left(\dfrac{0.1767}{\bar{\lambda}_{sb}}\right)^4 + \left(\dfrac{0.1225}{\bar{\lambda}_{sb}}\right)^5 & if \quad 0.113 \le \bar{\lambda}_{sb} < 0.701 \\ \dfrac{0.0551}{\bar{\lambda}_{sb}} - \left(\dfrac{0.8117}{\bar{\lambda}_{sb}}\right)^2 + \left(\dfrac{1.314}{\bar{\lambda}_{sb}}\right)^3 \\ -\left(\dfrac{1.1673}{\bar{\lambda}_{sb}}\right)^4 + \left(\dfrac{0.8674}{\bar{\lambda}_{sb}}\right)^5 & if \quad 0.701 \le \bar{\lambda}_{sb} \le 2.37 \end{cases} \tag{4.20}$$

As the Equations 4.1–4.4, Equations 4.8–4.11 and Equation 4.20 are derived by using the traditionally accepted empirical procedure of calibrating the expression for the lower bound limiting curve based on the available test results, it seems only the parameters like the cross-sectional geometry and the material yield strength are the significant contributing factors for the cross-sectional resistance (Rotter 2005). Consequently, the quantification of other important attributes like strain hardening, elastic-plastic interaction, geometric and material nonlinearity, and imperfection sensitivity is lacking in those Equations (4.1–4.4, 4.8–4.11 and 4.20) (Rotter 2005). Thus, to impart those lacking attributes, Equation 4.20 is approximately transformed into the form of the traditional RRD based shell buckling curve in Equation 4.21 without losing originality in the geometry using nonlinear regression analyses (see Figure 4.5).

$$\frac{M_{u.pr}}{M_p} = \begin{cases} 0.5011\left(\bar{\lambda}_{sb}\right)^{-0.466} & if \quad 0.1129 \le \bar{\lambda}_{sb} \le 0.2311 \\ 1 - 0.46\left(\dfrac{\bar{\lambda}_{sb} - 0.2311}{0.701 - 0.2311}\right)^{0.7137} & if \quad 0.2311 < \bar{\lambda}_{sb} \le 0.701 \\ \dfrac{0.27}{\bar{\lambda}_{sb}^{\,2}} & if \quad 0.701 < \bar{\lambda}_{sb} \le 2.37 \end{cases} \tag{4.21}$$

While the modified capacity curve is shown in Figure 4.6 where

$$\frac{M_{u.pr}}{M_{cr}} = \frac{M_{u.pr}}{M_p} \cdot \frac{M_p}{M_{cr}} = \frac{M_{u.pr}}{M_p} \cdot \left(\bar{\lambda}_{sb}\right)^2 \tag{4.22}$$

After substituting Equation 4.21 in 4.22, $\frac{M_{u.pr}}{M_{cr}}$ in terms of $\bar{\lambda}_{sb}$ is also obtained. So, the modified capacity curve in Figure 4.6 is plotted for the set of $\left(\frac{M_{u.pr}}{M_{cr}}; \frac{M_{u.pr}}{M_p}\right)$ data points calibrated for the range of $\bar{\lambda}_{sb}$ using Equations 4.21 and 4.22. The following parameters are estimated from Figure 4.5 and Equation 4.21.

Plastic *or* squash limit relative slenderness, $\bar{\lambda}_{osb}$ = 0.2311;

Elastic limit relative slenderness, $\bar{\lambda}_{psb}$ = 0.701;

Plastic range factor, β_p = 0.46;

Plastic severity factor *or* elastic-plastic interaction exponent, η_{in} = 0.7137;

Elastic reduction factor, $\alpha_e = \alpha_I \alpha_G$ = 0.27 where α_G and α_I are the geometric nonlinearity and imperfection sensitivity factors respectively.

Both α_G and α_I are found to be dependent on the length domain categorization of the member based on the dimensionless length parameters expressed in the following Equations 4.23 and 4.24 (Rotter et al. 2014, Fajuyitan and Sadowski 2018).

$$\omega_{lcs} = \frac{L_{ub}}{\sqrt{t \cdot r_{mid}}} \tag{4.23}$$

$$\Omega_{lcs} = \frac{L_{ub}}{r_{mid}} \sqrt{\frac{t}{r_{mid}}} \tag{4.24}$$

While α_I also depends on characteristic geometric imperfection amplitude known as the equivalent geometric deviation, δ_{ei} which can be estimated according to the following Equation 4.25 proposed by Fajuyitan and Sadowski (2018).

$$\alpha_I = \frac{1}{1 + x_{ip}\left(\frac{\delta_{ei}}{t}\right)^{0.7}} \tag{4.25}$$

where the scaling factor, x_{ip} is again shown to be dependent on ω_{lcs} and Ω_{lcs}. Variation of α_G and α_I are studied by Rotter et al. (2014) and Fajuyitan and Sadowski (2018) by extensive GMINA calculations over various length domains like short, medium, transitional and long cylindrical CHS shells. However, the practicality of those proposals made by Rotter et al. (2014) and Fajuyitan and Sadowski (2018) for α_G and α_I still needs to be assessed experimentally. It is beyond the scope of the present study to discuss the applicability of α_G and α_I in accordance with the proposed Equation 4.21 considering all those four domains which involves numerous calculations. Hence, the applicability of α_G and α_I based on the proposed Equation 4.21 in only short and medium-length domains is assessed further herein using the proposals made by Rotter et al. (2014) and Fajuyitan and Sadowski (2018). The cylindrical CHS shells in the short length domain $\left(\omega_{lcs} \le 4.8\right)$ are insensitive to geometric nonlinearity and imperfections with almost perfect plastic shell behaviour (Fajuyitan et al. 2018, Fajuyitan and Sadowski 2018, Wang et al. 2020).

For medium length cylinders domain $\left(4.8 < \omega_{lcs} \le 0.5\frac{r_{mid}}{t}\right)$, $\alpha_G = 0.85$ and $x_{ip} = 1.7$ considering the most vulnerable scenario according to Rotter et al. (2014). As $\alpha_G = 0.85$, $\alpha_I = 0.3177$ for $\alpha_e = 0.27$ from Equation 4.21 and therefore the maximum limit of $\frac{\delta_{ei}}{t}$ for the proposed curve is 1.396 based on Equation 4.25. Based on the expression for the characteristic imperfection amplitude in section D.1.2.2 of EC3: EN 1993-1-6 (2007) and the calibrated the maximum value of $\frac{\delta_{ei}}{t}$, the respective maximum permissible values of $\frac{r_{mid}}{t}$

are 3120, 1219 and 500 for which Equation (53) holds good for FTQ (Fabrication Tolerance Quality) parameters 40 (Class A), 25 (Class B) and 16 (Class C).

To date, publicly available documented studies related to material strain hardening and elastic-plastic interaction zones in the context of the RRD based traditional shell buckling capacity curve are lacking as per the authors' knowledge. Therefore, from Equation 4.21, 0.5011 and -0.466 are considered as the strain hardening coefficient and exponents for the proposed RRD based capacity curve, respectively.

4.1.2 Compact, Yield, and Elastic Slenderness Limits

From Figure 4.1, the abscissa value of 0.349 $\left(=\bar{\lambda}_{l.b}\right)$ corresponding to the ordinate value of unity $\left(i.e.,\ \frac{M_{u.pr}}{M_e}=1\right)$ for the proposed curve that represents Equation 4.1 is considered as the yield limit. From Figure 4.3, a compact section limit 0.205 $\left(=\bar{\lambda}_{l.b}\right)$ is proposed with a corresponding $\frac{M_{u.pr}}{M_p}$ value of unity as per Equation 4.8, and that limit corresponds to a $\frac{M_{u.pr}}{M_e}$ value of 1.323 according to Equations 4.1–4.4. From Figures 4.1 and 4.2, the point of convergence of the two components of the proposed moment-resistance capacity curve defined by Equations 4.1–4.4 beneath the yield section resistance limit is chosen as the elastic section limit. The obtained elastic section limit is 0.621 $\left(=\bar{\lambda}_{l.b}\right)$. The sections with the proposed elastic section limit as cross-section slenderness exhibit a cross-section capacity value of ~ 0.695 times of M_e. Thus, the sections with cross-section slenderness less than *or* equal to the proposed elastic limit are the sections with absolute zero deformation capacity. While the sections with cross-section slenderness between the proposed elastic and yield section limits can exhibit negligible deformation capacity with slight inelastic squashing of the material. It can be observed from Figure 4.2 that the effect of material plastification increases and the effect of local buckling decreases on the section moment resistance capacity with the reduction in the section slenderness value beyond the proposed elastic limit. And, the cross-sections with slenderness value between the proposed yield and compact limits (*i.e.*, yielding sections) exhibit the moment resistance capacity solely due to the material plastification. Further, from

Figures 4.2 and 4.3, it is understood that the material strain hardening effectuates the moment resistance capacity of the cross-sections with slenderness limit less than the proposed compact limit.

Table 4.3 depicts the disparities among the existing compact and yield section slenderness limits for CHSs under pure bending in various international design standards (BS 5950:Part-1 1990, EN 1993-1-1 2005, IS 800 2007, CSA S16-14 2014, AISC 360-16 2016, AS 4100:1998 2016). The compact and yield section slenderness limits in Table 4.3 are normalized and expressed in terms of the cross-section slenderness parameter $\overline{\lambda}_{cs.IA}$ (see Equations 2.29–2.31). While Table 4.4 showcases the contrast between the proposed and the existing cross-section classification slenderness limits for CHSs according to various international design standards. However, it should be noted that the proposed slenderness limits in Table 4.4 shall have the same value when normalized with-respect-to any of the slenderness parameters specified in Equations 2.27–2.29, thereby eliminating the discrepancies which are mentioned earlier in Table 4.3.

4.2 EQUIVALENT CHS DIAMETER

Since Chan and Gardner (2008a) proposed expressions (Equations 2.22 and 2.23) for the equivalent CHS diameter of EHS, some additional independent experimental and FE programs (McCann et al. 2018, Chen and Young 2019) were carried out to study the cross-sectional bending behaviour of EHSs. Chan and Gardner (2008a) performed three-point and four-point bending experiments (EXPs) on EHSs. McCann et al. (2018) conducted Finite Element Analyses (FEAs) on slender EHS cantilever members. While Chen and Young (2019) performed both EXPs and FEAs on CF EHSs.

Haque et al. (2012) and Chen and Young (2019) reported significant conservatism involved in utilizing those Equations 2.22 and 2.23 formulated by Chan and Gardner (2008a) for predicting the maximum cross-sectional bending strength, M_u. Chan and Gardner (2008a) and McCann et al. (2018) also indicated varying cross-sectional strength prediction curves with-respect-to the cross-sectional aspect ratio, $r\left(=\frac{a}{b}\right)$ of EHSs based on those Equations 2.22 and 2.23 and thus consequently implying different slenderness limits for different aspect ratios. Therefore, firstly,

the efficiency of Equations 2.22 and 2.23 is analysed using the available data of carbon steel EHSs under bending from the literature (Chan and Gardner 2008a, McCann et al. 2018, Chen and Young 2019). The data including geometrical, material and other cross-sectional strength properties of the EHS test specimens and FE models analysed under bending load from the literature are calibrated and catalogued in Tables 4.5 and 4.6 using the formulae provided in Section 2.2.1.

In Figures 4.7 and 4.8, the M_u/M_e value of EHSs in the investigations from the literature (Chan and Gardner 2008a, McCann et al. 2018, Chen and Young 2019) alongside the proposed CHS moment-resistance prediction curve is plotted against the respective EC3: EN 1993-1-1 (2005) cross-section slenderness value calibrated based on Equation 2.22 *or* Equation 2.23. The respective EC3: EN 1993-1-1 (2005) cross-section slenderness value which is calculated based on Equation 2.22 or Equation 2.23 and the maximum cross-sectional moment resistance capacity, M_u value exhibited by the EHSs are also catalogued in Tables 4.5 and 4.6. Further, it is to be noted that the data of EHS cantilever models from McCann et al. (2018) with only FTQ Class-A imperfections specified according to Annex D (Section D.1.2.2) of EN 1993-1-6 (2007) for circular shells is considered herein.

Alongside the findings of Haque et al. (2012) and Chen and Young (2019), it is observed from Figures 4.7 and 4.8 that the equivalent CHS diameter Equations 2.22 and 2.23 which are proposed by Chan and Gardner (2008a) result in significant conservatism with-respect-to the proposed curve represented by Equation 4.3. However, the extent of conservatism is found to be much higher in the case of EHSs under major axis bending.

4.2.1 Equivalent-Resistance-Capacity-Method (ERCM)

In the interest of promoting the reliable application of the CHS cross-section classification criteria also to the EHSs, it is intended to acquire empirical expressions for the equivalent CHS diameter of the EHS under bending based on ERCM which involves fitting the data of EHS bending analysis results from the literature (Chan and Gardner 2008a, McCann et al. 2018, Chen and Young 2019) by preserving consistency with the CHS bending capacity prediction curve. The concept of ERCM is already used in the determination of the equivalent CHS

diameter expression (Equation 3.1) for the EHSs under axial compression in the previous Chapter 3.

Thus, the following empirical Equations 4.26 and 4.27 for the equivalent CHS diameter, D_{eq} are deduced based on the ERCM by using the data of material, geometry and sectional strength properties in Tables 4.5 and 4.6 so that the consistency with the proposed CHS bending capacity curve is maintained.

For EHS under major axis bending:

$$\frac{D_{eq}}{2a}=\frac{D_{NSb.mj}}{2a}=\begin{cases}\left(0.1286r\right)^3+\left(0.0922r\right)^2-\left(0.031r\right)+0.5448 & if \quad r>1.357\\ \dfrac{1}{r^2} & if \quad r\le 1.357\end{cases} \tag{4.26}$$

For EHS under minor axis bending:

$$\frac{D_{eq}}{2a}=\frac{D_{NSb.mn}}{2a}=-\left(0.3123r\right)^3+\left(0.5648r\right)^2-\left(0.2996r\right)+1.01 \tag{4.27}$$

According to ERCM, both the EHS and the CHS with its respective D_{eq} based on Equation 4.26 *or* Equation 4.27 shall exhibit the same value of cross-sectional resistance capacity $\left(\frac{M_u}{M_e} \quad or \quad \frac{M_u}{M_p}\right)$, provided both the EHS and CHS have the same $f_{y.mea}$ and t values.

The respective equivalent CHS diameter values under bending and the EC3: EN 1993-1-1 (2005) cross-section slenderness values which are calculated using Equations 4.26 and 4.27 for all the EHS members in the investigations carried out by Chan and Gardner (2008a), McCann et al. (2018) and Chen and Young (2019) are also tabulated in Tables 4.5 and 4.6. It should be noted that for the EHSs under major axis bending and with $r=\frac{a}{b}\le 1.357$, the equivalent CHS diameter expression proposed by Chan and Gardner (2008a) is also recommended herein as well.

The applicability of Equations 4.26 and 4.27 is verified in Figures 4.9 and 4.10 by plotting the M_u/M_e value of EHSs from Tables 4.5 and 4.6 alongside the proposed CHS moment-resistance prediction curve against the respective EC3: EN 1993-1-1 (2005) cross-section slenderness value calibrated based on Equation 4.26 *or* Equation 4.27. By comparing Figures 4.7 and 4.8 with Figures 4.9 and 4.10, it is evident that the usage of the equivalent CHS diameter Equations 4.26 and 4.27 for calibrating the cross-section slenderness resulted in improved consistency with reduced scatter and conservatism between the M_u/M_e values and the proposed CHS moment-resistance curve represented by Equation 4.3.

Further, using the Equations 2.22 and 2.23 proposed by Chan and Gardner (2008a) for calculating the cross-sectional slenderness will necessitate the designer to propose higher cross-section slenderness limits than the existing *or* proposed limits for CHSs as those Equations 2.22 and 2.23 are already proved to be conservative. Lan et al. (2019) suggested the yield limit for $\bar{\lambda}_{l.b}$ of CHS and EHSs as 0.50 by using Equations 2.22 and 2.23. But, 0.4233 is the estimated yield limit for $\bar{\lambda}_{l.b}$ of CHS and EHSs in Section 4.1.2 based on the interpretations from Figure 4.1. Therefore, it is recommended to utilise the proposed Equations 4.26 and 4.27 for determining the cross-section slenderness of the EHS, so that it is feasible to implement the CHS cross-section slenderness limits and moment resistance prediction curves proposed in the previous Sections 4.1 also for EHSs. Accordingly, the respective $\bar{\lambda}_{l.b}$ and $\bar{\lambda}_{cs}$ values of EHSs as per Equations 2.32 and 2.33 in Tables 4.5 and 4.6 are calculated using Equations 4.26 and 4.27.

4.3 RELIABILITY ANALYSIS

The accuracy and suitability of the proposed bending resistance capacity prediction curves represented by Equations 4.1–4.4 and Equations 4.8–4.11 are evaluated using the reliability analysis procedure for the design of structural steel members presented in the literature (Ellingwood et al. 1980, Hsiao et al. 1990, Victorsson 2011, AISI S100-16 2016), similar to the procedure detailed in Section 3.3. Additionally, the reliability of the codal design curves represented by Equations 4.5–4.7 is also evaluated herein. A target reliability index, β_o of 2.5 is recommended as a lower bound for structural steel members corresponding to the load

combination 1.2DL+1.6LL (1.2×Dead Load + 1.6×Live Load) and a fixed dead-to-live load ratio of 0.2 is to be utilised according to the North American specifications (AISI S100-16 2016). The reliability index of the prediction curves is calculated using Equation 3.9.

According to North American specifications (AISI S100-16 2016), $C_{\varphi} = 1.521$, F_m = 1.00, M_m = 1.10, V_M = 0.10, V_Q = 0.21 and V_F = 0.05. $\varphi = 0.90$ for structural steel tubular members subjected to bending as per the LRFD method (Hsiao et al. 1990, Chen and Kim 1997). The $\frac{M_u}{M_{AS4100}}$, $\frac{M_u}{M_{AISC360}}$, $\frac{M_u}{M_{EC3}}$ and $\frac{M_u}{M_{u.pr}}$ ratios of all the CHSs in Tables 4.1 and 4.2 and EHSs in Tables 4.5 and 4.6 are calibrated and tabulated as per the Equations 4.5–4.8. While the corresponding values of mean (P_m) and coefficient-of-variation (V_P) of $\frac{M_u}{M_{AS4100}}$, $\frac{M_u}{M_{AISC360}}$, $\frac{M_u}{M_{EC3}}$ and $\frac{M_u}{M_{u.pr}}$ ratios for all the CHSs in Tables 4.1 and 4.2 and EHSs in Tables 4.5 and 4.6 together are calibrated and presented in Table 4.7. Based on Equation 3.9, β values of the codal curves representing Equations 4.5–4.7 and the proposed curve representing any one of the Equations 4.1–4.4 and Equations 4.8–4.11 are also calibrated in Table 4.7. From Table 4.7, only the proposed curve represented by Equations 4.1–4.4 and Equations 4.8–4.11 is found to have a β value greater than the target value of 2.5. It is also estimated that the proposed curve represented by Equations 4.1–4.4 and Equations 4.8–4.11 exhibits a β value of 2.5 for a higher φ value of 0.96.

4.4 SUMMARY AND DISCUSSION

4.4.1 Discussion on the Codal and Proposed Cross-sectional Criteria

In this section, the contrast between the proposed and the existing codal design criteria for CHSs under bending is discussed in terms of their appropriateness in applicability and limitations based on the observations made from Figure 4.1 and Tables 4.4 and 4.7.

From Table 4.7, the codal design Equations 4.5–4.7 are found to be unreliable as they have a β value lesser than the target value of 2.5. The lesser β values of the codal design curves could also be partially attributed to their extrapolation beyond their specified maximum value

of $\bar{\lambda}_{l.b}$. While the proposed prediction curve represented by Equations 4.1–4.4 and Equations 4.8–4.11 is found to provide more accurate and the least scattered sectional moment capacity predictions reliably as they have a β value greater than the target value of 2.5. Moreover, from Figure 4.1, the predictions from the codal design Equations 4.5–4.7 are either significantly conservative *or* unsafe for the CHSs within a particular range of $\bar{\lambda}_{l.b}$. The reliability assessment of the proposed bending capacity prediction curve representing Equations 4.1–4.4 and Equations 4.8–4.11 is already carried out in the previous Section 4.3 and therefore it is assumed that the proposed RRD based prediction curve represented by Equation 4.21 also has the same β value.

From Figure 4.1, the AS 4100:1998 (2016) design curve (Equation 4.5) predictions are highly conservative for slender and very slender CHSs with the $\bar{\lambda}_{l.b}$ value between 0.5 and 2.1, *e.g.*, Elchalakani (2014) and thus the AS 4100:1998 (2016) design curve is the least reliable among the curves plotted. Although, the AISC 360-16 (2016) curve (Equation 4.7) among the codal design curves has a better β value (~ 2.5) (see Table 4.7), it can be seen that the AISC 360-16 (2016) design curve (Equation 4.7) predictions are unsafe for the CHSs with the $\bar{\lambda}_{l.b}$ value ranging between 0.225 and 0.6 (*i.e.*, approximately in the elastic-plastic interaction range). Further, it can also be observed that the EC3: EN 1993-1-1 (2005) design curve (Equation 4.6) predictions are slightly unsafe for the CHSs with the $\bar{\lambda}_{l.b}$ value ranging between 0.2 and 0.25, and significantly over-conservative for the CHSs with the $\bar{\lambda}_{l.b}$ value between 0.25 and 1.10.

From Table 4.4, the proposed compact section limit is closer to those of the values specified for the same in the Australian (AS 4100:1998 2016) and Indian (IS 800 2007) design standards. While the existing compact section limit specified in EC3: EN 1993-1-1 (2005), AISC 360-16 (2016) and CSA S16-14 (2014) are found to be unsafe. The proposed yield section limit is almost the same as the value specified in the Australian design standard (AS 4100:1998 2016). The yield section limit specified in Indian (IS 800 2007) design standard is slightly unsafe, and the yield section limit specified in EC3: EN 1993-1-1 (2005) is found to be over-conservative. While the yield section limits specified in AISC 360-16 (2016) and CSA S16-14 (2014) are found to be very unsafe.

A comparison between the prediction curves and the normalized moment capacity exhibited by the CHSs in Tables 4.1 and 4.2 and EHSs in Tables 4.5 and 4.6 with-respect-to their $\bar{\lambda}_{l,b}$ value is shown in Figure 4.11. It is to be noted that the comparisons are made based on the unfactored moment resistance predictions and assuming proportional loading. While a plot of the proposed prediction curve representing Equation 4.2 and the normalized moment capacities with-respect-to $\frac{1}{\bar{\lambda}_{cs}}$ values is shown in Figure 4.12. From both the Figures 4.11 and 4.12, it can be seen that both the experimental (EXP) data of cold-formed (CF) and hot-finished (HF) sections exhibited significant scatter with-respect-to the proposed curve in the plastification and strain hardening zones. While, in the slender sections with the slenderness value between the proposed elastic and yield limits, it appears that the moment capacity predictions based on the proposed curves seem to be slightly on the conservative side for the hot-finished (HF) sections. But, on close observation (see Figures 4.11 and 4.12), it is found that there is not enough experimental data of hot-finished (HF) sections available with the slenderness value between the proposed elastic and yield limits, while the cold-formed (CF) sections data exhibited significant scatter with-respect-to the proposed curve.

4.4.2 Summary

The key findings drawn for the structural design of carbon steel CHS and EHSs under bending at the cross-section level based on the Direct-Strength-Method (DSM), including material strain hardening effects are summarised below.

- The moment resistance capacity prediction curve and a new set of cross-section slenderness limits for CHSs are established by using a comprehensive data from the literature on CHSs covering a wide range of cross-section slenderness values and material yield strength range, thereby eliminating the discrepancies existing among the compact and yield slenderness limits specified among various international design standards.

- The moment capacity predictions from the codal design curves are found to be either over-conservative *or* unsafe within a particular range of cross-sectional slenderness,

e.g., the AISC 360-16 (2016) design curve predictions are found to be unsafe for the CHSs with the $\bar{\lambda}_{l,b}$ value ranging between 0.225 and 0.6.

- The proposed expression for the bending resistance curve has been transformed into the traditional cylindrical shell buckling capacity curve equation format as a practical solution according to the newly introduced Reference-Resistance-Design (RRD) guidelines (EC3: EN 1993-1-6:A1 2017).

- The scope of the proposed CHS bending resistance curve based on the existing RRD based cylindrical shell buckling capacity guidelines is assessed for the short and medium-length domains.

- The efficiency of the equivalent CHS diameter expressions for the EHSs under bending proposed in the previous study is assessed and found that they resulted in significant conservatism and inconsistency in estimating the cross-sectional moment resistance capacity.

- The improved empirical expressions have been developed herein for the equivalent CHS diameter of EHS based on the Equivalent-Resistance-Capacity-Method (ERCM) by using the data of EHSs from the literature in such a way that the proposed CHS cross-section classification slenderness limits and strength prediction curves are also applicable for EHSs too.

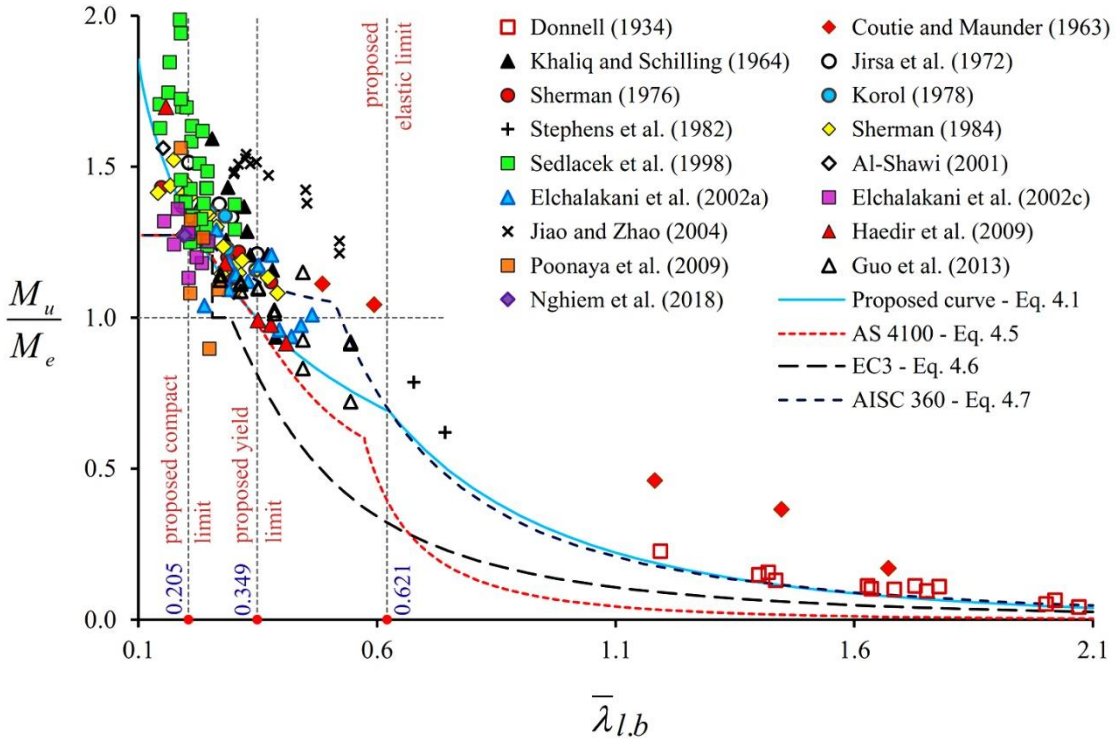

Figure 4.1 *Normalized bending capacity versus local buckling slenderness of CHSs from experimental programs alongside the prediction curves*

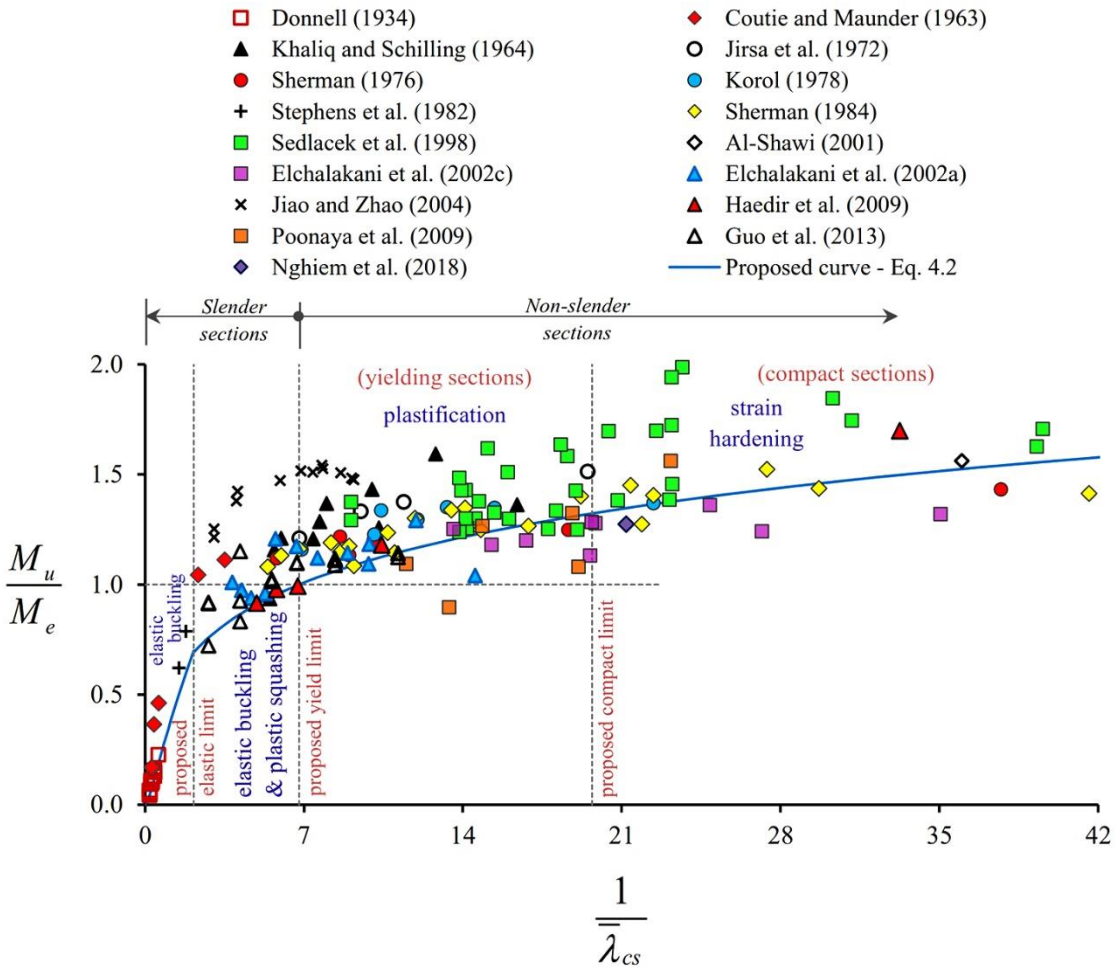

Figure 4.2 *Normalized bending capacity versus inversed-AISC cross-section slenderness of CHSs from experimental programs alongside the proposed curve*

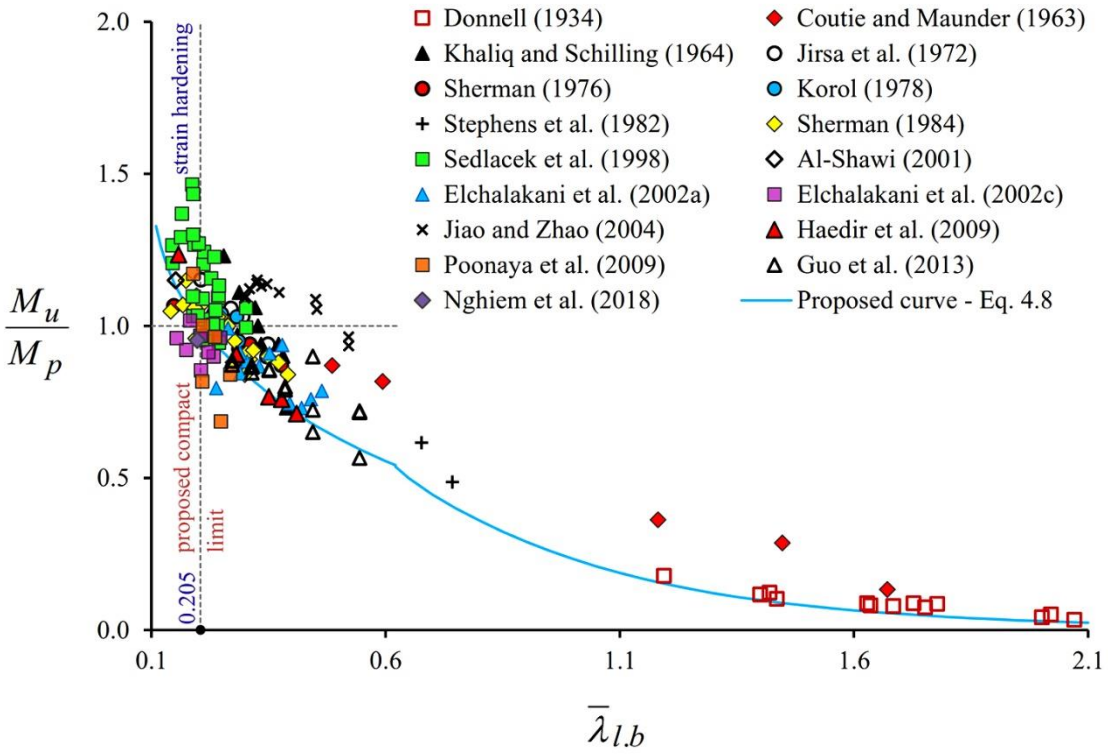

Figure 4.3 *Normalized bending capacity versus local buckling slenderness of CHSs from experimental programs alongside the proposed curve*

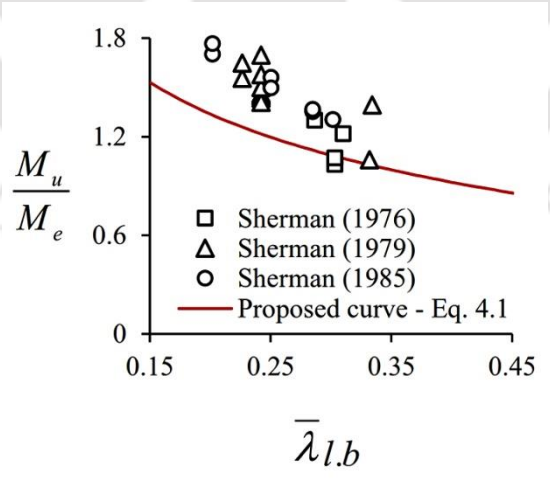

Figure 4.4 *Normalized bending capacity versus local buckling slenderness of CHSs with ovalisation restraint from experimental programs alongside the proposed curve*

[**Source:** Sherman (1992)]

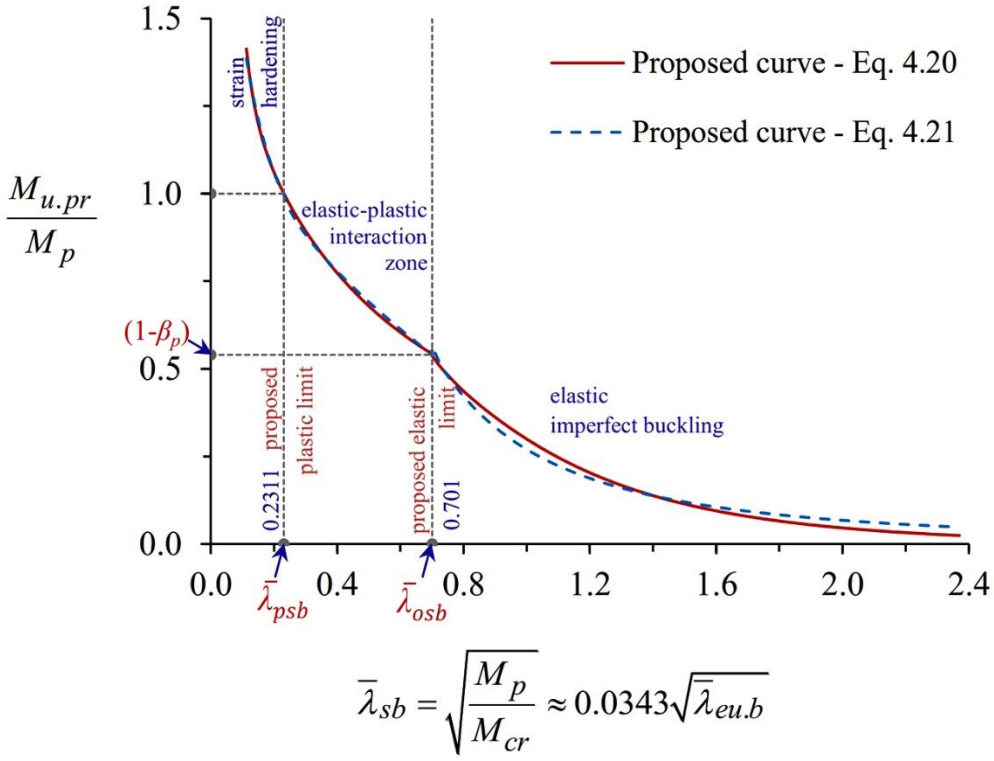

Figure 4.5 *Approximation of the proposed CHS bending capacity curve to the RRD based traditional capacity curve form*

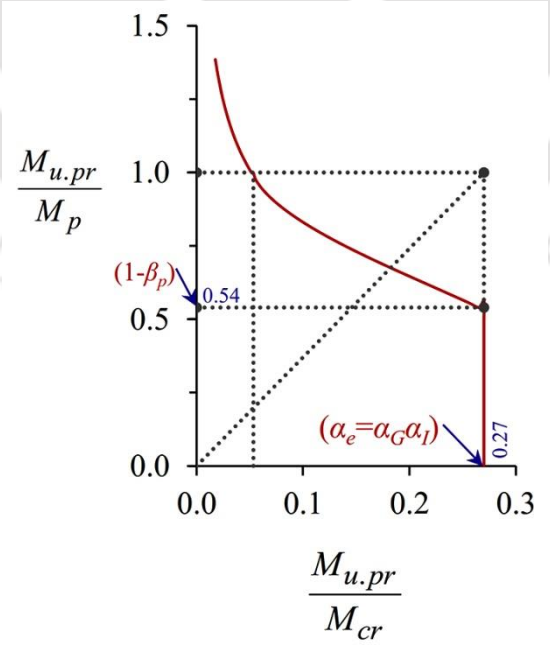

Figure 4.6 *Modified form of the approximated RRD based traditional capacity curve*

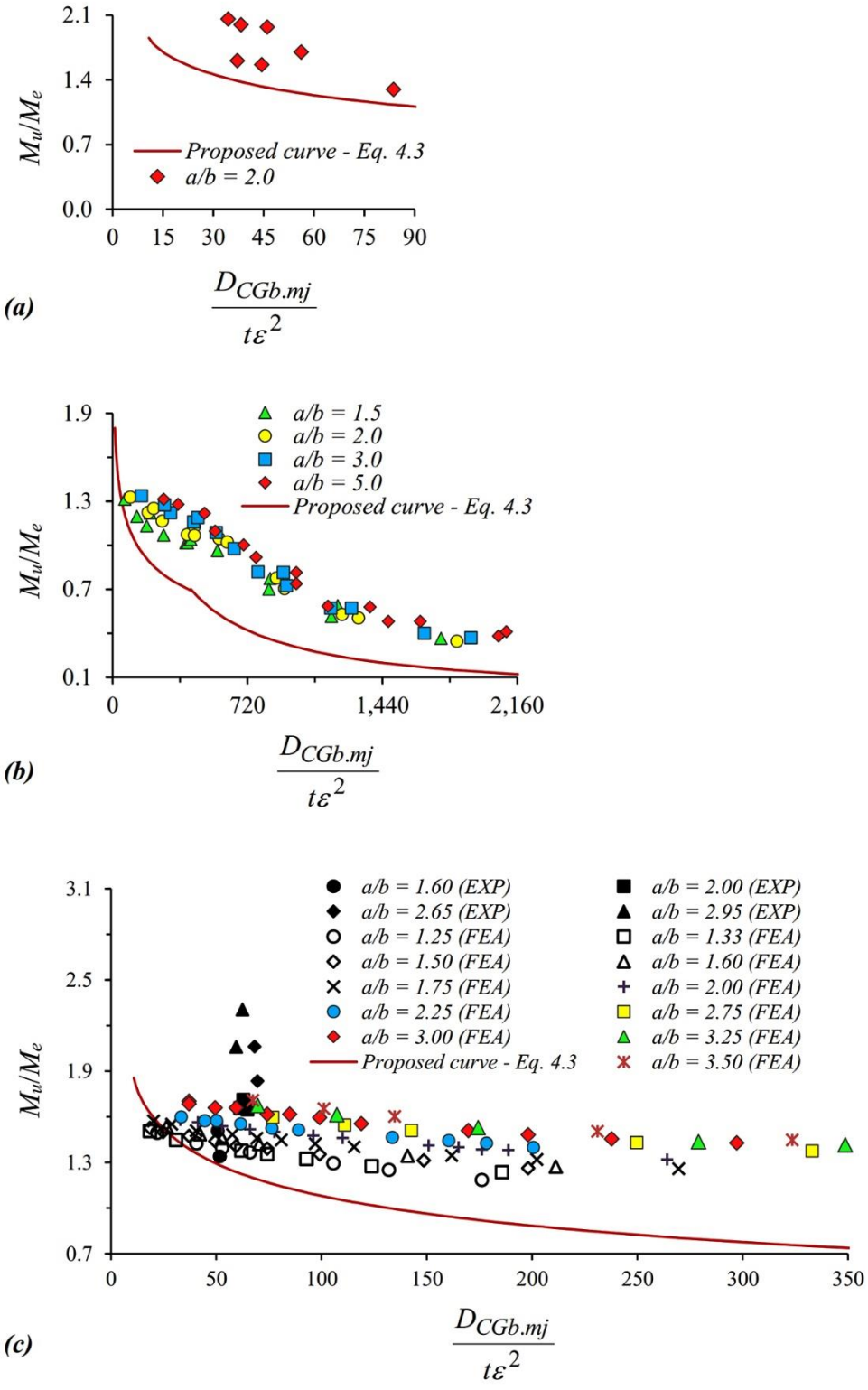

Figure 4.7 *Normalized bending capacity versus EN 1993-1-1 (2005) cross-section slenderness under major axis bending by Chan and Gardner (2008a) for EHSs from (a) Chan and Gardner (2008a); (b) McCann et al. (2018); and (c) Chen and Young (2019)*

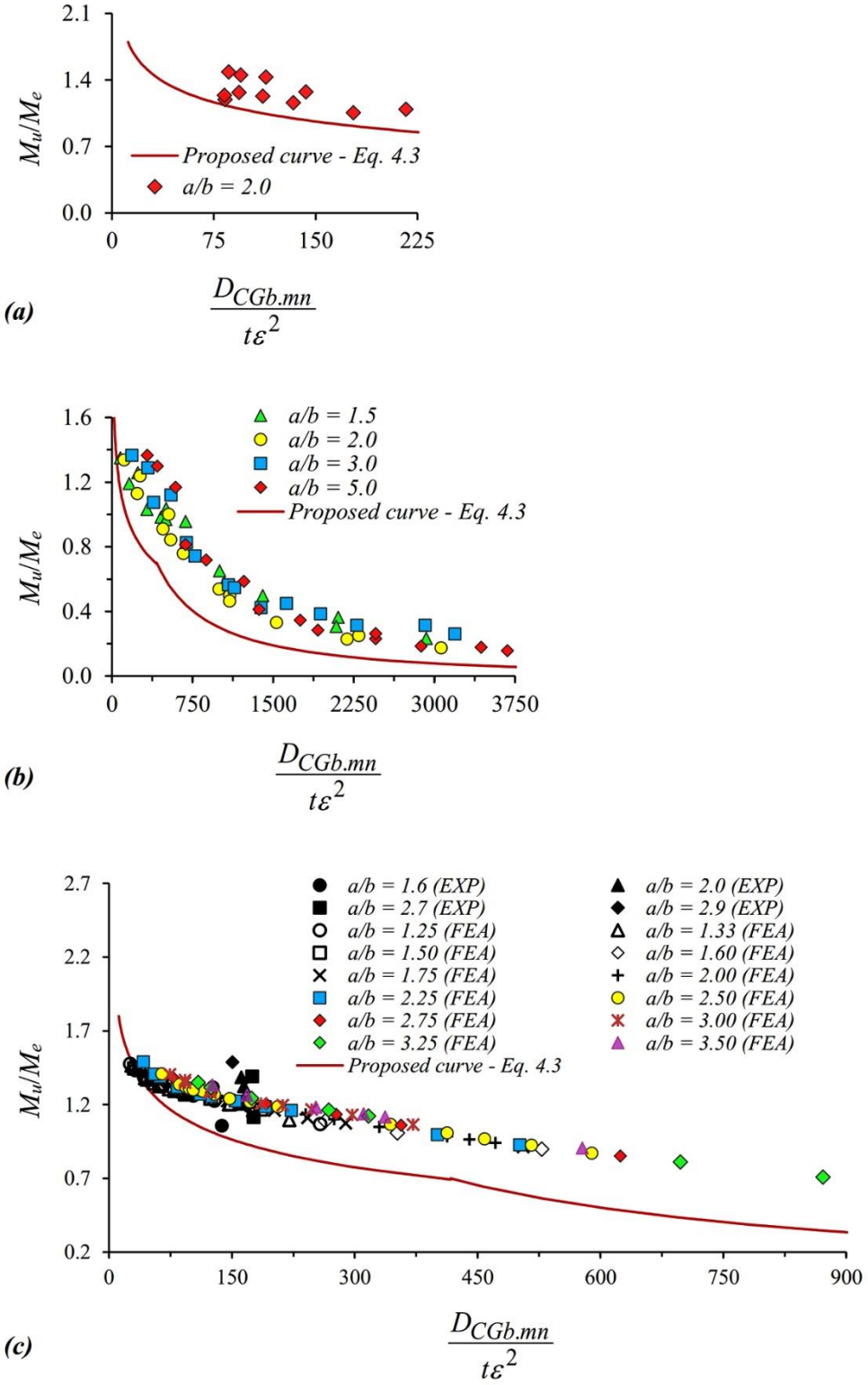

Figure 4.8 *Normalized bending capacity versus EN 1993-1-1 (2005) cross-section slenderness under minor axis bending by Chan and Gardner (2008a) for EHSs from (a) Chan and Gardner (2008a); (b) McCann et al. (2018); and (c) Chen and Young (2019)*

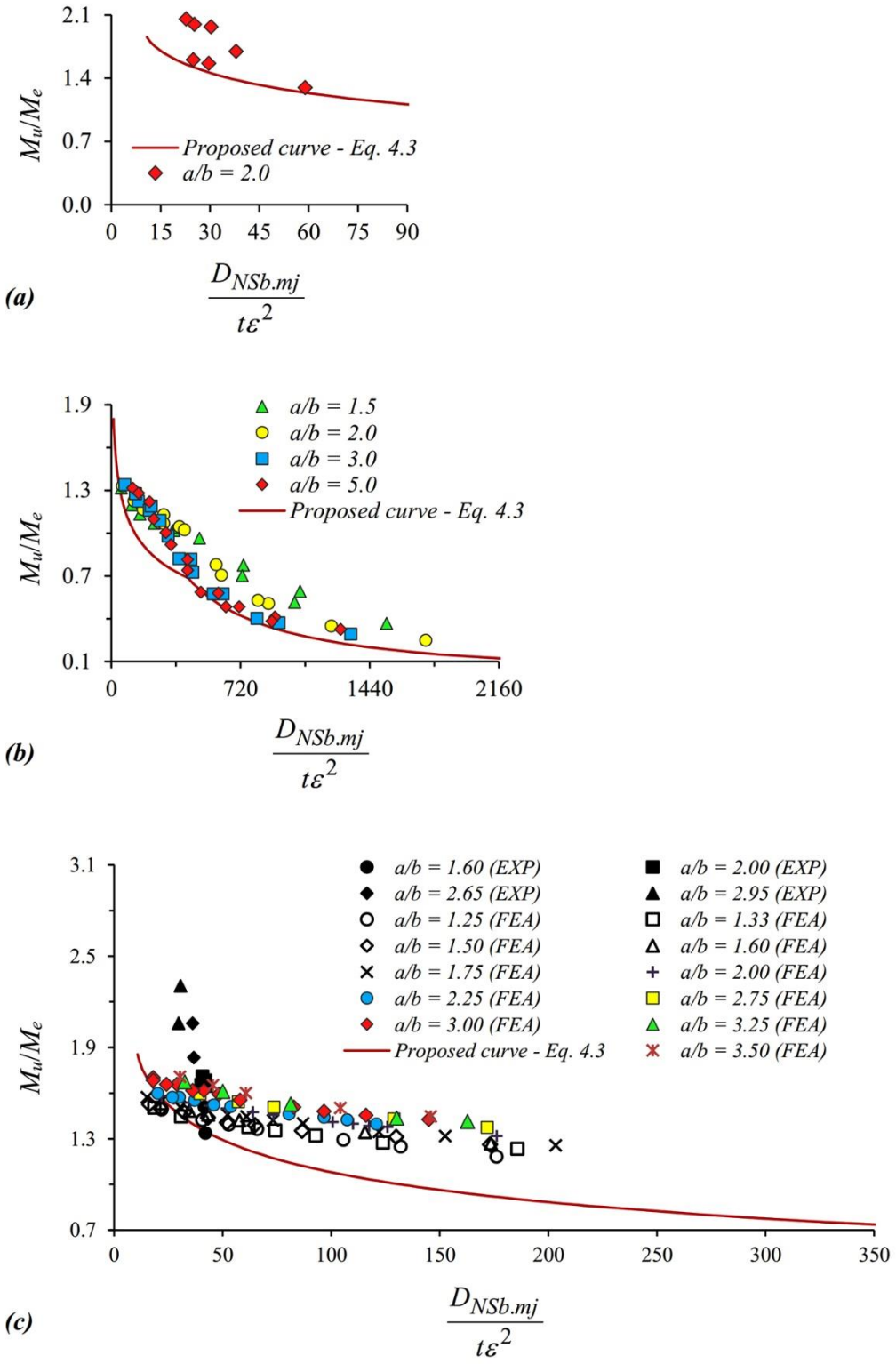

Figure 4.9 *Normalized bending capacity versus the proposed EN 1993-1-1 (2005) cross-section slenderness under major axis bending for EHSs from (a) Chan and Gardner (2008a); (b) McCann et al. (2018); and (c) Chen and Young (2019)*

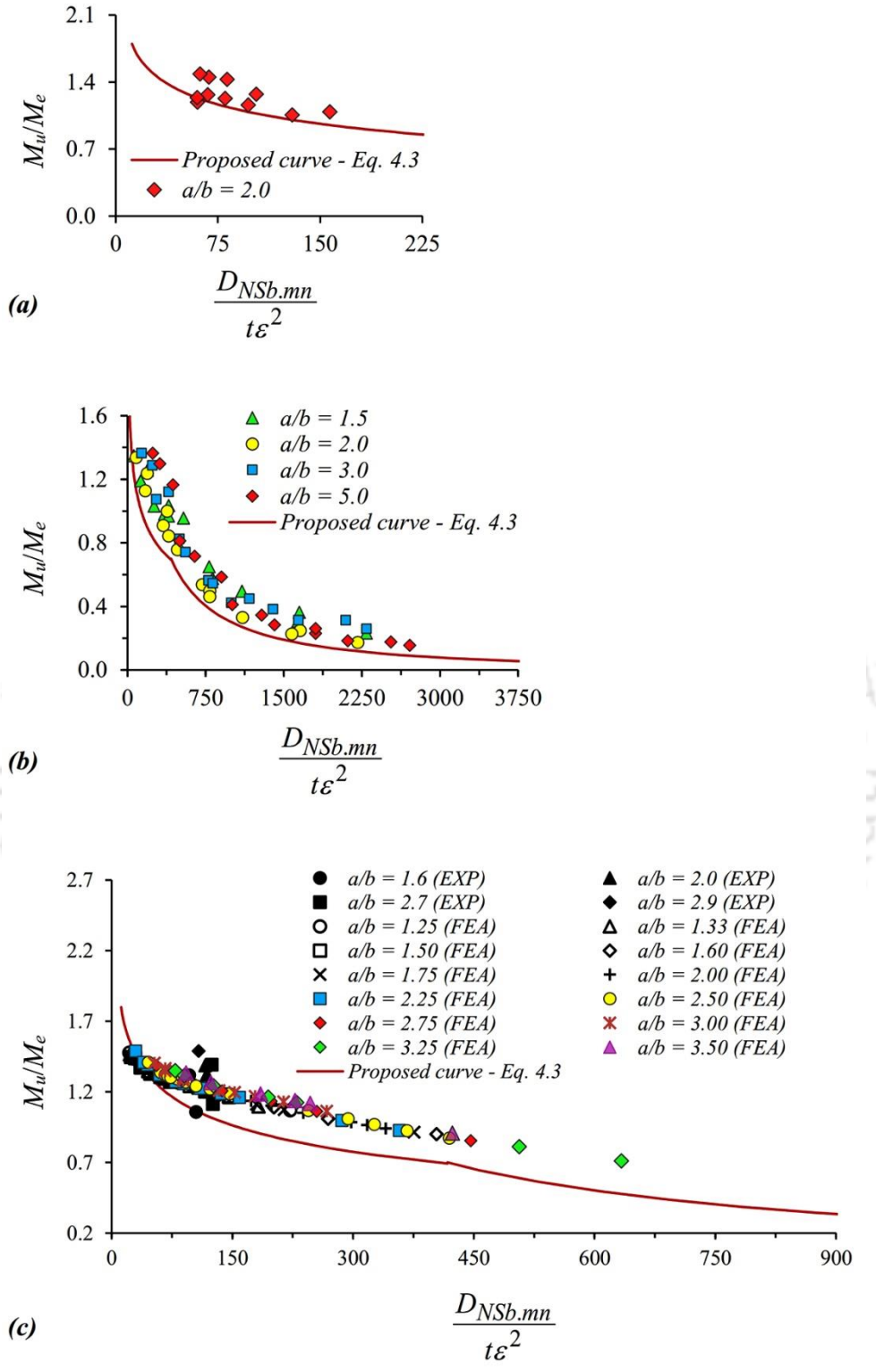

Figure 4.10 *Normalized bending capacity versus the proposed EN 1993-1-1 (2005) cross-section slenderness under minor axis bending for EHSs from (a) Chan and Gardner (2008a); (b) McCann et al. (2018); and (c) Chen and Young (2019)*

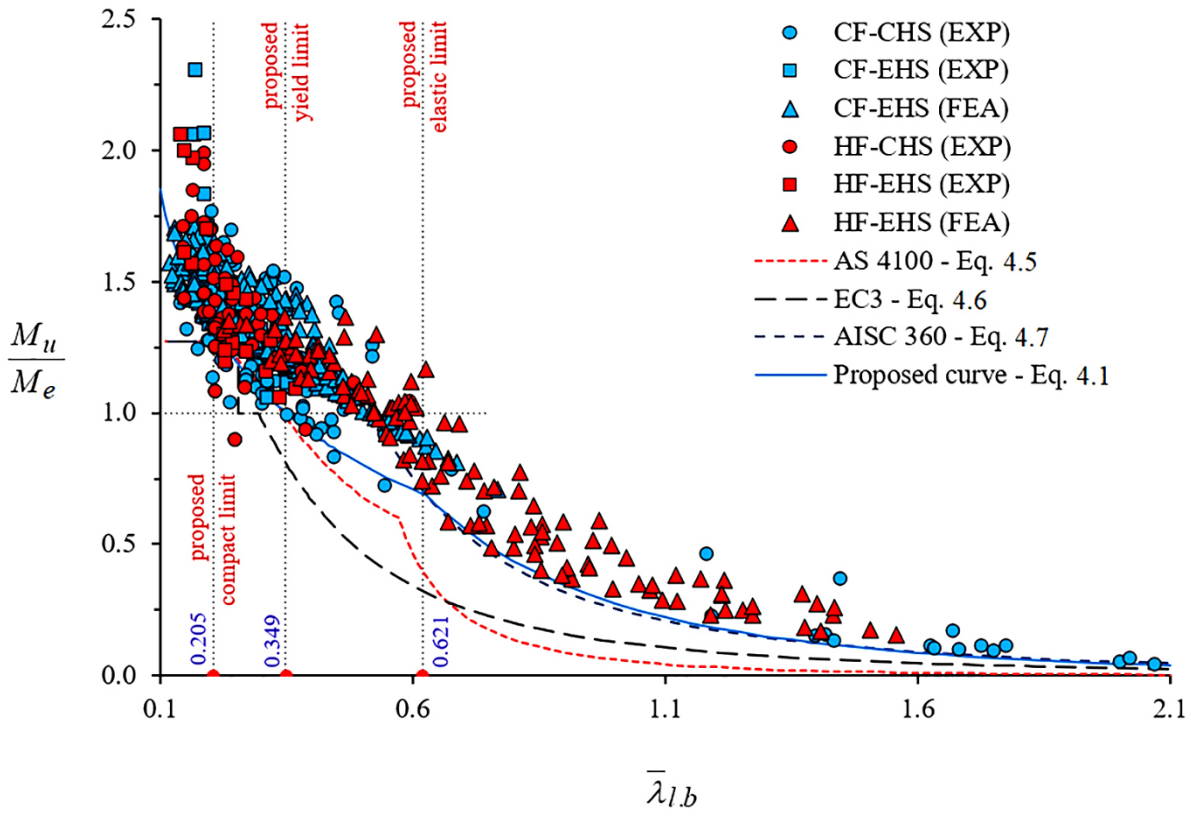

Figure 4.11 *Normalized bending capacity versus cross-sectional local buckling slenderness of CHSs and EHSs from various experimental and FEA programs alongside the prediction curves*

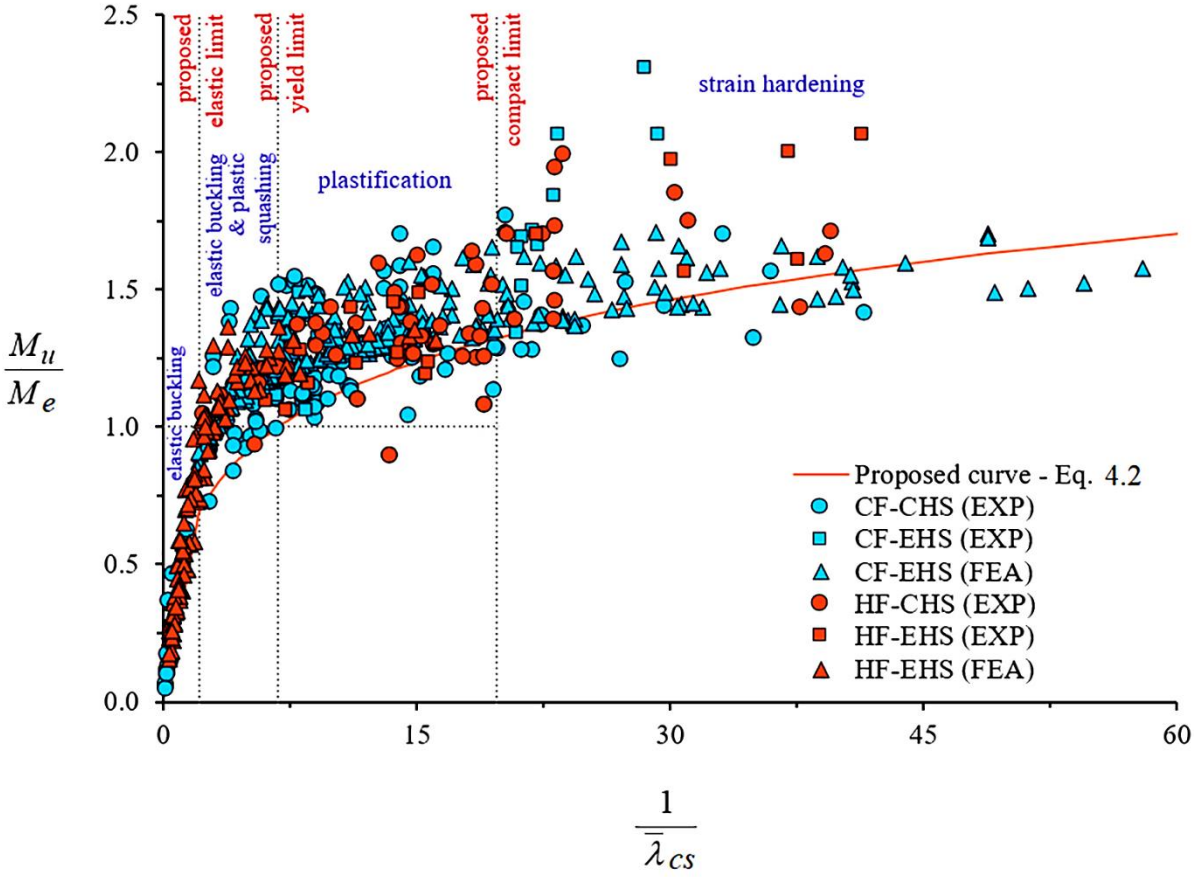

Figure 4.12 *Normalized bending capacity versus inversed AISC 360-16 (2016) cross-sectional slenderness of CHSs and EHSs under bending from various experimental and FEA programs alongside the proposed curve*

Table 4.1 *Properties of CHSs under bending in various experimental programs*

Reference – (CF/HF CHSs)	D (mm)	t (mm)	E (GPa)	$f_{y.mea}$ (MPa)	M_e (kNm)	M_p (kNm)	M_u (kNm)	$\bar{\lambda}_{l.b}$	$\bar{\lambda}_{cs}$	$M_{u.pr}$ (kNm)	$\frac{M_u}{M_{AS4100}}$	$\frac{M_u}{M_{AISC360}}$	$\frac{M_u}{M_{EC3}}$	$\frac{M_u}{M_{u.pr}}$
Donnell (1934) – (CF)	144.0	0.073	215.8	393	0.465	0.592	0.052	1.73	3.61	0.033	13.656	1.491	2.740	1.589
	144.0	0.071	215.8	393	0.452	0.575	0.043	1.75	3.71	0.031	12.328	1.311	2.406	1.408
	95.3	0.073	215.8	393	0.204	0.260	0.031	1.40	2.37	0.025	8.028	1.229	2.303	1.201
	95.3	0.071	215.8	393	0.199	0.253	0.031	1.42	2.44	0.024	8.898	1.335	2.498	1.310
	144.0	0.054	215.8	393	0.346	0.441	0.018	2.00	4.85	0.016	12.459	0.997	1.813	1.169
	144.0	0.053	215.8	393	0.340	0.432	0.022	2.02	4.94	0.015	16.059	1.255	2.282	1.483
	95.3	0.054	215.8	393	0.151	0.193	0.017	1.63	3.21	0.013	10.763	1.304	2.409	1.350
	95.3	0.054	215.8	393	0.150	0.191	0.015	1.64	3.24	0.012	10.030	1.206	2.226	1.251
	144.0	0.069	215.8	393	0.439	0.558	0.048	1.78	3.82	0.028	15.199	1.571	2.882	1.703
	95.3	0.070	215.8	393	0.195	0.248	0.025	1.43	2.49	0.023	7.676	1.133	2.118	1.116
	144.0	0.051	215.8	393	0.323	0.412	0.014	2.07	5.19	0.013	11.900	0.873	1.585	1.052
	95.3	0.051	215.8	393	0.141	0.180	0.014	1.68	3.43	0.011	11.036	1.261	2.323	1.327
	47.9	0.051	215.8	393	0.036	0.045	0.008	1.19	1.72	0.007	6.893	1.313	2.508	1.236
Coutie and Maunder (1963) – HF	32.2	0.152	204.0	275.8	0.034	0.043	0.037	0.49	0.29	0.028	1.582	1.051	2.262	1.360
	32.1	0.102	204.0	275.8	0.022	0.029	0.023	0.59	0.43	0.016	2.111	1.353	2.994	1.460
Coutie and Maunder (1963) – CF	76.2	0.152	204.0	689.5	0.477	0.608	0.220	1.18	1.69	0.090	13.515	2.610	4.991	2.452
	76.2	0.102	204.0	689.5	0.318	0.406	0.116	1.45	2.53	0.036	22.247	3.244	6.058	3.204
	76.2	0.076	204.0	689.5	0.239	0.304	0.041	1.67	3.38	0.018	18.164	2.103	3.877	2.205
Khaliq and Schilling (1964) – HF	109.0	1.88	199.6	268.9	4.481	5.802	7.136	0.25	0.08	5.321	1.326	1.281	1.251	1.341
	103.4	1.38	199.0	268.9	3.029	3.907	4.337	0.29	0.10	3.371	1.272	1.207	1.432	1.286
	104.9	1.09	198.8	268.9	2.459	3.162	3.162	0.33	0.13	2.548	1.241	1.128	1.461	1.241
	103.4	0.94	218.9	268.9	2.065	2.652	2.493	0.33	0.14	2.116	1.182	1.064	1.407	1.178
	103.6	0.76	201.1	268.9	1.691	2.168	1.583	0.39	0.18	1.591	1.054	0.853	1.338	0.995
	100.2	2.95	199.9	358.5	7.623	9.990	10.387	0.22	0.06	9.638	1.075	1.070	1.070	1.078
	124.8	2.31	199.4	358.5	9.594	12.438	12.064	0.28	0.10	10.762	1.107	1.054	1.257	1.121
	112.0	1.60	200.8	358.5	5.418	6.995	7.414	0.32	0.13	5.675	1.303	1.193	1.519	1.306
	89.2	0.99	193.6	358.5	2.145	2.761	2.595	0.37	0.17	2.070	1.306	1.093	1.625	1.253
	117.0	1.19	200.3	358.5	4.464	5.740	5.166	0.38	0.18	4.244	1.280	1.051	1.612	1.217
Jirsa et al. (1972) – HF	273.1	5.92	199.5	379.2	123.17	160.18	169.48	0.27	0.09	141.909	1.179	1.132	1.376	1.194
	273.1	8.89	200.3	334.4	157.87	207.53	239	0.21	0.05	208.310	1.189	1.097	1.189	1.147
	406.4	6.60	199.9	342.0	279.11	361.03	372	0.29	0.11	306.391	1.202	1.133	1.339	1.214
	508.0	6.48	200.8	376.5	475.82	613.35	576	0.35	0.15	476.119	1.232	1.078	1.491	1.210

Table 4.1 (**Cont'd.**)

Reference – (CF/HF CHSs)	D (mm)	t (mm)	E (GPa)	$f_{y.mea}$ (MPa)	M_e (kNm)	M_p (kNm)	M_u (kNm)	$\bar{\lambda}_{l.b}$	$\bar{\lambda}_{cs}$	$M_{u.pr}$ (kNm)	$\frac{M_u}{M_{AS4100}}$	$\frac{M_u}{M_{AISC360}}$	$\frac{M_u}{M_{EC3}}$	$\frac{M_u}{M_{u.pr}}$
Korol (1978) – CF	114.3	3.96	199.6	308.9	11.32	14.91	15.50	0.19	0.04	15.444	1.076	1.076	1.076	1.003
	168.3	3.96	199.3	304.8	25.03	32.61	33.26	0.23	0.06	31.147	1.062	1.044	1.044	1.068
	168.3	4.78	200.2	368.9	35.98	47.10	48.50	0.23	0.06	44.775	1.077	1.059	1.059	1.083
	273.1	5.56	199.9	306.1	93.82	121.86	126.72	0.25	0.08	112.499	1.115	1.077	1.061	1.126
	323.9	6.35	199.3	375.8	185.37	240.56	247.76	0.28	0.10	208.469	1.174	1.119	1.337	1.188
	355.6	6.35	200.2	297.9	178.09	230.73	230.71	0.26	0.08	207.953	1.096	1.056	1.295	1.109
	406.4	6.35	199.7	308.9	242.86	313.94	298.22	0.29	0.10	271.007	1.088	1.033	1.228	1.100
	508.0	6.35	199.1	360.6	447.18	576.28	518	0.35	0.14	449.324	1.171	1.030	1.413	1.153
Sherman (1976) – HF	272.2	14.86	200.6	290.3	212.89	285.96	304.79	0.15	0.03	328.005	1.124	1.125	1.125	0.929
	273.9	7.80	199.1	304.1	128.27	167.95	160.15	0.21	0.05	167.400	0.981	0.981	0.981	0.957
Sherman (1976) – CF	273.9	5.61	198.5	404.0	125.70	163.28	150.86	0.29	0.10	140.148	1.064	1.010	1.200	1.076
	273.1	4.93	200.8	421.3	115.18	149.25	140.28	0.31	0.12	123.071	1.132	1.051	1.294	1.140
	273.1	3.53	200.6	288.2	57.36	73.95	65.05	0.30	0.11	62.048	1.039	0.972	1.174	1.048
	272.9	2.46	199.0	309.6	43.44	55.79	48.59	0.38	0.17	41.514	1.227	1.014	1.538	1.170
Stephens et al. (1982) – CF	1529.1	5.13	202.0	375.8	3506.44	4477.74	2759.6	0.68	0.55	2099.175	2.943	1.344	2.861	1.315
	1523.4	3.43	204.0	306.1	1901.27	2425.25	1180	0.74	0.67	958.726	3.387	1.288	2.678	1.231
Sherman (1984) – CF	457.2	26.65	199.3	279.2	1024.48	1381.05	1448.26	0.14	0.02	1612.958	1.110	1.110	1.110	0.898
	457.2	18.72	199.8	298.6	811.19	1075.20	1235.72	0.17	0.04	1161.511	1.197	1.197	1.197	1.064
	457.2	16.54	199.9	337.9	822.70	1085.34	1193.31	0.20	0.05	1110.437	1.139	1.139	1.139	1.075
	457.2	13.11	200.0	298.6	589.48	771.94	825.73	0.21	0.05	774.875	1.100	1.100	1.100	1.066
	457.2	9.93	200.1	293.7	448.78	583.66	560.23	0.24	0.07	552.927	1.006	0.981	0.981	1.013
	457.2	6.86	199.2	324.8	349.66	451.72	379.42	0.30	0.11	380.528	0.988	0.927	1.110	0.997
	457.2	6.15	201.1	314.4	304.84	393.22	349.94	0.31	0.12	325.722	1.067	0.991	1.220	1.074
	457.2	6.33	201.0	308.9	307.79	397.18	361.41	0.30	0.11	332.980	1.076	1.007	1.216	1.085
	609.6	12.93	200.1	314.4	1113.47	1447.40	1490.59	0.25	0.07	1340.207	1.101	1.064	1.051	1.112
	609.6	6.78	201.2	373.0	714.35	919.32	808.97	0.37	0.17	689.401	1.222	1.023	1.521	1.173
	457.2	25.40	200.2	374.4	1320.31	1775.15	1897.22	0.17	0.03	1926.463	1.129	1.129	1.129	0.985
	457.2	19.61	198.9	389.6	1102.22	1463.73	1404.24	0.19	0.05	1496.071	1.001	1.001	1.001	0.939
	457.2	18.92	200.4	370.3	1015.58	1346.68	1426.60	0.19	0.04	1385.997	1.103	1.103	1.103	1.029
	457.2	16.38	200.0	424.0	1024.08	1350.58	1295.96	0.22	0.06	1304.411	0.994	0.994	0.994	0.994
	457.2	13.26	199.8	410.9	819.99	1074.15	1106.05	0.24	0.07	997.956	1.099	1.062	1.059	1.108
	457.2	10.03	200.0	410.3	632.80	823.18	781.89	0.28	0.09	717.047	1.077	1.029	1.236	1.090
	457.2	6.78	198.8	433.7	461.99	596.75	537.04	0.35	0.15	462.278	1.183	1.035	1.432	1.162
	457.2	10.24	199.2	405.4	637.17	829.22	729.59	0.27	0.09	727.273	0.991	0.949	1.145	1.003
	609.6	13.74	200.2	379.2	1421.70	1850.51	1850.18	0.26	0.08	1656.462	1.103	1.062	1.301	1.117
	609.6	7.04	201.0	429.6	852.36	1097.39	921.77	0.39	0.19	797.389	1.229	0.988	1.567	1.156
	609.6	10.01	199.4	399.2	1110.33	1436.47	1321.43	0.32	0.12	1170.964	1.124	1.034	1.301	1.128

Table 4.1 (**Cont'd.**)

Reference – (CF/HF CHSs)	D (mm)	t (mm)	E (GPa)	$f_{y.mea}$ (MPa)	M_e (kNm)	M_p (kNm)	M_u (kNm)	$\bar{\lambda}_{l.b}$	$\bar{\lambda}_{cs}$	$M_{u.pr}$ (kNm)	$\frac{M_u}{M_{AS4100}}$	$\frac{M_u}{M_{AISC360}}$	$\frac{M_u}{M_{EC3}}$	$\frac{M_u}{M_{u.pr}}$
Sedlacek et al. (1998) – HF	219.0	4.51	205	290	46.33	60.19	60.2	0.24	0.07	56.842	1.051	1.021	1.021	1.059
	219.3	4.40	205	290	45.37	58.91	57	0.24	0.07	55.302	1.022	0.988	0.987	1.031
	121.3	7.23	205	309	21.56	29.10	36.8	0.14	0.03	33.566	1.341	1.341	1.341	1.096
	121.4	7.19	205	309	21.51	29.02	35	0.15	0.03	33.437	1.278	1.278	1.278	1.047
	220.1	6.01	205	309	65.12	85.17	87	0.21	0.06	84.386	1.049	1.049	1.049	1.031
	220.0	5.89	205	309	63.87	83.48	80	0.22	0.06	82.357	0.984	0.984	0.984	0.971
	193.7	12.53	205	560	170.10	230.73	338	0.19	0.04	235.259	1.561	1.561	1.561	1.437
	193.7	12.28	205	560	167.33	226.68	325	0.19	0.04	230.312	1.526	1.526	1.526	1.411
	121.3	7.41	205	402	28.64	38.71	50	0.16	0.03	42.251	1.371	1.371	1.371	1.183
	121.2	7.20	205	402	27.89	37.64	51.5	0.17	0.03	40.885	1.450	1.450	1.450	1.260
	246.2	6.99	205	412	125.91	164.84	180	0.24	0.07	153.311	1.164	1.125	1.123	1.174
	246.2	7.28	205	412	130.65	171.24	180	0.24	0.07	160.727	1.112	1.082	1.082	1.120
	246.3	8.34	205	373	133.86	176.19	212	0.21	0.05	174.619	1.244	1.244	1.244	1.214
	246.4	8.21	205	373	132.10	173.78	216	0.21	0.05	171.636	1.284	1.284	1.284	1.258
	133.6	3.76	205	304	14.73	19.27	21	0.21	0.05	19.301	1.120	1.120	1.120	1.088
	133.4	3.77	205	304	14.73	19.23	18.4	0.21	0.05	19.321	0.981	0.981	0.981	0.952
	178.0	4.73	205	341	37.06	48.43	56	0.23	0.06	46.547	1.199	1.187	1.187	1.203
	178.0	4.75	205	341	37.22	48.64	48.3	0.23	0.06	46.791	1.029	1.019	1.019	1.032
	219.1	4.32	205	290	44.52	57.79	63.6	0.24	0.07	54.028	1.167	1.128	1.122	1.177
	219.0	4.38	205	290	45.08	58.53	58.6	0.24	0.07	54.903	1.058	1.023	1.021	1.067
	139.7	5.09	205	495	34.59	45.65	56	0.23	0.07	42.832	1.299	1.272	1.272	1.307
	139.7	5.19	205	495	35.20	46.48	46.7	0.23	0.06	43.799	1.061	1.042	1.042	1.066
	139.7	7.34	205	478	45.91	61.55	78	0.19	0.04	62.746	1.334	1.334	1.334	1.243
	139.7	7.53	205	478	46.91	62.97	65	0.19	0.04	64.509	1.088	1.088	1.088	1.008
	168.2	8.18	205	488	76.61	102.31	130	0.20	0.05	102.241	1.333	1.333	1.333	1.272
	168.4	8.35	205	488	78.11	104.41	108	0.20	0.05	104.746	1.086	1.086	1.086	1.031
	133.2	3.96	205	440	22.22	29.13	33	0.24	0.07	26.921	1.214	1.174	1.166	1.226
	133.2	3.96	205	440	22.21	29.12	27.5	0.24	0.07	26.909	1.013	0.979	0.972	1.022
	133.4	5.63	205	373	25.83	34.28	44.55	0.19	0.04	35.555	1.355	1.355	1.355	1.253
	133.2	5.63	205	373	25.76	34.19	37.5	0.19	0.04	35.465	1.143	1.143	1.143	1.057
	219.3	4.53	207	471	75.78	98.45	104.2	0.30	0.11	82.170	1.257	1.177	1.417	1.268
	219.3	4.53	207	471	75.78	98.45	98	0.30	0.11	82.170	1.182	1.107	1.332	1.193
Al-Shawi (2001) – CF	48.3	3.20	207.0	381.0	1.829	2.484	2.856	0.15	0.03	2.788	1.227	1.227	1.227	1.024
Nghiem et al. (2018) – CF	457.2	22.9	200	472.3	1526.82	2041.90	1945	0.20	0.05	2056.364	1.001	1.001	1.001	0.946

Table 4.1 (**Cont'd.**)

Reference – (CF/HF CHSs)	D (mm)	t (mm)	E (GPa)	$f_{y.mea}$ (MPa)	M_e (kNm)	M_p (kNm)	M_u (kNm)	$\overline{\lambda}_{l.b}$	$\overline{\lambda}_{cs}$	$M_{u.pr}$ (kNm)	$\frac{M_u}{M_{AS4100}}$	$\frac{M_u}{M_{AISC360}}$	$\frac{M_u}{M_{EC3}}$	$\frac{M_u}{M_{u.pr}}$
Elchalakani et al. (2002c) – CF	101.8	2.53	199.8	365	6.98	9.11	8.75	0.25	0.07	8.419	1.029	0.995	0.984	1.039
	88.6	2.79	209.5	432	6.77	8.89	7.99	0.23	0.07	8.403	0.945	0.927	0.927	0.951
	76.3	2.45	217.1	415	4.22	5.55	5.07	0.22	0.06	5.372	0.943	0.943	0.943	0.944
	89.3	3.35	217.9	412	7.72	10.19	9.86	0.20	0.05	10.225	1.004	1.004	1.004	0.964
	60.7	2.44	211.1	433	2.70	3.58	3.06	0.21	0.05	3.574	0.889	0.889	0.889	0.856
	76.2	3.24	211.1	456	5.93	7.87	7.61	0.20	0.05	7.839	1.009	1.009	1.009	0.971
	60.7	3.01	204.7	408	3.06	4.09	4.16	0.18	0.04	4.279	1.069	1.069	1.069	0.972
	33.7	1.98	204.2	442	0.65	0.88	0.81	0.17	0.04	0.932	0.976	0.976	0.976	0.869
	33.8	2.63	207.1	460	0.86	1.18	1.13	0.15	0.03	1.298	1.036	1.036	1.036	0.870
Elchalakani et al. (2002a) – CF	110.1	1.1	190.9	408	4.15	5.33	3.89	0.42	0.21	3.715	1.147	0.868	1.515	1.047
	109.9	1.0	190.9	408	3.77	4.84	3.67	0.44	0.23	3.278	1.251	0.908	1.693	1.120
	109.7	0.9	190.9	408	3.39	4.35	3.42	0.46	0.26	2.852	1.369	0.948	1.906	1.199
	110.4	1.25	190.9	408	4.72	6.08	4.53	0.39	0.19	4.391	1.101	0.878	1.411	1.032
	98.6	1.7	212.3	410	5.06	6.55	5.78	0.30	0.11	5.457	1.051	0.981	1.189	1.059
	98.8	1.2	191.2	404	3.59	4.62	4.33	0.38	0.17	3.416	1.331	1.096	1.673	1.267
	99.2	1.4	191.2	404	4.19	5.41	4.92	0.35	0.15	4.173	1.205	1.048	1.464	1.179
	99.6	1.6	191.2	404	4.80	6.21	5.38	0.33	0.13	4.958	1.087	0.984	1.284	1.085
	100.0	1.8	199.8	365	4.89	6.34	5.35	0.29	0.10	5.421	0.976	0.924	1.094	0.987
	99.8	2.3	212.3	410	6.89	8.97	8.89	0.26	0.08	8.028	1.094	1.053	1.291	1.107
	87.3	2.4	217.9	412	5.45	7.13	5.67	0.24	0.07	6.685	0.842	0.817	0.817	0.848
	100.6	2.1	191.2	404	6.34	8.23	7.50	0.29	0.10	7.028	1.055	1.000	1.184	1.067
Jiao and Zhao (2004) – CF	31.9	1.56	200.3	1327	1.42	1.90	2.15	0.33	0.14	1.459	1.479	1.331	1.761	1.474
	31.9	1.76	200.3	1284	1.53	2.05	2.30	0.31	0.12	1.630	1.401	1.301	1.601	1.411
	31.9	1.96	200.3	1350	1.76	2.38	2.61	0.30	0.11	1.910	1.354	1.269	1.525	1.366
	38.0	1.58	200.3	1398	2.22	2.94	3.26	0.37	0.17	2.133	1.594	1.331	1.988	1.528
	38.2	1.78	200.3	1361	2.41	3.21	3.65	0.35	0.15	2.416	1.536	1.349	1.856	1.511
	38.1	1.98	200.3	1330	2.56	3.43	3.91	0.32	0.13	2.667	1.465	1.335	1.716	1.466
	57.2	1.58	200.3	1360	5.07	6.64	7.22	0.45	0.25	4.353	1.871	1.331	2.562	1.659
	76.0	1.59	200.3	1377	9.32	12.11	11.68	0.52	0.33	7.276	1.914	1.238	2.867	1.605
	31.8	1.97	200.3	1350	1.75	2.36	2.58	0.30	0.11	1.901	1.344	1.262	1.510	1.357
	38.1	1.97	200.3	1330	2.56	3.42	3.94	0.33	0.13	2.657	1.482	1.349	1.739	1.483
	57.1	1.56	200.3	1360	5.00	6.54	6.90	0.45	0.25	4.276	1.825	1.291	2.506	1.614
	76.0	1.59	200.3	1377	9.33	12.12	11.32	0.52	0.33	7.281	1.854	1.199	2.777	1.555

Table 4.1 (**Cont'd.**)

Reference – (CF/HF CHSs)	D (mm)	t (mm)	E (GPa)	$f_{y.mea}$ (MPa)	M_e (kNm)	M_p (kNm)	M_u (kNm)	$\bar{\lambda}_{l.b}$	$\bar{\lambda}_{cs}$	$M_{u.pr}$ (kNm)	$\frac{M_u}{M_{AS4100}}$	$\frac{M_u}{M_{AISC360}}$	$\frac{M_u}{M_{EC3}}$	$\frac{M_u}{M_{u.pr}}$
Guo et al. (2013) – CF	150	2	188	224.7	7.63	9.84	8.72	0.27	0.09	8.744	0.985	0.944	1.143	0.997
	150	2	188	224.7	7.63	9.84	8.58	0.27	0.09	8.744	0.969	0.929	1.124	0.981
	200	2	188	224.7	13.71	17.62	14.91	0.31	0.12	14.535	1.021	0.943	1.175	1.026
	200	2	188	224.7	13.71	17.62	15.23	0.31	0.12	14.535	1.043	0.963	1.200	1.048
	250	2	188	224.7	21.55	27.64	23.61	0.35	0.15	21.461	1.123	0.978	1.365	1.100
	250	2	188	224.7	21.55	27.64	23.69	0.35	0.15	21.461	1.127	0.981	1.369	1.104
	300	2	188	224.7	31.15	39.91	31.91	0.38	0.18	29.422	1.146	0.933	1.450	1.085
	300	2	188	224.7	31.15	39.91	31.56	0.38	0.18	29.422	1.133	0.922	1.434	1.073
	200	2	188	224.7	13.7	17.62	15.24	0.31	0.12	14.535	1.043	0.964	1.201	1.049
	200	2	188	224.7	13.7	17.62	15.32	0.31	0.12	14.535	1.049	0.969	1.207	1.054
	400	2	188	224.7	55.65	71.19	51.54	0.44	0.24	48.155	1.200	0.865	1.632	1.070
	400	2	188	224.7	55.65	71.19	46.32	0.44	0.24	48.155	1.079	0.777	1.466	0.962
	600	2	188	224.7	125.85	160.71	90.90	0.54	0.36	95.429	1.149	0.782	1.781	0.953
	600	2	188	224.7	125.85	160.71	115.67	0.54	0.36	95.429	1.463	0.994	2.266	1.212
	400	2	188	224.7	55.65	71.19	64.00	0.44	0.24	48.155	1.491	1.073	2.026	1.329
	600	2	188	224.7	125.85	160.71	115.00	0.54	0.36	95.429	1.454	0.989	2.253	1.205
Poonaya et al. (2009) – CF	59.3	2.80	150	306	2.05	2.73	3.20	0.19	0.04	2.819	1.227	1.227	1.227	1.135
	59.0	2.30	150	306	1.71	2.26	1.85	0.21	0.05	2.247	0.849	0.849	0.849	0.823
	46.9	1.80	150	306	0.85	1.12	1.12	0.21	0.05	1.107	1.040	1.040	1.040	1.012
	59.4	1.80	150	306	1.39	1.83	1.76	0.24	0.07	1.716	1.019	0.994	0.994	1.026
	58.6	1.60	150	306	1.22	1.59	1.09	0.25	0.07	1.459	0.740	0.715	0.705	0.747
	74.5	1.75	150	306	2.18	2.84	2.38	0.27	0.09	2.513	0.935	0.899	1.094	0.947
Haedir et al. (2009) – CF	33.8	2.70	199.6	479	0.91	1.26	1.55	0.16	0.03	1.366	1.334	1.334	1.334	1.134
	86.5	1.97	208.2	455	4.92	6.40	5.80	0.28	0.10	5.532	1.036	0.987	1.180	1.048
	85.1	1.31	205.7	470	3.35	4.33	3.32	0.35	0.15	3.340	1.014	0.885	1.230	0.994
	84.7	1.11	202.0	457	2.75	3.55	2.69	0.38	0.17	2.627	1.074	0.887	1.347	1.024
	84.4	0.94	202.0	457	2.33	2.99	2.13	0.41	0.20	2.115	1.091	0.844	1.423	1.007

Table 4.2 *Properties of CHSs with ovalisation restraint under bending in various experimental programs*

Reference – (CF/HF CHSs)	D (mm)	t (mm)	E (GPa)	$f_{y.mea}$ (MPa)	M_e (kNm)	M_p (kNm)	M_u (kNm)	$\bar{\lambda}_{l.b}$	$\bar{\lambda}_{cs}$	$M_{u.pr}$ (kNm)	$\frac{M_u}{M_{AS4100}}$	$\frac{M_u}{M_{AISC360}}$	$\frac{M_u}{M_{EC3}}$	$\frac{M_u}{M_{u.pr}}$
Sherman (1976) – CF	273.9	5.61	198.5	404.0	125.70	163.275	163.28	0.29	0.10	140.148	1.151	1.093	1.299	1.165
	273.1	4.93	200.8	421.3	115.18	149.254	140.30	0.31	0.12	123.071	1.133	1.051	1.294	1.140
	273.1	3.53	200.6	288.2	57.36	73.948	59.16	0.30	0.11	62.048	0.945	0.884	1.068	0.953
	273.1	3.53	200.6	288.2	57.36	73.948	61.38	0.30	0.11	62.048	0.981	0.917	1.108	0.989
Sherman (1985) – CF	457	16.26	199.7	350	838.97	1106.177	1426.97	0.20	0.05	1117.969	0.656	1.336	1.336	1.276
	457	16.26	199.7	350	838.97	1106.177	1482.29	0.20	0.05	1117.969	0.682	1.388	1.388	1.326
	458	10.29	200.3	341	540.59	703.591	844.31	0.25	0.08	646.937	1.291	1.248	1.227	1.305
	458	10.29	200.3	341	540.59	703.591	809.13	0.25	0.08	646.937	1.237	1.196	1.176	1.251
	457	9.77	199.1	417	626.57	814.608	847.19	0.28	0.10	701.037	1.194	1.135	1.352	1.208
	457	9.77	199.1	417	626.57	814.608	855.34	0.28	0.10	701.037	1.206	1.146	1.365	1.220
	458	6.35	198.8	303	304.26	392.629	396.56	0.30	0.11	330.142	1.190	1.115	1.341	1.201
	458	6.35	198.8	303	304.26	392.629	396.56	0.30	0.11	330.142	1.190	1.115	1.341	1.201
Sherman (1979) – CF	102	2.70	200	328.6	6.69	8.75	10.41	0.23	0.06	8.424	1.232	1.221	1.221	1.236
	102	2.70	200	328.6	6.69	8.75	11.02	0.23	0.06	8.424	1.304	1.293	1.293	1.308
	114	2.79	200	346.8	9.17	11.96	15.55	0.24	0.07	11.160	1.381	1.335	1.332	1.393
	114	2.79	200	346.8	9.17	11.96	13.27	0.24	0.07	11.160	1.179	1.140	1.137	1.189
	114	2.79	200	346.8	9.17	11.96	13.39	0.24	0.07	11.160	1.190	1.150	1.147	1.200
	114	2.79	200	346.8	9.17	11.96	13.15	0.24	0.07	11.160	1.168	1.130	1.127	1.179
	114	2.79	200	346.8	9.17	11.96	12.96	0.24	0.07	11.160	1.147	1.109	1.106	1.157
	114	2.79	200	346.8	9.17	11.96	13.75	0.24	0.07	11.160	1.222	1.181	1.178	1.232
	114	2.79	200	346.8	9.17	11.96	14.47	0.24	0.07	11.160	1.285	1.242	1.239	1.297
	155	2.08	200	362.8	13.68	17.65	19.06	0.33	0.14	14.025	1.364	1.228	1.623	1.359
	155	2.08	200	357.9	13.50	17.42	14.28	0.33	0.13	13.890	1.031	0.931	1.222	1.028

[Source: Sherman (1992)**]**

Table 4.3 *Existing cross-section classification slenderness limits for CHSs under bending*

Design Standard	Slenderness parameter	Compact limit	Yield limit
AS 4100:1998 (2016)	$\overline{\lambda}_{cs.IA}$	50	120
IS 800 (2007)	$\overline{\lambda}_{cs.IA}$	52	146
BS 5950:Part-1 (1990)	$\overline{\lambda}_{cs.IA}$	62.69	87.97
EN 1993-1-1 (2005)	$\overline{\lambda}_{cs.IA}$	65.79	84.59
AISC 360-16 (2016)	$\overline{\lambda}_{cs.IA}$	58.79	260.36
CSA S16-14 (2014)	$\overline{\lambda}_{cs.IA}$	71.98	263.97

Table 4.4 *Existing and proposed cross-section classification slenderness limits for CHSs under bending*

Design Standard	Slenderness parameter	Compact limit		Yield limit		Elastic limit	
		Existing	Proposed	Existing	Proposed	Existing	Proposed
AS 4100:1998 (2016)	$\overline{\lambda}_{cs.IA}$	50	42.65	120	123.84	—	392.11
IS 800 (2007)	$\overline{\lambda}_{cs.IA}$	52	42.65	146	123.84	—	392.11
BS 5950:Part-1 (1990)	$\overline{\lambda}_{cs.E}$	66.7	45.37	93.6	131.75	—	417.14
EN 1993-1-1 (2005)	$\overline{\lambda}_{cs.E}$	70	45.37	90	131.75	—	417.14
AISC 360-16 (2016)	$\overline{\lambda}_{cs}$	0.07	0.0508	0.31	0.1474	—	0.4668
CSA S16-14 (2014)	$\overline{\lambda}_{cs}$	0.0857	0.0508	0.3143	0.1474	—	0.4668

Table 4.5 *Properties of EHSs under major axis bending in various experimental and FE investigations*

Reference – (HF/CF - EXP/FEA)	$2a \times 2b \times t$ (mm×mm×mm)	a/b (= r)	E (GPa)	$f_{y.mea}$ (MPa)	M_e (kNm)	M_p (kNm)	$D_{CGb.mj}$ (mm)	$\frac{D_{CGb.mj}}{t\varepsilon^2}$	$D_{NSb.mj}$ (mm)	$\frac{D_{NSb.mj}}{t\varepsilon^2}$	$\bar{\lambda}_{l.b}$	$\bar{\lambda}_{cs}$	M_u (kNm)	$\frac{M_u}{M_{AS4100}}$	$\frac{M_u}{M_{AISC360}}$	$\frac{M_u}{M_{EC3}}$	$\frac{M_u}{M_{u.pr}}$
Chan and Gardner (2008a) – (HF - EXP)	401.3 × 200.8 × 12.13	2.00	215.10	395	350.08	491.17	320.91	44.47	214.23	29.69	0.164	0.032	548	1.229	1.229	1.229	1.064
	399.9 × 201.1 × 14.48	1.99	220.10	397.5	409.85	578.44	318.15	37.17	213.35	24.92	0.148	0.027	659	1.263	1.263	1.263	1.044
	491.7 × 260.9 × 7.78	1.89	223.80	413	383.14	526.01	370.70	83.74	261.02	58.96	0.226	0.062	497	1.027	1.019	1.019	1.030
	399.0 × 202.1 × 9.57	1.98	197.10	401	285.29	397.06	315.19	56.20	212.72	37.93	0.193	0.045	485	1.335	1.335	1.335	1.250
	403.1 × 198.5 × 11.94	2.03	215.10	395	345.39	485.07	327.35	46.08	215.53	30.34	0.165	0.033	681	1.549	1.549	1.549	1.346
	400.9 × 197.8 × 14.34	2.03	220.10	397.5	404.35	571.56	324.98	38.33	214.32	25.28	0.149	0.027	808	1.569	1.569	1.569	1.302
	405.5 × 200.7 × 15.33	2.02	221.25	378.5	418.82	593.11	327.73	34.43	216.72	22.77	0.141	0.024	862	1.617	1.617	1.617	1.309
McCann et al. (2018) – (HF - FEA)	274.8 × 183.2 × 4.2	1.5	216.64	390.6	70.09	94.00	164.88	65.25	144.16	57.05	0.226	0.062	92.11	1.040	1.032	1.032	1.043
	274.8 × 183.2 × 2.1	1.5	216.64	390.6	35.95	47.82	164.88	130.50	144.16	114.10	0.320	0.124	43.03	1.136	1.043	1.320	1.140
	274.8 × 183.2 × 1.5	1.5	216.64	390.6	25.86	34.33	164.88	182.70	144.16	159.74	0.378	0.173	29.28	1.245	1.027	1.563	1.187
	274.8 × 183.2 × 1.0	1.5	216.64	390.6	17.35	22.98	164.88	274.05	144.16	239.61	0.463	0.260	18.55	1.449	1.004	2.015	1.269
	274.8 × 183.2 × 0.7	1.5	216.64	390.6	12.19	16.13	164.88	391.50	144.16	342.31	0.554	0.371	12.39	1.643	1.141	2.584	1.357
	274.8 × 183.2 × 4.2	1.5	216.64	1200	215.32	288.77	164.88	200.46	144.16	175.27	0.396	0.190	262.70	1.405	1.117	1.803	1.314
	274.8 × 183.2 × 2.1	1.5	216.64	1200	110.43	146.92	164.88	400.92	144.16	350.54	0.560	0.380	112.31	1.660	1.170	2.638	1.368
	274.8 × 183.2 × 1.5	1.5	216.64	1200	79.45	105.47	164.88	561.29	144.16	490.76	0.663	0.532	76.65	3.304	1.579	3.379	1.553
	274.8 × 183.2 × 1.0	1.5	216.64	1200	53.29	70.60	164.88	841.94	144.16	736.14	0.812	0.799	41.26	5.969	1.946	3.965	1.828
	274.8 × 183.2 × 0.7	1.5	216.64	1200	37.44	49.54	164.88	1202.77	144.16	1051.63	0.971	1.141	22.09	8.662	2.174	4.282	2.012
	274.8 × 183.2 × 4.2	1.5	216.64	2500	448.59	601.60	164.88	417.63	144.16	365.15	0.572	0.396	466.56	1.726	1.248	2.796	1.419
	274.8 × 183.2 × 2.1	1.5	216.64	2500	230.07	306.09	164.88	835.26	144.16	730.30	0.809	0.792	161.29	5.324	1.747	3.563	1.642
	274.8 × 183.2 × 1.5	1.5	216.64	2500	165.53	219.73	164.88	1169.36	144.16	1022.42	0.957	1.109	85.21	7.189	1.840	3.632	1.703
	274.8 × 183.2 × 1.0	1.5	216.64	2500	111.02	147.09	164.88	1754.04	144.16	1533.63	1.172	1.664	40.66	10.427	2.035	3.895	1.909
	274.8 × 183.2 × 0.7	1.5	216.64	2500	78.00	103.22	164.88	2505.78	144.16	2190.90	1.401	2.377	21.54	14.928	2.282	4.275	2.230
	300 × 150 × 4.2	2	216.64	390.6	70.93	97.79	240.00	94.98	160.15	63.38	0.238	0.069	94.25	1.075	1.044	1.044	1.083
	300 × 150 × 2.1	2	216.64	390.6	36.36	49.74	240.00	189.96	160.15	126.75	0.337	0.137	44.54	1.207	1.082	1.444	1.201
	300 × 150 × 1.5	2	216.64	390.6	26.15	35.70	240.00	265.94	160.15	177.45	0.399	0.192	30.49	1.351	1.069	1.739	1.261
	300 × 150 × 1.0	2	216.64	390.6	17.54	23.90	240.00	398.91	160.15	266.18	0.488	0.289	18.85	1.538	1.016	2.207	1.319
	300 × 150 × 0.7	2	216.64	390.6	12.32	16.77	240.00	569.87	160.15	380.26	0.584	0.412	12.88	1.936	1.309	2.913	1.447
	300 × 150 × 4.2	2	216.64	900	163.44	225.31	240.00	218.84	160.15	146.03	0.362	0.158	204.63	1.305	1.125	1.623	1.278
	300 × 150 × 2.1	2	216.64	900	83.77	114.60	240.00	437.69	160.15	292.06	0.512	0.317	94.54	1.693	1.073	2.504	1.428
	300 × 150 × 1.5	2	216.64	900	60.26	82.26	240.00	612.77	160.15	408.88	0.605	0.444	61.68	2.288	1.383	3.041	1.452
	300 × 150 × 1.0	2	216.64	900	40.41	55.06	240.00	919.15	160.15	613.32	0.741	0.665	28.48	3.830	1.459	3.035	1.395
	300 × 150 × 0.7	2	216.64	900	28.39	38.64	240.00	1313.07	160.15	876.17	0.886	0.950	14.37	5.365	1.532	3.067	1.424
	300 × 150 × 4.2	2	216.64	1800	326.88	450.63	240.00	437.69	160.15	292.06	0.512	0.317	349.04	1.602	1.016	2.369	1.351
	300 × 150 × 2.1	2	216.64	1800	167.54	229.21	240.00	875.38	160.15	584.12	0.724	0.634	130.34	3.837	1.530	3.201	1.470
	300 × 150 × 1.5	2	216.64	1800	120.52	164.52	240.00	1225.53	160.15	817.76	0.856	0.887	63.65	4.942	1.485	2.993	1.385
	300 × 150 × 1.0	2	216.64	1800	80.82	110.13	240.00	1838.30	160.15	1226.64	1.048	1.331	28.07	6.682	1.512	2.941	1.402
	300 × 150 × 0.7	2	216.64	1800	56.78	77.28	240.00	2626.14	160.15	1752.35	1.253	1.901	14.08	8.941	1.596	3.029	1.515

Table 4.5 (**Cont'd.**)

Reference – (HF/CF - EXP/FEA)	$2a \times 2b \times t$ (mm×mm×mm)	a/b (= r)	E (GPa)	$f_{y.mea}$ (MPa)	M_e (kNm)	M_p (kNm)	$D_{CGb.mj}$ (mm)	$\frac{D_{CGb.mj}}{t\varepsilon^2}$	$D_{NSb.mj}$ (mm)	$\frac{D_{NSb.mj}}{t\varepsilon^2}$	$\bar{\lambda}_{l.b}$	$\bar{\lambda}_{cs}$	M_u (kNm)	$\frac{M_u}{M_{AS4100}}$	$\frac{M_u}{M_{AISC360}}$	$\frac{M_u}{M_{EC3}}$	$\frac{M_u}{M_{u.pr}}$
	326 × 108.67 × 4.2	3	216.64	390.6	69.34	99.58	391.20	154.82	190.95	75.57	0.260	0.082	92.83	1.128	1.087	1.339	1.142
	326 × 108.67 × 2.1	3	216.64	390.6	35.54	50.64	391.20	309.63	190.95	151.13	0.368	0.164	43.46	1.309	1.103	1.623	1.261
	326 × 108.67 × 1.5	3	216.64	390.6	25.56	36.35	391.20	433.48	190.95	211.59	0.435	0.230	29.66	1.472	1.080	1.979	1.324
	326 × 108.67 × 1.0	3	216.64	390.6	17.14	24.33	391.20	650.22	190.95	317.38	0.533	0.344	16.75	1.526	1.014	2.327	1.271
	326 × 108.67 × 0.7	3	216.64	390.6	12.04	17.07	391.20	928.89	190.95	453.40	0.637	0.492	8.73	2.078	1.092	2.363	1.086
	326 × 108.67 × 4.2	3	216.64	700	124.26	178.46	391.20	277.45	190.95	135.42	0.348	0.147	158.57	1.298	1.136	1.571	1.275
	326 × 108.67 × 2.1	3	216.64	700	63.69	90.76	391.20	554.89	190.95	270.85	0.493	0.294	69.28	1.571	1.030	2.266	1.343
	326 × 108.67 × 1.5	3	216.64	700	45.81	65.14	391.20	776.85	190.95	379.19	0.583	0.411	37.52	1.505	1.023	2.276	1.132
	326 × 108.67 × 1.0	3	216.64	700	30.72	43.60	391.20	1165.28	190.95	568.78	0.714	0.617	17.58	2.674	1.094	2.297	1.055
	326 × 108.67 × 0.7	3	216.64	700	21.58	30.60	391.20	1664.68	190.95	812.55	0.853	0.881	8.67	3.715	1.122	2.263	1.047
	326 × 108.67 × 4.2	3	216.64	1150	204.15	293.18	391.20	455.81	190.95	222.48	0.447	0.241	242.68	1.549	1.110	2.110	1.378
	326 × 108.67 × 2.1	3	216.64	1150	104.63	149.11	391.20	911.61	190.95	444.97	0.631	0.483	85.27	2.236	1.203	2.612	1.201
	326 × 108.67 × 1.5	3	216.64	1150	75.26	107.02	391.20	1276.26	190.95	622.95	0.747	0.676	43.07	3.207	1.204	2.501	1.149
	326 × 108.67 × 1.0	3	216.64	1150	50.47	71.63	391.20	1914.38	190.95	934.43	0.915	1.014	18.69	4.408	1.201	2.391	1.114
	326 × 108.67 × 0.7	3	216.64	1150	35.45	50.27	391.20	2734.83	190.95	1334.90	1.094	1.448	10.28	6.468	1.384	2.674	1.287
	346 × 69.2 × 4.2	5	216.64	390.6	65.41	98.74	692.00	273.86	300.39	118.88	0.326	0.129	85.96	1.265	1.151	1.487	1.266
	346 × 69.2 × 2.1	5	216.64	390.6	33.54	50.22	692.00	547.71	300.39	237.75	0.462	0.258	36.82	1.481	1.030	2.055	1.300
	346 × 69.2 × 1.5	5	216.64	390.6	24.13	36.05	692.00	766.79	300.39	332.85	0.546	0.361	22.19	1.467	1.002	2.280	1.215
	346 × 69.2 × 1.0	5	216.64	390.6	16.19	24.13	692.00	1150.19	300.39	499.28	0.669	0.542	9.47	2.080	0.975	2.082	0.956
	346 × 69.2 × 0.7	5	216.64	390.6	11.37	16.93	692.00	1643.13	300.39	713.26	0.799	0.774	5.49	3.507	1.173	2.398	1.105
	346 × 69.2 × 4.2	5	216.64	500	83.73	126.39	692.00	350.56	300.39	152.17	0.369	0.165	107.18	1.375	1.155	1.708	1.323
	346 × 69.2 × 2.1	5	216.64	500	42.94	64.28	692.00	701.11	300.39	304.34	0.522	0.330	43.08	1.536	0.996	2.305	1.287
	346 × 69.2 × 1.5	5	216.64	500	30.89	46.14	692.00	981.56	300.39	426.08	0.618	0.462	25.16	2.015	1.149	2.510	1.154
	346 × 69.2 × 1.0	5	216.64	500	20.72	30.89	692.00	1472.34	300.39	639.12	0.757	0.693	10.00	2.844	1.044	2.161	0.993
	346 × 69.2 × 0.7	5	216.64	500	14.56	21.67	692.00	2103.34	300.39	913.03	0.905	0.990	5.98	4.687	1.299	2.591	1.206
	346 × 69.2 × 4.2	5	216.64	700	117.22	176.95	692.00	490.78	300.39	213.04	0.437	0.231	142.83	1.551	1.134	2.090	1.393
	346 × 69.2 × 2.1	5	216.64	700	60.11	90.00	692.00	981.56	300.39	426.08	0.618	0.462	44.39	1.827	1.042	2.276	1.046
	346 × 69.2 × 1.5	5	216.64	700	43.25	64.60	692.00	1374.18	300.39	596.51	0.731	0.647	25.07	2.982	1.165	2.432	1.118
	346 × 69.2 × 1.0	5	216.64	700	29.01	43.24	692.00	2061.28	300.39	894.77	0.895	0.971	11.07	4.203	1.182	2.361	1.098
	346 × 69.2 × 0.7	5	216.64	700	20.38	30.34	692.00	2944.68	300.39	1278.24	1.070	1.387	6.60	6.699	1.475	2.860	1.369

Table 4.5 (**Cont'd.**)

Reference – (HF/CF - EXP/FEA)	$2a \times 2b \times t$ (mm×mm×mm)	a/b (= r)	E (GPa)	$f_{y.mea}$ (MPa)	M_e (kNm)	M_p (kNm)	$D_{CGb.mj}$ (mm)	$\frac{D_{CGb.mj}}{t\varepsilon^2}$	$D_{NSb.mj}$ (mm)	$\frac{D_{NSb.mj}}{t\varepsilon^2}$	$\bar{\lambda}_{l.b}$	$\bar{\lambda}_{cs}$	M_u (kNm)	$\frac{M_u}{M_{AS4100}}$	$\frac{M_u}{M_{AISC360}}$	$\frac{M_u}{M_{EC3}}$	$\frac{M_u}{M_{u.pr}}$
Chen and Young (2019)	140.7 × 87.9 × 2.93	1.60	208	388	12.00	16.29	90.09	50.76	73.96	41.68	0.197	0.047	18.1	1.184	1.184	1.184	1.119
– (CF - EXP)	141.2 × 87.5 × 2.91	1.61	208	388	11.96	16.24	91.14	51.71	74.25	42.13	0.198	0.048	16.0	1.051	1.051	1.051	0.996
	148.1 × 72.6 × 2.73	2.04	210	341	9.55	13.26	120.85	64.23	79.23	42.11	0.197	0.047	16.1	1.324	1.324	1.324	1.251
	148.1 × 72.4 × 2.71	2.05	210	341	9.47	13.15	121.18	64.89	79.26	42.44	0.198	0.047	15.6	1.293	1.293	1.293	1.225
	148.3 × 72.4 × 2.87	2.05	210	341	10.02	13.92	121.51	61.43	79.38	40.13	0.193	0.045	16.6	1.302	1.302	1.302	1.216
	148.5 × 71.9 × 2.83	2.07	210	341	9.87	13.73	122.68	62.90	79.56	40.80	0.194	0.046	16.9	1.345	1.345	1.345	1.261
	176.0 × 66.7 × 4.84	2.64	200	418	24.95	35.95	185.76	68.27	98.78	36.30	0.188	0.043	51.4	1.618	1.618	1.618	1.493
	176.4 × 66.1 × 4.81	2.67	200	418	24.80	35.77	188.3	69.63	99.32	36.73	0.189	0.043	45.5	1.441	1.441	1.441	1.334
	149.8 × 52.0 × 5.06	2.88	205	410	17.39	25.48	172.62	59.52	86.42	29.80	0.168	0.034	35.8	1.617	1.617	1.617	1.416
	150.7 × 50.5 × 5.02	2.98	205	410	17.22	25.32	179.89	62.52	88.09	30.61	0.170	0.035	39.7	1.811	1.811	1.811	1.595
Chen and Young (2019)	250 × 200 × 12	1.25	208	388	167.24	227.80	160	22.01	160	22.01	0.143	0.025	249.8	1.173	1.173	1.173	0.955
– (CF - FEA)	250 × 200 × 6.5	1.25	208	388	97.21	129.52	160	40.64	160	40.64	0.195	0.046	138.4	1.118	1.118	1.118	1.051
	250 × 200 × 5	1.25	208	388	76.22	100.95	160	52.83	160	52.83	0.222	0.060	106.2	1.094	1.094	1.094	1.096
	250 × 200 × 4	1.25	208	388	61.76	81.46	160	66.04	160	66.04	0.248	0.075	84.3	1.077	1.072	1.072	1.135
	250 × 200 × 2.5	1.25	208	388	39.34	51.58	160	105.67	160	105.67	0.314	0.119	50.9	1.141	1.086	1.294	1.219
	250 × 200 × 2	1.25	208	388	31.68	41.44	160	132.09	160	132.09	0.351	0.149	39.6	1.181	1.087	1.367	1.254
	250 × 200 × 1.5	1.25	208	388	23.91	31.22	160	176.11	160	176.11	0.405	0.199	28.3	1.263	1.067	1.563	1.292
	200 × 150 × 10	1.33	208	388	84.67	116.29	112.5	18.57	112.5	18.57	0.132	0.021	127.4	1.182	1.182	1.182	0.929
	200 × 150 × 6	1.33	208	388	54.22	72.99	112.5	30.96	112.5	30.96	0.170	0.035	78.5	1.137	1.137	1.137	1.001
	200 × 150 × 3	1.33	208	388	28.46	37.73	112.5	61.91	112.5	61.91	0.240	0.070	39.2	1.101	1.082	1.082	1.127
	200 × 150 × 2.5	1.33	208	388	23.91	31.62	112.5	74.30	112.5	74.30	0.263	0.084	32.4	1.128	1.090	1.064	1.162
	200 × 150 × 2	1.33	208	388	19.28	25.43	112.5	92.87	112.5	92.87	0.294	0.105	25.5	1.167	1.110	1.322	1.203
	200 × 150 × 1.5	1.33	208	388	14.58	19.18	112.5	123.83	112.5	123.83	0.340	0.140	18.6	1.233	1.119	1.452	1.257
	200 × 150 × 1	1.33	208	388	9.80	12.86	112.5	185.74	112.5	185.74	0.416	0.210	12.1	1.442	1.133	1.862	1.370
	300 × 200 × 8	1.50	208	388	152.16	206.49	180	37.15	157.38	32.48	0.174	0.037	224.1	1.157	1.157	1.157	1.030
	300 × 200 × 6	1.50	208	388	116.69	157.26	180	49.53	157.38	43.31	0.201	0.049	168	1.131	1.131	1.131	1.079
	300 × 200 × 4	1.50	208	388	79.54	106.45	180	74.30	157.38	64.96	0.246	0.073	110.6	1.141	1.103	1.092	1.153
	300 × 200 × 2	1.50	208	388	40.66	54.04	180	148.60	157.38	129.92	0.348	0.147	53.4	1.335	1.170	1.616	1.312
	300 × 200 × 1.5	1.50	208	388	30.66	40.68	180	198.13	157.38	173.23	0.402	0.196	38.7	1.475	1.159	1.906	1.372
	150 × 100 × 8	1.50	208	388	34.79	48.51	90	18.57	78.69	16.24	0.123	0.018	53.1	1.199	1.199	1.199	0.915
	150 × 100 × 6	1.50	208	388	27.29	37.54	90	24.77	78.69	21.65	0.142	0.024	40.9	1.177	1.177	1.177	0.956
	150 × 100 × 2.5	1.50	208	388	12.29	16.51	90	59.44	78.69	51.97	0.220	0.059	17.3	1.106	1.106	1.106	1.103
	150 × 100 × 1.5	1.50	208	388	7.54	10.06	90	99.06	78.69	86.62	0.284	0.098	10.2	1.194	1.136	1.353	1.209
	400 × 250 × 16	1.60	208	388	496.50	687.57	256	26.42	210.27	21.70	0.142	0.025	761.1	1.204	1.204	1.204	0.978
	400 × 250 × 10	1.60	208	388	326.53	445.20	256	42.27	210.27	34.72	0.180	0.039	484.5	1.165	1.165	1.165	1.054
	400 × 250 × 8	1.60	208	388	265.68	360.35	256	52.83	210.27	43.40	0.201	0.049	387.3	1.145	1.145	1.145	1.093
	400 × 250 × 6	1.60	208	388	202.66	273.43	256	70.45	210.27	57.86	0.232	0.065	288	1.137	1.116	1.116	1.144

Table 4.5 (**Cont'd.**)

Reference – (HF/CF - EXP/FEA)	$2a \times 2b \times t$ (mm×mm×mm)	a/b (= r)	E (GPa)	$f_{y.mea}$ (MPa)	M_e (kNm)	M_p (kNm)	$D_{CGb.mj}$ (mm)	$\frac{D_{CGb.mj}}{t\varepsilon^2}$	$D_{NSb.mj}$ (mm)	$\frac{D_{NSb.mj}}{t\varepsilon^2}$	$\bar{\lambda}_{l.b}$	$\bar{\lambda}_{cs}$	M_u (kNm)	$\frac{M_u}{M_{AS4100}}$	$\frac{M_u}{M_{AISC360}}$	$\frac{M_u}{M_{EC3}}$	$\frac{M_u}{M_{u.pr}}$
	400 × 250 × 3	1.60	208	388	103.93	139.12	256	140.89	210.27	115.72	0.329	0.131	139.6	1.300	1.179	1.533	1.299
	400 × 250 × 2	1.60	208	388	69.87	93.28	256	211.34	210.27	173.58	0.403	0.196	88.8	1.487	1.167	1.922	1.382
	350 × 200 × 14	1.75	208	388	314.80	440.04	245	28.89	184.79	21.79	0.143	0.025	487.9	1.217	1.217	1.217	0.990
	350 × 200 × 7	1.75	208	388	168.69	230.88	245	57.79	184.79	43.59	0.202	0.049	250.2	1.165	1.165	1.165	1.113
	350 × 200 × 5	1.75	208	388	122.89	167.17	245	80.90	184.79	61.02	0.239	0.069	177.9	1.172	1.137	1.137	1.181
	350 × 200 × 3.5	1.75	208	388	87.30	118.22	245	115.57	184.79	87.17	0.285	0.098	122.3	1.239	1.177	1.401	1.254
	350 × 200 × 2	1.75	208	388	50.63	68.24	245	202.26	184.79	152.55	0.377	0.172	66.7	1.445	1.195	1.812	1.379
	350 × 200 × 1.5	1.75	208	388	38.16	51.36	245	269.67	184.79	203.40	0.436	0.230	48	1.597	1.171	2.149	1.436
	210 × 120 × 12	1.75	208	388	91.51	130.22	147	20.23	110.88	15.26	0.119	0.017	143.9	1.235	1.235	1.235	0.930
	210 × 120 × 6	1.75	208	388	50.53	69.79	147	40.45	110.88	30.51	0.169	0.034	76.2	1.184	1.184	1.184	1.039
	210 × 120 × 3.5	1.75	208	388	30.72	41.89	147	69.34	110.88	52.30	0.221	0.059	44.8	1.146	1.146	1.146	1.145
	210 × 120 × 2.5	1.75	208	388	22.30	30.26	147	97.08	110.88	73.23	0.261	0.083	31.7	1.200	1.157	1.421	1.215
	210 × 120 × 1.5	1.75	208	388	13.60	18.36	147	161.80	110.88	122.04	0.338	0.138	18.3	1.327	1.189	1.588	1.320
	500 × 250 × 16	2.00	208	388	699.36	983.15	400	41.28	266.91	27.54	0.160	0.031	1093.6	1.228	1.228	1.228	1.052
	500 × 250 × 10	2.00	208	388	456.19	633.01	400	66.04	266.91	44.07	0.203	0.050	692.2	1.192	1.192	1.192	1.142
	500 × 250 × 8.5	2.00	208	388	391.91	542.05	400	77.70	266.91	51.85	0.220	0.059	587.9	1.178	1.178	1.178	1.175
	500 × 250 × 6	2.00	208	388	281.60	387.35	400	110.07	266.91	73.45	0.262	0.083	411	1.233	1.188	1.460	1.249
	500 × 250 × 4	2.00	208	388	190.41	260.77	400	165.11	266.91	110.17	0.321	0.124	266.4	1.331	1.220	1.549	1.334
	500 × 250 × 3.5	2.00	208	388	167.20	228.74	400	188.69	266.91	125.91	0.343	0.142	230.7	1.377	1.224	1.663	1.366
	400 × 200 × 16	2.00	208	388	434.98	616.77	320	33.02	213.53	22.03	0.143	0.025	687.2	1.241	1.241	1.241	1.011
	400 × 200 × 10	2.00	208	388	286.81	400.16	320	52.83	213.53	35.25	0.181	0.040	440.9	1.207	1.207	1.207	1.096
	400 × 200 × 5.5	2.00	208	388	164.18	226.27	320	96.06	213.53	64.10	0.245	0.072	242.2	1.207	1.167	1.159	1.219
	400 × 200 × 3.5	2.00	208	388	106.35	145.77	320	150.95	213.53	100.73	0.307	0.114	150.1	1.303	1.214	1.481	1.313
	400 × 200 × 3	2.00	208	388	91.56	125.32	320	176.11	213.53	117.52	0.331	0.133	126.7	1.346	1.217	1.595	1.344
	400 × 200 × 2	2.00	208	388	61.58	84.06	320	264.17	213.53	176.27	0.406	0.199	81.2	1.555	1.212	2.017	1.441
	270 × 120 × 8	2.25	208	388	96.60	137.17	243	50.15	146.42	30.22	0.168	0.034	152	1.236	1.236	1.236	1.082
	270 × 120 × 6.5	2.25	208	388	80.10	113.03	243	61.72	146.42	37.19	0.186	0.042	124.4	1.220	1.220	1.220	1.122
	270 × 120 × 4.5	2.25	208	388	56.97	79.73	243	89.16	146.42	53.72	0.224	0.061	86.2	1.193	1.188	1.188	1.196
	270 × 120 × 2.5	2.25	208	388	32.51	45.13	243	160.48	146.42	96.70	0.300	0.109	46.9	1.315	1.233	1.479	1.327
	270 × 120 × 2	2.25	208	388	26.18	36.27	243	200.60	146.42	120.88	0.336	0.137	36.6	1.374	1.234	1.640	1.368
	180 × 80 × 8	2.25	208	388	40.66	58.69	162	33.43	97.62	20.15	0.137	0.023	65	1.255	1.255	1.255	1.003
	180 × 80 × 6	2.25	208	388	31.77	45.29	162	44.58	97.62	26.86	0.158	0.030	50	1.236	1.236	1.236	1.053
	180 × 80 × 3.5	2.25	208	388	19.49	27.37	162	76.42	97.62	46.05	0.207	0.052	29.7	1.197	1.197	1.197	1.159
	180 × 80 × 2	2.25	208	388	11.48	15.97	162	133.74	97.62	80.59	0.274	0.091	16.8	1.266	1.213	1.463	1.282
	180 × 80 × 1.5	2.25	208	388	8.70	12.06	162	178.31	97.62	107.45	0.317	0.121	12.4	1.344	1.238	1.554	1.350
	500 × 200 × 16	2.50	208	388	623.20	897.48	500	51.60	276.83	28.57	0.163	0.032	1007.4	1.270	1.270	1.270	1.097
	500 × 200 × 12	2.50	208	388	481.56	687.24	500	68.79	276.83	38.09	0.189	0.043	763.5	1.245	1.245	1.245	1.152
	500 × 200 × 8	2.50	208	388	330.74	467.72	500	103.19	276.83	57.13	0.231	0.065	507.1	1.224	1.204	1.204	1.230

***Table 4.5** (Cont'd.)*

Reference – (HF/CF - EXP/FEA)	$2a \times 2b \times t$ (mm×mm×mm)	a/b (= r)	E (GPa)	$f_{y.mea}$ (MPa)	M_e (kNm)	M_p (kNm)	$D_{CGb.mj}$ (mm)	$\frac{D_{CGb.mj}}{t\varepsilon^2}$	$D_{NSb.mj}$ (mm)	$\frac{D_{NSb.mj}}{t\varepsilon^2}$	$\bar{\lambda}_{l.b}$	$\bar{\lambda}_{cs}$	M_u (kNm)	$\frac{M_u}{M_{AS4100}}$	$\frac{M_u}{M_{AISC360}}$	$\frac{M_u}{M_{EC3}}$	$\frac{M_u}{M_{u.pr}}$
	500 × 200 × 4	2.50	208	388	170.35	238.71	500	206.38	276.83	114.27	0.327	0.129	245.6	1.389	1.263	1.632	1.389
	500 × 200 × 3.5	2.50	208	388	149.61	209.40	500	235.87	276.83	130.59	0.349	0.148	212.3	1.446	1.264	1.752	1.419
	250 × 100 × 10	2.50	208	388	94.50	137.33	250	41.28	138.42	22.85	0.146	0.026	153.3	1.274	1.274	1.274	1.047
	250 × 100 × 7	2.50	208	388	69.19	99.19	250	58.97	138.42	32.65	0.175	0.037	110.1	1.250	1.250	1.250	1.114
	250 × 100 × 5	2.50	208	388	50.92	72.33	250	82.55	138.42	45.71	0.207	0.052	79	1.219	1.219	1.219	1.178
	250 × 100 × 3	2.50	208	388	31.47	44.30	250	137.59	138.42	76.18	0.267	0.086	46.8	1.268	1.219	1.487	1.284
	250 × 100 × 1.5	2.50	208	388	16.09	22.49	250	275.18	138.42	152.36	0.377	0.172	22.3	1.519	1.257	1.905	1.450
	275 × 100 × 6.5	2.75	208	388	75.60	108.95	302.5	76.84	156.22	39.68	0.192	0.045	120.7	1.254	1.254	1.254	1.171
	275 × 100 × 4.5	2.75	208	388	53.80	76.88	302.5	110.99	156.22	57.32	0.231	0.065	83.1	1.234	1.213	1.213	1.240
	275 × 100 × 3.5	2.75	208	388	42.43	60.37	302.5	142.70	156.22	73.69	0.262	0.083	64	1.276	1.229	1.509	1.292
	275 × 100 × 2	2.75	208	388	24.75	34.99	302.5	249.72	156.22	128.96	0.347	0.146	35.4	1.450	1.273	1.751	1.426
	275 × 100 × 1.5	2.75	208	388	18.69	26.37	302.5	332.96	156.22	171.95	0.401	0.194	25.7	1.601	1.262	2.065	1.491
	300 × 100 × 16	3.00	208	388	190.01	286.21	360	37.15	175.72	18.13	0.130	0.020	323.5	1.337	1.337	1.337	1.045
	300 × 100 × 10	3.00	208	388	128.35	188.86	360	59.44	175.72	29.01	0.165	0.033	212.8	1.302	1.302	1.302	1.129
	300 × 100 × 7	3.00	208	388	93.38	135.79	360	84.91	175.72	41.45	0.197	0.047	151	1.270	1.270	1.270	1.199
	300 × 100 × 6	3.00	208	388	81.08	117.43	360	99.06	175.72	48.35	0.212	0.055	129.2	1.252	1.252	1.252	1.227
	300 × 100 × 3.5	3.00	208	388	48.84	70.03	360	169.82	175.72	82.89	0.278	0.094	73.7	1.316	1.257	1.509	1.333
	300 × 100 × 2.5	3.00	208	388	35.33	50.47	360	237.75	175.72	116.05	0.329	0.131	51.4	1.409	1.277	1.663	1.408
	300 × 100 × 2	3.00	208	388	28.45	40.55	360	297.19	175.72	145.06	0.368	0.164	40.6	1.528	1.287	1.894	1.472
	150 × 50 × 8	3.00	208	388	23.75	35.78	180	37.15	87.86	18.13	0.130	0.020	40	1.323	1.323	1.323	1.033
	150 × 50 × 6	3.00	208	388	18.76	27.82	180	49.53	87.86	24.18	0.150	0.027	31.1	1.302	1.302	1.302	1.083
	150 × 50 × 4	3.00	208	388	13.17	19.23	180	74.30	87.86	36.27	0.184	0.041	21.3	1.270	1.270	1.270	1.161
	150 × 50 × 2.5	3.00	208	388	8.55	12.34	180	118.88	87.86	58.02	0.233	0.066	13.3	1.245	1.221	1.221	1.252
	150 × 50 × 1.5	3.00	208	388	5.27	7.54	180	198.13	87.86	96.71	0.300	0.109	7.8	1.351	1.266	1.519	1.363
	325 × 100 × 10	3.25	208	388	147.11	217.69	422.5	69.76	197.23	32.56	0.174	0.037	246.3	1.315	1.315	1.315	1.172
	325 × 100 × 6.5	3.25	208	388	99.74	145.68	422.5	107.32	197.23	50.10	0.216	0.057	160.8	1.266	1.266	1.266	1.252
	325 × 100 × 4	3.25	208	388	63.25	91.52	422.5	174.39	197.23	81.41	0.276	0.092	96.7	1.327	1.269	1.529	1.344
	325 × 100 × 2.5	3.25	208	388	40.25	57.91	422.5	279.03	197.23	130.25	0.349	0.147	57.8	1.462	1.279	1.770	1.436
	325 × 100 × 2	3.25	208	388	32.39	46.52	422.5	348.79	197.23	162.82	0.390	0.184	45.8	1.602	1.290	2.039	1.508
	350 × 100 × 12	3.50	208	388	196.00	293.64	490	67.42	221.07	30.42	0.168	0.034	334.7	1.341	1.341	1.341	1.176
	350 × 100 × 8	3.50	208	388	136.74	201.99	490	101.13	221.07	45.62	0.206	0.052	226.1	1.299	1.299	1.299	1.255
	350 × 100 × 6	3.50	208	388	104.90	153.87	490	134.84	221.07	60.83	0.238	0.069	168	1.296	1.258	1.258	1.305
	350 × 100 × 3.5	3.50	208	388	62.94	91.51	490	231.15	221.07	104.28	0.312	0.118	94.6	1.403	1.300	1.610	1.412
	350 × 100 × 2.5	3.50	208	388	45.47	65.87	490	323.61	221.07	146.00	0.369	0.165	65.8	1.554	1.306	1.929	1.495

Table 4.6 *Properties of EHSs under minor axis bending in various experimental and FE investigations*

Reference – (HF/CF - EXP/FEA)	$2a \times 2b \times t$ (**mm×mm×mm**)	a/b (= r)	E (**GPa**)	$f_{y.mea}$ (**MPa**)	M_e (**kNm**)	M_p (**kNm**)	$D_{CGb.mn}$ (**mm**)	$\frac{D_{CGb.mn}}{t\varepsilon^2}$	$D_{NSb.mn}$ (**mm**)	$\frac{D_{NSb.mn}}{t\varepsilon^2}$	$\bar{\lambda}_{l.b}$	$\bar{\lambda}_{cs}$	M_u (**kNm**)	$\frac{M_u}{M_{AS4100}}$	$\frac{M_u}{M_{AISC360}}$	$\frac{M_u}{M_{EC3}}$	$\frac{M_u}{M_{u.pr}}$
Chan and Gardner (2008a)	396.1 × 207.6 × 7.8	1.9	221.60	429	176.14	221.98	755.61	177.99	550.13	129.59	0.337	0.137	186	1.040	0.933	1.244	1.035
– (HF - EXP)	396.1 × 207.5 × 9.7	1.9	197.10	401	200.09	254.39	755.82	133.65	550.25	97.30	0.310	0.116	232	1.077	1.000	1.230	1.084
	401.5 × 201 × 12.1	2.0	215.10	395	234.24	301.01	802.12	111.15	579.29	80.27	0.269	0.088	288	1.054	1.012	1.230	1.067
	400.3 × 200 × 14.5	2.0	220.10	397.5	270.62	351.76	801.12	93.58	578.41	67.57	0.244	0.072	343	1.036	1.002	0.995	1.046
	403.2 × 201.1 × 15.6	2.0	221.25	378.5	277.70	362.77	808.32	83.30	583.44	60.12	0.230	0.064	331	0.949	0.936	0.936	0.954
	403.3 × 202.2 × 15.6	2.0	221.25	378.5	279.60	365.21	804.53	82.90	581.14	59.89	0.229	0.064	346	0.985	0.972	0.972	0.989
	495.3 × 255.9 × 7.78	1.9	223.80	413	266.82	333.73	959.01	216.63	696.26	157.28	0.369	0.165	291	1.172	0.984	1.455	1.127
	400.5 × 199.4 × 9.6	2.0	197.10	401	192.29	244.15	804.49	142.85	580.52	103.08	0.319	0.123	245	1.207	1.109	1.399	1.211
	402.2 × 200.1 × 12.0	2.0	215.10	395	230.92	296.51	808.58	113.45	583.40	81.85	0.272	0.089	330	1.231	1.180	1.429	1.247
	400.5 × 199.2 × 14.3	2.0	220.10	397.5	267.25	347.16	805.18	94.98	580.93	68.52	0.246	0.073	388	1.191	1.151	1.140	1.202
	403.4 × 199.5 × 15.3	2.0	221.25	378.5	270.05	352.21	815.54	86.02	587.91	62.01	0.233	0.066	401	1.190	1.166	1.166	1.197
McCann et al. (2018)	274.8 × 183.2 × 8.7	1.5	216.64	390.6	109.32	141.29	412.2	78.75	323.32	61.77	0.235	0.067	147.51	1.086	1.060	1.060	1.093
– (HF - FEA)	274.8 × 183.2 × 4.2	1.5	216.64	390.6	56.45	71.24	412.2	163.13	323.32	127.95	0.339	0.139	67.25	1.178	1.054	1.413	1.171
	274.8 × 183.2 × 2.1	1.5	216.64	390.6	29.12	36.34	412.2	326.25	323.32	255.90	0.479	0.278	30.01	1.445	0.972	2.049	1.249
	274.8 × 183.2 × 1.5	1.5	216.64	390.6	20.99	26.11	412.2	456.75	323.32	358.26	0.567	0.389	20.61	1.617	1.156	2.597	1.331
	274.8 × 183.2 × 1.0	1.5	216.64	390.6	14.09	17.49	412.2	685.13	323.32	537.39	0.694	0.583	13.48	3.977	1.722	3.642	1.673
	274.8 × 183.2 × 8.7	1.5	216.64	1200	335.85	434.07	412.2	241.94	323.32	189.77	0.412	0.206	422.35	1.508	1.160	1.973	1.388
	274.8 × 183.2 × 4.2	1.5	216.64	1200	173.42	218.86	412.2	501.16	323.32	393.09	0.594	0.426	167.97	1.958	1.256	2.779	1.356
	274.8 × 183.2 × 2.1	1.5	216.64	1200	89.46	111.65	412.2	1002.31	323.32	786.18	0.839	0.853	58.15	5.659	1.752	3.546	1.638
	274.8 × 183.2 × 1.5	1.5	216.64	1200	64.47	80.21	412.2	1403.23	323.32	1100.65	0.993	1.194	31.98	7.890	1.920	3.767	1.777
	274.8 × 183.2 × 1.0	1.5	216.64	1200	43.30	53.73	412.2	2104.85	323.32	1650.97	1.216	1.791	15.69	11.755	2.184	4.161	2.062
	274.8 × 183.2 × 8.7	1.5	216.64	2500	699.69	904.31	412.2	504.04	323.32	395.35	0.595	0.429	724.02	2.123	1.350	2.984	1.451
	274.8 × 183.2 × 4.2	1.5	216.64	2500	361.29	455.96	412.2	1044.07	323.32	818.94	0.857	0.888	208.49	5.414	1.625	3.275	1.516
	274.8 × 183.2 × 2.1	1.5	216.64	2500	186.38	232.61	412.2	2088.15	323.32	1637.87	1.212	1.777	57.23	9.820	1.834	3.497	1.730
	274.8 × 183.2 × 1.5	1.5	216.64	2500	134.32	167.10	412.2	2923.40	323.32	2293.02	1.434	2.487	31.27	13.690	2.024	3.784	1.993
	300 × 150 × 8.7	2	216.64	390.6	93.18	119.46	600.0	114.63	433.24	82.77	0.272	0.090	124.64	1.153	1.106	1.338	1.168
	300 × 150 × 4.2	2	216.64	390.6	48.58	60.51	600.0	237.45	433.24	171.45	0.392	0.186	54.86	1.286	1.032	1.642	1.209
	300 × 150 × 2.1	2	216.64	390.6	25.18	30.93	600.0	474.89	433.24	342.90	0.554	0.372	22.89	1.470	1.022	2.314	1.214
	300 × 150 × 1.5	2	216.64	390.6	18.17	22.23	600.0	664.85	433.24	480.06	0.656	0.521	13.77	2.473	1.212	2.603	1.196
	300 × 150 × 1.0	2	216.64	390.6	12.21	14.90	600.0	997.28	433.24	720.10	0.803	0.781	6.55	3.969	1.317	2.691	1.240
	300 × 150 × 8.7	2	216.64	900	214.70	275.26	600.0	264.12	433.24	190.71	0.413	0.207	265.70	1.488	1.142	1.949	1.368
	300 × 150 × 4.2	2	216.64	900	111.94	139.43	600.0	547.11	433.24	395.05	0.595	0.429	94.43	1.727	1.099	2.431	1.183
	300 × 150 × 2.1	2	216.64	900	58.01	71.27	600.0	1094.22	433.24	790.10	0.841	0.857	28.84	4.368	1.347	2.726	1.260
	300 × 150 × 1.5	2	216.64	900	41.86	51.23	600.0	1531.91	433.24	1106.14	0.996	1.200	13.87	5.317	1.289	2.529	1.194
	300 × 150 × 1.0	2	216.64	900	28.14	34.33	600.0	2297.87	433.24	1659.21	1.219	1.800	7.02	8.158	1.511	2.877	1.427

Table 4.6 (**Cont'd.**)

Reference – (HF/CF - EXP/FEA)	$2a \times 2b \times t$ (**mm×mm×mm**)	a/b (= r)	E (**GPa**)	$f_{y.mea}$ (**MPa**)	M_e (**kNm**)	M_p (**kNm**)	$D_{CGb.mn}$ (**mm**)	$\frac{D_{CGb.mn}}{t\varepsilon^2}$	$D_{NSb.mn}$ (**mm**)	$\frac{D_{NSb.mn}}{t\varepsilon^2}$	$\bar{\lambda}_{l.b}$	$\bar{\lambda}_{cs}$	M_u (**kNm**)	$\frac{M_u}{M_{AS4100}}$	$\frac{M_u}{M_{AISC360}}$	$\frac{M_u}{M_{EC3}}$	$\frac{M_u}{M_{u.pr}}$
	300 × 150 × 8.7	2	216.64	1800	429.40	550.52	600.0	528.25	433.24	381.43	0.585	0.414	429.19	1.865	1.256	2.792	1.384
	300 × 150 × 4.2	2	216.64	1800	223.89	278.85	600.0	1094.22	433.24	790.10	0.841	0.857	103.60	4.065	1.254	2.537	1.172
	300 × 150 × 2.1	2	216.64	1800	116.01	142.55	600.0	2188.45	433.24	1580.20	1.190	1.714	26.45	6.843	1.309	2.501	1.231
	300 × 150 × 1.5	2	216.64	1800	83.72	102.46	600.0	3063.83	433.24	2212.28	1.408	2.400	14.55	9.562	1.451	2.718	1.420
	326 × 108.67 × 8.7	3	216.64	390.6	69.34	89.02	978.0	186.85	704.42	134.58	0.347	0.146	94.63	1.384	1.215	1.673	1.361
	326 × 108.67 × 4.2	3	216.64	390.6	36.95	45.57	978.0	387.04	704.42	278.77	0.500	0.302	39.69	1.574	1.019	2.292	1.339
	326 × 108.67 × 2.1	3	216.64	390.6	19.34	23.41	978.0	774.08	704.42	557.54	0.707	0.605	14.34	3.327	1.388	2.921	1.342
	326 × 108.67 × 1.5	3	216.64	390.6	13.99	16.85	978.0	1083.71	704.42	780.56	0.836	0.847	7.89	4.842	1.508	3.053	1.410
	326 × 108.67 × 1.0	3	216.64	390.6	9.43	11.30	978.0	1625.56	704.42	1170.84	1.024	1.270	4.24	7.972	1.861	3.632	1.724
	326 × 108.67 × 8.7	3	216.64	700	124.26	159.53	978.0	334.85	704.42	241.18	0.465	0.262	160.04	1.751	1.210	2.439	1.532
	326 × 108.67 × 4.2	3	216.64	700	66.22	81.67	978.0	693.62	704.42	499.59	0.669	0.542	54.69	2.941	1.377	2.941	1.351
	326 × 108.67 × 2.1	3	216.64	700	34.66	41.95	978.0	1387.23	704.42	999.18	0.946	1.084	14.65	5.668	1.474	2.916	1.365
	326 × 108.67 × 1.5	3	216.64	700	25.08	30.19	978.0	1942.13	704.42	1398.85	1.120	1.517	9.61	9.278	1.924	3.707	1.794
	326 × 108.67 × 1.0	3	216.64	700	16.90	20.26	978.0	2913.19	704.42	2098.27	1.371	2.276	5.28	15.608	2.460	4.621	2.389
	326 × 108.67 × 8.7	3	216.64	1150	204.14	262.08	978.0	550.11	704.42	396.23	0.596	0.430	228.70	2.312	1.465	3.237	1.572
	326 × 108.67 × 4.2	3	216.64	1150	108.78	134.17	978.0	1139.51	704.42	820.75	0.858	0.890	59.50	5.152	1.544	3.111	1.440
	326 × 108.67 × 2.1	3	216.64	1150	56.93	68.91	978.0	2279.03	704.42	1641.51	1.213	1.781	17.88	10.080	1.880	3.583	1.774
	326 × 108.67 × 1.5	3	216.64	1150	41.20	49.60	978.0	3190.64	704.42	2298.11	1.435	2.493	10.72	15.364	2.268	4.239	2.234
	346 × 69.2 × 8.7	5	216.64	390.6	43.03	56.78	1730.0	330.52	1273.49	243.30	0.467	0.264	58.74	1.864	1.283	2.604	1.628
	346 × 69.2 × 4.2	5	216.64	390.6	24.07	29.80	1730.0	684.64	1273.49	503.98	0.672	0.547	19.58	2.951	1.369	2.919	1.341
	346 × 69.2 × 2.1	5	216.64	390.6	12.87	15.47	1730.0	1369.28	1273.49	1007.95	0.950	1.093	5.31	5.613	1.451	2.868	1.343
	346 × 69.2 × 1.5	5	216.64	390.6	9.37	11.17	1730.0	1916.99	1273.49	1411.13	1.125	1.531	2.66	6.980	1.439	2.771	1.343
	346 × 69.2 × 1.0	5	216.64	390.6	6.35	7.51	1730.0	2875.48	1273.49	2116.70	1.377	2.296	1.17	9.371	1.468	2.756	1.427
	346 × 69.2 × 8.7	5	216.64	500	55.08	72.69	1730.0	423.09	1273.49	311.44	0.528	0.338	71.55	2.011	1.321	3.043	1.679
	346 × 69.2 × 4.2	5	216.64	500	30.81	38.15	1730.0	876.39	1273.49	645.13	0.760	0.700	22.08	4.300	1.566	3.237	1.489
	346 × 69.2 × 2.1	5	216.64	500	16.48	19.81	1730.0	1752.79	1273.49	1290.26	1.075	1.400	5.68	7.251	1.586	3.074	1.474
	346 × 69.2 × 1.5	5	216.64	500	12.00	14.30	1730.0	2453.90	1273.49	1806.36	1.272	1.959	2.76	8.756	1.531	2.901	1.459
	346 × 69.2 × 1.0	5	216.64	500	8.13	9.62	1730.0	3680.85	1273.49	2709.55	1.558	2.939	1.26	12.546	1.633	3.028	1.658
	346 × 69.2 × 8.7	5	216.64	700	77.12	101.76	1730.0	592.32	1273.49	436.02	0.625	0.473	89.98	3.051	1.686	3.672	1.688
	346 × 69.2 × 4.2	5	216.64	700	43.13	53.41	1730.0	1226.95	1273.49	903.18	0.900	0.980	25.27	6.561	1.832	3.658	1.701
	346 × 69.2 × 2.1	5	216.64	700	23.07	27.73	1730.0	2453.90	1273.49	1806.36	1.272	1.959	6.04	9.967	1.743	3.302	1.660
	346 × 69.2 × 1.5	5	216.64	700	16.80	20.02	1730.0	3435.46	1273.49	2528.91	1.505	2.743	2.98	12.544	1.723	3.206	1.726

Table 4.6 (**Cont'd.**)

Reference – (HF/CF - EXP/FEA)	$2a \times 2b \times t$ (mm×mm×mm)	a/b (= r)	E (GPa)	$f_{y.mea}$ (MPa)	M_e (kNm)	M_p (kNm)	$D_{CGb.mn}$ (mm)	$\frac{D_{CGb.mn}}{t\varepsilon^2}$	$D_{NSb.mn}$ (mm)	$\frac{D_{NSb.mn}}{t\varepsilon^2}$	$\bar{\lambda}_{l.b}$	$\bar{\lambda}_{cs}$	M_u (kNm)	$\frac{M_u}{M_{AS4100}}$	$\frac{M_u}{M_{AISC360}}$	$\frac{M_u}{M_{EC3}}$	$\frac{M_u}{M_{u.pr}}$
Chen and Young (2019)	141 × 87.5 × 3	1.61	208	388	9.33	11.84	227.21	126.74	173.30	96.67	0.300	0.109	12.3	1.202	1.127	1.352	1.213
– (CF - EXP)	141.4 × 87.6 × 2.7	1.61	208	388	8.70	11.01	228.24	138.04	173.99	105.22	0.313	0.119	9.2	0.990	0.916	1.138	0.996
	147.8 × 73 × 2.7	2.02	210	341	6.39	8.02	299.24	160.82	215.68	115.91	0.327	0.130	7.7	1.164	1.057	1.369	1.163
	148.1 × 72.6 × 2.7	2.04	210	341	6.27	7.87	302.12	164.81	217.52	118.66	0.331	0.133	8.3	1.288	1.164	1.525	1.285
	148.4 × 72.7 × 2.7	2.04	210	341	6.42	8.06	302.92	161.60	218.08	116.34	0.328	0.130	8.9	1.339	1.215	1.577	1.338
	148.6 × 72.1 × 2.7	2.06	210	341	6.33	7.94	306.27	164.60	220.21	118.35	0.331	0.132	7.8	1.198	1.084	1.418	1.196
	176.3 × 65.5 × 4.8	2.69	200	418	13.61	17.45	474.53	174.75	338.80	124.77	0.348	0.147	18.95	1.415	1.240	1.712	1.390
	176.7 × 65.1 × 4.8	2.71	200	418	13.54	17.36	479.61	176.63	342.60	126.17	0.350	0.148	15.1	1.139	0.994	1.381	1.117
	150.4 × 52.3 × 5	2.88	205	410	8.94	11.67	432.51	150.92	310.29	108.27	0.320	0.124	13.3	1.414	1.297	1.644	1.418
	150.4 × 51.7 × 5	2.91	205	410	8.79	11.47	437.53	153.28	314.21	110.08	0.323	0.126	10.8	1.175	1.074	1.372	1.177
Chen and Young (2019)	250 × 200 × 20	1.25	208	388	217.99	300.13	312.50	25.80	268.86	22.20	0.144	0.025	321.9	1.160	1.160	1.160	0.947
– (CF - FEA)	250 × 200 × 16	1.25	208	388	184.78	249.67	312.50	32.25	268.86	27.74	0.161	0.031	265.1	1.127	1.127	1.127	0.967
	250 × 200 × 12	1.25	208	388	146.82	194.63	312.50	43.00	268.86	36.99	0.186	0.042	203.4	1.088	1.088	1.088	0.999
	250 × 200 × 8	1.25	208	388	103.67	134.80	312.50	64.49	268.86	55.49	0.228	0.063	137.2	1.050	1.039	1.039	1.054
	250 × 200 × 6.5	1.25	208	388	86.06	111.09	312.50	79.38	268.86	68.29	0.252	0.077	111.7	1.078	1.041	1.019	1.090
	250 × 200 × 6	1.25	208	388	80.01	103.03	312.50	85.99	268.86	73.98	0.263	0.084	103	1.090	1.050	1.287	1.103
	250 × 200 × 5	1.25	208	388	67.64	86.67	312.50	103.19	268.86	88.78	0.288	0.100	85.4	1.122	1.064	1.263	1.135
	250 × 200 × 4	1.25	208	388	54.89	69.99	312.50	128.99	268.86	110.98	0.322	0.125	67.4	1.171	1.071	1.365	1.173
	250 × 200 × 2	1.25	208	388	28.24	35.66	312.50	257.98	268.86	221.95	0.455	0.251	30.2	1.422	1.002	1.958	1.255
	200 × 150 × 16	1.33	208	388	101.98	140.59	266.67	27.52	221.29	22.84	0.146	0.026	149.4	1.151	1.151	1.151	0.945
	200 × 150 × 10	1.33	208	388	71.42	94.83	266.67	44.03	221.29	36.54	0.185	0.041	98.6	1.084	1.084	1.084	0.993
	200 × 150 × 8	1.33	208	388	59.34	77.78	266.67	55.04	221.29	45.67	0.206	0.052	79.8	1.056	1.056	1.056	1.021
	200 × 150 × 6	1.33	208	388	46.21	59.80	266.67	73.38	221.29	60.89	0.238	0.069	60.3	1.056	1.025	1.025	1.064
	200 × 150 × 5.5	1.33	208	388	42.76	55.16	266.67	80.05	221.29	66.43	0.249	0.075	55.3	1.067	1.031	1.016	1.078
	200 × 150 × 3	1.33	208	388	24.45	31.02	266.67	146.76	221.29	121.79	0.337	0.138	29.4	1.186	1.062	1.418	1.179
	200 × 150 × 2.5	1.33	208	388	20.56	26.01	266.67	176.11	221.29	146.14	0.369	0.165	23.9	1.249	1.049	1.551	1.201
	200 × 150 × 2	1.33	208	388	16.60	20.94	266.67	220.14	221.29	182.68	0.413	0.206	18.2	1.316	1.011	1.723	1.211
	300 × 200 × 20	1.50	208	388	257.39	349.67	450.00	37.15	352.96	29.14	0.165	0.033	370.2	1.130	1.130	1.130	0.981
	300 × 200 × 16	1.50	208	388	217.62	290.14	450.00	46.44	352.96	36.42	0.184	0.041	302.9	1.093	1.093	1.093	1.000
	300 × 200 × 12	1.50	208	388	172.48	225.61	450.00	61.91	352.96	48.56	0.213	0.055	231	1.052	1.052	1.052	1.032
	300 × 200 × 8	1.50	208	388	121.48	155.87	450.00	92.87	352.96	72.85	0.261	0.082	155.6	1.080	1.041	1.281	1.093
	300 × 200 × 6	1.50	208	388	93.64	118.99	450.00	123.83	352.96	97.13	0.301	0.110	116.2	1.133	1.062	1.276	1.143
	300 × 200 × 4	1.50	208	388	64.15	80.74	450.00	185.74	352.96	145.69	0.369	0.165	74.9	1.253	1.053	1.554	1.205
	150 × 100 × 12	1.50	208	388	36.53	50.55	225.00	30.96	176.48	24.28	0.151	0.027	52.8	1.135	1.135	1.135	0.945
	150 × 100 × 8	1.50	208	388	27.20	36.27	225.00	46.44	176.48	36.42	0.184	0.041	37.3	1.077	1.077	1.077	0.985

Table 4.6 (**Cont'd.**)

Reference – (HF/CF - EXP/FEA)	$2a \times 2b \times t$ (mm×mm×mm)	a/b (= r)	E (GPa)	$f_{y.mea}$ (MPa)	M_e (kNm)	M_p (kNm)	$D_{CGb.mn}$ (mm)	$\frac{D_{CGb.mn}}{t\varepsilon^2}$	$D_{NSb.mn}$ (mm)	$\frac{D_{NSb.mn}}{t\varepsilon^2}$	$\bar{\lambda}_{l.b}$	$\bar{\lambda}_{cs}$	M_u (kNm)	$\frac{M_u}{M_{AS4100}}$	$\frac{M_u}{M_{AISC360}}$	$\frac{M_u}{M_{EC3}}$	$\frac{M_u}{M_{u.pr}}$
	150 × 100 × 6	1.50	208	388	21.56	28.20	225.00	61.91	176.48	48.56	0.213	0.055	28.6	1.042	1.042	1.042	1.022
	150 × 100 × 4	1.50	208	388	15.19	19.48	225.00	92.87	176.48	72.85	0.261	0.082	19.3	1.072	1.033	1.271	1.085
	150 × 100 × 2.5	1.50	208	388	9.89	12.50	225.00	148.60	176.48	116.55	0.330	0.132	11.9	1.167	1.057	1.380	1.166
	400 × 250 × 25	1.60	208	388	534.13	722.49	640.00	42.27	489.41	32.32	0.174	0.037	763.1	1.122	1.122	1.122	0.998
	400 × 250 × 20	1.60	208	388	451.23	598.97	640.00	52.83	489.41	40.40	0.194	0.046	622.6	1.084	1.084	1.084	1.016
	400 × 250 × 16	1.60	208	388	377.03	492.90	640.00	66.04	489.41	50.50	0.217	0.057	504.3	1.051	1.051	1.051	1.041
	400 × 250 × 12	1.60	208	388	295.30	380.17	640.00	88.06	489.41	67.34	0.251	0.076	381.9	1.070	1.034	1.016	1.082
	400 × 250 × 11.5	1.60	208	388	284.53	365.60	640.00	91.89	489.41	70.26	0.256	0.079	366.3	1.076	1.039	1.287	1.089
	400 × 250 × 11	1.60	208	388	273.63	350.92	640.00	96.06	489.41	73.46	0.262	0.083	350.5	1.082	1.043	1.281	1.096
	400 × 250 × 10.5	1.60	208	388	262.61	336.14	640.00	100.64	489.41	76.96	0.268	0.087	334.7	1.090	1.047	1.275	1.104
	400 × 250 × 10	1.60	208	388	251.46	321.24	640.00	105.67	489.41	80.80	0.275	0.091	318.8	1.098	1.051	1.268	1.112
	400 × 250 × 8	1.60	208	388	205.55	260.57	640.00	132.09	489.41	101.01	0.307	0.114	254	1.142	1.064	1.299	1.151
	400 × 250 × 6	1.60	208	388	157.52	198.14	640.00	176.11	489.41	134.67	0.355	0.152	186	1.221	1.056	1.489	1.192
	400 × 250 × 4	1.60	208	388	107.29	133.92	640.00	264.17	489.41	202.01	0.434	0.228	116.9	1.378	1.013	1.851	1.241
	400 × 250 × 3	1.60	208	388	81.34	101.13	640.00	352.23	489.41	269.35	0.501	0.304	82	1.482	0.956	2.162	1.259
	400 × 250 × 2	1.60	208	388	54.81	67.88	640.00	528.34	489.41	404.02	0.614	0.456	49.3	2.159	1.252	2.742	1.289
	350 × 200 × 20	1.75	208	388	297.91	400.67	612.50	50.56	455.14	37.57	0.187	0.042	417.3	1.100	1.100	1.100	1.014
	350 × 200 × 16	1.75	208	388	251.39	331.78	612.50	63.20	455.14	46.97	0.209	0.053	340	1.062	1.062	1.062	1.034
	350 × 200 × 12	1.75	208	388	198.85	257.47	612.50	84.27	455.14	62.62	0.242	0.071	259.1	1.061	1.025	1.023	1.070
	350 × 200 × 7	1.75	208	388	123.93	156.65	612.50	144.47	455.14	107.35	0.317	0.121	151.9	1.156	1.064	1.335	1.160
	350 × 200 × 5	1.75	208	388	90.89	113.78	612.50	202.26	455.14	150.29	0.375	0.170	105.6	1.265	1.052	1.581	1.211
	350 × 200 × 3.5	1.75	208	388	64.89	80.64	612.50	288.94	455.14	214.70	0.448	0.243	69.7	1.403	1.004	1.915	1.247
	350 × 200 × 2	1.75	208	388	37.82	46.66	612.50	505.64	455.14	375.73	0.592	0.425	34.6	1.828	1.181	2.614	1.278
	210 × 120 × 16	1.75	208	388	78.47	108.85	367.50	37.92	273.08	28.18	0.162	0.032	113.9	1.140	1.140	1.140	0.982
	210 × 120 × 12	1.75	208	388	64.35	86.54	367.50	50.56	273.08	37.57	0.187	0.042	89.2	1.089	1.089	1.089	1.004
	210 × 120 × 10	1.75	208	388	56.06	74.23	367.50	60.68	273.08	45.09	0.205	0.051	75.7	1.061	1.061	1.061	1.022
	210 × 120 × 6	1.75	208	388	36.75	47.14	367.50	101.13	273.08	75.15	0.265	0.085	46.7	1.080	1.039	1.271	1.093
	210 × 120 × 3.5	1.75	208	388	22.65	28.47	367.50	173.36	273.08	128.82	0.347	0.146	27	1.207	1.060	1.458	1.188
	210 × 120 × 2.5	1.75	208	388	16.54	20.62	367.50	242.71	273.08	180.35	0.410	0.204	18.4	1.327	1.025	1.732	1.224
	500 × 250 × 25	2.00	208	388	662.75	884.38	1000.00	66.04	722.06	47.69	0.211	0.054	907.1	1.075	1.075	1.075	1.050
	500 × 250 × 20	2.00	208	388	558.41	731.16	1000.00	82.55	722.06	59.61	0.236	0.067	738.6	1.065	1.039	1.039	1.073
	500 × 250 × 17	2.00	208	388	489.60	633.76	1000.00	97.12	722.06	70.13	0.256	0.079	634.4	1.083	1.045	1.296	1.095
	500 × 250 × 16.5	2.00	208	388	477.66	617.12	1000.00	100.06	722.06	72.25	0.260	0.082	616	1.085	1.047	1.290	1.099
	500 × 250 × 16	2.00	208	388	465.58	600.36	1000.00	103.19	722.06	74.51	0.264	0.084	598.1	1.089	1.049	1.285	1.103
	500 × 250 × 14	2.00	208	388	415.87	532.16	1000.00	117.93	722.06	85.16	0.282	0.096	525.6	1.110	1.058	1.264	1.124
	500 × 250 × 10	2.00	208	388	309.52	390.01	1000.00	165.11	722.06	119.22	0.334	0.135	375.2	1.186	1.068	1.410	1.182

Table 4.6 (**Cont'd.**)

Reference – (HF/CF - EXP/FEA)	$2a \times 2b \times t$ (mm×mm×mm)	a/b (= r)	E (GPa)	$f_{y.mea}$ (MPa)	M_e (kNm)	M_p (kNm)	$D_{CGb.mn}$ (mm)	$\frac{D_{CGb.mn}}{t\varepsilon^2}$	$D_{NSb.mn}$ (mm)	$\frac{D_{NSb.mn}}{t\varepsilon^2}$	$\bar{\lambda}_{l.b}$	$\bar{\lambda}_{cs}$	M_u (kNm)	$\frac{M_u}{M_{AS4100}}$	$\frac{M_u}{M_{AISC360}}$	$\frac{M_u}{M_{EC3}}$	$\frac{M_u}{M_{u.pr}}$
	500 × 250 × 8.5	2.00	208	388	267.17	334.70	1000.0	194.24	722.06	140.26	0.362	0.158	315.8	1.245	1.062	1.532	1.207
	500 × 250 × 6	2.00	208	388	193.48	240.04	1000.0	275.18	722.06	198.70	0.431	0.224	213.3	1.383	1.024	1.849	1.249
	500 × 250 × 4	2.00	208	388	131.64	162.07	1000.0	412.77	722.06	298.04	0.527	0.337	129.7	1.523	0.999	2.302	1.272
	500 × 250 × 3.5	2.00	208	388	115.78	142.26	1000.0	471.73	722.06	340.62	0.564	0.385	109	1.544	1.097	2.468	1.272
	400 × 200 × 20	2.00	208	388	339.33	452.80	800.0	66.04	577.65	47.69	0.211	0.054	463.1	1.072	1.072	1.072	1.047
	400 × 200 × 16	2.00	208	388	285.91	374.35	800.0	82.55	577.65	59.61	0.236	0.067	377.4	1.063	1.037	1.037	1.070
	400 × 200 × 14	2.00	208	388	256.72	332.94	800.0	94.35	577.65	68.12	0.252	0.077	332.9	1.076	1.040	1.018	1.088
	400 × 200 × 13.5	2.00	208	388	249.16	322.36	800.0	97.84	577.65	70.65	0.257	0.080	321.7	1.081	1.043	1.291	1.093
	400 × 200 × 13	2.00	208	388	241.48	311.68	800.0	101.60	577.65	73.36	0.262	0.083	310.3	1.086	1.046	1.285	1.099
	400 × 200 × 12.5	2.00	208	388	233.69	300.91	800.0	105.67	577.65	76.30	0.267	0.086	298.9	1.091	1.049	1.279	1.105
	400 × 200 × 12	2.00	208	388	225.80	290.05	800.0	110.07	577.65	79.48	0.272	0.090	287.4	1.097	1.052	1.273	1.112
	400 × 200 × 10	2.00	208	388	193.07	245.63	800.0	132.09	577.65	95.37	0.298	0.108	240.4	1.130	1.062	1.267	1.141
	400 × 200 × 5.5	2.00	208	388	112.50	140.05	800.0	240.15	577.65	173.41	0.402	0.196	127.7	1.327	1.042	1.715	1.234
	400 × 200 × 4	2.00	208	388	83.40	103.07	800.0	330.21	577.65	238.43	0.472	0.269	87.6	1.450	0.989	2.037	1.261
	400 × 200 × 3	2.00	208	388	63.35	77.91	800.0	440.28	577.65	317.91	0.545	0.359	61.1	1.536	1.045	2.382	1.273
	270 × 120 × 16	2.25	208	388	100.95	138.11	607.5	62.69	433.32	44.71	0.204	0.051	140.4	1.092	1.092	1.092	1.050
	270 × 120 × 12	2.25	208	388	82.40	109.27	607.5	83.59	433.32	59.62	0.236	0.067	109.3	1.068	1.042	1.042	1.076
	270 × 120 × 8	2.25	208	388	59.76	76.77	607.5	125.38	433.32	89.43	0.289	0.101	75.1	1.119	1.061	1.257	1.132
	270 × 120 × 6.5	2.25	208	388	50.11	63.59	607.5	154.31	433.32	110.07	0.321	0.124	61.4	1.165	1.068	1.355	1.168
	270 × 120 × 4.5	2.25	208	388	36.17	45.17	607.5	222.89	433.32	158.99	0.385	0.180	42	1.300	1.057	1.646	1.230
	270 × 120 × 2.5	2.25	208	388	20.95	25.74	607.5	401.21	433.32	286.17	0.517	0.323	20.9	1.512	0.969	2.252	1.271
	270 × 120 × 2	2.25	208	388	16.93	20.72	607.5	501.51	433.32	357.72	0.578	0.404	15.7	1.623	1.137	2.537	1.274
	180 × 80 × 16	2.25	208	388	37.86	55.00	405.0	41.79	288.88	29.81	0.167	0.034	56.4	1.170	1.170	1.170	1.021
	180 × 80 × 12	2.25	208	388	32.25	44.81	405.0	55.72	288.88	39.75	0.193	0.045	45.4	1.106	1.106	1.106	1.033
	180 × 80 × 8	2.25	208	388	24.42	32.37	405.0	83.59	288.88	59.62	0.236	0.067	32.2	1.062	1.036	1.036	1.070
	180 × 80 × 6	2.25	208	388	19.51	25.26	405.0	111.45	288.88	79.49	0.272	0.090	24.8	1.096	1.051	1.271	1.110
	180 × 80 × 3.5	2.25	208	388	12.31	15.47	405.0	191.05	288.88	136.27	0.357	0.154	14.6	1.233	1.062	1.507	1.201
	500 × 200 × 20	2.50	208	388	424.25	559.66	1250.0	103.19	889.91	73.46	0.262	0.083	556.4	1.108	1.068	1.311	1.122
	500 × 200 × 19.5	2.50	208	388	416.22	547.77	1250.0	105.84	889.91	75.35	0.265	0.085	543.8	1.111	1.069	1.307	1.125
	500 × 200 × 19	2.50	208	388	408.08	535.77	1250.0	108.62	889.91	77.33	0.269	0.087	531.2	1.114	1.071	1.302	1.129
	500 × 200 × 18.5	2.50	208	388	399.81	523.67	1250.0	111.56	889.91	79.42	0.272	0.090	518.4	1.118	1.072	1.297	1.132
	500 × 200 × 18	2.50	208	388	391.43	511.46	1250.0	114.66	889.91	81.63	0.276	0.092	505.5	1.121	1.073	1.291	1.136
	500 × 200 × 16	2.50	208	388	356.67	461.60	1250.0	128.99	889.91	91.83	0.293	0.104	453	1.140	1.077	1.270	1.152
	500 × 200 × 12	2.50	208	388	281.05	356.80	1250.0	171.99	889.91	122.44	0.338	0.138	343	1.206	1.079	1.444	1.199
	500 × 200 × 6	2.50	208	388	151.26	186.54	1250.0	343.97	889.91	244.88	0.478	0.277	161.4	1.494	1.006	2.115	1.292
	500 × 200 × 5	2.50	208	388	127.60	156.59	1250.0	412.77	889.91	293.86	0.524	0.332	128.7	1.548	1.007	2.328	1.296

Table 4.6 (**Cont'd.**)

Reference – (HF/CF - EXP/FEA)	$2a \times 2b \times t$ (mm×mm×mm)	a/b (= r)	E (GPa)	$f_{y.mea}$ (MPa)	M_e (kNm)	M_p (kNm)	$D_{CGb.mn}$ (mm)	$\frac{D_{CGb.mn}}{t\varepsilon^2}$	$D_{NSb.mn}$ (mm)	$\frac{D_{NSb.mn}}{t\varepsilon^2}$	$\bar{\lambda}_{l.b}$	$\bar{\lambda}_{cs}$	M_u (kNm)	$\frac{M_u}{M_{AS4100}}$	$\frac{M_u}{M_{AISC360}}$	$\frac{M_u}{M_{EC3}}$	$\frac{M_u}{M_{u.pr}}$
	500 × 200 × 4.5	2.50	208	388	115.54	141.45	1250.00	458.63	889.91	326.51	0.552	0.369	112	1.562	1.080	2.449	1.291
	500 × 200 × 4	2.50	208	388	103.33	126.20	1250.00	515.96	889.91	367.32	0.586	0.415	95.6	1.562	1.166	2.591	1.283
	500 × 200 × 3.5	2.50	208	388	90.96	110.83	1250.00	589.67	889.91	419.80	0.626	0.474	79.3	2.295	1.264	2.750	1.264
	250 × 100 × 16	2.50	208	388	73.05	101.93	625.00	64.49	444.96	45.92	0.207	0.052	102.9	1.106	1.106	1.106	1.071
	250 × 100 × 12	2.50	208	388	60.55	81.40	625.00	85.99	444.96	61.22	0.239	0.069	81	1.084	1.051	1.051	1.092
	250 × 100 × 11	2.50	208	388	56.90	75.78	625.00	93.81	444.96	66.79	0.250	0.075	75.1	1.090	1.054	1.037	1.102
	250 × 100 × 10.5	2.50	208	388	54.99	72.89	625.00	98.28	444.96	69.97	0.256	0.079	72.1	1.095	1.057	1.311	1.108
	250 × 100 × 10	2.50	208	388	53.03	69.96	625.00	103.19	444.96	73.46	0.262	0.083	69	1.100	1.059	1.301	1.113
	250 × 100 × 7	2.50	208	388	39.99	51.26	625.00	147.42	444.96	104.95	0.313	0.119	49.6	1.161	1.074	1.333	1.167
	250 × 100 × 5	2.50	208	388	30.00	37.73	625.00	206.38	444.96	146.93	0.370	0.166	35.6	1.278	1.072	1.589	1.228
	275 × 100 × 16	2.75	208	388	80.69	112.14	756.25	78.04	540.67	55.79	0.228	0.063	111.8	1.101	1.088	1.088	1.105
	275 × 100 × 10	2.75	208	388	58.44	76.76	756.25	124.86	540.67	89.27	0.289	0.101	74.9	1.141	1.082	1.282	1.154
	275 × 100 × 6.5	2.75	208	388	41.37	52.54	756.25	192.09	540.67	137.34	0.358	0.155	49.9	1.259	1.081	1.541	1.224
	275 × 100 × 4.5	2.75	208	388	30.06	37.44	756.25	277.47	540.67	198.37	0.430	0.224	34.1	1.422	1.054	1.900	1.285
	275 × 100 × 3.5	2.75	208	388	23.95	29.54	756.25	356.75	540.67	255.05	0.488	0.288	25.4	1.516	1.003	2.174	1.301
	275 × 100 × 2	2.75	208	388	14.19	17.25	756.25	624.31	540.67	446.34	0.645	0.504	12.1	2.589	1.318	2.844	1.266
	300 × 100 × 16	3.00	208	388	88.40	122.44	900.00	92.87	648.24	66.89	0.250	0.076	120.8	1.129	1.091	1.073	1.141
	300 × 100 × 12	3.00	208	388	73.06	97.46	900.00	123.83	648.24	89.19	0.289	0.101	94.9	1.156	1.096	1.299	1.169
	300 × 100 × 7	3.00	208	388	48.07	61.12	900.00	212.28	648.24	152.90	0.378	0.173	57.5	1.313	1.085	1.648	1.252
	300 × 100 × 6	3.00	208	388	42.20	53.14	900.00	247.66	648.24	178.38	0.408	0.202	49.3	1.386	1.075	1.803	1.281
	300 × 100 × 5	3.00	208	388	36.02	44.91	900.00	297.19	648.24	214.06	0.447	0.242	40.7	1.474	1.056	2.009	1.311
	300 × 100 × 4	3.00	208	388	29.51	36.44	900.00	371.49	648.24	267.57	0.500	0.302	31.4	1.559	1.009	2.270	1.326
	150 × 50 × 10	3.00	208	388	12.53	18.00	450.00	74.30	324.12	53.51	0.223	0.060	17.6	1.107	1.103	1.103	1.109
	150 × 50 × 8	3.00	208	388	11.05	15.30	450.00	92.87	324.12	66.89	0.250	0.076	14.9	1.114	1.077	1.059	1.126
	150 × 50 × 6	3.00	208	388	9.13	12.18	450.00	123.83	324.12	89.19	0.289	0.101	11.7	1.140	1.081	1.281	1.153
	150 × 50 × 4	3.00	208	388	6.71	8.61	450.00	185.74	324.12	133.79	0.353	0.151	8.1	1.245	1.080	1.516	1.217
	325 × 100 × 16	3.25	208	388	96.18	132.82	1056.25	109.00	767.37	79.19	0.272	0.089	129.9	1.163	1.116	1.351	1.178
	325 × 100 × 14	3.25	208	388	88.30	119.68	1056.25	124.57	767.37	90.50	0.291	0.102	116.2	1.176	1.113	1.316	1.189
	325 × 100 × 10	3.25	208	388	69.41	90.55	1056.25	174.39	767.37	126.70	0.344	0.143	86.3	1.250	1.104	1.504	1.233
	325 × 100 × 6.5	3.25	208	388	49.02	61.82	1056.25	268.30	767.37	194.92	0.427	0.220	57	1.444	1.078	1.921	1.310
	325 × 100 × 5.5	3.25	208	388	42.47	53.04	1056.25	317.08	767.37	230.36	0.464	0.260	47.7	1.522	1.055	2.118	1.333
	325 × 100 × 2.5	3.25	208	388	20.71	25.12	1056.25	697.57	767.37	506.79	0.688	0.573	16.8	3.249	1.433	3.038	1.396
	325 × 100 × 2	3.25	208	388	16.76	20.23	1056.25	871.97	767.37	633.49	0.769	0.716	11.9	4.448	1.588	3.276	1.507
	350 × 100 × 16	3.50	208	388	104.00	143.27	1225.00	126.41	897.47	92.61	0.294	0.105	138.7	1.200	1.132	1.336	1.213
	350 × 100 × 12	3.50	208	388	85.79	113.78	1225.00	168.55	897.47	123.48	0.339	0.140	108.5	1.253	1.119	1.505	1.245
	350 × 100 × 8	3.50	208	388	62.85	80.21	1225.00	252.82	897.47	185.22	0.416	0.209	74.4	1.431	1.093	1.880	1.313
	350 × 100 × 6.5	3.50	208	388	52.89	66.52	1225.00	311.16	897.47	227.97	0.461	0.258	60.2	1.534	1.068	2.129	1.347
	350 × 100 × 6	3.50	208	388	49.40	61.82	1225.00	337.09	897.47	246.96	0.480	0.279	55.2	1.571	1.054	2.231	1.357
	350 × 100 × 3.5	3.50	208	388	30.54	37.30	1225.00	577.87	897.47	423.37	0.629	0.478	27.7	2.436	1.326	2.883	1.325

Table 4.7 *Reliability index of the cross-sectional resistance prediction curves for CHSs and EHSs under bending*

	$\frac{M_u}{M_{AS4100}}$	$\frac{M_u}{M_{AISC360}}$	$\frac{M_u}{M_{EC3}}$	$\frac{M_u}{M_{u.pr}}$
Mean, P_m	2.1659	1.1827	1.6931	1.2239
COV, V_P	1.2661	0.2072	0.4436	0.1861
Reliability index, β	1.0812	2.497	2.2779	2.7217

CHAPTER 5

ELLIPTICAL-HOLLOW-SECTIONS UNDER COMBINED AXIAL COMPRESSION AND BENDING

The plastic interaction response and cross-section classification criteria for the EHSs under combined axial-compression and bending (uni-/bi-axial) are investigated in this chapter. Firstly, the development of plastic interaction criteria for steel EHSs with various cross-sectional aspect ratios subjected to combined axial compression and bending is undertaken. Following the analytical work, expressions for the equivalent CHS diameter of stocky EHSs are derived using the plastic-interaction stress-block analyses performed herein this chapter and the equivalent CHS diameter expressions based on ERCM proposed in Chapters 3 and 4. Lastly, the derived plastic-interaction relations and the equivalent CHS diameter expressions are utilised to assess the experimental data available from the relevant literature.

5.1 PLASTIC LIMIT STATE INTERACTION CRITERIA

To take advantage of the plastically reserved strength of the stocky EHS under the interaction of combined axial-compression and uni/bi-axial bending moments, *or* address the local instability, the knowledge of cross-sectional stress-block pattern in the plastic limit state at susceptible failure location is an essential requisite (Charalampakis 2011, Baptista 2012a). As the interest in the in-elastic response of steel structural sections under a combination of different loading–histories is relatively recent, the pertinent literature (Trahair 2004, Belingardi and Peroni 2007, Nowzartash and Mohareb 2009, Chan et al. 2010a, Charalampakis 2011, Gardner et al. 2011, Baptista 2012b, 2012a) is limited to date. With the steady escalation in the usage of EHSs in an extensive range of infrastructure projects as discussed in Section 1.1.2, the development of plastic interaction criteria for steel EHSs subjected to combinations of combined axial compression and uni/bi-axial bending moments is necessitated.

Under combined axial compression and bending, the Plastic-Neutral-Axis (PNA) of the cross-section shift relative to the position under bending load alone (Gardner et al. 2011, Baptista 2012a, 2012b). The geometric profile of an EHS complicates the process of determining this shift, particularly in the case of plastic stress distribution under the interaction of the loads applied. Under bi-axial bending, the PNA of the cross-section orients its direction according to the magnitude of the resolved moments along the cross-sectional principal axes. Assuming that the material in the entire cross-section yields either in tension *or* compression, the PNA is defined by the axis located between the fibres yielding in compression and those yielding in tension. The following are the other assumptions made for the derivation of the PNA location and interaction criteria, while the basic formulae for calibrating the cross-sectional geometric and strength properties of EHSs are already provided in Section 2.2.1.

- The cross-sectional geometrical profile is assumed to remain undistorted under the action of internal forces induced. This assumption is substantive for EHS with lower diameter to thickness ratios, where the cross-sectional ovalisation/distortion is trivial (Nowzartash and Mohareb 2009). In such sections, the full plastic resistance capacity can conventionally be attained, or nearly attained, before the occurrence of local buckling.

- The distribution of the cross-sectional longitudinal strains (associated with its normal stresses) is based on the classical Bernoulli hypothesis that, after deformation, the cross-

sections remain plane and normal to the longitudinal axis of the structural element, *e.g.*, Baptista (2012a).

- The material is assumed to yield following the maximum distortional energy density yield criterion (Boresi et al. 1993), *e.g.*, Nowzartash and Mohareb (2009).

- Shear stresses due to bending are supposed to be very small and they are not taken into account.

In the following sub-sections (5.1.1 and 5.1.2), the PNA location parameters have been derived by adopting a similar methodology of Gardner et al. (2011), considering appropriate transformation between parametric and Polar coordinate systems for the angles measured and the relevant formulae; and opting of consistent reference axis system for the angles measured.

5.1.1 Axial Compression plus Major Axis Bending

An approximate method for determining the PNA position and plastic interaction relationship for the EHS under axial compression plus major axis bending is described in this sub-section with-reference-to Figure 5.1. When a compressive axial force N_h is applied on an EHS subjected to major axis bending such that $\frac{N_h}{N_y} \leq 1$, the compression zone of the cross-section increases thereby shifting the PNA to a new location as shown in Figure 5.1. As shown in Figures 5.1b and 5.1c, *h* is assumed as the PNA shift from the minor axis due to N_h. Ω_h is the central Polar angle for each element with ψ_h as the respective parametric angle of Ω_h. Both, Ω_h and ψ_h are measured in the counter-clockwise direction with-respect-to the major axis diameter as indicated. The plastic limit state stress distribution along the cross-section shown in Figure 5.1a can be split into two parts, one due to major axis bending as in Figure 5.1b and the other due to the axial compressive load as in Figure 5.1c.

From Figure 5.1c, the area of cross-section effective under N_h is expressed as in Equation 5.1 and thereby N_h can be evaluated by using Equation 5.2.

$$A_{cmp.h} = 4a_m t \int_{\psi_h}^{\frac{\pi}{2}} \sqrt{\sin^2\psi + \frac{b_m^2}{a_m^2}\cos^2\psi} \cdot d\psi \tag{5.1}$$

$$N_h = 4a_m t f_{y.mea} \int_{\psi_h}^{\frac{\pi}{2}} \sqrt{\sin^2\psi + \frac{b_m^2}{a_m^2}\cos^2\psi} \cdot d\psi \tag{5.2}$$

For determining the PNA shift *h* from the minor axis due to N_h as illustrated in Figure 5.1, N_h is normalised as follows:

$$n_h = \frac{N_h}{4a_m t f_{y.mea}} \tag{5.3}$$

Therefore, the following Equation 5.4 is obtained from Equations 5.2 and 5.3.

$$n_h = \int_{\psi_h}^{\frac{\pi}{2}} \sqrt{\sin^2\psi + \frac{b_m^2}{a_m^2}\cos^2\psi} \cdot d\psi \tag{5.4}$$

The above integral in Equation 5.4 is evaluated for a ψ_h range of 0 to $\frac{\pi}{2}$ by substituting the respective $\frac{b_m^2}{a_m^2}$ from Equation 2.5 for a range of *r* (= a/b) values between 1 and 3.5. The resulting normalized relationships between n_h and ψ_h is approximately represented by a simple function as expressed in the following Equation 5.5.

$$\psi_h = \begin{cases} \psi_{h1}n_h^4 + \psi_{h2}n_h^3 + \psi_{h3}n_h^2 + \psi_{h4}n_h + \psi_{h5} & \text{if} \quad \left(\psi_{h1}n_h^4 + \psi_{h2}n_h^3 + \psi_{h3}n_h^2 + \psi_{h4}n_h + \psi_{h5}\right) \le \frac{\pi}{2} \\ \pi - \left(\psi_{h1}n_h^4 + \psi_{h2}n_h^3 + \psi_{h3}n_h^2 + \psi_{h4}n_h + \psi_{h5}\right) & \text{if} \quad \left(\psi_{h1}n_h^4 + \psi_{h2}n_h^3 + \psi_{h3}n_h^2 + \psi_{h4}n_h + \psi_{h5}\right) > \frac{\pi}{2} \end{cases} \tag{5.5}$$

where the respective expressions for ψ_{h1}, ψ_{h2}, ψ_{h3}, ψ_{h4} and ψ_{h5} are estimated by the non-linear regression fitting for a range of r (= a/b) values between 1 and 3.5 and are given in Equations 5.6–5.10 as follows:

$$\psi_{h1} = -0.0725r^5 + 0.8051r^4 - 3.224r^3 + 5.3059r^2 - 3.4583r + 0.6437 \tag{5.6}$$

$$\psi_{h2} = 0.1534r^5 - 1.7189r^4 + 7.0098r^3 - 12.034r^2 + 8.2626r - 1.673 \tag{5.7}$$

$$\psi_{h3} = -0.0944r^5 + 1.0669r^4 - 4.4291r^3 + 7.9469r^2 - 6.0522r + 1.5619 \tag{5.8}$$

$$\psi_{h4} = 0.017r^5 - 0.1913r^4 + 0.7888r^3 - 1.4034r^2 + 1.0479r - 1.2591 \tag{5.9}$$

$$\psi_{h5} = -0.00003r^4 + 0.0012r^3 - 0.0077r^2 + 0.0154r + 1.562 \tag{5.10}$$

From Figures 5.1b and 5.1c, the PNA shift h from the minor axis is expressed in both the parametric and Polar forms as follows:

$$h = a \cdot \cos\psi_h = k_h \cdot \cos\Omega_h \tag{5.11}$$

where k_h is the respective radial distance expressed in the following Equation 5.12 based on Equation 2.2.

$$k_h = \sqrt{a^2\cos^2\psi_h + b^2\sin^2\psi_h} = \frac{ab}{\sqrt{a^2\sin^2\Omega_h + b^2\cos^2\Omega_h}} \tag{5.12}$$

From Figures 5.1a and 5.1b and Equation 5.11, the distance from the extreme compressive fibre to PNA of the cross-section can be expressed as follows:

$$c_{PNA} = (a - h) + 2h = a + h = a \cdot (1 + \cos\psi_h) \tag{5.13}$$

The proportion of the cross-sectional depth in compression, α_{mj} is therefore given by

$$\alpha_{mj} = \frac{c_{PNA}}{2a} = \frac{1 + \cos\psi_h}{2} \tag{5.14}$$

From Figure 5.1b, the plastic state limiting moment acting about the minor axis can be represented as follows:

$$M_{lpy} = 4a_m^2 t f_{y.mea} \int_0^{\psi_h} \cos\psi \sqrt{\sin^2\psi + \frac{b_m^2}{a_m^2}\cos^2\psi} \cdot d\psi \tag{5.15}$$

In the following Equations 5.16 and 5.17, N_h from Equation 5.2 is normalised with N_y using Equation 2.18, while M_{lpy} from Equation 5.15 is normalised with M_{py} using Equation 2.15.

$$\frac{N_h}{N_y} = \frac{\int_{\psi_h}^{\frac{\pi}{2}} \sqrt{\sin^2\psi + \frac{b_m^2}{a_m^2}\cos^2\psi} \cdot d\psi}{\int_0^{\frac{\pi}{2}} \sqrt{\sin^2\psi + \frac{b_m^2}{a_m^2}\cos^2\psi} \cdot d\psi} \tag{5.16}$$

$$\frac{M_{lpy}}{M_{py}} = \frac{\int_0^{\psi_h} \cos\psi \sqrt{\sin^2\psi + \frac{b_m^2}{a_m^2}\cos^2\psi} \cdot d\psi}{\int_0^{\frac{\pi}{2}} \cos\psi \sqrt{\sin^2\psi + \frac{b_m^2}{a_m^2}\cos^2\psi} \cdot d\psi} \tag{5.17}$$

By substituting the respective $\frac{b_m^2}{a_m^2}$ from Equation 2.5 and varying ψ_h values from 0 to $\frac{\pi}{2}$ in Equations 5.16 and 5.17, the plastic interaction curve equation is obtained as follows:

$$\left(\frac{|N_h|}{N_y}\right)^{n_{ry}} + \left(\frac{|M_{lpy}|}{M_{py}}\right)^{m_{ry}} = 1.0 \tag{5.18}$$

where the following respective Equations 5.19 and 5.20 for n_{ry} and m_{ry} are estimated by non-linear regression fitting for a range of r (= a/b) values between 1 and 3.5.

$$n_{ry} = \frac{2.071 - 5.4664r + 3.5057r^2}{1 - 2.6857r + 1.7428r^2} \tag{5.19}$$

$$m_{ry} = \frac{0.8901 - 0.8049r + 0.4967r^2}{1 - 0.8517r + 0.5062r^2} \tag{5.20}$$

Considering the ovalisation of EHSs under bending, the plastic interaction curve Equation 5.18 is further modified in Equation 5.21 for the moment, M_{dy} to be designed for along with N_h.

$$\left(\frac{|N_h|}{N_y}\right)^{n_{ry}} + \left(\frac{|M_{dy}|}{0.95M_{py}}\right)^{m_{ry}} = 1.0 \tag{5.21}$$

5.1.2 Axial Compression plus Minor Axis Bending

The same approach can be followed during the determination of the PNA position and plastic interaction relationship for the EHS under axial compression plus minor axis bending scenario with-reference-to Figure 5.2. When a compressive axial force N_n is applied on an EHS subjected to minor axis bending such that $\frac{N_n}{N_y} \leq 1$, the compression zone of the section increases thereby shifting the PNA to a new location as shown in Figure 5.2. As shown in Figures 5.2b and 5.2c, h_{mn} is assumed as the PNA shift from the major axis due to N_n. Ω_n is the central Polar angle for each element with ψ_n as the respective parametric angle of Ω_n. Both, Ω_n and ψ_n are measured in the counter-clockwise direction with-respect-to the major axis diameter as indicated. The plastic limit state stress distribution along the cross-section shown in Figure 5.2a can be split into two parts, one due to bending as in Figure 5.2b and the other due to the axial compressive load as in Figure 5.2c.

From Figure 5.2c, the area of cross-section under N_n is expressed as in Equation 5.22 and thereby N_n can be evaluated by using Equation 5.23.

$$A_{cmp.n} = 4a_m t \int_0^{\psi_n} \sqrt{\sin^2\psi + \frac{b_m^2}{a_m^2}\cos^2\psi} \cdot d\psi \tag{5.22}$$

$$N_n = 4a_m t f_{y.mea} \int_0^{\psi_n} \sqrt{\sin^2\psi + \frac{b_m^2}{a_m^2}\cos^2\psi} \cdot d\psi \tag{5.23}$$

For determining the PNA shift h_{mn} from the major axis due to N_n as illustrated in Figure 5.2, N_n is normalised as follows:

$$n_n = \frac{N_n}{4a_m t f_{y.mea}} \tag{5.24}$$

Therefore, the following Equation 5.25 is obtained from Equations 5.23 and 5.24.

$$n_n = \int_0^{\psi_n} \sqrt{\sin^2\psi + \frac{b_m^2}{a_m^2}\cos^2\psi} \cdot d\psi \tag{5.25}$$

The above integral is evaluated for a ψ_n range of 0 to $\frac{\pi}{2}$ by substituting the respective $\frac{b_m^2}{a_m^2}$ from Equation 2.5 for a range of r (= a/b) values between 1 and 3.5. The resulting normalised relationships between n_n and ψ_n may be approximately represented by a simple function as expressed in the following Equation 5.26.

$$\psi_n = \begin{cases} \psi_{n1}n_n^4 + \psi_{n2}n_n^3 + \psi_{n3}n_n^2 + \psi_{n4}n_n + \psi_{n5} & \text{if} \quad \left(\psi_{n1}n_n^4 + \psi_{n2}n_n^3 + \psi_{n3}n_n^2 + \psi_{n4}n_n + \psi_{n5}\right) \le \frac{\pi}{2} \\ \pi - \left(\psi_{n1}n_n^4 + \psi_{n2}n_n^3 + \psi_{n3}n_n^2 + \psi_{n4}n_n + \psi_{n5}\right) & \text{if} \quad \left(\psi_{n1}n_n^4 + \psi_{n2}n_n^3 + \psi_{n3}n_n^2 + \psi_{n4}n_n + \psi_{n5}\right) > \frac{\pi}{2} \end{cases} \tag{5.26}$$

where the respective expressions for ψ_{n1}, ψ_{n2}, ψ_{n3}, ψ_{n4} and ψ_{n5} are estimated by non-linear regression fitting for a range of r (= a/b) values between 1 and 4 and are given in the following Equations 5.27–5.31.

$$\psi_{n1} = -0.0616r^5 + 0.6799r^4 - 2.6711r^3 + 4.1432r^2 - 2.3042r + 0.2137 \quad (5.27)$$

$$\psi_{n2} = 0.0681r^5 - 0.5982r^4 + 1.2058r^3 + 2.5202r^2 - 8.0062r + 4.8104 \quad (5.28)$$

$$\psi_{n3} = 0.0672r^5 - 1.0356r^4 + 6.2992r^3 - 18.4r^2 + 22.774r - 9.7045 \quad (5.29)$$

$$\psi_{n4} = -0.0728r^5 + 0.9249r^4 - 4.5662r^3 + 10.624r^2 - 10.206r + 4.2958 \quad (5.30)$$

$$\psi_{n5} = -0.0012r^4 + 0.0103r^3 - 0.0267r^2 + 0.0249r - 0.0072 \quad (5.31)$$

From Figures 5.2b and 5.2c, the PNA shift h_{mn} from the major axis is expressed in both the parametric and Polar forms as follows:

$$h_{mn} = b \cdot \sin\psi_n = k_n \cdot \sin\Omega_n \quad (5.32)$$

where k_n is the respective radial distance expressed in the following Equation 5.33 based on Equation 2.2.

$$k_n = \sqrt{a^2\cos^2\psi_n + b^2\sin^2\psi_n} = \frac{ab}{\sqrt{a^2\sin^2\Omega_n + b^2\cos^2\Omega_n}} \quad (5.33)$$

From Figures 5.2a and 5.2b and Equation 5.32, the distance from the extreme compressive fibre to the PNA of the cross-section can be expressed as follows:

$$d_{PNA} = (b - h_{mn}) + 2h_{mn} = b + h_{mn} = b \cdot (1 + \sin\psi_n) \quad (5.34)$$

The proportion of the cross-sectional depth in compression, α_{mn} is therefore given by

$$\alpha_{mn} = \frac{d_{PNA}}{2b} = \frac{1 + \sin\psi_n}{2} \quad (5.35)$$

From Figure 5.2b, the plastic state limiting moment acting about the major axis can be represented as per the following equation.

$$M_{lpz} = 4a_m b_m t f_{y.mea} \int_{\psi_n}^{\frac{\pi}{2}} \sin\psi \sqrt{\sin^2\psi + \frac{b_m^2}{a_m^2}\cos^2\psi} \cdot d\psi \tag{5.36}$$

In the following Equations 5.37 and 5.38, N_n from Equation 5.23 is normalized with N_y using Equation 2.18, while M_{lpz} from Equation 5.36 is normalized with M_{pz} using Equation 2.17.

$$\frac{N_n}{N_y} = \frac{\int_0^{\psi_n} \sqrt{\sin^2\psi + \frac{b_m^2}{a_m^2}\cos^2\psi} \cdot d\psi}{\int_0^{\frac{\pi}{2}} \sqrt{\sin^2\psi + \frac{b_m^2}{a_m^2}\cos^2\psi} \cdot d\psi} \tag{5.37}$$

$$\frac{M_{lpz}}{M_{pz}} = \frac{\int_{\psi_n}^{\frac{\pi}{2}} \sin\psi \sqrt{\sin^2\psi + \frac{b_m^2}{a_m^2}\cos^2\psi} \cdot d\psi}{\int_0^{\frac{\pi}{2}} \sin\psi \sqrt{\sin^2\psi + \frac{b_m^2}{a_m^2}\cos^2\psi} \cdot d\psi} \tag{5.38}$$

By substituting the respective $\frac{b_m^2}{a_m^2}$ from Equation 2.5 and varying ψ_n values from 0 to $\frac{\pi}{2}$ in Equations 5.37 and 5.38, the plastic interaction curve equation is obtained as follows:

$$\left(\frac{|N_n|}{N_y}\right)^{n_{rz}} + \left(\frac{|M_{lpz}|}{M_{pz}}\right)^{m_{rz}} = 1.0 \tag{5.39}$$

where the following respective Equations 5.40 and 5.41 for n_{rz} and m_{rz} are estimated by non-linear regression fitting for a range of r (= a/b) values between 1 and 3.5.

$$n_{rz} = 0.0305r^2 - 0.2702r + 2.1726 \tag{5.40}$$

$$m_{rz} = 0.0046r^4 - 0.0533r^3 + 0.2271r^2 - 0.4027r + 1.1143 \quad (5.41)$$

Considering the ovalisation of EHSs under bending, the plastic interaction curve Equation 5.39 is further modified in Equation 5.42 for the moment, M_{dz} to be designed for along with N_n.

$$\left(\frac{|N_n|}{N_y}\right)^{n_{rz}} + \left(\frac{|M_{dz}|}{0.95M_{pz}}\right)^{m_{rz}} = 1.0 \quad (5.42)$$

5.1.3 Bi-axial (Oblique) Bending

When dissymmetric sections like RHS, CHS and EHSs are subjected to pure uni-/bi-axial elastic/elastic-plastic/plastic bending, half of the cross-sectional area will be in tension, while the other half will be in compression (Nowzartash and Mohareb 2009). The technique for determining the plastic interaction relation and PNA orientation for the EHS under pure bi-axial plastic bending is described in this sub-section, with-reference-to Figure 5.3. For an EHS under pure bi-axial (oblique) bending at governing plastic limit condition, the PNA orientation depends on the respective resulting normal components of the applied bending moment loads reduced along the two principal axes with sign conventions assumed herein to be following the right-hand-rule.

$M_{lpz.r}$ and $M_{lpy.r}$ are the resulting normal components of the plastic state limiting moments reduced along the two principal axes just enough to affect the cross-section in reaching the governing plastic limit condition based on the applied loads, *i.e.*, the material along the entire cross-section has just reached the yield limit either in tension *or* compression portion. The plastic limit stress distribution along the cross-section can be split into two equal parts, one due to tensile stress and the other due to compressive stress. It is illustrated in Figure 5.3 that the PNA passes through the centre $\mathrm{O}(0,0)$ and oriented with an inclination angle γ with-respect-to the major axis *z*–*z*. The slope of PNA is the ratio of respective resulting bending curvatures $\kappa_{lpy.r}$ and $\kappa_{lpz.r}$ about the principal axes due to $M_{lpy.r}$ and $M_{lpz.r}$, and is given as follows (Baptista 2012a, Charif et al. 2014, Wang et al. 2018b):

$$\tan\gamma = \frac{\kappa_{lpy.r}}{\kappa_{lpz.r}} = \frac{\left(\frac{M_{lpy.r}}{EI_y}\right)}{\left(\frac{M_{lpz.r}}{EI_z}\right)} = \left(\frac{M_{lpy.r}}{M_{lpz.r}}\right)\cdot\left(\frac{I_z}{I_y}\right) \tag{5.43}$$

It is shown in Figure 5.3 that the tangents at the extreme fibre in tension and compression zones contact the mid-surface (*or* median) profile of the cross-section at $T_1(i, j)$ and $T_2(-i, -j)$, respectively. From the fundamentals of the Cartesian co-ordinate geometry, the slope of the tangents at $T_1(i, j)$ and $T_2(-i, -j)$ is expressed in the following Equation 5.44 based on the first-order derivative of the expression in Equation 2.4.

$$\frac{dy}{dz}_{(i,j)} = \frac{dy}{dz}_{(-i,-j)} = -\frac{b_m^2}{a_m^2}\cdot\frac{i}{j} \tag{5.44}$$

As the tangents at $T_1(i, j)$ and $T_2(-i, -j)$ are parallel to PNA, their slope is equal to the slope of PNA and thus the following Equation 5.45 is obtained from Equations 5.43 and 5.44.

$$\tan\gamma = \left(\frac{M_{lpy.r}}{M_{lpz.r}}\right)\cdot\left(\frac{I_z}{I_y}\right) = -\frac{b_m^2}{a_m^2}\cdot\frac{i}{j} \tag{5.45}$$

It is shown in Figure 5.3 that the chord $\overline{T_1T_2}$ is inclined at an angle θ_t at the centre $O(0,0)$ with-respect-to the major axis *z*–*z*. From the fundamentals of the Cartesian co-ordinate geometry, the slope of the chord $\overline{T_1T_2}$ can be obtained according to the following equation.

$$\tan\theta_t = \frac{j}{i} \tag{5.46}$$

where θ_t can be determined by eliminating $\frac{j}{i}$ from Equations 5.45 and 5.46 as follows:

$$\theta_t = \arctan\left(-\frac{b_m^2}{a_m^2}\cdot\cot\gamma\right) = \arctan\left(-\frac{b_m^2}{a_m^2}\cdot\frac{M_{lpz.r}}{M_{lpy.r}}\cdot\frac{I_y}{I_z}\right) \tag{5.47}$$

Based on Equation 2.2, the radial distance k_t in Figure 5.3 which is equal to half the length of the chord $\overline{T_1T_2}$ is as follows:

$$\overline{OT_1} = \overline{OT_2} = k_t = \frac{a_m b_m}{\sqrt{a_m^2 \sin^2\theta_t + b_m^2 \cos^2\theta_t}} \tag{5.48}$$

From Figure 5.3, the vertical depth D_{bi} of the cross-section under tension *or* compression can be obtained by the following Equation 5.49.

$$D_{bi} = k_t \cdot \cos\theta_b = \frac{a_m b_m \cos\theta_b}{\sqrt{a_m^2 \sin^2\theta_t + b_m^2 \cos^2\theta_t}} \tag{5.49}$$

where θ_b is the intersection angle of D_{bi} and $\overline{OT_1}$ at the centre $\mathrm{O}(0,0)$ and can be obtained as follows from Figure 5.3:

$$\theta_b = \frac{\pi}{2} - \theta_t + \gamma \tag{5.50}$$

From Figure 5.3, it should be noted that the central Polar angles θ_b and θ_t are measured in the counter-clockwise direction. While the PNA angle γ which is also a central Polar angle measured in the clockwise direction with-respect-to major axis *z–z*.

For obtaining the plastic interactive equation, the corresponding parametric angle of the PNA angle γ can be estimated according to the following Equation 5.51 based on Equations 2.2 and 2.3.

$$\psi_{bi} = \sin^{-1}\left(\frac{a_m \cdot \sin\gamma}{\sqrt{a_m^2 \sin^2\gamma + b_m^2 \cos^2\gamma}}\right) \tag{5.51}$$

From Figure 5.3, the component of plastic state limiting moment about the minor axis *y–y* can be expressed as follows:

$$M_{lpy.r} = 2a_m^2 t f_{y.mea} \int_{2\pi-\psi_{bi}}^{\pi-\psi_{bi}} \cos\psi \sqrt{\sin^2\psi + \frac{b_m^2}{a_m^2}\cos^2\psi} \cdot d\psi \tag{5.52}$$

Similarly, the component of plastic state limiting moment about the major axis *z–z* in Figure 5.3 can be expressed as follows:

$$M_{lpz.r} = 2a_m b_m t f_{y.mea} \int_{2\pi-\psi_{bi}}^{\pi-\psi_{bi}} \sin\psi \sqrt{\sin^2\psi + \frac{b_m^2}{a_m^2}\cos^2\psi} \cdot d\psi \tag{5.53}$$

Without losing the generality of the formulation, Equations 5.52 and 5.53 are rewritten in the following Equations 5.54 and 5.55.

$$M_{lpy.r} = 4a_m^2 t f_{y.mea} \int_{0}^{\psi_{bi}} \cos\psi \sqrt{\sin^2\psi + \frac{b_m^2}{a_m^2}\cos^2\psi} \cdot d\psi \tag{5.54}$$

$$M_{lpz.r} = 4a_m b_m t f_{y.mea} \int_{\psi_{bi}}^{\frac{\pi}{2}} \sin\psi \sqrt{\sin^2\psi + \frac{b_m^2}{a_m^2}\cos^2\psi} \cdot d\psi \tag{5.55}$$

Using Equations 2.15 and 5.54, $M_{lpy.r}$ is normalised with M_{py} in Equation 5.56. While $M_{lpz.r}$ is normalised with M_{pz} in Equation 5.57 using Equations 2.17 and 5.55.

$$\frac{M_{lpy.r}}{M_{py}} = \frac{\int_{0}^{\psi_{bi}} \cos\psi \sqrt{\sin^2\psi + \frac{b_m^2}{a_m^2}\cos^2\psi} \cdot d\psi}{\int_{0}^{\frac{\pi}{2}} \cos\psi \sqrt{\sin^2\psi + \frac{b_m^2}{a_m^2}\cos^2\psi} \cdot d\psi} \tag{5.56}$$

$$\frac{M_{lpz.r}}{M_{pz}} = \frac{\int_{\psi_{bi}}^{\frac{\pi}{2}} \sin\psi \sqrt{\sin^2\psi + \frac{b_m^2}{a_m^2}\cos^2\psi} \cdot d\psi}{\int_{0}^{\frac{\pi}{2}} \sin\psi \sqrt{\sin^2\psi + \frac{b_m^2}{a_m^2}\cos^2\psi} \cdot d\psi} \tag{5.57}$$

The following plastic interaction curve Equation 5.58 is obtained by substituting the respective $\frac{b_m^2}{a_m^2}$ values from Equation 2.5 and varying ψ_{bi} values from 0 to $\frac{\pi}{2}$ in Equations 5.56 and 5.57.

$$\left(\frac{\left|M_{lpy.r}\right|}{M_{py}}\right)^2+\left(\frac{\left|M_{lpz.r}\right|}{M_{pz}}\right)^{z_r}=1.0 \tag{5.58}$$

where the following Equation 5.59 for z_r is estimated by non-linear regression fitting for a range of $r\left(=a/b\right)$ values between 1 and 3.5.

$$z_r=\frac{1.9093-1.5962r+0.7155r^2}{1-0.8855r+0.4r^2} \tag{5.59}$$

Considering the ovalisation of EHSs under bending, the interaction curve Equation 5.58 is further modified in the following Equation 5.60 for the respective moments $M_{dy.r}$ and $M_{dz.r}$ to be designed for along *y*–*y* and *z*–*z* axes.

$$\left(\frac{\left|M_{dy.r}\right|}{0.95M_{py}}\right)^2+\left(\frac{\left|M_{dz.r}\right|}{0.95M_{pz}}\right)^{z_r}=1.0 \tag{5.60}$$

5.1.4 Axial Compression plus Bi-axial Bending

The determination of the PNA position and interactive relationship for the EHS under bi-axial plastic bending with axial compression is described in this sub-section with-reference-to Figure 5.4. Similar to the case of an EHS under bi-axial bending, the PNA orientation at the governing plastic limit depends on the respective resulting normal components of the applied bending moment loads reduced along the two principal axes with sign conventions assumed to be following the right-hand-rule as shown in Figure 5.4. Additionally, there will also be a shift *w* ($=\overline{CQ}\ =\ \overline{OD}$) of PNA from centre $\mathrm{O}\left(0,0\right)$ (see Figure 5.4) due to the axial compression load N_c. $M_{lpz.c}$ and $M_{lpy.c}$ are the resulting normal components of the plastic state limiting moments reduced along the two principal axes just enough to affect the cross-section in reaching the governing plastic limit condition based on the applied loads, (*i.e.*, the material along the entire cross-section has just reached the yield limit either in tension *or* compression portion) under the action of N_c. The governing plastic limit condition stress distribution along

the cross-section shown in Figure 5.4 can be split into two parts, one due to tensile stress and the other due to compressive stress. For convenience, all the angles measured counter-clockwise direction with-respect-to the major axis (*z*–*z*) are assumed to be positive (*+ve*), while the angles measured clockwise direction with-respect-to the major axis (*z*–*z*) are assumed to be negative (*-ve*).

As illustrated in Figure 5.4, the PNA is oriented with an inclination angle γ_c with-respect-to the major axis *z*–*z* intersecting the mid-surface (*or* median) profile of the cross-section at P(z_1, y_1) and Q(z_2, y_2); and the major axis *z*–*z* at N such that $\angle NOP = \theta_1$ and $\angle NOQ = \theta_2$. Thus, the radial distances $\overline{OP}$ (= k_1) and $\overline{OQ}$ (= k_2) can be obtained as per the following Equations 5.61 and 5.62 based on Equation 2.2.

$$\overline{OP} = k_1 = \frac{a_m b_m}{\sqrt{a_m^2 \sin^2\theta_1 + b_m^2 \cos^2\theta_1}} \tag{5.61}$$

$$\overline{OQ} = k_2 = \frac{a_m b_m}{\sqrt{a_m^2 \sin^2\theta_2 + b_m^2 \cos^2\theta_2}} \tag{5.62}$$

The Cartesian form of P (z_1, y_1) is ($k_1 \cos\theta_1$, $k_1 \sin\theta_1$) and Q (z_2, y_2) is ($k_2 \cos\theta_2$, $k_2 \sin\theta_2$). The slope of PNA (*or* $\overline{PQ}$) is expressed in the following Equation 5.63.

$$\tan\gamma_c = \frac{y_2 - y_1}{z_2 - z_1} = \frac{k_2 \sin\theta_2 - k_1 \sin\theta_1}{k_2 \cos\theta_2 - k_1 \cos\theta_1} \tag{5.63}$$

It is shown in Figure 5.4 that the tangents at the extreme fibre in tension and compression zones contact the mid-surface (*or* median) profile of the cross-section at R_1 and R_2 such that $\overline{R_1 R_2}$ is inclined at an angle θ_r at the centre O(*0*, *0*) with-respect-to the major axis *z*–*z*. Similar to Equations 5.43 and 5.47, γ_c and θ_r can be expressed as follows:

$$\gamma_c = \arctan\left(\frac{M_{lpy.c}}{M_{lpz.c}} \cdot \frac{I_z}{I_y}\right) \tag{5.64}$$

$$\theta_r = \arctan\left(-\frac{b_m^2}{a_m^2}\cdot\cot\gamma_c\right) = \arctan\left(-\frac{b_m^2}{a_m^2}\cdot\frac{M_{lpz.c}}{M_{lpy.c}}\cdot\frac{I_y}{I_z}\right) \tag{5.65}$$

From Equations 5.63 and 5.64, the following Equation 5.66 is obtained.

$$\frac{k_2\sin\theta_2 - k_1\sin\theta_1}{k_2\cos\theta_2 - k_1\cos\theta_1} = \left(\frac{M_{lpy.c}}{M_{lpz.c}}\right)\cdot\left(\frac{I_z}{I_y}\right) = \tan\gamma_c \tag{5.66}$$

Then, the following Equation 5.67 is obtained by substituting k_1 and k_2 from Equations 5.61 and 5.62 in Equation 5.66.

$$\frac{\sin\theta_2\sqrt{a_m^2\sin^2\theta_1 + b_m^2\cos^2\theta_1} - \sin\theta_1\sqrt{a_m^2\sin^2\theta_2 + b_m^2\cos^2\theta_2}}{\cos\theta_2\sqrt{a_m^2\sin^2\theta_1 + b_m^2\cos^2\theta_1} - \cos\theta_1\sqrt{a_m^2\sin^2\theta_2 + b_m^2\cos^2\theta_2}} = \tan\gamma_c \tag{5.67}$$

From ΔDPO, $\angle DPO = (\gamma_c - \theta_1)$ and the PNA shift is given by

$$\overline{OD} = w = k_1\cdot\left|\sin(\gamma_c - \theta_1)\right| = \frac{a_m b_m\cdot\left|\sin(\gamma_c - \theta_1)\right|}{\sqrt{a_m^2\sin^2\theta_1 + b_m^2\cos^2\theta_1}} \tag{5.68}$$

From ΔDQO, $\angle DQO = (\pi - \theta_2 + \gamma_c)$ and the PNA shift is given by

$$\overline{OD} = w = k_2\cdot\left|\sin(\pi - \theta_2 + \gamma_c)\right| = \frac{a_m b_m\cdot\left|\sin(\theta_2 - \gamma_c)\right|}{\sqrt{a_m^2\sin^2\theta_2 + b_m^2\cos^2\theta_2}} \tag{5.69}$$

The following equation is obtained from Equations 5.68 and 5.69.

$$\frac{\left|\sin(\gamma_c - \theta_1)\right|}{\sqrt{a_m^2\sin^2\theta_1 + b_m^2\cos^2\theta_1}} = \frac{\left|\sin(\theta_2 - \gamma_c)\right|}{\sqrt{a_m^2\sin^2\theta_2 + b_m^2\cos^2\theta_2}} \tag{5.70}$$

The Cartesian coordinates of R_1 and R_2 are $(k_r\cos\theta_r,\ k_r\sin\theta_r)$ and $(-k_r\cos\theta_r,\ -k_r\sin\theta_r)$, respectively. Where the radial distance k_r is equal to half the length of $\overline{R_1R_2}$ is as follows based on Equation 2.2:

$$\overline{OR_1} = \overline{OR_2} = k_r = \frac{a_m b_m}{\sqrt{a_m^2 \sin^2\theta_r + b_m^2 \cos^2\theta_r}} \tag{5.71}$$

If $\angle R_1OD = \angle OR_2C = \theta_w$. From Figure 5.4,

$$\theta_w + \theta_r - \gamma_c = \frac{\pi}{2} \tag{5.72}$$

From ΔOR_2C and from Equations 5.71 and 5.72, $\angle OR_2C = \theta_w = \frac{\pi}{2} + \gamma_c - \theta_r$ and then

$$\overline{R_2C} = d_b = k_r \cdot |\cos\theta_w| = k_r \cdot \left|\cos\left(\frac{\pi}{2} + \gamma_c - \theta_r\right)\right| = \frac{a_m b_m \cdot |\sin(\gamma_c - \theta_r)|}{\sqrt{a_m^2 \sin^2\theta_r + b_m^2 \cos^2\theta_r}} \tag{5.73}$$

From Figure 5.4, it should be noted that θ_1, θ_2, θ_r, θ_w and γ_c are the central Polar angles. It can be seen from Figure 5.4 that the stress block diagram depends on the PNA shift *w* and the locus of $\overline{R_1R_2}$ by rotating around major and minor axes from the case of combined major axis bending plus axial compression to the case of combined minor axis bending plus axial compression.

The plastic interactive surface for EHSs under combined biaxial bending plus axial compression is a plane that intersects the interaction curves represented by Equations 5.18, 5.39 and 5.58 and the expression for the same is obtained as follows:

$$\left(\frac{|N_c|}{N_y}\right)^{1.9332} + \left[\left(\frac{|M_{lpy.c}|}{M_{py}}\right)^2 + \left(\frac{|M_{lpz.c}|}{M_{pz}}\right)^2\right]^{\frac{1}{2.25}} = 1.0; \qquad \text{if } \frac{a}{b} = r = 1.00 \tag{5.74}$$

$$\left(\frac{|N_c|}{N_y}\right)^{1.8511} + \left[\left(\frac{|M_{lpy.c}|}{M_{py}}\right)^2 + \left(\frac{|M_{lpz.c}|}{M_{pz}}\right)^{1.9852}\right]^{\frac{1}{2.22}} = 1.0; \qquad \text{if } \frac{a}{b} = r = 1.33 \tag{5.75}$$

$$\left(\frac{|N_c|}{N_y}\right)^{1.81}+\left[\left(\frac{|M_{lpy.c}|}{M_{py}}\right)^{2}+\left(\frac{|M_{lpz.c}|}{M_{pz}}\right)^{1.9463}\right]^{\frac{1}{2.20}}=1.0; \qquad \text{if } \frac{a}{b}=r=1.67 \tag{5.76}$$

$$\left(\frac{|N_c|}{N_y}\right)^{1.76}+\left[\left(\frac{|M_{lpy.c}|}{M_{py}}\right)^{2}+\left(\frac{|M_{lpz.c}|}{M_{pz}}\right)^{1.9046}\right]^{\frac{1}{2.18}}=1.0; \qquad \text{if } \frac{a}{b}=r=2.00 \tag{5.77}$$

$$\left(\frac{|N_c|}{N_y}\right)^{1.73}+\left[\left(\frac{|M_{lpy.c}|}{M_{py}}\right)^{2}+\left(\frac{|M_{lpz.c}|}{M_{pz}}\right)^{1.8593}\right]^{\frac{1}{2.16}}=1.0; \qquad \text{if } \frac{a}{b}=r=2.50 \tag{5.78}$$

$$\left(\frac{|N_c|}{N_y}\right)^{1.69}+\left[\left(\frac{|M_{lpy.c}|}{M_{py}}\right)^{2}+\left(\frac{|M_{lpz.c}|}{M_{pz}}\right)^{1.8320}\right]^{\frac{1}{2.13}}=1.0; \qquad \text{if } \frac{a}{b}=r=3.00 \tag{5.79}$$

$$\left(\frac{|N_c|}{N_y}\right)^{1.64}+\left[\left(\frac{|M_{lpy.c}|}{M_{py}}\right)^{2}+\left(\frac{|M_{lpz.c}|}{M_{pz}}\right)^{1.8168}\right]^{\frac{1}{2.07}}=1.0; \qquad \text{if } \frac{a}{b}=r=3.50 \tag{5.80}$$

A summary of the proposed plastic interaction expressions for various loading combinations based on Equations 5.18, 5.39, 5.58 and 5.74–5.80 are tabulated in Table 5.1. Where N_a is the resulting axial compressive component and; M_{ay} and M_{az} are the respective resulting bending moment components reduced normally about the principal axes of the cross-section due to the applied loads. The plastic limit interaction surfaces in the positive octant of the $N_a - M_{ay} - M_{az}$ space for the EHSs with $\frac{a}{b}$ ratios of 1.0, 2.0 and 3.0 are depicted in Figure 5.5. The data points on the interactive surface represents the resultant loading components reduced along the principal axes at the governing plastic limit condition as shown in Figures 5.1–5.4. While, the contour mappings of the plastic limit interaction surfaces at variable axial-compressive load levels with an interval of 0.1 is shown in Figure 5.6. Further, in Figure 5.7, the variation between the plastic lmit interaction relationshps with-respect-to the cross-

sectional aspect ratio at various compressive load levels is assessed and found that the variation increases and becomes significant with increase in the axial-compressive load level.

5.2 EQUIV. CIRCULAR-HOLLOW-SECTION DIAMETER

Gardner et al. (2011) utilised the PNA location parameters to vary the equivalent CHS diameter of the compact EHS under the combined axial compression and bending loads linearly between the equivalent CHS diameters calculated based on Equations 2.21–2.23 for the loading scenarios of pure axial compression and bending. And, in Chapters 3 and 4, usage of Equations 2.21–2.23 is found to provide over-conservative and inconsistent cross-sectional strength and classification predictions.

Therefore, in this section, the PNA location parameters derived in the previous Section 5.1 and the equivalent CHS diameter expressions (Equations 3.1, 4.26 and 4.27) proposed in Chapters 3 and 4 are used for formulating the equivalent CHS diameter of the compact EHS under the combined axial compression and bending loads based on the technique of linear variation adopted by Gardner et al. (2011).

5.2.1 Axial Compression plus Major Axis Bending

The equivalent CHS diameter of the compact EHS under combined axial compression and major axis bending is expressed in the following Equation 5.81 by assuming a simple linear transition pattern between $D_{eq.c3}$ and $D_{NSb.mj}$, depending on the estimated α_{mj} using Equation 5.14.

$$D_{eq} = D_{cb.mj} = D_{NSb.mj} + \left(D_{eq.c3} - D_{NSb.mj}\right)\cdot\left(2\alpha_{mj} - 1\right) = D_{NSb.mj} + \left(D_{eq.c3} - D_{NSb.mj}\right)\cdot\cos\psi_h \tag{5.81}$$

where ψ_h can be determined from Equations 5.5–5.10 based on N_h and $r\left(=\frac{a}{b}\right)$ values; $D_{eq.c3}$ and $D_{NSb.mj}$ can be determined from Equations 3.1 and 4.26, respectively.

From Figure 5.1 and Table 5.1, due to the presence of the applied resultant axial force N_a, the plastic limit state strong-axis moment capacity M_{lpy} can be lower than the applied resultant strong-axis flexural moment M_{ay} (M° Kenzie 1998). Where M_{lpy} can be calibrated using Equation 5.18 assuming that N_h is equal to N_a.

5.2.2 Axial Compression plus Major Axis Bending

The equivalent CHS diameter of the compact EHS under combined axial compression and major axis bending is expressed in the following Equation 5.82 by assuming a simple linear transition pattern between $D_{eq.c3}$ and $D_{NSb.mn}$, depending on the estimated α_{mn} using Equation 5.35.

$$\begin{aligned} D_{eq} = D_{cb.mn} &= D_{NSb.mn} + \left(D_{eq.c3} - D_{NSb.mn}\right)\cdot(2\alpha_{mn} - 1) \\ &= D_{NSb.mn} + \left(D_{eq.c3} - D_{NSb.mn}\right)\cdot \sin\psi_n \end{aligned} \tag{5.82}$$

where ψ_n can be determined from Equations 5.26–5.31 based on N_n and $r\left(=\frac{a}{b}\right)$ values; $D_{eq.c3}$ and $D_{NSb.mn}$ can be determined from Equations 3.1 and 4.27, respectively.

From Figure 5.2 and Table 5.1, due to the presence of the applied resultant axial force N_a, the plastic limit state strong-axis moment capacity M_{lpz} can be lower than the applied resultant strong-axis flexural moment M_{az} (M° Kenzie 1998). Where M_{lpz} can be calibrated using Equation 5.39 assuming that N_n is equal to N_a.

5.2.3 Bi-axial (Oblique) Bending

For the compact EHS under pure bi-axial bending, it can be seen from Figure 5.3 that the stress block diagram entirely depends on the locus of $\overline{T_1T_2}$ by rotating around major and minor axes

from the case of pure major axis bending to the case of pure minor axis bending. Thus, the equivalent CHS diameter for EHS under bi-axial plastic bending can be approximately calculated as a resultant of $D_{NSb.mj}$ and $D_{NSb.mn}$ of the EHS based on θ_t as shown in the following Equation 5.83.

$$D_{eq} = D_{NSb.bi} = \sqrt{\left(D_{NSb.mj} \cdot \cos\theta_t\right)^2 + \left(D_{NSb.mn} \cdot \sin\theta_t\right)^2} \tag{5.83}$$

where $D_{NSb.mj}$ and $D_{NSb.mn}$ can be determined from Equations 4.26 and 4.27, respectively.

From Table 5.1 and Figure 5.3, due to the presence of the applied resultant weak-axis flexural moment M_{az}, the plastic limit state strong-axis moment capacity $M_{lpy.r}$ can be lower than the applied resultant strong-axis flexural moment M_{ay} (Stoakes and Fahnestock 2016). $M_{lpy.r}$ can be calibrated using Equation 5.58 assuming that $M_{lpz.r}$ is equal to M_{az}. Later, θ_t can be determined from Equation 5.47.

From Figure 5.3, for the case of EHS under the absence of minor axis bending load (*i.e.*, $M_{lpz.r} = 0$), $\theta_t = 0$; $\theta_b = 0$; $\gamma = -\frac{\pi}{2}$; and $\overline{T_1T_2} = 2k_t = 2a_m$. And, for the case of EHS under the absence of major axis bending load (*i.e.*, $M_{lpy.r} = 0$), $\theta_t = \frac{\pi}{2}$; $\theta_b = 0$; $\gamma = 0$; and $\overline{T_1T_2} = 2k_t = 2b_m$.

5.2.4 Axial Compression plus Bi-axial Bending

Similar to Equation 5.83 and with-reference to Figure 5.4, the expression for the equivalent CHS diameter for EHS under combined bi-axial plastic bending plus axial compression can be approximately calculated as a resultant of $D_{cb.mj}$ and $D_{cb.mn}$ as shown in the following Equation 5.84.

$$D_{eq} = D_{NSbc.bi} = \sqrt{\left(D_{cb.mj} \cdot \cos\theta_r\right)^2 + \left(D_{cb.mn} \cdot \sin\theta_r\right)^2} \tag{5.84}$$

where $D_{cb.mj}$ and $D_{cb.mn}$ shall be calculated from Equations 5.81 and 5.82, respectively at $N_h = N_n = N_c = N_a$.

From Table 5.1 and Figure 5.4, due to the presence of the applied resultant axial force N_a and weak-axis flexural moment M_{az}, the plastic limit state strong-axis moment capacity $M_{lpy.c}$ can be lower than the applied resultant strong-axis flexural moment M_{ay} (M° Kenzie 1998, Stoakes and Fahnestock 2016). $M_{lpy.c}$ can be calibrated using any one of the Equations 5.74–5.80 assuming that N_c is equal to N_a and $M_{lpz.c}$ is equal to M_{az}. Later, γ_c can be obtained from Equation 5.64. And, θ_1 and θ_2 can be obtained by solving Equations 5.67 and 5.70. While θ_r and θ_w can be obtained from Equations 5.65 and 5.72, respectively.

From Figure 5.4, for the case of EHS under the absence of minor axis bending load (*i.e.*, $M_{lpz.c} = 0$), $\theta_r = 0$; $\theta_w = 0$; $\gamma_c = -\frac{\pi}{2}$; and $\overline{R_1R_2} = 2k_r = 2a_m$. And, for the case of EHS under the absence of major axis bending load (*i.e.*, $M_{lpy.c} = 0$), $\theta_r = \frac{\pi}{2}$; $\theta_w = 0$; $\gamma_c = 0$; and $\overline{R_1R_2} = 2k_r = 2b_m$.

The proposed formulae for D_{eq} under various loading combinations are summarised in Table 5.2.

5.3 SUMMARY AND DISCUSSION

5.3.1 Discussion on the Scope of the Proposed Cross-sectional Formulae

In this section, the application of the formulae proposed in the previous Sections 5.1 and 5.2 is discussed. EHSs with $r\left(=\frac{a}{b}\right)$ value of ~ 2.0 subjected to combined axial compression and

uni-/bi-axial bending loads in the experimental program of Chan et al. (2010a) are analysed based on the proposed interaction formulae in Section 5.1. Based on the equations specified in Section 2.2.1, the cross-sectional geometrical and mechanical properties of the EHSs along with the components of the applied forces collected from Chan et al. (2010a) are tabulated in Table 5.3. While 387 MPa and 214.5 GPa are assumed as the respective average values of $f_{y.mea}$ and E of all the specimens based on the tensile coupon test results from Gardner et al. (2011) and Chan et al. (2010a). The test data of specimens E01–E08 is also available in Gardner et al. (2011) apart from Chan et al. (2010a).

Unlike in the pure axial compression *or* bending only scenarios where the equivalent CHS diameter Equations 3.1, 4.26 and 4.27 are derived to be solely dependent on the cross-sectional geometric aspects like t, P_M and r (= a/b), the equivalent CHS diameter Equations 5.81–5.84 for the combined scenarios in Section 5.2 are derived based on the plastic interaction equilibrium according to the applied loads apart from the cross-sectional geometric aspects like t, P_M and r (= a/b). In Table 5.4, the plastic interaction assessment of the EHSs from Chan et al. (2010a) is made based on the expression for EHSs with $\frac{a}{b}$ ratio of 2.0 in Table 5.1. The elastic interaction relation for EHSs with any cross-sectional aspect ratio can be assumed as follows:

$$\left(\frac{|N_a|}{N_y}\right)+\left(\frac{|M_{ay}|}{M_{ey}}\right)+\left(\frac{|M_{az}|}{M_{ez}}\right)\leq 1.0 \tag{5.85}$$

In Table 5.5, the equivalent CHS diameter of the EHS specimens only for whose normalised plastic resistance is greater than *or* equal to unity in Table 5.4 is calibrated by following the procedures described in Section 5.2. While the equivalent CHS diameter of the other EHS specimens (E02, E09–E12) is to be derived based on the Elastic-Neutral-Axis (ENA) location and elastic interaction equilibrium criteria which can be obtained by following a similar methodology described in Sections 5.1 and 5.2. The derivation of ENA parameters and elastic interaction equilibrium criteria are not within the scope of the research of this thesis as only the cross-sections which can develop in-elastic strength are preferred for ELCF conditions.

5.3.2 Summary

Derivation of analytical expressions capable of determining the plastic interaction curves and surfaces of Elliptical-Hollow-Sections (EHSs) under combined axial-compression and bending (uni-/bi-axial) loads is presented in detail. The relations offer cross-section classification criteria between compact and yielding cross-sections and cross-sectional strength design criteria to withstand a given combination of applied loads. The proposed plastic interaction criteria are derived from an exact integration of the cross-section stress field at the limiting plastic state and are valid for any position of the cross-sectional Plastic-Neutral-Axis (PNA). Following the analytical work, expressions for the equivalent CHS diameter of EHSs with various cross-sectional aspect ratios which can develop plastic strength are proposed based on the following.

- Equivalent CHS diameter expression for the cases of EHSs under pure axial compression and pure bending which are derived based on Equivalent-Resistance-Capacity-Method (ERCM).
- The proportion of the cross-section under compressive and tensile stresses and the position of PNA due to the interaction behaviour of the applied loads.

Further, the proposed plastic interaction and equivalent CHS diameter expressions developed in this study are used to assess the behaviour of EHSs from the experimental programs presented in the literature.

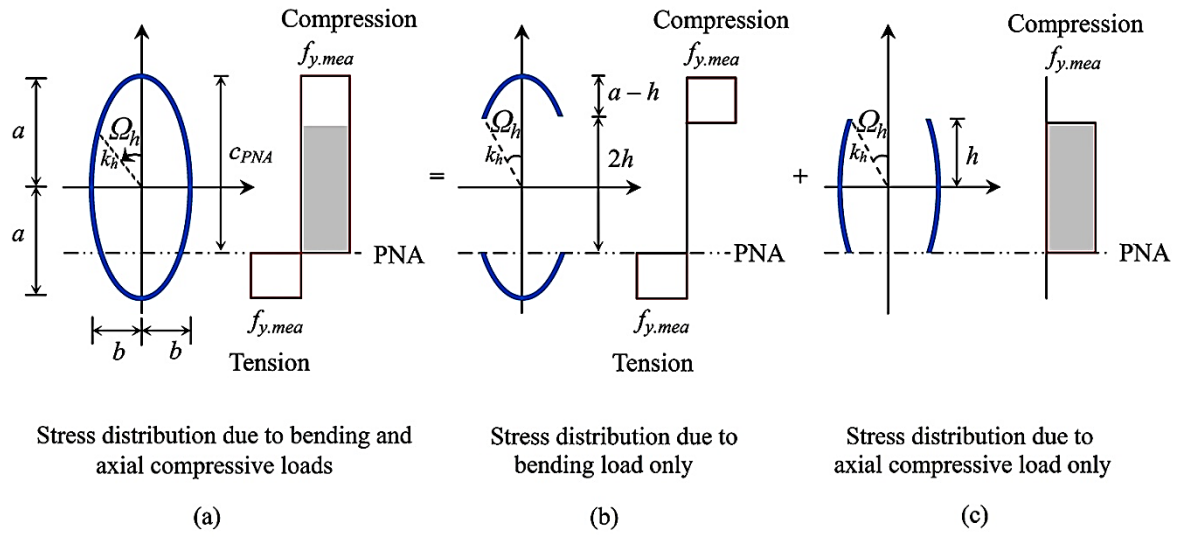

Figure 5.1 *Plastic limit state stress block diagram along EHS cross-section under major axis bending load plus axial compressive load*

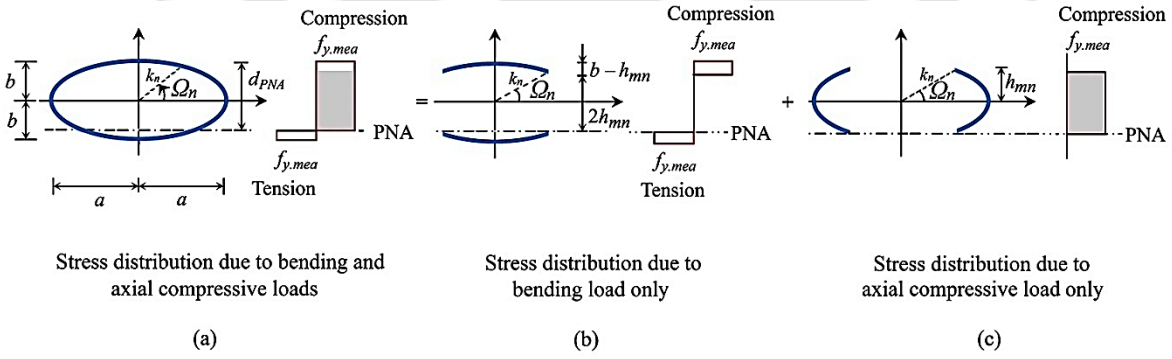

Figure 5.2 *Plastic limit state stress block diagram along EHS cross-section under minor axis bending load plus axial compressive load*

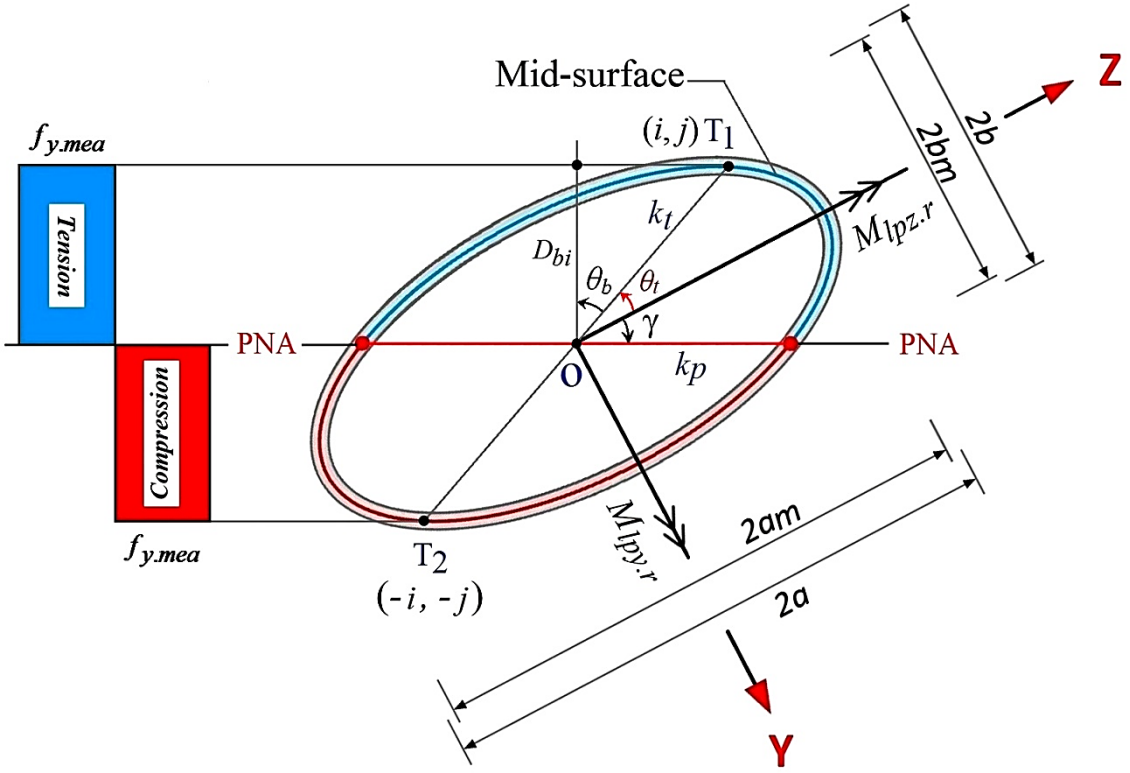

Figure 5.3 *Plastic limit state stress block diagram along EHS cross-section under bi-axial bending load*

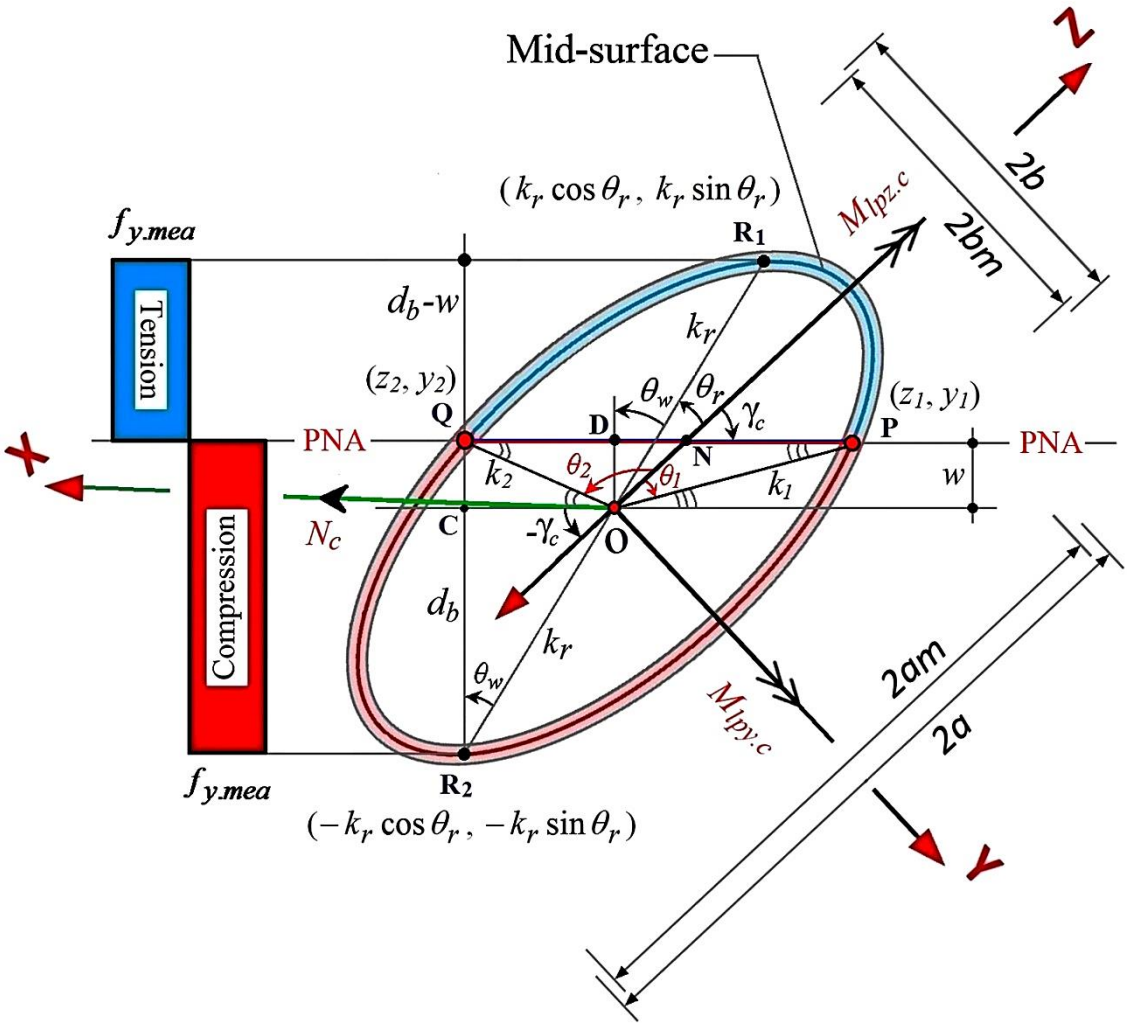

Figure 5.4 *Plastic limit state stress block diagram along EHS cross-section under combined axial compression and bi-axial bending loads*

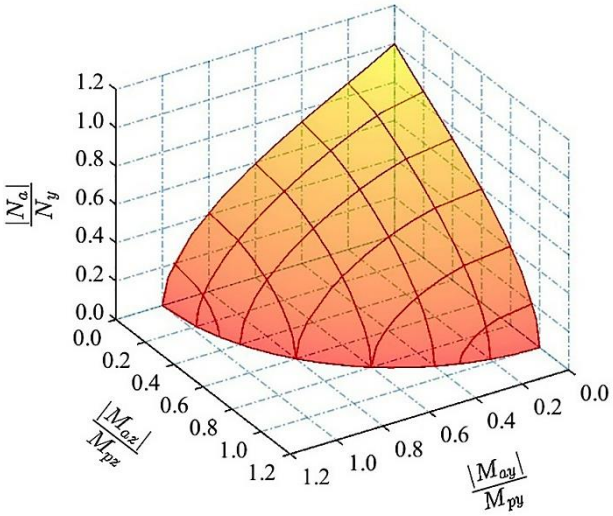

(a)

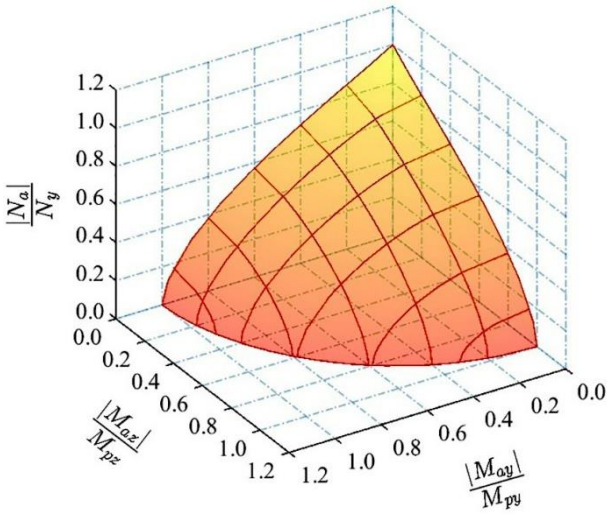

(b)

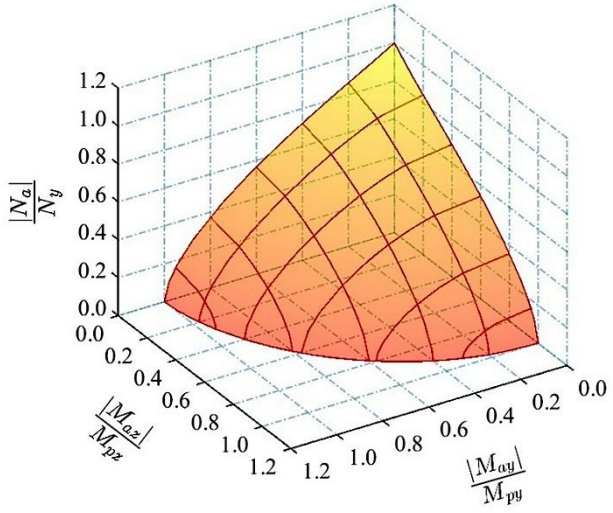

(c)

Figure 5.5 *Plastic limit interaction of EHSs with (a) a/b = 1; (b) a/b = 2; (c) a/b = 3*

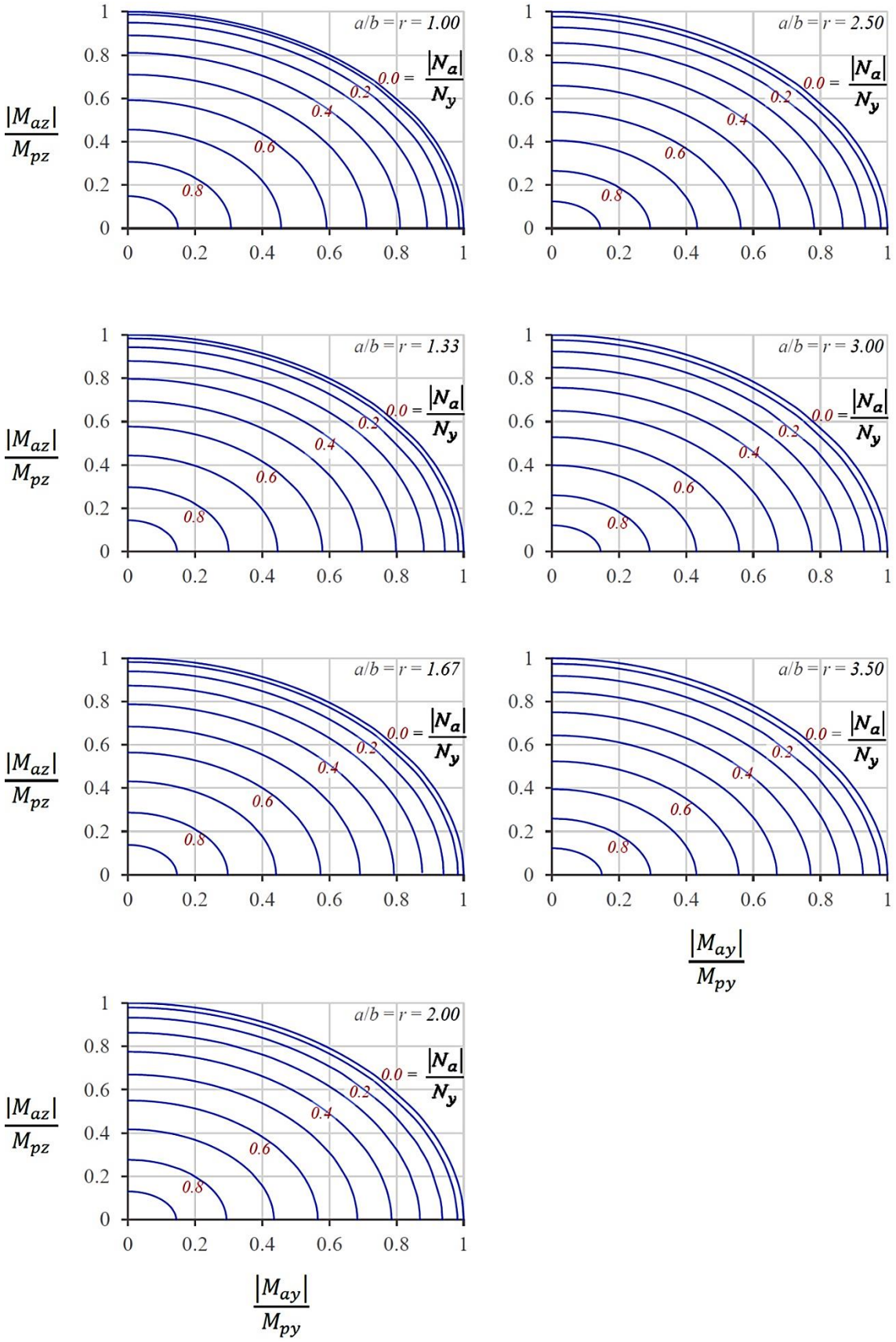

Figure 5.6 *Contour mapping of plastic limit interaction surface of EHSs with varying axial-compressive load level*

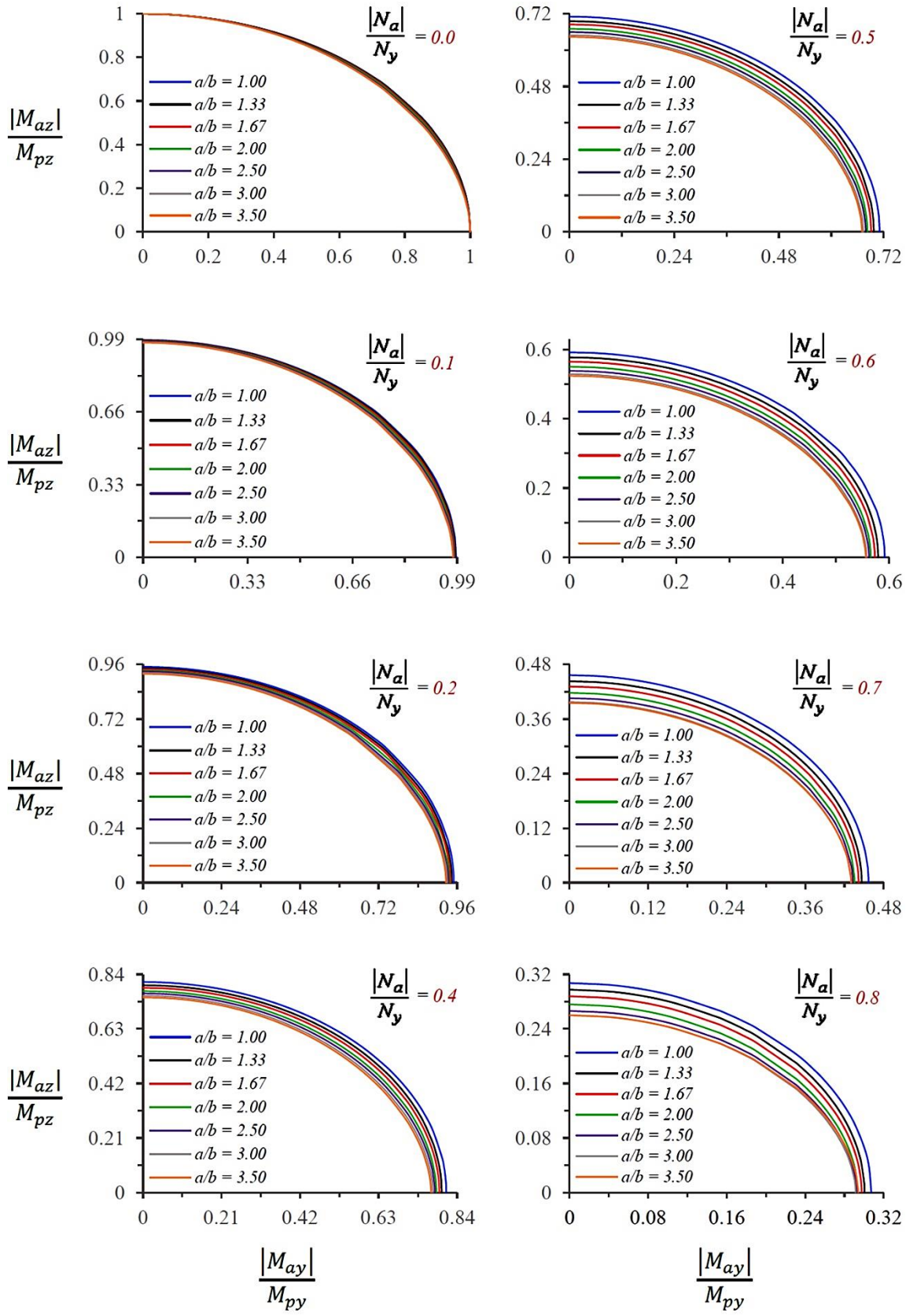

Figure 5.7 *Plastic limit interaction curves for EHSs at various axial-compressive load levels with respect to the cross-sectional aspect ratio*

Table 5.1 *Proposed plastic interaction expressions*

Load combination	Interaction relationship
Axial compression plus major axis bending	$\left(\frac{\lvert N_a\rvert}{N_y}\right)^{n_{ry}} + \left(\frac{\lvert M_{ay}\rvert}{M_{py}}\right)^{m_{ry}} \le 1.0$; n_{ry} and m_{ry} are from Equations 5.19 and 5.20
Axial compression plus minor axis bending	$\left(\frac{\lvert N_a\rvert}{N_y}\right)^{n_{rz}} + \left(\frac{\lvert M_{az}\rvert}{M_{pz}}\right)^{m_{rz}} \le 1.0$; n_{rz} and m_{rz} are from Equations 5.40 and 5.41
Bi-axial bending	$\left(\frac{\lvert M_{ay}\rvert}{M_{py}}\right)^{2} + \left(\frac{\lvert M_{az}\rvert}{M_{pz}}\right)^{z_r} \le 1.0$; z_r is from Equation 5.59
Axial compression plus bi-axial bending	$\left(\frac{\lvert N_a\rvert}{N_y}\right)^{1.9332} + \left[\left(\frac{\lvert M_{ay}\rvert}{M_{py}}\right)^{2} + \left(\frac{\lvert M_{az}\rvert}{M_{pz}}\right)^{2}\right]^{\frac{1}{2.25}} \le 1.0$; if $\frac{a}{b} = r = 1.00$
	$\left(\frac{\lvert N_a\rvert}{N_y}\right)^{1.8511} + \left[\left(\frac{\lvert M_{ay}\rvert}{M_{py}}\right)^{2} + \left(\frac{\lvert M_{az}\rvert}{M_{pz}}\right)^{1.9852}\right]^{\frac{1}{2.22}} \le 1.0$; if $\frac{a}{b} = r = 1.33$
	$\left(\frac{\lvert N_a\rvert}{N_y}\right)^{1.81} + \left[\left(\frac{\lvert M_{ay}\rvert}{M_{py}}\right)^{2} + \left(\frac{\lvert M_{az}\rvert}{M_{pz}}\right)^{1.9463}\right]^{\frac{1}{2.20}} \le 1.0$; if $\frac{a}{b} = r = 1.67$
	$\left(\frac{\lvert N_a\rvert}{N_y}\right)^{1.76} + \left[\left(\frac{\lvert M_{ay}\rvert}{M_{py}}\right)^{2} + \left(\frac{\lvert M_{az}\rvert}{M_{pz}}\right)^{1.9046}\right]^{\frac{1}{2.18}} \le 1.0$; if $\frac{a}{b} = r = 2.00$
	$\left(\frac{\lvert N_a\rvert}{N_y}\right)^{1.73} + \left[\left(\frac{\lvert M_{ay}\rvert}{M_{py}}\right)^{2} + \left(\frac{\lvert M_{az}\rvert}{M_{pz}}\right)^{1.8593}\right]^{\frac{1}{2.16}} \le 1.0$; if $\frac{a}{b} = r = 2.50$
	$\left(\frac{\lvert N_a\rvert}{N_y}\right)^{1.69} + \left[\left(\frac{\lvert M_{ay}\rvert}{M_{py}}\right)^{2} + \left(\frac{\lvert M_{az}\rvert}{M_{pz}}\right)^{1.8320}\right]^{\frac{1}{2.13}} \le 1.0$; if $\frac{a}{b} = r = 3.00$
	$\left(\frac{\lvert N_a\rvert}{N_y}\right)^{1.64} + \left[\left(\frac{\lvert M_{ay}\rvert}{M_{py}}\right)^{2} + \left(\frac{\lvert M_{az}\rvert}{M_{pz}}\right)^{1.8168}\right]^{\frac{1}{2.07}} \le 1.0$; if $\frac{a}{b} = r = 3.50$

Table 5.2 *Proposed equivalent CHS diameter expressions*

Load combination	Equivalent CHS diameter, D_{eq} expression
Pure axial compression	$D_{eq.c3} = 2a \cdot \left[0.1011r^2 - 0.0774r + 0.9763 \right] \cdot \left(\frac{t}{P_M} \right)^{118.35 - \sqrt{118.38^2 - (r-3.64)^2}}$
Major axis bending only	$D_{NSb.mj} = \begin{cases} 2a\left[(0.1286r)^3 + (0.0922r)^2 - (0.031r) + 0.5448 \right] & if \quad r > 1.357 \\ \frac{2a}{r^2} & if \quad r \le 1.357 \end{cases}$
Minor axis bending only	$D_{NSb.mn} = 2a\left[-(0.3123r)^3 + (0.5648r)^2 - (0.2996r) + 1.01 \right]$
Axial compression plus major axis bending	$D_{cb.mj} = D_{NSb.mj} + \left(D_{eq.c3} - D_{NSb.mj} \right) \cdot \left(2\alpha_{mj} - 1 \right)$ $= D_{NSb.mj} + \left(D_{eq.c3} - D_{NSb.mj} \right) \cdot \cos\psi_h$
Axial compression plus minor axis bending	$D_{cb.mn} = D_{NSb.mn} + \left(D_{eq.c3} - D_{NSb.mn} \right) \cdot \left(2\alpha_{mn} - 1 \right)$ $= D_{NSb.mn} + \left(D_{eq.c3} - D_{NSb.mn} \right) \cdot \sin\psi_n$
Bi-axial bending	$D_{NSb.bi} = \sqrt{\left(D_{NSb.mj} \cdot \cos\theta_t \right)^2 + \left(D_{NSb.mn} \cdot \sin\theta_t \right)^2}$
Axial compression plus bi-axial bending	$D_{NSbc.bi} = \sqrt{\left(D_{cb.mj} \cdot \cos\theta_r \right)^2 + \left(D_{cb.mn} \cdot \sin\theta_r \right)^2}$

Table 5.3 *Components of the applied forces, geometrical and mechanical properties of EHS specimens from Chan et al. (2010a)*

EHS Id.	$2a \times 2b \times t$ **(mm×mm×mm)**	a/b **(= *r*)**	a_m **(mm)**	b_m **(mm)**	I_y **(mm^4)**	I_z **(mm^4)**	M_{ey} **(kNm)**	M_{py} **(kNm)**	M_{ez} **(kNm)**	M_{pz} **(kNm)**	N_y **(kN)**	N_a *or* N_h *or* N_n *or* N_c **(kN)**	M_{ay} **(kNm)**	M_{az} **(kNm)**
E01	150 × 76.15 × 4.81	1.97	72.60	35.67	3687696	1258505	19.33	27.13	12.99	16.75	662.19	343	0	10.6
E02	150.2 × 75.9 × 4.88	1.98	72.66	35.51	3741081	1266221	19.28	27.08	12.91	16.67	661.12	181	0	14.4
E03	148.7 × 76 × 6.65	1.96	71.03	34.68	4766124	1613224	24.81	35.27	16.43	21.69	880.40	500	0	13.6
E04	149.55 × 75.8 × 6.8	1.97	71.38	34.50	4921155	1640544	25.47	36.27	16.75	22.15	902.43	248	0	19.7
E05	150.5 × 76.65 × 4.94	1.96	72.78	35.36	3794139	1272356	19.51	27.44	13.02	16.81	669.33	490	18.5	0
E06	150.2 × 76.95 × 4.84	1.95	72.68	36.06	3742453	1296168	19.29	27.05	13.04	16.82	658.39	235	27.4	0
E07	148.4 × 76.1 × 6.72	1.95	70.84	34.69	4786689	1627918	24.97	35.50	16.56	21.88	888.04	712	30	0
E08	148.55 × 76 × 6.74	1.95	70.91	34.63	4807618	1628419	25.05	35.63	16.58	21.92	890.90	342	42.4	0
E09	150.1 × 76.15× 4.78	1.97	72.66	35.66	3672220	1250926	18.94	26.58	12.72	16.40	648.26	325	8.9	8.6
E10	149.7 × 75.74× 4.75	1.98	72.48	35.50	3617397	1228277	18.70	26.25	12.55	16.18	642.21	162	4.2	12.9
E11	150.2 × 76.78 × 4.99	1.96	72.61	35.90	3840028	1323130	19.79	27.79	13.34	17.24	677.50	207	21.7	5.7
E12	149.95 × 76.1 × 4.79	1.97	72.58	35.66	3669632	1251911	18.94	26.58	12.73	16.42	649.06	136	14	10.2
E13	148.6 × 76.1 × 6.6	1.95	71.00	34.75	4731246	1607539	24.64	35.02	16.35	21.57	874.03	466	12.4	13.6
E14	148.73 × 76.1 × 6.57	1.95	71.08	34.77	4723814	1603241	24.58	34.93	16.31	21.51	870.89	319	8.4	17.6
E15	148.7 × 76.1 × 6.59	1.95	71.06	34.76	4733450	1606706	24.64	35.01	16.34	21.56	873.24	233	6	18.9
E16	148.38 × 76 × 6.64	1.95	70.87	34.68	4733600	1607968	24.69	35.10	16.38	21.62	877.68	279	29.1	7.3
E17	150.15 × 75.35 × 6.8	1.99	71.68	34.28	4955944	1625024	25.55	36.41	16.69	22.07	903.80	240	24.9	13.4
E18	148.6 × 76.13 × 6.64	1.95	70.98	34.75	4756424	1616503	24.77	35.21	16.43	21.70	879.11	203	19.6	15.6

Table 5.4 *Plastic interaction assessment of EHS specimens from Chan et al. (2010a)*

EHS Id.	$\left(\frac{\lvert N_a \rvert}{N_y}\right)^{1.76} + \left[\left(\frac{\lvert M_{ay} \rvert}{M_{py}}\right)^{2} + \left(\frac{\lvert M_{az} \rvert}{M_{pz}}\right)^{1.9046}\right]^{\frac{1}{2.18}}$	**Remarks**
E01	1.006	> 1.0
E02	0.984	< 1.0
E03	1.037	> 1.0
E04	1.006	> 1.0
E05	1.225	> 1.0
E06	1.145	> 1.0
E07	1.500	> 1.0
E08	1.335	> 1.0
E09	0.957	< 1.0
E10	0.924	< 1.0
E11	0.990	< 1.0
E12	0.902	< 1.0
E13	1.085	> 1.0
E14	1.042	> 1.0
E15	1.004	> 1.0
E16	1.043	> 1.0
E17	1.027	> 1.0
E18	1.001	> 1.0

Table 5.5 *Calibration of the equivalent CHS diameter of EHSs from Chan et al. (2010a) based on the plastic-interaction equilibrium*

EHS Id.	$D_{eq.c3}$ **(mm)**	$D_{NSb.mj}$ **(mm)**	$D_{NSb.mn}$ **(mm)**	n_h	n_n	ψ_h **(rad.)**	ψ_n **(rad.)**	$D_{cb.mj}$ **(mm)**	$D_{cb.mn}$ **(mm)**	$M_{lpz.c}$ **(kNm)**	$M_{lpy.c}$ **(kNm)**	γ_c **(rad.)**	θ_r **(rad.)**	$D_{eq}= D_{NSbc.bi}$ **(mm)**
E01	197.24	80.01	213.72	—	0.635	—	0.9915	—	199.93	10.5	0	0	1.5708	199.93
E03	193.48	79.20	210.69	—	0.684	—	1.0446	—	195.81	13.6	0	0	1.5708	195.81
E04	195.53	79.72	213.36	—	0.330	—	0.6028	—	203.25	19.7	0	0	1.5708	203.25
E05	199.06	80.29	216.22	0.880	—	0.5684	—	180.39	—	0	10.73	-1.5708	0	180.39
E06	196.35	79.98	212.39	0.432	—	1.1283	—	129.81	—	0	22.28	-1.5708	0	129.81
E07	192.64	79.01	209.68	0.966	—	0.4356	—	182.04	—	0	10.33	-1.5708	0	182.04
E08	193.11	79.11	210.30	0.462	—	1.0950	—	131.33	—	0	28.50	-1.5708	0	131.33
E13	193.14	79.13	210.20	0.642	0.642	0.8893	0.9973	150.95	195.87	13.6	1.42	-0.0355	1.4235	195.01
E14	193.43	79.21	210.54	0.441	0.441	1.1178	0.7534	129.20	198.83	17.6	0	0	1.5708	198.83
E15	193.35	79.19	210.46	0.321	0.321	1.2451	0.5864	115.72	200.99	18.9	5.06	-0.0907	1.2075	192.32
E16	192.80	79.01	209.86	0.383	0.383	1.1803	0.6743	122.33	199.21	7.3	27.32	-0.9044	0.1861	125.74
E17	197.57	80.12	216.02	0.318	0.318	1.2485	0.5888	117.32	205.77	13.4	23.44	-0.5207	0.3794	132.98
E18	193.07	79.13	210.13	0.278	0.278	1.2900	0.5203	110.70	201.65	15.6	19.56	-0.4029	0.5122	138.12

CHAPTER 6

ELLIPTICAL-HOLLOW-SECTION BRACES UNDER CYCLIC LOADING – A FINITE ELEMENT STUDY

In this chapter, the performance of concentrically loaded EHS bracing members under the ELCF loading history recommended by ECCS (1986) is examined by conducting FE modelling simulations using Abaqus (2009). The FE study emphasizes the cyclic response of twenty hot-rolled carbon steel EHS braces of constant cross-sectional steel area and wall thickness by employing NLCHM model. The cross-sectional aspect ratio (*a/b*) of the EHS brace models is varied between 1 and 2, while the non-dimensional global slenderness $\left(\overline{\lambda}\right)$ is varied between 0.3 and 2.0. The adopted FE modelling procedure is validated by accurate replication of the hysteretic response of test specimens from relevant experimental programs detailed in the literature. Further, a parametric study has been conducted to investigate the hysteresis behaviour of the EHS brace models. The effects of *a*/*b* ratio and $\overline{\lambda}$ on the cyclic performance in terms of compressive resistance, mid-length hinge lateral deflection and energy dissipation at various ductility levels have been assessed and the design implications based on the respective proposed predictive equations have been presented.

The experiments on large-scale bracing members which undergo significant out-of-plane deformations are limited by the available financial support and laboratory space and facilities. Therefore, a comprehensive non-linear FE simulation study is necessitated to accurately assess the cyclic energy dissipation capacity of the EHS bracing members for promoting them as seismic-resistant as well as architectural structural members.

6.1 FINITE ELEMENT MODELLING

A general-purpose commercial FE software, Abaqus (2009) has been used to analyse the performance of EHS steel brace models under ELCF loading. The attributes of shell FE modelling framework adopted herein and presented in the subsequent sub-sections follow those published in Nip et al. (2010b) and Sheehan and Chan (2014).

6.1.1 Geometric and Material Characteristics

Twenty 3 mm thick EHS tubular braces with five sets of brace length $\left(L_{br}\right)$ ranging from 900–2500 mm and *a/b* ratios ranging from 1–2 are modelled with a constant material cross-sectional area, *A* of ~ 431 mm^2, which is equal to that of the 40×40×3-CS-HR SHS brace used in the experimental investigation of Nip et al. (2010b). S355J2H grade (EN 10210-2 2006) HR-CS (Hot-Rolled Carbon-Steel) is assumed herein as the reference material during material modelling of all the twenty EHS braces. The material properties (mechanical and NLCHM model parameters) of S355J2H grade HR-CS are extracted from the experimental program of Nip et al. (2010a) (see Table 2.3). Therefore, the cross-sectional yield resistance, N_y of all the twenty EHS brace models is 200.415 kN. The schematic diagrams of the EHS cross-section of the brace models are shown in Figure 6.1.

Stiffener support endplates are being used to impede the premature fracture at brace ends and also to facilitate an adequate length of weld alongside the supports during the experimental testing (Goggins et al. 2006, Nip et al. 2010b, Sheehan and Chan 2014). Hence, a couple of 125×50×8 mm rectangular longitudinal stiffeners of the same brace material properties are also modelled and rigidly fastened to the brace models at each of the supports along the cross-sectional major axis diameter extremities. Both the brace ends are restrained against all the

translational and rotational movements, except for the translational movement at the loading end.

The non-dimensional cross-sectional and global slenderness ratios are the most important factors that control the brace cyclic performance in terms of ductility, compressive resistance, fracture life, energy dissipation capacity and mid-length hinge deflection (Jain et al. 1980, Popov and Black 1981, Tremblay 2002, Elchalakani et al. 2003, Goggins et al. 2005, Fell et al. 2006, Nip et al. 2010b, 2013, Haddad et al. 2011b, Xu et al. 2020). During the seismic design of structures, an understanding of the effects of non-dimensional cross-sectional and global slenderness ratios would enable more informed choices to be made on member selection.

Based on Equation 2.36 as per Clause 6.3.1.2 of EC3: EN 1993-1-1 (2005), the non-dimensional global slenderness $\bar{\lambda}$ for the cross-sectional yielding EHS brace members which are preferred under ELCF conditions is obtained as follows:

$$\bar{\lambda} = \sqrt{\frac{Af_{y.mea}}{N_{cr}}} = \sqrt{\frac{Af_{y.mea}}{\left(\frac{\pi^2 EI_z}{L_{eff}^2}\right)}} = \sqrt{\frac{f_{y.mea}}{\left(\frac{\pi^2 E}{\left(L_{eff}/r_{g.z}\right)^2}\right)}} = \frac{\sqrt{\varepsilon_{y.mea}}}{\pi} \cdot \left(\frac{L_{eff}}{r_{g.z}}\right) \tag{6.1}$$

where L_{eff} is the effective length of the member based on the support conditions and $\varepsilon_{y.mea}$ is the material yield strain. L_{eff} of all the EHS brace models for the support conditions considered herein is equal to 0.65 times of the unstiffened-length (*i.e.*, $L_{br} - 250$ mm) of the brace with 0.65 as the effective length factor, K_{eff}. $\varepsilon_{y.mea}$ is equal to $\frac{f_{y.mea}}{E}$. The elastic critical buckling load, N_{cr} can be calculated as follows (Euler 1759):

$$N_{cr} = \frac{\pi^2 EI_z}{\left(L_{eff}\right)^2} = \frac{\pi^2 EA}{\left(\frac{L_{eff}}{r_{g.z}}\right)^2} \tag{6.2}$$

where $r_{g.z}$ can be obtained from the expression in Table 2.1.

The EHS brace cross-sectional slenderness, $\bar{\lambda}_{cs.E}\left(=\frac{D_{eq.c3}}{t\varepsilon^2}\right)$ values can be determined using Equation 3.1. The yield displacement, δ_y of a brace model/specimen can be approximated as the product of L_{br} and $\varepsilon_{y.mea}$ (Shaback 2001, Tremblay 2002).

The geometric and material yield characteristics of the EHS brace member models are calibrated and tabulated in Table 6.1 as per the details provided earlier in this sub-section. All the four cross-sections (see Figure 6.1) are deemed as non-slender/yielding cross-sections according to the proposed cross-section slenderness limits in Table 3.5.

6.1.2 Meshing

S4R, a three-dimensional four-node doubly curved quadrilateral robust general-purpose reduced integrated and structured stress/displacement shell element with six degrees of freedom, hourglass control, finite membrane strains and five integration points through the thickness available in Abaqus (2009) element library based on thick-shell theory is employed herein for meshing the brace models (Laulusa et al. 2006). As the formulation of this element accounts for large strains and rotations (transverse shear deformations) and thus allowing the changes in thickness with deformation, it has been successfully employed in previous studies (Chan and Gardner 2009, Nip et al. 2010b, Haddad et al. 2011a, Xu et al. 2020) for accurately predicting the behaviour of HSS bracing and compression members.

Considering the computational time, a similar meshing pattern described in the FE simulation studies of Nip et al. (2010b) and Sheehan and Chan (2014) is adopted for meshing the EHS brace models herein. The extent of the refined mesh in the longitudinal direction is set to ~ *4a* at the mid-length region as shown in Figure 6.2 for a typical brace model. A similar pattern is adopted for meshing from both the ends of the brace models (including the stiffeners) to the extent of ~ *6a* in the longitudinal direction. Therefore, ensuring a sufficiently large refined area in the zones where the plastic hinge and local buckling is most likely to occur when subjected to axial cyclic loading. The aspect ratio of the element in the regions of refined mesh is as low as 1 to 1; whereas a ratio of 2 to 1 is adopted elsewhere of the model as shown in Figure 6.2. The number of S4R elements used for modelling the EHS brace members ranges from 36,000

– 81,000. The stiffeners are rigidly tied to the brace models using the "*Tie*" option available in the "*Constraint*" module of Abaqus (2009).

6.1.3 Boundary Conditions and Imperfections

All the six degrees of freedom of all the nodes at both ends of the members (with rigidly tied stiffeners) were restrained, except for the axial displacement at the loading end which is enabled for translational movement along the global axis as shown in Figure 6.3a.

In reality, all structural members contain initial geometric imperfections. These imperfections trigger out-of-plane deflections at stresses below the theoretical critical buckling limits. In this study, both global and local initial geometric imperfections are seeded into the FE models by defining the nodes directly in their imperfect configuration based on the superposition of weighted eigenmode analysis data. Their respective typical lowest buckling mode shapes resulted from linear eigenvalue buckling analysis (obtained through the Lanczos method) for a typical FE brace model (EHS17) are shown in Figure 6.3c.

Global imperfection amplitude, ω_{g0} equal to $\frac{L_{br}}{500}$ reflect the maximum allowable out-of-straightness tolerance as per EN 10210-2 (2006), EN 10219-2 (2006), AS/NZS 1163 (2016), ASTM A501-01 (2005) specifications (Chan and Gardner 2009, Wardenier et al. 2010). ω_{g0} equal to $\frac{L_{br}}{1000}$ is incorporated into the FE models herein as per the imperfection sensitivity analyses of Hassan et al. (2018) and Zhou et al. (2018).

Local imperfection amplitude, ω_{l0} range of $\frac{t}{6.67}$ to $\frac{t}{10}$ reflect the maximum allowable thickness tolerance as per EN 10210-2 (2006), EN 10219-2 (2006), AS/NZS 1163 (2016), ASTM A501-01 (2005) specifications. But, usage of higher values of ω_{l0} with a range of $\frac{t}{3}$ to $\frac{t}{5}$ is also shown to provide better accuracy in the replicating the experimental structural response by Sun and Butterworth (1998), Gardner (2002), Huang and Young (2012) and Shokouhian and Shi (2015). Also, based on Dawson and Walker (1972) predictive model, Gardner et al. (2010) and Gardner and Nethercot (2004) proposed modified models for

determining ω_{l0} in hot-rolled, cold-formed carbon steel and stainless-steel HSSs. Initial local imperfections are embodied into the respective FE models herein with values of ω_{l0} ranging between $\frac{t}{25}$ and $\frac{t}{50}$ based on the imperfection sensitivity analyses carried out by Nip (2009) and Hassan et al. (2018).

The presence of longitudinal residual stresses in structural members can have a significant influence on brace (*or* column) buckling strengths, by causing premature yielding of the cross-section resulting in a reduction in stiffness and loss of load-carrying capacity. Most of the residual stresses are induced during the production process.

The EHS braces are modelled herein as hot-finished members; therefore the significant portion of the residual stresses that are to be induced during the modelling are only those which could arise due to uneven cooling of the members during their manufacturing. In hot-finished CHSs and EHSs, uneven cooling arises due to the differing thermal conditions present at the outer and inner surfaces, with the outer surface cooling rapidly. This generally leaves the outer surface of the tube with longitudinal and radial compressive stresses; and the inner surface with the equilibrating tensile stress. The magnitude of such tensile and compressive residual stresses are generally found to be in the region of 15% of $f_{y.mea}$. Also, indicating a lower level of such residual stresses, a distinct yield point was observed in the tensile coupon result of S355 J2H grade hot-rolled carbon-steel from Nip et al. (2010a), which is used herein as reference material for modelling of the EHS braces. For these reasons, residual stresses are not explicitly incorporated into the EHS FE brace models, *e.g.*, Chan and Gardner (2009).

The axial tension-compression cyclic displacement loading history (Figure 6.3b) outlined in the ECCS (1986) protocol is chosen to apply with a strain rate of $3\times10^{-4}s^{-1}$ which is within the quasi-static testing range as per BS 7270 (2006) at the loading end through a "*reference point*" to which all the circumferential nodes of the model in the loading plane are tied to by "*Kinematic Coupling*" available in the "*Constraint*" module of Abaqus (2009). In the ECCS (1986) loading history, δ_y is the controlling parameter for increasing the amplitude of loading cycles (Figure 6.3b). The attributes of the ECCS (1986) loading history are already detailed in Section 2.3.2. Nip et al. (2010b), Goggins et al. (2006), Salawdeh and Goggins (2013), Sheehan and Chan (2014) and Zhou et al. (2018) are amongst those who chose to follow the

recommendations of ECCS (1986) protocol while testing steel HSS braces. The non-linear geometric parameter (NLGEOM) is also assigned in the analysis step to deal with large displacement analysis.

6.1.4 Validation of the FE Modelling Approach

To validate the FE modelling approach detailed in the foregoing sub-sections, FE simulations are carried out to replicate the cyclic behaviour of two SHS and RHS bracing specimens in the experimental program of Nip et al. (2010b). During material modelling the mechanical and NLCHM model parameters of the specimens are extracted from the experimental program of Nip et al. (2010a) (see Table 2.3). A comparison of the cyclic performance of the FE models of those test specimens in terms of hysteretic loops and deformation patterns shown in Figures 6.4a–6.4i depict that the FE modelling approach adopted herein can capture the key features of experimental cyclic behaviour of the HSS steel bracing members with reasonable accuracy. Therefore, the FE modelling approach adopted herein is capable of simulating the hysteretic behaviour well for the EHS steel brace models under quasi-static axial cyclic tension-compression displacement loads. The difference between the experimental and FE results in Figures 6.4a–6.4e could be due to consideration of the initial elastic stiffness during elastic unloading giving rise to a steeper drop in the unloading curves than those of the test specimens. Such discrepancies are particularly large for unloading after tensile displacement (Nip et al. 2010b). Further, due to the limited number of parameters ($\sigma|_0$, C_{kin}, γ_{kin}, Q_∞, b_{iso}) in the NLCHM model considered herein employing Abaqus (2009) and the sensitivity of the initial geometric imperfections, the hysteretic behaviour cannot always be replicated accurately at maximum and minimum strains. It can readily be seen that, on the compression side, relatively, there is a good agreement between the experimental and FE results. And hence, it can be expected that estimation of cyclic brace parameters like maximum compressive resistance; post-local-buckling compressive resistance and mid-length-lateral-deflection at various ductility levels; which are required for the brace design, would be accurately estimated. Such parameters would be exploited further in the parametric study in Section 6.3.

6.2 CYCLIC PERFORMANCE TERMINOLOGY

6.2.1 Hysteresis Loop Characteristics

Hysteretic loops can be produced by plotting the cyclic axial displacement against the respective axial resistance exhibited by the bracing member *or* system subjected to cyclic loading. The complex nature of the hysteresis loops can be attributed to the combination of elastic and inelastic buckling behaviour of the brace. In Figure 6.5a, a better understanding of this behaviour can be gained by tracking a typical hysteresis loop of a brace during the first displacement loading cycle.

Upon the application of the compressive axial displacement, initially, the brace exhibits a traditional linear elastic axial resistance-displacement relationship as indicated in segment O–A until the limit δ_y is reached. The behaviour of the brace in this linear elastic segment O–A depends on the slenderness ratio and the initial geometric global imperfection (camber) of the brace. The slenderer the brace is, the more pronounced is the linear elastic buckling behaviour. Upon increasing the applied displacement level beyond δ_y, a gradual transition to nonlinear inelastic behaviour (partial plasticization) occurs in segment A–B until the inelastic stability limit (local instability point 'B') is reached with the formation of a plastic hinge at the mid-length and the attainment of the inelastic buckling capacity. If the brace is sufficiently slender, the increased applied axial compressive displacement during this segment (A–B) of the overall axial resistance-displacement loop will be accompanied by the mid-length lateral deflection, Δ_{mid} at an approximately constant axial compressive resistance force. Segment A–B is attributed by the increase in the plastic moment at the mid-length hinge with-respect-to the applied axial compressive displacement at the same incremental rate. Where point 'B' is characterised by the plastic moment limit *or* peak moment resistance at the mid-length hinge thereby represents the peak compressive resistance, $F_{cr.\max}$ post initial buckling of the brace in the applied axial displacement cycle. After the brace exhibits $F_{cr.\max}$ (*i.e.*, at point 'B'), the further increase in the axial compressive displacement to the maximum limit (point 'C') of the loading cycle results in a gradual drop in the axial compressive resistance and force with an increase in Δ_{mid}. The post local buckling axial compressive resistance exhibited by the brace at any point up to point 'C' after exhibiting $F_{cr.\max}$ is denoted as F_c.

With the reversal of the applied axial compressive displacement (at point 'C'), the axial compressive resistance and Δ_{mid} reduce. Segment C–D of the loop represents the elastic unloading of the brace. Where Point 'D' represents a state of zero resistance exerted by the brace. The slope of the loop in segment C–D is lower than that of segment O–A due to formation of the visible kink at the mid-length of the brace.

With further increase in the reversed axial displacement (beyond point 'D'), tensile axial resistance begins to develop where an initial elastic response is expected in segment D–E of the loop. The slope of the loop in segment D–E is lower than that of segment O–A because of the cumulative plastic strains that the specimen is expected to have experienced during the previous loading. The cumulative plastic strain will cause the specimen to yield earlier, resulting in 85–100 % (Gioncu and Mazzolani 2013) degradation in the brace member stiffness. From a microscopic point of view, the reduction in stiffness is related to dislocation movements and growth of voids in the material. Dislocations move along certain slip planes in compression and will slip in the opposite direction when unloaded in tension. However, the original microstructure can't be reconstituted. As a result, residual deformation occurs at the hinge zone. Permanent strain increases due to the accumulated plastic deformation from the previous loading and due to material non-homogeneity (imperfections and orthotropic nature). Point 'E' in segment E–F of the loop indicates that the brace starts to yield again at the mid-length (the plastic hinge redevelops at the mid-length) because of inelastic local buckling with the rotation opposite to that of the brace corresponding to segment B–C. The increased axial tensile displacement in segment E–F of the hysteresis loop leads to an increase in the tensile axial resistance force accompanied by elongation and straightening of the brace. Point 'F' is characterised with no Δ_{mid} and a noticeable elongation in the length of the brace, *i.e.*, the brace will be completely straight such that there is no applied moment at mid-length hinge zone with a straight kink. With further increase in the tensile axial displacement load till the maximum limit as indicated in segment F–G of the loop, pure plastic axial elongation is expected with the maximum tensile yield resistance of the brace is gradually reached at some point and continues to be almost constant till point 'G'.

Upon the reversal of the tensile axial displacement load at point 'G', linear elastic tensile unloading starts as indicated in segment G–I with the decrease in the brace elongation. The slope of segment G–I shall be almost same as that of segment O–A.

6.2.2 Cyclic Backbone Curve

Cyclic backbone curve *or* cyclic envelope, which is the locus of the axial brace resistance points (in both compression and tension) at the extremes of the first loading cycle of each displacement ductility, μ_δ level as highlighted in Figure 6.5b. Figure 6.5b shows a typical hysteretic response of a brace specimen (40×40×3×1250-CS-HR) from the experimental program of Nip et al. (2010b). In this test, the brace was loaded first in tension but also buckled in the first cycle when the load was reversed. During the second and subsequent cycles, the compressive resistance degraded significantly due to the Baushinger effect and residual out-of-plane deformations from previous cycles (Popov and Black 1981). At every cycle, the brace accumulated permanent elongation and, hence, could only develop its yield resistance after larger axial deformation was imposed in tension. The amount of inelastic rotation imposed to the hinge at every cycle increased as the brace elongated with the increment in the applied axial displacement. Eventually, local buckling develops at the susceptible hinge locations inducing high localized strains in the steel material and thereby gradually reducing the sectional stiffness and axial resistance force. In the later stage, fracture initiates at the hinge locations.

6.2.3 Mid-length Lateral Deflection

The mid-length lateral deflection, Δ_{mid} under the elastic buckling and plastic mechanism scenarios is illustrated in Figures 6.6a and 6.6b, respectively. Δ_{mid} after the formation of the plastic hinge must be accounted for in the design as it can lead to the damage and collapse of non-structural elements such as walls and cladding elements (Tremblay 2002).

6.2.4 Displacement Ductility

The displacement ductility, μ_δ of a loading cycle is the ratio of the maximum applied displacement, δ of the cycle to the axial tensile yield displacement, δ_y.

6.2.5 Cyclic Energy Dissipation

The area encompassed by the hysteresis loop is the energy dissipated by the brace during that particular cycle. The first loading cycle at μ_δ of 4 is found to be the cycle with the largest amount of energy dissipation $W_{\mu\delta.4}$ (Tremblay 2002, Goggins et al. 2005, Nip 2009). Hence, $W_{\mu\delta.4}$ can be used as a reliable basis for comparing the performance of the specimens under various cyclic loading protocols. The cumulative energy dissipation, $W_{\mu\delta.4cum}$ of the brace is the area under the hysteretic loops up to the first loading cycle at μ_δ of 4.

6.3 PARAMETRIC STUDY

FEAs are carried out on the EHS brace models by employing the approach discussed in Section 6.1. Hysteretic curves of the EHS brace models extracted from FEAs are plotted in Figures 6.7–6.9. It can be seen from Figures 6.7–6.9 that the behaviour of the brace under tension is merely affected either by the change in L_{br} *or* a/b ($\overline{\lambda}$ *or* $\frac{D_{eq.c3}}{t\varepsilon^2}$) value. But, local buckling of the brace under compression occurs earlier (*i.e.*, at lesser number of loading cycles) either with the increase in L_{br} *or* a/b ($\overline{\lambda}$ *or* $\frac{D_{eq.c3}}{t\varepsilon^2}$) value. Also, EHS braces with higher L_{br} *or* a/b ($\overline{\lambda}$ *or* $\frac{D_{eq.c3}}{t\varepsilon^2}$) value offer lesser post-buckling compressive resistance and energy dissipation capacities.

In all the models, the compression resistance reduced after subsequent loading cycles due to the cumulative elongation and residual lateral deflection at the mid-length. The cyclic performance of the EHS brace models is compared with various international design specifications, including results from the available literature. Hysteretic parameters like $F_{cr.max}$, F_c, Δ_{mid}, $W_{\mu\delta.4}$ and $W_{\mu\delta.4cum}$ are investigated in this section. However, it is to be noted that analysing brace fracture ductility is not possible herein due to the limitations of the material model adopted.

Apart from the data of the EHS FE brace models, experimental data of the carbon-steel HSS braces (listed in Table 6.2) from Shaback (2001), Haddad (2004), Goggins (2004), Goggins et al. (2006), Nip (2009), Sheehan and Chan (2014), and Sheehan et al. (2015) is also used for the parametric study. Although, various versions of δ_y are followed in the literature (Shaback 2001, Goggins 2004, Haddad 2004, Nip 2009, Sheehan and Chan 2014, Sheehan et al. 2015) herein, it is to be noted that δ_y values in Tables 6.1 and 6.2 are estimated as the product of the respective tensile yield strain $\left(=\frac{f_{y.mea}}{E}\right)$ and unsupported length (= L_{br}) of the entire brace as mentioned in Section 6.1.1 of this chapter.

6.3.1 Maximum Compressive Resistance

The unfactored predictive normalised compression resistance for HSS members as per the CSA S16-14 (2014) and AISC LRFD (2000) specifications is given by Equations 6.3 and 6.4, respectively as follows:

$$\frac{F_{cr.\max}}{N_y} = \frac{1}{\left(1+\bar{\lambda}^{2.68}\right)^{\frac{1}{1.34}}} \tag{6.3}$$

$$\frac{F_{cr.\max}}{N_y} = \begin{cases} 0.658^{\bar{\lambda}^2} & if \quad \bar{\lambda} \le 1.5 \\ \dfrac{0.877}{\bar{\lambda}^2} & if \quad \bar{\lambda} > 1.5 \end{cases} \tag{6.4}$$

In Figure 6.10, experimental data of carbon steel HSS braces from Shaback (2001), Haddad (2004), Goggins (2004), Nip (2009), and Sheehan and Chan (2014) are plotted alongside the unfactored predictive normalised compression resistance curves specified in AISC LRFD (2000) and CSA S16-14 (2014). It can be seen that the CSA S16-14 (2014) predictions are safer, while the AISC LRFD (2000) predictions are unsafe for the members in the intermediate slenderness range $\left(0.5 < \bar{\lambda} \le 1.2\right)$. It is to be noted that L_{eff} of the bracing members from Goggins (2004), Nip (2009) and Sheehan and Chan (2014) is calculated as 0.65 times of their

unstiffened length. While L_{eff} of the bracing members from Shaback (2001) and Haddad (2004) is extracted as it is from the sources.

In Figure 6.11, the normalised $F_{cr.\max}$ values of the FE models obtained from Figures 6.7–6.9 are plotted against their respective $\overline{\lambda}$ and compared with the unfactored predictive resistance curves specified in AISC LRFD (2000) and CSA S16-14 (2014). Both the CSA S16-14 (2014) and AISC LRFD (2000) predictions are found to safe for all the EHS FE models.

6.3.2 Post-Local-buckling Compressive Resistance

Various predictive Equations have been proposed to evaluate the design values of the post-buckling compressive resistance, F_c of steel sections under axial compression, which is a critical loading scenario for ascertaining the evolving forces in other frame members under cyclic loading (Elghazouli 2003). The respective F_c value at a μ_δ level can be obtained from the compressive cyclic-backbone curve *or* cyclic envelope generated according to the brace performance.

The design (*or* minimum) F_c according to ANSI/AISC 341-16 (2016) is 26 % of $F_{cr.max}$ calculated as per Equation 6.4 regardless of $\overline{\lambda}$ and δ.

CSA S16-14 (2014) column strength design specifies a prediction of the design F_c in terms of $\overline{\lambda}$ and N_y as per the following Equation 6.5.

$$F_c = \frac{N_y}{\left(1+0.35\overline{\lambda}\right)\left(1+\overline{\lambda}^{2.68}\right)^{0.7463}} \tag{6.5}$$

While AIJ (1990) provides empirical expressions shown in the following Equation 6.6 to estimate the design F_c values.

$$F_c = \begin{cases} N_y; & if \quad \bar{\lambda} \le 0.15 \\ \dfrac{N_y}{11\bar{\lambda} - 0.65}; & if \quad 0.15 \le \bar{\lambda} \le 0.3 \\ \dfrac{N_y}{6\bar{\lambda} + 0.85}; & if \quad \bar{\lambda} > 0.3 \end{cases} \tag{6.6}$$

For brace members made of carbon steel with a nominal tensile yield strength of 350 MPa, F_c prediction values as per the AIJ (1990) Equation 6.6 corresponds to a cyclic compression displacement of ~ $3\delta_y$ at 1% compression strain (Tremblay 2002).

Tremblay (2002) has collected test results of 76 brace specimens with various cross-sectional shapes from various independent experimental programs and derived an expression for F_c at various μ_δ levels for Class 1 cross-sectional bracing members as follows:

$$F_c = \begin{cases} N_y\left(0.058 + 0.23\bar{\lambda}^{-1.40}\right) \le F_{cr.max} & at \quad \mu_\delta = 2 \quad if \quad \bar{\lambda} \ge 0.3653 \\ N_y\left(0.084 + 0.12\bar{\lambda}^{-1.61}\right) \le F_{cr.max} & at \quad \mu_\delta = 3 \quad if \quad \bar{\lambda} \ge 0.2829 \\ N_y\left(0.091 + 0.063\bar{\lambda}^{-2.05}\right) \le F_{cr.max} & at \quad \mu_\delta = 4 \quad if \quad \bar{\lambda} \ge 0.2719 \\ N_y\left(0.095 + 0.046\bar{\lambda}^{-2.22}\right) \le F_{cr.max} & at \quad \mu_\delta = 5 \quad if \quad \bar{\lambda} \ge 0.2613 \end{cases} \tag{6.7}$$

In Equation 6.7, the expression for predicting F_c values at μ_δ level of 4 is obtained by interpolation by proportional parts based on the predictions at μ_δ levels of 2,3 and 5. Further, it is to be noted that the predictive F_c at any μ_δ level cannot exceed N_y value of the member as per Tremblay (2002).

Experimental investigation of Nakashima et al. (1992) led to an analytical predictive model based on the formation of a plastic hinge mechanism during the inelastic response of bracing members. The predictive F_c value at various μ_δ levels is given by the following Equation 6.8.

$$F_c = N_y \left(\frac{1-\alpha\beta_b}{1-\beta_b}\right)^{\frac{4}{3}} \leq F_{cr.max} \tag{6.8}$$

Where $\alpha = \frac{8r_{st}^{0.75}}{5\bar{\lambda}^{1.5}}$ and $\beta_b = \alpha^{1/3} - \sqrt{\alpha^{2/3} + \frac{5}{3}\bar{\lambda}^2\mu_\delta}$. And, the strain hardening ratio, r_{st} of steel is generally reckoned to be 0.015 (Tremblay 2002). While the predictive F_c at any μ_δ level cannot exceed the N_y value of the member.

In Figure 6.12, the predictive curves for post-local-buckling compressive resistance, F_c of steel bracing members as per ANSI/AISC 341-16 (2016), CSA S16-14 (2014), AIJ (1990), Tremblay (2002) and Nakashima et al. (1992) are plotted. The ANSI/AISC 341-16 (2016) and CSA S16-14 (2014) curves are independent of μ_δ level.

The post-local-buckling compressive resistance in all the EHS brace models reduced after subsequent loading cycles (see Figures 6.7–6.9) due to the accumulated elongation and residual mid-length lateral deflection. The F_c value at various μ_δ levels of the FE models in the current study are normalized with-respect-to their cross-sectional axial tensile yield force, N_y ($=Af_{y.mea}$) and are plotted against their respective $\bar{\lambda}$ along with the predictive curves from Tremblay (2002), AIJ (1990) and Nakashima et al. (1992) in Figure 6.13.

It can be seen from Figure 6.13 that the EHS FE brace models with higher *a*/*b* ratio offer lesser F_c values at higher μ_δ levels and the variation between these values increased with μ_δ level. While the variation between the F_c values decreased with increase in $\bar{\lambda}$ and the effect of *a*/*b* ratio on F_c is insignificant if $\bar{\lambda} \geq \sim 1.15$.

In Figure 6.14, experimental F_c data of carbon steel HSS braces from Shaback (2001), Haddad (2004), Goggins (2004), Nip (2009), and Sheehan and Chan (2014) are plotted alongside the predictive curves specified in Tremblay (2002) and Nakashima et al. (1992). From Figures 6.13 and 6.14, it can be seen that the predictions from Nakashima et al. (1992) curve at higher μ_δ levels for most of the intermediate slenderness range $\left(0.5 < \bar{\lambda} \leq 1.2\right)$ are unsafe. While the predictions from Tremblay (2002) curves seems to be safer. However, Figures 6.13b and 6.13c indicate that the predictions from Tremblay (2002) curves within a considerable $\bar{\lambda}$ range of

0.18–0.45 could be unsafe for the EHS braces with higher cross-sectional aspect ratio *or* slenderness. Therefore, the following Equation 6.9 is proposed based on a lower-bound non-linear regression analysis plot by making a slight adjustment for the Tremblay (2002) curves (Equation 6.7) within that $\bar{\lambda}$ range (0.18–0.45) to accommodate the HSS braces with higher cross-sectional aspect ratio *or* slenderness as shown in the Figures 6.13 and 6.14.

$$F_c = \begin{cases} \dfrac{N_y}{10^3}\left(\dfrac{216.3}{\bar{\lambda}} + \dfrac{102.132}{\bar{\lambda}^2} - \dfrac{23.027}{\bar{\lambda}^3}\right) & if \quad \bar{\lambda} \geq 0.3020, \quad else \quad N_y; \quad at \quad \mu_\delta = 2 \\ \dfrac{N_y}{10^3}\left(\dfrac{164.35}{\bar{\lambda}} + \dfrac{49.29}{\bar{\lambda}^2} - \dfrac{7.39}{\bar{\lambda}^3}\right) & if \quad \bar{\lambda} \geq 0.2418, \quad else \quad N_y; \quad at \quad \mu_\delta = 3 \\ \dfrac{N_y}{10^3}\left(\dfrac{113.29}{\bar{\lambda}} + \dfrac{41.16}{\bar{\lambda}^2} - \dfrac{4.71}{\bar{\lambda}^3}\right) & if \quad \bar{\lambda} \geq 0.2016, \quad else \quad N_y; \quad at \quad \mu_\delta = 4 \\ \dfrac{N_y}{10^3}\left(\dfrac{103.42}{\bar{\lambda}} + \dfrac{25.831}{\bar{\lambda}^2} - \dfrac{2.289}{\bar{\lambda}^3}\right) & if \quad \bar{\lambda} \geq 0.1763, \quad else \quad N_y; \quad at \quad \mu_\delta = 5 \end{cases} \tag{6.9}$$

6.3.3 Mid-length Lateral Deflection

The formulae for the estimation of Δ_{mid} are discussed herein. Tremblay (2002) proposed the following Equations 6.10a and 6.10b.

$$\Delta_{mid} = \frac{2}{\pi}\sqrt{\delta L_{br}} \tag{6.10a}$$

$$\Delta_{mid} = \frac{1}{\sqrt{2}}\sqrt{\delta L_{eff}} \tag{6.10b}$$

Equation 6.10a is for lower δ values where the brace undergoes elastic buckling as shown in Figure 6.6a, while Equation 6.10b is for higher δ values where the brace exhibits a plastic mechanism as shown in Figure 6.6b. Both the Equations 6.10a and 6.10b do not account the permanent residual axial deformation resulting from the preceding load cycles and hence Tremblay (2002) modified Equations 6.10a and 6.10b to Equations 6.11a and 6.11b, respectively as follows:

$$\Delta_{mid} = \frac{2}{\pi}\sqrt{\left(\mu_c + \mu_t - 1\right)\delta_y L_{br}} \tag{6.11a}$$

$$\Delta_{mid} = \frac{1}{\sqrt{2}}\sqrt{\left(\mu_c + \mu_t - 1\right)\delta_y L_{eff}} \tag{6.11b}$$

where μ_c and μ_t refer to the compressive displacement ductility of the cycle in question and the tensile displacement ductility of the previous half-cycle, respectively. It should be noted that not all specimens can achieve the plastic mechanism (Figure 6.6b) considered in Equations 6.10b and 6.11b before failure. In reality, braces are mostly expected to exhibit an elasto-plastic behaviour that lies between each of these two cases, *i.e.*, elastic buckling and plastic mechanism (Figures 6.6a and 6.6b).

Shaback (2001) conducted tests on SHS bracing members and derived an empirical expression shown in the following Equation 6.12 using the resulting data.

$$\frac{\Delta_{mid}}{L_{br}}(\%) = -\frac{1}{9}\mu^{1.9} + 2\mu \tag{6.12}$$

By utilising the test data of CHS bracing members from Sheehan and Chan (2014), Sheehan et al. (2015) derived similar empirical expressions shown in the following Equations 6.13a and 6.13b for estimating Δ_{mid}.

$$\frac{\Delta_{mid}}{L_{br}}(\%) = -0.05\mu^2 + 1.88\mu - 0.41; \quad \text{for hot-finished HSS bracing members} \tag{6.13a}$$

$$\frac{\Delta_{mid}}{L_{br}}(\%) = -0.15\mu^2 + 3.10\mu - 1.60; \quad \text{for cold-formed HSS bracing members} \tag{6.13b}$$

All the Equations 6.10–6.13 have no comprehensive involvement of the material property, elastic buckling, plastic mechanism, cross-sectional shape and support conditions of the members. But, Sheehan et al. (2015) had also derived an empirical expression for estimating Δ_{mid} of hollow and concrete-filled hot-finished and cold-formed braces of all cross-sectional shapes that involves $\overline{\lambda}$. The empirical expression involving $\overline{\lambda}$ of the bracing member proposed by Sheehan et al. (2015) is as follows:

$$\frac{\Delta_{mid}}{L_{br}}(\%) = 7.6\sqrt{\mu} - 1.5\bar{\lambda}\sqrt{\mu} + 4.2\bar{\lambda} - 9.5 \tag{6.14}$$

The Δ_{mid} value at various μ_δ levels of the FE models in the current study are normalized with-respect-to their L_{br} and are plotted against their respective $\bar{\lambda}$ along with the predictive line (Equation 6.14) from Sheehan et al. (2015) in Figure 6.15. It can be seen from Figure 6.15 that the EHS FE brace models with higher *a*/*b* ratio exhibit higher Δ_{mid} values at a higher μ_δ level due to lesser compressive strengths triggered by a plate-type behaviour of the cross-section during local buckling (Zhao and Packer 2009, Silvestre and Gardner 2011) and the variation between these values decreased with increase in $\bar{\lambda}$. Further, the effect of *a*/*b* ratio on Δ_{mid} is found to be insignificant if $\bar{\lambda} \geq\sim 1.15$. In Figure 6.16, experimental Δ_{mid} data of carbon steel HSS braces from Shaback (2001), Haddad (2004), Nip (2009) and Sheehan et al. (2015) are plotted alongside the predictive line (Equation 6.14) from Sheehan et al. (2015).

From Figures 6.15 and 6.16, it can be seen that the predictions from Sheehan et al. (2015) line at all μ_δ levels for the braces within the slenderness $(\bar{\lambda})$ range of 0.6–2.0 are on the safer side. While the predictions of Sheehan et al. (2015) line at all μ_δ levels are certainly unsafe for the HSS braces within the slenderness $(\bar{\lambda})$ range of 0.0–0.6. Ideally, Δ_{mid} values shall drastically decrease and become zero as $\bar{\lambda}$ tends to zero, which is not the case with Sheehan et al. (2015) predictive line (Equation 6.14). This scenario is evident in Figure 6.15.

Therefore, the following Equation 6.15 is proposed to address the estimation of Δ_{mid} values for the braces within the slenderness $(\bar{\lambda})$ range of 0.0–0.6.

$$\frac{\Delta_{mid}}{L_{br}}(\%)=\begin{cases}\left(\dfrac{4.837-42.718\bar{\lambda}+93.563\bar{\lambda}^2}{1-3.635\bar{\lambda}+16.28\bar{\lambda}^2}\right) & if \quad \bar{\lambda}\geq 0.249, \quad else \quad 0; \quad at \quad \mu_\delta=2\\ \left(\dfrac{0.671-14.443\bar{\lambda}+74.613\bar{\lambda}^2}{1-0.653\bar{\lambda}+10.283\bar{\lambda}^2}\right) & if \quad \bar{\lambda}\geq 0.116, \quad else \quad 0; \quad at \quad \mu_\delta=3\\ \left(\dfrac{-0.0316+1.362\bar{\lambda}+65.4\bar{\lambda}^2}{1-0.0015\bar{\lambda}+7.891\bar{\lambda}^2}\right) & if \quad \bar{\lambda}\geq 0.014, \quad else \quad 0; \quad at \quad \mu_\delta=4\\ \left(\dfrac{0.0473+23.912\bar{\lambda}+54.46\bar{\lambda}^2}{1+2.564\bar{\lambda}+5.32\bar{\lambda}^2}\right) & if \quad \bar{\lambda}\geq 0.001, \quad else \quad 0; \quad at \quad \mu_\delta=5\end{cases} \tag{6.15}$$

The predictive curves representing Equation 6.15 are also plotted in Figures 6.15 and 6.16 for comparison purpose. These predictive curves show a satisfactory estimation of Δ_{mid} values at all μ_δ levels. However, it is to be noted that Equation 6.15 may slightly underestimate Δ_{mid} values of the EHS braces with a higher cross-sectional aspect ratio (*a*/*b*) at a higher μ_δ level as shown in Figure 6.15b. While the Sheehan et al. (2015) predictive line representing Equation 6.14 seems to consistently underestimate Δ_{mid} values of the EHS braces within the slenderness $\left(\bar{\lambda}\right)$ range of 0.7–1.5 at all μ_δ levels as seen in Figures 6.15a and 6.15b.

6.3.4 Cyclic Energy Dissipation

The first loading cycle at μ_δ level of 4 is found to be the cycle with the largest amount of energy dissipation, $W_{\mu\delta.4}$ (Tremblay 2002, Goggins et al. 2005, Nip 2009). Hence, Figure 6.17 in which the $W_{\mu\delta.4}$ values of the EHS FE brace models are plotted against their respective $\bar{\lambda}$ represent a more useful basis for comparing the energy dissipation capacity of different HSS brace specimens under various cyclic loading protocols. Besides, the test results of SHS specimens in the experimental program of Nip (2009) are also depicted. The expression for the non-linear regression fit based energy index curve using the $W_{\mu\delta.4}$ values is given in the following Equation 6.16.

$$\frac{W_{\mu\delta.4}}{N_y\delta_y} = \frac{-0.288}{\bar{\lambda}^2} + \frac{3.55}{\bar{\lambda}} + 1.427 \tag{6.16}$$

The $W_{\mu\delta.4}$ curve followed a decreasing trajectory with an increase in the $\bar{\lambda}$ value.

The cumulative energy dissipation, $W_{\mu\delta.4cum}$ of the EHS brace models is normalised and plotted against their respective $\bar{\lambda}$ in Figure 6.18. Although, CHS braces (*i.e.*, EHS with *a/b* = 1.0) exhibited the highest $W_{\mu\delta.4cum}$ values, the effect of *a/b* ratio is found to be insignificant on the $W_{\mu\delta.4cum}$ values of higher slender sections with $\bar{\lambda} \geq 1.15$.

6.4 SUMMARY

The performance of carbon-steel EHS FE brace models under ELCF loading following the recommendations of ECCS (1986) protocol is analysed. A parametric study is performed on the brace characteristics like maximum compressive resistance; post-local-buckling compressive resistance and lateral deflection at various displacement ductility levels; and energy dissipative indices. The respective predictive envelopes are developed and compared with various codal specifications and the results of independent experimental investigations on HSS bracing members from the literature. The cross-sectional aspect ratio effect on the hysteretic parameters of the EHS brace models with-respect-to their non-dimensional slenderness is also assessed. The following are the deductions drawn from the parametric study.

- Slender sectional EHS braces exhibit lesser compressive resistance and energy dissipation values at all ductility levels.
- Braces with higher cross-sectional aspect ratio *or* slenderness show higher lateral deflection near the mid-length region of the braces at all ductility levels.
- For the EHS braces with non-dimensional global slenderness lesser than ~1.15, the cross-sectional aspect ratio *or* slenderness has a significant effect on the normalised hysteresis parameters like post-local-buckling compressive resistance, lateral deflection and energy dissipative indices at higher displacement ductility levels; and the significance of the effect increases with the ductility level.

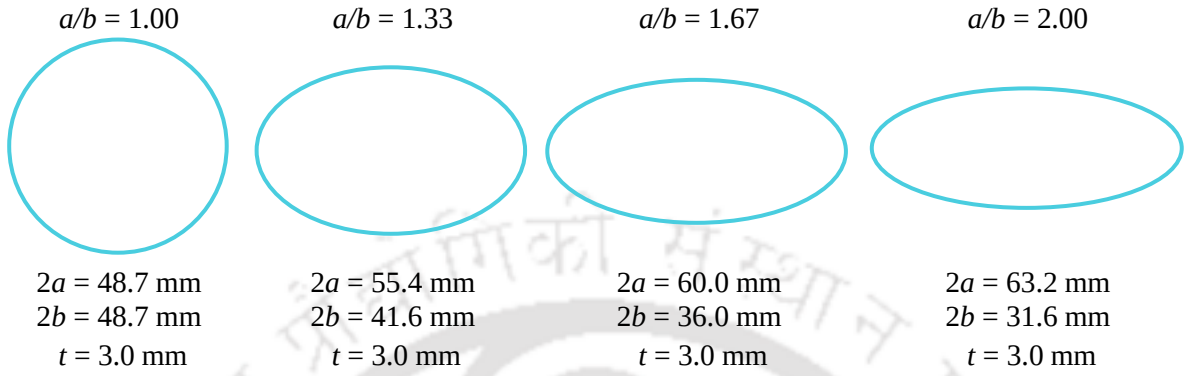

Figure 6.1 *Selected cross-sectional geometric features for FE modelling of the EHS braces* [not to scale]

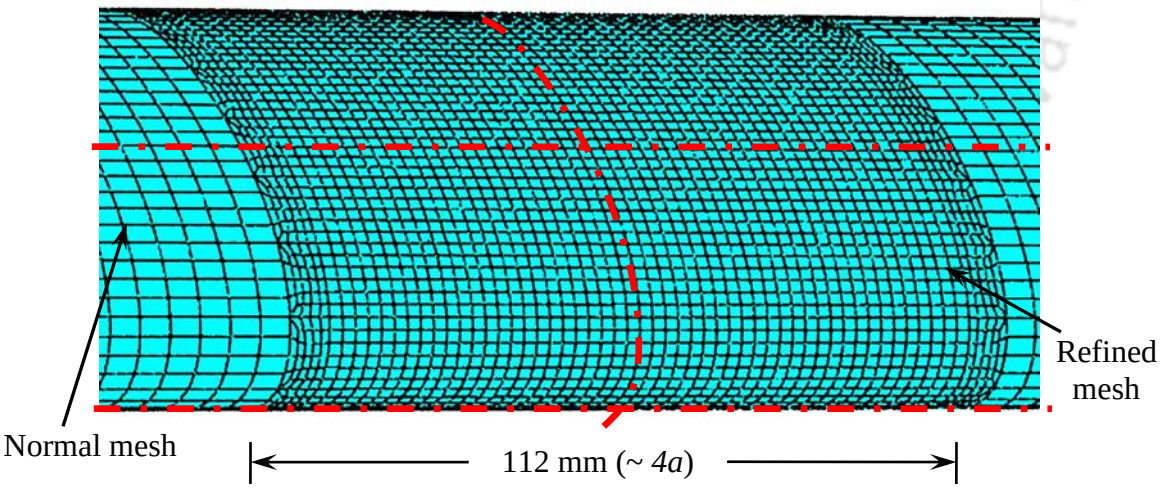

Figure 6.2 *FE mesh pattern at mid-length zone of EHS17 brace model*

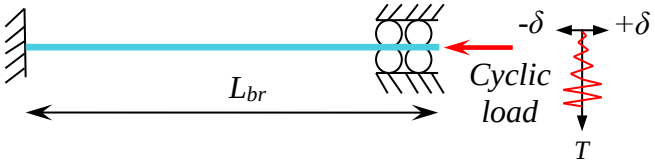

a) Schematic of the applied boundary conditions

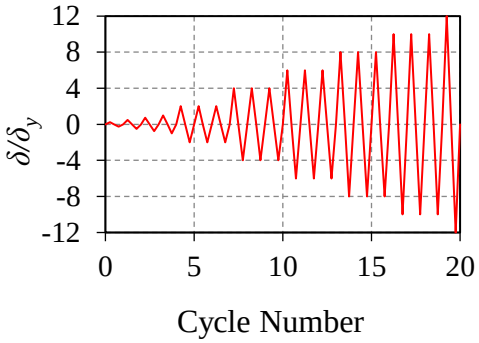

b) ECCS (1986) cyclic loading history

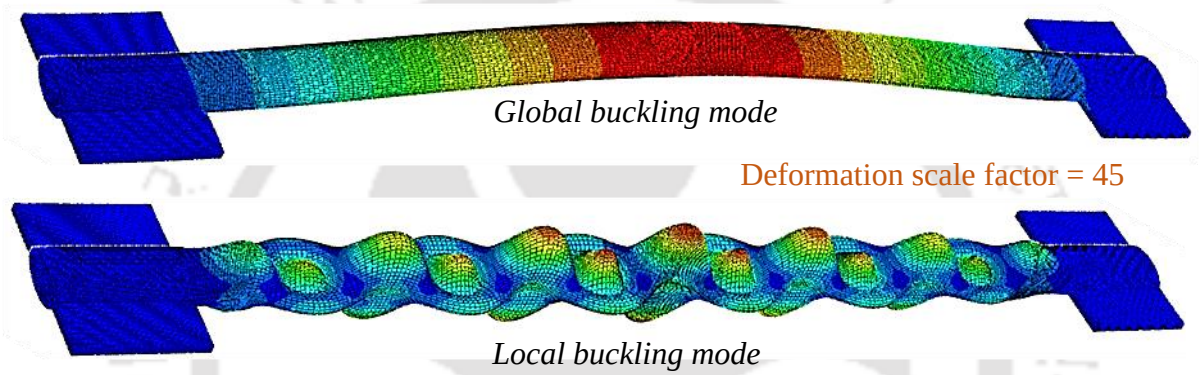

c) Initial global and local buckling shapes of EHS17 brace model

Figure 6.3 *Boundary conditions and initial eigen buckling shapes of a typical FE brace model*

Figure 6.4 *Cyclic performance comparison of the specimens in Nip et al. (2010b) with those of their respective FE simulated models*

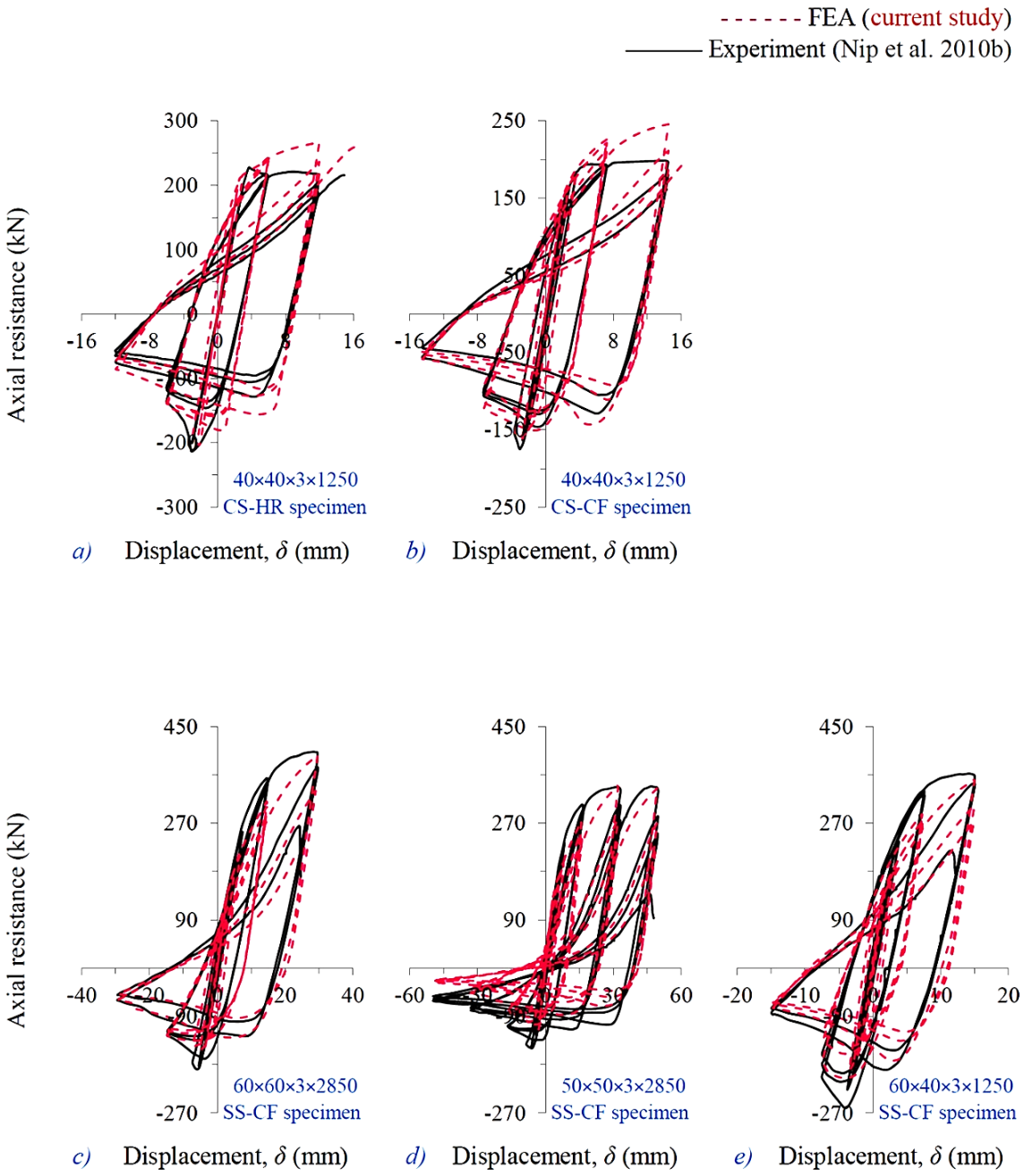

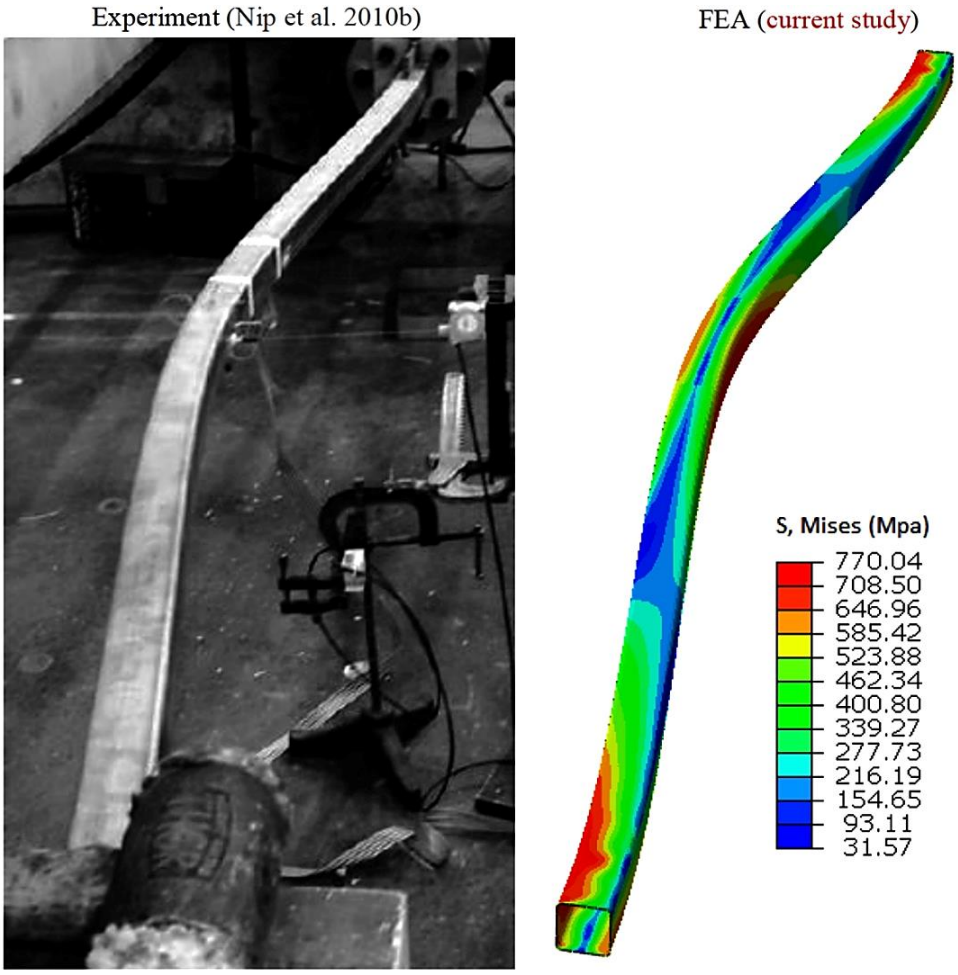

f) Global buckling of *60×60×3×2850 SS-CF specimen*

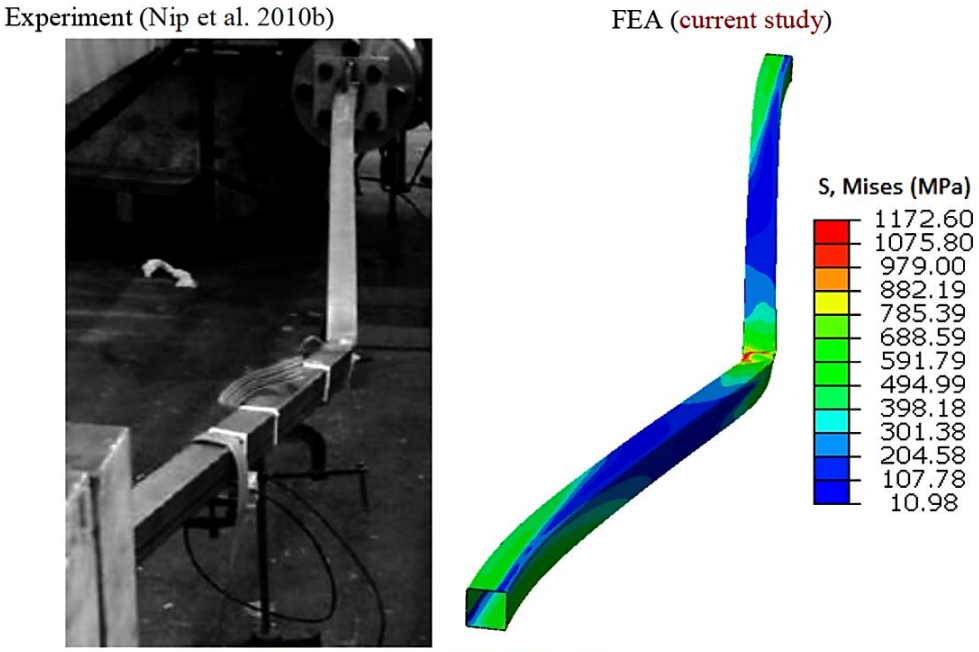

g) Plastic mechanism in *50×50×3×2850 SS-CF specimen*

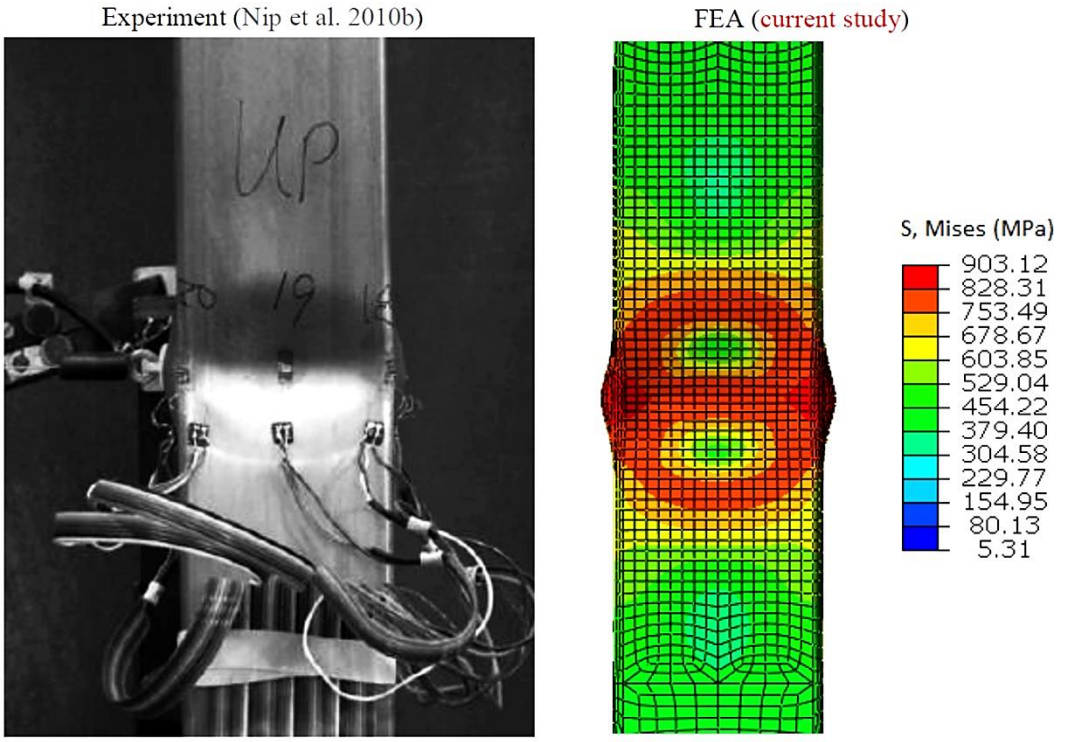

h) Local buckling of *60×40×3×1250 SS-CF specimen*

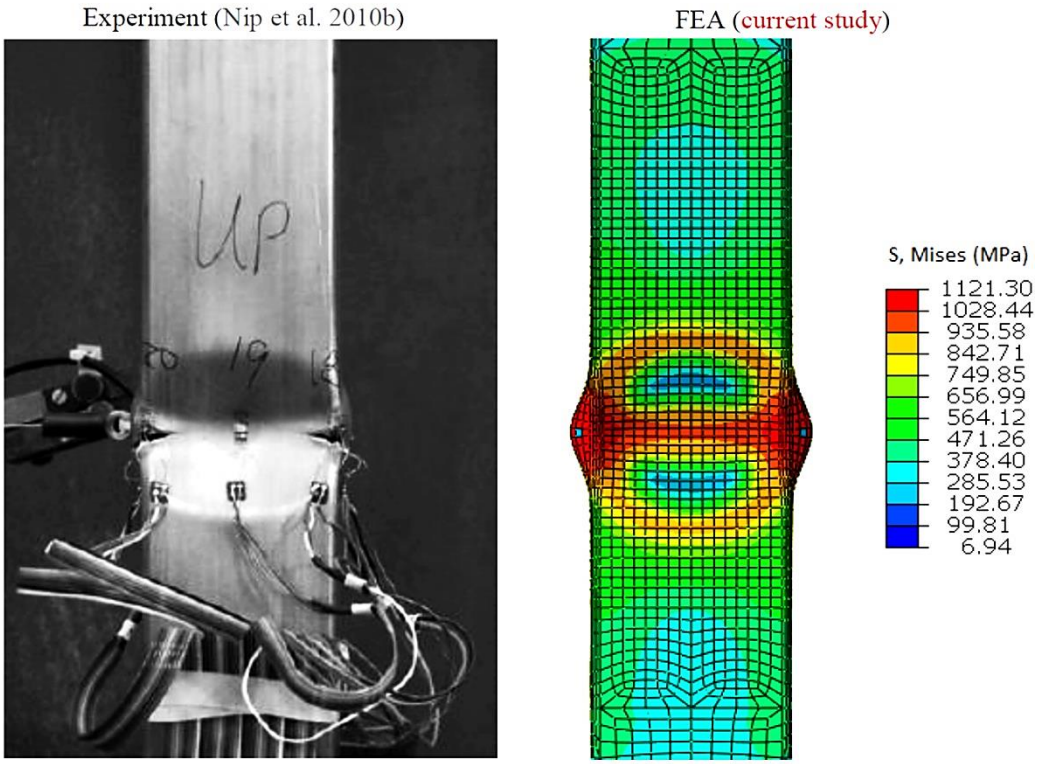

i) Small openings at corners of *60×40×3×1250 SS-CF specimen*

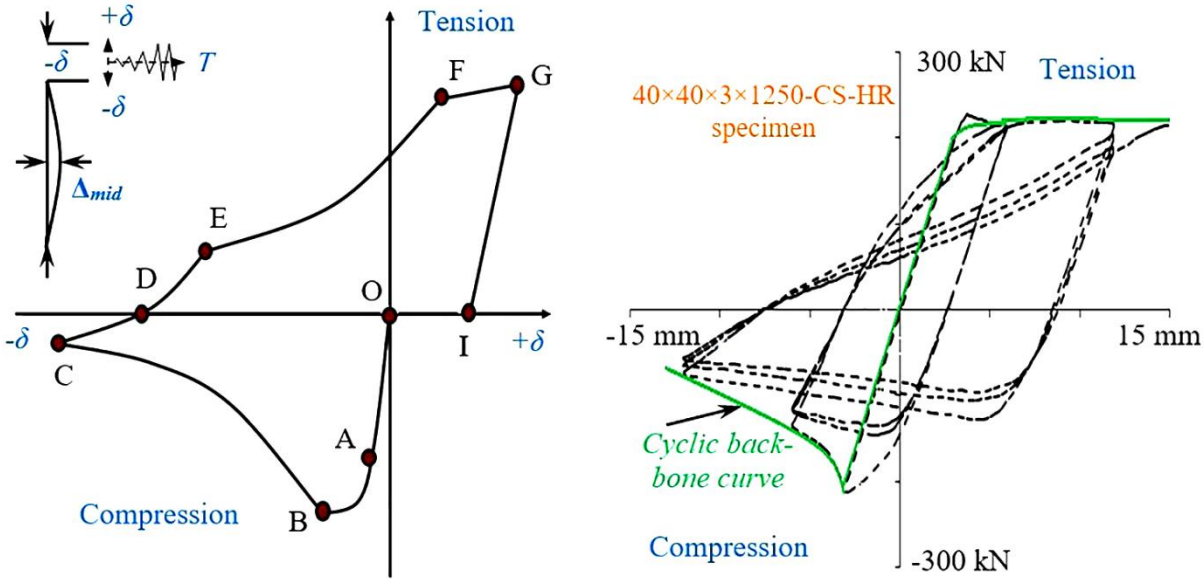

a) Axial resistance-displacement hysteresis loop [**Source:** Popov et al. (1976)]

b) Brace hysteretic response under cyclic loading [**Source:** Nip et al. (2010b)]

Figure 6.5 *Typical hysteretic behaviour of brace member*

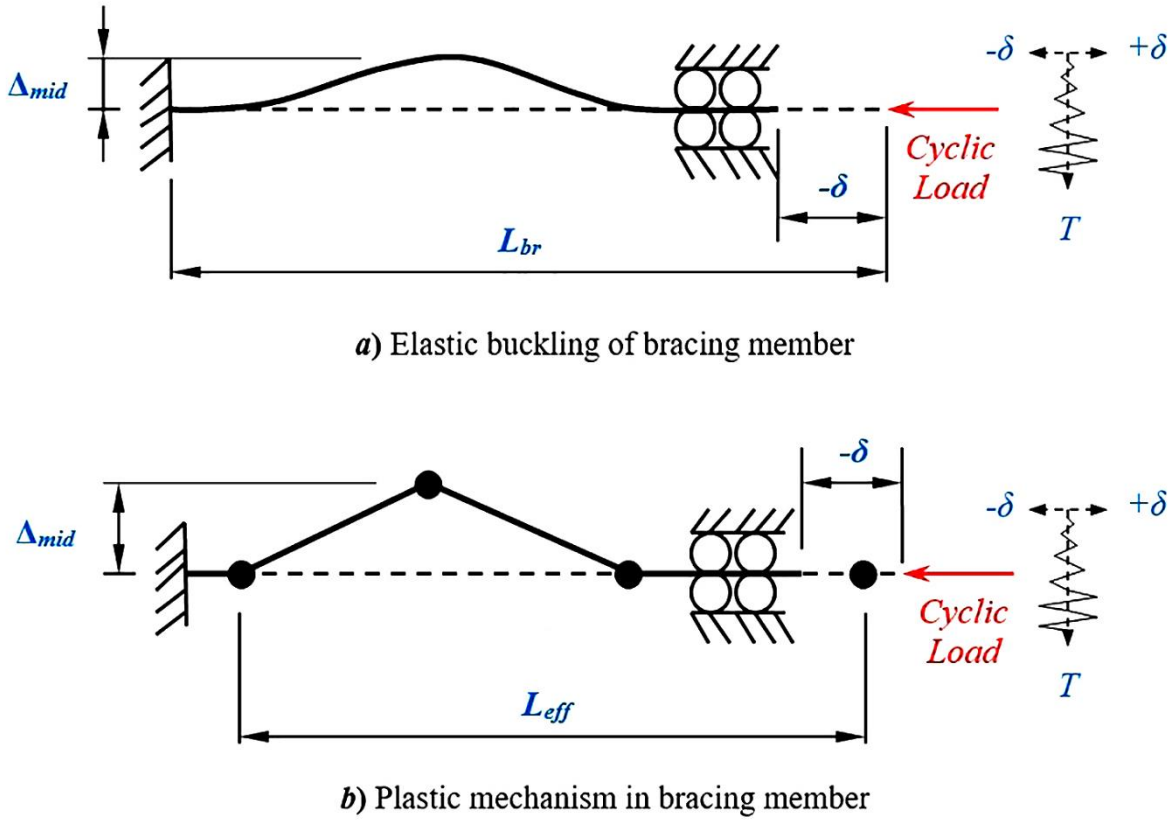

Figure 6.6 *Mid-length lateral deflection during elastic buckling and plastic mechanism in bracing member*

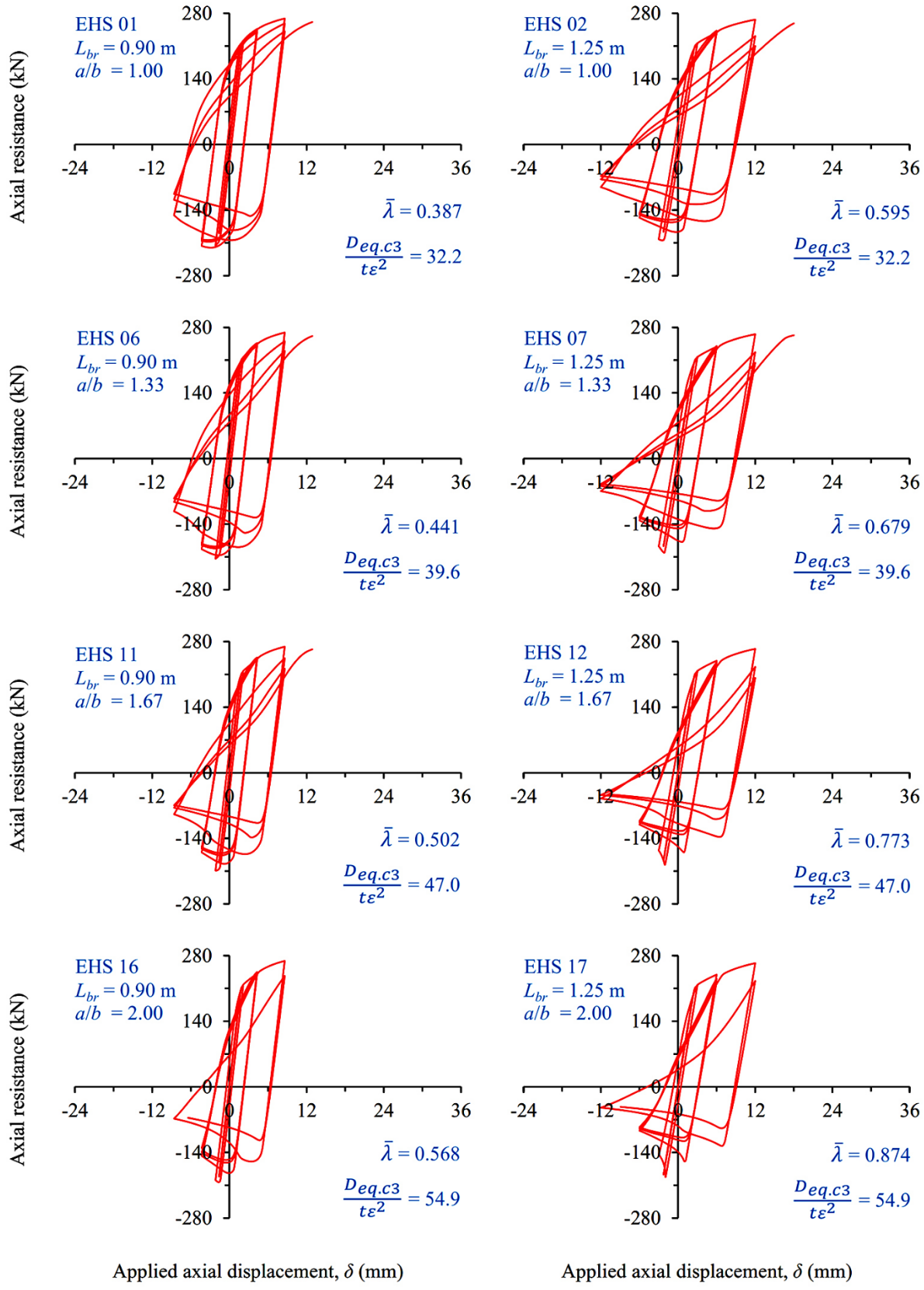

Figure 6.7 *Cyclic response of the brace models with unsupported length 0.90 m and 1.25 m*

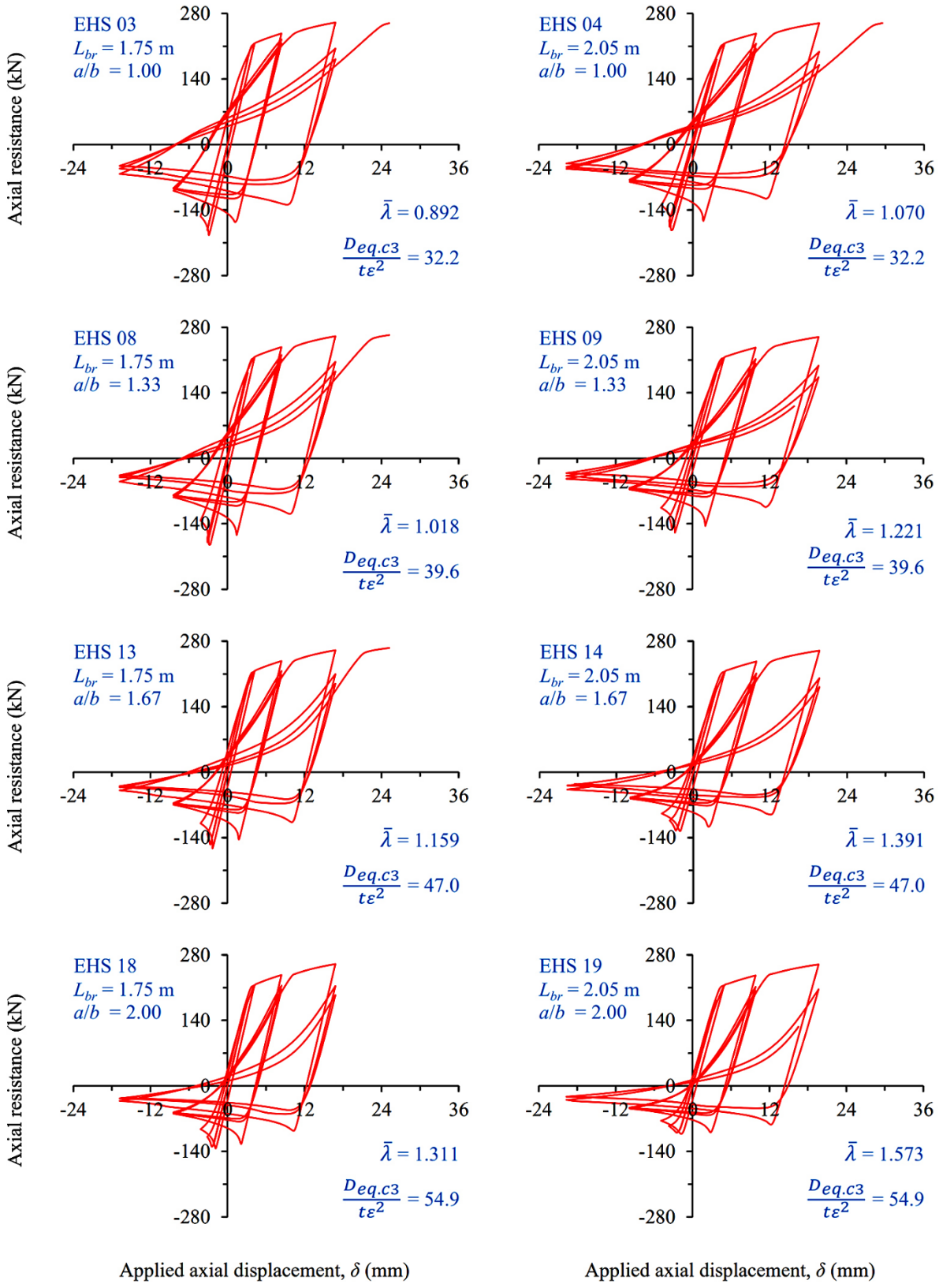

Figure 6.8 *Cyclic response of the brace models with unsupported length 1.75 m and 2.05 m*

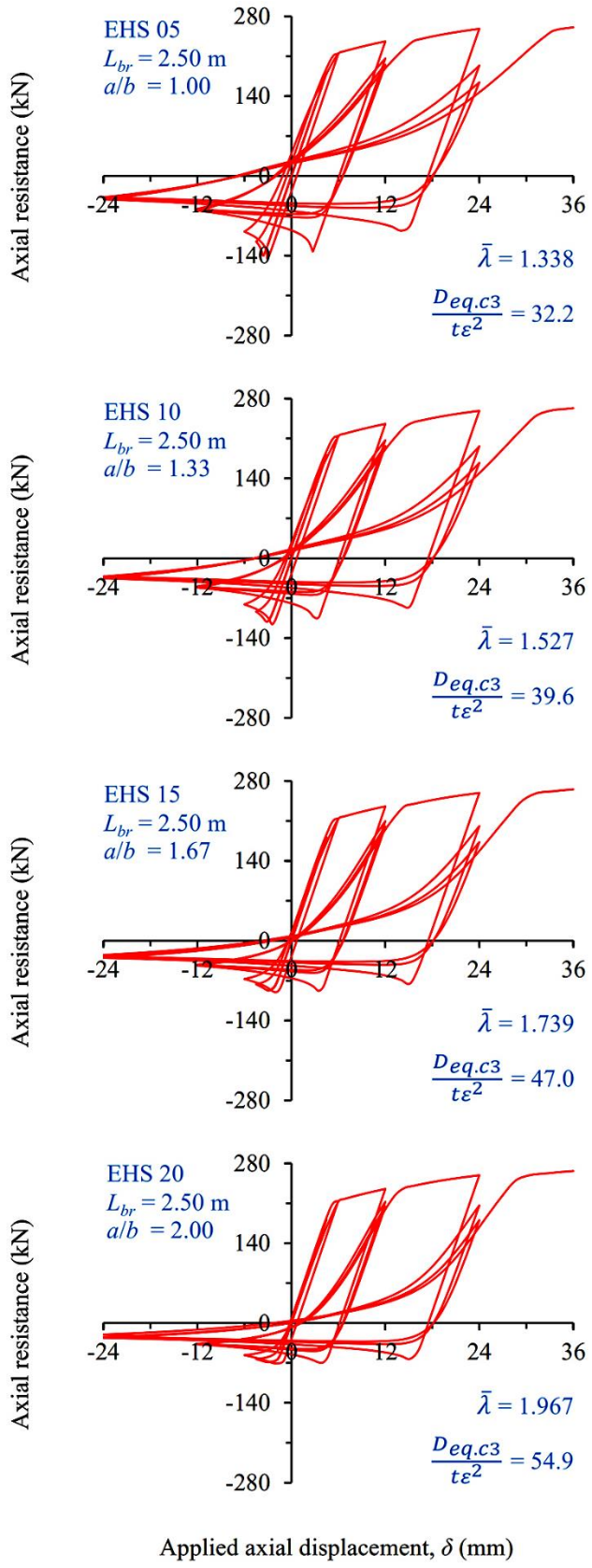

Figure 6.9 *Cyclic response of the brace models with unsupported length 2.50 m*

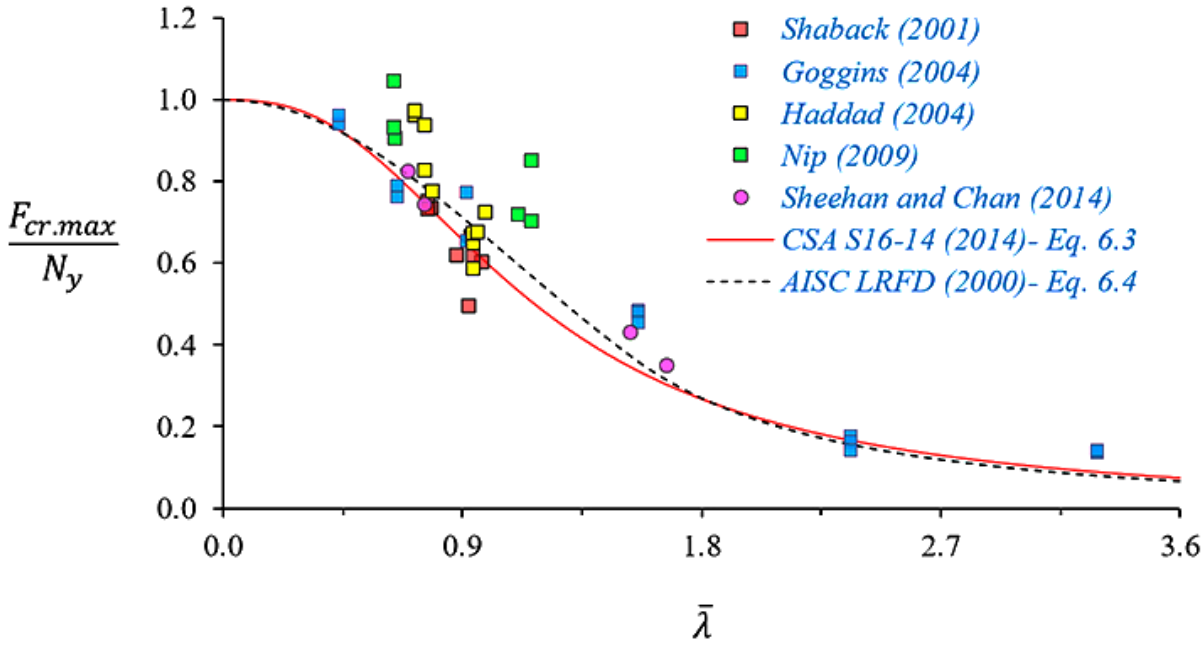

Figure 6.10 *Normalised maximum compressive resistance of HSS brace members from various experimental investigations and the codal prediction curves*

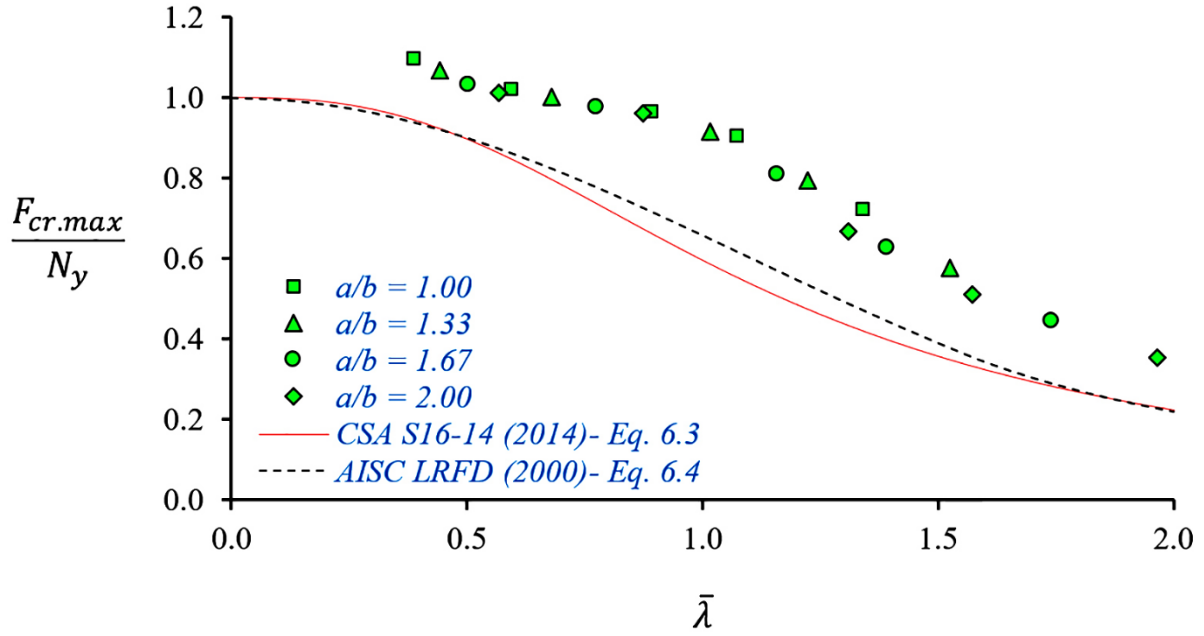

Figure 6.11 *Normalised maximum compressive resistance of the EHS FE brace models and the codal prediction curves*

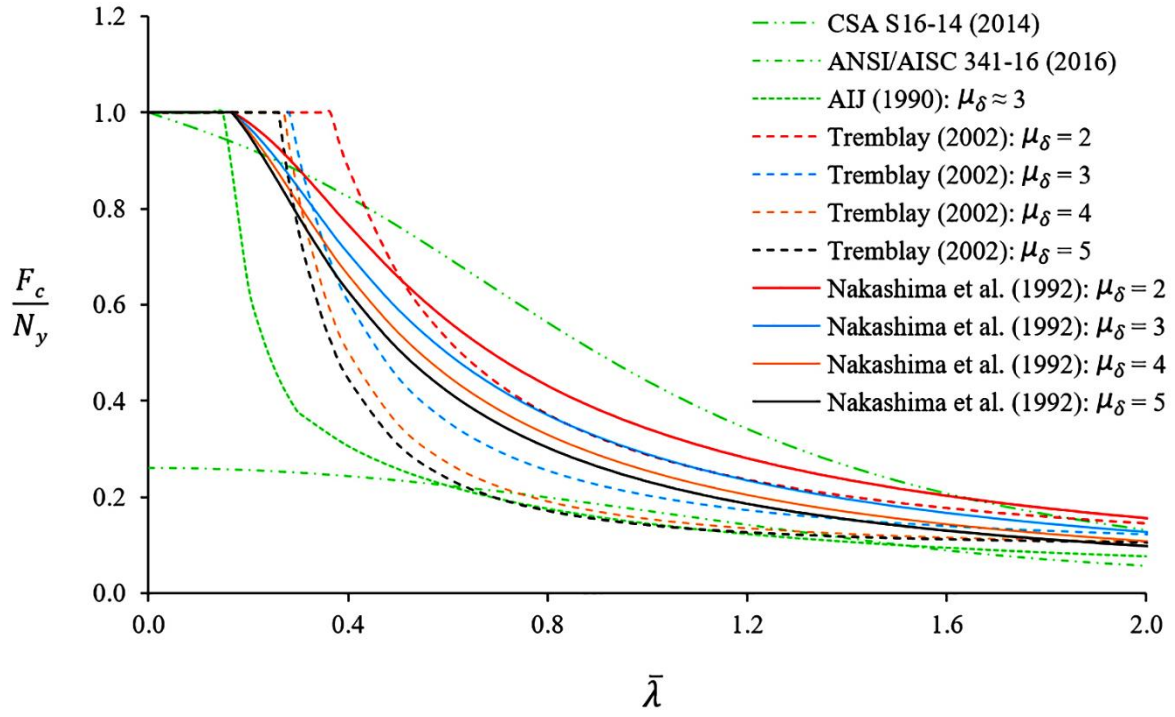

Figure 6.12 *Predictive curves for compressive resistance of steel bracing members post local-buckling*

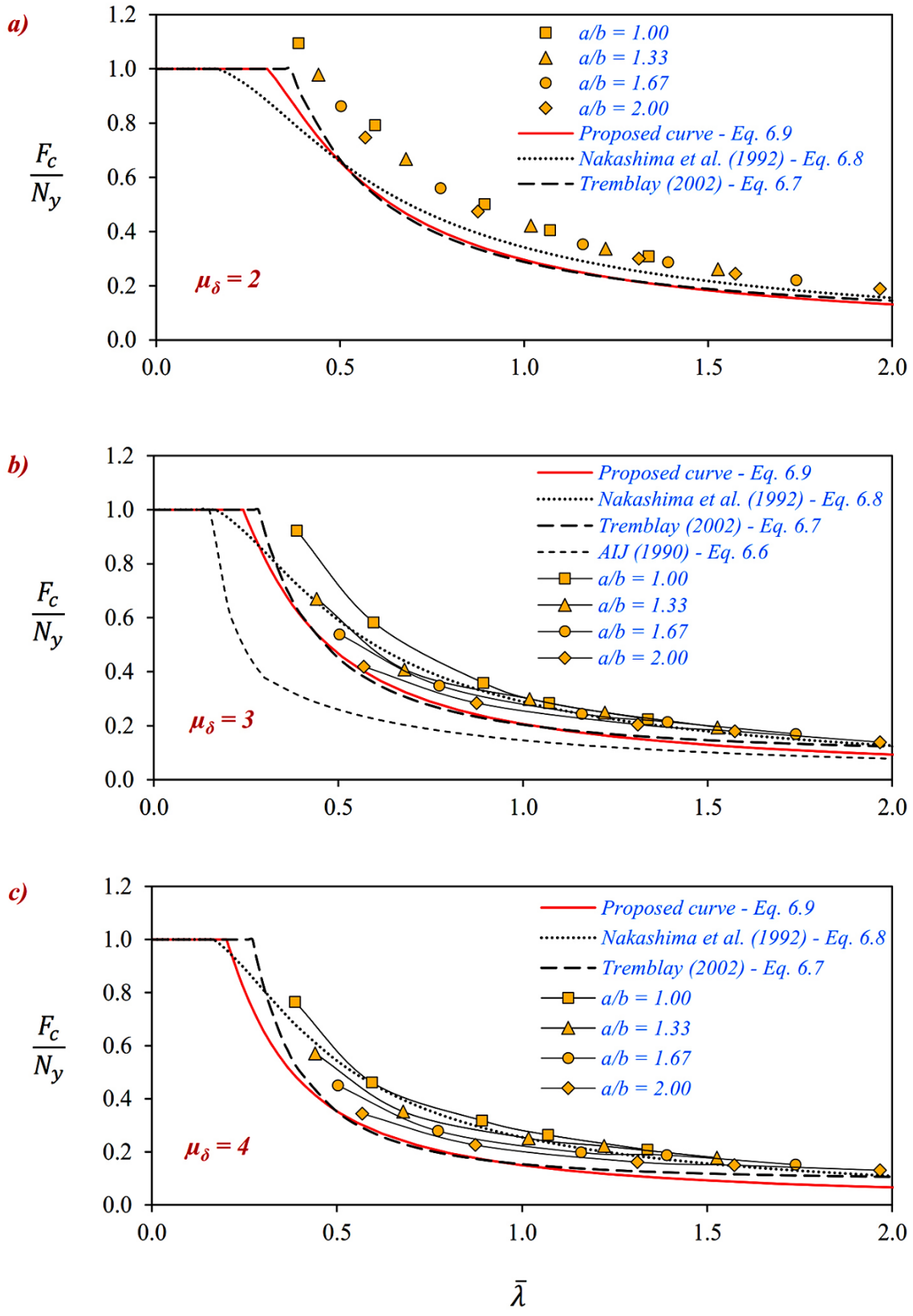

Figure 6.13 *Normalised compressive resistance of FE modelled EHS bracing members post local-buckling alongside the predictive curves at various displacement ductility levels*

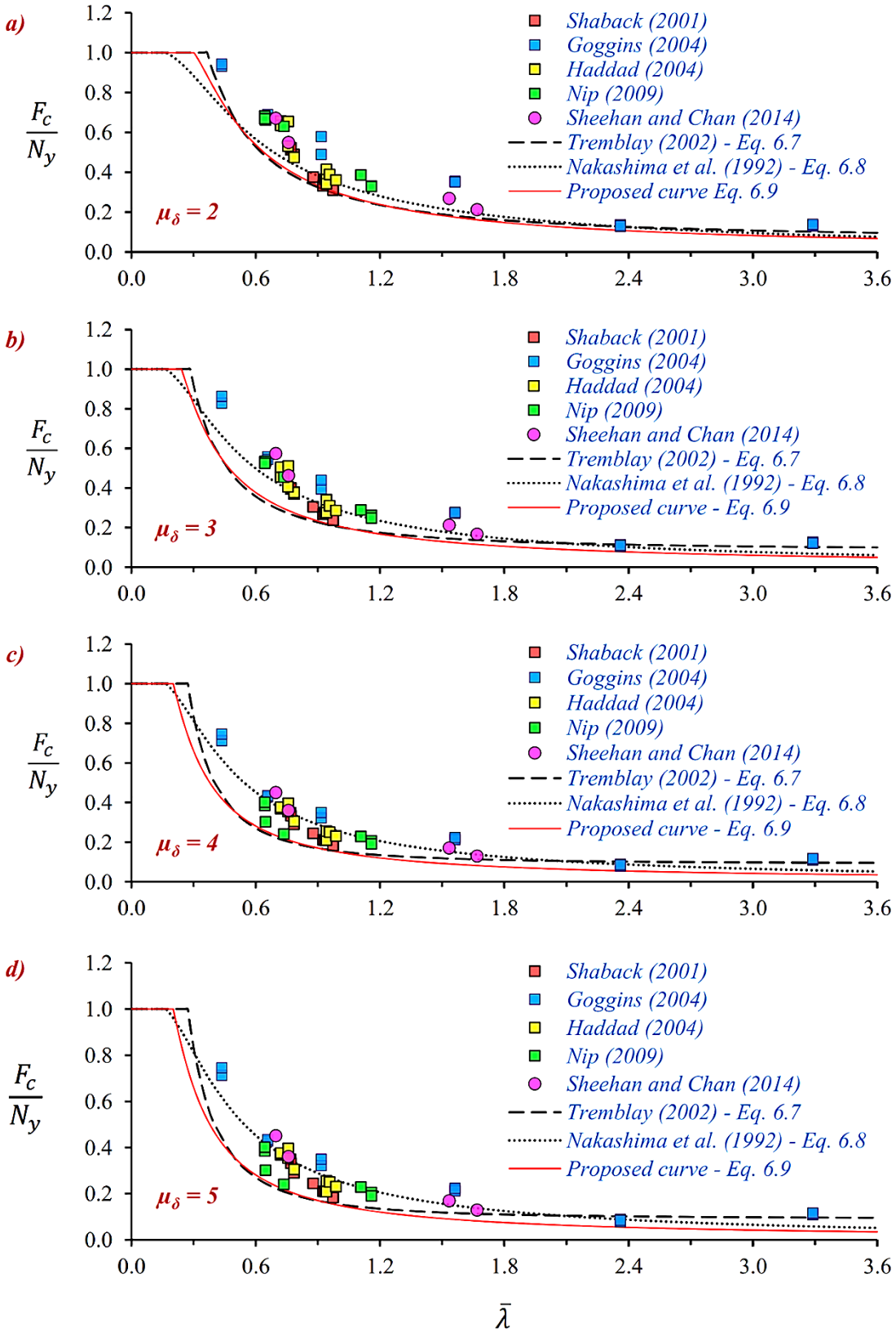

Figure 6.14 *Normalised compressive resistance of carbon-steel HSS bracing members post local-buckling alongside the predictive curves at various displacement ductility levels*

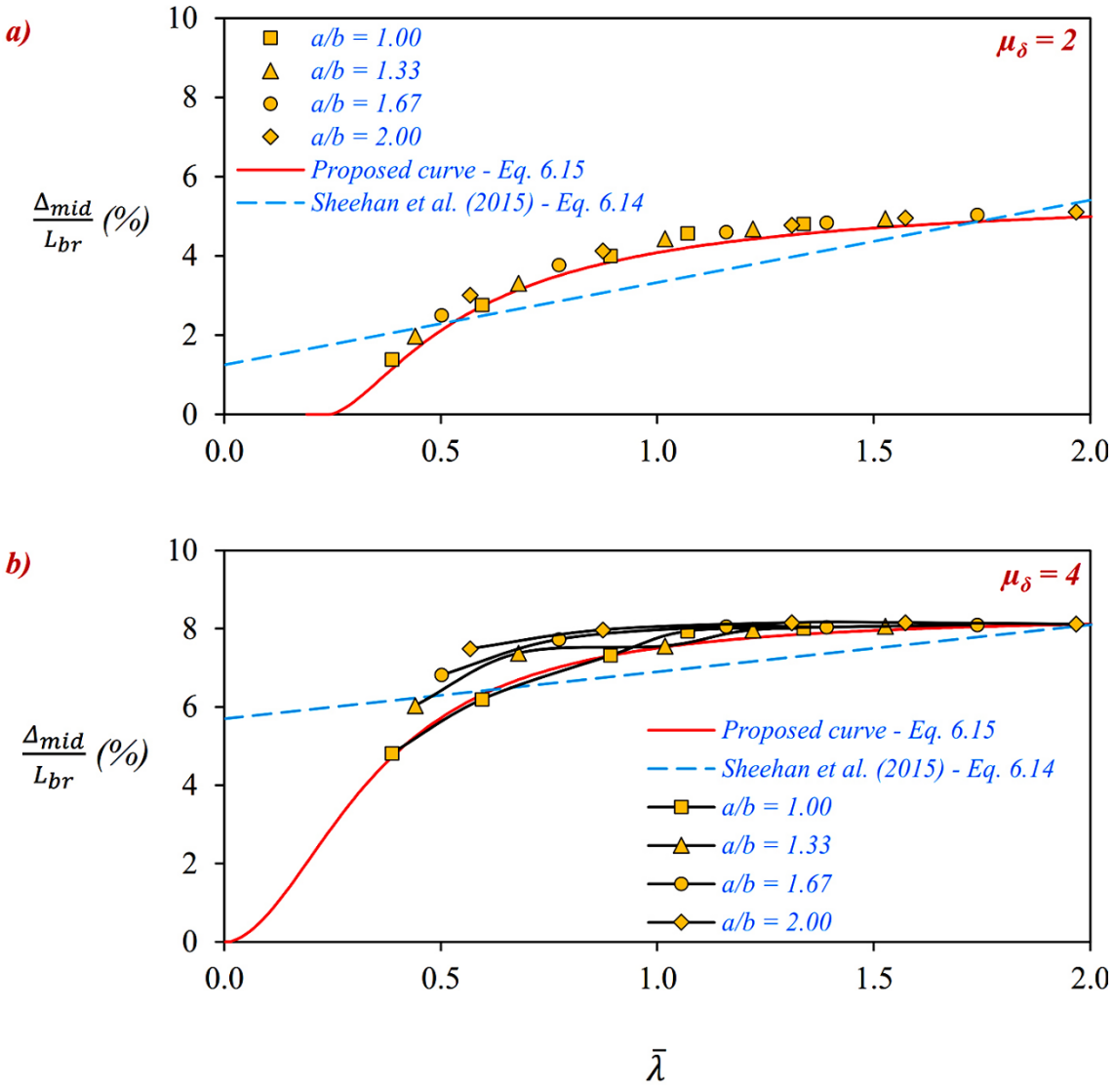

Figure 6.15 *Normalised mid-length lateral deflection of FE modelled EHS bracing members alongside the predictive curves at various displacement ductility levels*

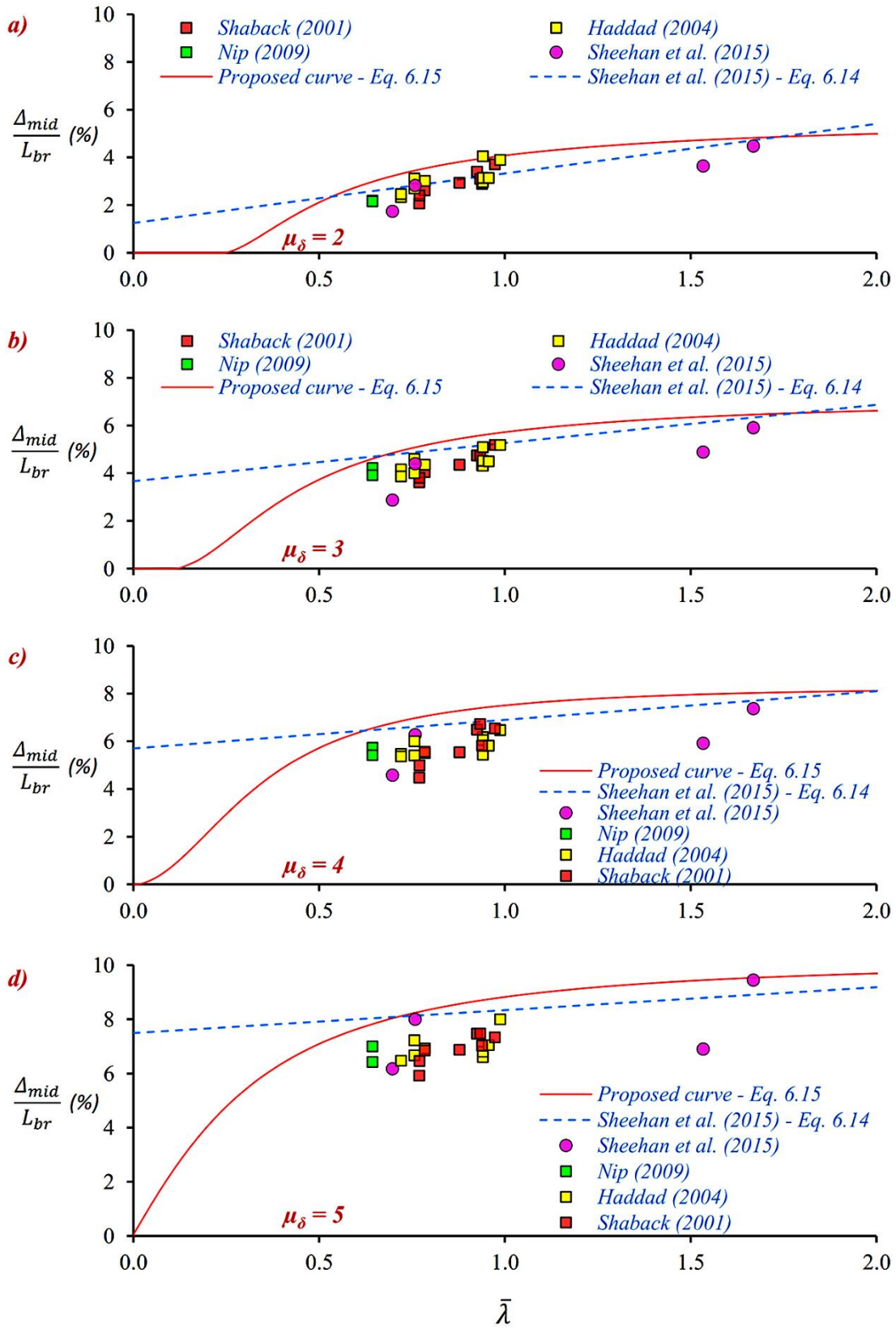

Figure 6.16 *Normalised mid-length lateral deflection of carbon-steel HSS bracing members alongside the predictive curves at various displacement ductility levels*

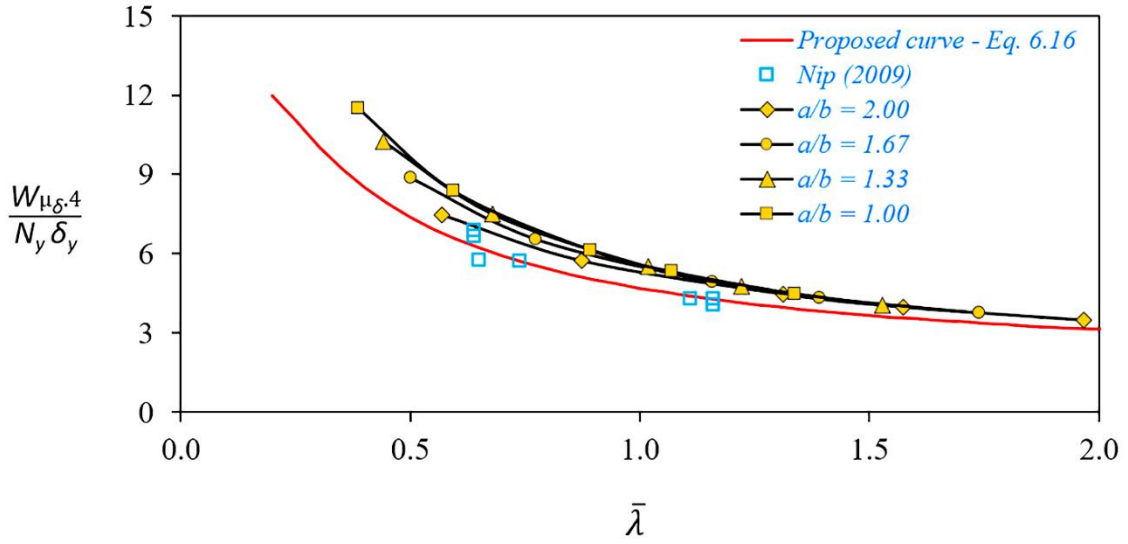

Figure 6.17 *Normalised energy dissipation of HSS bracing members during the first loading cycle at the displacement ductility level of 4*

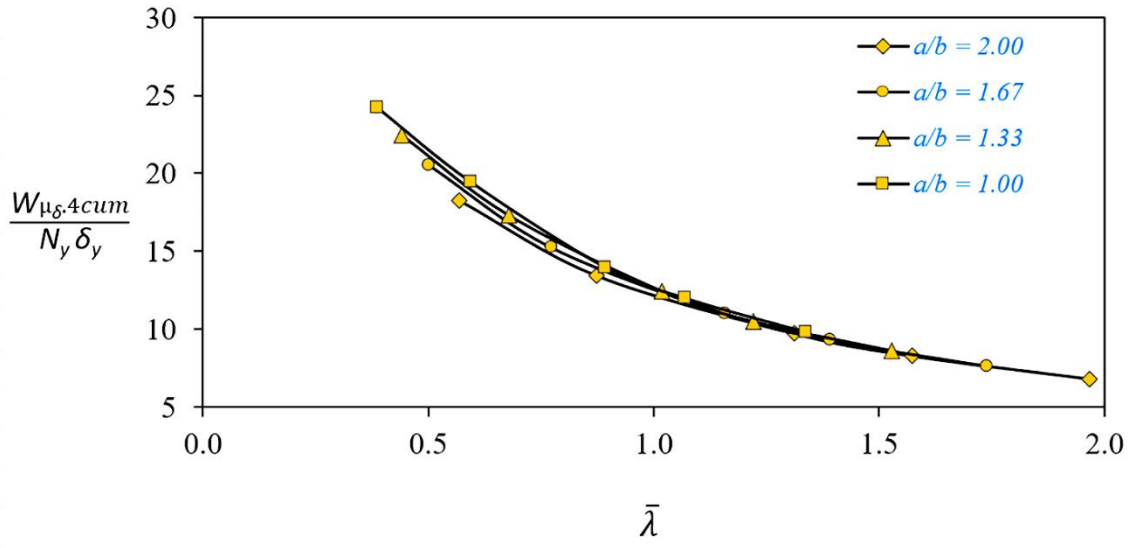

Figure 6.18 *Normalised cumulative energy dissipation of EHS FE brace models under ECCS (1986) cyclic loading upto the first loading cycle at the displacement ductility level of 4*

Table 6.1 *Geometric and material yield characteristics of the EHS brace member models*

Specimen Id.	$2a \times 2b \times t$ **(mm × mm × mm)**	$r\left(=\frac{a}{b}\right)$	$r_{g.z}$ **(mm)**	L_{br} **(mm)**	$\frac{D_{eq.c3}}{t\varepsilon^2}$	$\bar{\lambda}$	δ_y **(mm)**
EHS 01	48.7 × 48.7 × 3	1.00	16.2	900	32.2	0.387	2.1
EHS 02	48.7 × 48.7 × 3	1.00	16.2	1250	32.2	0.595	3.0
EHS 03	48.7 × 48.7 × 3	1.00	16.2	1750	32.2	0.892	4.2
EHS 04	48.7 × 48.7 × 3	1.00	16.2	2050	32.2	1.070	4.9
EHS 05	48.7 × 48.7 × 3	1.00	16.2	2500	32.2	1.338	6.0
EHS 06	55.4 × 41.6 × 3	1.33	14.2	900	39.6	0.441	2.1
EHS 07	55.4 × 41.6 × 3	1.33	14.2	1250	39.6	0.679	3.0
EHS 08	55.4 × 41.6 × 3	1.33	14.2	1750	39.6	1.018	4.2
EHS 09	55.4 × 41.6 × 3	1.33	14.2	2050	39.6	1.221	4.9
EHS 10	55.4 × 41.6 × 3	1.33	14.2	2500	39.6	1.527	6.0
EHS 11	60.0 × 36.0 × 3	1.67	12.5	900	47.0	0.502	2.1
EHS 12	60.0 × 36.0 × 3	1.67	12.5	1250	47.0	0.773	3.0
EHS 13	60.0 × 36.0 × 3	1.67	12.5	1750	47.0	1.159	4.2
EHS 14	60.0 × 36.0 × 3	1.67	12.5	2050	47.0	1.391	4.9
EHS 15	60.0 × 36.0 × 3	1.67	12.5	2500	47.0	1.739	6.0
EHS 16	63.2 × 31.6 × 3	2.00	11.0	900	54.9	0.568	2.1
EHS 17	60.0 × 36.0 × 3	2.00	11.0	1250	54.9	0.874	3.0
EHS 18	60.0 × 36.0 × 3	2.00	11.0	1750	54.9	1.311	4.2
EHS 19	60.0 × 36.0 × 3	2.00	11.0	2050	54.9	1.573	4.9
EHS 20	60.0 × 36.0 × 3	2.00	11.0	2500	54.9	1.967	6.0

Table 6.2 *Properties of the HSS brace specimens from various experimental investigations*

Test Program Reference	Test Specimen I.D.	Brace Properties							
		L_{br} (mm)	L_{eff} (mm)	A (mm^2)	$r_{g.z}$ (mm)	E (GPa)	$f_{y,\,mea}$ (MPa)	δ_y (mm)	$\bar{\lambda}$
Shaback (2001)	1B-SHS-128×126.1×7.65	3452	2589	3665	48.3	207	421	7.02	0.77
	2A-SHS-154.2×151.2×8.01	4040	3111	4645	58.6	207	442	8.63	0.78
	2B-SHS-152.8×151.2×9.24	4028	3021	5308	57.1	207	442	8.60	0.77
	3A-SHS-127.4×126.4×6.46	4456	3164	3114	48.5	207	461	9.92	0.97
	3B-SHS-128×126.1×7.65	4446	3157	3665	48.3	207	421	9.04	0.94
	3C-SHS-127.2×126.1×9.42	4414	2913	4423	47.5	207	461	9.83	0.92
	4A-SHS-153.5×151.6×8.09	4944	3708	4695	58.2	207	442	10.56	0.93
	4B-SHS-152.4×150.7×9.18	4914	3440	5246	57.5	207	442	10.49	0.88
Goggins (2004)	CyIS1-SHS-40×40×2.5	1100	715	359	15.1	209.7	309	1.62	0.44
	CyIS2-SHS-40×40×2.5	1100	715	359	15.1	209.7	309	1.62	0.44
	CyIS3-SHS-20×20×2.0	1100	715	134	7.2	209.7	309	1.62	0.92
	CyIS4-SHS-20×20×2.0	1100	715	134	7.2	209.7	309	1.62	0.92
	CyIS5-RHS-50×25×2.5	1100	715	350	10.0	209.7	309	1.62	0.66
	CyIS6-RHS-50×25×2.5	1100	715	350	10.0	209.7	309	1.62	0.66
	CyLS1-SHS-40×40×2.5	3300	2145	359	15.1	209.7	309	4.86	1.56
	CyLS2-SHS-40×40×2.5	3300	2145	359	15.1	209.7	309	4.86	1.56
	CyLS3-SHS-40×40×2.5	3300	2145	359	15.1	209.7	309	4.86	1.56
	CyLS4-SHS-20×20×2.0	3300	2145	134	7.2	209.7	309	4.86	3.29
	CyLS5-SHS-20×20×2.0	3300	2145	134	7.2	209.7	309	4.86	3.29
	CyLS6-SHS-20×20×2.0	3300	2145	134	7.2	209.7	309	4.86	3.29
	CyLS7-RHS-50×25×2.5	3300	2145	350	10.0	209.7	309	4.86	2.36
	CyLS8-RHS-50×25×2.5	3300	2145	350	10.0	209.7	309	4.86	2.36
	CyLS9-RHS-50×25×2.5	3300	2145	350	10.0	209.7	309	4.86	2.36
Haddad (2004)	1-SHS-152.7×152.9×7.82	4950	3777	4675	58.4	207	432	10.33	0.94
	2-SHS-152.7×152.9×7.75	4950	3777	4675	58.4	207	432	10.33	0.94
	3-SHS-152.6×153.1×7.78	4950	3777	4675	58.4	207	432	10.33	0.94
	4-SHS-127.4×127.7×7.81	4450	3177	3665	48.3	207	432	9.29	0.96
	5-SHS-127.5×127.7×7.81	4450	2608	3665	48.3	207	432	9.29	0.78
	6-SHS-127.4×127.7×7.86	4450	2394	3665	48.3	207	432	9.29	0.72
	7-SHS-127.5×127.7×7.89	3150	2394	3665	48.3	207	432	6.57	0.72
	8-SHS-127.8×127.7×12.77	4450	3102	5391	45.7	207	432	9.29	0.99
	9-SHS128×127.6×12.81	4450	2376	5391	45.7	207	432	9.29	0.76
	10-SHS-127.6×127.8×12.84	3550	2375	5391	45.7	207	432	7.41	0.76
Nip (2009)	60×60×3 CS-HR-SHS	2050	1332.5	716	23.1	215.2	458	4.36	0.74
	40×40×3 CS-HR-SHS	2050	1332.5	423	15.0	219.6	478	4.46	1.16
	40×40×3 CS-HR-SHS	1250	812.5	423	15.0	219.6	478	2.72	0.64
	60×60×3 CS-CF-SHS	2050	1332.5	621	23.3	207.4	361	3.57	0.65
	40×40×4 CS-CF-SHS	2050	1332.5	506.5	14.5	201.6	410	4.17	1.11
	40×40×3 CS-CF-SHS	2050	1332.5	414	14.6	212.9	451	4.34	1.16
	40×40×3 CS-CF-SHS	1250	812.5	414	14.6	212.9	451	2.65	0.64
Sheehan and Chan (2014) and Sheehan et al. (2015)	HF-H-CHS 48.6×3.2	1500	975	454.1	16.1	206	415	3.02	0.70
	CF-H-CHS 48.6×3	1500	975	407.4	16.2	184	499	4.07	0.76
	HF-H-CHS 48.6×3.2	3000	1950	454.1	16.1	206	415	6.04	1.53
	CF-H-CHS 48.6×3	3000	1950	407.4	16.2	184	499	8.14	1.67

CHAPTER 7

ELLIPTICAL-HOLLOW-SECTION CANTILEVERS UNDER CYCLIC BENDING – A FINITE ELEMENT STUDY

In this chapter, the cyclic performance of EHS cantilever beams is analysed by conducting FE simulations using Abaqus (2009). A comprehensive non-linear FE study carried out on twenty cold-formed carbon steel beams of constant cross-sectional steel area and length under ELCF uni-axial bending load along major and minor axes separately is presented by employing NLCHM model in Abaqus (2009). The cross-sectional aspect ratio (major to minor axis diameter ratio), a/b and shell thickness, t of EHS beam models are varied between 1-2.33 and 4-6 mm respectively. The adopted FE modelling procedure is validated by accurate replication of the hysteretic response of test specimens from the experimental programs detailed in the literature. Further, a parametric study is conducted to investigate the hysteresis behaviour of the EHS beam models. The effect of a/b ratio and cross-section slenderness on cyclic rotation capacity and flexural over-strength of the EHS beam models is assessed. Empirical expressions for predicting the cyclic rotation capacity and flexural over-strength are also derived.

7.1 INTRODUCTION

By the end of the 20th century, the increasing adoption of performance-based seismic design and assessment methods for buildings has highlighted the importance of estimating seismic drifts, which can be directly related to localised demands of both structural and non-structural components (Tsitos et al. 2018). In the early days, emperical models were proposed to predict the area under the hysteresis loops, *i.e.*, the amount of cyclic energy dissipation by structural members. The energy is dissipated mainly through cyclic bending from the dissipative-zones/plastic-hinges in the beams *or* the beam-column joints. The need for hysteretic models is evident in the case of structural members with excessive levels of deformation *or* inelastic strain where locally initiated damage triggers strength and stiffness deterioration eventually leading to a significant reduction of the global structural integrity.

Until the first decade of the 21st century, HSS applications have typically been limited to structural members such as columns, truss elements and bracing members. Further HSS-applications such as beam and column members in low and mid-rise frames in seismic areas can provide benefits like reduced seismic weight, lesser surface area per length of the member, decreased lateral bracing, applications in modular construction and unique retrofit techniques (Fadden and McCormick 2014). Consequently, the necessity for reliable prediction of the damage potential of new and existing steel hollow and composite structural members has motivated studies on assessing and quantifying their deformation capacity and degradation rates.

Ductility and energy-absorption capacity are important elements of seismic resistant steel member design. It has been widely deduced in the modern-day earthquake resistant design philosophy that a rational technique should explicitly evaluate the structural nonlinear cyclic performance expected to occur under the design seismic load (Mamaghani 2008). AISC 341-16 (2016) categorises the flexural members of the seismic resisting system into moderately ductile members and highly ductile members. Nowadays, for safety and economic reasons, the concept of ductility-based design has become necessary during the design of structural resistance to severe earthquake, which is a shift away from the strength-based design. The ductility-based design draws attention to both strength and ductility. The design strength of a section can be substantially reduced if it can provide a good deformation capacity beyond the elastic limit. The assumed logical strategy and procedures behind adopting yield and failure limits especially for evaluating the available ductility of structural members and their

connections should be clearly defined to enable the designers in ensuring adequate available ductility of the structures based on the target ductility criterion (Park 1988).

7.1.1 Cyclic Envelope Characteristics

The nature of carbon steel (CS) HSSs under cyclic flexural loading was analysed in the past two decades, *e.g.*, Usami et al. (2000); Elchalakani et al. (2006); D'Aniello et al. (2012); and Fadden and McCormick (2014); *etc*. Besides reiterating the importance of cross-section slenderness limits, these independent large-scale studies have also shown that the cyclic flexural-overstrength ($s_{cy.}$) and rotation capacity ($R_{cy.}$) of steel HSS beams play an important role in estimating the cyclic degradation under ELCF bending loads. Using the illustrations in Figure 7.1, $s_{cy.}$ and $R_{cy.}$ of a steel cantilever beam are explained.

It is shown in Figure 7.1a that a typical steel cantilever member of length L is under cyclic lateral displacement, δ history at the cantilever tip and its respective normalised cyclic flexural moment-rotation (M_{Cy}–θ) envelope is shown in Figure 7.1b. As shown in Figure 7.1a, M_{Cy} is the resultant cyclic moment produced at fixed-end. And, subsequently, θ is the rotation angle *or* drift angle made by an imaginary chord joining the two ends of the column which is measured at the rigid end. From Figure 7.1b, the cyclic flexural-overstrength ($s_{cy.}$) is defined in the following Equation 7.1 as the ratio of the maximum cyclic resistance moment, M_{uCy} of the section to the nominal plastic section capacity, M_p of the member.

$$s_{cy.} = \frac{M_{uCy}}{M_p} \tag{7.1}$$

$s_{cy.}$ indicates the non-dimensional measure of the ultimate bending capacity due to the amount of cyclic strain hardening which can be exhibited before the complete development of plastic mechanism (Brescia 2008, D'Aniello et al. 2012).

The cyclic rotation capacity ($R_{cy.}$) represents the ability of a flexural member to fulfil the rotational prerequisite in terms of rotation ductility. From Figure 7.1b, the cyclic rotation capacity ($R_{cy.}$) can be determined as per the following Equation 7.2.

$$R_{cy.} = \frac{\theta_u}{\theta_p} - 1 \tag{7.2}$$

where, θ_p is the elastic component of member rotation upon reaching the resistance level of M_p initially and θ_u is the limiting rotation at which the moment resistance falls back below M_p in the post-peak zone (D'Aniello et al. 2012).

$R_{cy.}$ is considered as the most effective parameter for experimental purposes, *e.g.*, Elchalakani et al. (2006); D'Aniello et al. (2012); and Fadden and McCormick (2014); *etc*. In general, it was deduced that $R_{cy.}$ of a beam is essential to ensure that a determined portion of the input seismic energy is dissipated by inelastic behaviour. Therefore, steel beams need to undergo a ductile flexural pattern with a higher $R_{cy.}$ value. However, the evaluation of the minimum $R_{cy.}$ required is even more complex for a seismic design application, because it is also strictly related to the design value of the behaviour factor, the intensity measure of the seismic event and its frequency content (Brescia 2008, D'Aniello et al. 2012). Plastic design rules are being evolved for establishing the limiting beam cross-sectional dimensions to satisfy a predefined $R_{cy.}$ value. It should be noted that $R_{cy.}$ is defined based on the concept of resistance drop beyond the nominal plastic section capacity, M_p (Figure 7.1b) after reaching the maximum cyclic moment of resistance limit, M_{uCy}. However, a failure rule defined by a 20% resistance drop measured with-respect-to M_{uCy} is suggested in both FEMA 350 (2000) and AISC 341-16 (2016).

7.1.2 Problem Statement

During the first two decades of the 21st century, with the ever-increasing computational power and the development of efficient algorithms and software platforms for ELCF type of loading simulations, enhanced analytical models also have been evolved to accurately predict the behaviour and understand the different failure modes of HSS members under cyclic loads. To predict the cyclic flexural behaviour of box section columns, Usami et al. (2000) used a modified two-surface plasticity model (2SM) which was developed at Nagoya University, Japan. Recently, Varelis and Karamanos (2014) and Fadden and McCormick (2014) employed NLCHM within Abaqus (2009).

The compact cross-sections having higher $R_{cy.}$ value with the lesser effect of ovalisation are highly ductile *or* plastic and can develop large inelastic deformations and plastic hinges, *e.g.*,

Kyriakides and Shaw (1987); Lee et al. (2001); Elchalakani et al. (2004); *etc*. Hence, these are preferred in the design of high dissipative structural configurations (Elchalakani et al. 2004, D'Aniello et al. 2012). It is assumed that the semi-compact (elasto-plastic) cross-sections could also exhibit some amount of R_{cy}, especially due to the cyclic hardening of the material. Therefore, the assessment of the adequacy of plastic and elasto-plastic cross-sections to satisfy the cyclic flexural demands imposed under seismic conditions is entailed. Also, there is no study on the cross-sectional parameters of EHS under ELCF bending load available to date to the best of the authors' knowledge.

Therefore, the main objective of this study is to assess the cyclic flexural performance of EHS steel beams under the ELCF bending load by evaluating the parameters like $R_{cy.}$ and $s_{cy.}$ with-respect-to their a/b ratio using FE modelling approach and furnish a comprehensive structural and reliable earthquake-resistant guidance according to the state of the art in seismic engineering to promote the wider application of EHS in practice.

7.2 FINITE ELEMENT MODELLING

Abaqus (2009) has been used to analyse the performance of EHS steel cantilever beam models under the ELCF bending load. The attributes of shell FE modelling framework adopted herein and presented in the subsequent sub-sections follow those reported in Nip et al. (2010b) and Fadden and McCormick (2014).

7.2.1 Geometric and Material Characteristics

Twenty EHS steel cantilever beams (Table 7.1) with four sets of 't' ranging between 4 mm and 6 mm, a/b ratios ranging between 1 and 2.33 are modelled with A_o ~ 1740 mm^2 which is equal to that of a 150×75×5 mm ($2a$×$2b$×t) EHS beam model and with a span length (L) of 1500 mm. P_M values in Table 7.1 are calculated according to Equation 2.1. While W_{ey}, W_{py}, W_{ez}, and W_{pz} values are calibrated as per the expressions catalogued in Table 2.1. All the twenty models are analysed under cyclic bending load about both major and minor axis separately making it a total of 40 (20+20) FE analyses (FEAs). The mechanical and NLCHM model parameters are extracted from Nip et al. (2010a) for S235JRH grade CF-CS (see Table 2.3), which is assumed herein as the reference material during material modelling of EHS beams whose geometric

properties are catalogued in Table 7.1. The cross-section classification is made based on the cross-section slenderness, $\bar{\lambda}_{cs.E}\left(=\frac{D_{NSb.mj}}{t\varepsilon^2}\ or\ \frac{D_{NSb.mn}}{t\varepsilon^2}\right)$ values calculated as per Equations 4.26 and 4.27. Barring EHS17Cb specimen model under minor axis bending which can be almost classified as an Elasto-plastic cross-section, all cross-sections are deemed either Compact (*i.e.*, Class 1 *or* Class 2) *or* Elasto-plastic (*i.e.*, Class 3) under major *or* minor axis bending according to the proposed EC3: EN 1993-1-1 (2005) slenderness limits in Table 4.4.

Apart from the twenty EHS models listed in Table 7.1, eight other EHS cantilever beam models whose geometrical and material properties listed in Table 7.2 are also considered for the cyclic bending performance study through FEAs. Unlike the models listed in Table 7.1, models listed in Table 7.2 are of different steel grades whose mechanical and NLCHM model parameters are already catalogued in Table 2.3.

7.2.2 Meshing

S4R, a three-dimensional four-node doubly curved quadrilateral robust general-purpose reduced integrated and structured stress/displacement shell element with six degrees of freedom, hourglass control, finite membrane strains and five integration points through the thickness available in Abaqus (2009) element library based on thick-shell theory is employed herein for meshing the brace models (Laulusa et al. 2006). As the formulation of this element accounts for large strains and rotations (transverse shear deformations) and thus allowing the changes in thickness with deformation, it has been successfully employed in previous studies (Nip et al. 2010b, Fadden and McCormick 2014) for accurately simulating the behaviour of HSS beams, bracings and compression members under cyclic loading.

Considering the computational time, a similar meshing pattern described in the FE simulation study of Fadden and McCormick (2014) is adopted for meshing the EHS cantilever models herein. The extent of the refined mesh in the longitudinal direction is set to ~ 4*a* including the transition zone from the fixed end as shown in Figure 7.2 for a typical cantilever beam model. Therefore, ensuring a sufficiently large refined area at the fixed end zone where the plastic hinge and local buckling are most likely to occur when the beam is subjected to cyclic lateral bending displacement load history at the free end. The espoused element ratio in the regions of refined mesh is as low as 1 and in the elastic regions (*i.e.*, coarse mesh zones) of the model is

1 to 2 (Figure 7.2). The number of S4R elements used in the analyses for various models ranges from ~ 4,500 – 6,500.

7.2.3 Boundary Conditions and Imperfections

Boundary conditions simulating a fixed-end cantilever beam with one end (bottom end) completely fixed (*i.e.*, all the six degrees of freedom restrained for all nodes at the end) and the opposite end free to displace laterally according to the cyclic bending displacement loading history (see Figures 7.1a and 7.3).

In reality, all structural members contain initial geometric imperfections. These imperfections trigger out-of-plane deflections at stresses below the theoretical critical buckling limits. In this study, both global and local initial geometric imperfections are seeded into the FE models by defining the nodes directly in their imperfect configuration based on the superposition of weighted eigenmode analysis data. Their respective typical lowest buckling mode shapes resulted from linear eigenvalue buckling analysis (obtained through the Lanczos method) for a typical FE cantilever model (EHS15Cb) are shown in Figure 7.4. Local imperfection amplitude, ω_{l0} range of $\frac{t}{6.67}$ to $\frac{t}{10}$ reflect the maximum allowable thickness tolerance as per EN 10210-2 (2006), EN 10219-2 (2006), AS/NZS 1163 (2016), ASTM A501-01 (2005) specifications. But, usage of higher values of ω_{l0} with a range of $\frac{t}{3}$ to $\frac{t}{6}$ is also shown to provide better accuracy in the replicating the experimental structural response by Sun and Butterworth (1998), Gardner (2002), Huang and Young (2012), Fadden (2013) and Shokouhian and Shi (2015). Also, based on Dawson and Walker (1972) predictive model, Gardner et al. (2010) and Gardner and Nethercot (2004) proposed modified models for determining ω_{l0} in hot-rolled, cold-formed carbon steel and stainless-steel HSSs. Initial local imperfections are embodied into the respective FE models herein with values of ω_{l0} ranging between $\frac{t}{4.5}$ and $\frac{t}{6}$ based on the imperfection sensitivity analyses carried out by Sun and Butterworth (1998), Gardner (2002), Huang and Young (2012) and Fadden (2013).

Global imperfection amplitude, ω_{g0} equal to $L_{eff.}/250$ reflect the current allowable out-of-straightness tolerance for EHS tubes with $2a < 250mm$ in EN 10210-2 (2006), where L_{eff} is effective length of the column member based on its critical buckling load. While, the maximum allowable out-of-straightness tolerance limit of $L_{eff.}/500$ is stipulated for hollow sections of other shapes, namely circular, square and rectangular in EN 10210-2 (2006), EN 10219-2 (2006), AS/NZS 1163 (2016), ASTM A501-01 (2005) specifications (Chan and Gardner 2009, Wardenier et al. 2010). However, $L_{eff.}/500$ is also stipulated as out-of-straightness tolerance for EHSs with $2a > 250mm$ in EN 10210-2 (2006). Hence, EHSs with lesser outer major diameter values under combined axial compression and bending loadings are envisaged to possess higher global imperfection amplitudes which can be greater than $L_{eff.}/500$. Global imperfection amplitude of $L_{eff.}/500$ was successfully used in numerical studies of Law and Gardner (2013b), Law and Gardner (2013a) and Coelho et al. (Coelho et al. 2013)(2013). An imperfection amplitude of $L_{eff.}/360$ is used during the numerical study of EHS columns under compression load by Scullion et al. (2012).

However, it is to be noted that the inclusion of ω_{g0} is not effective in the absence of the axial compressive load. But, the description of ω_{g0} inclusion herein is to accommodate the cyclic bending specimens with axial compression load from in the experimental studies of Chung et al. (2007) and Nakashima and Liu (2005) in the upcoming FE modelling procedure validation Section 7.2.4.

The EHS cantilevers are modelled herein as cold-formed members. And, according to EN 1993-1-1 (2005), the performance of Cold-Formed (CF) and Hot-Finished (HF) HSSs do not differ with-regard-to the tension and bending resistances. Therefore, as already mentioned in Section 1.3, the residual stresses are not explicitly incorporated into the EHS cantilever models herein due to the absence of axial compressive force.

SAC protocol (ANSI/AISC 341-16 2016) loading pattern described in Section 2.3.2 (Figure 7.5) representing a far-field earthquake motion is being endorsed for interpreting the member behaviour of a moment connection during laboratory tests to make their quotients commensurable at an international level in seismic design (Fadden and McCormick 2014). The reference for increasing the amplitude of loading cycles in this protocol is the drift angle, θ which is the rotation of the imaginary straight line joining fixed end and the free (or pinned) end of the laterally loaded beam as shown in Figures 7.1a and 7.3. For small θ up to 0.3 rad.,

lateral displacement, δ to be applied at the free end of the beam along the major *or* minor axis as shown in Figure 7.3 can be calculated as the product of θ and L. The lateral cyclic loading history contains six cycles at each level of 0.00375, 0.005, 0.0075 rad., followed by four cycles at the level of 0.01 rad. and two cycles at each level of 0.015, 0.02, 0.03, 0.04, 0.05 rad. *etc.*, as shown in Figure 7.5. D'Aniello et al. (2012) and Fadden and McCormick (2014) are amongst those who chose to practice the SAC protocol (ANSI/AISC 341-16 2016) loading pattern while testing steel hollow tubular beams in the recent years. Hence, the SAC cyclic loading pattern outlined in AISC 341-16 (2016) is chosen to apply with a strain rate of $3\times10^{-4}s^{-1}$ which is within the quasi-static testing range as per BS 7270 (2006) at the free end of the cantilever models through a "*reference point*" that acts as a pin to which all the circumferential nodes of the model in the loading plane are tied to by "*Kinematic Coupling*" available in the "*Constraint*" module of Abaqus (2009). The non-linear geometric parameter (NLGEOM) is also assigned in the analysis step to deal with large displacement analysis.

7.2.4 Validation of the FE Modelling Approach

To substantiate the FE modelling approach labelled previously in this Section 7.2, FEAs are carried out in the initial part of the study to replicate the cyclic behaviour of three CF-CS RHS cantilever beams from Fadden (2013) and three CF-CS SHS columns each from Chung et al. (2007) and Nakashima and Liu (2005).

During modelling the specimens of Fadden (2013), the mechanical and NLCHM model parameters of ASTM A500 Gr.B steel are extracted from Fell (2008) (Table 2.3). A comparison of cyclic behaviour of FE models of those test specimens in terms of hysteretic loops is shown in Figures 7.6a, 7.6b and 7.6c.

Further, due to very close material properties, NLCHM model parameters of BCR295 steel from Suzuki (2018) (Table 2.3) are used in modelling three CF-CS SHS columns of Chung et al. (2007). Figures 7.6d, 7.6e and 7.6f show a comparison of cyclic behaviour of FE models of those test specimens in terms of hysteretic loops.

Also, the response of three specimens from Nakashima and Liu (2005) is simulated using the same FE modelling approach and the comparison between their experimental and simulated hysteresis loops is shown in Figures 7.6g, 7.6h and 7.6i. The NLCHM model parameters of

BCR295 grade CF-CS from Suzuki (2018) (Table 2.3) are used during material modelling of the specimens.

Lastly, a comparison between the deformation pattern near the plastic hinge region of the FE simulated models in the current study with those of the respective specimens available from Fadden (2013) and Nakashima and Liu (2005) is shown in Figures 7.6j–7.6m.

Figures 7.6a–7.6m indicate that the FE modelling approach described previously in this Section is capable of simulating the hysteretic behaviour well for the EHS steel cantilever models under the cyclic bending load. The initial stage differences between the experimental and FE modelling outcomes could be due to the consideration of a relatively similar material during the FE modelling instead of the original steel used in the experimental study of Nakashima and Liu (2005). Further, due to the limited number of parameters ($\sigma|_0$, C_{kin}, γ_{kin}, Q_∞, b_{iso}) in the NLCHM model considered herein employing Abaqus (2009) during FE modelling and the sensitivity of the initial geometric imperfections, the hysteretic pattern cannot always be replicated accurately at maximum and minimum strains.

7.3 PARAMETRIC STUDY

By employing the FE simulation mechanism discussed in the previous Section 7.2, M_{Cy}-θ hysteresis loops of EHS cantilever beam models catalogued in Tables 7.1 and 7.2 are shown in Figures 7.7–7.13. A backbone envelope which is the locus of the tips of moment-rotation hysteresis curves during the first cycle at each level of rotation applied for all the models in their respective all-positive quadrant is also constructed in Figures 7.7–7.13. $s_{cy.}$ and $R_{cy.}$ of all the models are calibrated for their respective backbone envelope in Tables 7.3 and 7.4 following the terminology explained in Figure 7.1 and Equations 7.1 and 7.2. δ_p and δ_{uCy} in Tables 7.3 and 7.4 are the corresponding displacements at free-end of the beam for the drift angles θ_p (= δ_p/L) and θ_u (= δ_{uCy}/L) measured at the fixed end. Hence, $R_{cy.}$ in Equation 7.2 is deciphered in terms of δ_p and δ_{uCy} and expressed as shown in the following Equation 7.3.

$$R_{cy.} = \frac{\theta_u}{\theta_p} - 1 = \frac{\delta_{uCy}}{\delta_p} - 1 \tag{7.3}$$

Further, the effects of a/b ratio and $\bar{\lambda}_{cs.E}\left(=\frac{D_{NSb.mj}}{t\varepsilon^2}\ or\ \frac{D_{NSb.mn}}{t\varepsilon^2}\right)$ on their hysteretic parameters like $R_{cy.}$ and $s_{cy.}$ are investigated.

7.3.1 Results and Discussion

Although EHS01Cb–EHS20Cb models have different a/b ratio and t values, it should be noted that they all have the same A and L values.

In case of EHS cantilever models under major-axis *or* minor-axis cyclic bending, it is observed from Figures 7.8–7.11 (from top to bottom) that with the increase in t value and with same a/b ratio, M_{uCy} decreases due to decrease in cross-section moduli values with same A, while θ_u increases as the ductility increases with increase in t value.

In case of EHS cantilever models under major-axis cyclic bending, it is observed from Figures 7.8 and 7.9 (from left to right) that with the increase in a/b ratio, both M_{uCy} and θ_u increases for sections with the same t value due to the increase in cross-section moduli values.

In case of EHS cantilever models under minor-axis cyclic bending, it is observed from Figures 7.10 and 7.11 (from left to right) that with the increase in a/b ratio, M_{uCy} decreases due to decrease in cross-section moduli with same A, while θ_u increases as the ductility increases with increase in t value. Further, from Figures 7.10 and 7.11 (from left to right) it is observed that with the increase in a/b ratio, M_{uCy} decreases and θ_u increases for sections with same t value due to the gradual change in the behaviour from tubular type pattern to ductile plate type pattern.

The normalized cyclic moment resistance and the rotation capacity values from Tables 7.3 and 7.4 are plotted against their respective cross-section slenderness, $\bar{\lambda}_{cs.E}\left(=\frac{D_{NSb.mj}}{t\varepsilon^2}\ or\ \frac{D_{NSb.mn}}{t\varepsilon^2}\right)$ values calculated as per Equations 4.26 and 4.27 in Figures 7.14–7.16. The empirical expressions for the lower-bound fit curves of the predictive maximum sectional cyclic moment, $M_{uCy.pr}$ and rotation capacity, $R_{cy.pr}$ of the EHSs are derived using the data plotted in Figures 7.14–7.16 from tables 7.3 and 7.4 and are expressed in the following Equations 7.4–7.6.

$$\frac{M_{uCy.pr}}{M_e} = \frac{3033.036 - 135.35\overline{\lambda}_{cs.E}^{0.5} + 0.121\overline{\lambda}_{cs.E}}{893.62 + 88.59\overline{\lambda}_{cs.E}^{0.5} - 6.0685\overline{\lambda}_{cs.E}} \quad \text{if} \quad 10.81 \le \overline{\lambda}_{cs.E} < 251.31 \tag{7.4}$$

$$s_{cy.pr} = \frac{M_{uCy.pr}}{M_p} = \frac{1818.785 - 101.034\overline{\lambda}_{cs.E}^{0.5} - 0.5565\overline{\lambda}_{cs.E}}{893.62 + 27.245\overline{\lambda}_{cs.E}^{0.5} - 4.9406\overline{\lambda}_{cs.E}} \tag{7.5}$$

$$\text{if} \quad 10.81 \le \overline{\lambda}_{cs.E} < 251.31$$

$$R_{cy.pr} = \left(\frac{5823.364}{\overline{\lambda}_{cs.E}}\right)^{0.5} - \frac{348.6}{\overline{\lambda}_{cs.E}} + \left(\frac{84.894}{\overline{\lambda}_{cs.E}}\right)^{1.5} - 3.7534 \quad \text{if} \quad 10.81 \le \overline{\lambda}_{cs.E} < 251.31 \tag{7.6}$$

In Figures 7.14 and 7.15, the prediction curves representing Equations 4.3 and 4.10 are also plotted for comparison purpose.

7.3.2 Shear-force Check

The extent of involvement of shear force developed in the cross-section of the beams at the fixed end on their $R_{cy.}$ and $s_{cy.}$ values is checked by comparing their maximum shear force, V_u obtained from FEAs with their respective plastic section shear resistance, V_p in Tables 7.3 and 7.4. The expression for V_p is given in Equation 7.7 which is specified in EC3: EN 1993-1-1 (2005).

$$V_p = \frac{A_v\left(f_{y.mea}/\sqrt{3}\right)}{\gamma_{M0}} \tag{7.7}$$

Where γ_{M0} is the partial factor corresponding to the cross-section resistance and is taken in this study as 1.00 as per the stipulations of EC3: EN 1993-1-1 (2005) and A_v is the shear area of the cross-section. The expression for A_v of EHS according to Chan (2007) is given as follows:

$$A_v = \begin{cases} 2(2a - t)t; & \text{for major-axis cyclic bending} \\ 2(2b - t)t; & \text{for minor-axis cyclic bending} \end{cases} \tag{7.8}$$

While V_u values are obtained by dividing the M_{uCy} values with their respective L values.

From Tables 7.3 and 7.4, either in major-axis cyclic bending *or* minor-axis cyclic bending maximum of V_u values tabulated is only ~13.9% of the respective V_p value which is much lesser than 50% as per clause 6.2.8 of EC3: EN 1993-1-1 (2005) to neglect the effect of shear force on bending resistance when the sections are under bending and shear. On the other hand, in Tables 7.3 and 7.4, all the $s_{cy.}$ values are greater than 1, except for EHS22Cb model under minor-axis cyclic bending.

Hence, the proposed Equations 7.4–7.6 are based only on pure cyclic flexural bending and are completely free from the effect of shear. Also, the effect of lateral torsion is assumed to be negligible due to the lesser magnitudes of the L values considered for the EHS models herein.

7.4 SUMMARY

The performance of carbon-steel EHS FE cantilever beam models under ELCF uni-axial bending load following the SAC protocol (ANSI/AISC 341-16 2016) loading pattern is analysed. A parametric study is performed on the cross-sectional characteristics like cyclic rotation capacity and flexural over-strength. The deductions from the parametric study are summarised as follows:

- The empirical expressions for the predictive cyclic-moment-resistance-capacity and cyclic-rotation-capacity curves of EHSs with-respect-to their CHS cross-section slenderness are established.
- The effect of cross-sectional aspect ratio on cyclic-moment-resistance and cyclic-rotation capacities of EHSs with-respect-to their non-dimensional CHS cross-sectional slenderness is found to be insignificant.
- The difference of sectional cyclic moment from normal moment resistance capacity is found to be ~ 30%.

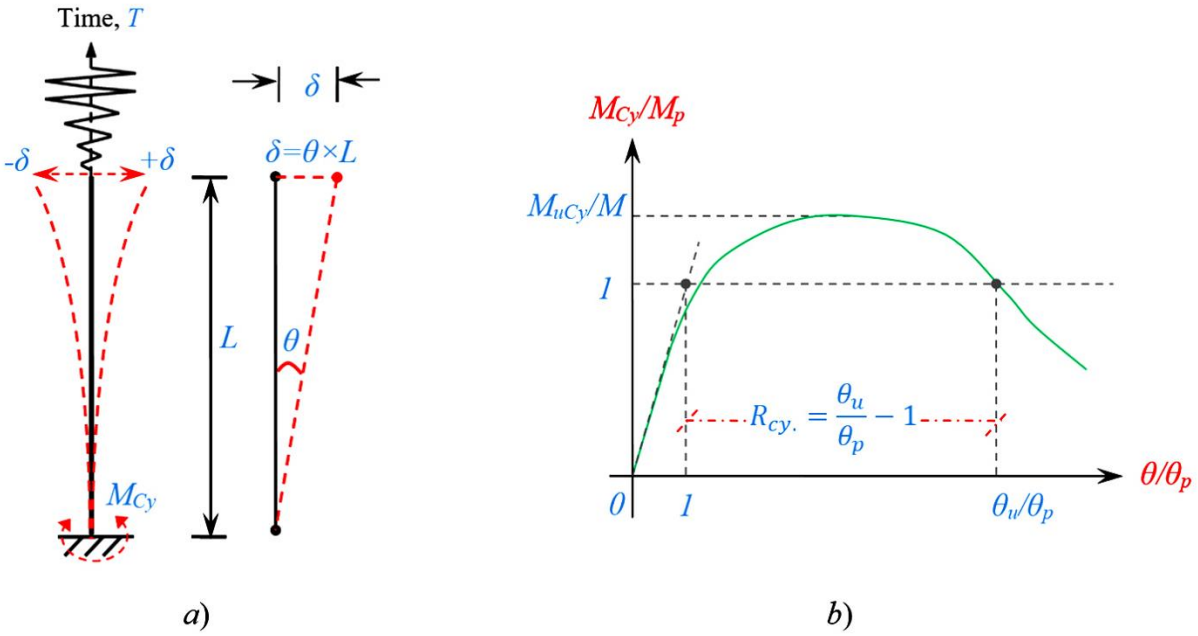

Figure 7.1 *a) Schematic representation of a cantilever beam member with lateral cyclic displacement history applied at the tip; b) Relevant general normalised M_{Cy}–θ cyclic envelope*

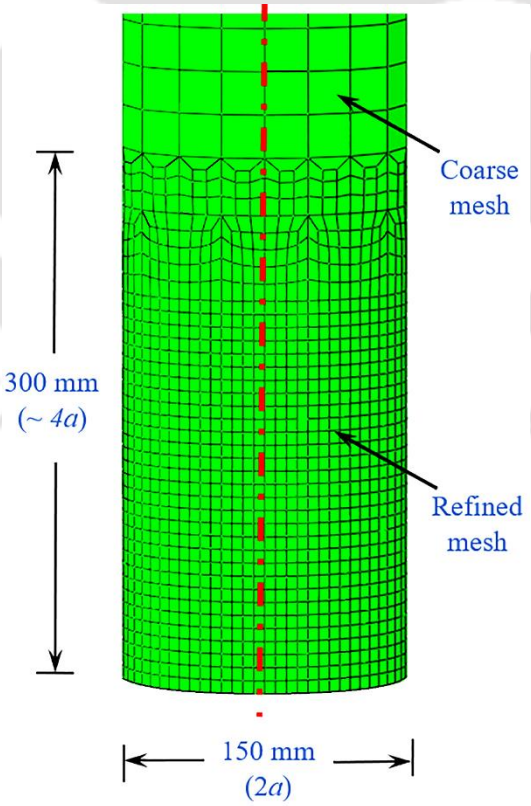

Figure 7.2 *FE mesh pattern at fixed end of EHS15Cb (150×75×5×1500 mm) beam model*

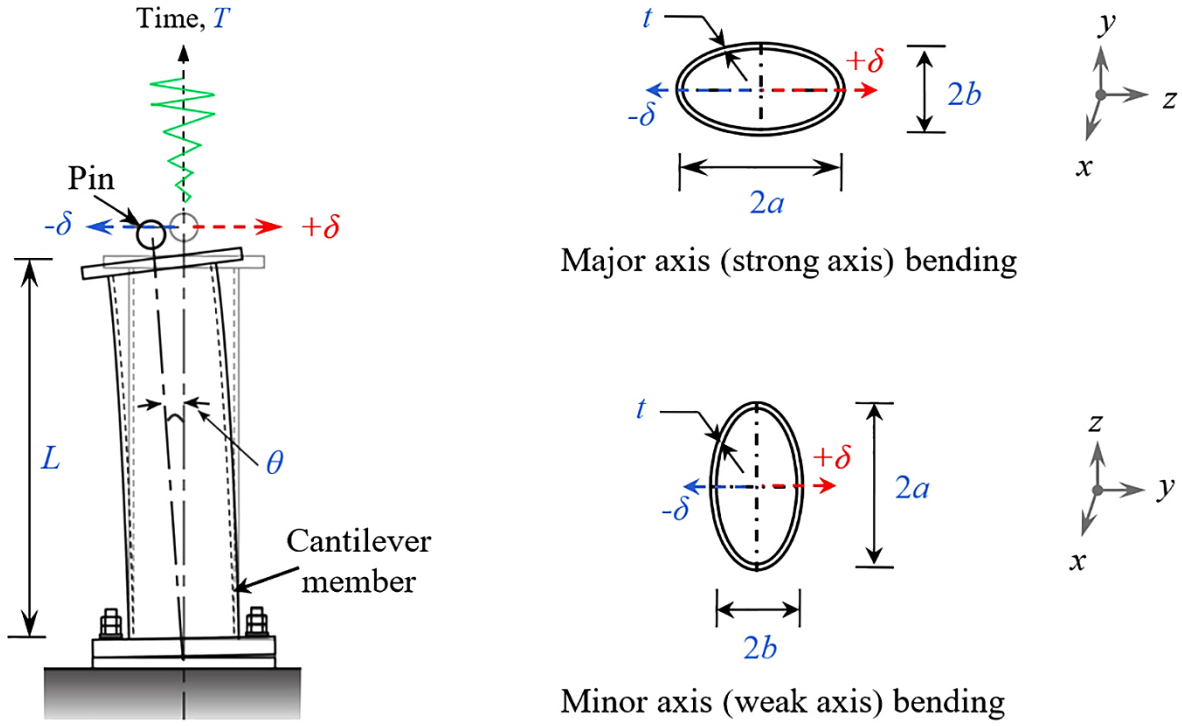

Figure 7.3 *Schematic of the applied boundary conditions and the cross-sectional views of the cantilever tip*

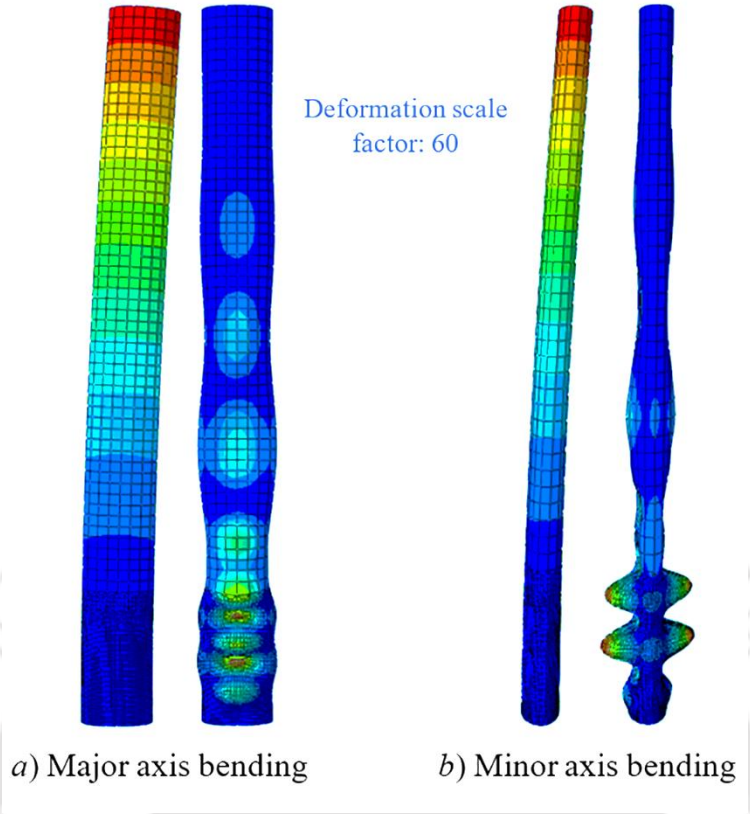

Figure 7.4 *Initial global and local buckling mode shapes of EHS15Cb (150×75×5×1500 mm) cantilever beam model*

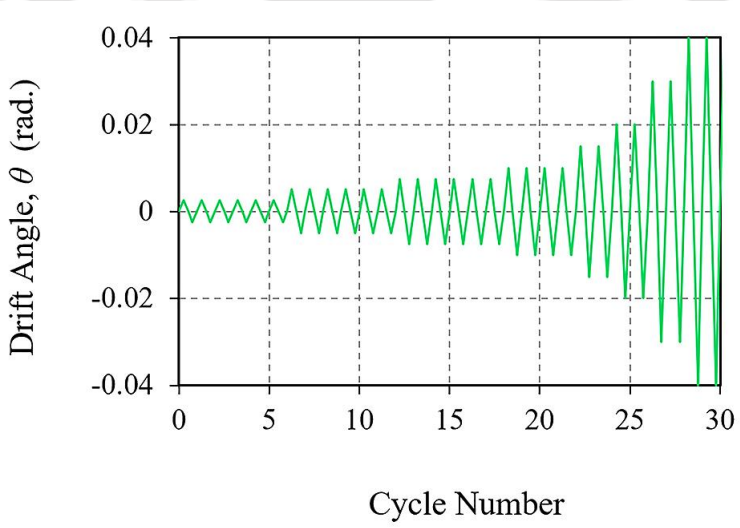

Figure 7.5 *SAC protocol (ANSI/AISC 341-16 2016) cyclic loading sequence*

Figure 7.6 *Comparison between cyclic performance obtained in the performed FE simulation study with those of the specimens in the experimental studies*

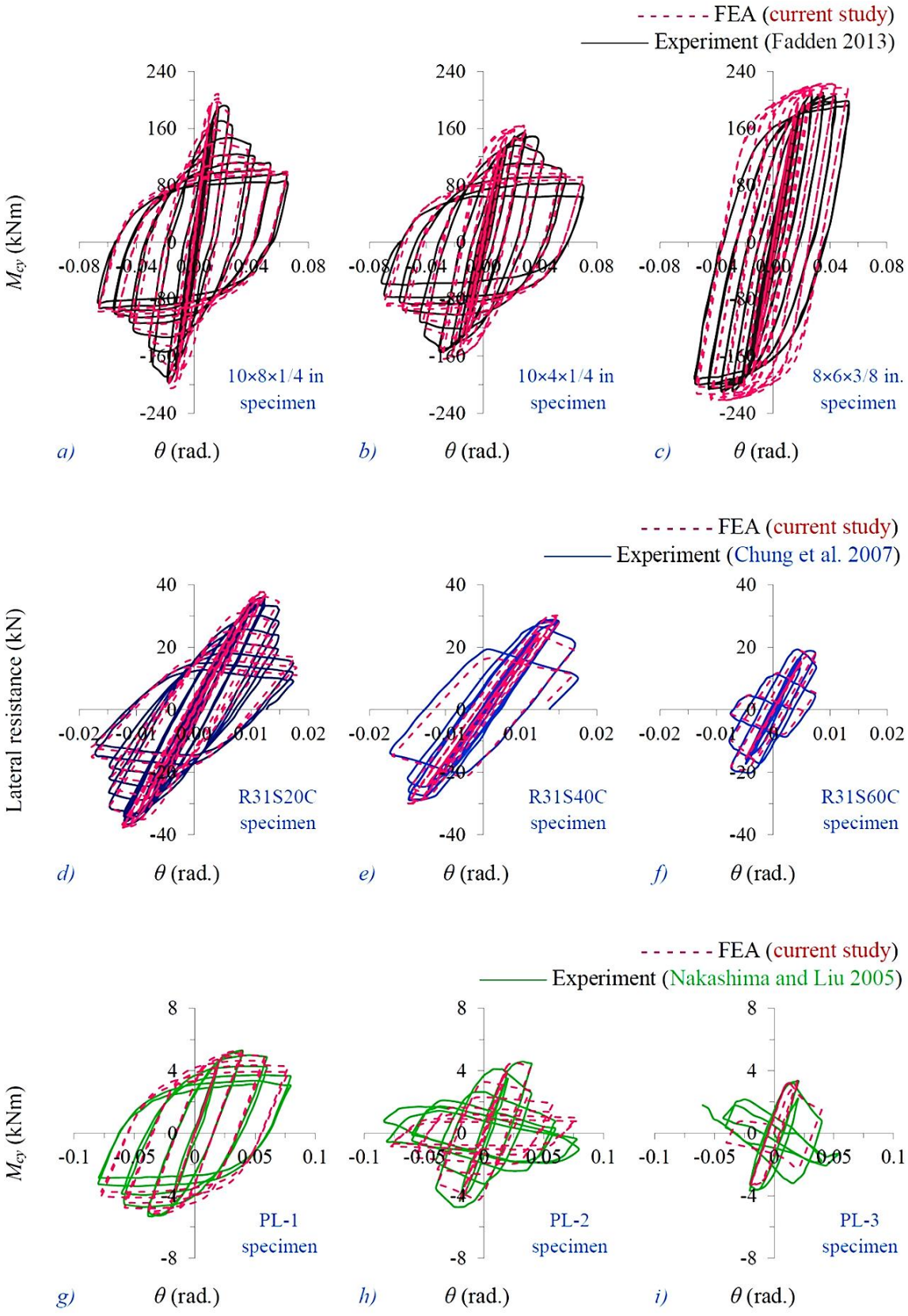

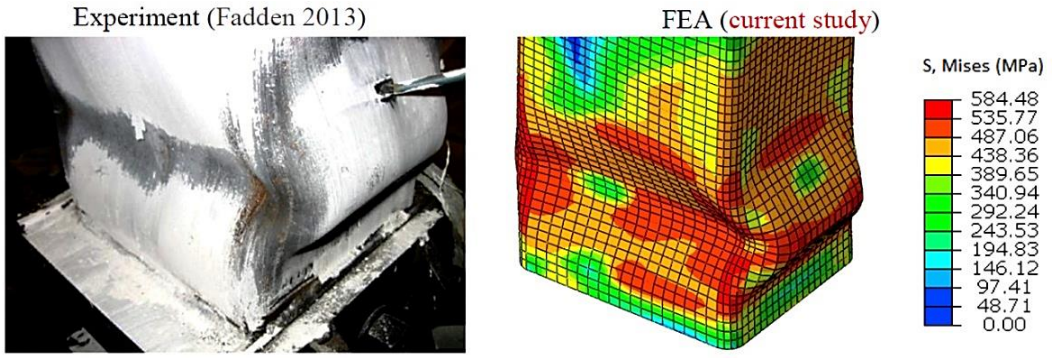

j) Plastic hinge region of *10×8×1/4 in. specimen*

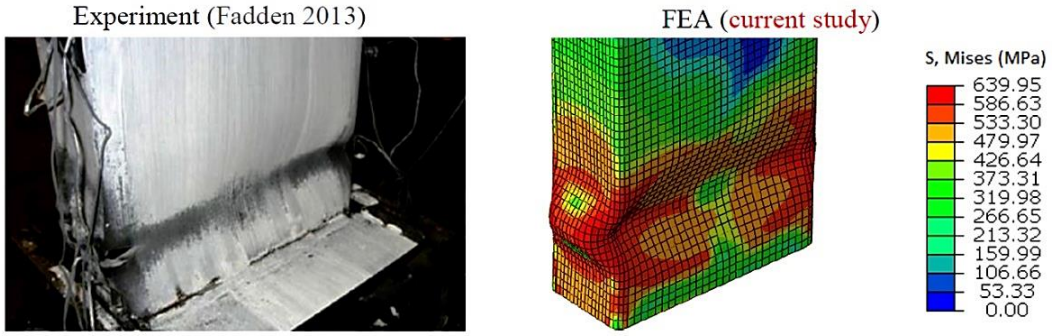

k) Plastic hinge region of *10×4×1/4 in. specimen*

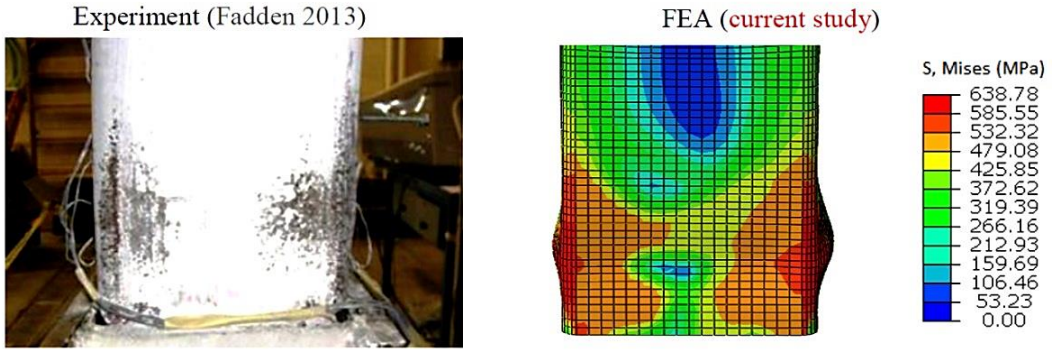

l) Plastic hinge region of *8×6×3/8 in. specimen*

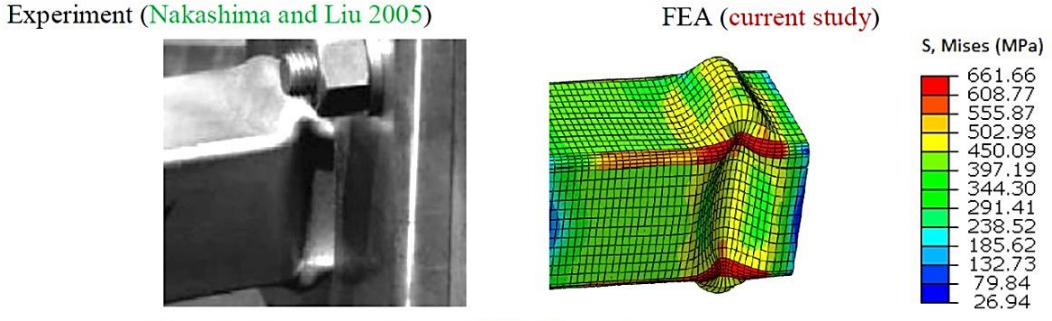

m) Plastic hinge region of *PL-2 specimen*

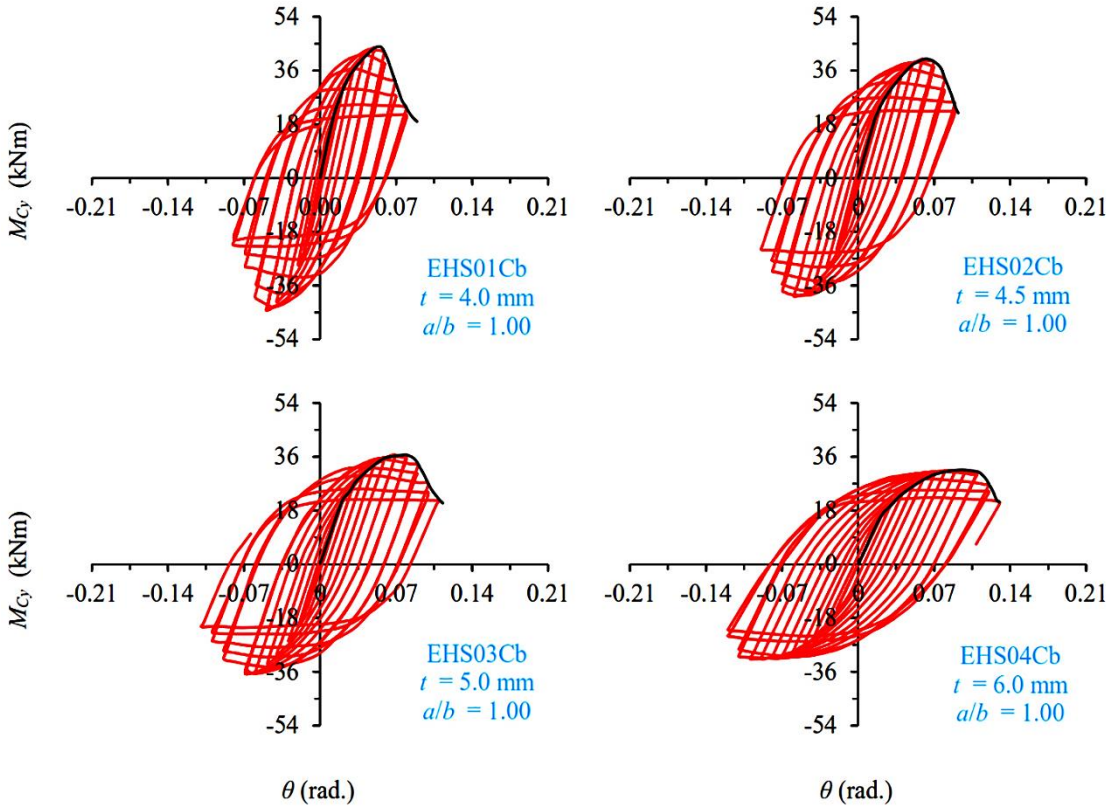

Figure 7.7 *Hysteresis loops and cyclic envelope of EHS01Cb–EHS04Cb models with aspect ratios 1.00 under uni-axial cyclic bending*

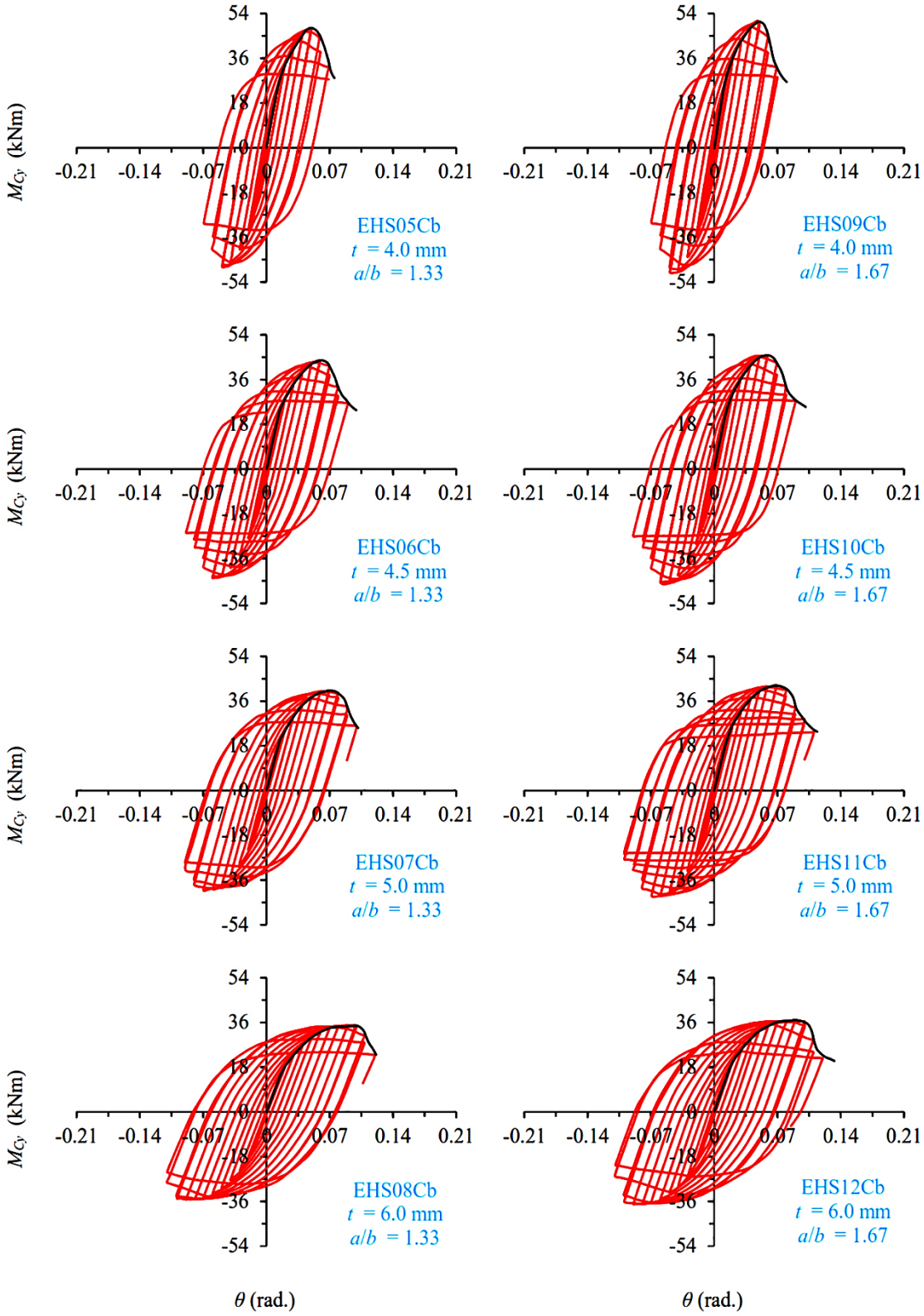

Figure 7.8 *Hysteresis loops and cyclic envelope of EHS05Cb–EHS12Cb models with aspect ratios 1.33 and 1.67 under major axis cyclic bending*

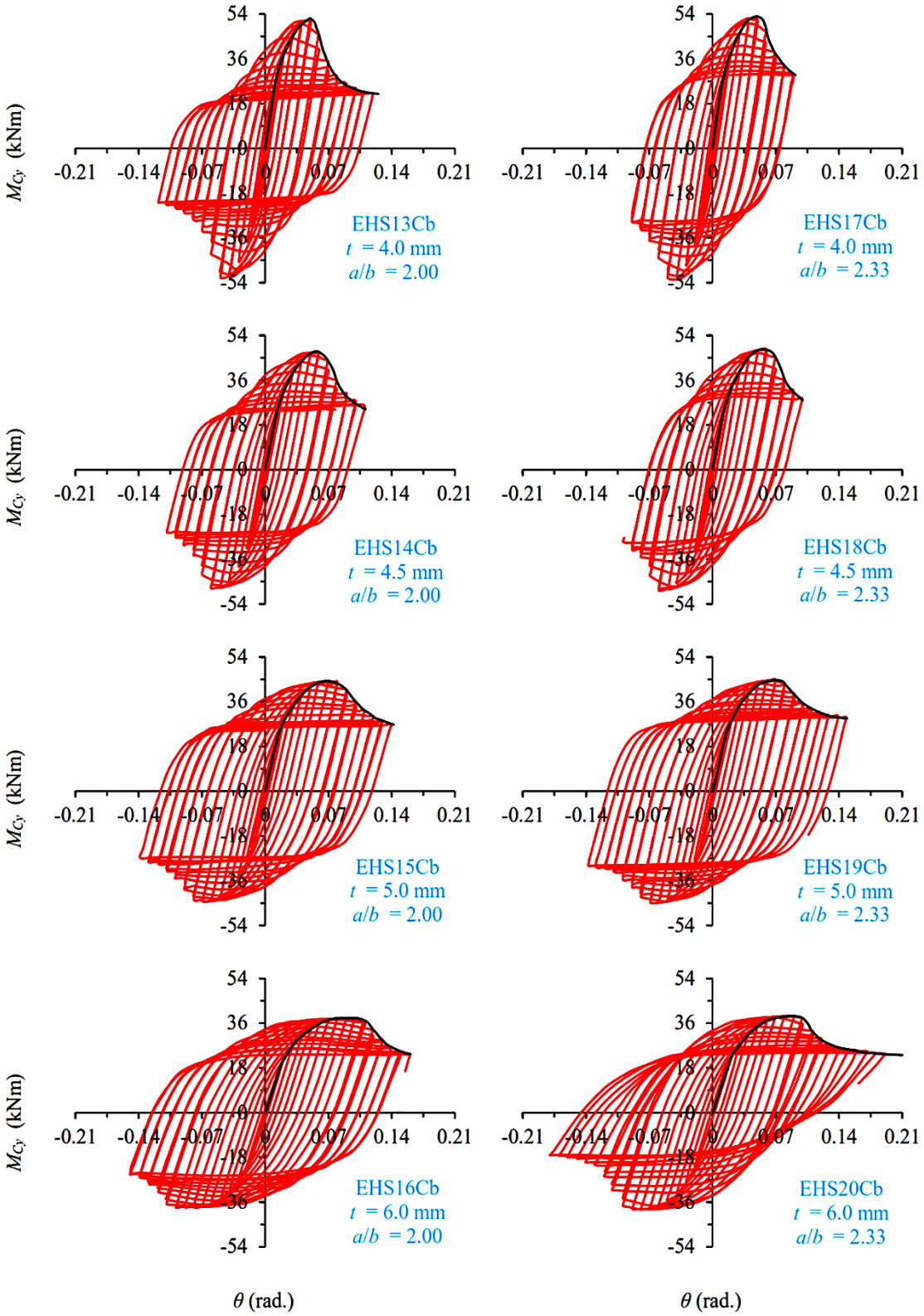

Figure 7.9 *Hysteresis loops and cyclic envelope of EHS13Cb–EHS20Cb models with aspect ratios 2.00 and 2.33 under major axis cyclic bending*

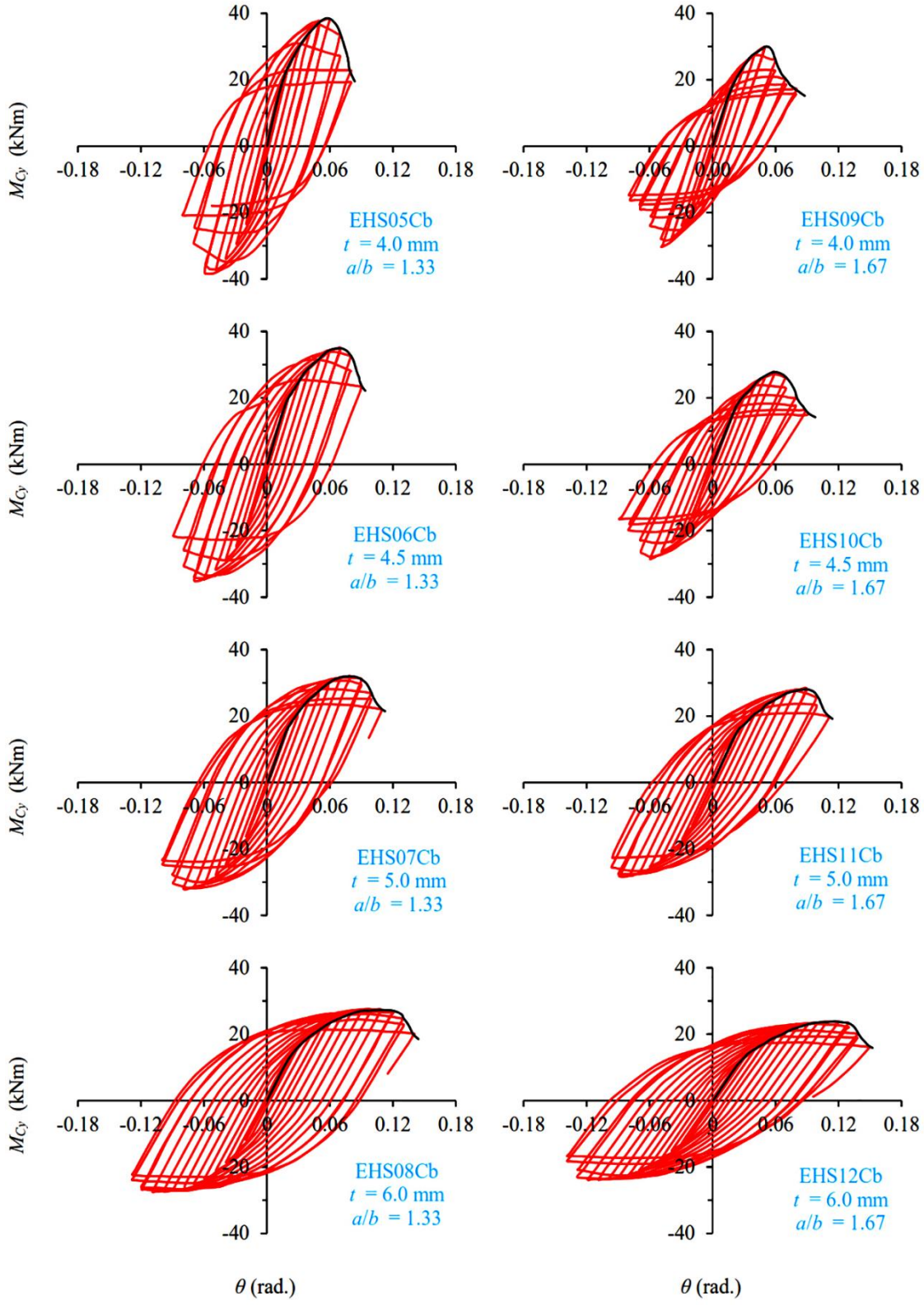

Figure 7.10 *Hysteresis loops and cyclic envelope of EHS05Cb–EHS12Cb models with aspect ratios 1.33 and 1.67 under minor axis cyclic bending*

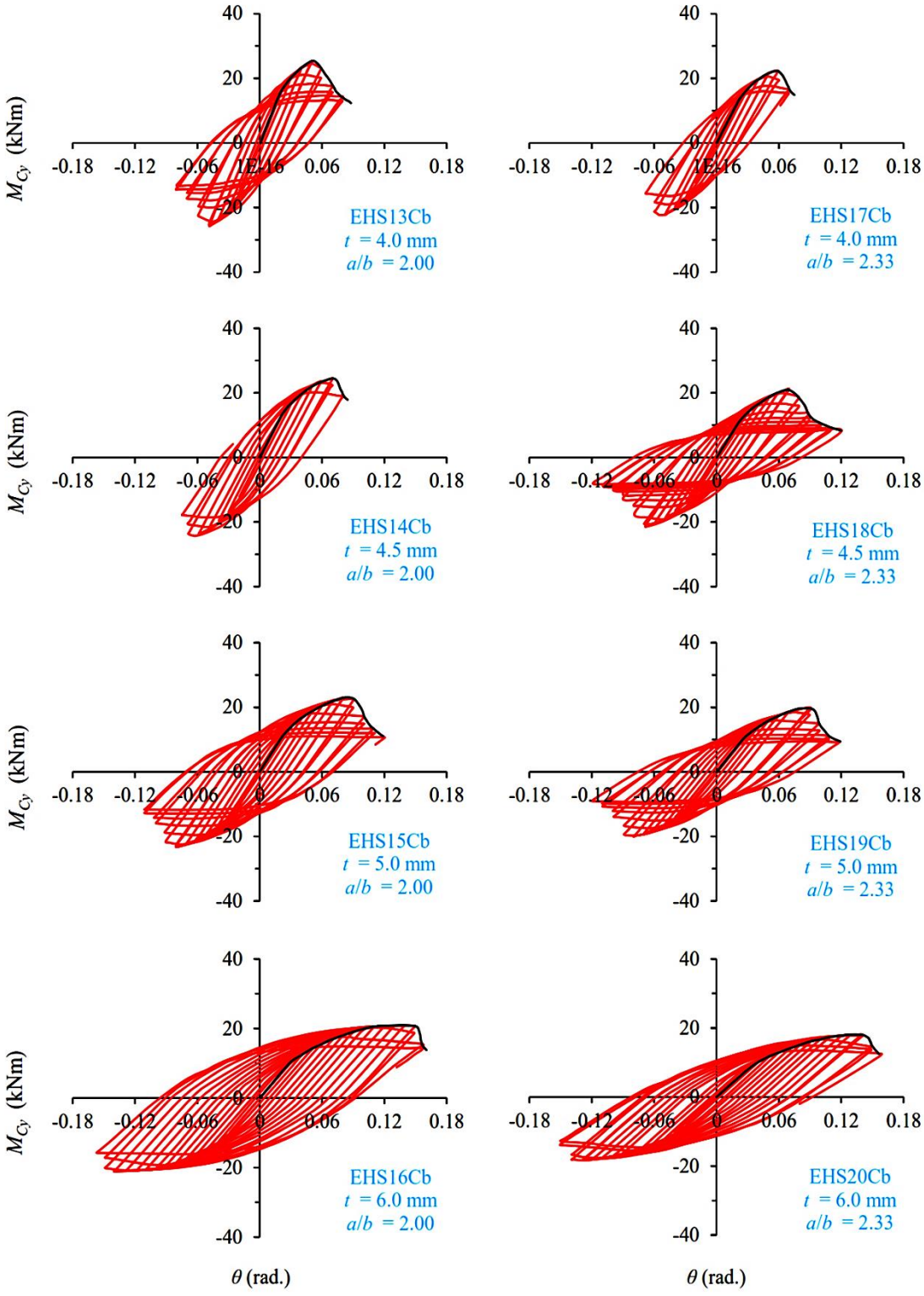

Figure 7.11 *Hysteresis loops and cyclic envelope of EHS13Cb–EHS20Cb models with aspect ratios 2.00 and 2.33 under minor axis cyclic bending*

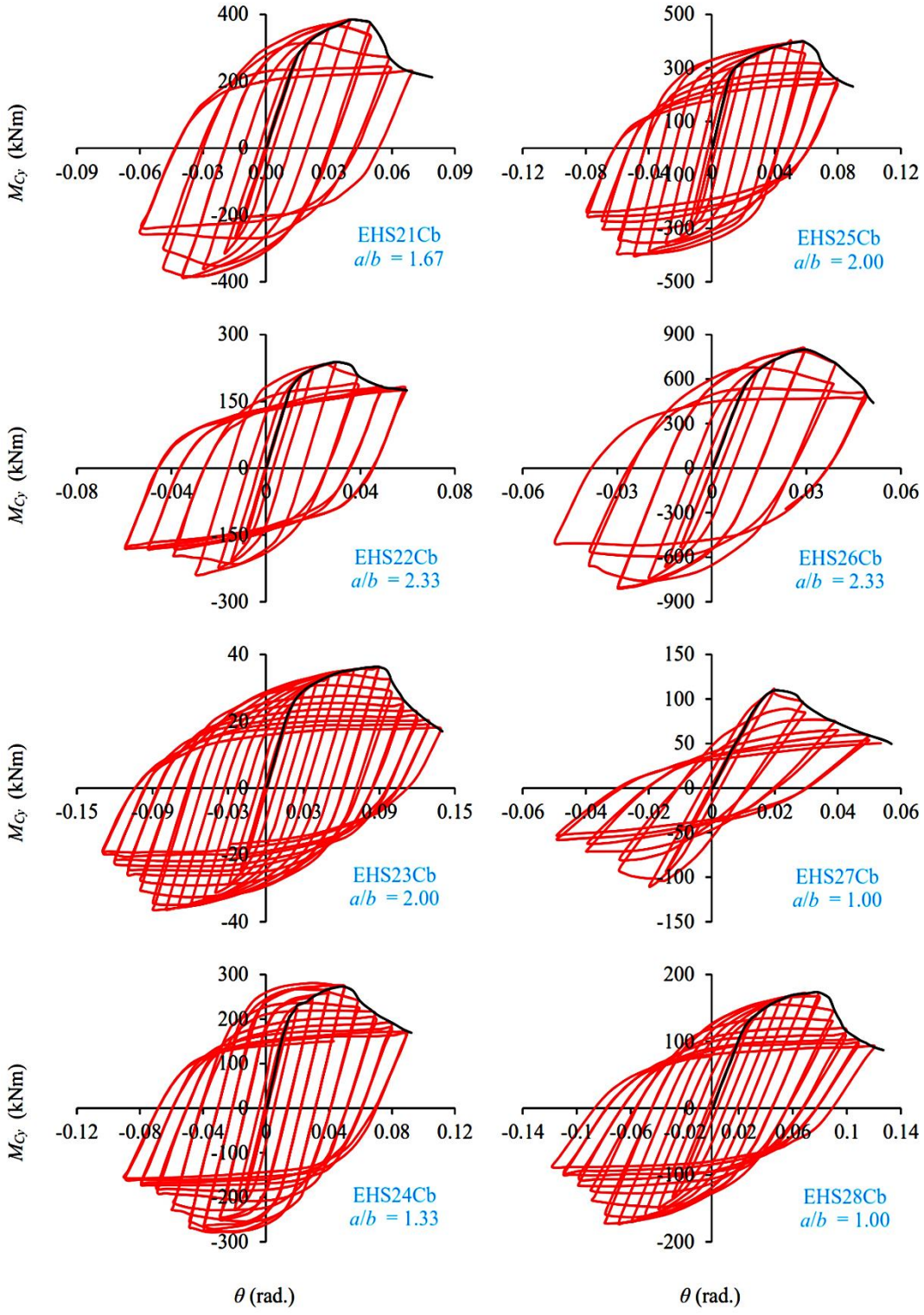

Figure 7.12 *Hysteresis loops and cyclic envelope of EHS21Cb–EHS28Cb models under major axis cyclic bending*

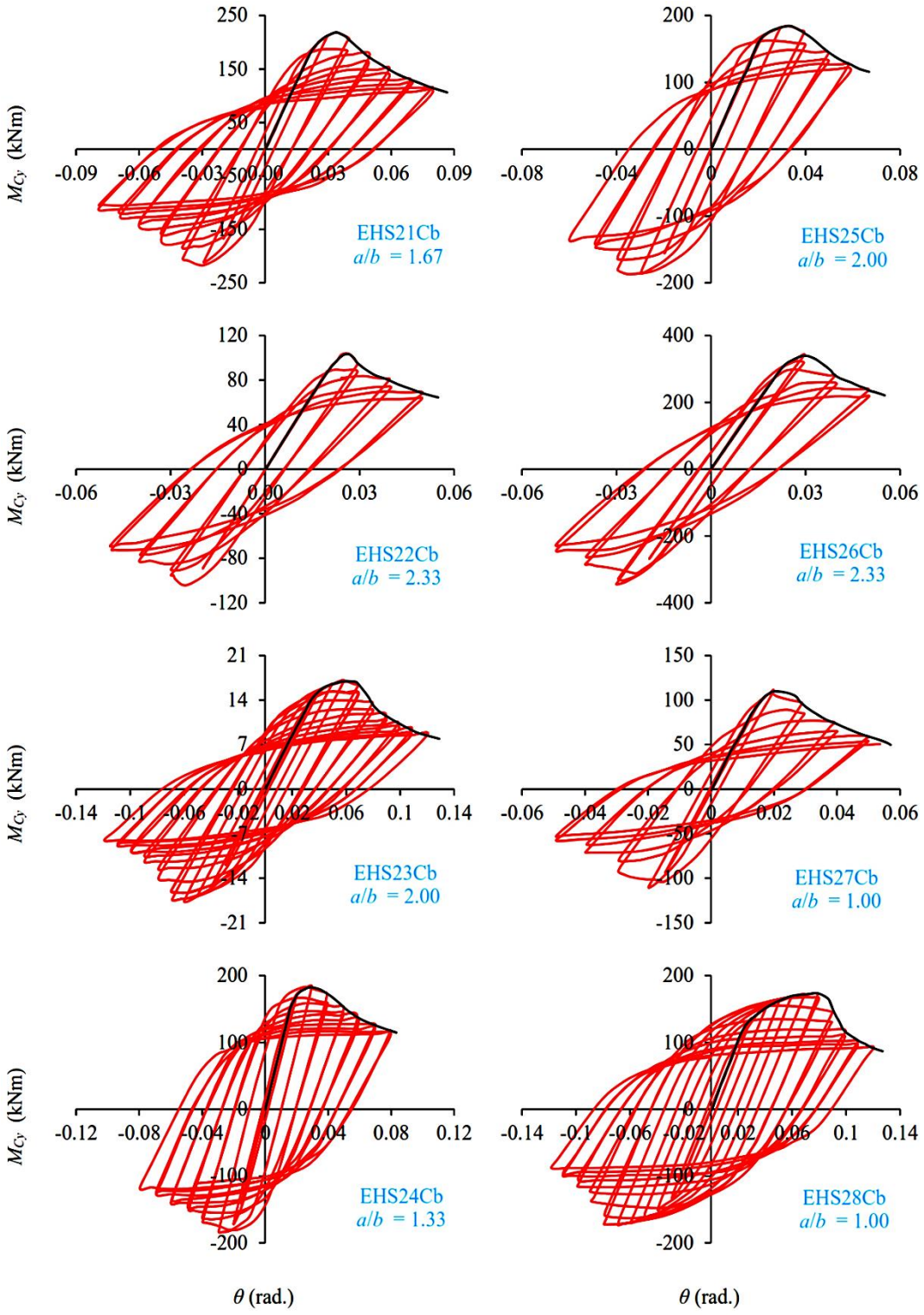

Figure 7.13 *Hysteresis loops and cyclic envelope of EHS21Cb–EHS28Cb models under minor axis cyclic bending*

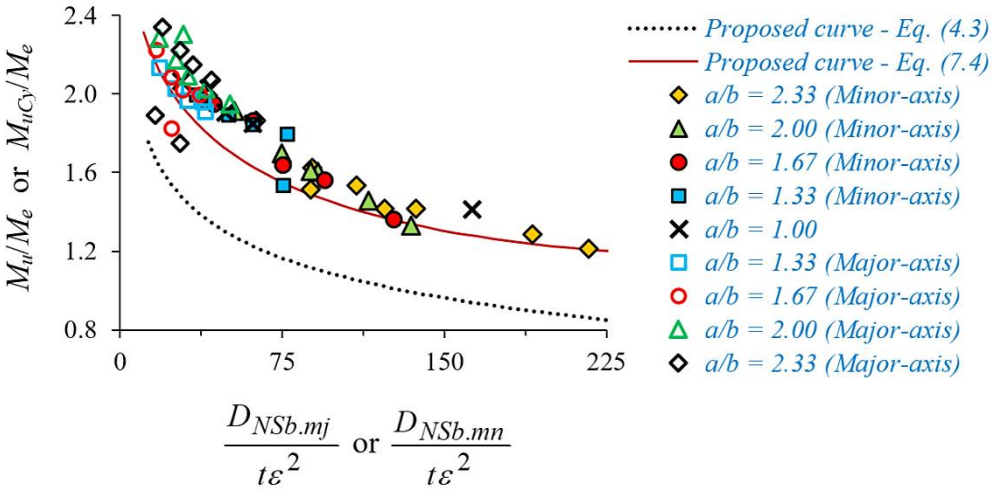

Figure 7.14 *Maximum moment normalised with elastic section moment versus CHS cross-section slenderness of EHS cantilever beams under uni-axial bending and the predictive curves*

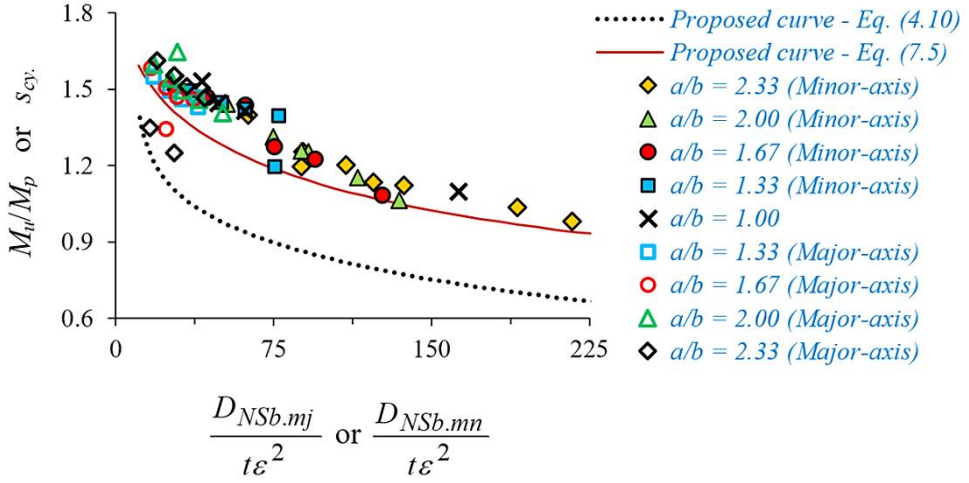

Figure 7.15 *Maximum moment normalised with plastic section moment versus CHS cross-section slenderness of EHS cantilever beams under uni-axial bending and the predictive curves*

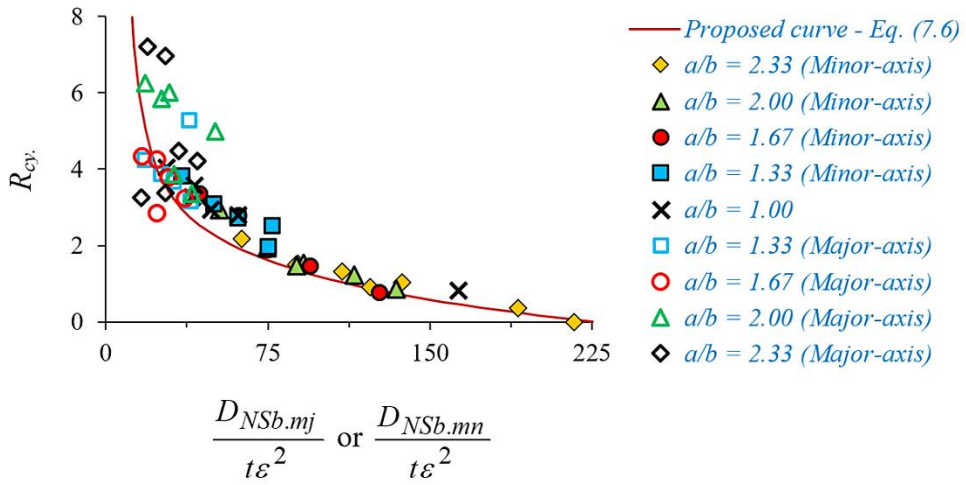

Figure 7.16 *Cyclic rotation capacity versus CHS cross-section slenderness of EHS cantilever beams under uni-axial bending and the predictive curve*

Table 7.1 *Geometric properties of the EHS cantilever models under ELCF bending load*

Specimen Id.	$2a \times 2b \times t$ (mm×mm×mm)	a/b	P_M (mm)	Major-axis bending			Minor-axis bending		
				$\frac{D_{NSb.mj}}{t\varepsilon^2}$	W_{ey} (mm^3)	W_{py} (mm^3)	$\frac{D_{NSb.mn}}{t\varepsilon^2}$	W_{ez} (mm^3)	W_{pz} (mm^3)
EHS01Cb	142.5×142.5×4	1.00	435.3	61.4	58644	76750	61.4	58644	76750
EHS02Cb	127.5×127.5×4.5	1.00	386.6	48.8	51673	68111	48.8	51673	68111
EHS03Cb	115.8×115.8×5	1.00	348.2	39.9	46241	61425	39.9	46241	61425
EHS04Cb	98.3×98.3×6	1.00	290.1	28.2	37870	51188	28.2	37870	51188
EHS05Cb	162×121.5×4	1.33	435.3	39.3	62191	83261	77.2	53149	68304
EHS06Cb	145×108.7×4.5	1.33	386.6	31.2	54891	73966	61.5	46746	60569
EHS07Cb	131.6×98.8×5	1.33	348.3	25.6	49162	66706	50.2	41754	54590
EHS08Cb	111.8×83.9×6	1.33	290.3	18.1	40444	55747	35.5	34065	45437
EHS09Cb	175.2×105.1×4	1.67	435.0	36.5	63452	86675	94.9	47810	60800
EHS10Cb	156.8×94.2×4.5	1.67	386.7	29.1	56091	77081	75.4	42043	53975
EHS11Cb	142.4×85.5×5	1.67	348.3	23.8	50267	69546	61.7	37415	48528
EHS12Cb	120.8×72.5×6	1.67	290.0	16.8	41280	57982	43.6	30253	40157
EHS13Cb	184.6×92.3×4	2.00	435.1	39.8	63726	88589	114.9	43125	54514
EHS14Cb	165.2×82.6×4.5	2.00	386.6	31.6	56288	78723	91.4	37757	48243
EHS15Cb	150×75×5	2.00	348.2	25.8	50454	71030	74.7	33517	43331
EHS16Cb	127.2×63.6×6	2.00	289.9	18.3	41436	59205	52.8	26924	35736
EHS17Cb	191.3×82×4	2.33	434.8	42.5	63352	89434	136.9	38972	49112
EHS18Cb	171.4×73.4×4.5	2.33	386.7	33.8	56075	79645	109.2	34081	43468
EHS19Cb	155.5×66.8×5	2.33	348.3	27.6	50259	71832	88.9	30225	39061
EHS20Cb	131.9×56.5×6	2.33	290.0	19.5	41249	59850	63.0	24050	32019

Table 7.2 *Geometric and material properties of the additional EHS cantilever models under ELCF bending load*

Specimen Id.	$2a \times 2b \times t$ (mm×mm×mm)	a/b	P_M (mm)	L (m)	Steel grade	Major-axis bending			Minor-axis bending		
						$\frac{D_{NSb.mj}}{t\varepsilon^2}$	W_{ey} (mm^3)	W_{py} (mm^3)	$\frac{D_{NSb.mn}}{t\varepsilon^2}$	W_{ez} (mm^3)	W_{pz} (mm^3)
EHS21Cb	400 × 240 × 6.5	1.67	1001	3.00	S355J2H	23.6	549740	745740	126.7	417091	524831
EHS22Cb	400 × 171.43 × 5	2.33	919	2.50	A992 Gr.50	27.7	357023	499295	216.7	223577	276449
EHS23Cb	150 × 75 × 4	2.00	351	1.50	Q345B	29.3	41332	57781	88.3	27755	35431
EHS24Cb	300 × 225 × 7	1.33	807	2.25	A653 Gr.50	38.4	374866	501203	75.5	320588	411283
EHS25Cb	400 × 200 × 7	2.00	948	2.70	A992 Gr.50	50.8	531436	735431	134.5	361984	453916
EHS26Cb	560 × 240 × 8	2.33	1284	3.00	S355J2H	16.4	1112364	1558701	190.6	693922	861506
EHS27Cb	300 × 300 × 3	1.00	933	2.70	Q345B	163.0	205875	264648	163.0	205875	264648
EHS28Cb	200 × 200 × 8	1.00	603	2.70	S355J2H	41.0	222831	295091	41.0	222831	295091

Table 7.3 *Cross-sectional properties of the EHS cantilever models under ELCF major-axis bending load*

Specimen Id.	a/b	$\frac{D_{NSb.mj}}{t\varepsilon^2}$	M_e (kNm)	M_p (kNm)	δ_p (mm)	M_{uCy} (kNm)	δ_{uCy} (kNm)	$s_{cy.}$ (kNm)	$R_{cy.}$ (kNm)	A_v (mm^2)	V_p (kN)	V_u (kN)	$\frac{V_u}{V_p}$
EHS01Cb	1.00	61.4	23.75	31.08	27.91	43.92	105.75	1.413	2.79	1108	253.32	29.00	0.1145
EHS02Cb	1.00	48.8	20.93	27.58	32.91	39.87	129.78	1.445	2.94	1107	253.09	26.30	0.1039
EHS03Cb	1.00	39.9	18.73	24.88	36.42	36.67	155.10	1.474	3.26	1108	253.32	24.27	0.0958
EHS04Cb	1.00	28.2	15.34	20.73	39.50	31.65	198.75	1.527	4.03	1108	253.23	21.16	0.0836
EHS05Cb	1.33	39.3	25.19	33.72	24.84	48.19	103.80	1.429	3.18	1264	288.99	32.09	0.1110
EHS06Cb	1.33	31.2	22.23	29.96	26.82	43.8	125.78	1.462	3.69	1264	289.00	29.06	0.1006
EHS07Cb	1.33	25.6	19.91	27.02	30.12	40.39	147.00	1.495	3.88	1265	289.33	26.91	0.0930
EHS08Cb	1.33	18.1	16.38	22.58	34.95	34.96	183.90	1.548	4.26	1270	290.27	23.21	0.0800
EHS09Cb	1.67	36.5	25.70	35.10	23.39	51.36	98.85	1.463	3.23	1369	313.08	33.67	0.1075
EHS10Cb	1.67	29.1	22.72	31.22	25.80	45.9	123.24	1.470	3.78	1371	313.38	30.80	0.0983
EHS11Cb	1.67	23.8	20.36	28.17	28.50	42.45	150.00	1.507	4.26	1373	314.02	28.35	0.0903
EHS12Cb	1.67	16.8	16.72	23.48	34.43	37.19	183.53	1.584	4.33	1378	314.96	24.57	0.0780
EHS13Cb	2.00	39.8	25.81	35.88	23.30	52.32	101.58	1.458	3.36	1445	330.33	34.83	0.1054
EHS14Cb	2.00	31.6	22.80	31.88	26.21	47.67	127.65	1.495	3.87	1446	330.67	31.76	0.0960
EHS15Cb	2.00	25.8	20.43	28.77	27.60	44.36	189.00	1.542	5.85	1450	331.51	29.36	0.0886
EHS16Cb	2.00	18.3	16.78	23.98	32.24	38.3	233.85	1.597	6.25	1454	332.52	25.48	0.0766
EHS17Cb	2.33	42.5	25.66	36.22	21.23	53.1	110.72	1.466	4.22	1499	342.64	35.26	0.1029
EHS18Cb	2.33	33.8	22.71	32.26	24.95	48.79	136.82	1.513	4.48	1502	343.43	32.40	0.0943
EHS19Cb	2.33	27.6	20.36	29.09	28.35	45.18	225.75	1.553	6.96	1505	344.03	29.87	0.0868
EHS20Cb	2.33	19.5	16.71	24.24	31.86	39.08	261.75	1.612	7.22	1510	345.28	25.95	0.0752
EHS21Cb	1.67	23.6	211.65	287.11	45.69	386.33	175.80	1.346	2.85	5116	1137.07	128.00	0.1126
EHS22Cb	2.33	27.7	136.74	191.23	27.00	239.23	118.25	1.251	3.38	3950	873.44	95.69	0.1096
EHS23Cb	2.00	29.3	15.83	22.13	26.10	36.44	183.08	1.647	6.01	1168	258.27	24.29	0.0941
EHS24Cb	1.33	38.4	140.20	187.45	28.04	274.88	176.63	1.466	5.30	4102	885.74	122.17	0.1379
EHS25Cb	2.00	50.8	203.54	281.67	33.13	396.61	198.18	1.408	4.98	5502	1216.63	146.89	0.1207
EHS26Cb	2.33	16.4	428.26	600.10	32.40	810	138.00	1.350	3.26	8832	1963.18	270.00	0.1375
EHS27Cb	1.00	163.0	78.85	101.36	41.04	111.27	74.79	1.098	0.82	1782	394.05	41.21	0.1046
EHS28Cb	1.00	41.0	85.79	113.61	60.16	173.8	275.00	1.530	3.57	3072	682.84	64.37	0.0943

Table 7.4 *Cross-sectional properties of the EHS cantilever models under ELCF minor-axis bending load*

Specimen Id.	a/b	$\frac{D_{NSb.mn}}{t\varepsilon^2}$	M_e (kNm)	M_p (kNm)	δ_p (mm)	M_{uCy} (kNm)	δ_{uCy} (kNm)	$s_{cy.}$ (kNm)	$R_{cy.}$ (kNm)	A_v (mm^2)	V_p (kN)	V_u (kN)	$\frac{V_u}{V_p}$
EHS01Cb	1.00	61.4	23.75	31.08	27.91	43.92	105.75	1.413	2.79	1108	253.32	29.00	0.1145
EHS02Cb	1.00	48.8	20.93	27.58	32.91	39.87	129.78	1.445	2.94	1107	253.09	26.30	0.1039
EHS03Cb	1.00	39.9	18.73	24.88	36.42	36.67	155.10	1.474	3.26	1108	253.32	24.27	0.0958
EHS04Cb	1.00	28.2	15.34	20.73	39.50	31.65	198.75	1.527	4.03	1108	253.23	21.16	0.0836
EHS05Cb	1.33	77.2	21.53	27.66	31.58	38.63	110.70	1.396	2.51	940	214.91	25.66	0.1194
EHS06Cb	1.33	61.5	18.93	24.53	35.40	34.90	131.82	1.423	2.72	938	214.41	23.38	0.1090
EHS07Cb	1.33	50.2	16.91	22.11	39.83	32.02	162.90	1.448	3.09	938	214.48	21.43	0.0999
EHS08Cb	1.33	35.5	13.80	18.40	44.70	27.50	215.55	1.494	3.82	934	213.59	18.45	0.0864
EHS09Cb	1.67	94.9	19.36	24.62	38.21	30.17	93.53	1.225	1.45	809	184.92	20.32	0.1099
EHS10Cb	1.67	75.4	17.03	21.86	41.19	27.84	118.64	1.274	1.88	807	184.57	19.00	0.1029
EHS11Cb	1.67	61.7	15.15	19.65	44.21	28.20	167.16	1.435	2.78	805	184.05	18.86	0.1025
EHS12Cb	1.67	43.6	12.25	16.26	51.74	23.86	224.84	1.467	3.35	797	182.31	16.05	0.0880
EHS13Cb	2.00	114.9	17.47	22.08	41.25	25.47	92.25	1.154	1.24	706	161.50	17.26	0.1069
EHS14Cb	2.00	91.4	15.29	19.54	47.18	24.54	119.76	1.256	1.54	703	160.70	16.17	0.1006
EHS15Cb	2.00	74.7	13.57	17.55	51.30	23.05	150.38	1.313	1.93	700	160.04	15.44	0.0965
EHS16Cb	2.00	52.8	10.90	14.47	60.45	20.88	237.90	1.443	2.94	691	158.03	14.05	0.0889
EHS17Cb	2.33	136.9	15.78	19.89	48.14	22.34	98.40	1.123	1.04	624	142.67	14.89	0.1044
EHS18Cb	2.33	109.2	13.80	17.60	52.52	21.17	121.80	1.203	1.32	620	141.73	14.33	0.1011
EHS19Cb	2.33	88.9	12.24	15.82	59.62	19.86	149.95	1.255	1.52	617	141.18	13.17	0.0933
EHS20Cb	2.33	63.0	9.74	12.97	75.38	18.16	240.00	1.400	2.18	606	138.55	12.16	0.0878
EHS21Cb	1.67	126.7	160.58	202.06	72.18	218.40	126.48	1.081	0.75	3036	674.73	72.80	0.1079
EHS22Cb	2.33	216.7	85.63	105.88	59.00	104.00	0.00	0.982	0.00	1664	368.02	41.60	0.1130
EHS23Cb	2.00	88.3	10.63	13.57	48.60	17.07	120.08	1.258	1.47	568	125.60	11.38	0.0906
EHS24Cb	1.33	75.5	119.90	153.82	37.64	184.10	111.11	1.197	1.95	3052	659.02	81.82	0.1242
EHS25Cb	2.00	134.5	138.64	173.85	59.29	184.70	110.62	1.062	0.87	2702	597.48	68.41	0.1145
EHS26Cb	2.33	190.6	267.16	331.68	73.11	344.00	99.56	1.037	0.36	3712	825.10	114.67	0.1390
EHS27Cb	1.00	163.0	78.85	101.36	41.04	111.27	74.79	1.098	0.82	1782	394.05	41.21	0.1046
EHS28Cb	1.00	41.0	85.79	113.61	60.16	173.80	275.00	1.530	3.57	3072	682.84	64.37	0.0943

CHAPTER 8

ELLIPTICAL-HOLLOW-SECTION COLUMNS UNDER CYCLIC BENDING – A FINITE ELEMENT STUDY

In this chapter, the performance of carbon-steel EHS cantilever columns is analysed under the combined action of constant axial compressive load and ELCF major-axis *or* minor-axis bending load by conducting FE simulations using Abaqus (2009). A comprehensive non-linear FE study carried out on sixteen EHS cantilever columns with constant cross-sectional steel area, four sets of column length ranging between 300 mm to 600 mm and cross-sectional aspect ratio (major to minor axis diameter ratio) ranging between 1 and 2. A parametric study is conducted to assess their axial compressive load and cyclic moment interaction behaviour under various axial compressive load levels. The effects of cross-sectional aspect ratio and axial compressive load level on ductility and cyclic energy dissipation capacity of the columns are examined. Further, the empirical expressions for axial compressive load – cyclic moment interaction curves; and the hysteretic properties like ductility and cyclic energy dissipation capacities are derived.

8.1 INTRODUCTION

Structural damage and failure under cyclic loading are analogous to lack of ductility due to the inelastic behaviour of structural members (Kuroda 2002). After the 1994 Northridge earthquake and 1995 Kobe earthquake, the increasing adoption of performance-based seismic design and assessment methods for buildings has highlighted the importance of estimating seismic drifts and earthquake energy dissipation capacities, which can be directly related to localised demands of both structural and non-structural components (Tsitos et al. 2018).

The earthquake energy energy is dissipated mainly through cyclic bending from the dissipative-zones/plastic-hinges in the beams *or* the beam-column joints. In the early days, emperical models were proposed to predict the area under the hysteresis loops, *i.e.*, the amount of earthquake energy dissipation by structural members. The need for hysteretic models is evident in the case of structural members with excessive levels of deformation *or* inelastic strain where locally initiated damage triggers strength and stiffness deterioration eventually leading to a significant reduction of the global structural integrity. Conservation of overall structural integrity without collapse is one of the foremost objectives of earthquake resistant design which also deals with some of the latest retrofitting methods using thin-walled steel HSSs (Usami and Ge 1994, Mamaghani 2004).

Thin-walled HSSs are being preferred over their reinforced concrete counterparts because of their higher stiffness to cross-sectional area ratio. However, the performance of these members during severe earthquakes like 1985 Mexico City and 1995 Hyogo-ken-Nanbu (Kobe) earthquakes have shown that these components are pregnable to local buckling under cyclic lateral loading (Bruneau et al. 1996). HSS applications have typically been limited to structural members such as columns, beams, truss elements and bracing members. HSS-applications such as beam and column members in low and mid-rise frames in seismic areas can provide benefits like reduced seismic weight, lesser surface area per length of the member, decreased lateral bracing, applications in modular construction and unique retrofit techniques (Fadden and McCormick 2014). Extensive studies have been performed on the seismic behaviour of the braces, gusset plates and beams until the first two decades of the 21st century, but the investigations about columns as the most important structural members are sparser (Momenzadeh and Shen 2018). Consequently, the necessity for reliable prediction of the damage potential of new and existing steel hollow and composite columns has motivated studies on assessing and quantifying their deformation capacity and degradation rates.

Initially, HSSs were used instead of concrete bridge piers as cantilever columns because of their lighter weight and shorter construction period (Usami and Ge 1994, 1998). Experimental and numerical studies on thin-walled steel bridge piers/columns under combined constant axial compressive and cyclic flexural loads have revealed that critical local buckling originates in the compression part of the cross-section within an effective failure range (Usami et al. 1995).

Along with HSSs, usage of concrete-filled steel tube (CFST) sections as a bridge pier has become a popular structural application during the first decade of the 21st century as they have enhanced structural performance in terms of earthquake-resistant properties such as high strength, high ductility, and large absorption capacity than those of bare steel *or* bare reinforced concrete (Usami and Ge 1994, Han and Yang 2005, Han et al. 2006).

Ductility and energy-absorption capacity are important elements of earthquake-resistant steel member design. It has been widely deduced in the modern-day earthquake resistant design philosophy that a rational technique should explicitly evaluate the structural nonlinear cyclic performance expected to occur under the design seismic load (Mamaghani 2008). AISC 341-16 (2016) categorises the flexural members of the seismic resisting system into moderately ductile members and highly ductile members. Nowadays, for safety and economic reasons, the concept of ductility-based design has become necessary during the design of structural resistance to severe earthquake, which is a shift away from the strength-based design. The ductility-based design draws attention to both strength and ductility. The design strength of a section can be substantially reduced if it can provide a good deformation capacity beyond the elastic limit. The assumed logical strategy and procedures behind adopting yield and failure limits especially for evaluating the available ductility of structural members and their connections should be clearly defined to enable the designers in ensuring adequate available ductility of the structures based on the target ductility criterion (Park 1988).

8.1.1 Cyclic Envelope Characteristics

In this Section, the cyclic ductility and energy dissipation indices of the cantilever column with compact *or* plastic cross-section under combined lateral cyclic bending and axial compression are discussed based on Figures 8.1a and 8.1b. The displacement ductility, μ of a typical steel cantilever member of a length, L under the combined action of constant axial compressive load, N_a and lateral cyclic force, H_c which displaces the free end in terms of lateral displacement, δ

history as illustrated in Figure 8.1a and its respective generalized cyclic flexural moment-rotation (M_{Cy}-θ) envelope shown in Figure 8.1b is defined as the ratio of the ultimate rotation, $\theta_{0.85u}$ $\left(\approx \delta_u/L\right)$ to the yield rotation, θ_y $\left(\approx \delta_y/L\right)$ as expressed in the following Equation 8.1.

$$\mu = \frac{\theta_{0.85u}}{\theta_y} \approx \frac{\delta_u}{\delta_y} \tag{8.1}$$

The ultimate rotation, $\theta_{0.85u}$ $\left(\approx \delta_u/L\right)$ is the rotation of the column that corresponds to the moment of resistance of the section which is 0.85 times the maximum resistance moment, M_{uCy} of the section in the post-peak zone. While, δ_u is the displacement corresponding to $0.85M_{uCy}$ of the member in the post-peak zone of the cyclic envelope and δ_y is the yield displacement corresponding to the reduced yield section capacity, M_{er} of the member.

When both H_c and N_a are acting together, the resultant total moment, M_{Cy} produced at fixed-end is given by Equation 8.2. Subsequently, θ is the rotation angle *or* drift angle made by an imaginary chord joining the two ends of the column, measured at the rigid end as shown in Figure 8.1a. For small θ up to 0.3 rad., lateral displacement, δ to be applied at the free end of the column as shown in Figure 8.1a can be calculated as the product of θ and L. Thus, the expression for obtaining θ is given in Equation 8.3.

$$M_{Cy} = \left(H_c \times L\right) + \left(N_a \times \delta\right) \tag{8.2}$$

$$\theta \approx \frac{\delta}{L} \tag{8.3}$$

The reduced yield section moment capacity, M_{er} measured along M_{Cy}-θ envelope response and the respective yield rotation, θ_y $\left(\approx \delta_y/L\right)$ under the combined action of H_c and N_a are shown in Figure 8.1b. The yield resistance, H_{y0} and the corresponding yield displacement, δ_{y0} under zero axial compressive loading (N_a = 0) can be calibrated using the following Equations 8.4 and 8.5, respectively.

$$H_{y0} = \frac{M_e}{L} \tag{8.4}$$

$$\delta_{y0} = \frac{H_{y0} L^3}{3EI} \tag{8.5}$$

where, M_e is the cross-sectional yield moment capacity under pure bending (*i.e.*, in absence of axial compressive loading so that $N_a = 0$). For EHSs, M_e shall be calculated accordingly using Equations 2.14 and 2.16. While, the corresponding member rotation shall be calibrated as follows:

$$\theta_{y0} = \frac{\delta_{y0}}{L} = \frac{\left(\frac{H_{y0} L^3}{3EI}\right)}{L} = \frac{\left(H_{y0} \times L\right)}{\left(\frac{3EI}{L}\right)} = \frac{M_e}{\left(\frac{3EI}{L}\right)} \tag{8.6}$$

The reduced elastic section moment, M_{er} and plastic section moment, M_{pr} capacities under the combined action of H_c and N_a are given by the following Equations 8.7 and 8.8, respectively (Sahoo and Rai 2007, Trahair et al. 2008, Cheng et al. 2013).

$$M_{er} = M_e \times \left(1 - \frac{N_a}{N_y}\right) \tag{8.7}$$

$$\begin{aligned} M_{pr} &= M_p && \left(\text{at } \frac{N_a}{N_y} < 0.15 \text{ for plastic and compact sections}\right) \\ &= 1.18 \times M_p \times \left(1 - \frac{N_a}{N_y}\right) && \left(\text{at } \frac{N_a}{N_y} \geq 0.15 \text{ for plastic and compact sections}\right) \\ &= M_{er} && \text{(for semi-compact and slender sections)} \end{aligned} \tag{8.8}$$

where, M_p is the cross-sectional plastic moment capacity under pure bending (*i.e.*, in absence of axial compressive loading so that $N_a = 0$). For EHSs, M_p shall be calculated accordingly using Equations 2.15 and 2.17. While the cross-sectional squash load *or* axial compressive yield capacity N_y for EHSs can be computed by using any one of the Equations 2.18 and 2.19.

The ultimate rotation, $\theta_{0.85u}$ *or* ultimate displacement, δ_u ($= \theta_{0.85u} \times L$) is computed with-respect-to moment of resistance of the section which is 0.85 times of M_{uCy} in the post-peak zone (Figure 8.1b) based on the criterion that most structures exhibit some capacity for deformation beyond the peak of the strength-deformation *or* moment-rotation response with some reduction in strength just before fracture *or* failure (Park 1988). For ductile materials like steel,

displacement ductility can be quantified by assuming fracture *or* crack initiation as a failure criterion. Hence, the displacement at which the specimen starts to fracture during the test is considered to be the ultimate displacement. Also, the fracture strength for high ductile metals is estimated to be 80–90% of the ultimate strength (Pope 1996). Therefore, it is reasonable to recognize at least some part of the post-peak displacement capacity and rationally $\theta_{0.85u}$ values are being assumed for the corresponding values of $0.85M_{uCy}$ beyond post-peak zone based on fracture *or* local buckling criterion described in Park (1988) while gauging ductility, *e.g.*, Han et al. (2006), Cheng et al. (2013) and Liao et al. (2016).

In the early days, expository models were proposed to gauge the area under the hysteresis loops, which represents the amount of cyclic energy dissipation by structural members. The energy is dissipated mainly by means of cyclic bending from the dissipative zones which are located in plastic hinges in the beams, columns or the beam-column joints. The cyclic energy dissipation capacity ($\overline{E}_{cy}$) is obtained by normalising the accumulated hysteretic energy, $E_{tot.cy}$ (*i.e.*, the area under the M_{Cy}-θ hysteretic loops of each loading cycle till the cycle where $\theta_{0.85u}$ is measured) with-respect-to $E_{e.cy}$ (= $M_{er} \times \theta_y$) as described in Equation 8.9 (Cheng et al. 2013).

$$\overline{E}_{cy} = \frac{E_{tot.cy}}{\left(M_{er} \times \theta_y\right)} = \frac{E_{tot.cy}}{E_{e.cy}} \tag{8.9}$$

8.1.2 Problem Statement

During the first two decades of the 21st century, with the ever-increasing computational potential and the development of efficient algorithms and software platforms for ELCF type of loading simulations, matured analytical models also have been developed to accurately predict and understand the behaviour of HSS members under cyclic loads. To predict the cyclic flexural behaviour of box section columns, Usami et al. (2000) used a modified two-surface plasticity model (2SM) which was developed at Nagoya University, Japan. Recently, Varelis and Karamanos (2014) and Fadden and McCormick (2014) employed NLCHM within Abaqus (2009).

The earthquake resistant design requires strong-column weak-beam behaviour with thin-walled steel hollow columns generally vulnerable to damage caused by local and overall interaction

buckling. In case of EHS under combined compression and minor axis bending, local buckling originates in the zone of maximum radius of curvature, similar to the case of pure axial compression and pure minor axis bending (Gardner and Chan 2007, Chan et al. 2010b). Whereas under combined compression and major axis bending, local buckling will trigger at a point that form/relocate towards the centroidal axis as the compressive part of the loading increases (Gardner and Chan 2007, Chan et al. 2010b). But, a comprehensive understanding of the cyclic flexural behaviour of EHS columns through overall interaction between axial load and moment due to lateral cyclic bending load with an accurate means of modelling is necessary prior to the predictable upsurge in practising EHSs. Yet, to the best of authors' knowledge, no research has been made on EHS columns under lateral cyclic bending load. As with any new cross-sectional shape, carrying out investigations on its various aspects is necessary to accredit its inclusion in different design specifications.

Therefore, the main objective of this study is to assess the cyclic flexural performance of EHS steel columns under the interaction of combined constant axial compressive load (with various axial load levels) and ELCF uniaxial bending load by evaluating hysteretic parameters like strength, ductility and energy absorption capacity with-respect-to their *a*/*b* ratios using FE modelling approach and furnish a comprehensive structural and rational earthquake-resistant guidance according to the state of the art in seismic engineering to promote their wider application in practice.

8.2 FINITE ELEMENT MODELLING

Abaqus (2009) has been used to analyse the performance of EHS steel cantilever column models under combined uni-axial ELCF lateral bending load and constant axial compressive load. The attributes of shell FE modelling framework adopted herein and presented in the subsequent sub-sections follow those reported in Nip et al. (2010b) and Fadden and McCormick (2014).

8.2.1 Geometric and Material Characteristics

Sixteen 3.6 mm thick EHS steel cantilever columns, EHS01c - EHS16c (Table 8.1) with four sets of column length '*L*' ranging between 300 mm to 600 mm, *a/b* ratios ranging between 1

and 2 are modelled with A_s ~ 511 mm^2. Shell thickness, t adopted is 3.6 mm which is offsetting from top surface to bottom surface in the section module during FE modelling. All the sixteen models are analysed under combined uniaxial lateral cyclic bending load about either axis separately and a constant axial compressive load, N_a which is n times of the axial compressive capacity, N_c of the columns respectively, making it a total of 112 [(4 + 12 + 12) × 4)] FEAs. The axial load level ratio, n of the column sections is defined as follows:

$$n = \frac{N_a}{N_c} \tag{8.10}$$

All the sixteen models are also analysed under monotonically increasing quasi-static axial compression displacement to obtain their respective N_c values with buckling about either axis separately, adding another 28 (4 + 12 + 12) FEAs to previously mentioned 112 FEAs. The cross-sectional schematic diagrams of the EHS column models and their geometric attributes considered for this FE simulation study are provided in Figure 8.2 and Table 8.1. P_M values in Table 8.1 are calculated according to Equation 2.1. While I_y, W_{ey}, W_{py}, I_z, W_{ez}, and W_{pz} values are calibrated as per the expressions catalogued in Table 2.1.

The mechanical and NLCHM model parameters are extracted from Nip et al. (2010a) for S235JRH grade CF-CS (see Table 2.3), which is assumed herein as the reference material during material modelling of EHS cantilever columns under lateral cyclic bending. Also, the monotonic tensile stress-strain curve (Figure 8.3) of S235JRH grade CF-CS obtained from Nip et al. (2010a) is used during estimation of N_c of EHS column models in the present study. The values of M_e and M_p are calculated using Equations 2.14 to 2.17. While, values of $D_{eq.c3}$, $D_{NSb.mj}$ and $D_{NSb.mn}$ are calculated using Equations 3.1, 4.26 and 4.27, respectively.

The respective column non-dimensional global slenderness, $\overline{\lambda}$ is calibrated according to Equation 2.36 and tabulated in Tables 8.2 and 8.3. For the practical range of EHS column slenderness values ($\overline{\lambda} \leq$ ~1.5) for sections with $\frac{a}{b} \leq 2.0$ considered, the non-dimensional global slenderness for lateral-torsional-buckling (LTB) $\overline{\lambda}_{LT}$ is always less than 0.4 (Law and Gardner 2013b). 0.4 being the tolerance limit for $\overline{\lambda}_{LT}$ below which LTB can be neglected (Law and Gardner 2012). However, the Japanese design guideline conservatively limits the column slenderness ratio to $0.25 \leq \overline{\lambda} \leq 0.60$ and the constant axial compressive thrust to a maximum of 20% of N_y during the design of steel bridge piers and thus ensuring reasonable

safety even in the event of a strong earthquake (Usami 1996). The axial yield capacity, N_y of all the EHS column sections is calculated as per Equation 2.19 and is equal to ~ 209.5 kN.

8.2.2 Meshing

Like in Sections 6.1.2 and 7.2.2, S4R, a three-dimensional four-node doubly curved quadrilateral robust general-purpose reduced integrated and structured stress/displacement shell element is employed herein for meshing the brace models.

Monotonic lateral bending experiments by Mamaghani (2008) on thin-walled steel box-section columns under constant axial compressive thrust to a maximum of 20% of N_y revealed that local buckling occurred near the column base at the height of about 0.7 times the width of the section. Elkady and Lignos (2017) observed that the plastic hinge length for wide-flange columns with fixed-flexible conditions under combined uniaxial cyclic loading and maximum constant compressive axial thrust of 50% of N_y applied at the flexible end is around 2.7 times the depth of the cross-section. As 0.6 is the maximum of the axial load ratio, n values considered in this study, the extent of the refined mesh in the longitudinal direction is set to ~6a (= 3 × 2a) including the transition zone from the fixed end as shown in Figure 8.4 for a typical cantilever column model. Therefore, ensuring sufficiently large refined area in the zone where the plastic hinge and local buckling is most likely to occur when the FE cantilever column models are subjected to cyclic uniaxial flexural and constant axial compressive loads together at the free end. The espoused element ratio in refined and coarser mesh regions is as low as 1 and 1.2 respectively (Figure 8.4). The number of S4R elements used in the analyses for various models ranges from ~ 1,500 – 3,600.

8.2.3 Boundary Conditions and Imperfections

Boundary conditions simulating a fixed-end cantilever column with one end (bottom end) completely fixed, *i.e.*, all the six degrees of freedom restrained for all nodes and the opposite end free and flexible to displace according to the combined cyclic flexural loading, H_c and constant axial thrust, N_a (Figures 8.5 and 8.6). Except for the pattern of cyclic flexural loading, H_c, the details of these very boundary conditions under practical testing laboratory environment are clearly described in the experimental facilities section of Cheng et al. (2013).

In reality, all structural members contain initial geometric imperfections. These imperfections trigger out-of-plane deflections at stresses below the theoretical critical buckling limits. ω_{g0} $\left(=L_{eff}/\alpha_g\right)$ and ω_{l0} $\left(=t/\beta_l\right)$ are global and local imperfection amplitudes with α_g and β_l as the respective imperfection factors. L_{eff} is effective length of the column member based on its critical buckling load. In case of cantilever columns with member length L, L_{eff} is equal to $2L$.Global imperfection amplitude of $L_{eff.}$/250 reflect the current allowable out-of-straightness tolerance for EHS tubes with $2a < 250mm$ in EN 10210-2 (2006). While, the maximum allowable out-of-straightness tolerance limit of $L_{eff.}$/500 is stipulated for hollow sections of other shapes, namely circular, square and rectangular in EN 10210-2 (2006), EN 10219-2 (2006), AS/NZS 1163 (2016), ASTM A501-01 (2005) specifications (Chan and Gardner 2009, Wardenier et al. 2010). However, $L_{eff.}$/500 is also stipulated as out-of-straightness tolerance for EHSs with $2a > 250mm$ in EN 10210-2 (2006). Hence, EHSs with lesser outer major diameter values under combined axial compression and bending loadings are envisaged to possess higher global imperfection amplitudes which can be greater than $L_{eff.}$/500.

Global imperfection amplitude of $L_{eff.}$/500 was successfully used in numerical studies of Law and Gardner (2013b), Law and Gardner (2013a) and Coelho et al. (Coelho et al. 2013)(2013). An imperfection amplitude of $L_{eff.}$/360 is used during the numerical study of EHS columns under compression load by Scullion et al. (2012). Therefore, a global imperfection amplitude range of $L_{eff.}$/400 to $L_{eff.}$/900 which is within the allowable out-of-straightness tolerance of $L_{eff.}$/250 for EHS tubes with $2a < 250mm$ as per EN 10210-2 (2006) is chosen during FE modelling of EHS columns in this study as indicated in Tables 8.4 and 8.5. It is to be noted that global imperfections are not considered during FE modelling when there is no axial compression load acting on the column, *i.e.*, at N_a = 0.

Local imperfection amplitude, ω_{l0} range of $\frac{t}{6.67}$ to $\frac{t}{10}$ reflect the maximum allowable thickness tolerance as per EN 10210-2 (2006), EN 10219-2 (2006), AS/NZS 1163 (2016), ASTM A501-01 (2005) specifications. But, usage of higher values of ω_{l0} with a range of $\frac{t}{3}$ to $\frac{t}{6}$ is also shown to provide better accuracy in the replicating the experimental structural response by Sun and Butterworth (1998), Gardner (2002), Huang and Young (2012), Fadden (2013) and Shokouhian and Shi (2015). Also, based on Dawson and Walker (1972) predictive model, Gardner et al. (2010) and Gardner and Nethercot (2004) proposed modified models for

determining ω_{l0} in hot-rolled, cold-formed carbon steel and stainless-steel HSSs. Initial local imperfections are embodied into the respective FE models herein with values of ω_{l0} ranging between $\frac{t}{3}$ and $\frac{t}{6}$ based on the imperfection sensitivity analyses carried out by Sun and Butterworth (1998), Gardner (2002), Huang and Young (2012) and Fadden (2013).

Both global and local initial geometric imperfections are seeded into the FE models by defining the nodes directly in their imperfect configuration based on the superposition of weighted eigenmode analysis data. Their respective typical lowest buckling mode shapes resulted from linear eigenvalue buckling analysis (obtained through the Lanczos method) for a typical FE cantilever column model are shown in Figure 8.7. Values of the imperfection amplitudes ω_{g0} $\left(= L_{eff}/\alpha_g\right)$ and ω_{l0} $(= t/\beta_l)$ and their respective imperfection factors α_g and β_l used during the modelling of EHS columns are tabulated in Tables 8.4 and 8.5.

In this study, the cyclic loading history, H_C is applied according to the pattern specified in SAC protocol (ANSI/AISC 341-16 2016). SAC protocol (ANSI/AISC 341-16 2016) loading pattern described in Section 2.3.2 (Figure 7.5) representing a far-field earthquake motion is being endorsed for interpreting the member behaviour of a moment connection during laboratory tests to make their quotients commensurable at an international level in seismic design (Fadden and McCormick 2014). The reference for increasing the amplitude of loading cycles in this protocol is the drift angle, θ which is the rotation of the imaginary straight line joining fixed end and the pinned end of the laterally loaded column as shown in Figures 8.5. For small θ up to 0.3 rad., lateral displacement, δ to be applied at the pinned end of the column along the major *or* minor axis as shown in Figure 8.6 can be calculated as the product of θ and L. The lateral cyclic loading history contains six cycles at each level of 0.00375, 0.005, 0.0075 rad., followed by four cycles at the level of 0.01 rad. and two cycles at each level of 0.015, 0.02, 0.03, 0.04, 0.05 rad. *etc.*, as shown in Figure 7.5. H_c is chosen to apply with a strain rate of $3\times10^{-4}s^{-1}$ which is within the quasi-static testing range as per BS 7270 (2006) at the pinned end of the cantilever column models through a "*reference point*" that acts as a pin to which all the circumferential nodes of the model in the loading plane are tied to by "*Kinematic Coupling*" available in the "*Constraint*" module of Abaqus (2009). The non-linear geometric parameter (NLGEOM) is also assigned in the analysis step to deal with large displacement analysis.

8.2.4 Validation of the FE Modelling Approach

The validation study performed in Section 7.2.4 is also valid for the modelling approach detailed in this Section 8.2.

8.3 PARAMETRIC STUDY

Axial compressive capacity, N_c of all the EHS column models under quasi-static monotonically increasing axial compression displacement at the pinned end in the absence of lateral displacement is found by performing FE simulations and catalogued in Tables 8.2 and 8.3. Also, their N_c/ N_y ratio with-respect-to their value is plotted in Figures 8.8a and 8.8b. It is to be noted that the true stress-strain values based on the stress-strain curve shown in Figure 8.3 are used for the EHS column models while obtaining the N_c values. Later, based on the N_c value of a column model and its buckling axis, the respective N_a value to be applied along with the cyclic lateral flexural load for a chosen n value is calibrated using Equation 8.10 and tabulated in Tables 8.2 and 8.3.

Based on N_a values, the equivalent CHS diameters and the respective cross-section slenderness ratios under combined axial-compression and bending are also calculated and tabulated in Tables 8.2 and 8.3 using Equations 5.77 and 5.78. On camparison with the existing and proposed EN 1993-1-1 (2005) slenderness limits (*i.e.*,compact section limit in case of bending and yield section limit in case of axial-compression) in Tables 3.5 and 4.4, the values in Tables 8.2 and 8.3 are lesser and thus all the cross-sections considered in this study are assumed to be either plastic or compact cross-sections under combined axial-compression and bending.

By employing the FE simulation mechanism discussed in the previous Section 8.2, FE simulation study is carried out on the EHS columns under combined global axial-compression and cyclic lateral flexural load along cross-sectional major *or* minor axis to study the cyclic-moment and axial compression-interaction, cyclic ductility and cyclic energy dissipation capacity indices. M_{Cy}–θ hysteresis loops of EHS cantilever column models are shown in Figures 8.9–8.16. A backbone envelope which is the locus of the tips of cyclic moment-rotation hysteresis curves during the first cycle at each level of rotation applied for all the models in their respective all-positive quadrant is also constructed in Figures 8.9–8.16.

8.3.1 Results and Discussion

Moment-rotation (*i.e.*, fixed end moment-drift angle) hysteresis curves of the EHS cantilever column models under combined global axial compression load and cyclic lateral bending load along cross-sectional major axis are shown in Figures 8.9–8.12. Respective imperfection amplitudes ω_{g0} and ω_{l0} utilised for carrying out the FE analyses are also provided in Table 8.4. M_{er} and M_{pr} value of all the EHS columns is calculated as per the Equations 8.7 and 8.8 and tabulated in Table 8.4. M_{uCy}, θ_y, δ_y, $\theta_{0.85u}$ and δ_u of all the models are calibrated for their respective cyclic moment-rotation backbone curve following a similar terminology explained in Figure 8.1 and tabulated in Table 8.4. $E_{e.cy}$ (= $M_{er} \times \theta_y$) value of all the column models is also calibrated and given in Table 8.4. The accumulated hysteretic energy, $E_{tot.cy}$ of all the columns (*i.e.*, the area under the M_{Cy}-θ hysteretic loops of each loading cycle till the cycle where θ_u is measured) obtained from FE analyses is also provided in Table 8.4.

In Figure 8.17, the interaction between cyclic plastic moment ratio, M_{uCy}/M_p with the applied global axial compression yield ratio, N_a/N_y is illustrated for columns with various global slenderness, $\overline{\lambda}$ values alongside the respective cross-section aspect ratio, *r* values. From left to right in Figures 8.9–8.12, M_{uCy} value increases with increase in the cross-sectional aspect ratio, *r*. Incidentally, M_{uCy}/M_p value also increases with increase in *r* value in Figure 8.17 from top to bottom. From top to bottom in Figures 8.9–8.12, it is found that with increase in length, *L* of the member *or* global slenderness, $\overline{\lambda}$, there is hardly any variation among the M_{uCy} values and thus the effect of $\overline{\lambda}$ on M_{uCy}/M_p is observed to be negligible in Figure 8.17. On the basis of FEA results presented in Table 8.4 and from Figure 8.17, empirical formulation depicting the interaction of cyclic plastic moment ratio, M_{uCy}/M_p with applied global axial compression yield ratio, N_a/N_y are expressed in Equation 8.11 from multiple non-linear regression analyses based on a lower bound fit for the data plotted in Figure 8.17. Interaction curves for EHS columns for various cross-sectional aspect ratios based on Equation 8.11 are plotted in Figure 8.18.

$$\left(\frac{N_a}{N_y}\right)^{\left(1.2063+\frac{0.6407}{r}-\frac{0.5375}{r^2}+\frac{0.454}{r^3}\right)} - \left(0.0202-\frac{0.9534}{r}+\frac{1.2143}{r^2}-\frac{0.6498}{r^3}\right)\left(\frac{M_{uCy}}{M_p}\right)^{\left(4.0847-\frac{4.6085}{r}+\frac{5.2854}{r^2}-\frac{2.6983}{r^3}\right)} = 1 \quad (8.11)$$

Cyclic ductility, $\mu_{cyb,mjr}\left(=\delta_u/\delta_y\right)$ value of all the EHS columns listed in Table 8.2 are calculated using the values of δ_u and δ_y values in Table 8.4 and plotted in Figure 8.19. Ductility is observed to reduce linearly with increase in the axial compression load ratio. From top to bottom in Figure 8.19, ductility increased with increase in the cross-sectional aspect ratio, *r*. Expression for the ductility of EHS columns based on the results presented in Table 8.4 and from Figure 8.19 from multiple non-linear regression analyses is derived as

$$\mu = \mu_{cyb,mjr} = \frac{\delta_u}{\delta_y} = -1.26\left(\frac{N_a}{N_y}\right) + \left\{\left(1.3747r - 7.1565\right)\bar{\lambda} + \left(0.6865r + 14.041\right)\right\} \quad (8.12)$$

As per Equation 8.9, cyclic energy dissipation capacity, $\bar{E}_{cy,mjr}\left(=E_{tot.cy}/E_{e.cy}\right)$ value is calculated using the values of $E_{tot.cy}$ and $E_{e.cy}$ values in Table 8.4 and plotted in Figure 8.20. From top to bottom in Figure 8.20, $\bar{E}_{cy,mjr}$ increased with increase in the cross-sectional aspect ratio, *r*. Expression for $\bar{E}_{cy,mjr}$ of EHS columns based on the values presented in Table 8.4 and from Figure 8.20 from multiple non-linear regression analyses is given as

$$\begin{aligned}\bar{E}_{cy} = \bar{E}_{cy,mjr} = &\left[\left\{\left(381.272\times 3.463^{r}\right)-1143.45\right\}\bar{\lambda} + \left(-1025.292r + 2217.156\right)\right]\times\left(\frac{N_a}{N_y}\right)^2 \\ &+\left[\left(-2413.304r + 2099.029\right)\bar{\lambda} + \left(935.51r - 1195.113\right)\right]\times\left(\frac{N_a}{N_y}\right) \\ &+\left[\left(602.336r - 386.572\right)\bar{\lambda} + 284.663\right]\end{aligned} \quad (8.13)$$

From Figures 8.17, 8.19 and 8.20 and from Equations 8.11–8.13, unlike in the case of cyclic-ductility and cyclic-energy dissipation capacity, the effect of non-dimensional global slenderness, $\bar{\lambda}$ on cyclic-moment–axial-compression interaction is found to be negligible for each of the cross-sectional aspect ratio and cross-sectional slenderness values considered.

Moment-rotation (*i.e.*, fixed end moment-drift angle) hysteresis curves of the EHS cantilever column models under combined global axial compression load and cyclic lateral bending load along cross-sectional minor axis are shown in Figures 8.13–8.16. Respective global and local imperfection amplitudes, ω_{g0} and ω_{l0} utilised for carrying out the FE analyses are also provided in Table 8.5. M_{er} and M_{pr} value of all the EHS columns is calculated as per the Equations 8.7 and 8.8 and tabulated in Table 8.5. M_{uCy}, θ_y, δ_y, $\theta_{0.85u}$ and δ_u of all the models are calibrated for their respective cyclic moment-rotation backbone curve following a similar terminology explained in Figure 8.1 and tabulated in Table 8.5. $E_{e.cy}$ (= $M_{er} \times \theta_y$) value of all the column models is also calibrated and given in Table 8.5. The accumulated hysteretic energy, $E_{tot.cy}$ of all the columns (*i.e.*, the area under the M_{Cy}-θ hysteretic loops of each loading cycle till the cycle where θ_u is measured) obtained from FE analyses is also provided in Table 8.5.

In Figure 8.21, the interaction between cyclic plastic moment ratio, M_{uCy}/M_p with the applied global axial compression yield ratio, N_a/N_y is illustrated for columns with various global slenderness, $\overline{\lambda}$ values alongside the respective cross-section aspect ratio, *r* values. From left to right in Figures 8.13–8.16, M_{uCy} value decreases with increase in the cross-sectional aspect ratio, *r*. Incidentally, M_{uCy}/M_p value also decreases with increase in *r* value in Figure 8.21 from top to bottom. From top to bottom in Figures 8.13–8.16, it is found that with increase in length, *L* of the member *or* global slenderness, $\overline{\lambda}$, there is hardly any variation among the M_{uCy} values and thus the effect of $\overline{\lambda}$ on M_{uCy}/M_p is observed to be negligible in Figure 8.21. On the basis of FEA results presented in Table 8.5 and from Figure 8.21, empirical formulation depicting the interaction of cyclic plastic moment ratio, M_{uCy}/M_p with applied global axial compression yield ratio, N_a/N_y are expressed in Equation 8.14 from multiple non-linear regression analyses based on a lower bound fit for the data plotted in Figure 8.21. Interaction curves for EHS columns for various cross-sectional aspect ratios based on Equation 8.14 are plotted in Figure 8.22.

$$\left(\frac{N_a}{N_y}\right)^{\left(2.2236-\frac{3.961}{r}+\frac{6.327}{r^2}-\frac{2.8222}{r^3}\right)}+$$

$$\left(0.1791r^3-0.6908r^2+0.918r-0.0387\right)\left(\frac{M_{uCy}}{M_p}\right)^{\left(-0.4596r^3+1.6363r^2-1.9496r+2.8428\right)}=1 \quad (8.14)$$

Cyclic ductility, $\mu_{cyb,mnr}\left(=\delta_u/\delta_y\right)$ value of all the EHS columns considered in Table 8.3 are calculated using the values of δ_u and δ_y values in Table 8.5 and plotted in Figure 8.23. Ductility is observed to reduce linearly with increase in the axial compression load ratio. From top to bottom in Figure 8.23, ductility decreased with increase in the cross-sectional aspect ratio, *r*. Expression for the ductility of EHS columns based on the results presented in Table 8.5 and from Figure 8.23 from multiple non-linear regression analyses is derived as

$$\mu=\mu_{cyb,mnr}=\frac{\delta_u}{\delta_y}=$$

$$-1.26\left(\frac{N_a}{N_y}\right)+\left\{\left(-3.2545r^2+14.089r-16.863\right)\bar{\lambda}+\left(29.288r^{-0.3462}-14.377\right)\right\} \quad (8.15)$$

As per Equation 8.9, cyclic energy dissipation capacity, $\bar{E}_{cy,mnr}\left(=E_{tot.cy}/E_{e.cy}\right)$ value is calculated using the values of $E_{tot.cy}$ and $E_{e.cy}$ values in Table 8.5 and plotted in Figure 8.24. From top to bottom in Figure 8.24, $\bar{E}_{cy,mnr}$ decreased with increase in the cross-sectional aspect ratio, *r*. Expression for $\bar{E}_{cy,mnr}$ of EHS columns based on the results presented in Table 8.5 and from Figure 8.24 from multiple non-linear regression analyses is given as

$$\bar{E}_{cy}=\bar{E}_{cy,mnr}=\left[\left(-192.506r+431.009\right)\bar{\lambda}+\left(-56.658r^{3.711}+1217.942\right)\right]\times\left(\frac{N}{N_y}\right)^2$$

$$+\left[\left(346.419r-831.466\right)\bar{\lambda}+\left(239.614r^2-553.669r+187.51\right)\right]\times\left(\frac{N}{N_y}\right)$$

$$+\left[\left(-115.697r+326.164\right)\bar{\lambda}+\left(\frac{410.24}{r+0.0572}-104.694\right)\right] \quad (8.16)$$

From Figures 8.21, 8.23 and 8.24 and from Equations 8.14–8.16, unlike in the case of cyclic-ductility and cyclic-energy dissipation capacity, the effect of non-dimensional global

slenderness, $\overline{\lambda}$ on cyclic-moment–axial-compression interaction is found to be negligible for each of the cross-sectional aspect ratio and cross-sectional slenderness values considered.

8.4 SUMMARY

The performance of carbon-steel EHS FE cantilever column models under combined axial compression and ELCF uni-axial bending load following the SAC protocol (ANSI/AISC 341-16 2016) loading pattern is analysed. A parametric study is performed on the characteristics like cyclic-moment–axial-compression interaction, cyclic dutility and energy dissipation capacity. The deductions from the parametric study are summarised as follows:

- The empirical expressions for the cyclic-moment–axial-compression interaction and cyclic-ductility and cyclic-energy dissipation capacity curves of EHS columns are established.
- Based on the proposed empirical expressions, cyclic-ductility and cyclic-energy dissipation capacity are found to be dependent on the co-existing influence of non-dimensional global slenderness and cross-sectional aspect ratio *or* local slenderness
- Unlike in the case of cyclic-ductility and cyclic-energy dissipation capacity, the effect of non-dimensional global slenderness on cyclic-moment–axial-compression interaction is found to be negligible for each of the cross-sectional aspect ratio and cross-sectional slenderness values considered.

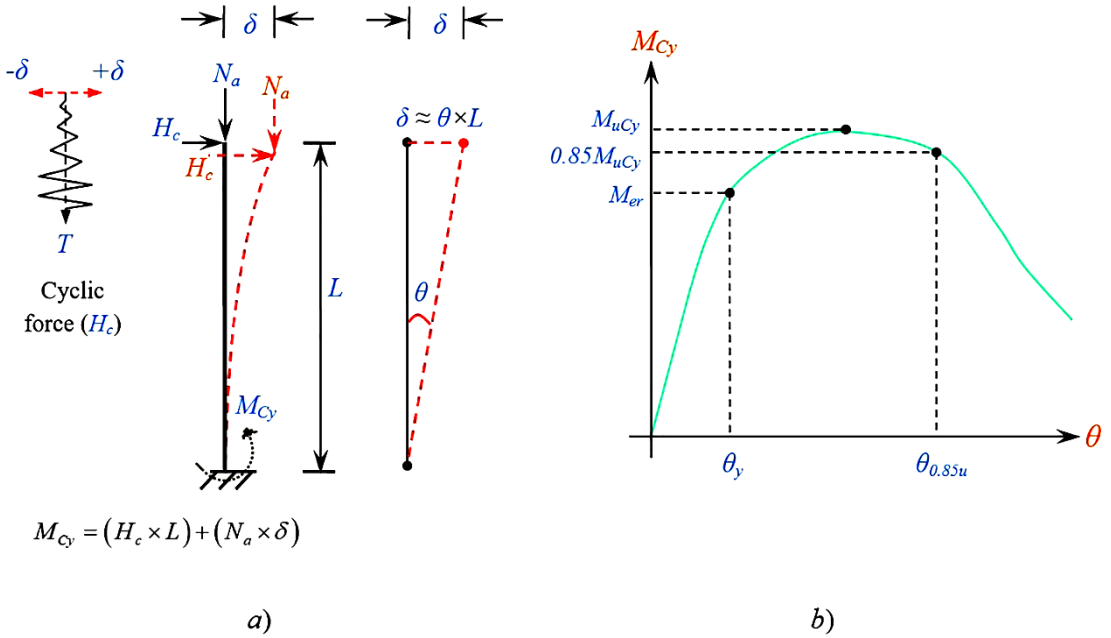

Figure 8.1 *a) Schematic boundary and applied loading conditions on a cantilever column; b) Generalized M_{Cy}-θ response of a typical cantilever steel column with compact or plastic cross-section*

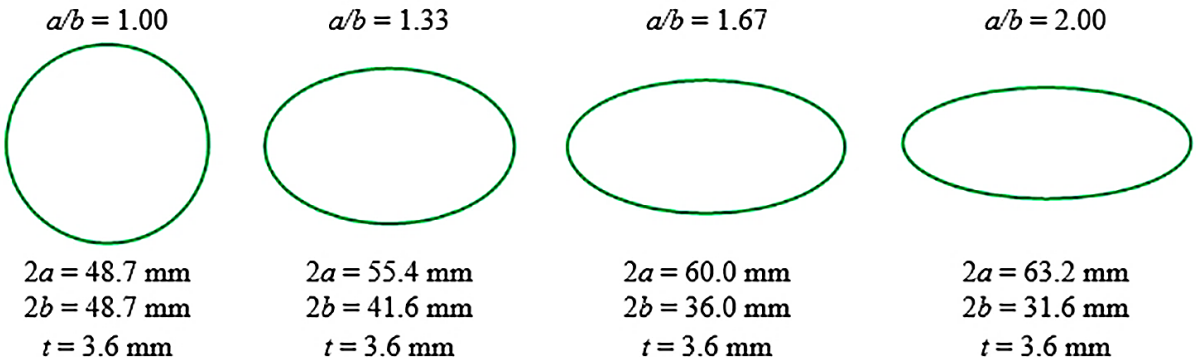

Figure 8.2 *Selected EHS cross-sectional dimensions for FE modelling*

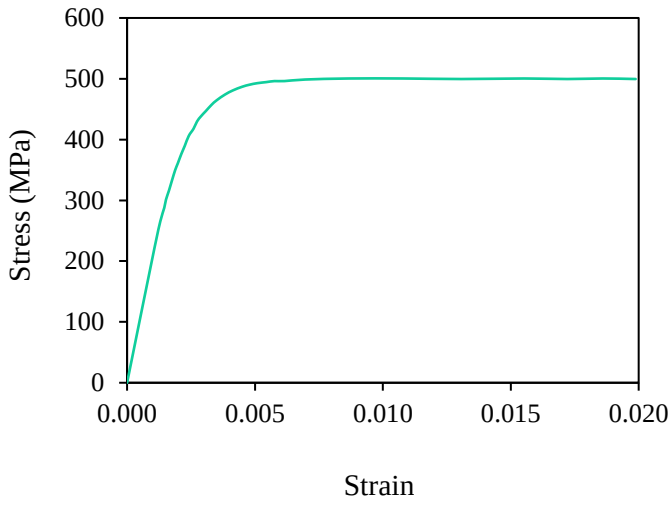

Figure 8.3 *Monotonic tensile stress-strain curve of Gr. S235JRH CF-CS*

Source: Nip et al. (2010a)

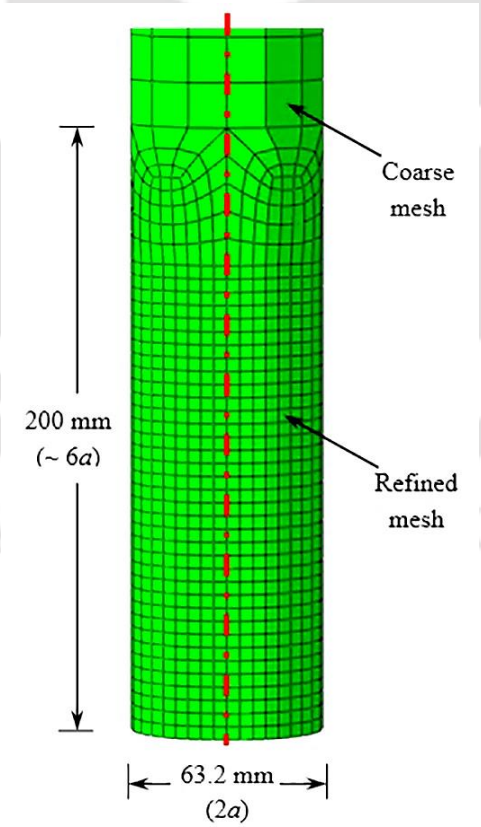

Figure 8.4 *FE mesh pattern at fixed end of EHS16c (63.2 × 31.6 × 3.6 × 600 mm) column model*

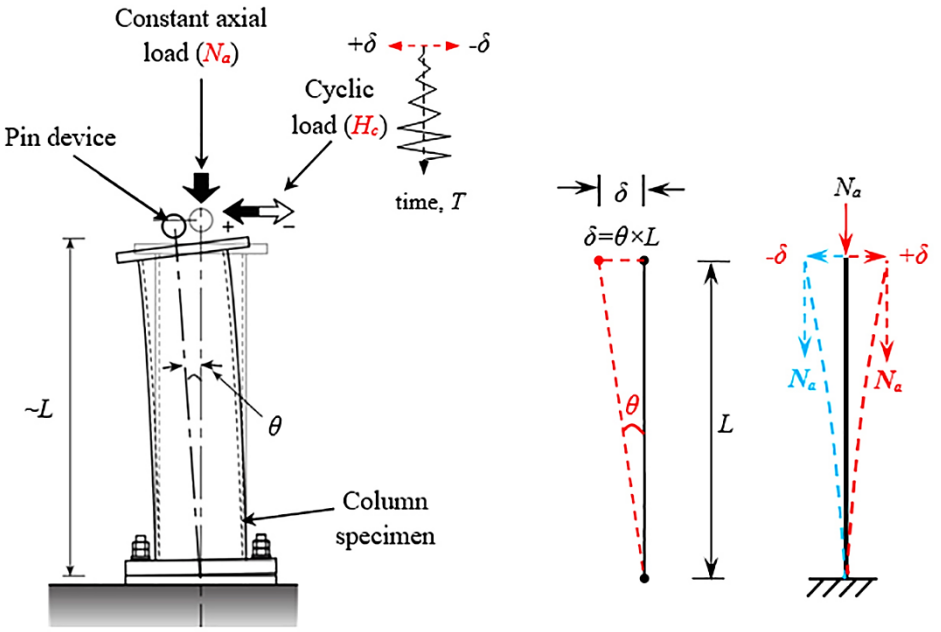

Figure 8.5 *Schematic of applied boundary conditions*

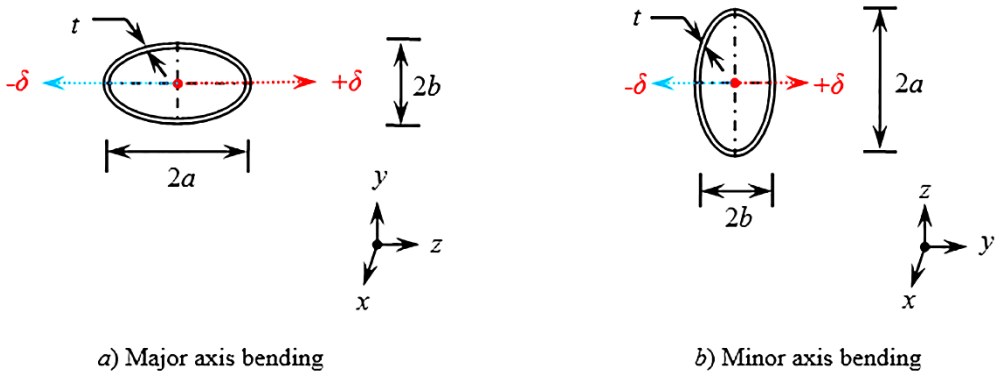

a) Major axis bending

b) Minor axis bending

Figure 8.6 *Direction of cyclic flexural load at the cross-section level near flexible/free end of the column*

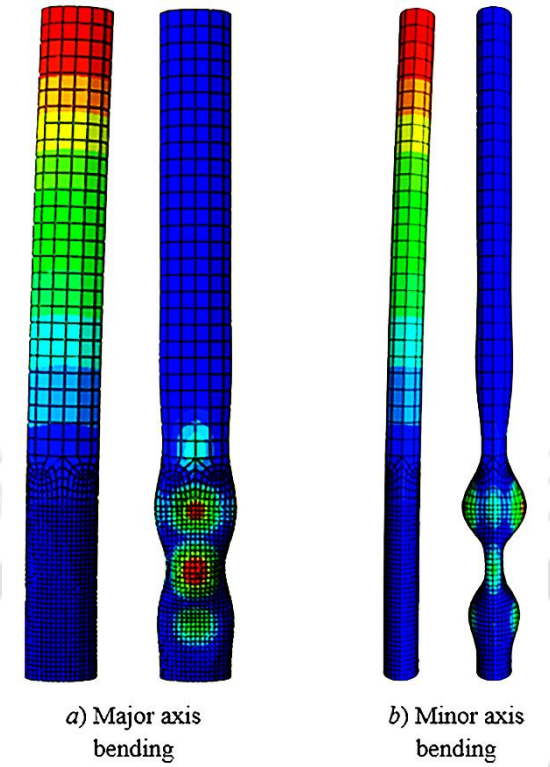

Figure 8.7 *Initial global and local buckling shapes of EHS16c (63.2 × 31.6 × 3.6 × 600 mm) column model with a deformation scale factor of 15*

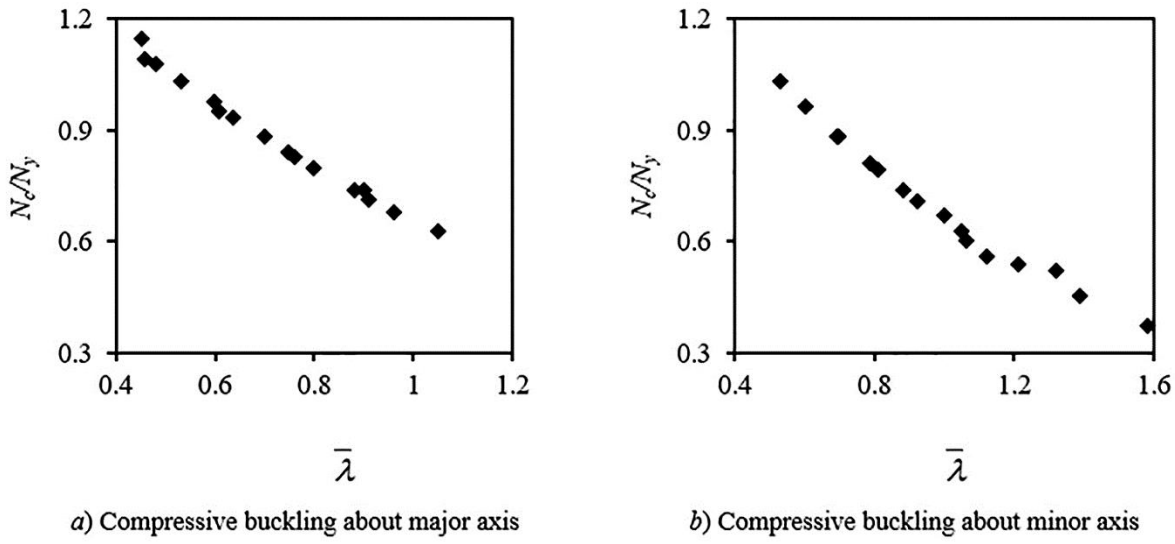

Figure 8.8 *Normalised axial compressive buckling capacities of EHS column models*

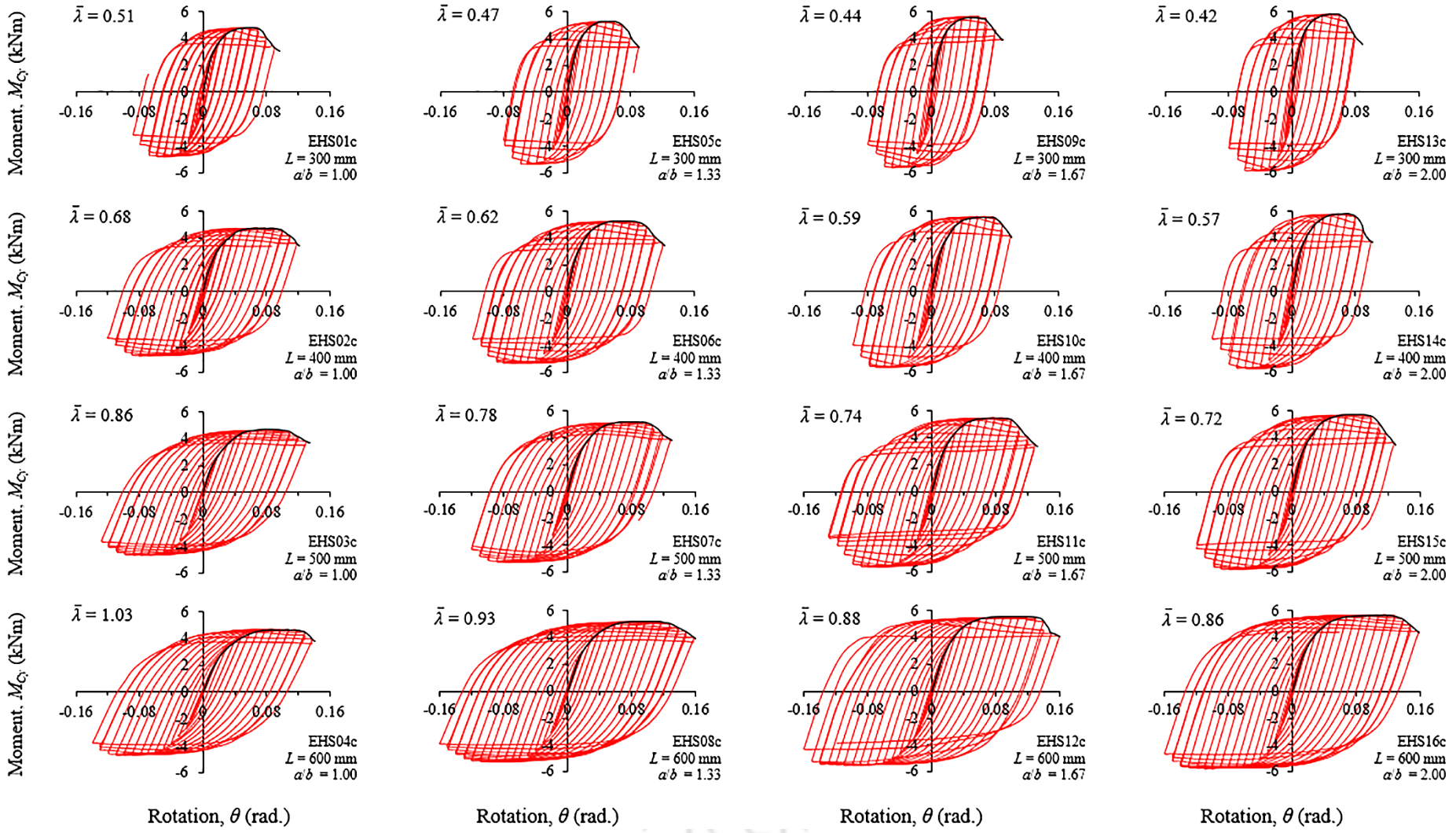

Figure 8.9 *Moment-rotation hysteresis curves of EHS cantilever column models under major axis bending at n = 0.00*

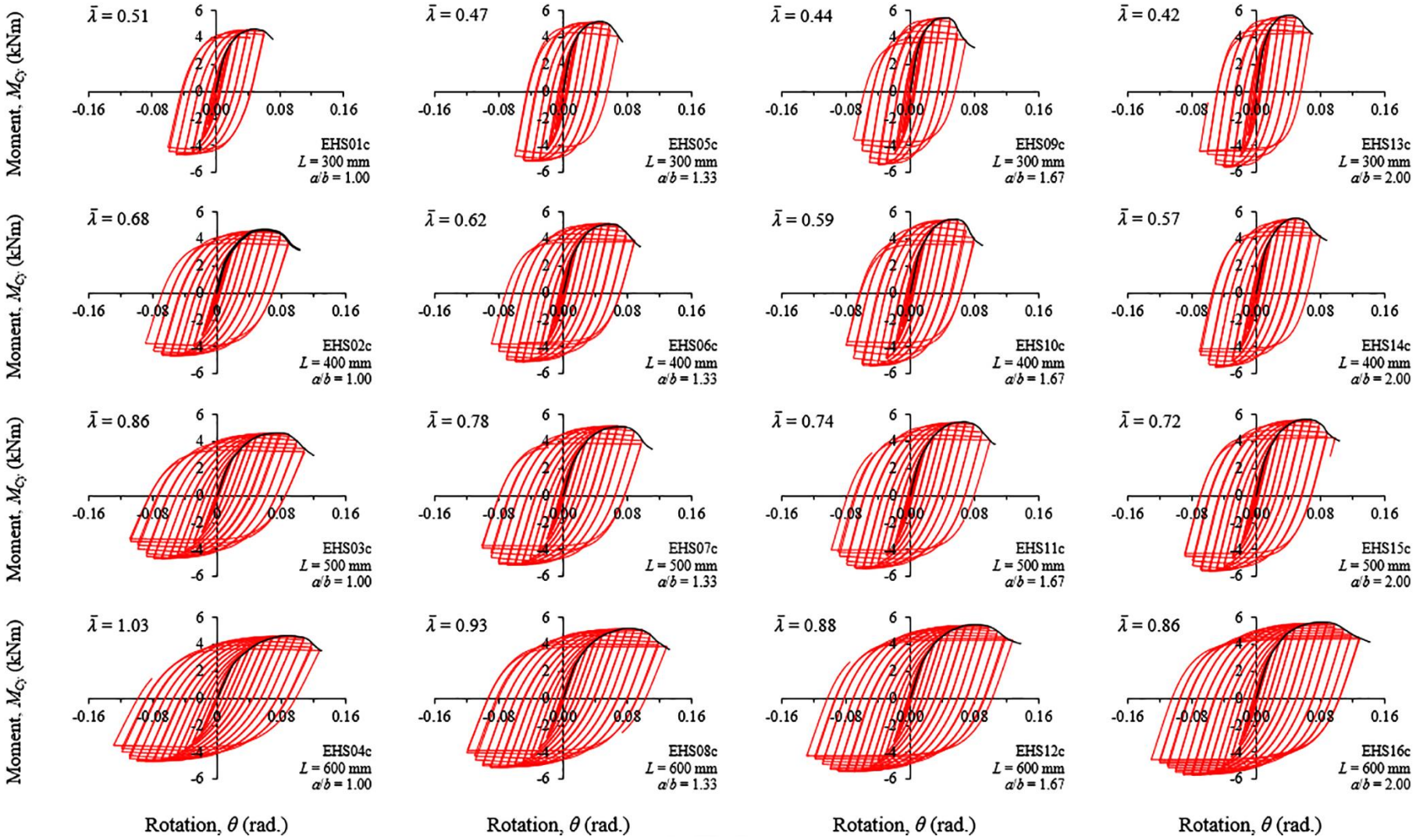

Figure 8.10 *Moment-rotation hysteresis curves of EHS cantilever column models under major axis bending at n = 0.20*

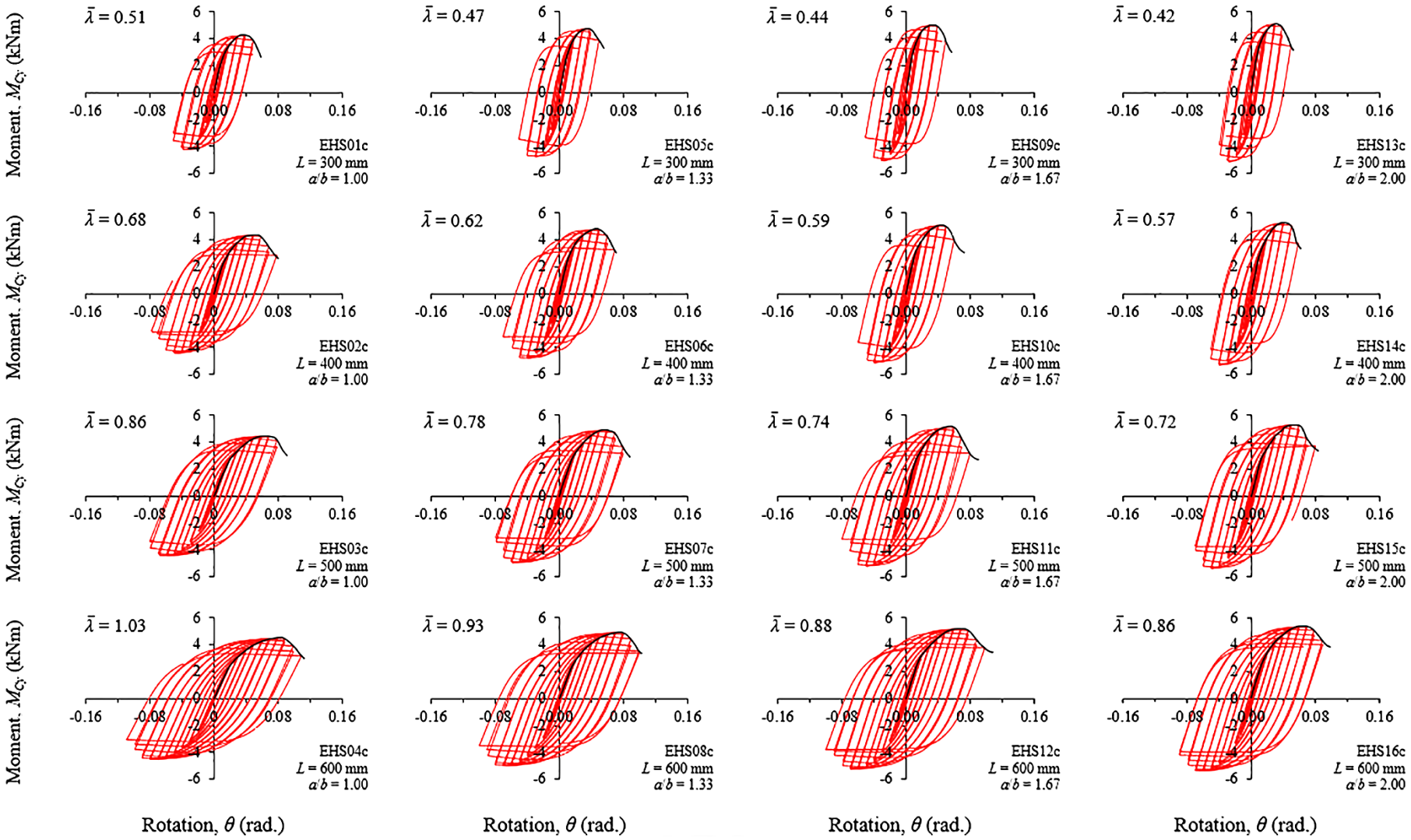

Figure 8.11 *Moment-rotation hysteresis curves of EHS cantilever column models under major axis bending at n = 0.40*

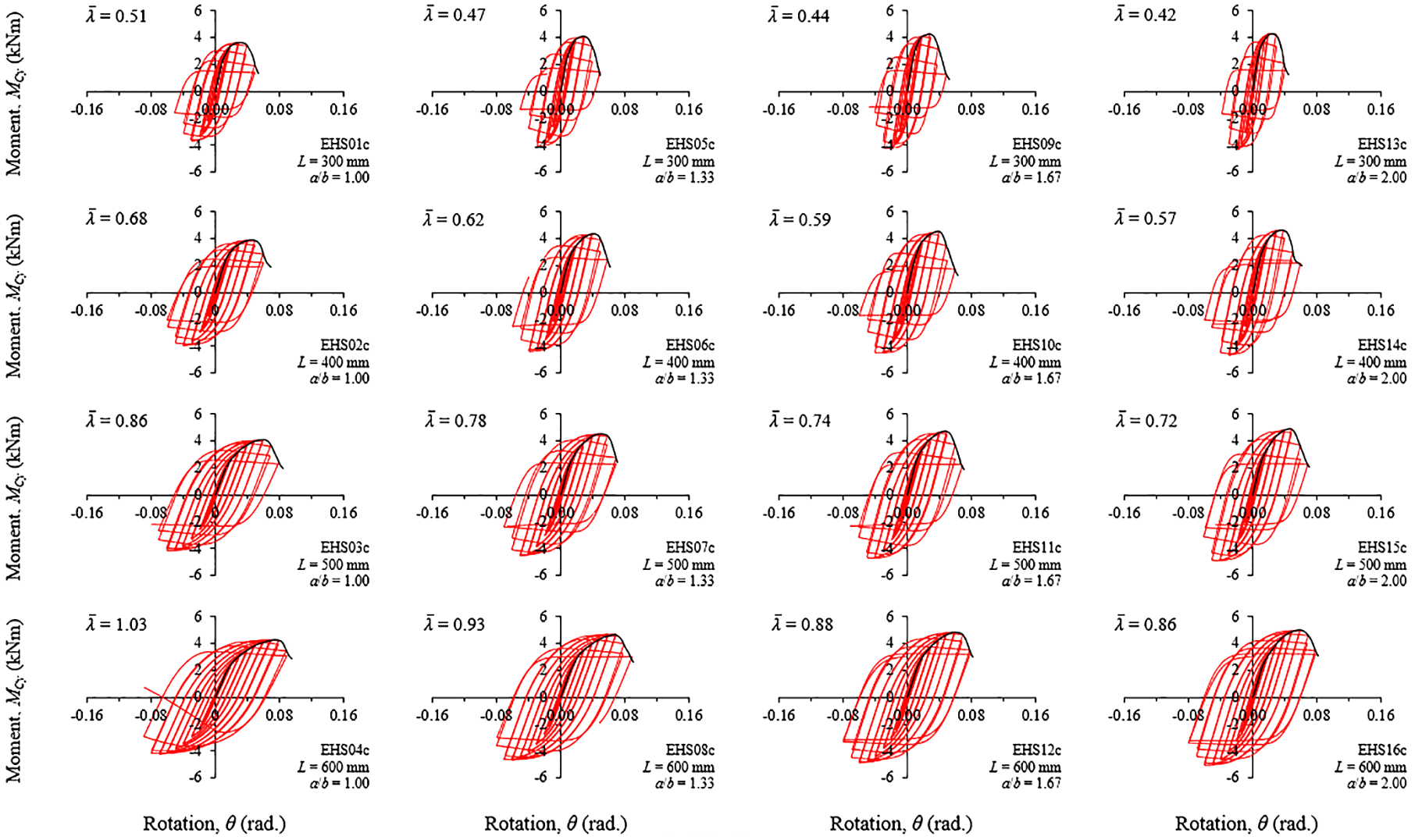

Figure 8.12 *Moment-rotation hysteresis curves of EHS cantilever column models under major axis bending at n = 0.60*

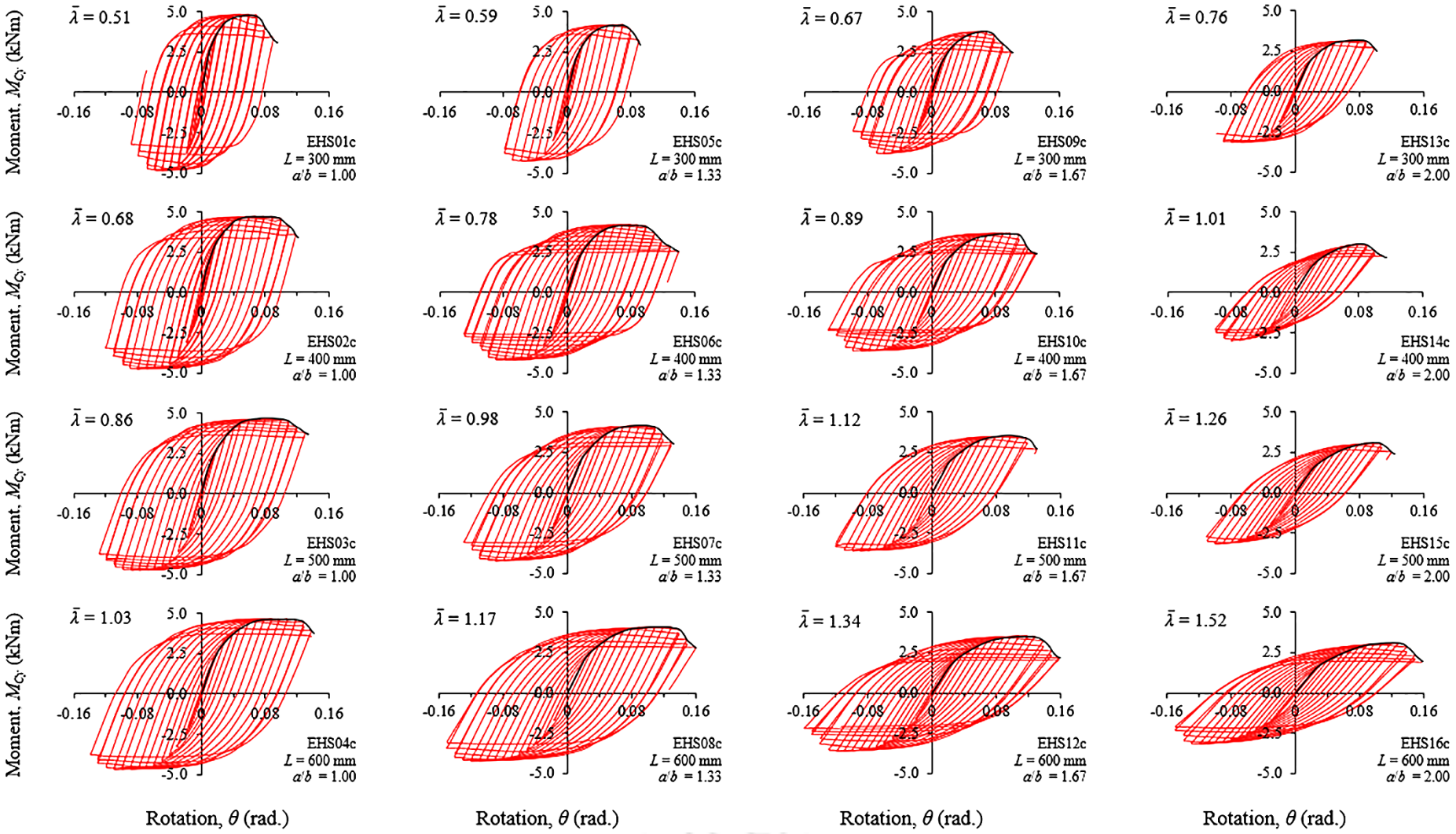

Figure 8.13 *Moment-rotation hysteresis curves of EHS cantilever column models under minor axis bending at n = 0.00*

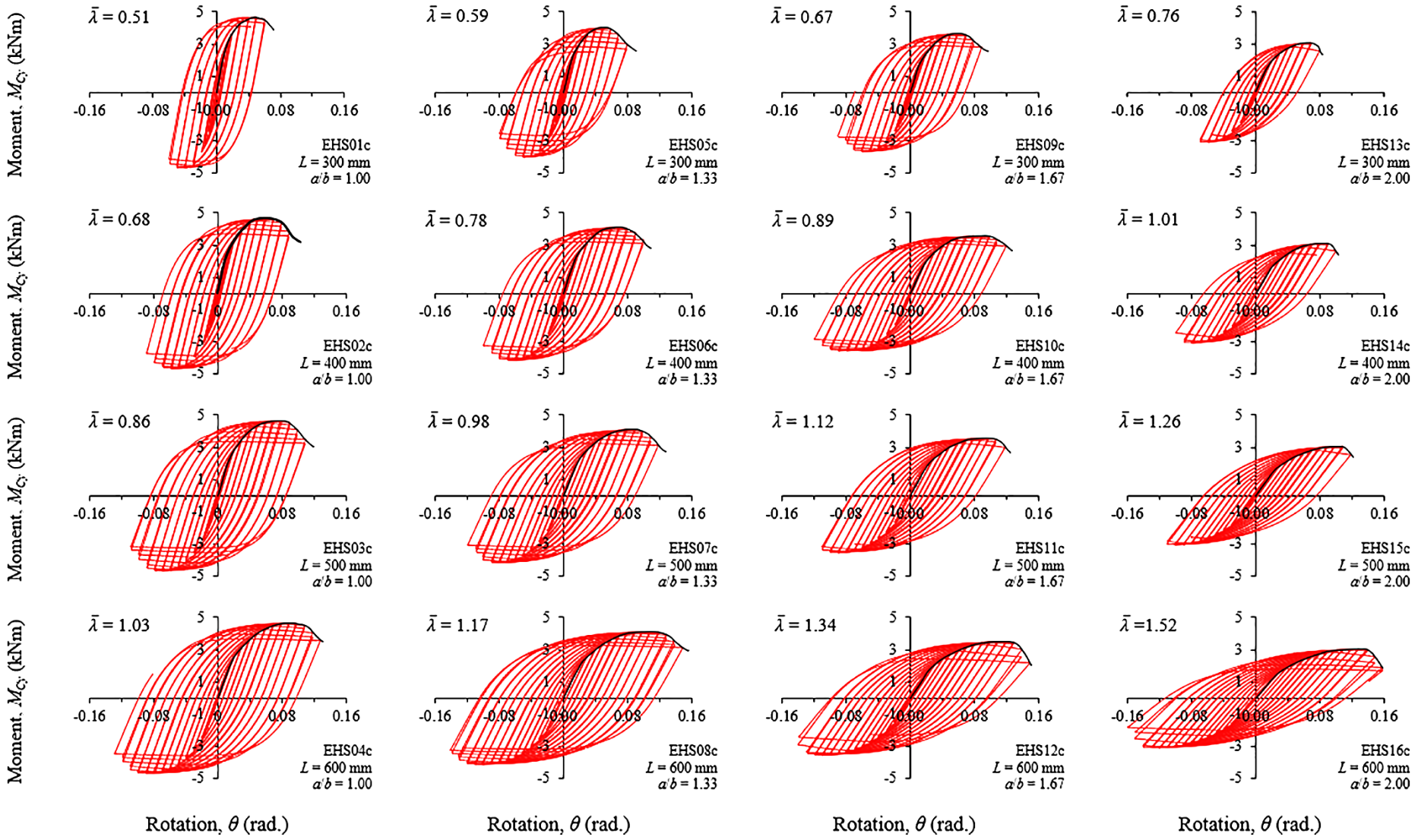

Figure 8.14 *Moment-rotation hysteresis curves of EHS cantilever column models under minor axis bending at n = 0.20*

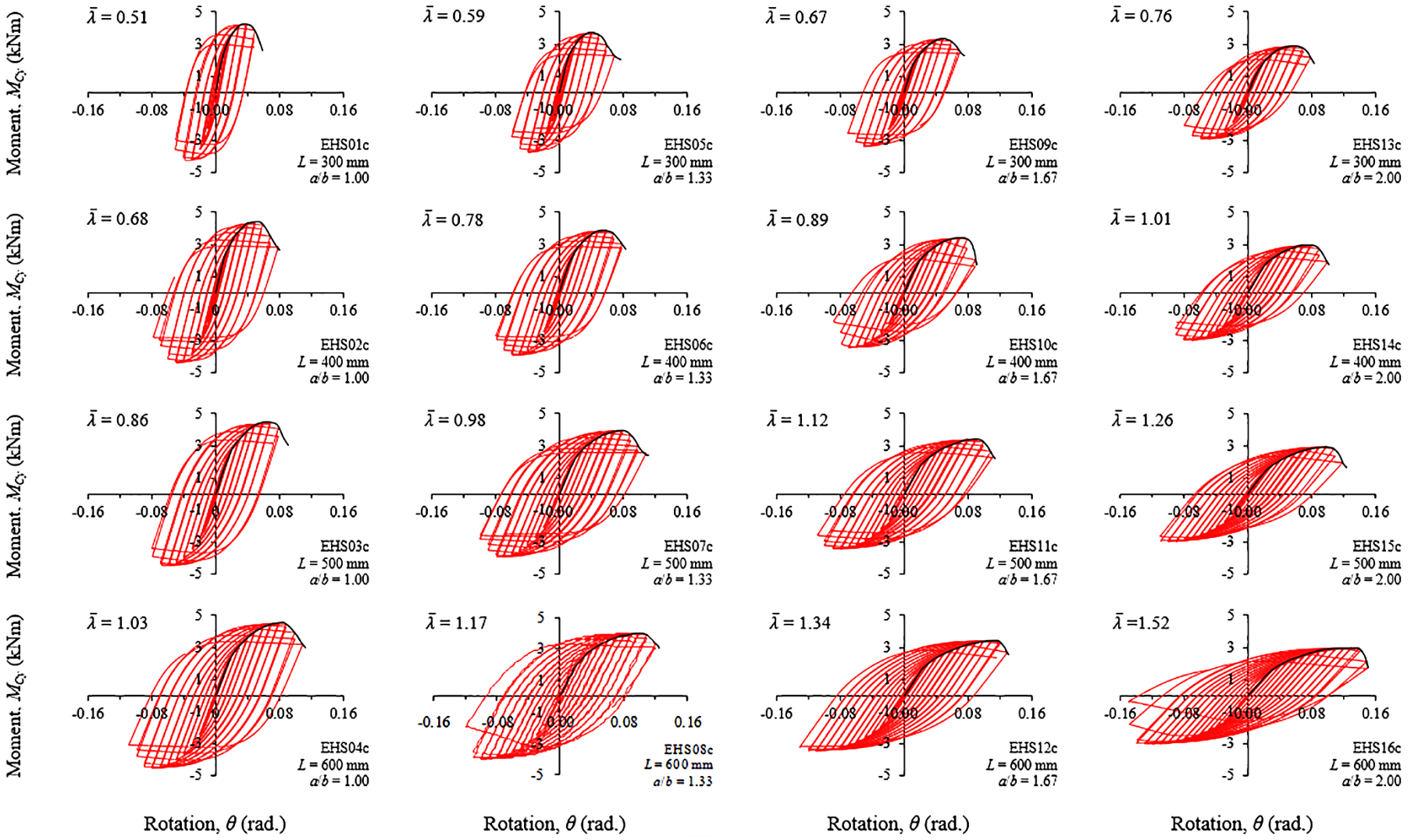

Figure 8.15 *Moment-rotation hysteresis curves of EHS cantilever column models under minor axis bending at n = 0.40*

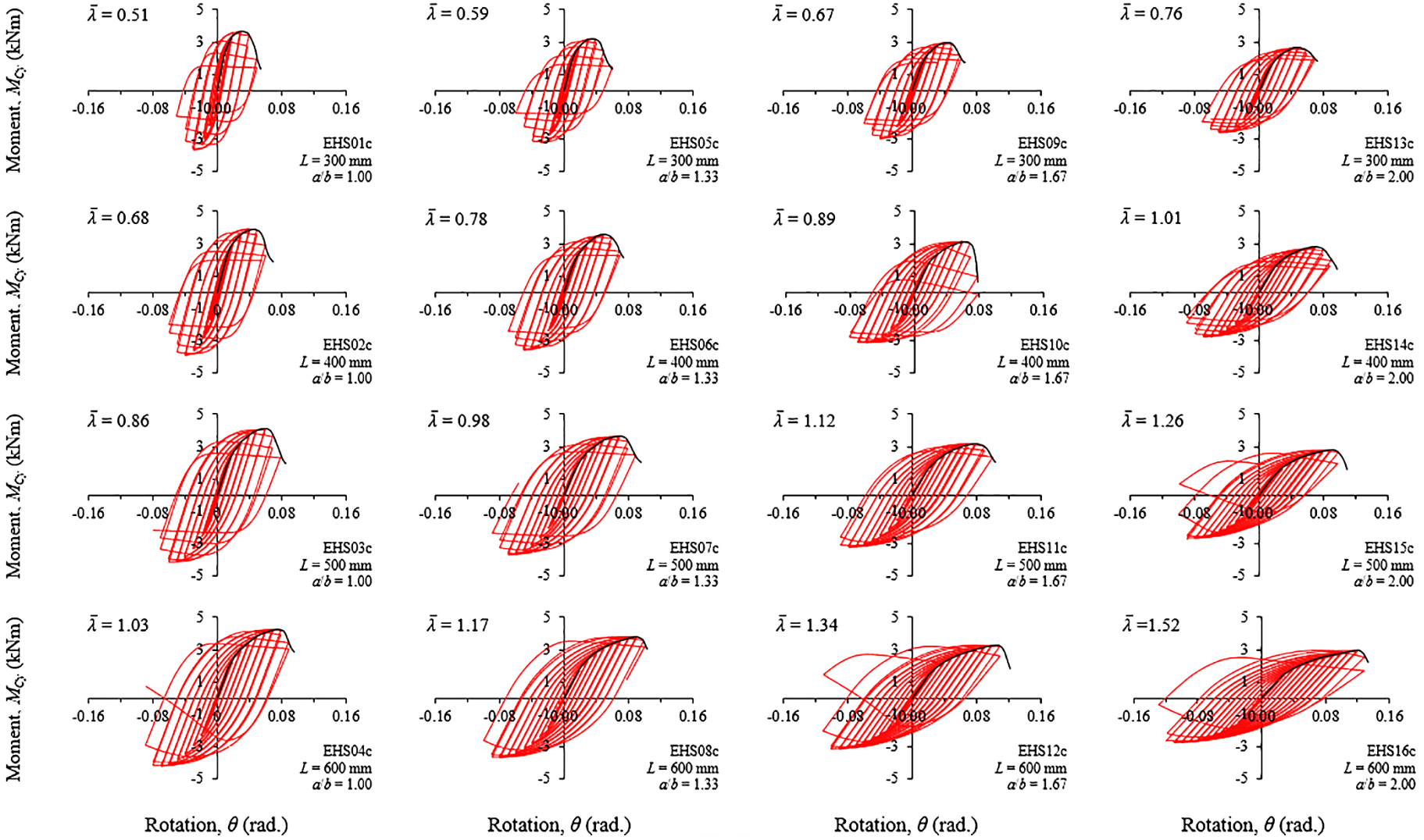

Figure 8.16 *Moment-rotation hysteresis curves of EHS cantilever column models under minor axis bending at n = 0.60*

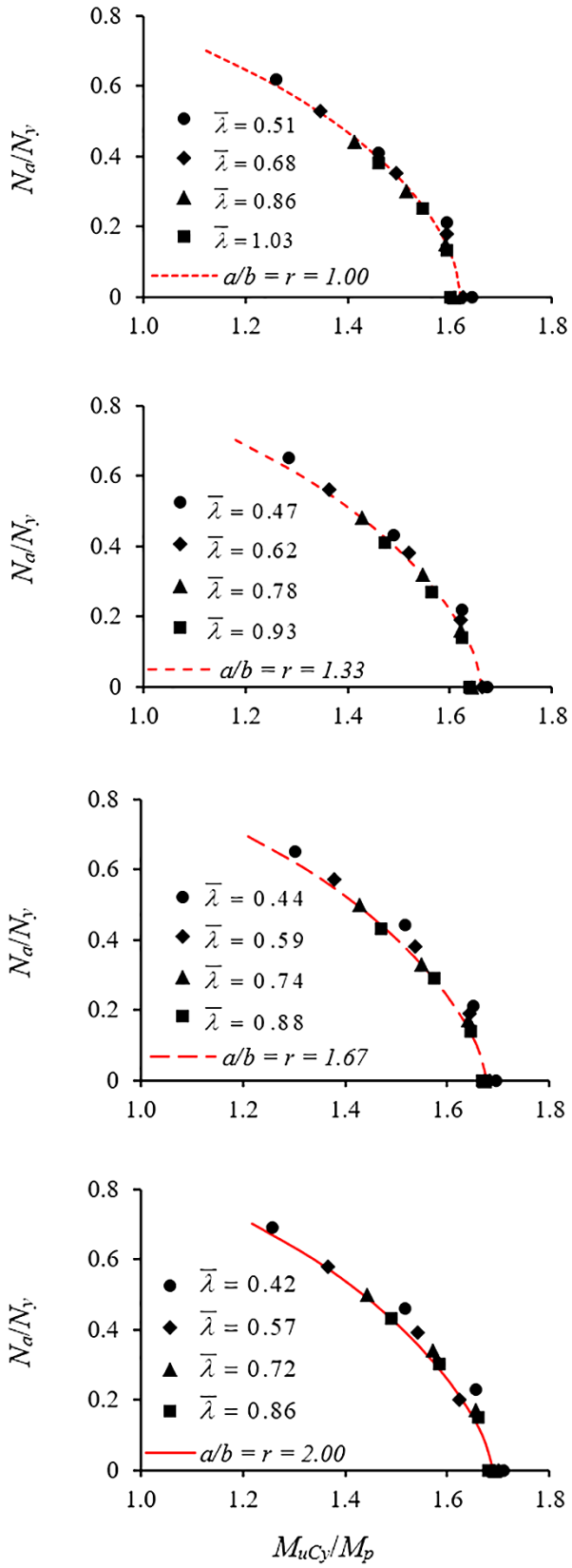

Figure 8.17 *Plastic interaction charts for EHS columns under combined global axial compression load and cyclic lateral flexural load along cross-sectional major axis*

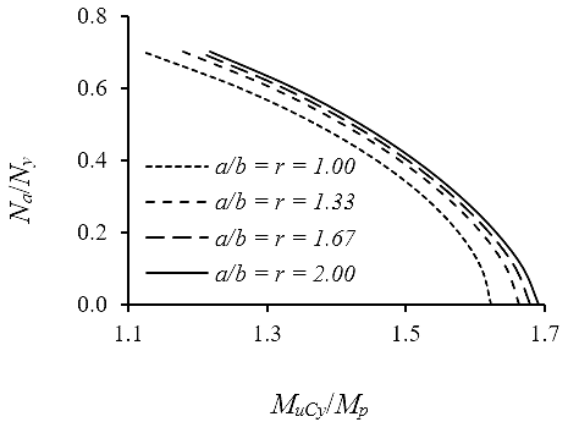

Figure 8.18 *Plastic interaction curves for EHS columns of various cross-sectional aspect ratios under combined global axial compression load and cyclic lateral flexural load along cross-sectional major axis*

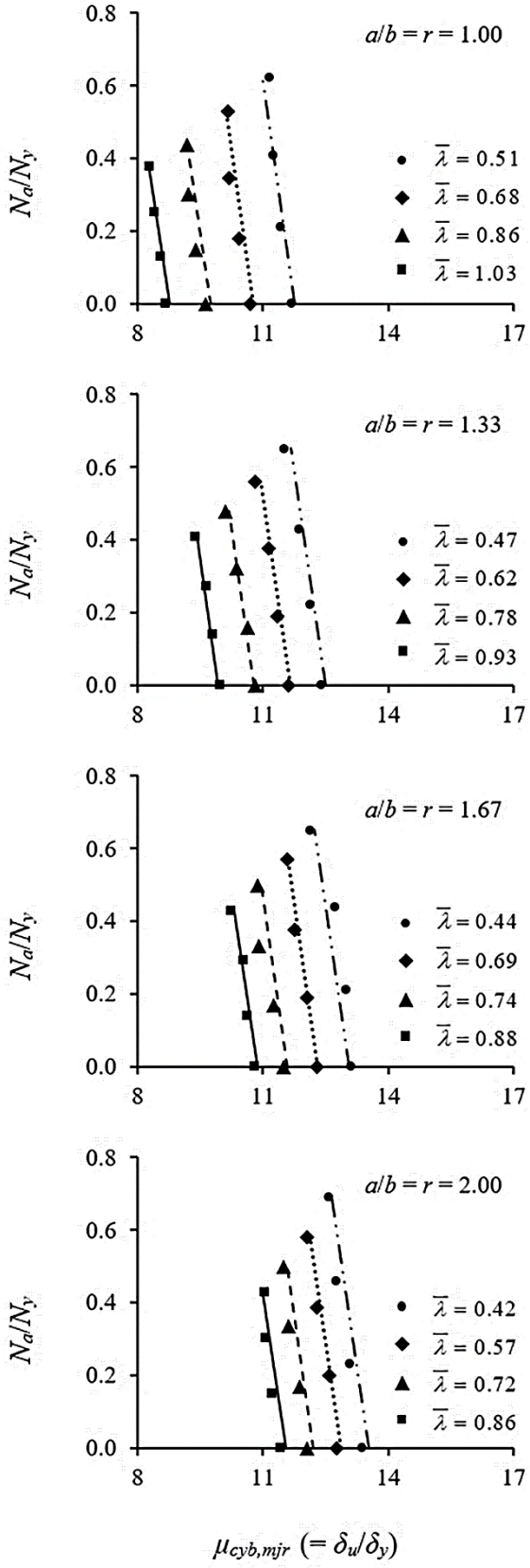

Figure 8.19 *Cyclic ductility plots for EHS columns under combined global axial compression load and cyclic lateral flexural load along cross-sectional major axis*

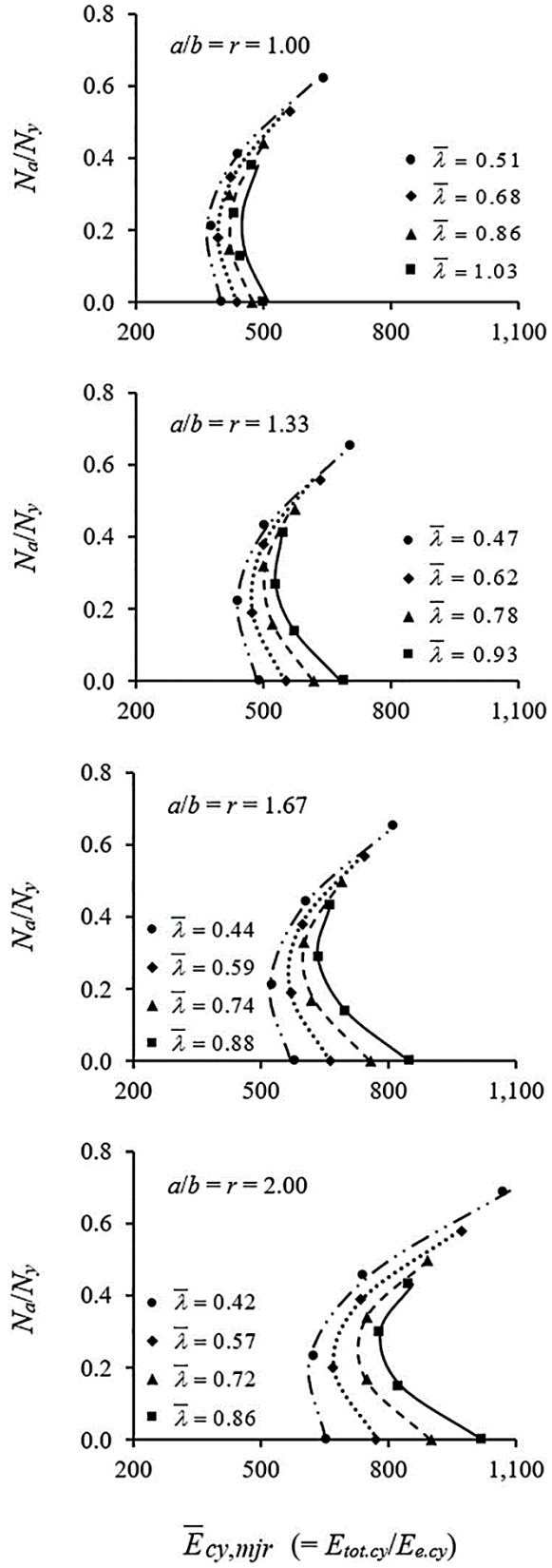

Figure 8.20 *Cyclic energy dissipation capacity plots for EHS columns under combined global axial compression load and cyclic lateral flexural load along cross-sectional major axis*

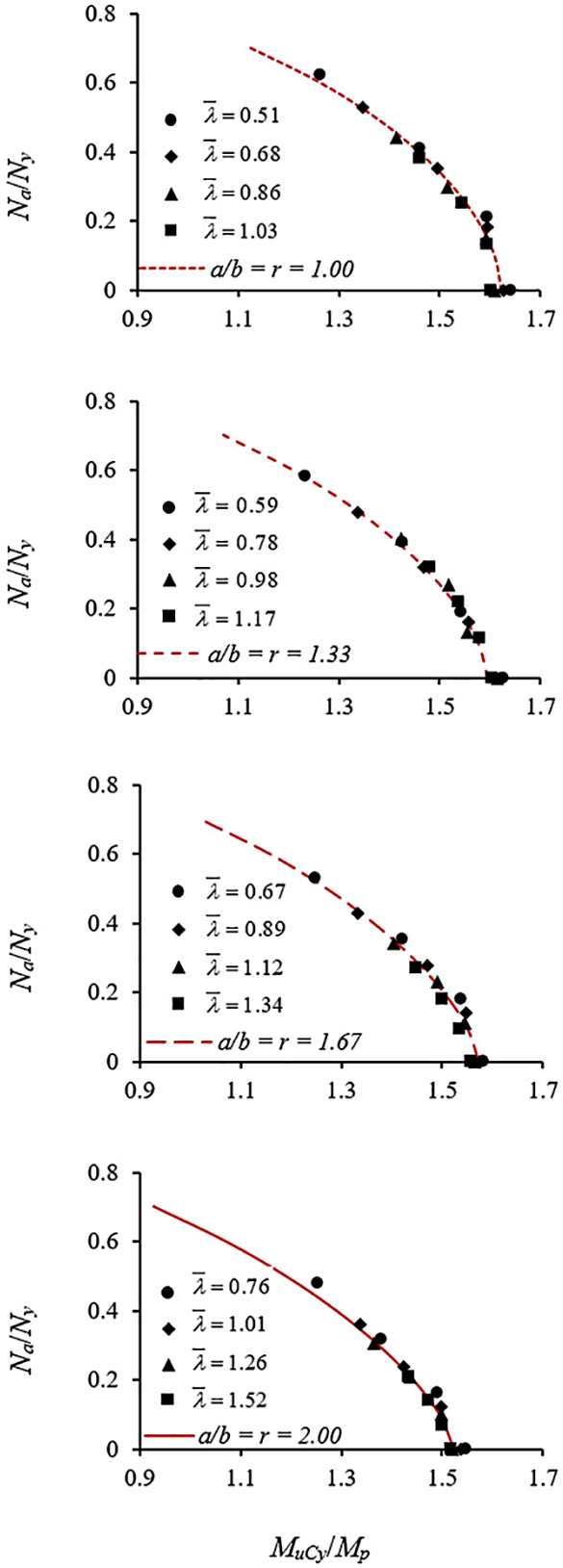

Figure 8.21 *Plastic interaction charts for EHS columns under combined global axial compression load and cyclic lateral flexural load along cross-sectional minor axis*

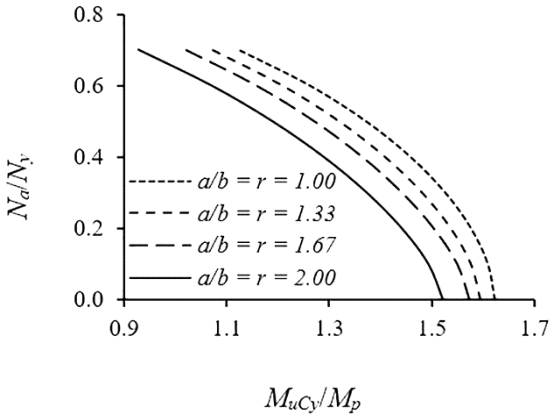

Figure 8.22 *Plastic interaction curves for EHS columns of various cross-sectional aspect ratios under combined global axial compression load and cyclic lateral flexural load along cross-sectional minor axis*

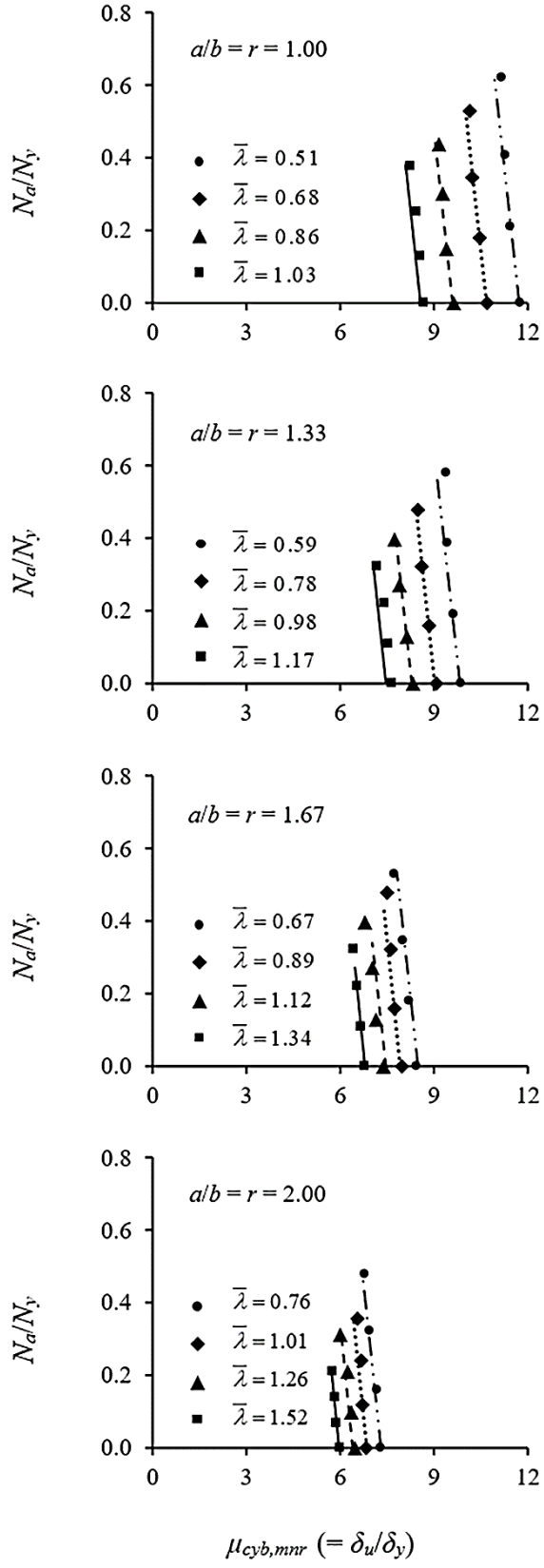

Figure 8.23 *Cyclic ductility plots for EHS columns under combined global axial compression load and cyclic lateral flexural load along cross-sectional minor axis*

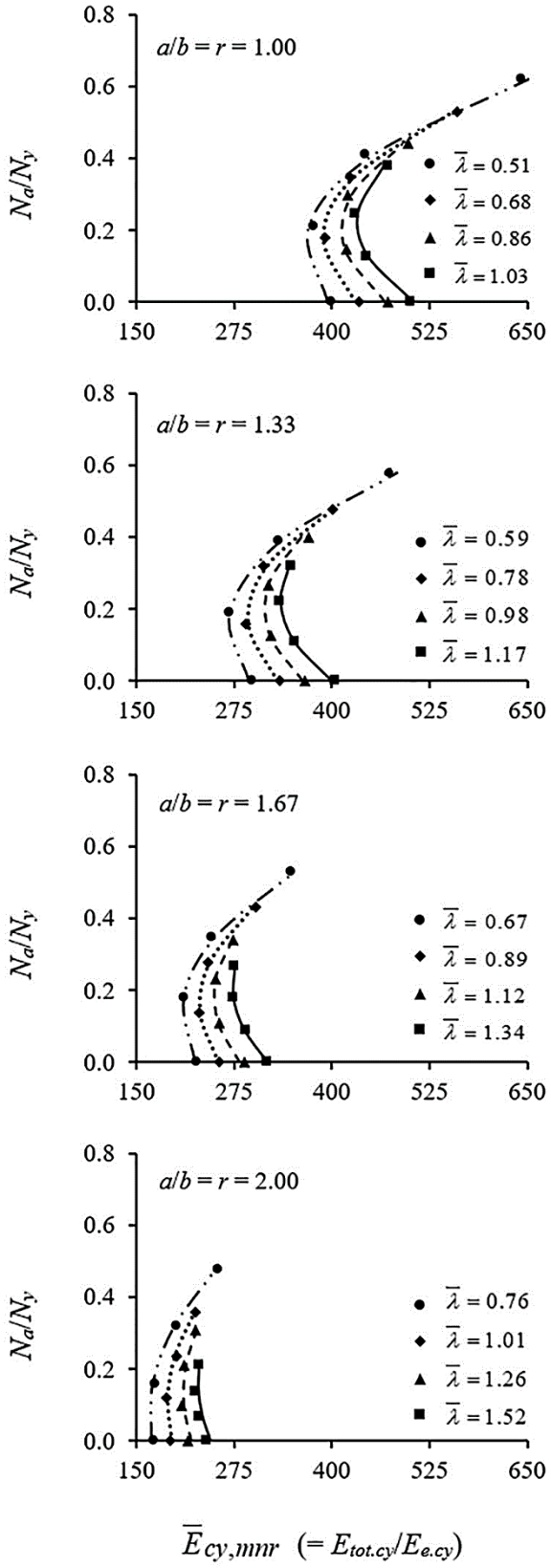

Figure 8.24 *Cyclic energy dissipation capacity plots for EHS columns under combined global axial compression load and cyclic lateral flexural load along cross-sectional minor axis*

Table 8.1 *Geometric properties of EHS cantilever column models*

Specimen Id.	$2a \times 2b \times t$ (mm × mm × mm)	$\frac{a}{b}$	$\frac{P_M}{t}$	$D_{eq.c3}$ (mm)	I_y (mm^4)	I_z (mm^4)
EHS01c - EHS04c	48.7 × 48.7 × 3.6	1.00	39.42	48.70	130565	130565
EHS05c - EHS08c	55.4 × 41.6 × 3.6	1.33	39.42	59.94	159119	100090
EHS09c - EHS12c	60 × 36 × 3.6	1.67	39.42	71.14	176864	76916
EHS13c - EHS16c	63.2 × 31.6 × 3.6	2.00	39.42	82.97	187249	59885

Specimen Id.	r (or) $\frac{a}{b}$	Major axis bending					Minor axis bending				
		$D_{NSb.mj}$ (mm)	W_{ey} (mm^3)	W_{py} (mm^3)	M_e (kNm)	M_p (kNm)	$D_{NSb.mn}$ (mm)	W_{ez} (mm^3)	W_{pz} (mm^3)	M_e (kNm)	M_p (kNm)
EHS01c - EHS04c	1.00	48.70	5362	7338	2.12	2.91	48.70	5362	7338	2.12	2.91
EHS05c - EHS08c	1.33	31.24	5744	8007	2.27	3.17	61.21	4812	6511	1.91	2.58
EHS09c - EHS12c	1.67	31.60	5895	8369	2.33	3.31	75.35	4273	5765	1.66	2.28
EHS13c - EHS16c	2.00	33.74	5926	8555	2.35	3.39	91.21	3790	5124	1.50	2.03

Table 8.2 *Global and local slenderness of the EHS column models under cyclic flexural load along cross-section major axis and axial compression along column global axis*

Specimen Id.	r (a/b)	L (mm)	$\bar{\lambda}$	N_c (kN)	n	N_a (kN)	n_h	ψ_h (deg.)	$D_{cb.mj}$ (mm)	$\frac{D_{cb.mj}}{t\varepsilon^2}$
EHS01c	1.00	300	0.51	216	0.0	0.0	0.000	90.00	48.7	22.8
					0.2	43.2	0.336	70.75	48.7	22.8
					0.4	86.3	0.672	51.50	48.7	22.8
					0.6	129.4	1.008	32.24	48.7	22.8
EHS02c	1.00	400	0.68	185	0.0	0.0	0.000	90.00	48.7	22.8
					0.2	37.0	0.288	73.52	48.7	22.8
					0.4	74.1	0.575	57.02	48.7	22.8
					0.6	111.1	0.863	40.53	48.7	22.8
EHS03c	1.00	500	0.86	155	0.0	0.0	0.000	90.00	48.7	22.8
					0.2	31.0	0.241	76.19	48.7	22.8
					0.4	61.9	0.482	62.38	48.7	22.8
					0.6	92.9	0.723	48.56	48.7	22.8
EHS04c	1.00	600	1.03	132	0.0	0.0	0.000	90.00	48.7	22.8
					0.2	26.3	0.205	78.24	48.7	22.8
					0.4	52.7	0.411	66.48	48.7	22.8
					0.6	79.0	0.616	54.71	48.7	22.8
EHS05c	1.33	300	0.47	226	0.0	0.0	0.000	90.00	31.2	14.6
					0.2	45.1	0.306	72.34	39.9	18.7
					0.4	90.2	0.612	53.94	48.1	22.5
					0.6	135.3	0.918	33.79	55.1	25.8
EHS06c	1.33	400	0.62	196	0.0	0.0	0.000	90.00	31.2	14.6
					0.2	39.3	0.265	74.70	38.8	18.2
					0.4	78.5	0.531	58.96	46.0	21.5
					0.6	117.8	0.796	42.05	52.5	24.6
EHS07c	1.33	500	0.78	168	0.0	0.0	0.000	90.00	31.2	14.6
					0.2	33.5	0.228	76.89	37.7	17.7
					0.4	67.0	0.455	63.55	44.0	20.6
					0.6	100.6	0.683	49.48	49.9	23.4
EHS08c	1.33	600	0.93	143	0.0	0.0	0.000	90.00	31.2	14.6
					0.2	28.7	0.194	78.85	36.8	17.2
					0.4	57.3	0.387	67.58	42.2	19.7
					0.6	85.9	0.581	55.88	47.3	22.2
EHS09c	1.67	300	0.44	228	0.0	0.0	0.000	90.00	31.6	14.8
					0.2	44.6	0.284	73.59	42.8	20.0
					0.4	91.1	0.567	56.26	53.6	25.1
					0.6	136.7	0.851	36.37	63.4	29.7
EHS10c	1.67	400	0.59	200	0.0	0.0	0.000	90.00	31.6	14.8
					0.2	40.0	0.249	75.63	41.4	19.4
					0.4	80.0	0.497	60.68	51.0	23.9
					0.6	119.3	0.746	44.11	60.0	28.1
EHS11c	1.67	500	0.74	174	0.0	0.0	0.000	90.00	31.6	14.8
					0.2	34.8	0.216	77.51	40.1	18.8
					0.4	69.5	0.433	64.68	48.5	22.7
					0.6	104.3	0.649	50.84	56.6	26.5
EHS12c	1.67	600	0.88	150	0.0	0.0	0.000	90.00	31.6	14.8
					0.2	29.9	0.187	79.24	39.0	18.2
					0.4	59.9	0.373	68.29	46.2	21.6
					0.6	89.8	0.560	56.74	53.3	24.9
EHS13c	2.00	300	0.42	240	0.0	0.0	0.000	90.00	33.7	15.8
					0.2	48.0	0.282	73.63	47.6	22.3
					0.4	96.0	0.565	56.11	61.2	28.6
					0.6	144.0	0.847	35.34	73.9	34.6
EHS14c	2.00	400	0.57	205	0.0	0.0	0.000	90.00	33.7	15.8
					0.2	41.0	0.241	76.07	45.6	21.3
					0.4	82.0	0.483	61.41	57.3	26.8
					0.6	121.7	0.724	45.06	68.5	32.1
EHS15c	2.00	500	0.72	176	0.0	0.0	0.000	90.00	33.7	15.8
					0.2	35.1	0.207	78.08	43.9	20.5
					0.4	70.2	0.414	65.67	54.0	25.3
					0.6	105.0	0.621	52.33	63.8	29.9
EHS16c	2.00	600	0.86	155	0.0	0.0	0.000	90.00	33.7	15.8
					0.2	31.0	0.182	79.53	42.7	20.0
					0.4	62.0	0.365	68.69	51.6	24.2
					0.6	90.0	0.547	57.27	60.3	28.3

Table 8.3 *Global and local slenderness of the EHS column models under cyclic flexural load along cross-section minor axis and axial compression along column global axis*

Specimen Id.	r (a/b)	L (mm)	$\overline{\lambda}$	N_c (kN)	n	N_a (kN)	n_n	ψ_n (deg.)	$D_{cb.mn}$ (mm)	$\frac{D_{cb.mn}}{t\varepsilon^2}$
EHS01c	1.00	300	0.51	216	0.0	0.0	0.000	0.00	48.7	22.8
					0.2	43.2	0.336	19.25	48.7	22.8
					0.4	86.3	0.672	38.50	48.7	22.8
					0.6	129.4	1.008	57.75	48.7	22.8
EHS02c	1.00	400	0.68	185	0.0	0.0	0.000	0.00	48.7	22.8
					0.2	37.0	0.288	16.49	48.7	22.8
					0.4	74.1	0.575	32.97	48.7	22.8
					0.6	111.1	0.863	49.46	48.7	22.8
EHS03c	1.00	500	0.86	155	0.0	0.0	0.000	0.00	48.7	22.8
					0.2	31.0	0.241	13.82	48.7	22.8
					0.4	61.9	0.482	27.63	48.7	22.8
					0.6	92.9	0.723	41.44	48.7	22.8
EHS04c	1.00	600	1.03	132	0.0	0.0	0.000	0.00	48.7	22.8
					0.2	26.3	0.205	11.77	48.7	22.8
					0.4	52.7	0.411	23.53	48.7	22.8
					0.6	79.0	0.616	35.29	48.7	22.8
EHS05c	1.33	300	0.59	202	0.0	0.0	0.000	0.00	61.2	28.7
					0.2	40.5	0.274	20.76	60.8	28.4
					0.4	80.9	0.547	40.04	60.4	28.3
					0.6	121.4	0.821	57.61	60.1	28.1
EHS06c	1.33	400	0.78	166	0.0	0.0	0.000	0.00	61.2	28.7
					0.2	33.3	0.225	17.16	60.8	28.5
					0.4	66.5	0.450	33.37	60.5	28.3
					0.6	99.8	0.674	48.42	60.3	28.2
EHS07c	1.33	500	0.98	140	0.0	0.0	0.000	0.00	61.2	28.7
					0.2	28.0	0.190	14.52	60.9	28.5
					0.4	56.0	0.379	28.41	60.6	28.4
					0.6	84.1	0.569	41.49	60.4	28.3
EHS08c	1.33	600	1.17	113	0.0	0.0	0.000	0.00	61.2	28.7
					0.2	22.7	0.153	11.76	61.0	28.5
					0.4	45.3	0.306	23.14	60.7	28.4
					0.6	68.0	0.459	34.02	60.5	28.3
EHS09c	1.67	300	0.67	186	0.0	0.0	0.000	0.00	75.4	35.3
					0.2	37.1	0.231	22.23	73.8	34.5
					0.4	74.2	0.463	40.75	72.6	34.0
					0.6	111.0	0.694	56.61	71.8	33.6
EHS10c	1.67	400	0.89	149	0.0	0.0	0.000	0.00	75.4	35.3
					0.2	29.8	0.185	18.13	74.0	34.7
					0.4	59.5	0.371	33.76	73.0	34.2
					0.6	89.3	0.556	47.40	72.3	33.8
EHS11c	1.67	500	1.12	118	0.0	0.0	0.000	0.00	75.4	35.3
					0.2	23.7	0.147	14.58	74.3	34.8
					0.4	47.3	0.294	27.53	73.4	34.4
					0.6	71.0	0.440	39.09	72.7	34.0
EHS12c	1.67	600	1.34	95	0.0	0.0	0.000	0.00	75.4	35.3
					0.2	19.0	0.118	11.86	74.5	34.9
					0.4	38.0	0.236	22.66	73.7	34.5
					0.6	57.1	0.354	32.48	73.1	34.2
EHS13c	2.00	300	0.76	170	0.0	0.0	0.000	0.00	91.2	42.7
					0.2	34.0	0.200	22.93	88.0	41.2
					0.4	68.0	0.400	40.51	85.9	40.2
					0.6	101.0	0.600	54.84	84.5	39.5
EHS14c	2.00	400	1.01	126	0.0	0.0	0.000	0.00	91.2	42.7
					0.2	25.2	0.148	17.60	88.7	41.5
					0.4	50.4	0.297	31.94	86.9	40.7
					0.6	75.6	0.445	43.93	85.5	40.0
EHS15c	2.00	500	1.26	109	0.0	0.0	0.000	0.00	91.2	42.7
					0.2	21.8	0.128	15.44	89.0	41.7
					0.4	43.6	0.257	28.34	87.3	40.9
					0.6	65.4	0.385	39.30	86.0	40.3
EHS16c	2.00	600	1.52	78	0.0	0.0	0.000	0.00	91.2	42.7
					0.2	14.6	0.092	11.33	89.6	41.9
					0.4	29.2	0.184	21.28	88.2	41.3
					0.6	43.8	0.275	30.05	87.1	40.8

Table 8.4 *Cyclic properties of EHS column models under cyclic bending along cross-section major axis and global axial compression*

Specimen Id.	r (a/b)	L (mm)	$\bar{\lambda}$	n	ω_{g0}	ω_{l0}	N_a (kN)	$\frac{N_a}{N_y}$	M_{er} (kNm)	δ_y (mm)	M_{pr} (kNm)	M_{uCy} (kNm)	δ_u (mm)	$E_{e.cy}$ (J)	$E_{tot.cy}$ (kJ)
EHS01c	1.00	300	0.51	0.0	-	0.90	0.0	0.00	2.12	2.26	2.91	4.78	26.49	16.00	6.39
				0.2	1.00	1.00	43.2	0.21	1.68	1.82	2.71	4.64	20.79	10.19	3.84
				0.4	1.20	1.80	86.3	0.41	1.25	1.33	2.03	4.25	15.00	5.55	2.45
				0.6	1.20	0.90	129.4	0.62	0.81	1.04	1.31	3.67	11.60	2.80	1.80
EHS02c	1.00	400	0.68	0.0	-	0.90	0.0	0.00	2.12	4.17	2.91	4.73	44.46	22.10	9.60
				0.2	1.62	0.81	37.0	0.18	1.74	3.38	2.82	4.64	35.20	14.70	5.76
				0.4	1.20	0.81	74.1	0.35	1.38	2.61	2.23	4.35	26.61	9.00	3.81
				0.6	1.14	0.81	111.1	0.53	1.00	2.14	1.62	3.92	21.70	5.35	3.00
EHS03c	1.00	500	0.86	0.0	-	0.90	0.0	0.00	2.12	6.77	2.91	4.68	65.00	28.70	13.50
				0.2	2.00	0.81	31.0	0.15	1.80	5.75	2.91	4.63	54.00	20.70	8.64
				0.4	1.80	1.00	61.9	0.30	1.48	4.70	2.41	4.41	43.41	13.90	5.84
				0.6	1.36	0.81	92.9	0.44	1.19	3.57	1.92	4.11	32.67	8.50	4.23
EHS04c	1.00	600	1.03	0.0	-	0.90	0	0.00	2.12	9.68	2.91	4.66	84.00	34.20	17.10
				0.2	2.40	0.81	26.3	0.13	1.84	8.80	2.91	4.64	75.30	27.00	12.00
				0.4	2.10	0.81	52.7	0.25	1.59	7.36	2.57	4.50	62.10	19.50	8.40
				0.6	1.85	0.81	79.0	0.38	1.31	5.77	2.12	4.25	47.70	12.60	5.94
EHS05c	1.33	300	0.47	0.0	-	0.90	0.0	0.00	2.26	2.00	3.15	5.30	24.84	15.10	7.38
				0.2	1.33	1.80	45.1	0.22	1.76	1.60	2.90	5.15	19.41	9.36	4.12
				0.4	1.20	0.80	90.2	0.43	1.29	1.18	2.12	4.72	14.00	5.06	2.55
				0.6	1.00	0.80	135.3	0.65	0.79	0.99	1.30	4.07	11.41	2.60	1.83
EHS06c	1.33	400	0.62	0.0	-	0.90	0.0	0.00	2.26	3.54	3.15	5.27	41.13	20.00	11.00
				0.2	1.35	0.90	39.3	0.19	1.83	2.91	3.01	5.14	32.96	13.30	6.30
				0.4	1.35	0.80	78.5	0.38	1.40	2.29	2.30	4.82	25.50	8.00	4.00
				0.6	1.20	0.80	117.8	0.56	0.99	1.98	1.64	4.32	21.40	4.90	3.10
EHS07c	1.33	500	0.78	0.0	-	0.90	0.0	0.00	2.26	5.75	3.15	5.21	62.14	26.00	16.10
				0.2	1.26	0.81	33.5	0.16	1.90	4.74	3.13	5.14	50.40	18.00	9.36
				0.4	1.26	0.81	67.0	0.32	1.54	3.90	2.53	4.90	40.50	12.00	6.00
				0.6	1.26	0.81	100.6	0.48	1.18	3.18	1.94	4.53	32.10	7.50	4.30
EHS08c	1.33	600	0.93	0.0	-	0.90	0.0	0.00	2.26	8.23	3.15	5.19	82.20	31.00	21.33
				0.2	1.44	0.81	28.7	0.14	1.94	7.11	3.15	5.15	69.69	23.00	13.23
				0.4	1.44	0.81	57.3	0.27	1.65	5.89	2.71	4.96	57.00	16.20	8.60
				0.6	1.44	0.81	85.9	0.41	1.33	5.01	2.20	4.67	47.00	11.10	6.10
EHS09c	1.67	300	0.44	0.0	-	0.72	0.0	0.00	2.29	1.83	3.25	5.61	24.03	14.00	8.10
				0.2	1.33	1.20	44.6	0.21	1.81	1.46	3.03	5.46	18.94	8.80	4.62
				0.4	1.20	0.80	91.1	0.44	1.28	1.03	2.15	5.02	13.10	4.40	2.67
				0.6	0.92	0.80	136.7	0.65	0.80	0.86	1.35	4.31	10.44	2.30	1.86
EHS10c	1.67	400	0.59	0.0	-	0.72	0.0	0.00	2.29	3.14	3.25	5.57	38.50	18.00	11.97
				0.2	1.35	1.20	40.0	0.19	1.86	2.58	2.63	5.44	31.05	12.00	6.84
				0.4	1.35	0.80	80.0	0.38	1.42	2.03	2.02	5.09	23.80	7.20	4.30
				0.6	1.35	0.72	119.3	0.57	0.99	1.73	1.40	4.56	20.05	4.30	3.20
EHS11c	1.67	500	0.74	0.0	-	0.90	0.0	0.00	2.29	5.02	3.25	5.54	57.60	23.00	17.46
				0.2	1.20	0.81	34.8	0.17	1.90	4.21	3.19	5.43	47.40	16.00	9.90
				0.4	1.20	0.81	69.5	0.33	1.53	3.53	2.57	5.13	38.52	10.80	6.48
				0.6	1.20	0.81	104.3	0.50	1.15	2.79	1.92	4.73	30.24	6.42	4.44
EHS12c	1.67	600	0.88	0.0	-	0.90	0.0	0.00	2.29	7.34	3.25	5.52	79.36	28.00	23.80
				0.2	1.35	0.81	29.9	0.14	1.97	6.30	3.25	5.45	67.00	20.70	14.49
				0.4	1.35	0.81	59.9	0.29	1.63	5.11	2.73	5.21	54.00	13.90	8.82
				0.6	1.35	0.81	89.8	0.43	1.31	4.40	2.18	4.87	45.00	9.60	6.36
EHS13c	2.00	300	0.42	0.0	-	0.75	0.0	0.00	2.27	1.78	3.29	5.80	23.81	13.50	8.82
				0.2	2.40	0.80	48.0	0.23	1.75	1.41	2.99	5.61	18.45	8.22	5.13
				0.4	1.20	0.90	96.0	0.46	1.23	0.95	2.09	5.14	12.15	3.90	2.88
				0.6	1.00	0.90	144.0	0.69	0.70	0.77	1.20	4.26	9.70	1.80	1.92
EHS14c	2.00	400	0.57	0.0	-	0.72	0.0	0.00	2.27	2.96	3.29	5.76	37.80	16.80	12.96
				0.2	3.20	0.81	41.0	0.20	1.82	2.37	3.09	5.50	29.80	10.80	7.20
				0.4	1.32	0.81	82.0	0.39	1.39	1.76	2.36	5.23	21.61	6.12	4.50
				0.6	1.35	0.81	121.7	0.58	0.95	1.47	1.63	4.63	17.73	3.50	3.40
EHS15c	2.00	500	0.72	0.0	-	0.72	0.0	0.00	2.27	4.63	3.29	5.74	55.90	21.00	18.90
				0.2	1.20	0.72	35.1	0.17	1.88	3.83	3.21	5.61	45.54	14.40	10.80
				0.4	1.20	0.72	70.2	0.34	1.50	2.94	2.56	5.33	34.20	8.82	6.60
				0.6	1.20	0.72	105.0	0.50	1.14	2.28	1.94	4.89	26.20	5.20	4.62
EHS16c	2.00	600	0.86	0.0	-	0.72	0.0	0.00	2.27	6.87	3.29	5.70	78.65	26.00	26.55
				0.2	1.20	0.72	31.0	0.15	1.93	5.88	3.29	5.63	66.00	18.90	15.60
				0.4	1.20	0.72	62.0	0.30	1.59	4.53	2.71	5.37	50.22	12.00	9.36
				0.6	1.20	0.72	90.0	0.43	1.29	3.59	2.21	5.05	39.69	7.71	6.51

Table 8.5 *Cyclic properties of EHS column models under cyclic bending along cross-section minor axis and global axial compression*

Specimen Id.	r (a/b)	L (mm)	$\bar{\lambda}$	n	ω_{g0}	ω_{l0}	N (kN)	$\frac{N}{N_y}$	M_{er} (kNm)	δ_y (mm)	M_{pr} (kNm)	M_{uCy} (kNm)	δ_u (mm)	$E_{e.cy}$ (J)	$E_{tot.cy}$ (kJ)
EHS01c	1.00	300	0.51	0.0	-	0.90	0.0	0.00	2.12	2.26	2.91	4.78	26.49	16.00	6.39
				0.2	1.00	1.00	43.2	0.21	1.68	1.82	2.30	4.64	20.79	10.19	3.84
				0.4	1.20	1.80	86.3	0.41	1.25	1.33	1.72	4.25	15.00	5.55	2.45
				0.6	1.20	0.90	129.4	0.62	0.81	1.04	1.11	3.67	11.60	2.80	1.80
EHS02c	1.00	400	0.68	0.0	-	0.90	0.0	0.00	2.12	4.17	2.91	4.73	44.46	22.10	9.60
				0.2	1.62	0.81	37.0	0.18	1.74	3.38	2.39	4.64	35.20	14.70	5.76
				0.4	1.20	0.81	74.1	0.35	1.38	2.61	1.89	4.35	26.61	9.00	3.81
				0.6	1.14	0.81	111.1	0.53	1.00	2.14	1.37	3.92	21.70	5.35	3.00
EHS03c	1.00	500	0.86	0.0	-	0.90	0.0	0.00	2.12	6.77	2.91	4.68	65.00	28.70	13.50
				0.2	2.00	0.81	31.0	0.15	1.80	5.75	2.91	4.63	54.00	20.70	8.64
				0.4	1.80	1.00	61.9	0.30	1.48	4.70	2.04	4.41	43.41	13.90	5.84
				0.6	1.36	0.81	92.9	0.44	1.19	3.57	1.63	4.11	32.67	8.50	4.23
EHS04c	1.00	600	1.03	0.0	-	0.90	0.0	0.00	2.12	9.68	2.91	4.66	84.00	34.20	17.10
				0.2	2.40	0.81	26.3	0.13	1.84	8.80	2.91	4.64	75.30	27.00	12.00
				0.4	2.10	0.81	52.7	0.25	1.59	7.36	2.18	4.50	62.10	19.50	8.40
				0.6	1.85	0.81	79.0	0.38	1.31	5.77	1.80	4.25	47.70	12.60	5.94
EHS05c	1.33	300	0.59	0.0	-	0.80	0.0	0.00	1.89	2.78	2.56	4.19	27.36	17.50	5.22
				0.2	1.20	2.40	40.5	0.19	1.53	2.29	2.44	3.98	22.00	11.70	3.15
				0.4	1.33	1.53	80.9	0.39	1.15	1.67	1.84	3.68	15.75	6.40	2.13
				0.6	1.20	1.20	121.4	0.58	0.79	1.25	1.27	3.18	11.70	3.30	1.56
EHS06c	1.33	400	0.78	0.0	-	0.72	0.0	0.00	1.89	4.95	2.56	4.18	45.00	23.40	7.83
				0.2	1.35	0.81	33.3	0.16	1.59	4.15	2.54	4.02	36.63	16.50	4.77
				0.4	1.20	0.81	66.5	0.32	1.29	3.41	2.05	3.79	29.43	11.00	3.42
				0.6	1.20	0.72	99.8	0.48	0.98	2.65	1.57	3.45	22.44	6.50	2.61
EHS07c	1.33	500	0.98	0.0	-	1.80	0.0	0.00	1.89	7.94	2.56	4.17	66.00	30.00	10.98
				0.2	1.80	1.20	28.0	0.13	1.64	7.01	2.56	4.01	57.00	23.00	7.38
				0.4	1.60	0.78	56.0	0.27	1.38	5.80	2.21	3.92	45.63	16.00	5.10
				0.6	1.26	0.72	84.1	0.40	1.13	4.51	1.82	3.67	34.77	10.20	3.77
EHS08c	1.33	600	1.17	0.0	-	1.80	0.0	0.00	1.89	11.11	2.56	4.14	85.00	35.00	14.14
				0.2	2.40	1.00	22.7	0.11	1.68	10.18	2.56	4.07	77.00	28.50	10.08
				0.4	2.10	0.90	45.3	0.22	1.47	9.06	2.36	3.97	67.00	22.20	7.41
				0.6	1.71	0.80	68.0	0.32	1.29	7.44	2.05	3.82	53.50	16.00	5.58
EHS09c	1.67	300	0.67	0.0	-	1.80	0.0	0.00	1.66	3.43	2.24	3.61	29.00	19.00	4.32
				0.2	1.01	1.50	37.1	0.18	1.36	2.87	2.17	3.51	23.58	13.00	2.75
				0.4	0.90	1.20	74.2	0.35	1.08	2.25	1.72	3.24	17.98	8.10	2.00
				0.6	0.86	0.81	111.0	0.53	0.78	1.73	1.24	2.85	13.32	4.50	1.57
EHS10c	1.67	400	0.89	0.0	-	1.44	0.0	0.00	1.66	5.90	2.24	3.59	46.80	24.50	6.30
				0.2	1.80	1.20	29.8	0.14	1.43	5.17	2.24	3.53	40.03	18.50	4.23
				0.4	1.60	0.90	59.5	0.28	1.20	4.33	1.90	3.35	33.00	13.00	3.15
				0.6	1.53	1.20	89.3	0.43	0.95	3.37	1.51	3.04	25.20	8.00	2.42
EHS11c	1.67	500	1.12	0.0	-	0.80	0.0	0.00	1.66	9.34	2.24	3.57	68.50	31.00	8.90
				0.2	1.82	0.72	23.7	0.11	1.48	8.45	2.24	3.52	60.00	25.00	6.40
				0.4	150	0.72	47.3	0.23	1.28	7.42	2.04	3.40	52.00	19.00	4.80
				0.6	1.26	0.72	71.0	0.34	1.10	5.91	1.75	3.20	40.00	13.00	3.56
EHS12c	1.67	600	1.34	0.0	-	0.72	0.0	0.00	1.66	13.01	2.24	3.55	88.20	36.00	11.43
				0.2	2.00	0.72	19.0	0.09	1.51	12.16	2.24	3.50	81.00	30.60	8.91
				0.4	1.65	0.72	38.0	0.18	1.36	11.03	2.17	3.42	72.00	25.00	6.84
				0.6	1.35	0.72	57.1	0.27	1.21	9.82	1.94	3.30	63.00	19.80	5.45
EHS13c	2.00	300	0.76	0.0	-	1.80	0.0	0.00	1.45	4.24	1.96	3.14	31.00	20.50	3.51
				0.2	1.00	1.33	34.0	0.16	1.22	3.39	1.95	3.03	24.30	13.80	2.40
				0.4	1.09	1.20	68.0	0.32	0.99	2.73	1.57	2.80	19.00	9.00	1.80
				0.6	0.81	0.80	101.0	0.48	0.75	2.04	1.20	2.54	13.80	5.10	1.30
EHS14c	2.00	400	1.01	0.0	-	3.60	0.0	0.00	1.45	7.03	1.96	3.12	48.00	25.50	4.95
				0.2	1.35	1.53	25.2	0.12	1.28	6.13	1.96	3.04	41.00	19.60	3.69
				0.4	1.35	1.33	50.4	0.24	1.10	5.09	1.76	2.89	34.00	14.00	2.80
				0.6	1.26	1.00	75.6	0.36	0.93	4.30	1.48	2.71	28.00	10.00	2.25
EHS15c	2.00	500	1.26	0.0	-	1.53	0.0	0.00	1.45	10.86	1.96	3.09	70.00	31.50	6.75
				0.2	1.27	1.00	21.8	0.10	1.31	9.62	1.96	3.04	61.00	25.20	5.22
				0.4	1.27	0.80	43.6	0.21	1.15	8.48	1.83	2.92	53.00	19.50	4.10
				0.6	1.20	0.72	65.4	0.31	1.00	7.20	1.59	2.77	43.00	14.40	3.24
EHS16c	2.00	600	1.52	0.0	-	0.80	0.0	0.00	1.45	15.27	1.96	3.08	91.80	36.90	8.82
				0.2	1.85	0.80	14.6	0.07	1.35	14.22	1.96	3.05	83.43	32.00	7.36
				0.4	1.60	0.80	29.2	0.14	1.25	12.96	1.96	2.99	75.60	27.00	6.10
				0.6	1.35	0.80	43.8	0.21	1.15	11.48	1.83	2.91	66.00	22.00	5.04

CHAPTER 9

CONCLUSIONS

In this chapter, the main conclusions drawn from the research work documented in this dissertation are summarised. More detailed concluding comments may be found at the end of each of the individual chapters. Suggestions for future work are also presented at the end of the chapter.

9.1 RESEARCH SUMMARY

The focus of the research work documented in this dissertation is to explore the behaviour and design of carbon-steel EHS members (braces, beams and columns) under ELCF loading. The cyclic behaviour of EHS members was investigated through numerical modelling by performing FEAs using the general FE software package, Abaqus (2009). The accuracy of the numerical models was verified by-means-of test results available in the literature, showing that the modelling approaches adopted as part of this dissertation work can provide a realistic representation of the cyclic response of EHS members. The validated models were then used for conducting the parametric studies and establishing the empirical relationships for predictive capacities of the EHS members in-order-to provide reliable design guidance for the practical implementation of EHSs into the structures that are susceptible to ELCF type loadings.

For any HSS member, the determination of cross-section slenderness parameter which personifies the cross-sectional stability is a basic requirement of the designer (Gardner and Nethercot 2011). Thus, the accuracy of the existing equivalent CHS diameter theories for calibrating the cross-sectional slenderness parameters for EHS and the appropriateness of the existing CHS cross-sectional slenderness limits and resistance capacity curves in various international design standards (BS 5950:Part-1 1990, EN 1993-1-1 2005, IS 800 2007, CSA S16-14 2014, AISC 360-16 2016, AS 4100:1998 2016) under different loading cases are analysed as a part of this dissertation initially before conducting the parametric studies by performing the FE simulations on EHS member models under ELCF loads. This process has predominantly defined the shape and flow of the thesis. The literature review revealed widespread interest in the subject, though limited laboratory test data existed.

The following sub-sections briefly conclude the findings of the study performed as a part of this dissertation. At the end of the chapter, recommendations for future works associated with the research work doccumented in this dissertation are also presented.

9.1.1 New CHS Cross-sectional Slenderness and Capacity Criteria

The primary objective of developing the equivalent CHS diameter theories for the EHS is to bring applicability of the CHS cross-sectional design criteria also to the EHSs. In Chapters 3 and 4, the existing inconsistent CHS cross-sectional slenderness limits and resistance capacity

curves for the separate cases of axial compression and bending in various international design standards (BS 5950:Part-1 1990, EN 1993-1-1 2005, IS 800 2007, CSA S16-14 2014, AISC 360-16 2016, AS 4100:1998 2016) are analysed and found to be either over conservative *or* unsafe based on comparison with a compilation of available laboratory test data and results based on FE modelling simulations of CHSs from the literature.

Therefore, a unified set of cross-sectional resistance capacity curves and slenderness limits for CHSs under axial compression and bending loads that can be used uniformly across various global design standards (BS 5950:Part-1 1990, EN 1993-1-1 2005, IS 800 2007, CSA S16-14 2014, AISC 360-16 2016, AS 4100:1998 2016), by using a comprehensive data of CHS results from the literature is established based on lower bound empirical data fittings using non-linear regression analyses.

9.1.2 Equivalent CHS Diameter and Plastic Interaction Equations

After the establishment of new CHS cross-sectional resistance capacity curves and slenderness limits for the loading cases of axial compression and bending separately in Chapters 3 and 4, the equivalent CHS diameter theories proposed by Chan and Gardner (2008a, 2008b) and Ruiz-Terán and Gardner (2008) are reviewed and found to be inconsistent and over-conservative in estimating the proposed cross-sectional capacities by using the available laboratory test data and results based on FE modelling simulations of EHSs from the literature.

Improved empirical expressions are acquired for the equivalent CHS diameter of the EHS for the loading cases of axial compression and bending separately based on ERCM which involves fitting the data of EHS tests and simulations from the literature by preserving consistency with the newly proposed CHS bending capacity prediction curves in Chapters 3 and 4.

Further, in Chapter 5, expressions for the equivalent CHS diameter of EHSs which can develop plastic strength and with various cross-sectional aspect ratios under combinations of axial-compression, uni-axial bending and bi-axial bending loads are proposed using: *a*) the equivalent CHS diameter expressions derived in Chapters 3 and 4; and *b*) the proportion of the cross-section under compressive and tensile stresses and the position of PNA due to the interaction behaviour of the applied loads. The derivation of analytical expressions capable of determining the plastic interaction curves and surfaces of EHS is also presented in detail in

Chapter 5. The relationships derived in Chapter 5 can be utilised for establishing the cross-section classification criteria between compact and yielding cross-sections and cross-sectional strength design criteria to withstand a given combination of applied loads.

9.1.3 Cyclic Behaviour of EHS Members

The primary objective of the work documented in this dissertation is to analyse the behaviour of carbon-steel EHS members under ELCF loading through FE simulations and provide reliable earthquake-resistant guidance according to the state of the art in seismic engineering for promoting the wider application of EHS in practice. The cross-sectional classification of the EHS member FE models is estimated using the newly proposed equivalent CHS diameter relationships, interaction relationships and cross-sectional slenderness limits in Chapters 3, 4 and 5 based on the applied loading combinations.

Before the execution of parametric study on EHS members under ELCF loading by FEAs, the FE modelling approaches adopted are substantiated by accurately replicating the hysteretic behaviour of HSS members subjected to cyclic axial *or* bending loads in the independent experimental programs conducted by others (*e.g.*, Nip, 2009; Fadden, 2013). While the NLCHM model parameters used for the FE models of the EHS members analysed under cyclic displacement loading are adopted from Table 2.3 where the NLCHM data of various steels obtained from different sources are compiled. And, the details of the cyclic loading histories adopted for performing the FE simulations are presented in Section 2.3.2.

In Chapter 6, the effect of cross-sectional aspect ratio and non-dimensional brace slenderness on cyclic post-buckling compressive resistance, mid-length lateral deflection, and energy dissipation at various displacement ductility levels are investigated by analyzing the hysteresis response of EHS steel brace models under global-axial cyclic displacement loading history. The equations for the respective predictive envelopes are developed and compared with various codal specifications and the results of independent experimental investigations on HSS bracing members from the literature. And, it is found that for the EHS braces with non-dimensional global brace slenderness lesser than ~1.15, the cross-sectional aspect ratio *or* cross-sectional slenderness has a significant effect on the normalised hysteresis parameters like post-local-buckling compressive resistance, lateral deflection and energy dissipative indices at higher

displacement ductility levels; and the significance of such effect increases with the ductility level.

In Chapter 7, the non-linear FE simulation study has been extended to analyse the performance of cold-formed carbon steel EHS cantilever beam models under ELCF uni-axial bending load along cross-sectional major and minor axes separately is presented. A parametric study is conducted to investigate the hysteresis behaviour of the EHS beam models. The effect of cross-sectional aspect ratio on cyclic-moment-resistance and cyclic-rotation capacities of EHSs with-respect-to their non-dimensional CHS cross-sectional slenderness is found to be insignificant. The empirical expressions for the predictive cyclic-moment-resistance-capacity and cyclic-rotation-capacity curves of EHSs with-respect-to their CHS cross-section slenderness are established.

Lastly, in Chapter 8, the performance of carbon-steel EHS cantilever column models is analysed under the combined action of constant global-axial compressive load and cross-sectional major-axis *or* minor-axis cyclic bending load. A parametric study is conducted to assess their axial compressive load and cyclic moment interaction behaviour alongside the cyclic ductility and energy dissipation capacity under various axial compressive load levels. Considering the axial compressive load ratio first, the cyclic bending strength, ductility and energy dissipation capacity can be greatly affected. Increasing axial load ratio normally results in poorer hysteretic behaviour. The effects of cross-sectional aspect ratio and axial compressive load level on ductility and cyclic energy dissipation capacity of the columns are examined. Further, the empirical expressions for axial compressive load – cyclic moment interaction curves; and the hysteretic properties like ductility and cyclic energy dissipation capacities are derived. The effects of non-dimensional global slenderness and compressive axial load level on cyclic ductility and cyclic energy dissipation capacity of the columns are also examined. Unlike in the case of cyclic-ductility and cyclic-energy dissipation capacity, the effect of non-dimensional global slenderness on cyclic-moment–axial-compression interaction is found to be negligible for each of the cross-sectional aspect ratios and cross-sectional slenderness values considered.

Therefore, it can be concluded that the general aim of this thesis and its associated specific objectives have been sufficiently covered in the research work of this dissertation.

9.2 SUGGESTIONS FOR FURTHER WORK

The findings in the research work of this dissertation provide a good starting point for further exploration in various related areas. This final section presents such potential areas of further work identified in association with the research work of this dissertation.

9.2.1 Extension to Present Research Work

A reliable numerical method can be utilised to predict the fatigue fracture of the EHS members under cyclic loading. Since the damage prediction method is based on the strain-induced in a localised area, it applies to different member types and locations of fracture, provided suitable mesh sizes and average areas of strain output are carefully chosen. By utilising the enhanced calibrated constitutive cyclic and damage evolution material models, the predictive expressions on member cyclic ductility, strength and energy dissipation capacities and the interaction of EHS members can be assessed with greater accuracy, which may lead to a more efficient design.

The implications of the findings presented herein on the behaviour and design of the EHS members have been deduced mainly from their numerically simulated cyclic response under quasi-static loading. A more complete understanding of the performance of the EHS members in earthquakes, however, requires enhanced testing and FEAs on the members under dynamic loading. In dynamic experimental testing, strain rate effects of the material can be observed. When cyclic tests are no longer displacement controlled, an asymmetric hysteretic response may also be discovered (Elghazouli et al. 2005).

Also, apart from the global-axial cyclic compression-tension, uni-axial cyclic bending and combined global-axial compression and uni-axial cyclic bending scenarios considered herein, the research work in this thesis can be further extended to other loading combinations involving impact, blast, torsion and bi-axial cyclic bending.

Other than loading scenarios, the research work in this dissertation can be extended towards the topic of perforations (cut-outs/holes/access openings). Perforations (cut-outs/holes/access openings) of various shapes (*e.g.*, circular, rectangular, hexagonal, flat-ovals, *etc*.,) and sizes are made on the module columns to enable access for inter-module connection. Additionally, perforations are also created on structural members for permanent *or* temporary access, for

various needs such as ductwork; bridging; connection to other members; aesthetic appearance; wind load reduction; seismic weight reduction; material optimisation as well as various services *viz.*, inspections, installation of hidden electrical and electric wires, fresh and waste-water plumbing, *etc.*(Singh and Singh 2018, Devi et al. 2019, Devi and Singh 2020, Singh and Chan 2021). But, the provision of perforation can lead to adverse effects on the failure mechanism and structural capacity of the members. Hence, it is imperative to study the influence of various forms of perforation on the cyclic performance of an EHS member for the efficient use of constructional steel material and design, while satisfying the perforation functionalities.

Further, the research work carried out in this dissertation is limited to analysing the cyclic performance of EHS braces, beams and columns. Hence, it may be extended to other members like EHS arches and connections (T–type and K–Type).

9.2.2 Other Thoughts

Addition of infill material to HSS members has been known to enhance the resistance capacity. Therefore, the research work presented in this dissertation can be extended to EHS members with infill material such as ordinary concrete, fibre reinforced concrete, geopolymer concrete, *etc*. EHSs can be fully *or* partially filled with the infill material *or* the infill may be sandwiched between an outer and an inner tube (*i.e.*, double skin).

This page is intentionally left blank

REFERENCES

Abaqus 6.9-EF. 2009. Abaqus/Standard user's manual and Abaqus CAE manual. Dassault Systemes Simulia Corp., Providence, RI, USA.

Abela, J.M., and Gardner, L. 2012. Elastic buckling of elliptical tubes subjected to generalised linearly varying stress distributions. Thin-Walled Structures, **58**: 40–50.

Agius, D., Kajtaz, M., Kourousis, K.I., Wallbrink, C., Wang, C.H., Hu, W., and Silva, J. 2017. Sensitivity and optimisation of the Chaboche plasticity model parameters in strain-life fatigue predictions. Materials & Design, **118**: 107–121. Elsevier.

Ahn, K., Lim, I.G., Yoon, J., and Huh, H. 2016. A simplified prediction method for the local buckling load of cylindrical tubes. International Journal of Precision Engineering and Manufacturing, **17**(9): 1149–1156.

AIJ. 1990. Standard for Limit State Design of Steel Structures.

AISC 360-16. 2016. Specification for Structural Steel Buildings. American Institute of Steel Construction (AISC), Chicago, IL, USA.

AISC LRFD. 2000. Load and resistance factor design specification for steel hollow structural sections. American Institute of Steel Construction, Chicago, IL, USA.

AISI S100-16. 2016. North American specification for the design of cold-formed steel structural members. American Iron and Steel Institute, Washington, DC, USA.

AISI S100-16C. 2016. Commentary on North American specification for the design of cold-formed steel structural members. American Iron and Steel Institute, Washington, DC, USA.

AISI S902-13. 2013. Stub-column test method for effective area of cold-formed steel columns. American Iron and Steel Institute (AISI), Washington, DC, USA.

Akiyama, H. 1985. Earthquake-Resistant Limit-State Design for Buildings. University of Tokyo Press.

Al-Shawi, F.A.N. 2001. On the rotation capacity of structural steel circular hollow sections in plastic analysis. Journal of Constructional Steel Research, **57**(1): 29–43.

Almkvist, G., and Berndt, B. 2016. Gauss, Landen, Ramanujan, the arithmetic-geometric mean, ellipses, π, and the Ladies Diary (1988). *In* In: Pi: The Next Generation. *Edited by* D.H. Bailey and J.M. Borwein. Springer, Cham. pp. 125–150.

Anderson, M., Carter, C.J., and Schlafly, T.J. 2015. steelwise: Are you properly specifying materials? Modern Steel Construction, **55**(2): 17–27. American Institute of Steel Construction.

Androić, B., Dujmović, D., and Pišković, J. 2014. Application of cold formed hollow steel sections. Građevinar, **66**(10): 929–934. Hrvatski savez građevinskih inženjera.

ANSI/AISC 341-16. 2016. Seismic provisions for structural steel buildings. American Institute of Steel Construction, Chicago, IL, USA.

ANSI/AISC 358-16, and ANSI/AISC 358-18s. 2018. Prequalified Connections for Special and Intermediate Steel Moment Frames for Seismic Applications, including Supplement No. 1. *In* An American National Standard. American Institute of Steel Construction (AISC).

Archambault, M.H., Tremblay, R., and Filiatrault, A. 1995. Etude du comportement seismique des contreventements ductile en X avec profiles tubulaires en acier, Rapport no. EPM/GCS, 9. Montreal, Canada.

Armstrong, P.J., and Frederick, C.O. 1966. A mathematical representation of the multiaxial Bauschinger effect. *In* Central Electricity Generating Board & Berkeley Nuclear Laboratories, Research & Development Department Report 2007; 24 : 11-26. RD/B/N 731.

AS/NZS 1163. 2016. Cold-formed structural steel hollow sections. Standards Australia/Standards New Zealand, Sydney, Australia.

AS/NZS 4600:2005. 2010. Australian/New Zealand standard: Cold-formed Steel Structures. Standards Australia Limited/Standards New Zealand.

AS 4100:1998. 2016. Steel Structures. Standards Australia, Sydney, Australia.

Ashraf, M., Gardner, L., and Nethercot, D.A. 2006. Finite element modelling of structural stainless steel cross-sections. Thin-walled structures, **44**(10): 1048–1062. Elsevier.

ASME-LCF. 1963. Low-cycle fatigue. Naval Engineers Journal, **75**(5): 967–970. Blackwell Publishing Ltd.

Astaneh-Asl, A. 2003. Behavior and seismic design of steel piles. *In* Proceedings of the Conference on Behaviour of Steel Structures in Seismic Areas (STESSA 2003). *Edited by* Federico Mazzolani. CRC Press, Naples, Italy. pp. 123–128.

ASTM A501-01. 2005. Standard specification for hot-formed welded and seamless carbon steel structural tubing. ASTM International, West Conshohocken, PA, USA.

ASTM E606/E606M. 2012. Standard Test Method for Strain-Controlled Fatigue Testing BT - Standard Test Method for Strain-Controlled Fatigue Testing. ASTM International, West Conshohocken, PA, USA.

ATC-24. 1992. Guidelines for Cyclic Seismic Testing of Components of Steel Structures for Buildings. Applied Technology Council, Redwood City, CA, USA.

Aung, H. 2007. An analysis of the study of mechanical properties and microstructural relationship of HSLA steels used in ship hulls. World Maritime University Dissertations,.

Badnava, H., Pezeshki, S.M., Nejad, K.F., and Farhoudi, H.R. 2012. Determination of combined hardening material parameters under strain controlled cyclic loading by using the genetic algorithm method. Journal of mechanical science and technology, **26**(10): 3067–3072. Springer.

Bagby, F.L. 1960. Materials in space. *In* Advances in Space Science. *Edited by* F.I. Ordway. Academic Press, London, UK. pp. 143–213.

Bagnoli, F., and Bernabei, M. 2008. Fatigue analysis of a P180 aircraft main landing gear wheel flange. Engineering Failure Analysis, **15**(6): 654–665. Elsevier.

Bagnoli, F., Dolce, F., Colavita, M., and Bernabei, M. 2008. Fatigue fracture of a main landing gear swinging lever in a civil aircraft. Engineering Failure Analysis, **15**(6): 755–765. Elsevier.

Baig, M.N., Fan, J., and Nie, J. 2006. Strength of concrete filled steel tubular columns. Tsinghua Science and Technology, **11**(6): 657–666. TUP.

Ballio, G., Calado, L., and Castiglioni, C.A. 1997. Low cycle fatigue behaviour of structural steel members and connections. Fatigue & Fracture of Engineering Materials & Structures, **20**(8): 1129–1146. Wiley Online Library.

Ballio, G., and Castiglioni, C.A. 1995. A unified approach for the design of steel structures

under low and/or high cycle fatigue. Journal of Constructional Steel Research, **34**(1): 75–101. Elsevier.

Bambach, M.R. 2006. Local buckling and post-local buckling redistribution of stress in slender plates and sections. Thin-Walled Structures, **44**(10): 1118–1128.

Bambach, M.R., and Rasmussen, K.J.R. 2004. Effective widths of unstiffened elements with stress gradient. Journal of structural engineering, **130**(10): 1611–1619. American Society of Civil Engineers.

Baptista, A.M. 2012a. Analytical evaluation of the elastic and plastic resistances of double symmetric rectangular hollow sections under axial force and biaxial bending. International Journal of Non-Linear Mechanics, **47**(9): 1033–1044.

Baptista, A.M. 2012b. Resistance of steel I-sections under axial force and biaxial bending. Journal of Constructional Steel Research, **72**: 1–11.

Basan, R., Franulovic, M., and Smokvina Hanza, S. 2010. Estimation of cyclic stress-strain curves for low-alloy steel from hardness. Metalurgija, **49**(2): 83–86. Croatian Metallurgical Society.

Bauschinger, J. 1886a. On the change of the position of the elastic limit of iron and steel under cyclic variations of stress. Mitt. Mech.-Tech. Lab., Munich, **13**(1): 1–115.

Bauschinger, J. 1886b. Über die Veränderung der Elastizitätsgrenze und der Festigkeit des Eisens und Stahls durch Strecken und Quetschen, durch Erwärmen und Abkühlen und durch oftmals wiederholte Beanspruchung. Mitt. Mech.-Techn. Lab. K. Techn. Hochsch. München, **13**: 1–115.

BCSA. 2016. Harlech Castle Footbridge. Available from https://www.steelconstruction.org/design-awards/2016/award/harlech-castle-footbridge/.

Belingardi, G., and Peroni, L. 2007. Experimental investigation of plastic collapse of aluminium extrusions in biaxial bending. International Journal of Mechanical Sciences, **49**(5): 554–566.

Bernuzzi, C., Calado, L., and Castiglioni, C.A. 2000. Low-cycle fatigue of structural steel components: A method for re-analysis of test data and a design approach based on ductility. Indian Society of Earthquake Technology (ISET), Journal of Eathquake

Technology - Special Issue on Experimental Techniques, **37**(4): 401:47–63.

Bernuzzi, C., and Cordova, B. 2016. Structural Steel Design to Eurocode 3 and AISC Specifications. *In* 1st edition. John Wiley & Sons, Ltd., Chichester, UK.

Bhowmick, A., and Shit, J. 2016. Finite element simulation of LCF behaviour of SA 333 C-Mn steel. International Journal of Innovative Technology and Research, **4**(3): 2955–2961.

Black, R.G., Wenger, W.A., and Popov, E.P. 1980. Inelastic buckling of steel struts under cyclic load reversals. Report No. UCB/EERC-80/40. Berkeley, CA, USA.

Boake, T.M. 2015. Architecturally Exposed Structural Steel: Specifications, Connections, Details. Birkhäuser Verlag GmbH, Basel, Switzerland.

Bock, M., and Real, E. 2015. Effective width equations accounting for element interaction for cold-formed stainless steel square and rectangular hollow sections. Structures, **2**: 81–90.

Boresi, A.P., Schmidt, R.J., and Sidebottom, O.M. 1993. Advanced Mechanics of Materials. *In* 5th edition. John Wiley & Sons, Inc., New York, NY, USA.

Bortolotti, E., Jaspart, J.P., Pietrapertosa, C., Nicaud, G., Petitjean, P.D., and Grimault, J.P. 2003. Testing and modelling of welded joints between elliptical hollow sections. *In* The 10th International Symposium on Tubular Structures. *Edited by* M.A. Jaurietta, J.A. Chica, and A. Alonso. A.A. Balkema, Madrid, Spain. pp. 259–266.

Bower, A.F. 2009. Applied Mechanics of Solids. CRC press, Boca Raton, FL, USA.

Boyle, I. 2014. Docklands Light Railway (DLR). Available from http://www.simplonpc.co.uk/DLR.html. [accessed 25 November 2019].

Brazier, L.G. 1927. On the flexure of thin cylindrical shells and other" thin" sections. *In* Proceedings of the Royal Society A. The Royal Society Publishing, London, UK. pp. 104–114.

Brescia, M. 2008. Rotation Capacity and Overstrength of Steel Members for Seismic Design. PhD Thesis. University of Naples Federico II, Naples, Italy.

Broggiato, G.B., Campana, F., and Cortese, L. 2008. The Chaboche nonlinear kinematic hardening model: calibration methodology and validation. Meccanica, **43**(2): 115–124. Springer.

Bruneau, M. 1998. Performance of steel bridges during the 1995 Hyogoken–Nanbu (Kobe, Japan) earthquake—a North American perspective. Engineering Structures, **20**(12): 1063–1078. Elsevier.

Bruneau, M., Uang, C.-M., and Sabelli, S.E.R. 2011. Ductile Design of Steel Structures. McGraw Hill Professional.

Bruneau, M., Wilson, J.C., and Tremblay, R. 1996. Performance of steel bridges during the 1995 Hyogo-ken Nanbu (Kobe, Japan) earthquake. Canadian Journal of Civil Engineering, **23**(3): 678–713. NRC Research Press.

Brunel, I. 1870. The Life of Isambard Kingdom Brunel, Civil Engineer. Longmans, Green & Co., London, UK.

BS 5950:Part-1. 1990. Structural use of steelwork in building:- Part 1. Code of practice for design in simple and continuous construction: hot rolled sections. British Standards Institution (BSI), London, UK.

BS 7270. 2006. Metallic Materials - Constant Amplitude Strain Controlled Fatigue - Method of Test. British Standards Institution, London, UK.

Buchanan, C., Gardner, L., and Liew, A. 2016. The continuous strength method for the design of circular hollow sections. Journal of Constructional Steel Research, **118**: 207–216.

Cai, Y., Quach, W.M., and Young, B. 2018. Tests of concrete-filled cold-formed and hot-finished steel elliptical tubular stub columns. *In* The 8th International Conference on Thin-Walled Structures (ICTWS 2018). University of Lisbon.

Chaboche, J.L. 1974. Une loi différentielle d'endommagement de fatigue avec cumulation non linéaire. Office Nationale d'Etudes et de Recherches Aérospatiales (ONERA), Paris, France.

Chaboche, J.L. 1986. Time-independent constitutive theories for cyclic plasticity. International Journal of Plasticity, **2**(2): 149–188.

Chaboche, J.L. 2008. A review of some plasticity and viscoplasticity constitutive theories. International Journal of Plasticity, **24**(10): 1642–1693. Elsevier.

Chaboche, J.L., Van, K.D., and Cordier, G. 1979. Modelization of the strain memory effect on the cyclic hardening of 316 stainless steel. Transactions of the 5th International

Conference on Structural Mechanics in Reactor Technology,: Div. L in 11/3 1-10. North-Holland Publishing Co., Berlin, Germany.

Chan, T.M. 2007. Structural Behaviour of Elliptical Hollow Sections. PhD Thesis. Imperial College London, London, UK.

Chan, T.M., Abela, J.M., and Gardner, L. 2010a. Biaxial bending and compression of elliptical hollow sections. *In* The 13th International Symposium on Tubular Structures. *Edited by* B. Young. CRC Press, Taylor & Francis Group, Hong Kong, China. pp. 303–312.

Chan, T.M., and Gardner, L. 2008a. Bending strength of hot-rolled elliptical hollow sections. Journal of Constructional Steel Research, **64**(9): 971–986.

Chan, T.M., and Gardner, L. 2008b. Compressive resistance of hot-rolled elliptical hollow sections. Engineering Structures, **30**(2): 522–532.

Chan, T.M., and Gardner, L. 2009. Flexural buckling of elliptical hollow section columns. Journal of Structural Engineering (ASCE), **135**(5): 546–557.

Chan, T.M., Gardner, L., and Law, K.H. 2010b. Structural design of elliptical hollow sections : a review. Proceedings of the ICE Structures and Buildings, **163**(6): 391–402.

Chan, T.M., Huai, Y.M., and Wang, W. 2015. Experimental investigation on lightweight concrete-filled cold-formed elliptical hollow section stub columns. Journal of Constructional Steel Research, **115**: 434–444. Elsevier.

Chang, K.-H., and Pan, W.F. 2009. Buckling life estimation of circular tubes under cyclic bending. International Journal of Solids and Structures, **46**(2): 254–270.

Chang, X., Yang, L., Zong, L., Zhao, M.H., and Yin, F. 2019. Study on cyclic constitutive model and ultra low cycle fracture prediction model of duplex stainless steel. Journal of Constructional Steel Research, **152**: 105–116. Elsevier.

Chaparro, B.M., Thuillier, S., Menezes, L.F., Manach, P.-Y., and Fernandes, J. V. 2008. Material parameters identification: Gradient-based, genetic and hybrid optimization algorithms. Computational Materials Science, **44**(2): 339–346. Elsevier.

Charalampakis, A.E. 2011. Full plastic capacity of equal angle sections under biaxial bending and normal force. Engineering Structures, **33**(6): 2085–2090.

Charif, A., Shannag, M.J., and Dghaither, S. 2014. Ductility of reinforced lightweight concrete

beams and columns . scielo .

Chen, L., Doerich, C., and Rotter, J.M. 2008. A study of cylindrical shells under global bending in the elastic-plastic range. Steel Construction, **1**(1): 59–65. John Wiley & Sons, Ltd.

Chen, M.T., and Young, B. 2019. Behavior of cold-formed steel elliptical hollow sections subjected to bending. Journal of Constructional Steel Research, **158**: 317–330.

Chen, M.T., and Young, B. 2018. Numerical investigation on stub column behavior of cold-formed steel elliptical hollow sections. *In* The 8th International Conference on Thin-Walled Structures (ICTWS 2018). Lisbon, Portugal.

Chen, W.F., and Han, D.J. 2007. Plasticity for Structural Engineers. Springer-Verlag, New York, NY, USA.

Chen, W.F., and Kim, S.E. 1997. LRFD Steel Design using Advanced Analysis. CRC Press, Boca Raton, FL, USA.

Chen, Y.N., and Kempner, J. 1976. Buckling of oval cylindrical shells under compression and asymmetric bending. AIAA Journal, **14**(9): 1235–1240.

Cheng, X., Chen, Y., and Nethercot, D.A. 2013. Experimental study on H-shaped steel beam-columns with large width-thickness ratios under cyclic bending about weak-axis. Engineering Structures, **49**: 264–274. Elsevier.

Choi, K.K., and Park, H.G. 2010. Evaluation of inelastic deformation capacity of beams subjected to cyclic loading. ACI Structural Journal, **107**(5): 507–515.

Choo, Y.S., Liang, J.X., and Lim, L. V. 2003. Static strength of elliptical hollow section X-joint under brace compression. *In* The 10th International Symposium on Tubular Structures. *Edited by* M.A. Jaurietta, J.A. Chica, and A. Alonso. A.A. Balkema, Madrid, Spain. pp. 253–258.

Chung, K., Chung, J., and Choi, S. 2007. Prediction of pre-and post-peak behavior of concrete-filled square steel tube columns under cyclic loads using fiber element method. Thin-Walled Structures, **45**(9): 747–758. Elsevier.

Clark, E., and Stephenson, R. 1850. The Britannia and Conway Tubular Bridges: With General Inquiries on Beams and on the Properties of Materials Used in Construction. Day and Son, London, UK.

Coelho, A.M.G., Simão, P.D., and Wadee, M.A. 2013. Imperfection sensitivity of column instability revisited. Journal of Constructional Steel Research, **90**: 265–282. Elsevier.

Coffin, L.F. 1959. The cyclic straining and fatigue of metals. Transactions of the Metallurgical Society of AIME, **215**: 794–807.

Coffin, L.F. 1962. Low cycle fatigue: A review. Applied Materials Research, **1**(3): 129–141.

Corus. 2008. Celsius oval HSS sizes and design strengths: AISC-LRFD version, Corus tubes, structural and conveyance business. UK: Corby. TATA Steel Europe , Structural Hollow Sections - Celsius Oval,.

Coutie, M.G., and Maunder, L. 1963. Bend-buckling of pressurized cylindrical Shells. *In* Proceedings of the Institution of Mechanical Engineers. pp. 130–139.

CSA S16-14. 2014. Design of steel structures. Canadian Standards Association (CSA).

D'Aniello, M., Landolfo, R., Piluso, V., and Rizzano, G. 2012. Ultimate behavior of steel beams under non-uniform bending. Journal of Constructional Steel Research, **78**: 144–158.

Dai, X., and Lam, D. 2010. Axial compressive behaviour of stub concrete-filled columns with elliptical stainless steel hollow sections. Steel and Composite Structures, **10**(6): 517–539. Techno-Press.

Davoli, P. 1999. Principles of current methodologies in high-cycle fatigue design of metallic structures. *In* High-Cycle Metal Fatigue: From Theory to Applications. *Edited by* K.D. Van and I.V. Papadopoulos. Springer-Verlag GmbH, Udine, Italy. pp. 1–56.

Dawson, R.G., and Walker, A.C. 1972. Post-buckling of geometrically imperfect plates. Journal of the Structural Division (ASCE), **98**(1): 75–94. ASCE.

DeLuca, D.P. 2001. Understanding fatigue. ASME International Gas Turbine Institute,: 7–10.

Desmond, T.P., Winter, G., and Peköz, T. 1981a. Edge stiffeners for thin-walled members. Journal of the Structural Division (ASCE), **107**(2): 329–353. ASCE.

Desmond, T.P., Winter, G., and Peköz, T. 1981b. Intermediate stiffeners for thin-walled members. Journal of the Structural Division (ASCE), **107**(4): 627–648. ASCE.

Devi, S.V., and Singh, K.D. 2020. Finite element study of the stiffening effects on torsional

capacity of perforated stainless steel slender semi-elliptical hollow section members. Structures, **26**: 66–78.

Devi, S.V., Singh, T.G., and Singh, K.D. 2019. Cold-formed steel square hollow members with circular perforations subjected to torsion. Journal of Constructional Steel Research, **162**: 105730.

DeWolf, J.T., Winter, G., and Peköz, T. 1973. Local and overall buckling of cold-formed compression members. Report No. 354. Cornell University, Ithaca, NY, USA.

Ding, F.X., Ding, X.Z., Liu, X.M., Wang, H.B., Yu, Z.W., and Fang, C.J. 2017. Mechanical behavior of elliptical concrete-filled steel tubular stub columns under axial loading. Steel and Composite Structures, **25**(3): 375–388. Techno Press.

Divakaran, V.N., Ravikumar, G.V. V, and Rao, P.S. 2015. Aircraft Landing Gear Design & Development-How Advanced Technologies are helping to meet the challenges? Infosys, Bengaluru, Karnataka, India.

Doerich, C., and Rotter, J.M. 2011. Generalised capacity curves for stability and plasticity: Application and limitations. Thin-Walled Structures, **49**(9): 1132–1140.

Doghri, I. 1993. Fully implicit integration and consistent tangent modulus in elasto-plasticity. International Journal for Numerical Methods in Engineering, **36**(22): 3915–3932. Wiley Online Library.

Donnell, L.H. 1934. A new theory for the buckling of thin cylinders under axial compression and bending. Transactions of ASME, **56**(12): 795–806.

Dowling, N.E. 2012. Mechanical Behavior of Materials: Engineering Methods for Deformation, Fracture, and Fatigue. *In* 4th edition. Pearson.

Dunne, F., and Petrinic, N. 2005. Introduction to Computational Plasticity. *Edited by* Oxford University. Oxford University Press, Oxford, UK.

Dutta, A., Dhar, S., and Acharyya, S.K. 2010. Material characterization of SS 316 in low-cycle fatigue loading. Journal of Materials Science, **45**(7): 1782–1789. Springer.

ECCS. 1986. Recommended Testing Procedure For Assessing The Behaviour Of Steel Elements Under Cyclic Loads, Technical Committee 1, TWG 1.3 — Seismic Design. European Convention for Constructional Steelworks, Brussels, Belgium.

Elchalakani, M. 2014. A closed-form solution for elastic buckling of thin-walled unstiffened circular cylinders in pure flexure. Thin-Walled Structures, **80**: 120–129.

Elchalakani, M., Zhao, X.L., and Grzebieta, R. 2002a. Bending tests to determine slenderness limits for cold-formed circular hollow sections. Journal of Constructional Steel Research, **58**(11): 1407–1430. Elsevier.

Elchalakani, M., Zhao, X.L., and Grzebieta, R. 2002b. Tests on concrete filled double-skin (CHS outer and SHS inner) composite short columns under axial compression. Thin-Walled Structures, **40**(5): 415–441. Elsevier.

Elchalakani, M., Zhao, X.L., and Grzebieta, R. 2003. Tests of cold-formed circular tubular braces under cyclic axial loading. Journal of Structural Engineering (ASCE), (April): 507–514.

Elchalakani, M., Zhao, X.L., and Grzebieta, R. 2004. Cyclic bending tests to determine fully ductile section slenderness limits for cold-formed circular hollow sections. Journal of Structural Engineering, **130**(7): 1001–1010. American Society of Civil Engineers.

Elchalakani, M., Zhao, X.L., and Grzebieta, R. 2006. Variable amplitude cyclic pure bending tests to determine fully ductile section slenderness limits for cold-formed CHS. Engineering Structures, **28**(9): 1223–1235.

Elchalakani, M., Zhao, X.L., and Grzebieta, R.H. 2002c. Plastic slenderness limits for cold-formed circular hollow sections. Australian Journal of Structural Engineering, **3**(3): 127–141. Taylor & Francis.

Elghazouli, A.Y. 2003. Seismic design procedures for concentrically braced frames. *In* Proceedings of the ICE - Structures and Buildings. pp. 381–394.

Elghazouli, A.Y., Broderick, B.M., Goggins, J., Mouzakis, H., Carydis, P., Bouwkamp, J., and Plumier, A. 2005. Shake table testing of tubular steel bracing members. Proceedings of the Institution of Civil Engineers - Structures and Buildings, **158**(4): 229–241.

Elkady, A., and Lignos, D.G. 2015. Analytical investigation of the cyclic behavior and plastic hinge formation in deep wide-flange steel beam-columns. Bulletin of Earthquake Engineering, **13**(4): 1097–1118. Springer.

Elkady, A., and Lignos, D.G. 2017. Stability requirements of deep steel wide-flange columns

under cyclic loading. *In* Proceedings of the Annual Stability Conference Structural Stability Research Council (SSRC). Structural Stability Research Council, San Antonio, TX, USA.

Ellingwood, B., Galambos, T.V., MacGregor, J.G., and Cornell, C.A. 1980. Probability Based Load Criterion for American National Standard A58: Building code requirements for minimum design loads in buildings and other structures. *In* NBS SP 577. U.S. Department of Commerce, National Bureau of Standards, Washington, DC, USA.

EN 10210-2. 2006. Hot finished structural hollow sections of non-alloy and fine grain steels - Part 2: Tolerances, dimension and sectional properties. *In* British Standards. European Commitee for Standardization (CEN), Brussels, Belgium.

EN 10219-2. 2006. Cold formed welded structural hollow sections of non-alloy and fine grain steels–Part 2: Tolerances, dimensions and sectional properties. *In* British Standards. European Committee for Standardization (CEN), Brussels, Belgium.

EN 1993-1-1. 2005. Eurocode 3: Design of steel structures - Part 1-1: General rules and rules for buildings. European Commitee for Standardization (CEN), Brussels, Belgium.

EN 1993-1-11. 2006. Eurocode 3–Design of steel structures, Part 1-11: Design of structures with tension components. CEN–Comité Européen de Normalisation, Brussels, Belgium.

EN 1993-1-3. 2006. Eurocode 3: Design of steel structures-Part 1-3: General rules-Supplementary rules for cold-formed members and sheeting. European Commitee for Standardization (CEN), Brussels, Belgium.

EN 1993-1-6:A1. 2017. Eurocode 3: Design of steel structures - Part 1-6: Strength and stability of shell structures, Amendment A1. CEN–Comité Européen de Normalisation, Brussels, Belgium.

EN 1993-1-6. 2007. Eurocode 3 - Design of Steel Structures - Part 1-6: Strength and Stability of Shell Structures. European Commitee for Standardization (CEN), Brussels, Belgium.

EN 1993-1-9. 2005. Eurocode 3: Design of steel structures - Part 1-9: Fatigue. European Commitee for Standardization (CEN), Brussels, Belgium.

EN 1993-2. 2006. Eurocode 3: Design of steel structures - Part 2: Steel bridges. CEN–Comité Européen de Normalisation, Brussels, Belgium.

EN 1998-1. 2004. Eurocode 8: Design of structures for earthquake resistance - Part 1 : General rules, seismic actions and rules for buildings. *In* Eurocode 8. European Commitee for Standardization (CEN), Brussels, Belgium.

Engel, P., and Badia, L. Della. 2013. Ospedale di Mestre (Hospital of Mestre). Available from https://www.promozioneacciaio.it/cms/it4857-ospedale-di-mestre.asp.

Espinós, A., Gardner, L., Romero, M.L., and Hospitaler, A. 2011. Fire behaviour of concrete filled elliptical steel columns. Thin-Walled Structures, **49**(2): 239–255. Elsevier.

Espinós, A., Romero, M.L., Portolés, J.M., and Hospitaler, A. 2014. Ambient and fire behavior of eccentrically loaded elliptical slender concrete-filled tubular columns. Journal of constructional steel research, **100**: 97–107. Elsevier.

Espinós, A., Romero, M.L., Serra, E., and Hospitaler, A. 2015. Experimental investigation on the fire behaviour of rectangular and elliptical slender concrete-filled tubular columns. Thin-Walled Structures, **93**: 137–148. Elsevier.

Euler, L. 1759. Sur la force des colonnes. Eneström Number 238. Memoires de l'academie des sciences de Berlin, **13**: 252–282.

Fadden, M., and McCormick, J. 2014. Finite element model of the cyclic bending behavior of hollow structural sections. Journal of Constructional Steel Research, **94**: 64–75.

Fadden, M.F. 2013. Cyclic Bending Behavior of Hollow Structural Sections and their Application in Seismic Moment Frame Systems. PhD Thesis. University of Michigan.

Fairbairn, W. 1849. An Account of the Construction of the Britannia and Conway Tubular Bridges, with A Complete History of their Progress. John Weale, London, UK.

Fajuyitan, O.K., and Sadowski, A.J. 2018. Imperfection sensitivity in cylindrical shells under uniform bending. Advances in Structural Engineering, **21**(16): 2433–2453. SAGE Publications Ltd STM.

Fajuyitan, O.K., Sadowski, A.J., Wadee, M.A., and Rotter, J.M. 2018. Nonlinear behaviour of short elastic cylindrical shells under global bending. Thin-Walled Structures, **124**: 574–587.

Fang, C., Zhou, F., and Wu, W. 2018. Performance of elliptical hollow sections under combined compression and cyclic bending. Journal of Structural Engineering, **144**(8):

4018102. American Society of Civil Engineers.

Feinstein, G., Erickson, B., and Kempner, J. 1971. Stability of oval cylindrical shells. Experimental Mechanics, **11**(11): 514–520. Springer.

Fell, B. V, Kanvinde, A.M., Deierlein, G.G., Myers, A., and Fu, X. 2006. Buckling and fracture of concentric braces under inelastic cyclic loading. *In* Steel TIPS Report. Moraga, CA, USA.

Fell, B.V. 2008. Large-Scale Testing and Simulation of Earthquake-Induced Ultra Low Cycle Fatigue in Bracing Members Subjected to Cyclic Inelastic Buckling. PhD Thesis. University of California, Davis.

FEMA 350. 2000. Recommended seismic design criteria for new steel moment frame buildings. Federal Emergency Management Agency, Washington, D.C, USA.

FEMA 461. 2007. Interim Testing Protocols for Determining the Seismic Performance Characteristics of Structural and Nonstructural Components. Federal Emergency Management Agency, Washington, DC, USA.

FEMA P695. 2009. Quantification of Building Seismic Performance Factors. *Edited by* ATC. Federal Emergency Management Agency, Washington, DC, USA.

Franco, L.A.L., Lourenco, N.J., Graca, M.L.A., Silva, O.M.M., de Campos, P.P., and von Dollinger, C.F.A. 2006. Fatigue fracture of a nose landing gear in a military transport aircraft. Engineering Failure Analysis, **13**(3): 474–479. Elsevier.

Fujimoto, T., Mukai, A., Nishiyama, I., Inai, E., Kai, M., Tanaka, Y., Tokinoya, H., Noguchi, T., Baba, T., Fukumoto, N., Murata, Y., Sakino, K., and Morino, S. 1997. Axial compression behavior of concrete filled steel tubular stub columns using high strength materials. Journal of Structural Construction Engineering, AIJ, **498**: 161–168.

Gabor, R., Vulcu, C., Stratan, A., Dubina, D., Voica, F., Marcu, D., and Alexandrescu, D. 2012. Experimental and numerical validation of the technical solution of a brace with pinned connections for seismic-resistant multi-story structures. *In* 15th World Conference on Earthquake Engineering (15WCEE). Lisbon, Portugal.

Gardner, L. 2002. A new approach to stainless steel structural design. Ph.D Thesis. Imperial College London.

Gardner, L. 2005. Structural behaviour of oval hollow sections. Advanced Steel Construction,: 29–53. HKISC.

Gardner, L. 2008. The continuous strength method. *In* Proceedings of the Institution of Civil Engineers - Structures and Buildings. ICE Publishing. pp. 127–133.

Gardner, L., and Chan, T.M. 2007. Cross-section classification of elliptical hollow sections. Steel and Composite Structures, **7**(3): 185–200.

Gardner, L., Chan, T.M., and Abela, J.M. 2011. Structural behaviour of elliptical hollow sections under combined compression and uniaxial bending. Advanced Steel Construction, **7**(1): 86–112.

Gardner, L., and Ministro, A. 2004. Testing and numerical modelling of structural steel oval hollow sections. Imperial College, UK, London,.

Gardner, L., and Nethercot, D.A. 2004. Numerical modeling of stainless steel structural components—a consistent approach. Journal of Structural Engineering (ASCE), **130**(10): 1586–1601. American Society of Civil Engineers.

Gardner, L., and Nethercot, D.A. 2011. Designers' Guide to Eurocode 3: Design of Steel Buildings - EN 1993-1-1, -1-3 and -1-8. *In* 2nd edition. *Edited by* H. Gulvanessian. ICE Publishing, London, UK.

Gardner, L., Saari, N., and Wang, F. 2010. Comparative experimental study of hot-rolled and cold-formed rectangular hollow sections. Thin-Walled Structures, **48**(7): 495–507. Elsevier.

Gardner, L., Yun, X., Macorini, L., and Kucukler, M. 2017. Hot-rolled steel and steel-concrete composite design incorporating strain hardening. Structures, **9**: 21–28.

Giakoumelis, G., and Lam, D. 2004. Axial capacity of circular concrete-filled tube columns. Journal of Constructional Steel Research, **60**(7): 1049–1068. Elsevier.

Gioncu, V., and Mazzolani, F. 2013. Seismic Design of Steel Structures. *In* 1st edition. CRC Press, Taylor & Francis Group, London, UK.

Goggins, J. 2004. Earthquake Resistant Hollow and Filled Steel Braces. PhD Thesis. University of Dublin, Trinity College, Dublin, Ireland.

Goggins, J.M., Broderick, B.M., Elghazouli, A.Y., and Lucas, A.S. 2005. Experimental cyclic

response of cold-formed hollow steel bracing members. Engineering Structures, **27**(7): 977–989.

Goggins, J.M., Broderick, B.M., Elghazouli, A.Y., and Lucas, A.S. 2006. Behaviour of tubular steel members under cyclic axial loading. *In* Journal of Constructional Steel Research. pp. 121–131.

Grimm, D.F. 1979. Local buckling of steel tubular columns. Lehigh University.

Gross, M.R. 1963. Low-cycle fatigue of materials for submarine construction. Naval Engineers Journal, **75**(4): 783–798. Wiley Online Library.

Grover, H.J. 1966. NAVAIR 01-1A-13: Fatigue of Aircraft Structures. NAVAIR, Columbus, OH, USA.

Guerrero, N., Marante, M.E., Picón, R., and Flórez-López, J. 2007. Model of local buckling in steel hollow structural elements subjected to biaxial bending. Journal of Constructional Steel Research, **63**(6): 779–790.

Gugerli, H. 1982. Inelastic Cyclic Behavior of Steel Members. University of Michigan.

Guo, L., Liu, Y., Jiao, H., and An, S. 2016. Behavior of thin-walled circular hollow section stub columns under axial compression. International Journal of Steel Structures, **16**(3): 777–787. Springer.

Guo, L., Yang, S., and Jiao, H. 2013. Behavior of thin-walled circular hollow section tubes subjected to bending. Thin-Walled Structures, **73**: 281–289. Elsevier.

Haddad, M. 2015. Concentric tubular steel braces subjected to seismic loading: Finite element modeling. Journal of Constructional Steel Research, **104**: 155–166.

Haddad, M., Brown, T., and Shrive, N. 2011a. Finite element modeling of concentric HSS braces under cyclic loading. Canadian Journal of Civil Engineering, **38**(5): 493–505.

Haddad, M., Brown, T., and Shrive, N. 2011b. Experimental cyclic loading of concentric HSS braces. Canadian Journal of Civil Engineering, **38**(1): 110–123.

Haddad, M.A. 2004. Design of Concentrically Braced Steel Frames for Earthquakes. PhD Thesis. Calgary, Alberta, Canada.

Haedir, J., Bambach, M.R., Zhao, X.L., and Grzebieta, R.H. 2009. Strength of circular hollow

sections (CHS) tubular beams externally reinforced by carbon FRP sheets in pure bending. Thin-Walled Structures, **47**(10): 1136–1147.

Halama, R., Sedlák, J., and Šofer, M. 2012a. Phenomenological modelling of cyclic plasticity. *In* Numerical Modelling. *Edited by* P. Miidla. InTech, Shanghai, China. pp. 329–354.

Halama, R., Šofer, M., and Fojtík, F. 2012b. Choice and calibration of cyclic plasticity model with regard to subsequent fatigue analysis. Engineering Mechanics, **19**: 87–97.

Hales, R., Holdsworth, S.R., O'Donnell, M.P., Perrin, I.J., and Skelton, R.P. 2002. A code of practice for the determination of cyclic stress-strain data. Materials at high temperatures, **19**(4): 165–185. Taylor & Francis.

Han, L.H., Huang, H., Tao, Z., and Zhao, X.L. 2006. Concrete-filled double skin steel tubular (CFDST) beam–columns subjected to cyclic bending. Engineering Structures, **28**(12): 1698–1714. Elsevier.

Han, L.H., Li, W., and Bjorhovde, R. 2014. Developments and advanced applications of concrete-filled steel tubular (CFST) structures: Members. Journal of Constructional Steel Research, **100**: 211–228.

Han, L.H., and Yang, Y.F. 2005. Cyclic performance of concrete-filled steel CHS columns under flexural loading. Journal of Constructional Steel Research, **61**(4): 423–452. Elsevier.

Han, L.H., Yang, Y.F., and Tao, Z. 2003. Concrete-filled thin-walled steel SHS and RHS beam-columns subjected to cyclic loading. Thin-Walled Structures, **41**(9): 801–833.

Han, S.W., Kim, W.T., and Foutch, D.A. 2007. Seismic behavior of HSS bracing members according to width–thickness ratio under symmetric cyclic loading. Journal of Structural Engineering (ASCE), **133**(2): 264–273. American Society of Civil Engineers.

Hancock, G.J. 2003. Cold-formed steel structures. Journal of Constructional Steel Research, **59**(4): 473–487.

Hancock, G.J., Kwon, Y.B., and Bernard, E.S. 1994. Strength design curves for thin-walled sections undergoing distortional buckling. Journal of Constructional Steel Research, **31**(2–3): 169–186. Elsevier.

Hancock, G.J., Murray, T., and Ellifrit, D.S. 2001. Cold-Formed Steel Structures to the AISI

Specification. *Edited by* M.D. Meyer. Marcel Dekker, Inc., New York, NY, USA.

Haque, T., and Packer, J.A. 2012. Elliptical hollow section T and X connections. Canadian Journal of Civil Engineering, **39**(8): 925–936. NRC Research Press.

Haque, T., Packer, J.A., and Zhao, X.L. 2012. Equivalent RHS approach for the design of EHS in axial compression or bending. Advances in Structural Engineering, **15**(1): 107–120. SAGE Publications Sage UK: London, England.

Hashimoto, O., Yasunami, H., Mizutani, S., Kobashi, Y., and Nakagawa, T. 1996. Investigation on the strength and ductility of steel piers with compact section. Bridge Found. Eng, **30**(8): 135–137.

Hassan, M.S., Salawdeh, S., and Goggins, J.M. 2018. Determination of geometrical imperfection models in finite element analysis of structural steel hollow sections under cyclic axial loading. Journal of Constructional Steel Research, **141**: 189–203.

Hassanein, M.F., Patel, V.I., El Hadidy, A.M., Al Abadi, H., and Elchalakani, M. 2018. Structural behaviour and design of elliptical high-strength concrete-filled steel tubular short compression members. Engineering Structures, **173**: 495–511.

Hayman, R. 1628. Certaine Epigrams out of the First Foure Bookes of the Excellent Epigrammatist, Master John Owen. Translated into English at Harbor-Grace in Bristols-Hope in Britaniola, anciently called New-found-land. Roger Michell, London, UK.

Hill, R. 1966. Generalized constitutive relations for incremental deformation of metal crystals by multislip. Journal of the Mechanics and Physics of Solids, **14**(2): 95–102. Elsevier.

Hodge, P.G., Hopkins, H.G., and Lee, E.H. 1956. The theory of piecewise linear isotropic plasticity. *In* Deformation and Flow of Solids/Verformung und Fliessen des Festkörpers. Springer. pp. 147–170.

Houliara, S., and Karamanos, S.A. 2011. Buckling of thin-walled long steel cylinders subjected to bending. Journal of Pressure Vessel Technology (ASME), **133**(1): 11201-(1-9). American Society of Mechanical Engineers.

Hsiao, L.-E., Yu, W.W., and Galambos, T. V. 1990. AISI LRFD method for cold-formed steel structural members. Journal of Structural Engineering (ASCE), **116**(2): 500–517. American Society of Civil Engineers.

Huang, Y. 2009. Simulating the Inelastic Seismic Behavior of Steel Braced Frames Including the Effects of Low-Cycle-Fatigue. PhD Thesis. University of California, Berkeley, CA, USA.

Huang, Y., and Young, B. 2012. Material properties of cold-formed lean duplex stainless steel sections. Thin-walled structures, **54**: 72–81. Elsevier.

Hutchinson, J.W. 1968. Buckling and initial postbuckling behavior of oval cylindrical shells under axial compression. Journal of Applied Mechanics, **35**(1): 66–72.

Imaoka, S. 2008. Chaboche nonlinear kinematic hardening model. ANSYS Release, **12**(1): 1–14.

IS 800. 2007. General construction in steel-Code of practice (Third Revision). Bureau of Indian Standards, New Delhi, India.

Jain, A.K., Hanson, R.D., and Goel, S.C. 1980. Hysteretic cycles of axially loaded steel members. Journal of the Structural Division, ASCE, **106**(8): 1777–1795.

Jamaluddin, N., Lam, D., Dai, X.H., and Ye, J. 2013. An experimental study on elliptical concrete filled columns under axial compression. Journal of Constructional Steel Research, **87**: 6–16.

Javidan, F., Heidarpour, A., Zhao, X.L., and Fallahi, H. 2017. Fundamental behaviour of high strength and ultra-high strength steel subjected to low cycle structural damage. Engineering Structures, **143**: 427–440.

Jiang, W., Woo, W., Wan, Y., Luo, Y., Xie, X., and Tu, S.T. 2017. Evaluation of through-thickness residual stresses by neutron diffraction and finite-flement method in thick weld plates. Journal of Pressure Vessel Technology, **139**(3): 31401. American Society of Mechanical Engineers.

Jiao, H., and Zhao, X.L. 2003. Imperfection, residual stress and yield slenderness limit of very high strength (VHS) circular steel tubes. Journal of Constructional Steel Research, **59**(2): 233–249. Elsevier.

Jiao, H., and Zhao, X.L. 2004. Section slenderness limits of very high strength circular steel tubes in bending. Thin-Walled Structures, **42**(9): 1257–1271.

Jin, K., Guo, X., Tao, J., Wang, H., Kim, N., and Gu, Y. 2016. A model of one-surface cyclic

plasticity with Lemaitre damage criterion for plastic instability prediction in the incremental forming process. International Journal of Mechanical Sciences, **114**: 88–97. Elsevier.

Jirsa, J.O., Lee, F.H., Wilhoit Jr., J.C., and Merwin, J.E. 1972. Ovaling of pipelines under pure bending. *In* Offshore Technology Conference. Offshore Technology Conference (OTC), Dallas, TX, USA. p. OTC 1569.

Johansson, M., and Gylltoft, K. 2002. Mechanical behavior of circular steel–concrete composite stub columns. Journal of Structural Engineering ASCE, **128**(8): 1073–1081. American Society of Civil Engineers.

Kalyanaraman, V. 1976. Performance of unstiffened compression elements. Report No. 362. AISI, Ithaca, NY, USA.

Kalyanaraman, V., and Peköz, T. 1978. Analytical study of unstiffened elements. Journal of the Structural Division (ASCE), **104**(9): 1507–1524. ASCE.

Karamanos, S.A. 2002. Bending instabilities of elastic tubes. International Journal of Solids and Structures, **39**(8): 2059–2085.

von Kármán, T. 1932. The strength of thin plates in compression. Transactions of ASME, **54**: 53–57.

von Kármán, T., and Tsien, H. 1941. The buckling of thin cylindrical shells under axial compression. Journal of the Aeronautical Sciences, **8**(8): 303–312.

Kato, B. 1990. Role of strain-hardening of steel in structural performance. ISIJ International, **30**(11): 1003–1009.

Kempner, J. 1962. Some results on buckling and postbuckling of cylindrical shells. *In* Collected Papers on Instability of Shell Structures, NASA Technical Note (TN) D-1510. NASA, Hampton, VA, USA. pp. 173–186.

Kempner, J., and Chen, Y. 1974. Buckling and initial postbuckling of oval cylindrical shells under combined axial compression and bending. Transactions of the New York Academy of Sciences, **36**(2): 171–191. Wiley Online Library.

Kempner, J., and Chen, Y.N. 1966. Large deflections of an axially compressed oval cylindrical shell. *In* Applied Mechanics- Proceedings of the Eleventh International Congress of

Applied Mechanics. *Edited by* Henry Görtler. Springer, Munich, Germany. pp. 299–305.

Kempner, J., and Chen, Y.N. 1967. Buckling and postbuckling of an axially compressed oval cylindrical shell. *In* Symposium on the Theory of Shells. *Edited by* D. Muster. McCutchan Pub. Corp., Berkeley, CA, USA. pp. 141–175.

Kempner, J., and Chen, Y.N. 1969. Postbuckling of an axially compressed oval cylindrical shell. *In* Applied Mechanics- Proceedings of the Twelfth International Congress of Applied Mechanics. *Edited by* M. Hetényi and W.G. Vincenti. Springer Berlin Heidelberg, Berlin, Heidelberg, Germany. pp. 246–256.

Khaliq, A.A., and Schilling, C.G. 1964. Plastic buckling strength of seamless steel tubes under bending loads, Report No. 57.019-800(2). *In* Research Bulletin of Applied Research Lab., U.S. Steel Corp. Monroeville, PA, USA.

Klook. 2016. What To Expect. Available from https://res.klook.com/images/fl_lossy.progressive,q_65/c_fill,w_1295,h_720,f_auto/w_80,x_15,y_15,g_south_west,l_klook_water/activities/d43fc2dd-Up-To-30-Off-Airport-Express-Tickets/HongKongAirportExpressTrainTickets(QRCodeDirectEntry).jpg. [accessed 23 January 2019].

Korol, R.M. 1978. Inelastic buckling of circular tubes in bending. Journal of the Engineering Mechanics Division, **104**(4): 939–950. ASCE.

Krawinkler, H. 1996. Cyclic loading histories for seismic experimentation on structural components. Earthquake Spectra, **12**(1): 1–12.

Krawinkler, H. 2009. Loading histories for cyclic tests in support of performance assessment of structural components. *In* 3rd International Conference on Advances in Experimental Structural Engineering. San Franscisco, CA, USA. pp. 1–10.

Krawinkler, H., Gupta, A., Medina, R., and Luco, N. 2000. Development of Loading Histories for Testing of Steel Beam-to-Column Assemblies, SAC Background Report SAC/BD-00/10. Redwood City, CA, USA.

Krolo, P., Grandić, D., and Smolčić, Ž. 2016. Experimental and numerical study of mild steel behaviour under cyclic loading with variable strain ranges. Advances in Materials Science and Engineering, **2016**. Hindawi.

Kurata, M., Nakashima, M., and Suita, K. 2005. Effect of column base behavior on the seismic response of steel moment frames. Journal of Earthquake Engineering, **9**(spec02): 415–438. Taylor & Francis.

Kuroda, M. 2002. Extremely low cycle fatigue life prediction based on a new cumulative fatigue damage model. International Journal of Fatigue, **24**(6): 699–703.

Kyriakides, S., and Shaw, P.K. 1987. Inelastic buckling of tubes under cyclic bending. Journal of Pressure Vessel Technology (ASME), **109**(2): 169–178.

Laird, C. 1977. The general cyclic stress-strain response of aluminum alloys. *In* Cyclic Stress-Strain and Plastic Deformation Aspects of Fatigue Crack Growth (ASTM STP 637). ASTM International, Philadelphia, PA, USA. pp. 3–35.

Lam, D., Gardner, L., and Burdett, M. 2010. Behaviour of axially loaded concrete filled stainless steel elliptical stub columns. Advances in Structural Engineering, **13**(3): 493–500. SAGE Publications Ltd STM.

Lam, D., and Testo, N. 2011. Structural design of concrete filled steel elliptical hollow sections. *In* Composite Construction in Steel and Concrete VI. pp. 252–262.

Lan, X., Chen, J., Chan, T.M., and Young, B. 2019. The continuous strength method for the design of high strength steel tubular sections in bending. Journal of Constructional Steel Research, **160**: 499–509.

Lan, X., Chen, J., Chan, T.M., and Young, B. 2018. The continuous strength method for the design of high strength steel tubular sections in compression. Engineering Structures, **162**: 177–187.

Laulusa, A., Bauchau, O.A., Choi, J.-Y., Tan, V.B.C., and Li, L. 2006. Evaluation of some shear deformable shell elements. International Journal of Solids and Structures, **43**(17): 5033–5054.

Law, K.H., and Gardner, L. 2012. Lateral instability of elliptical hollow section beams. Engineering Structures, **37**: 152–166.

Law, K.H., and Gardner, L. 2013a. Global instability of elliptical hollow section beam-columns under compression and biaxial bending. International Journal of Steel Structures, **13**(4): 745–759.

Law, K.H., and Gardner, L. 2013b. Buckling of elliptical hollow section members under combined compression and uniaxial bending. Journal of Constructional Steel Research, **86**: 1–16.

LEAPS. 2015. Academic skills on the LEAPS summer school. Available from http://www.leapsacademicskills.net/uploads/2/0/7/0/2070115/dsb.jpg. [accessed 7 February 2019].

Lee, K.-L., Pan, W.-F., and Kuo, J.N. 2001. The influence of the diameter-to-thickness ratio on the stability of circular tubes under cyclic bending. International Journal of Solids and Structures, **38**(14): 2401–2413.

Lee, S., and Goel, S.C. 1987. Seismic behavior of hollow and concrete-filled square tubular bracing members, Report UMCE, 87-11. Ann Arbor, MI, USA.

Lee, Y.L., Pan, J., Hathaway, R., and Barkey, M. 2005. Fatigue testing and analysis: Theory and practice. Butterworth-Heinemann, Burlington, MA, USA.

Leen, S.B., Deshpande, A., and Hyde, T.H. 2010. Experimental and numerical characterization of the cyclic thermomechanical behavior of a high temperature forming tool alloy. Journal of manufacturing science and engineering, **132**(5): 51013(1–12). American Society of Mechanical Engineers.

Lemaitre, J., and Chaboche, J.-L. 1994. Mechanics of solid materials. Cambridge University Press, Cambridge, UK.

Li, R., Eyckens, P., Gawad, J., Poucke, M. Van, Cooreman, S., and Bael, A. Van. 2017. Advanced plasticity modeling for ultra-low-cycle-fatigue simulation of steel pipe. Metals, **7**(4): 140. Multidisciplinary Digital Publishing Institute.

Liao, F.-Y., Han, L.H., Tao, Z., and Rasmussen, K.J.R. 2016. Experimental behavior of concrete-filled stainless steel tubular columns under cyclic lateral loading. Journal of Structural Engineering, **143**(4): 4016219. American Society of Civil Engineers.

Liew, J.Y.R., Shanmugam, N.E., and Lee, S.L. 1989. Local buckling of thin-walled steel box columns. Thin-walled structures, **8**(2): 119–145. Elsevier.

Liu, F., Wang, Y., and Chan, T.M. 2017. Behaviour of concrete-filled cold-formed elliptical hollow sections with varying aspect ratios. Thin-Walled Structures, **110**: 47–61. Elsevier.

Livesey, G. 2018. Ahead of the Curve. Canadian Architect,: 36–41. Toronto, Canada.

Lorenz, R. 1908. Achsensymmetrische Verzerrungen in dünnwandigen Hohlzylindern. Zeitschrift des Vereines Deutscher Ingenieure, **52**(43): 1706–1713.

Lorenz, R. 1911. Die nicht achsensymmetrische Knickung dünnwandiger Hohlzylinder. Phys. Z., **12**(7): 241–260.

Lundquist, E.E., and Burke, W.F. 1935. Strength Tests of Thin-Walled Duralumin Cylinders of Elliptic Section. NACA-TN-527. National Advisory Committee for Aeronautics, USA.

M° Kenzie, W.M.C. 1998. Members subject to combined axial and flexural loads. *In* Design of Structural Steelwork to BS 5950 and C-EC3. Macmillan Publishers Ltd., Palgrave, London, UK. pp. 123–144.

Ma, J.L., Chan, T.M., and Young, B. 2016. Experimental investigation on stub-column behavior of cold-formed high-strength steel tubular sections. Journal of Structural Engineering (ASCE), **142**(5): 4015174. American Society of Civil Engineers.

Ma, J.L., Chan, T.M., and Young, B. 2018. Design of cold-formed high-strength steel tubular stub columns. Journal of Structural Engineering (ASCE), **144**(6): 4018063. American Society of Civil Engineers.

Mahgub, M., Ashour, A., Lam, D., and Dai, X. 2017. Tests of self-compacting concrete filled elliptical steel tube columns. Thin Walled Structures, **110**(March 2016): 27–34. Elsevier.

Mamaghani, I.H.P. 2004. Seismic design and retrofit of thin-walled steel tubular columns. *In* 13th World Conference on Earthquake Engineering. Vancouver, B.C., Canada.

Mamaghani, I.H.P. 2008. Seismic design and ductility evaluation of thin-walled steel bridge piers of box sections. Transportation Research Record: Journal of the Transportation Research Board, **2050**: 137–142. Transportation Research Board of the National Academies.

Mamaghani, I.H.P., Usami, T., and Mizuno, E. 1997. Hysteretic behavior of compact steel box beam-columns. Journal of Structural Engineering, **43**: 187–194.

Mann, J.Y. 2013. Bibliography on the Fatigue of Materials, Components and Structures. Pergamon Press, London, UK.

Manson, S.S. 1962. Discussion:“Experimental Support for Generalized Equation Predicting

Low Cycle Fatigue." Journal of Basic Engineering, **84**(4): 537–541. American Society of Mechanical Engineers.

Manson, S.S. 1964. Fatigue behavior in strain cycling in the low and intermediate cycle range. *In* Proceedings of the 10th Sagamore Army Materials Research Conference: Fatigue-An Interdisciplinary Approach. *Edited by* John J. Burke, N.L. Reed, and V. Weiss. Raquette Lake, NY, USA. pp. 133–179.

Manson, S.S. 1966. Thermal Stress and Low-Cycle Fatigue. McGraw-Hill, New York, NY, USA.

Marquis, D. 2001. Cyclic plasticity model with nonlinear isotropic and kinematic hardening: NoLIKH model. *In* Handbook of Materials Behavior Models, 1st edition. *Edited by* J. Lemaitre. Academic Press, Cambridge, Massachusetts, USA. pp. 213–222.

Martinez-Saucedo, G., and Packer, J.A. 2006. Slotted end connections to hollow sections. *In* CIDECT 8G-10/06. Toronto, Canada.

Masubuchi, K. 1980. Analysis of Welded Structures: Residual Stresses, Distortion, and their Consequences. *In* 1st edition. Pergamon Press, Oxford, UK.

Mazzolani, F.M., Mandara, A., and Langseth, M. 1999. Plastic design of aluminium members according to EC9. *In* LIGHT-WEIGHT STEEL AND ALUMINIUM STRUCTURES: The Fourth International Conference on Steel and Aluminium Structures (ICSAS '99). *Edited by* P. Mäkeläinen and R. Hassinen. Elsevier Science, Espoo, Finland. pp. 457–464.

Mazzolani, F.M., and Piluso, V. 1997. Plastic design of seismic resistant steel frames. Earthquake Engineering and Structural Dynamics, **26**(2): 167–191. Wiley Online Library.

McCann, F., Fang, C., Gardner, L., and Silvestre, N. 2016. Local buckling and ultimate strength of slender elliptical hollow sections in compression. Engineering Structures, **111**: 104–118. Elsevier.

McCann, F., Gardner, L., and Silvestre, N. 2018. Postbuckling strength of slender elliptical hollow sections in bending. *In* The 8th International Conference on Thin-Walled Structures (ICTWS 2018). *Edited by* D. Camotim and N. Silvestre. Lisbon, Portugal.

Midorikawa, M., Okawa, I., Iiba, M., and Teshigawara, M. 2003. Performance-based seismic design code for buildings in Japan. Earthquake Engineering and Engineering Seismology,

4(1): 15–25.

Miller, T.H., and Peköz, T. 1994. Unstiffened strip approach for perforated wall studs. Journal of Structural Engineering (ASCE), **120**(2): 410–421. American Society of Civil Engineers.

Momenzadeh, S., and Shen, J. 2018. Seismic demand on columns in special concentrically braced frames. Engineering Structures, **168**: 93–107.

Mouritz, A.P. (*Editor*). 2012. Strengthening of metal alloys. *In* Introduction to Aerospace Materials. Woodhead Publishing. pp. 57–90.

Nakamura, S., Yasunami, H., Kobayashi, Y., Nakagawa, T., and Mizutani, S. 1997. An experimental study on the seismic performance of steel bridge piers with less-stiffened and compact sized section. *In* Nonlinear Numerical Analysis and Seismic Design of Bridge Piers (JSCE).

Nakashima, M., and Liu, D. 2005. Instability and complete failure of steel columns subjected to cyclic loading. Journal of Engineering Mechanics (ASCE), **131**(6): 559–567. American Society of Civil Engineers.

Nakashima, M., Nishino, T., Tsuji, B., and Iwasa, Y. 1992. Effect of strain hardening on post-buckling resistance of steel braces. *In* International Proceedings of Third Pacific Structural Steel Conference. Tokyo, Japan. pp. 561–568.

Nastar, N., Brandow, G., Anderson, J., and Nigbor, R. 2013. The effects of low-cycle fatigue in steel structures. *In* Sixth Congress on Forensic Engineering, Forensic Engineering 2012: Gateway to a Safer Tomorrow. *Edited by* A.M. Dolhon, M.J. Drerup, A.D. de Len, J.B. Kardon, D.S. Hancock, and S. Chen. ASCE, San Francisco, CA, USA. pp. 1121–1130.

Nghiem, A., Kang, T.H.K., Lee, M., Ramseyer, C., and Lee, C.H. 2018. Flexural testing of circular concrete-filled tubes without axial forces. ACI Structural Journal, **115**(2).

Nicholas, T. 2006. High cycle fatigue: A Mechanics of Materials Perspective. *In* 1st edition. Elsevier, London, UK.

Nip, A.K.H., Gardner, L., and Elghazouli, A.Y. 2013. Ultimate behaviour of steel braces under cyclic loading. Proceedings of the Institution of Civil Engineers - Structures and

Buildings, **166**(5): 219–234. ICE Publishing.

Nip, K.H. 2009. Cyclic Behaviour of Carbon Steel and Stainless Steel Tubular Members. PhD Thesis. Imperial College London, London, UK.

Nip, K.H., Gardner, L., Davies, C.M., and Elghazouli, A.Y. 2010a. Extremely low cycle fatigue tests on structural carbon steel and stainless steel. Journal of Constructional Steel Research, **66**(1): 96–110.

Nip, K.H., Gardner, L., and Elghazouli, A.Y. 2010b. Cyclic testing and numerical modelling of carbon steel and stainless steel tubular bracing members. Engineering Structures, **32**(2): 424–441.

Nishikawa, K., Yamamoto, S., Natori, T., Terao, K., Yasunami, H., and Terada, M. 1998. Retrofitting for seismic upgrading of steel bridge columns. Engineering Structures, **20**(4): 540–551.

Nishikawa, K., Yamamoto, S., Natori, T., Terao, O., Yasunami, H., and Terada, M. 1996. An experimental study on improvement of seismic performance of existing steel bridge piers. Journal of Structural Engineering (JSCE), **42**(3): 975–986.

Northwood, D.O. 1985. The development and applications of zirconium alloys. Materials & Design, **6**(2): 58–70.

Novak, J.S. 2016. Parameter estimation of cyclic plasticity models and strain-based fatigue curves in numerical analysis of mechanical components under thermal loads. Ph. D Thesis. University of Udine, Udine, UD, Italy.

Novak, J.S., Benasciutti, D., De Bona, F., Stanojević, A., and Huter, P. 2015. Thermo-mechanical finite element simulation and fatigue life assessment of a copper mould for continuous casting of steel. Procedia Engineering, **133**: 688–697.

Nowzartash, F., and Mohareb, M. 2009. Plastic interaction relations for elliptical hollow sections. Thin-Walled Structures, **47**(6): 681–691. Elsevier.

Nussbaumer, A., Borges, L., and Davaine, L. 2011. Fatigue Design of Steel and Composite Structures: Eurocode 3: Design of Steel Structures, Part 1-9 Fatigue; Eurocode 4: Design of Composite Steel and Concrete Structures. *In* 1st edition. *Edited by* ECCS. European Convention for Constructional Steelwork, Berlin, Germany.

NZS 1170.5. 2004. Structural design actions—Part 5: Earthquake actions—New Zealand. Standards New Zealand, Wellington, New Zealand.

O'Donnell, W.J., and Langer, B.F. 1964. Fatigue design basis for Zircaloy components. Nuclear Science and Engineering, **20**(1): 1–12. Taylor & Francis.

O'Shea, M.D., and Bridge, R.Q. 1997. Local buckling of thin-walled circular steel sections with or without internal restraint. Journal of Constructional Steel Research, **41**(2–3): 137–157. Elsevier.

Ogle, C. 2015. 1st Anniversary of New Watford Market!! ... Shhhh nobody knows! Available from https://www.swhertscommunityhub.org.uk/2015/10/1st-anniversary-of-new-watford-market.html.

Ostapenko, A., and Gunzelman, S. 1978. Local buckling tests on three steel large-diameter tubular columns. *In* 4th International Specialty Conference on Cold-Formed Steel Structures.

Ottosen, N.S., and Ristinmaa, M. 2005. The Mechanics of Constitutive Modeling. Elsevier Science, Lund, Sweden.

Oxyman. 2011. Royal Albert Bridge. Available from https://upload.wikimedia.org/wikipedia/commons/thumb/6/62/Royal_Albert_Bridge_%282%29.jpg/800px-Royal_Albert_Bridge_%282%29.jpg. [accessed 23 November 2019].

Packer, J.A. 2008. Going Elliptical. Modern Steel Construction,.

Packer, J.A., and Henderson, J.E. 1992. Design Guide for Hollow Structural Section Connections. Canadian Institute of Steel Construction, Willowdale, Ontario, Canada.

Packer, J.A., Wardenier, J., Choo, Y.S., and Chiew, S.P. 2009. Elliptical steel tubes. Steel News and Notes, Singapore Structural Steel Society, SN&N 25th Anniversary Issue,: 86–90.

Padilla-llano, D.A., Moen, C.D., and Eatherton, M.R. 2015. OpenSees simulation of steel column axial cyclic response including local buckling. *In* Proceedings of the Annual Stability Conference. Structural Stability Research Council, Nashville, Tennessee.

Pakhomenkov, A. V, Azimov, R.A., and Bukatyi, S.A. 2017. Calculation of low cycle fatigue life for gas-turbine engine critical parts. Russian Aeronautics, **60**(3): 421–427. Allerton Press Inc.

Park, R. 1988. Ductility evaluation from laboratory and analytical testing. *In* Proceedings of the 9th world conference on earthquake engineering, Tokyo-Kyoto, Japan. pp. 605–616.

Payne, T. 2000. Nonlinear Response of Steel Beams: DSO-00-01. US Department of the Interior Bureau of Reclamation, Washington, DC, USA.

Pereira, J.C.R., de Jesus, A.M.P., Fernandes, A.A., and Varelis, G. 2016. Monotonic, low-cycle fatigue, and ultralow-cycle fatigue behaviors of the X52, X60, and X65 piping steel grades. Journal of Pressure Vessel Technology, **138**(3): 031403(1)-031403(9). ASME.

Pezoa, I. 2014. VIAJES-Los Mejores Aeropuertos del Mundo (TRAVELS- The Top Airports of the World [in Chilean Spanish]). Available from https://chileanjourna.wordpress.com/2014/07/30/los-mejores-aeropuertos-del-mundo/. [accessed 7 February 2019].

Pietrapertosa, C., and Jaspart, J.P. 2003. Study of the behaviour of welded joints between elliptical hollow sections. *In* The 10th International Symposium on Tubular Structures. *Edited by* M.A. Jaurietta, J.A. Chica, and A. Alonso. A.A. Balkema, Madrid, Spain. pp. 601–608.

Pirondi, A., Bonora, N., Steglich, D., Brocks, W., and Hellmann, D. 2006. Simulation of failure under cyclic plastic loading by damage models. International Journal of Plasticity, **22**(11): 2146–2170. Elsevier.

Plantema, F.J. 1946. Collapsing stresses of circular cylinders and round tubes. *In* Report No. S. 280. Amsterdam, The Netherlands.

Polák, J. 1991. Cyclic Plasticity and Low Cycle Fatigue Life of Metals. Academia, Prague, Czechoslovakia.

Poonaya, S., Teeboonma, U., and Thinvongpituk, C. 2009. Plastic collapse analysis of thin-walled circular tubes subjected to bending. Thin-Walled Structures, **47**(6): 637–645.

Pope, J.E. 1996. Rules of thumb for mechanical engineers. Gulf Professional Publishing.

Popov, E.P., and Black, R.G. 1981. Steel struts under severe cyclic loadings. Journal of Structural Division (ASCE), **107**(9): 1857–1881.

Popov, E.P., Mahin, S.A., and Zayas, V.A. 1979. Cyclic inelastic buckling of thin tubular columns. Journal of the Structural Division (ASCE), **105**(11): 2261–2277. ASCE.

Popov, E.P., Takanashi, K., and Roeder, C.W. 1976. Structural steel bracing systems: Behavior under cyclic loading. Report No. EERC 76-17. Earthquake Engineering Research Center, Berkeley, CA, USA.

Portella, P.D., and Rie, K.T. 1998. Low Cycle Fatigue and Elasto-Plastic Behaviour of Materials. *In* 1st edition. Elsevier Science, Garmisch-Partenkirchen, Germany.

Puthli, R., and Packer, J.A. 2013. Structural design using cold-formed hollow sections. Steel Construction, **6**(2): 150–157. John Wiley & Sons, Ltd.

Qiu, W. 2017. Beam-Column behaviour of concrete-filled elliptical hollow sections. Ph.D. Thesis. Imperial College London.

Rashed, R. 2015. Classical Mathematics from Al-Khwarizmi to Descartes. Routledge, Abingdon, Oxfordshire, UK.

RHP. 2015. Kimbolton School, New Science Wing. Available from http://www.rhpartnership.co.uk/projects/kimbolton-school-new-science-wing/. [accessed 22 January 2019].

Roberti, R., Cornacchia, G., and Faccoli, M. 2011. On the extremely low cycle fatigue behavior of the concrete reinforcing bar B450C (FeB44k) Steel. *In* Convegno Nazionale IGF XXI. Cassino (FR), Italy. pp. 181–190.

Rolfe, S.T., and Munse, W.H. 1963. Crack propagation in low cycle fatigue of mild steel. Welding Journal Research Supplement, **42**: 2525–2615.

Rondal, J., Würker, K.G., Dutta, D., Wardenier, J., and Yeomans, N. 2003. Structural Stability of Hollow Sections. *Edited by* CIDECT - Comité International pour le Développement et lÉtude de la Construction Tubulaire. TUV Rheinland, Cologne(Köln), Germany.

Ross, D.A. 1978. The strength and behavior of fabricated tubular steel columns. Ph.D Thesis. Lehigh University.

Rotter, J.M. 1999. Proposal for generalisation of the elastic-plastic buckling interaction rule in Eurocode 3 Part 1.6, submission to CEN TC250/SC3/PT4 and ECCS TWG8.4.

Rotter, J.M. 2002. Shell buckling and collapse analysis for structural design: The new framework of the european standard. *In* New Approaches to Structural Mechanics, Shells and Biological Structures. *Edited by* H.R. Drew and S. Pellegrino. K1uwer Academic

Publishers, London, UK. pp. 355–378.

Rotter, J.M. 2005. Stability and plasticity in structural analysis: A new conceptual framework. *In* Fourth International Conference on Advances in Steel Structures. *Edited by* Z.Y. Shen, G.Q. Li, and S.L. Chan. Elsevier Science Ltd, Shanghai, China. pp. 1815–1826.

Rotter, J.M. 2006. The practical design of shell structures exploiting different methods of analysis. *In* Shell Structures, Theory and Applications: Proceedings of the 8th Conference on Shell Structures. *Edited by* W. Pietraszkiewicz and C. Szymczak. Taylor & Francis, London, Jastarnia, Poland. pp. 71–83.

Rotter, J.M. 2011. The new framework for shell buckling design and the european shell buckling recommendations fifth edition. Journal of Pressure Vessel Technology (ASME), **133**(011203): 1–9.

Rotter, J.M. 2013. Design of shells using reference resistances. *In* Amendment AM-1-6-2013-05 to EN 1993-1-6, approved by CEN TC250 SC3.

Rotter, J.M. 2016a. The new method of reference resistance design for shell structures. *In* International Colloquium on Stability and Ductility of Steel Structures (SDSS). *Edited by* D. Dubina and V. Ungureanu. Ernst&Sohn, Timisoara, Romania. pp. 623–630.

Rotter, J.M. 2016b. Advances in understanding shell buckling phenomena and their characterisation for practical design. *In* The 13th international Conference on Metal Structures (ICMS 2016). *Edited by* M.A. Gizejowski, J. Marcinowski, A. Kozlowski, and J. Ziółko. CRC Press, Zielona Góra, Poland. pp. 3–16.

Rotter, J.M. 2017. Shell buckling transformed: Mechanics, design processes and their inter-relation. Stahlbau, **86**(4): 315–324. John Wiley & Sons, Ltd.

Rotter, J.M., and Sadowski, A.J. 2014. Thin tubular members design for bending: uniform bending with small axial loads. *In* The 7th International European Conference on Steel and Composite Structures (Eurosteel 2014). *Edited by* R. Landolfo and F. Mazzolani. ECCS (European Convention for Constructional Steelworks), Naples, Italy.

Rotter, J.M., and Sadowski, A.J. 2017. Development of circular tube slenderness classifications under axial and bending actions. *In* The 8th European Conference on Steel and Composite Structures (Eurosteel 2017). *Edited by* J. Jönsson. Ernst & Sohn, Copenhaguen, Denmark.

Rotter, J.M., Sadowski, A.J., and Chen, L. 2014. Nonlinear stability of thin elastic cylinders of different length under global bending. International Journal of Solids and Structures, **51**(15): 2826–2839.

Roy, S.C., Goyal, S., Sandhya, R., and Ray, S.K. 2012. Low cycle fatigue life prediction of 316 L (N) stainless steel based on cyclic elasto-plastic response. Nuclear Engineering and Design, **253**: 219–225. Elsevier.

Roylance, D. 2000. Stresses in beams. Massachusetts Institute of Technology, Cambridge, Massachusetts, USA.

RSHP. 2017. NEO Bankside. Available from https://www.rsh-p.com/projects/neo-bankside/. [accessed 24 November 2019].

Ruiz-Terán, A.M., and Gardner, L. 2008. Elastic buckling of elliptical tubes. Thin-Walled Structures, **46**(11): 1304–1318.

SAE J1099. 1997. Technical report on fatigue properties: SAE J1099. *In* SAE International (SAE). Warrendale, PA, USA.

Sahoo, D.R., and Rai, D.C. 2007. Built-up battened columns under lateral cyclic loading. Thin-walled structures, **45**(5): 552–562. Elsevier.

Sakino, K., Nakahara, H., Morino, S., and Nishiyama, I. 2004. Behavior of centrally loaded concrete-filled steel-tube short columns. Journal of Structural Engineering (ASCE), **130**(2): 180–188. American Society of Civil Engineers.

Salawdeh, S., and Goggins, J.M. 2013. Numerical simulation for steel brace members incorporating a fatigue model. Engineering Structures, **46**: 332–349.

Schafer, B.W. 2008. Review: The Direct Strength Method of cold-formed steel member design. Journal of Constructional Steel Research, **64**(7): 766–778.

Schafer, B.W., and Ádány, S. 2006. Buckling analysis of cold-formed steel members using CUFSM: conventional and constrained finite strip methods. *In* Eighteenth international specialty conference on cold-formed steel structures. pp. 39–54.

Schafer, B.W., and Peköz, T. 1998a. Computational modeling of cold-formed steel: characterizing geometric imperfections and residual stresses. Journal of Constructional Steel Research, **47**(3): 193–210. Elsevier.

Schafer, B.W., and Peköz, T. 1998b. Direct strength prediction of cold-formed steel members using numerical elastic buckling solutions. *In* Fourteenth International Specialty Conference on Cold-Formed Steel Structures. St. Louis, MO, USA.

Scullion, T., Ali, F., and Nadjai, A. 2012. Finite element numerical evaluation of elliptical hollow section steel columns in fire. Thin-Walled Structures, **55**: 22–36. Elsevier.

SDB. 2015. "Y" Column using Elliptical Steel Sections. Available from http://www.sdblimited.com/Innovation.html. [accessed 23 January 2019].

Sedlacek, G., Dahl, W., Stranghöner, N., Kalinowski, B., Rondal, J., and Boeraeve, P. 1998. Investigation of the rotation behaviour of hollow section beams. *In* Technical Steel Research series. European Communities, Luxembourg City, Luxembourg.

Shaback, B., and Brown, T. 2003. Behaviour of square hollow structural steel braces with end connections under reversed cyclic axial loading. Canadian Journal of Civil Engineering, **30**(4): 745–753. NRC Research Press.

Shaback, J.B. 2001. Behavior of Square HSS Braces with End Connections under Reversed Cyclic Axial Loading. MSc Thesis. University of Calgary, Calgary, Alberta, Canada.

Shariati, M., Kolasangiani, K., Norouzi, G., and Shahnavaz, A. 2014. Experimental study of SS316L cantilevered cylindrical shells under cyclic bending load. Thin-Walled Structures, **82**: 124–131.

Sheehan, T., and Chan, T.M. 2014. Cyclic response of hollow and concrete-filled circular hollow section braces. *In* Proceedings of the Institution of Civil Engineers - Structures and Buildings. ICE Publishing. pp. 140–152.

Sheehan, T., Chan, T.M., and Lam, D. 2015. Mid-length lateral deflection of cyclically-loaded braces. Steel and Composite Structures, **18**(6): 1569–1582.

Sheehan, T., Dai, X.H., Chan, T.M., and Lam, D. 2012. Structural response of concrete-filled elliptical steel hollow sections under eccentric compression. Engineering Structures, **45**: 314–323.

Sherman, D.R. 1976. Test of circular steel tubes in bending. Journal of the Structural Division (ASCE), **102**(11): 2181–2195. ASCE.

Sherman, D.R. 1979. Experimental study of post local buckling behavior in tubular portal type

beam-columns. *In* Report to Shell Oil Company. University of Wisconsin, Milwaukee, WI, USA.

Sherman, D.R. 1984. Supplemental tests for bending capacity of fabricated pipes. University of Wisconsin--Milwaukee, Milwaukee, WI, USA.

Sherman, D.R. 1985. Bending capacity of fabricated pipe at fixed ends. Civil Engineering Department, University of Wisconsin-Milwaukee, Milwaukee, WI, USA.

Sherman, D.R. 1992. Tubular members. *In* Constructional Steel Design: An International Guide. *Edited by* P.J. Dowling, J.E. Harding, and R. Bjorhovde. Elsevier Applied Science, London, UK. pp. 91–104.

Shi, G., Wang, M., Wang, Y., and Wang, F. 2013. Cyclic behavior of 460 MPa high strength structural steel and welded connection under earthquake loading. Advances in Structural Engineering, **16**(3): 451–466. SAGE Publications.

Shimada, K., Komotori, J., and Shimizu, M. 1987. Applicability of the Manson-Coffin law and Miner's law to extremely low cycle fatigue. Nippon Kikai Gakkai Ronbunshu, A Hen/Transactions of the Japan Society of Mechanical Engineers, Part A, **53**(491): 1178–1185.

Shokouhian, M., and Shi, Y. 2015. Flexural strength of hybrid steel I-beams based on slenderness. Engineering Structures, **93**: 114–128. Elsevier.

Short, J. 2018. Conference Park - Warwick Conferences. Available from https://www.google.com/maps/contrib/110248359319610927597/photos/@52.3787336,-1.5609106,3a,75y,82.64h,106.6t/data=!3m7!1e1!3m5!1sAF1QipNLc1vrz_MkFzOBTTyAVZZQzM614lhKxWT37ydP!2e10!6shttps:%2F%2Flh5.googleusercontent.com%2Fp%2FAF1QipNLc1vrz_MkFzOBTTyAVZZQzM. [accessed 22 January 2019].

Silvestre, E., Mendiguren, J., Galdos, L., and Sáenz de Argandoña, E. 2015. Comparison of the hardening behaviour of different steel families: From mild and stainless steel to advanced high strength steels. International Journal of Mechanical Sciences, **101**–**102**: 10–20.

Silvestre, N., and Gardner, L. 2011. Elastic local post-buckling of elliptical tubes. Journal of Constructional Steel Research, **67**(3): 281–292.

Singh, T.G., and Chan, T.-M. 2021. Effect of access openings on the buckling performance of square hollow section module stub columns. Journal of Constructional Steel Research, **177**: 106438.

Singh, T.G., and Singh, K.D. 2018. Experimental investigation on performance of perforated cold–formed steel tubular stub columns. Thin-Walled Structures, **131**: 107–121. Elsevier.

Skvortsov, Y. V, Glushkov, S. V, and Aistov, A.I. 2017. Research on the low-cycle structural strength of the fuel tank membrane. Procedia Engineering, **185**: 110–118. Elsevier.

Sorenson, G.R., and Clemett, H.R. 1962. Low-cycle fatigue in small turbines. Experimental Mechanics, **2**(12): 353–358. Kluwer Academic Publishers.

Southwell, R.V. 1914. On the general theory of elastic stability. Philosophical Transactions of the Royal Society of London. Series A, **213**(497–508): 187–244. Royal Society.

STD. 2014. Steel Tubes and Pipes. Available from https://www.steeltubedirect.co.uk/shop/steel-tubes-and-pipes/P100012. [accessed 9 July 2014].

Stephens, M.J., Kulak, G.L., and Montgomery, C.J. 1982. Local buckling of thin walled tubular steel members, SER No. 103. Alberta, Canada.

Stoakes, C.D., and Fahnestock, L.A. 2016. Strong-axis stability of wide flange steel columns in the presence of weak-axis flexure. Journal of Structural Engineering, **142**(5): 4016004. American Society of Civil Engineers.

Sun, J., and Butterworth, J.W. 1998. Behaviour of steel single angle compression members axially loaded through one leg. *In* Proc. Australasian Struct. Engrg. Conference, Auckland. pp. 859–866.

Suresh, S. 1998. Fatigue of Materials. *In* 2nd edition. Cambridge University Press, Cambridge, UK.

Suzuki, Y. 2018. Earthquake-Induced Collapse of Steel Moment Resisting Frames with Conventional and High Performance Steel Columns. PhD Thesis. McGill University, Montreal.

Szekely, R. 2013. Oshawa rec users facing fee hikes for most services. Available from https://www.durhamregion.com/news-story/3511366-oshawa-rec-users-facing-fee-

hikes-for-most-services/. [accessed 22 January 2019].

Taherizadeh, A., Ghaei, A., Green, D.E., and Altenhof, W.J. 2009. Finite element simulation of springback for a channel draw process with drawbead using different hardening models. International Journal of Mechanical Sciences, **51**(4): 314–325. Elsevier.

Takeuchi, T., and Matsui, R. 2011. Cumulative cyclic deformation capacity of circular tubular braces under local buckling. Journal of Structural Engineering (ASCE), **137**(11): 1311–1318.

Tang, X., and Goel, S.C. 1989. Brace fractures and analysis of phase I structure. Journal of Structural Engineering (ASCE), **115**(8): 1960–1976. American Society of Civil Engineers.

Teng, J.G., and Hu, Y.M. 2007. Behaviour of FRP-jacketed circular steel tubes and cylindrical shells under axial compression. Construction and Building Materials, **21**(4): 827–838.

Tennyson, R.C., and Muggeridge, D.B. 1969. Buckling of axisymmetric imperfect circular cylindrical shells under axial compression. AIAA Journal, **7**(11): 2127–2131.

Tepper, S. 1976. Low-cycle fatigue analysis of the turbine disk for the National Aeronautics and Space Administration high-temperature turbine rig. *In* Thermal Fatigue of Materials and Components - ASTM STP 612. *Edited by* D.A. Spera and D.F. Mowbray. ASTM International. pp. 38–54.

Theofanous, M., Chan, T.M., and Gardner, L. 2009a. Structural response of stainless steel oval hollow section compression members. Engineering Structures, **31**(4): 922–934.

Theofanous, M., Chan, T.M., and Gardner, L. 2009b. Flexural behaviour of stainless steel oval hollow sections. Thin-Walled Structures, **47**(6–7): 776–787.

Timoshenko, S.P. 1910. Einige Stabilitätsprobleme der Elastizitätstheorie. Zeitschrift für Mathematik und Physik, **58**(4): 337–385.

Timoshenko, S.P., and Gere, J.M. 1961. Theory of Elastic Stability. *In* 2nd edition. McGraw-Hill Book Company, Inc., New York, NY, USA.

Toomer, G.J. (*Editor*). 1990. Apollonius: Conics Books V to VII: The Arabic Translation of the Lost Greek Original in the Version of the Banū Mūsā. Springer-Verlag, New York, NY, USA.

Trahair, N., Bradford, M.A., Nethercot, D., and Gardner, L. 2008. The Behaviour and Design of Steel Structures to EC3. *In* Fourth. Taylor & Francis, New York, NY, USA.

Trahair, N.S. 2004. Biaxial bending of steel angle section beams. Journal of Structural Engineering, **130**(4): 554–561. American Society of Civil Engineers.

Tremblay, R. 2002. Inelastic seismic response of steel bracing members. Journal of Constructional Steel Research, **58**(5–8): 665–701.

Tremblay, R., Bolduc, P., Neville, R., and DeVall, R. 2006. Seismic testing and performance of buckling-restrained bracing systems. Canadian Journal of Civil Engineering, **33**(2): 183–198. NRC Research Press.

Tremblay, R., Filiatrault, A., Timler, P., and Bruneau, M. 1995. Performance of steel structures during the 1994 Northridge earthquake. Canadian Journal of Civil Engineering, **22**(2): 338–360. NRC Research Press.

Tremblay, R., Haddad, M., Martinez, G., Richard, J., and Moffatt, K. 2008. Inelastic cyclic testing of large size steel bracing members. *In* The 14 World Conference on Earthquake Engineering. Beijing, China.

TSE. 2018. Paradise Street. Available from https://www.tatasteelconstruction.com/en_GB/tata-steel-case-studies/retail/Paradise-Street,-Liverpool. [accessed 7 February 2019].

Tsitos, A., Bravo-Haro, M.A., and Elghazouli, A.Y. 2018. Influence of deterioration modelling on the seismic response of steel moment frames designed to Eurocode 8. Earthquake Engineering & Structural Dynamics, **47**(2): 356–376. John Wiley & Sons, Ltd.

Tsitos, A., and Elghazouli, A.Y. 2017. Evaluation of loading protocols for assessing local seismic demands in steel buildings designed to EC8. *In* 16th World Conference on Earthquake (16WCEE). Santiago, Chile.

Tvergaard, V. 1976. Buckling of elastic-plastic oval cylindrical shells under axial compression. International Journal of Solids and Structures, **12**(9–10): 683–691.

Uenaka, K. 2014. Experimental study on concrete filled elliptical/oval steel tubular stub columns under compression. Thin-Walled Structures, **78**: 131–137.

Uriz, P. 2005. Towards earthquake resistant design of concentrically braced steel buildings.

University of California, Berkeley, CA.

Usami, T. 1996. Interim guidelines and new technologies for seismic design of steel structures. Committee on New Technology for Steel Structures (CNTSS), Japan Society of Civil Engineers (JSCE), **1706**.

Usami, T., Gao, S., and Ge, H. 2000. Elastoplastic analysis of steel members and frames subjected to cyclic loading. Engineering Structures, **22**(2): 135–145.

Usami, T., and Ge, H. 1994. Ductility of concrete-filled steel box columns under cyclic loading. Journal of Structural Engineering, **120**(7): 2021–2040. American Society of Civil Engineers.

Usami, T., and Ge, H.B. 1998. Cyclic behavior of thin-walled steel structures—numerical analysis. Thin-walled structures, **32**(1): 41–80. Elsevier.

Usami, T., Suzuki, M., Ge, H., and Mamaghani, I.H.P. 1995. A proposal for check of ultimate earthquake resistance of partially concrete filled steel bridge piers. Doboku Gakkai Ronbunshu (Journal of Structural Mechanics and Earthquake Engineering), **1995**(525): 69-82 (in Japanese). Japan Society of Civil Engineers.

Van, K.D. 1999. Introduction to fatigue analysis in mechanical design by the multiscale approach. *In* High-Cycle Metal Fatigue: From Theory to Applications. *Edited by* K.D. Van and I.V. Papadopoulos. Springer-Verlag GmbH, Udine, Italy. pp. 57–88.

Varelis, G.E., and Karamanos, S.A. 2014. Buckling of high-strength steel cylinders under cyclic bending in the inelastic range. Journal of Pressure Vessel Technology, **136**(2): 21207–21211. ASME.

Victorsson, V.K. 2011. The Reliability of Capacity-Designed Components in Seismic Resistant Systems. Ph.D. Thesis. Stanford University.

Voce, E. 1948. The relationship between stress and strain for homogeneous deformation. J Inst Met, **74**: 537–562.

Walpole, W.R. 1996. Behaviour of cold-formed steel RHS members under cyclic loading. Research Report, No. 96-4. Christchurch, New Zealand.

Wang, H., Guo, Y., Bai, Y., Zhang, B., Sun, Q., and Xue, J. 2017. Experimental and numerical study on the stability capacity of Q690 high-strength circular steel tubes under axial

compression. International Journal of Steel Structures, **17**(3): 843–861. Springer.

Wang, J., Fajuyitan, O.K., Orabi, M.A., Rotter, J.M., and Sadowski, A.J. 2020. Cylindrical shells under uniform bending in the framework of Reference Resistance Design. Journal of Constructional Steel Research, **166**: 105920.

Wang, J., Sadowski, A.J., and Rotter, J.M. 2018a. Influence of ovalisation on the plastic collapse of thick cylindrical tubes under uniform bending. International Journal of Pressure Vessels and Piping, **168**: 94–99.

Wang, J., Shi, Y., and Wang, Y. 2016. Constitutive model of low-yield point steel and its application in numerical simulation of buckling-restrained braces. Journal of Materials in Civil Engineering, **28**(3): 4015142. American Society of Civil Engineers.

Wang, T., McCormick, J., Yoshitake, N., Pan, P., Murata, Y., and Nakashima, M. 2008. Collapse simulation of a four-story steel moment frame by a distributed online hybrid test. Earthquake Engineering and Structural Dynamics, **37**(6): 955–974. Wiley Online Library.

Wang, X., Zhou, A., and Chui, Y.H. 2018b. Load-carrying capacity of intermediately slender parallel strand bamboo columns with a rectangular cross section under biaxial eccentric compression. BioResources, **13**(1): 313–330.

Wang, Y., and Wang, Z. 2016. Experimental investigation and FE analysis on constitutive relationship of high strength aluminum alloy under cyclic loading. Advances in Materials Science and Engineering, **2016**. Hindawi Publishing Corporation.

Wang, Y.Q., Chang, T., Shi, Y.J., Yuan, H.X., Yang, L., and Liao, D.F. 2014. Experimental study on the constitutive relation of austenitic stainless steel S31608 under monotonic and cyclic loading. Thin-Walled Structures, **83**: 19–27. Elsevier.

Wardenier, J., Packer, J.A., Zhao, X.L., and Van der Vegte, G.J. 2010. Hollow Sections in Structural Applications. *Edited by* CIDECT. Bouwen met Staal, Zoetermeer, The Netherlands.

Wen, Z. 2012. Modeling of Ductile Fracture in Steel Structures for Monotonic and Cyclic Loading. Ottawa, Ontario, Canada.

Whitbread, J.E. 1969. Model analysis of the Royal Albert Bridge, Saltash. Strain, **5**(3): 128–134. Wiley Online Library.

White, C.S. 1988. A combined isotropic-kinematic hardening model for large deformation metal plasticity. Ph.D Thesis. Massachusetts Institute of Technology, Cambridge, Massachusetts, USA.

Willibald, S., Packer, J.A., and Martinez-Saucedo, G. 2006a. Behaviour of gusset plate connections to ends of round and elliptical hollow structural section members. Canadian Journal of Civil Engineering, **33**(4): 373–383. NRC Research Press.

Willibald, S., Packer, J.A., Voth, A.P., and Zhao, X.L. 2006b. Through-plate joints to elliptical and circular hollow sections. *In* Tubular Structures XI - 11th. International Symposium on Tubular Structures. *Edited by* S. Willibald and J.A. Packer. CRC press, Québec City, Canada. p. 221.

Wilson, W.M. 1937. Tests of Steel Columns: Thin Cylindrical Shells, Laced Channels, Angles: Bulletin No. 292. *In* University of Illinois Engineering Experimental Station Bulletin. Urbana, IL, USA.

Wilson, W.M., and Newmark, N.M. 1933. The strength of thin cylindrical shells as columns, Bulletin No. 255. University of Illinois, Urbana, IL, USA.

Winter, G. 1947. Strength of thin steel compression flanges. Transactions of ASCE, **112**(1): 527–554.

WRM. 2016. Time for Cork Airport to offer autism friendly facilities. Available from http://westcorktimes.com/time-for-cork-airport-to-offer-autism-friendly-facilities/. [accessed 7 February 2019].

Xu, F., Chan, T.M., Sheehan, T., and Gardner, L. 2020. Prediction of ductile fracture for circular hollow section bracing members under extremely low cycle fatigue. Engineering Structures, **214**: 110579.

Xu, L., Nie, X., Fan, J., Tao, M., and Ding, R. 2016. Cyclic hardening and softening behavior of the low yield point steel BLY160: Experimental response and constitutive modeling. International Journal of Plasticity, **78**: 44–63.

Xu, Z., Gardner, L., and Sadowski, A.J. 2017. Nonlinear stability of elastic elliptical cylindrical shells under uniform bending. International Journal of Mechanical Sciences, **128**–**129**: 593–606.

Yang, F., and Mahin, S. 2005. Limiting net section fracture in slotted tube braces. *In* Steel TIPS Report. Moraga, CA, USA.

Yang, H., Lam, D., and Gardner, L. 2008. Testing and analysis of concrete-filled elliptical hollow sections. Engineering Structures, **30**(12): 3771–3781.

Yang, H., Liu, F., Chan, T., and Wang, W. 2017. Behaviours of concrete-filled cold-formed elliptical hollow section beam-columns with varying aspect ratios. Thin-Walled Structures, **120**: 9–28.

Yoo, C.H., and Lee, S.C. 2011. Buckling of Columns. *In* Stability of Structures: Principles and Applications. *Edited by* C.H. Yoo and S.C.B.T.-S. of S. Lee. Butterworth-Heinemann, Boston. pp. 1–73.

Yu, C.K., and Tall, L. 1971. Significance and application of stub column test results. Journal of the Structural Division (ASCE), **97**(7): 1841–1861.

Yu, W.W., and Davis, C.S. 1973. Cold-formed steel members with perforated elements. Journal of the Structural Division (ASCE), **99**(10): 2061–2077. ASCE.

Zakavi, S.J., Shiralivand, B., and Nourbakhsh, M. 2017. Evaluation of combined hardening model in ratcheting behavior of pressurized piping elbows subjected to in-plane moments. Journal of Computational and Applied Research in Mechanical Engineering, **7**(1): 57–71.

Zakavi, S.J., Zehsaz, M., and Eslami, M.R. 2010. The ratchetting behavior of pressurized plain pipework subjected to cyclic bending moment with the combined hardening model. Nuclear Engineering and Design, **240**(4): 726–737. Elsevier.

Zehsaz, M., Tahami, F.V., and Akhani, H. 2016. Experimental determination of material parameters using stabilized cycle tests to predict thermal ratchetting. UPB Scientific Bulletin, Series D: Mechanical Engineering, **78**(2): 17–30.

Zhao, K.M., and Lee, J.K. 2000. Generation of cyclic stress-strain curves for sheet metals. Journal of Engineering Materials and Technology, **123**(4): 391–397. ASME.

Zhao, O., Afshan, S., and Gardner, L. 2017. Structural response and continuous strength method design of slender stainless steel cross-sections. Engineering Structures, **140**: 14–25.

Zhao, O., and Gardner, L. 2018. The continuous strength method for the design of mono-

symmetric and asymmetric stainless steel cross-sections in bending. Journal of Constructional Steel Research, **150**: 141–152.

Zhao, X.L. 2000. Section capacity of very high strength (VHS) circular tubes under compression. Thin-Walled Structures, **37**(3): 223–240. Elsevier.

Zhao, X.L., Grzebieta, R., and Elchalakani, M. 2002. Tests of concrete-filled double skin CHS composite stub columns. Steel and Composite Structures, **2**(2): 129–146. Techno-Press.

Zhao, X.L., and Packer, J.A. 2009. Tests and design of concrete-filled elliptical hollow section stub columns. Thin-Walled Structures, **47**(6–7): 617–628.

Zhou, F., Fang, C., and Chen, Y. 2018. Experimental and numerical studies on stainless steel tubular members under axial cyclic loading. Engineering Structures, **171**: 72–85.

Zhu, Y., and Wilkinson, T. 2006. Finite element analysis of structural steel elliptical hollow sections in pure compression. *In* 11th International Symposium on Tubular Structures. *Edited by* J.A. Packer and S. Willibald. CRC press, Québec City, Canada. pp. 179–186.

Ziegler, F. 2012. Mechanics of Solids and Fluids. Springer-Verlag, New York, NY, USA.

Ziemian, R.D. (*Editor*). 2010. Guide to Stability Design Criteria for Metal Structures. *In* 6th edition. John Wiley & Sons, Inc., Hoboken, NJ, USA.

PUBLICATIONS

JOURNAL ARTICLES

- **Narendra, P.V.R.**, and Singh, K.D. 2016. Structural performance of elliptical hollow section (EHS) steel tubular braces under extremely low cycle fatigue loading - a finite element study. ***Thin-Walled Structures***, 109: 202–216.
- **Narendra, P.V.R.**, and Singh, K.D. 2017. Elliptical hollow section steel cantilever beams under extremely low cycle fatigue flexural load – A finite element study. ***Thin-Walled Structures***, 119: 126–150.
- **Narendra, P.V.R.**, Prasad, K., Krishna, E.H., Kumar, V., and Singh, K.D. 2019. Low-Cycle-Fatigue (LCF) behavior and cyclic plasticity modeling of E250A mild steel. ***Structures***, 20: 594–606.
- **Narendra, P.V.R.**, and Singh, K.D. 2019. Equivalent-Resistance-Capacity-Method (ERCM) for the design of steel Elliptical-Hollow-Sections (EHSs) under axial compression. ***Structures***, 22: 28–42.
- **Narendra, P.V.R.**, and Singh, K.D. 2020. Cross-sectional bending strength of steel Elliptical-Hollow-Sections (EHSs) based on Equivalent-Resistance-Capacity-Method (ERCM). ***Thin-Walled Structures***, 157: 106947.
- **Narendra, P.V.R.**, and Singh, K.D. Plastic-interaction-relations and cross-section slenderness for steel Elliptical-Hollow-Sections under combined axial-compression and bending. (*Under review*).
- **Narendra, P.V.R.**, and Singh, K.D. Elliptical-Hollow-Section (EHS) columns under combined axial-compression and strong-axis cyclic-bending loads – a finite element study. (*Under preparation*).
- **Narendra, P.V.R.**, and Singh, K.D. Elliptical-Hollow-Section (EHS) columns under combined axial-compression and weak-axis cyclic-bending loads – a finite element study. (*Under preparation*).

CONFERENCE PAPERS

- **Narendra, P.V.R.**, and Singh, K.D. 2016. Structural performance of elliptical hollow steel tubular braces under ultra-low cycle fatigue loading. In ***Sixth International Congress on Computational Mechanics and Simulation (ICCMS 2016)***. 869-872. Mumbai, India.
- **Narendra, P.V.R.**, and Singh, K.D. 2016. Numerical modelling of elliptical steel tubular bracing members under extremely low cycle fatigue loading. In ***Eighth International Conference on Steel and Aluminium Structures (ICSAS 2016)***. Hong Kong.
- **Narendra, P.V.R.**, and Singh, K.D. 2017. Elliptical hollow steel cantilever beams under extremely low cycle fatigue bending along major axis using finite element analysis. In ***Sixteenth International Symposium on Tubular Structures (ISTS 16)***. Melbourne, Australia.

This page is intentionally left blank